Symposium on

AMORPHOUS INSULATORS

in honour of Frank L. Galeener

Winter Park, CO, USA
August 7–11, 1994

Editors:

M.F. Thorpe
Michigan State University
East Lansing, MI
USA

A.C. Wright
University of Reading
Whiteknights, Reading
UK

July 25, 1995

Defense Technical Information Center
Building 5, Cameron Station
Alexandria, Virginia 22314

Department of Physics
Fort Collins, Colorado 80523
(303) 491-6206
FAX: (303) 491-7947

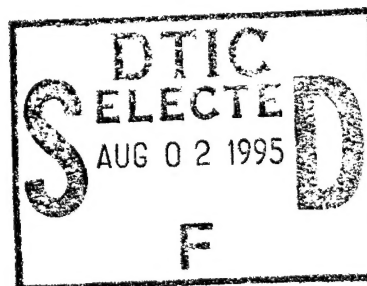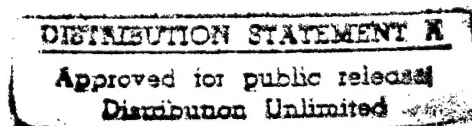Dear Center Personnel:

Enclosed please find a copy of the *Symposium on Amorphous Insulators*. This Symposium was partially supported by the Office of Naval Research under Contract N00014-94-1-0172. The enclosed copy is being submitted as specified by the Contract.

Sincerely,

Robert G. Leisure
Principal Investigator

cc: D. Rein

AMORPHOUS INSULATORS

N00014-94-1-0172

Accesion For	
NTIS CRA&I	☑
DTIC TAB	☐
Unannounced	☐
Justification	

By
Distribution /

Availability Codes	
Dist	Avail and / or Special
A-1	

19950731 008

Foreword: Frank Lee Galeener

Frank Lee Galeener
1936–1993

Frank Lee Galeener passed away on June 6, 1993 in Fort Collins, Colorado, where he was Professor of Physics at Colorado State University. He left in great sorrow his family, his students, his Faculty Colleagues, and everyone with whom his lifeline intersected, in and outside the Physics Community. He died of esophageal cancer. In his illness, as in all of his life, Frank displayed the consideration and style that was characteristically his. Immediately after his illness was diagnosed, his first thought was to secure the future of those who depended on him in any way, especially his family and his students at Colorado State. Having attended to that, he (with his wife Janet and his two sons Keith and Matthew at his side) waged a long, valiant, but in the end a losing battle with the merciless killer that it was his fate to encounter. Frank handled the inevitable in a manner that can only be described as inspiring to anyone who knew him and reflected precisely the responsible, considerate, and rational character by which he lived his entire life. In the last months of his life he concentrated on devoting all his personal attention to his family, his friends, and his students. Because of Frank's style, these final months became the highest-quality time that anyone had spent with him.

Frank was a Californian, born in Long Beach on July 31, 1936, in a family that moved to the Golden State in the days of the Dust Bowl, with a story behind them not unlike Steinbeck's *Grapes of Wrath*. For his college education he went to M.I.T., where he earned his S.B. degree in Physics in 1958 and his S.M. degree in Solid State Experimental Physics in 1962. His S.M. research was carried out under the joint direction of Benjamin Lax and George B. Wright in magneto-optical studies of III–V semiconductors, at a time when that field was just beginning to blossom. At the time of his S.M. research, Frank served on the staff of the M.I.T. Lincoln Laboratories, and upon completion of his S.M. he was appointed as a staff member of the M.I.T. National Magnet Laboratory (1961–1964). His intention was to be exposed to *real life* before continuing with his PhD studies.

He thus returned to graduate school (at Purdue University) as a mature physicist and, although an experimentalist at heart, Frank elected to do a theoretical thesis, so as to *round himself out* in order to become a more complete scientist. His thesis topic involved multiple scattering of electromagnetic waves in a magnetized solid state plasma consisting of a random distribution of semiconductor particles. His work, carried out in the group of J.K. Furdyna, has led to several new seminal concepts (e.g., magnetic-dipole-excited cyclotron

resonance) that were exploited by other students in at least five subsequent dissertations at Purdue. More importantly, Frank's thesis contained elements both of magneto-optics (on which he could draw from his own past experience) and of random media. It is thus likely that in his PhD research lay the early seeds of Frank's interest in random and amorphous media, the study of which had such a major impact later in his career.

Following the receipt of his PhD in physics from Purdue University in 1970, he became a founding member of the research staff at the Xerox Palo Alto Research Center, rising to manager of the Amorphous and Crystalline Semiconductors Research Area. He was promoted to Principal Scientist in 1977. During and just after his tenure at Xerox P.A.R.C., he was a Visiting Scholar at the University of Oxford (1982), a Visiting Professor at the Cavendish Laboratory of the University of Cambridge (1983–84), and a Visiting Scientist at the Laboratory for Elementary Particle Theory of the University of Paris VI (1988). His move to Colorado State University took place in 1987. He was a fellow of the American Physical Society and of the American Ceramic Society.

Although his PhD studies were in solid state theory, Frank Galeener remained a consummate experimentalist, developing a state-of-the-art Raman spectroscopy laboratory at Xerox P.A.R.C., which he later transferred to Colorado State University to form the nucleus of a diversified glass physics laboratory. Early in his post-PhD career, his interests became centered on the atomic and vibrational structure of amorphous solids and thin films. Among his most important achievements were his demonstration of LO–TO splitting in glasses, his empirical and theoretical determination of selection rules for Raman and infrared absorption in glasses, the definition and study of intermediate range structural order in glasses, and the identification of planar three-membered ring structures in glassy SiO_2. In recent years, he left the relative security of these subfields, in which he was an acknowledged leader, and bravely shifted into the arcane and highly competitive area of point defects and radiation-damage mechanisms in silica glasses, where he and his collaborators promptly discovered unanticipated dependencies of defect production efficiency on the fictive temperature of the glass and on the energy of the inducing X-ray photons. In recognition of his aggregate achievements in elucidating the structures of silica and other non-crystalline solids, Frank Galeener was chosen to receive the 1993 George W. Morey Award of the Glass and Optical Materials Division of the American Ceramic Society. His enthusiastic plans to go through with the award lecture, at least by way of a prerecorded video tape, were overtaken by his disease. The award was accepted posthumously by his widow Janet at the Society's November 1993 PAC RIM Meeting in Honolulu, Hawaii.

Frank Galeener was greatly admired for the energy and originality which he brought to the study of the physics and chemistry of glasses and for the extremely rigorous standard of proof which he imposed on all proposed models of glass structure including, especially, his own. He was greatly loved and will be long remembered by his numerous friends and colleagues for his courage, his kindness, and his rich sense of humor. He was generous, helpful, fair, and never less than considerate in his dealings with his students, his collaborators, and even his (very rare) detractors.

In the last few months of his life, some of Frank's friends got together and decided hold a symposium in his honor, that would be concerned with his main lifetime interest, Amorphous Insulators. This plan was presented to Frank over lunch at his home and he enthusiastically endorsed the idea. Characteristically he helped plan the format, suggested invited participants, and where the symposium was to be held. He wanted the meeting to be in a remote location in the Rocky Mountains of Colorado, that he had grown to love in recent years and Pingree Park was agreed upon, as it was a conference center operated by Colorado State University. Only one month before the symposium, forest fires severely damaged Pingree Park so that it was no longer available. Professor Robert G. Leisure of Colorado State University scrambled to find an alternative location, and succeeded admirably with the choice of the Iron Horse Resort and Retreat in Winter Park, also in the Rocky Mountains of Colorado.

The organizers would very much like to thank the Office of Naval Research, Colorado State University and Michigan State University for generous financial help. We should also like to thank Ms. Janet King for her help with organizing the program and this publication. This tribute to Frank Galeener was prepared by the guest editors, with much help from Professor Jack K. Furdyna (University of Notre Dame) and Dr David L. Griscom (Naval Research Laboratory).
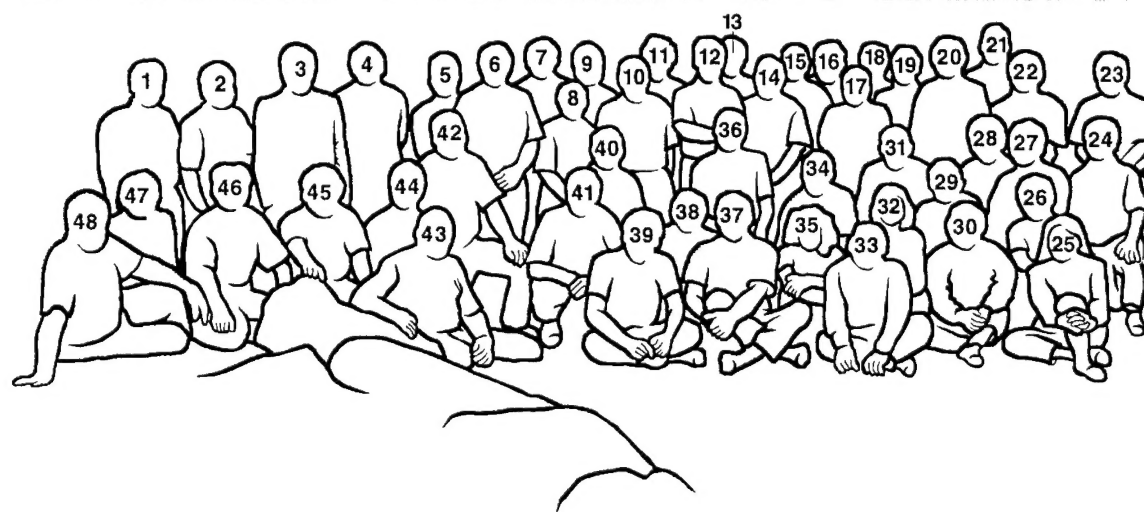
Michael F. Thorpe
Adrian C. Wright
Reading, UK, September, 1994

Organizing Committee
R.A. Barrio
R.J. Elliott
D.L. Griscom
R.G. Leisure
G. Lucovsky
A.C. Wright
G.B. Wright

Symposium Chair
M.F. Thorpe

[1] V. Mashkov, [2] D.L. Griscom, [3] A.N. Trukhin, [4] R.J. Elliott, [5] S.R. Elliott, [6] M.F. Thorpe, [7] A. Miller, [8] J. King, [9] A.C. Wright, [10] F. Wooten, [11] T. Frauenheim, [12] G. Jungnickel, [13] R. Martin, [14] M. Balkanski, [15] P. Boolchand, [16] B. Djordjevic, [17] P. Vashishta, [18] P.C. Taylor, [19] M.H. Grimsditch, [20] J.H. Simmons, [21] R.J. Nemanich, [22] S. Hyun, [23] L.F. Perondi, [24] K.L. Ngai, [25] L. Zhang, [26] J.H. Lee, [27] K. Tanaka, [28] R. Böhmer, [29] N. Rivier, [30] M. Zhang, [31] R. Zallen, [32] A. Yap, [33] R. Barrio, [34] D. Drabold, [35] J. Tagüeña, [36] S.A. Solin, [37] W. Austin, [38] R. Kerner, [39] M. Micoulaut, [40] R.G. Leisure, [41] L.W. Hobbs, [42] A.R. Silins, [43] G.B. Wright, [44] A.C. Hannon, [45] H. Hosono, [46] Y. Morimoto, [47] T. Isobe, [48] R.A. Weeks.
Not in photograph: H. Castillo, T. de Swiet, J.K. Furdyna, J. Galeener, P.M. Goldbart, G. Lucovsky, S.C. Moss, J.C. Phillips, P.N. Sen.

Contents

Section 1. Introduction and rings

Section 2. Structure

Section 3. Defects

Section 1. Introduction and rings

Evidence for rings in the dynamics of tetrahedral glasses

Roger Elliott [*]

Theoretical Physics, University of Oxford, 1 Keble Road, Oxford OX1 3NP, UK

Abstract

Following Galeener, the experimental evidence and qualitative arguments for the existence of small regular rings in amorphous SiO_2 and similar AX_2 tetrahedral glasses are reviewed. The vibrations of planar three-rings and puckered four-rings are calculated using central and non-central forces in a Born potential, while the rest of the network is modelled by Bethe lattices. It is shown that the symmetric oxygen motions in the rings, which are expected to have a large Raman polarisability, are nearly decoupled from the rest of network and are in quantitative agreement with the sharp 'defect' lines D_1 and D_2 observed in the Raman spectra of SiO_2 at 495 and 606 cm^{-1} respectively.

1. Introduction

Frank Galeener's scientific interests during the past decade were centred on the properties of glassy materials of which SiO_2 is the archetype. While his experimental work focused on the vibrational properties of these materials as studied by optical techniques, his insights into their structures were far broader. His single minded pursuit of these studies has added enormously to our understanding of these complex and interesting materials.

Over the past few years I collaborated with Frank in attempting to explain some of the features of the vibrational spectra, and in particular the sharp peaks in the Raman spectra which appeared to arise from well defined 'defects'. This collaboration was pursued in greater depth by my former student and long-time colleague Rafael Barrio. One of the last scientific tasks completed by Frank during his last illness was the writing of a paper [1] which reported these results and the implications for the structure which could be inferred from them.

2. Structure of amorphous solids

By definition, full information about the structure of an amorphous solid can never be elucidated, nor is it possible to find by experiment. This is by striking contrast with a perfect crystal where the periodic symmetry means that we can infer the structure on all length scales from the knowledge of the structure of a unit cell. Galeener, in a number of papers [2,3], has shown that it is useful to catalogue the elements of order on different scales. Short range order describes the nearest neighbour bonding environment of each atomic species. In glassy materials, strongly directional co-valent bonding is usually present. Thus, in SiO_2 we expect the Si to be surrounded by a tetrahedron of O atoms with bond lengths, r, close to the normal value of 1.61 Å and the O–Si–O bond angle, ϕ, close to the regular tetrahedral value of

---

[*] Corresponding author. Tel: +44-865 273 997. Telefax: +44-865 273 947. E-mail: r.elliott@physics.ox.ac.uk.
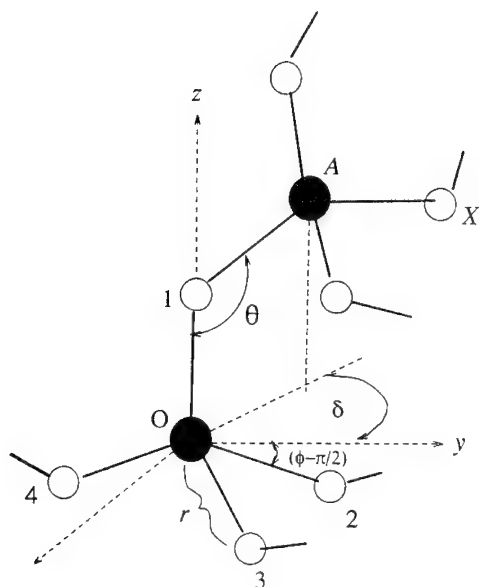
Fig. 1. Atomic arrangement of two adjacent silicon tetrahedra centred at position O and A sharing an oxygen at position 1, defining angles ϕ for O–Si–O, θ for Si–O–Si and δ the dihedral angle.

109.5°. The O atoms form bridges between two Si with bent Si–O–Si bond angles, θ, peaked at its normal value of 144° but having a broader distribution. Simple short-range order assumes that there is no correlation between the rotational positions of the two Si tetrahedra attached to a single oxygen. The relative rotational angle, δ, is called the dihedral angle and in real materials is affected, for example, by steric hindrance [4] (see Fig. 1).

These Si tetrahedra with their O bridges must couple together into a continuous network. Over distances involving several neighbours, this can be described as intermediate range order. One of the most pertinent questions relating to order on this scale is the size of the rings in the structure which provide the shortest non-repeating path which returns to the origin.

At larger distances it is possible that regular crystal-like arrangements of atoms might exist over finite volumes. In fact the width of the diffraction peaks observed by X-rays and neutrons indicate that such crystallites, if they exist must be very small. It has been suggested by Phillips [5,6] and others that such micro-crystals would be heavily strained and

would have a significant volume of connecting material which would be disordered and possibly show some surface like properties. While it is clear that for some purposes there is value in emphasising the possible existence of micro-crystallites, it would appear that their small volume means that they do not provide a good starting point for the description of many properties, and in particular the vibrational spectra.

Galeener [7] in his review strongly endorses the continuous random network model of Zachariasen [8] as elaborated by Warren and others [9] which incorporates the short range order properties discussed earlier. It has little to say about ring statistics and it does not allow for any crystallites. On a global scale, it maintains homogeneity and isotropy.

3. Ring statistics

The main difficulty in deciding the form of intermediate range order present in an amorphous system lies in the fact that there are no experiments which reveal these structures directly. Diffraction experiments yield pair distribution functions which give useful information about the short range order but which are less sensitive at longer ranges. One important way of gaining more insight into these structures is to construct models. The pioneering work of Bell and Dean [10] who constructed physical ball and stick models gave the first information of this type. Recently Vashishta and co-workers [11] have determined the structure of a 648-atom cluster using realistic inter-atomic potentials including three-body effects. This paper analyses the structure for the existence of n-membered rings for small values of n. Such a ring contains alternately n Si and n O atoms. They find a distribution which is peaked around $n = 6$ and $n = 8$ which occur in the crystalline form of crystabalite and quartz. However there are a significant number of smaller rings including some 8% with $n = 4$ and 1% with $n = 3$. There are no $n = 2$ rings which would occur if Si tetrahedra shared an edge. It seems likely that such ring statistics will be sensitive to the actual potential assumed. Bell and Dean found no rings with small n but they were largely forbidden by the subjective rules applied in the construction of their model.

4. Vibrational spectra

The vibrational modes of the glass depend in the last detail on the actual structure of the network. They can indeed be derived for the model clusters discussed above. In order to obtain a feeling for the factors which are most relevant in determining the spectra, it is valuable to have an analytic solution, albeit of a simplified model. The essential features of the spectrum are determined by the short range force constants and therefore by the short range order. There are, however, long range Coulomb effects which give rise to LO–TO splitting in those parts of the spectrum where there is local polarizability arising from the displacements. This was first pointed out by Lucovsky and Galeener sometime ago [12]. These long range Coulomb forces are neglected in the rest of this discussion.

The simplest model which has been widely used to represent the long range order while allowing for a simple analytical solution is the Bethe lattice (or Cayley tree) which consists of infinite branching chains with no loops so that it reduces to an effective one dimensional problem.

Sen and Thorpe [13] showed if only central forces between nearest neighbour atoms were assumed, the spectrum was greatly simplified. For SiO_2-like materials it consisted of two broad bands, each with a sharp peak at the maximum frequency. Even this highly simplified model allowed Galeener and Sen [14] to interpret the Raman spectra of these glasses.

Much more realistic spectra can be obtained if non-central forces are included and the simplest example of this is the so-called Born model where the potential between two neighbouring sites, δ, with small displacements $u(l)$ away from the equilibrium position of atoms can be written

$$V = \tfrac{1}{2}(\alpha - \beta)\left[(u(l) - u(l+\delta)) \cdot \boldsymbol{\delta}\right]^2$$
$$+ \tfrac{1}{2}\beta\left[u(l) - u(l+\delta)\right]^2. \tag{1}$$

Here the non-central force β represents the resistance to changes in the bond angles, and is more properly represented by a three body potential. Nevertheless the Born model has proved a very useful approximation in these materials. With non-central forces, the relative orientation of neighbouring Si tetrahedra becomes significant and it is necessary to make assumptions about the dihedral angle, δ. The most detailed calculations have been carried out by Barrio et al. [15] assuming that the dihedral angle is random.

The resulting density of states for the best fit with $\alpha = 507$ N/m, $\beta = 78$ N/m and $\theta = 154°$ is shown in Fig. 2. It consists of three main peaks in the region 400–500 cm^{-1}, 700–800 cm^{-1}, and 1000–1100 cm^{-1}. Similar peaks, with different weights reflecting the relative cross-sections of the two nuclei are found in neutron scattering [16].

The model may also be used to give the Raman and infrared intensities provided appropriate assumptions are made for the relevant polarizabilities. Martin and Galeener have viewed this semi-empirically [17] and it is generally believed that the strongest Raman intensity comes from those vibrations which simultaneously stretch (and compress) the Si–O bonds, in which the O atom moves along the bisector of the Si–O–Si bond angle. This emphasises the 400–500 cm^{-1} region of the spectrum where a strong peak is seen experimentally (see Fig. 3).

5. Defect lines

None of these theoretical considerations give any explanation of the sharp lines called D_1 and D_2 which occur universally in SiO_2 samples at 495 and 606 cm^{-1}, respectively, in the Raman spectrum. Their strength and position have been studied variously as a function of neutron bombardment [18], fictive temperature [19], trace water content [20], isotopic substitution of Si[21], isotopic substitution of O [22], tensile stress [23] and pressure compaction [24] as well as in Vycor glass [25] and sol–gel glasses [26].

The variation with isotopes shows that the motions involved are purely oxygen ones, while the strong Raman intensity suggests that several oxygens must be moving coherently. The possibility that they are associated with surfaces has been extensively examined by Brinker et al. [27].

After extensive investigation of other models, Galeener came firmly to the conclusion that these modes must be associated with small rings, specifically D_2 with $n = 3$ and D_1 with $n = 4$. One of the main initial difficulties with this interpretation lay in

the sharpness of the lines, since they occur at frequencies where the bulk density of states of the network is not zero. In order to be so sharp within this region, the defect modes must be effectively
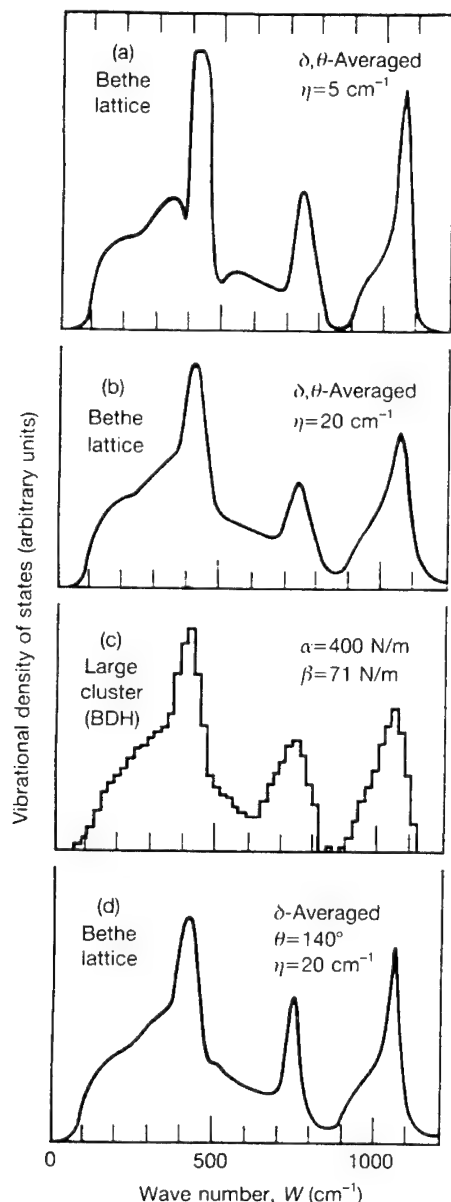
Fig. 2. Vibrational density of states in a Bethe lattice model (after Ref. [15]) for $\alpha = 507$ N/m, $\beta = 78$ N/m for different averages over distributions of θ and random δ compared with the histogram of modes in a large cluster [10]. The parameter η introduces an arbitrary broadening to smooth out spurious features.
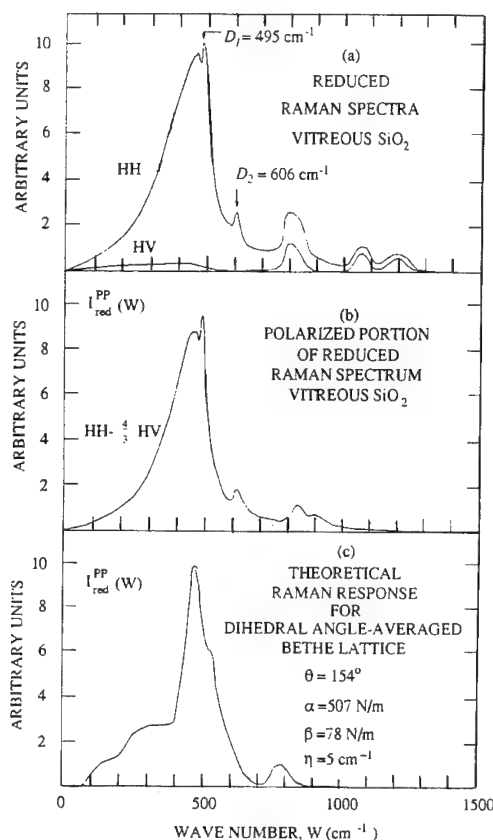
Fig. 3. Measured Raman response (a) and (b) in vitreous SiO_2 compared with a Bethe lattice calculation (c) (after Ref. [15]).

de-coupled from the rest of the lattice. This is consistent with an oxygen-only coherent motion within the rings which leaves the intermediate Si atoms stationary. It was shown by Barrio et al. [1] that the normal values of the force constants nearly satisfy this condition.

6. Dynamics of small rings

6.1. Planar three-ring

If we assume that it is more difficult to distort the O–Si–O away from $\phi = 109.5°$ than to distort the Si–O–Si angle, θ, from its preferred angle of about 150°, then geometry requires that in a planar ring $\theta = 130.5°$. On these assumptions, this structure should be stable since any puckering of the ring will

decrease θ even further away from the preferred value. If the ring was distorted in a regular way, it could take the form of a 'crown' with the O atoms on one side of the plane defined by the Si, or of a 'chair' where two atoms lie on one side of that plane and one on the other. In the model calculations of Vashishta et al. [11], the small number of three-rings found appear to favour the crown configuration with $\phi = 102°$ and $\theta = 131°$. This runs against the normal intuition that it is more difficult to distort ϕ than θ and must be due either to the special nature of the three-body forces in the model, or to the effects of more distant neighbours.

In order to have zero response for the Si atoms in the ring, and hence no coupling to the rest of the network in an oxygen breathing motion, we see from Fig. 4 that this requires the exact cancellation of force F which arises from the central forces f with the force G which arises from the non-central forces g. This requires

$$(\alpha/\beta) = \tan \tfrac{1}{2}\theta \ \tan \tfrac{1}{2}\phi, \tag{2}$$

which specifies $\beta/\alpha = 0.326$. The frequency of the O motion is then given by

$$\tfrac{1}{2}m_0 \omega^2 = \alpha \ \cos^2 \tfrac{1}{2}\theta + \beta \ \sin^2 \tfrac{1}{2}\theta$$
$$= \alpha \ \cos^2 \tfrac{1}{2}\theta \left(1 + \tan \tfrac{1}{2}\theta \ \cos \tfrac{1}{2}\phi \right), \tag{3}$$

and in order to obtain D_2 at the appropriate position gives $\alpha = 390$ N/m and $\beta = 127$ N/m. However, the de-coupling is quite insensitive to changes in
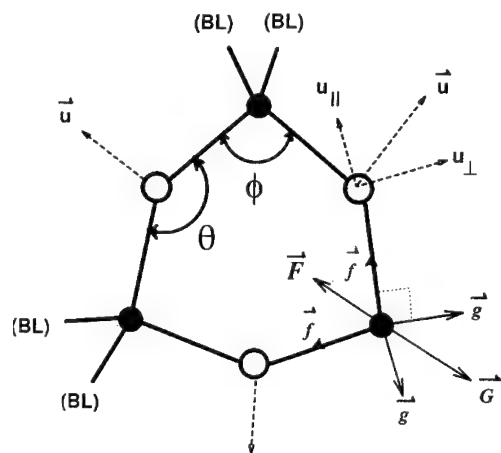
Fig. 4. Planar three-ring showing forces generated at a Si site by O motions. (BL = Bethe lattice).
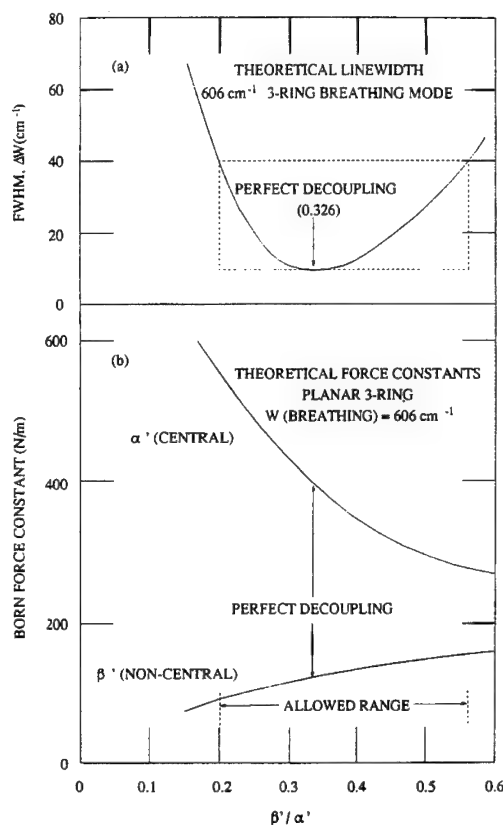
Fig. 5. Sensitivity of linewidth of the three-ring breathing mode D_2 to variations in the force constants α and β.

these parameters, as is shown in Fig. 5. Force constants unchanged from those used in the Bethe lattice calculation still show a comparatively narrow line at approximately the correct frequency. Although no detailed calculations have been carried out for this case, it is also clear that line width is insensitive to motions out of the plane which would exist if the ring was puckered in any way, as is demonstrated later by actual calculations of this type of effect for a four-ring.

6.2. Regular four-ring dynamics

Similar considerations suggest the assignment of Raman line D_1 at 495 cm^{-1} to the breathing motion of regular four-rings. This is based on the appropriate observed energy of formation [25], the reported vibrational frequencies of ring molecules [26] and other factors. The situation here is more complicated

since a planar ring with ϕ fixed at the tetrahedral value gives $\theta = 160.5°$ which is larger than the energetically favoured value so that puckering is likely to take place. Possible regular arrangements which show a single breathing mode frequency are given in Fig. 6. Of these eight configurations, only two are capable of perfect de-coupling of the breathing mode to the surrounding lattice where the Si atoms stay still when the oxygens move along the bisector of θ. Apart from the planar ring, only the oxygen boat can show a cancellation of the central F and the non-central G forces.

Using an oxygen boat with $\theta = 154°$, as taken in the Bethe lattice calculation, gives perfect de-coupling when $\beta/\alpha = 0.207$ and a response at the correct frequency 495 cm^{-1} when $\alpha = 467$ N/m and $\beta = 97$ N/m. However the normal lattice force constants $\alpha = 507$ N/m and $\beta = 78$ N/m also give a sharp response at the slightly lower frequency (Fig.

REGULAR CONFORMATIONS OF A 4-RING
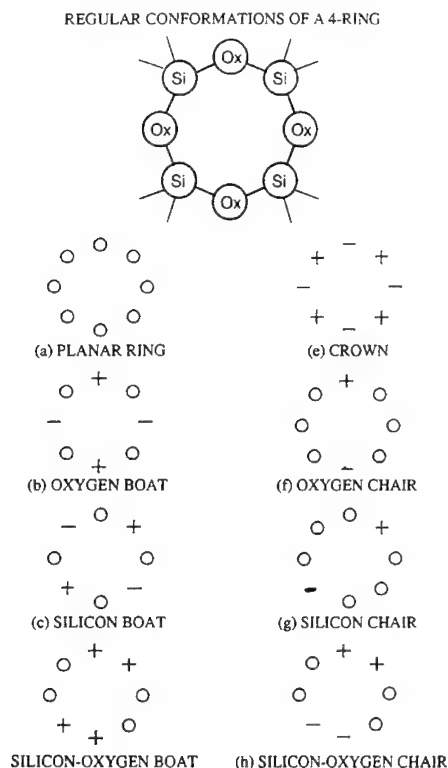
Fig. 6. Regular conformations of a four-ring. The symbols +, − and 0 refer to positions above, below or within the plane of the paper.
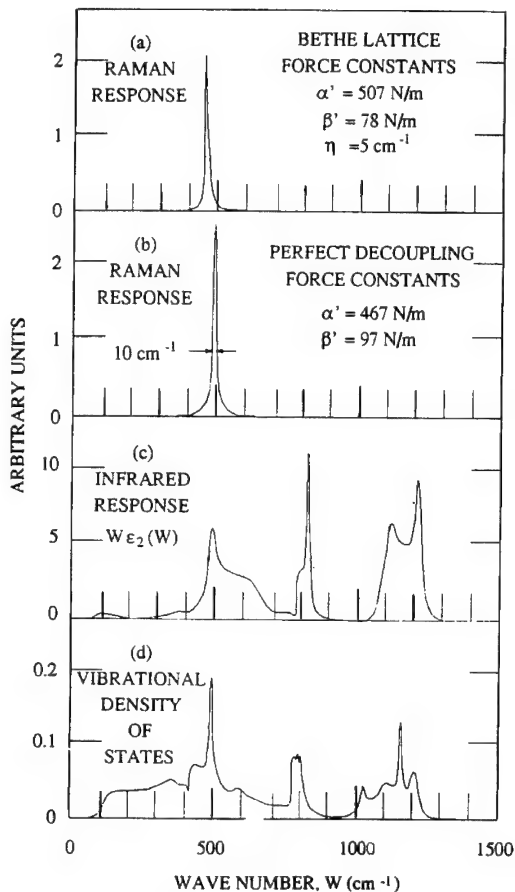
Fig. 7. Calculated Raman response of the four-ring oxygen boat for (a) the usual force constants and (b) for those giving perfect decoupling of the O motions. The infra-red response of the ring is broadened by coupling to the lattice modes as shown in (c), and exists across the whole range of the density of states in (d).

7). The line width is extremely insensitive to changes in the force constants (Fig. 8). Detailed calculations also show that it is relatively insensitive to changes in the puckering angle.

7. Conclusion

The short range bonding structures of the SiO_2 glasses are well established, while the long range isotropy and homogeneity of such glasses is well known. However, there is no conclusive experimental evidence available about the nature of intermediate range order, and in particular the ring statistics in
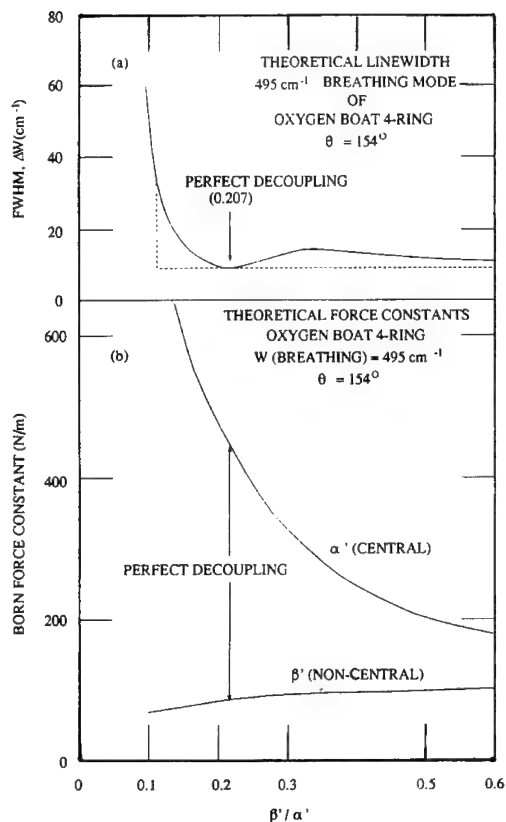
Fig. 8. Sensitivity of the linewidth of the oxygen breathing mode in a four-ring boat to changes in force constants.

these materials. The pair distribution functions obtained from diffraction experiments, and the bulk vibrational spectra obtained by optical or neutron experiments, are not sufficiently sensitive to these effects. Model calculations can and do give predictions of this intermediate range order, but they depend ultimately on the accuracy of the inter-atomic potential which have to be assumed.

This author is entirely persuaded by Galeener's hypothesis that small rings are a feature of such glasses and in particular that the sharp 'defect lines' observed in the Raman spectra are the signatures of such rings. This identification depends on the interpretation of a large mass of related experimental evidence, much of which was pieced together by Galeener in a sustained attack on this problem. In particular, since the planar three-ring does not occur in any known crystalline form of SiO_2, he has suggested that its presence may significantly inhibit

crystallisation upon quenching. The concentration of planar three-rings increases with the fictive temperature so that at the melting temperature there may be a large concentration of the structural units which must first be broken in order to build any known crystaline form. The existence of large concentrations of these rings may therefore be a key to understanding the strong glass forming tendency of molten SiO_2. In general, Galeener believes that the tendency to form a glass rather than a crystal may be due to specific elements of intermediate range order in the melt, in the form of small regular rings of bonds, which do not exist topologically in any crystaline form of the substance. Similar arguments have been applied to GeO and are no doubt relevant to other tetrahedral glasses.

References

[1] R.A. Barrio, F.L. Galeener, R.J. Elliott and E. Martinez, Phys. Rev. B48 (1993) 15672.
[2] F.L. Galeener, J. Non-Cryst. Solids 123 (1990) 182.
[3] F.L. Galeener, in: Disorder in Condensed Matter Physics, ed. J.A. Blackman and J. Taguena (Oxford University, Oxford, 1991) p. 45.
[4] F.L. Galeener, J. Non-Cryst. Solids 75 (1985) 399.
[5] J.C. Phillips, Solid State Phys. 37 (1982) 93.
[6] J.C. Phillips, Phys. Rev. B32 (1985) 5350, 6972; B33 (1986) 4443; B35 (1987) 6409.
[7] F.L. Galeener, Diffusion Defect Data 54&55 (1988) 305.
[8] W.H. Zachariasen, J. Am. Chem. Soc. 54 (1932) 3841.
[9] B.E. Warren, J. Appl. Phys. 8 (1937) 645; B.E. Warren and R.L. Mozzi, J. Appl. Cryst. 2. (1969) 164.
[10] R.J. Bell and P. Dean, Philos. Mag. 25 (1972) 1381.
[11] J.P. Rino, I. Ebbsjö, R.K. Kalia, G. Nakano and P. Vashishta, Phys. Rev. B47 (1993) 3053; Wei Jin, P. Vashishta, R.K. Kalia and J.P. Rino, Phys. Rev. B48 (1993) 9359.
[12] G. Lucovsky and F.L. Galeener, Phys. Rev. Lett. 37 (1976) 1474.
[13] P.N. Sen and M.F. Thorpe, Phys. Rev. B15 (1977) 4030.
[14] F.L. Galeener and P.N. Sen, Phys. Rev. B17 (1978) 1928.
[15] R.A. Barrio, F.L. Galeener and E. Martinez, Phys. Rev. B31 (1985) 7779.
[16] J.M. Carpenter and D.L. Price, Phys. Rev. Lett. 54 (1985) 441; J. Non-Cryst. Solids 92 (1987) 153.
[17] R.M. Martin and F.L. Galeener, Phys. Rev. B23 (1981) 3871.
[18] R.H. Stolen, J.T. Krause and C.R. Kurkjian, Disc. Faraday Soc. 50 (1970) 103.
[19] A.E. Geissberger and F.L. Galeener, Phys. Rev. B28 (1983) 3266.
[20] J.C. Mikkelsen Jr. and F.L. Galeener, Appl. Phys. Lett 37

(1980) 712; 38 (1981) 336; Solid State Commun. 37 (1981) 719.

[21] F.L. Galeener and A.E. Geissberger, Phys. Rev. B27 (1983) 6199.

[22] F.L. Galeener and J.C. Mikkelsen Jr., Phys. Rev. B23 (1981) 5527.

[23] G.E. Walrafen, P.N. Krishnan and S.W. Freiman, J. Appl. Phys. 52 (1981) 2832.

[24] W. Primak, The Compacted States of Vitreous Silica (Gordon and Breach, New York, 1975).

[25] C.A. Murray and T.J. Greytak, J. Chem. Phys. 71 (1979) 3555.

[26] A. Bertoluzza, C. Fagnano, M.A. Morelli, V. Gotardi and M. Guglielmi, J. Non-Cryst. Solids 48 (1982) 117.

[27] C.J. Brinker, D.R. Tallant, E.P. Roth and C.S. Ashley, J. Non-Cryst. Solids 82 (1986) 117.

[28] F.L. Galeener, Solid State Commun. 44 (1982) 1037.

[29] H. Steinfink, B. Post and I. Fankuchen, Acta Crystallogr. 8 (1955) 420.

Model of rings in the amorphous SiO_2.

Frank Galeener's legacy

Richard Kerner [*]

Laboratoire de Gravitation et Cosmologie Relativistes, Université Pierre et Marie Curie, CNRS, URA 769, Tour 22, 4-éme étage, Boite courrier 142 4, Place Jussieu, 75005 Paris, France

Abstract

This article discusses a theoretical approach to the description of the ring structure in the amorphous SiO_2 elaborated in common with Frank L. Galeener and Rafael Barrio in 1988–1990. After recalling briefly the theoretical model of agglomeration and growth of general networks, the first model of ring agglomeration, produced in 1988 and 1989, is presented. Partial results obtained with this model are shown and its shortcomings are criticized. Next, a brief description is given of the last version of the model of ring formation and growth, adapted also to other glasses, in particular to the amorphous B_2O_3, and elaborated partly along the recommendations concerning the model that Frank Galeener gave in one of his last letters.

*It happens sometimes that the trail left by a little snail
may be seen one thousand years later on the petrified sand.
Who can be sure to leave a trace that will be seen after a thousand years?*
Chinese poem (Song Dynasty, ~ 1000 years ago).

1. Introduction

Although as humans we may feel as frail and fragile as little snails when confronted with the unrelenting and pitiless flow of time, there is one magic property of the traces left by us in the minds and hearts of our fellow human beings that no snail's trail could possess: they can grow and develop, becoming bigger and more important with time.

Without any doubt this is happening with the reminiscence of our common work with Frank and the marvellous collaboration we had together since 1987, as well as the valuable contribution which Rafael Barrio has made after he joined our project on rings in amorphous SiO_2 in 1989.

Although we never published our results, the approach we developed to the problem has been used in the theoretical study of many glasses whose short-range structure turned out to be much simpler than that of the amorphous SiO_2, and has given rise to a number of papers, either published or about to appear (cf. Refs. [1–5]).

It can be said that the side-effects have momentarily overgrown the scope of our initial project that was concerned exclusively with the rings in amorphous SiO_2. This was also due to Frank's excep-

[*] Corresponding author. Tel: +33-1 44 27 72 86. Telefax: +33-1 44 27 72 87. E-mail: rk@ccr.jussieu.fr.

tional scientific honesty and the rigorous standards that he imposed on the quality of material that he would deem worth publishing. That is why partial results concerning the applications of our model to $xB_2O_3 + (1 - x)Li_2O$, $xSiS_2 + (1 - x)Li_2S$ and other binary glasses have been published since a few years, while the work on the amorphous SiO_2 still remains in a preparatory stage.

However, I feel the time is ripe to unveil, at least partly, the main content of our common theoretical work, and to pay tribute to Frank's inventiveness and to his extraordinarily deep insight in the domain of glass science. Frank's main concern during the few years of our common work has been related to rings in the amorphous SiO_2, whose characteristic breathing modes he discovered via Raman spectroscopy experiments (cf. Refs. [6,7]).

This article intends to be a tribute to a dear friend, a history of a ten years long search with its highs and lows, a sketch of our approach to the theory of the glass transition and its consequences for the short-range order in amorphous SiO_2 – all these things impose an internal structure of this contribution, which will also highlight:

(a) a description of the first model of agglomeration and growth;

(b) first attempts to model SiO_2 glass (in common with R. Barrio);

(c) a generalization of the model applied to binary glasses;

(d) last developments and new prospects.

2. First model of agglomeration and growth

In 1986 and 1987, I introduced, in collaboration with Dina Maria dos Santos, a model of agglomeration and growth of amorphous or quasi-crystalline networks that could be used – as it seemed – as a theoretical support for the description of local ring structure in amorphous SiO_2 (cf. Refs. [8,9]). Our first toy model was two-dimensional and was based on the idea that the energy cost of adding a new polygon to a network can be directly related to the local curvature it is supposed to introduce. Thus, in a tri-coordinate planar network with equal bond lengths, the hexagons were considered as zero-curvature entities, whereas a pentagon or a heptagon
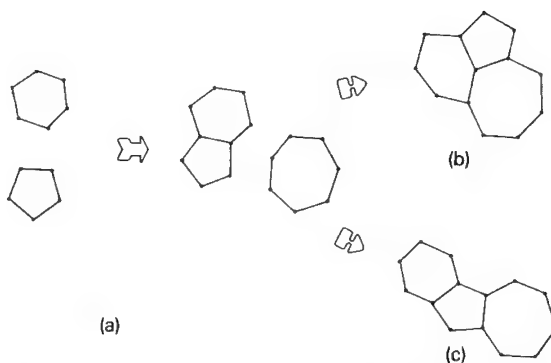
Fig. 1. Elementary agglomeration process: (a) two singlets form a doublet; (b) a cell; (c) a chain formed.

created equal amounts of positive, (resp. negative) curvature (Fig. 1)

If the initial probabilities of observing an n-sided polygon in the reservoir are denoted by $P_k^{(0)}$, with $k = 5$, 6 or 7, then the probabilities of six different doublets can be evaluated as

$$p_{km}^{(1)} = (1/Q)(2 - \delta_{km}) P_k^{(0)} P_m^{(0)} \, e^{-E_{km}/kT}, \qquad (1)$$

with $k \le m$, and Q the normalizing factor assuring that the sum of all probabilities of doublets is equal to 1.

This can be thought of as an idealized description of the first elementary step of the network formation. Now, supposing a maximal homogeneity of the network amounts to stating that on the average the probability of finding a k-sided polygon among these doublets is the same as the initial one, i.e., the probabilities do not evolve anymore during the agglomeration. Of course, the realistic hypothesis would be to assume that the saturation of this type is observed when some critical size of clusters is attained, probably much bigger than just two polygons sharing one side.

The probability of finding the elementary configuration (which in this model corresponds to a k-sided polygon, $k = 5$, 6, 7) among the doublets is given by

$$P_k^{(1)} = \tfrac{1}{2}\left(2 P_{kk}^{(1)} + \sum_{i \ne k} P_{ik}^{(1)}\right). \qquad (2)$$

The requirement of maximal local homogeneity at this stage amounts to setting

$$P_k^{(1)} - P_k^{(0)} = 0. \qquad (3)$$

Let us emphasize here that this set of equations refers to the probabilities observed in small volume elements which can exchange the singlets with the rest of the reservoir, thus changing *locally* the values of the $P_k^{(0)}$

Only two out of three equations above are independent, because the variables $P_k^{(0)}$, representing *probabilities*, satisfy the obvious constraint $\Sigma_k \ P_k^{(0)} = 1$.

These equations can be interpreted as a system of ordinary differential equations if we suppose that the amount of doublets is growing with time, while the number of singlets is decreasing. If we take into account the relative probabilities of elementary configurations computed on the set of singlets and doublets only (which may be a reasonable approximation at the very beginning of the agglomeration process), then we may introduce a time-dependent function $s = s(t)$ which is equal to 0 when there are no doublets formed, and equal to 1 when all the singlets have agglomerated. The only requirement concerning the function $s(t)$ is that it is positive and growing with t.

The probability $P_k(t)$ at a given time, t, can be evaluated then as

$$P_k(t) = (1 - s) P_k^{(0)} + s P_k^{(1)}. \tag{4}$$

Then, if the time derivative of the temperature, T, can be neglected, the derivative of $P_k(t)$ with respect to t is given by

$$\frac{\mathrm{d}P_k}{\mathrm{d}t} = \frac{\mathrm{d}s}{\mathrm{d}t}\frac{\mathrm{d}P_k}{\mathrm{d}s} = \frac{\mathrm{d}s}{\mathrm{d}t}\left(P_k^{(1)} - P_k^{(0)}\right). \tag{5}$$
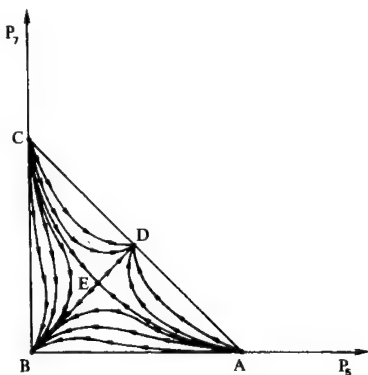
Fig. 2. The phase diagram of the differential system (6).

These equations are only an approximation whose validity is restrained to the infinitesimal neighborhoods of singular solutions.

From now on we can study the dynamical system and interpret its singular points (i.e., constant solutions corresponding to the vanishing right-hand side) as stable or unstable average statistics, following the nature of the eigenvalues of the linearized system in the vicinity of these solutions.

The overall behaviour of the system depends on the energies, E_{km}, we attribute to each elementary agglomeration process. In our first model (cf. Refs. [8,9]), we have chosen the energies to be proportional to the angular (curvature) defect introduced by a given polygon in planar tri-coordinate network, in which the mean value of the number of sides of a polygon is six in agreement with Euler's theorem. This means that we have set

$$E_{55} = 2\epsilon, \quad E_{56} = \epsilon, \quad E_{57} = 0, \quad E_{66} = 0,$$

$$E_{67} = \epsilon, \quad E_{77} = 2\epsilon. \tag{6}$$

No wonder that with such energy attributions the phase diagram of the system displayed perfect symmetry around the axis corresponding to the line $P_5 = P_7$. (Fig. 2).

The space of probabilities P_5, P_6 and P_7 is contained in a triangle; there are five singular solutions represented by the points A, B, C, D and E. The points A and C are unstable (repulsive), the points B and D are stable (attractive) and the point E is meta-stable (it is often called 'saddle point', but such a denomination makes sense only with two independent variables). It is obvious that the character of these singular points corresponds quite well to the physical reality of planar tri-coordinated networks: the trajectories converge towards the point B (pure hexagonal lattice) because it represents the natural tiling of the plane requiring no effort at all (zero curvature, and correspondingly, zero energetic cost, $E_{66} = 0$).

Another attractive point corresponds to the solution $P_5 = P_7 = \frac{1}{2}$, $P_6 = 0$; finally, the point E whose position varies with the temperature, T, clearly represents an amorphous configuration which is a mix-

ture of all the three types of ring; the configurational entropy computed as

$$S_{\text{conf}} = -k_B \sum_{i,m} P_{im}^{(1)} \ln P_{im}^{(1)} \tag{7}$$

has its maximum exactly at this point.

With growing temperature, the point E approaches the point $P_5 = P_7 = P_6 = \frac{1}{3}$ in the limit $T \to \infty$.

The description of the process of agglomeration and growth corresponds at this stage to the first *linear* approximation; the same approach may be continued onwards, with the analysis of the second step, consisting in joining of a third polygon (ring) to one of the doublets; this process is more differentiated, because it may lead either to chains or to cells (Fig. 1(b)).

The energies involved in the corresponding Boltzmann factors have been maintained as before, i.e., proportional to the absolute value of the curvature defect induced by a given configuration. The probabilities of all possible triplets, denoted by $P_{ijk}^{(2)}$, have been evaluated, taking into account different statistical weights coming from the fact that some of the triplets can be obtained in many different ways (e.g., $P_{567}^{(2)}$ contains the contributions from the processes like $(56) + (7)$, or $(67) + (5)$, etc, while the probability $P_{555}^{(2)}$ contains one contribution only).

From these, the new probabilities of elementary configurations $P_k^{(2)}$ can be evaluated by a similar procedure, and new set of equations can be produced, by requiring either $P_k^{(2)} - P_k^{(1)} = 0$, or by trying to find a parabola passing through the three points $P_k^{(0)}$, $P_k^{(1)}$ and $P_k^{(2)}$ and writing the second-order differential equation it satisfies.

The results of the second approximation (published in Ref. [9]) were quite close to those obtained in the first approximation, which could be interpreted as an illustration of the fact that our model was very primitive indeed, and whatever useful information it could give has been discovered already in the first approximation.

The model suffered from its lack of touch with real physical process. We badly needed contacts with the experimentalists, who would tell us if in real physical systems such progressive agglomeration of rings can occur, and if the energy costs and statistical weights of elementary agglomeration processes may

be evaluated with the help of some sound physical principles.

3. Application to amorphous SiO$_2$: first attempt

Frank Galeener was very much interested in a theoretical possibility of describing the rings in the amorphous SiO$_2$, whose presence he detected in the Raman spectroscopy experiments performed on various quenched or annealed glasses (cf. Refs. [6,7]), and we decided to try to adapt the model to a more complex case of three-dimensional networks, like the amorphous SiO$_2$. We worked together in 1988 and 1989, while Frank was visiting the University of Paris; later on, Rafael Barrio has joined the project and tested it on the computer program that he had elaborated.

Our results were not very convincing because in our first attempts we stuck too closely to the 'toy model' described in the previous section, which turned out to be too primitive when applied to three-dimensional structures. Nevertheless I think it is appropriate to present the main lines of our work because it will show most of the basic ingredients that have been applied since then quite successfully, although to other types of glass.

The main difference between the planar model of agglomerating equilateral polygons and the real rings in amorphous SiO$_2$ is that the latter are three-dimensional, and that the energy cost of creation of an edge-sharing doublet, and later a cell of three connected rings, cannot be put in a correspondence with any 'curvature versus flatness' argument. According to Frank's insight, the main contribution to the potential energy stored in a ring should come from the variations of the angle between the covalent bonds in the oxygen bridges Si–O–Si. These contributions may be evaluated from the Newton–Gibbs curve that gives the bond-bending energy versus the angle, θ, between the two adjacent bonds (Fig. 3).

It is known that in the amorphous SiO$_2$ the angles between the bonds around a Si atom are stiff and very close to 109°.47′, which is the central angle of a regular tetrahedron; in order to evaluate the potential energy stored in a ring made of n silicon atoms connected via n oxygen bonds, we had to figure out the most plausible geometrical form such a ring

Fig. 3. The Newton–Gibbs curve.

Fig. 5. (a) A 'crown' with puckering angle, Ψ; (b) Two puckered rings ('crowns') sharing a Si–O–Si bond.
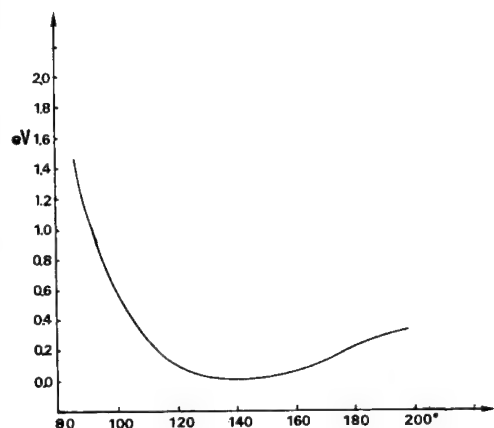
would take on when completely relaxed; then when it shared an oxygen bridge with another ring (forming a 'doublet', as in the planar toy model); finally, when it formed a 'cell' of three rings sharing two Si–O–Si bonds simultaneously with two other rings, or when it formed a 'fan' sharing one common oxygen bond with two other rings at once (Fig. 4).

Frank's idea was that the rings must be inevitably puckered whenever forced to share one or more bonds; if we know the difference between their relaxed form and the shape they take on after being put together, we will be able to compute the average

angle of their oxygen bonds, and then read on the Newton–Gibbs curve the energy difference that has to be assigned to the particular doublet; the same reasoning can be reproduced at the next step of agglomeration, when the triplets of rings are being considered.

Of course, any n-sided ring made of Si–O-bridges has many degrees of freedom; in order to reduce their number, we made the following symmetry assumptions, reducing the problem to a simple exercise in three-dimensional Euclidean geometry.

Consider *regular* rings of Si–O bonds with common bondlength, r, common Si–O–Si angle, $\Phi = \cos^{-1}(-\frac{1}{3}) = 109°47'$, and either planar or puckered in the crown configuration (Fig. 5).

Then, each ring can be obtained by taking the planar ring, and rotating each Si atom above the plane along the adjacent O–O line by the same angle, Ψ (the 'puckering angle'). Note that the O atoms all form a regular n-sided polygon which is unchanged by this procedure. Also, note that as the Ψ increases, the Si–O–Si angle, θ, decreases. A relationship giving θ as a function of Ψ for a given n has the following form:

$$\cos\theta = \left[\frac{R'_n}{r}\cos\left(\frac{\pi}{n}\right) - \frac{R_n}{r}\right]^2 - \left(\frac{R'_n}{r}\right)^2 \sin^2\left(\frac{\pi}{n}\right)$$
$$+ \cos^2\left(\frac{\Phi}{2}\right)\sin^2\Psi, \tag{8}$$

where R_n and R'_n are the radii of the circles circumscribing Si atoms and O atoms, respectively, and which are given by the formulae

$$R_n/r = \sin(\Phi/2)/\sin(\pi/2),$$
$$\frac{R'_n}{r} = \frac{R_n}{r}\cos\left(\frac{\pi}{n}\right) + \cos^2\left(\frac{\Phi}{2}\right)\cos\Psi. \tag{9}$$

Fig. 4. (a) A doublet formed by two rings; three different triplets of rings: (b) a chain; (c) a cell; (d) a fan.

Now, consider two such rings of order n and n', which share a common Si–O–Si bridge and both have identical Si–O–Si angles θ, everywhere. For a given pair (n, n') we can determine this common angle (denoted by $\theta_{nn'}$) by requiring the most symmetric (i.e., regular) shape for both crowns and by solving the equation that will give the common puckering angle, Ψ, which follows from the fact that the distance between two Si neighbors must be the same in both, because they share a common Si–O–Si bond. The equation determining Ψ in a given (n, n') pair is

$$\sin\left(\frac{\pi}{n}\right)\left[\frac{\sin(\Phi/2)\cos(\pi/n)}{\sin(\pi/n)} + \cos\left(\frac{\Phi}{2}\right)\cos\Psi \right.$$
$$\left. + \cos\left(\frac{\Phi}{2} + \Psi\right)\right] = 2\sin\left(\frac{\Phi}{2}\right)\sin\left(\frac{\pi(n'-2)}{2n'}\right),$$
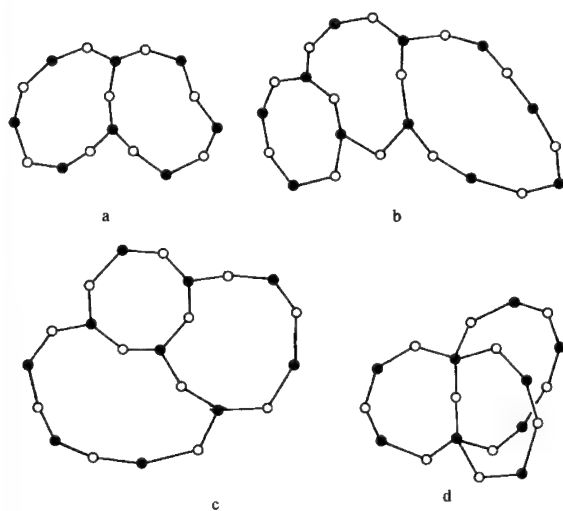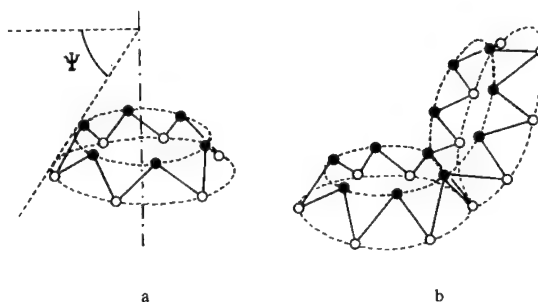
where $\Phi = 109°47'$.

The results for ten doublets of rings, n, $n' = 3, 4, 5, 6$, where each pair (n, n') is followed by the computed angle, $\theta_{n,n'}$, and the corresponding energy difference deduced from the Newton–Gibbs curve is given in Table 1.

For triplets of rings we have chosen the following rules for computing the average bond angle, $\theta_{nn'n''}$, from the angles of doublets involved:

$$\theta_{nn'n''} = \frac{\theta_{nn'} + \theta_{n'n''} + \theta_{n''n}}{3} \quad \text{for cells and fans}$$

and $\theta_{nn'n''} = \dfrac{\theta_{nn'} + \theta_{n'n''}}{2}$ for chains.

Again, the corresponding energy costs of the

Table 1
Results for doublet of rings n, $n' = 3, 4, 5, 6$, with the computed angle, $\theta_{nn'}$, and the corresponding energy difference, E_{NG}

n, n'	$\theta_{nn'}$	$E_{NG}(\theta_{nn'})$ (eV)
3 3:	109.5	0.860
3 4:	124.7	0.290
3 5:	129.7	0.190
3 6:	130.5	0.175
4 4:	148.4	0.001
4 5:	158.8	0.035
4 6:	160.3	0.048
5 5:	177.1	0.150
5 6:	167.8	0.095
6 6:	141.0	0.036

triplet forming could be read on the Newton–Gibbs curve, and then inserted into the definitions of the probabilities $P^{(1)}_{(nn')}$ and $P^{(2)}_{nn'n''}$ to be inserted in the equations defining the metastable singular points in the model of polygon agglomeration.

Here is an outline of the computational program as it has been produced by Rafael Barrio in 1989.

(I) We first define the initial probabilities of forming three-, four-, five- and sixfold rings, which we denote by $P^{(0)}_i$, with $\sum_{i=3}^{6} P^{(0)}_i = 1$.

We shall also suppose that the glass formation during annealing takes place at fictive (because it is a non-equilibrium process) temperature in SiO$_2$ equal to 1500 K, i.e., $\beta = 7.752$ eV^{-1}.

(II) Start forming pairs of rings, which define new pair probabilities

$$P^{(1)}_{ij} = (1/Q)(2 - \delta_{ij})P^{(0)}_i P^{(0)}_j E_{ij}, \tag{10}$$

where

$$Q = \sum_{i \le j} (2 - \delta_{ij})P^{(0)}_i P^{(0)}_j E_{ij}, \tag{11}$$

where the factor $(2 - \delta_{ij})$ comes from counting (ij) and (ji) as different agglomeration processes; the energy factors, E_{ij} are defined in the following way:

$$E_{ij} = e^{-\beta(i+j-1)E_{NG}(\theta_{ij})}, \tag{12}$$

with the energies $E_{ij}(\theta_{ij})$ taken from the Table 1.

(III) After forming the pairs, the singlet probabilities change:

$$P^{(1)}_i = \frac{1}{2}\sum_{j=3}^{6}(1 + \delta_{ij})P^{(1)}_{ij}. \tag{13}$$

Now we can try to solve the system of equations defining singular points, and draw the information from the meta-stable configuration found:

$$P^{(1)}_j - P^{(0)}_j = 0 \tag{14}$$

or proceed to the computation of the probabilities of different triplets, $P^{(2)}_{ijk}$, using a similar method; then, after defining the new set of probabilities, $P^{(2)}_j$ as

$$P^{(2)}_i = \frac{1}{3}\sum_{j=3}^{6}\sum_{k \ge j}(1 + \delta_{ij} + \delta_{ik})P^{(2)}_{ijk}, \tag{15}$$
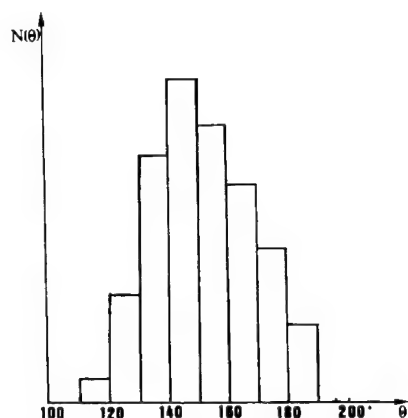
Fig. 6. The obtained distribution of Si–O–Si angles.

approach the development of probabilities introducing a continuous parameter, s, and setting

$$P_i(s) = P_i^{(0)} + s\left(P_i^{(1)} - P_i^{(0)}\right)$$
$$+ \frac{s^2}{4}\left(P_i^{(2)} - 2P_i^{(1)} + P_i^{(0)}\right) \qquad (16)$$

and find stationary solutions to a system of linear equations of the second order satisfied by functions $P_i(s)$

After the program has been performed and solved numerically, the results we have got were far from satisfactory. Although the (55), (56) and (66) pairs of rings were dominant, there were still too many three-sided rings (more than 12% versus 3% deduced by Frank Galeener from his Raman spectroscopy experiments); the only non-trivial result was the distribution of Si–O–Si angles, although it was a very coarse approximation, too (Fig. 6)

The reason for these unsatisfactory results could be easily understood: the approximation we used was too tough; we needed a more sophisticated scheme in which both energy and entropy (statistical weight of each configuration) should be evaluated with much better care.

That is why we have put aside for a while the problem of rings in pure amorphous SiO_2, looking for the application of the model to glasses whose local structure is simpler, and at the same time to make use of information that could be drawn form the behaviour of binary glasses.

4. Testing the model on covalent binary glasses

It has become clear after the analysis of the results of our first model based on the agglomeration of rings, that the approximation in which the rings were conceived as the only independent entities that agglomerated in doublets and triplets was too coarse and did not take into account all the intermediate structures present in the liquid SiO_2 close to the glass transition temperature.

This unrealistic approximation altered the statistical weights attributed to each configuration, because we ignored the number of ways in which a given ring could be created, thus attributing from the beginning equal chemical potential to all rings, which is certainly erroneous.

In order to repair this, we have tried (in collaboration with Matthieu Micoulaut) the approach in which the elementary configuration was taken to be the 'n-pod', i.e., a single atom of a glass-former (B, Si, or Ge) with m valencies ready to form a bridge. We have decided to apply the model to binary glasses, containing an alkaline modifier, e.g., $(xB_2O_3 + (1-x)Li_2O$ or $(xSiO_2 + (1-x)CaO$ or $(xSiS_2 + (1-x)Li_2S$. Such an approach has been also studied by Bray and co-workers [10,11].

By doing so, we drifted away from the initial goal which was the study of pure SiO_2; however, even without the possibility of analyzing the ring structure, we could test the model against the experimental data, which are abundant and which have a clearly pronounced and unambiguous character, like the dependence of the glass transition temperature on the modifier's rate, x, etc.

It was very encouraging to see how the model displayed its predictive power even at the lowest order approximation. We recall very briefly the main features of the new version, in which the probability factors corresponding to various ways of agglomeration are computed more attentively. In binary glasses they are much more important, because even at the first step of agglomeration we have to do with different elementary configurations, because the modifier (usually an alkali oxide or sulfide) either increases the valency of a glass-former, or decreases it by saturating oxygen bonds and making it impossible for them to participate in the agglomeration process.

It is very enlightening to compare the contrasting effects of the modifier on borate and silicate glasses. It has been observed experimentally that in a B_2O_3 glass, the alkali modifier Li_2O has the effect of transforming the three-valenced B atoms into four-valenced B_4 ions (for the concentration of Li_2O below 30%), whereas in SiO_2 the only result of adding some amount of modificator, be it Na_2O or CaO, is transforming a four-valenced Si atom into a three- or even two-valenced one.

We can treat both these cases simultaneously, at least if we consider the first agglomeration step only. Let us describe the simplest agglomeration process as a creation of a new oxygen bridge between two atoms whose valencies are equal to m and m', respectively, for an atom in its 'ordinary' state and for an atom in its 'modified' state.

We perform the analysis when only two types of atom are present, with respective valencies m and m', which is a good approximation when the amount of modificator does not exceed 10%. We denote the first type of atom by A and the second type by B; their relative parts in the entire 'soup' is denoted by x and $1 - x$, respectively.

The probabilities of the doublets are easily computed, as shown in Fig. 7.

The normalized probabilities of the doublets corresponding to the processes A + A and A + B are given then by the following formulae:

$$P_{AA} = \frac{m^2 x^2 E_{AA}}{m^2 x^2 E_{AA} + 2mm' x(1-x) E_{AB}} \tag{17}$$

and

$$P_{AB} = \frac{2mm' x(1-x) E_{AB}}{m^2 x^2 E_{AA} + 2mm' x(1-x) E_{AB}}, \tag{18}$$

where the factors E_{AA} and E_{AB} should include both Boltzmann factors containing the corresponding energies involved in these processes, as well as kinetic factors, if necessary. As usual, we evaluate the relative probability of observing the configuration A among the newly formed doublets

$$x^{(1)} = \tfrac{1}{2}(2P_{AA} + P_{AB}). \tag{19}$$

Now we can form the equation that tells us that the agglomeration process does not alter the relative probabilities of finding an A or a B atom in newly formed clusters; this amounts to

$$x^{(1)} - x = 0,$$

i.e.,
$$\frac{m^2 x^2 E_{AA} + mm' x(1-x) E_{AB}}{m^2 x^2 E_{AA} + 2mm' x(1-x) E_{AB}} - x = 0. \tag{20}$$

The corresponding ordinary differential equation will read then

$$dx/dt = x(1-x)\left[\left(E_{AA} - 2\frac{m'}{m}E_{AB}\right)x + \frac{m'}{m}E_{AB}\right]. \tag{21}$$

It has three obvious constant solutions (singular points), which are

$$x_1 = 0, \quad x_2 = 1, \quad \text{and}$$

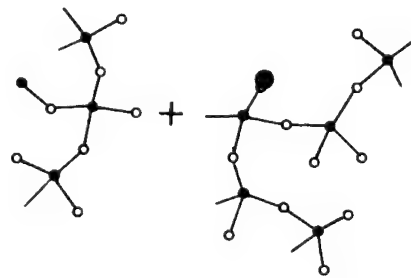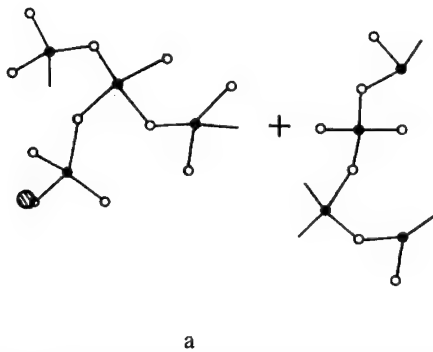$$x_{am} = \frac{(m'/m) E_{AA}}{2(m'/m) E_{AB} - E_{AA}}. \tag{22}$$

Fig. 7. Two elementary agglomeration processes with their unrenormalized probability factors. (a) A + A: $P_{AA} \sim m^2 x^2 E_{AA}$. (b) A + B: $P_{AB} \sim 2mm' x(1-x)E_{AB}$.
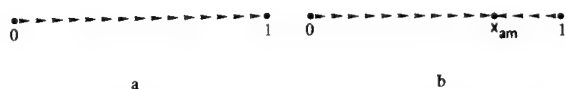
Fig. 8. Two diagrams representing the behaviour of the system: (a) when $m'E_{AB} < mE_{AA}$; (b) when $m'E_{AB} > mE_{AA}$.

Recalling that the variable x is a probability, the last of three solutions is contained between 0 and 1 under the condition that

$$(m'/m)E_{AB} > E_{AA}. \tag{23}$$

If the last equation is satisfied, then the intermediate solution, which we identify with tendency to form homogeneous amorphous configurations, is an *attractive* singular point, whereas two extremal solutions, $x = 0$ and $x = 1$, are *repulsive*; when the last equation is not satisfied, the point $x = 0$ is *repulsive*, whereas the solution $x = 1$ is *attractive* (Fig. 8).

Let us suppose now that the formation of larger clusters is a process that requires an activation energy specific to each pairing. Then we can admit that the most important contribution to the expressions E_{AA} and E_{AB} are the Boltzmann factors; i.e., let us put

$$E_{AA} = e^{-E_1/kT}, \quad E_{AB} = e^{-E_2/kT} \tag{24}$$

and the condition for the existence of the intermediate solution, x_{am}, which we interpret as the tendency to form locally an amorphous network, reads

$$\exp[(E_2 - E_1)/kT] \leq m'/m. \tag{25}$$

A good glass former should conserve this tendency even when the amount of the modifier tends to 0, i.e., with $x_{am} \to 1$, which happens when

$$\exp\left[\frac{E_2 - E_1}{kT}\right] = \frac{m'}{m} \quad \text{or} \quad \frac{E_2 - E_1}{kT} = \ln\left(\frac{m'}{m}\right). \tag{26}$$

This equation defines the relation between the entropic and energetic factors that are the most important for binary glass formation. If $m' > m$, the logarithm of m'/m is positive, which means that the energy, E_2, involved in the formation of the bond of type AB is greater than the energy needed to form the bond AA; in the case when $m' < m$, one must have $E_2 < E_1$.

This is in agreement with what should be intuitively expected from a good glass former, which should behave on a microscopic scale in a 'frustrated' way: indeed, our formulae show that the main contributions to the probability of formation of new clusters act always in opposite directions: when the modifier raises the number of possible bonds, thus creating more entropy and raising the probability of agglomeration $(m' > m)$, the corresponding Boltzmann factor is smaller, thus reducing the same probability, and vice versa.

It is this very undecided character of the process that leads to amorphous rather than a pure (crystalline) state

This view is akin of and greatly inspired by the theory of glass-forming proposed by Phillips in his pioneering works [12].
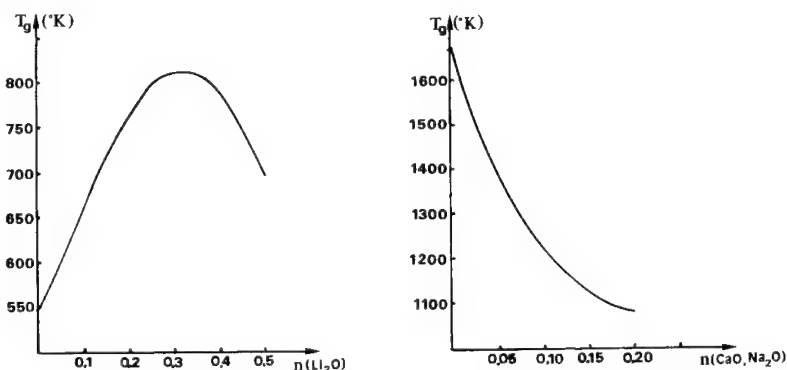
Fig. 9. Two curves $T_g(n)$ for binary glasses. Left: $xB_2O_3 + (1 - x)Li_2O$. Right: $xSiO_2 + (1 - x)(CaO, Na_2O)$.

The fairness of this approximate model can be tested against another characteristic behaviour of binary glasses, namely the dependence of the glass transition temperature on the modifier's rate, which in the vicinity of $x = 1$ is equal to $n = 1 - x$. Two characteristic curves are shown in Fig. 9.

Let us investigate the derivative of the glass transition temperature, T_g with respect to modifier concentration n in the vicinity of $n = 0$: we have to evaluate

$$\left[\frac{dT_g}{dn} \right]_{n=0} = -\left[\frac{dT_g}{dx} \right]_{x=1} = -\left[\left(\frac{dx}{dT} \right)^{-1} \right]_{x=1, T=T_0}, \tag{27}$$

where T_0 is the glass transition temperature at $n = 0$, i.e., in the absence of a modifier. The last expression is easily computed giving the result

$$\left[\frac{dT_g}{dn} \right]_{n=0} = \left[\frac{\left(2\frac{m'}{m}\frac{E_{AB}}{E_{AA}} - 1 \right)^2}{\frac{m'}{m}\frac{(E_{AB} - E_{AA})}{kT^2}} \right]_{T=T_0} = \frac{T_0}{\ln\left(\frac{m'}{m} \right)} \tag{28}$$

because we have

$$\frac{m'}{m}\frac{E_{AB}}{E_{AA}} = 1 \text{ at } T = T_0, \text{ and } \frac{(E_2 - E_1)}{kT_0} = \ln\left(\frac{m'}{m} \right).$$

The formula

$$\left[dT_g / dn \right]_{n=0} = T_0 / \left(\ln(m'/m) \right) \tag{29}$$

is very significant and may be interpreted as a universal law:

The modifier that increases the average coordination number of the glass former tends to raise the glass transition temperature (e.g., as in $B_2O_3 + nLi_2O$), while the modifier that decreases the average coordination number tends to lower the glass transition temperature (e.g., as in $SiO_2 + nCaO$).

We can now compare the experimental data represented in Fig. 11 with the last formula. For the alkali borate glass the derivative dT_g/dn at $T = T_0$ can be roughly estimated as 1200 K/mol, and $T_0 \approx 550$ K; this yields $\ln(m'/m) = 0.458$ and $m'/m = 1.58$, which is close to $\frac{3}{2}$.

For an ordinary silicate glass, we have the corresponding derivative of the order of -1900 K/mol at $T_0 = 1700$ K; this yields $\ln(m'/m) = -1.118$ and $m'/m = 0.327$, which is close to $\frac{1}{3}$. These values describe fairly well the two situations displayed in Fig. 10.

We can also evaluate the energy differences $E_2 - E_1$ for each of these glasses: $E_2 - E_1 = 0.021$ eV for borate glass, and $E_2 - E_1 = -0.181$ eV for silicate glass. These simple results together with a good agreement of the model applied to the description of rapid quenching (see Ref. [2]) have encouraged us to continue developing of the model along these lines, and to apply it to the situations when the rings start to appear, i.e., to continue the analysis of the next steps of agglomeration. The technical problems were quite important, because the number of configurations grows quasi-exponentially with each step.

Since 1993, Dina Maria dos Santos-Loff has drawn and computed eleven steps of the agglomeration process, taking into account the formation of hundreds possible rings and chains. We have applied the model to the pure B_2O_3 and SiO_2 glasses, with encouraging results, although the work is not yet

a   b
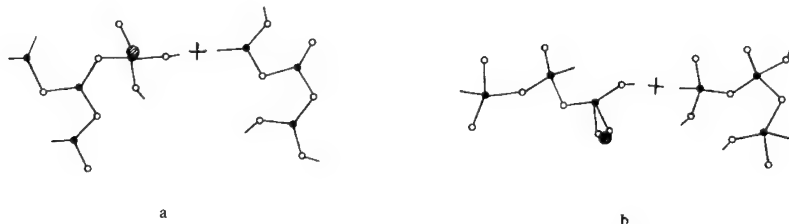
Fig. 10. Two elementary agglomeration processes: (a) in a $B_2O_3 + nLi_2O$ glass ($B_4 + B_3$ ($m' = 3$, $m = 2$)); b) in a $SiO_2 + n(CaO, Na_2O)$ glass ($Si_2 + Si_4$ ($m' = 1$, $m = 3$)).

finished. We present it briefly in the next section; it follows the recommendations concerning our model Frank gave us in one of his last letters.

5. New developments and prospects

Let us sketch the new approach to the problem of ring modeling in amorphous SiO_2 and incidentally in other glasses, elaborated recently in collaboration with D.M. dos Santos-Loff and M. Micoulaut along the lines suggested by Frank Galeener.

We follow the construction of clusters starting from the elementary configuration reduced to a single Si atom with for oxygen bonds (a singlet); these form oxygen bridges with next Si atoms, and so on.

Of course, in the liquid SiO_2 about to undergo a glass transition, such 'singlets' represent a rare virtual state, most of the SiO_2 molecules being already organized in clusters; however, during the glass transition, new oxygen bridges must form in order to produce the final solid network. Whatever the order in which this occurs, the configurational entropy relative to a given cluster can be evaluated with a fair exactitude by computing the number of independent agglomeration pathways leading to this cluster.

Parallelly, the energy cost of forming, or the energy *stored* in a given cluster, can also be treated as an additive quantity and evaluated by summing up the energies involved in each creation of a new oxygen bridge during the process. Whenever the

doublets or triplets of rings will be formed, we use the energies evaluated in Section 3 with the help of the Newton–Gibbs curve and the ring model.

At each step n we shall find normalized probabilities of each particular cluster being produced; the overall normalizing factors of these probabilities can be used as consecutive approximations for the big statistical sum, i.e., the partition function identifying different energies stored in a given cluster as Classical Ensemble state energies.

It should be emphasized at this point that by contrast with usual equilibrium thermodynamics, the 'partition function', $Z_{(r)}$, does not refer here to an ensemble of momentaneous states of the same system, but rather to an ensemble of evolution processes (or pathways) leading to the set of all geometrically acceptable clusters of a given size n. This approach has been recently tested on a simpler glass, B_2O_3 [12].

In order to obtain a reliable information concerning the ring distribution, one should follow this scheme up to the 15th or 16th step of agglomeration; at the moment, this is yet to be achieved. Nevertheless, some of the most important features of the model can be investigated at a lower degree of approximation.

Let us show how we shall evaluate the probabilities of the pathways, and then how we shall use them. The first step consisting in doublet creation has a relative probability equal to 1; because there are no alternatives (Fig. 11), we exclude here the
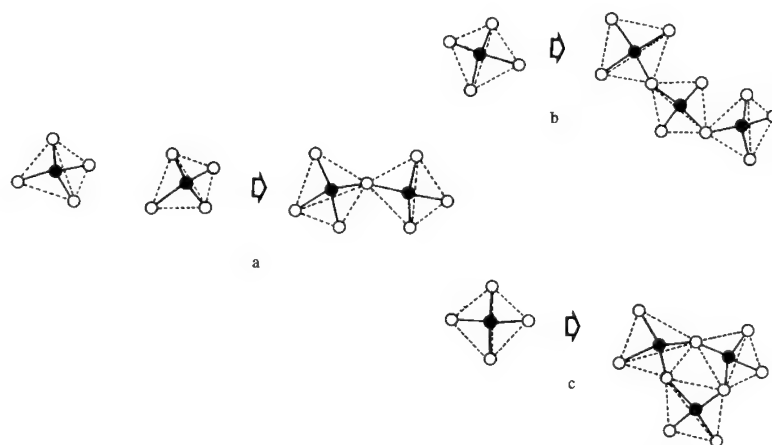
Fig. 11. First two steps of agglomeration in SiO_2: (a) the only doublet; (b) a chain; (c) a cell.

possibility of creation of two or three oxygen bridges between two Si atoms.

During the next step (Fig. 11(b)), two possibilities have to be taken into account, formation of a chain or of a three-ring. It is easy to see that the corresponding statistical factors (or multiplicities) are 24 and 108, respectively; we shall multiply them by the factors e_1 and e_3 that are supposed to take into account both energetic and kinetic factors characterizing each of the two processes.

The normalized probabilities of the two triplets displayed above are

$$p3A = \frac{24e_1}{24e_1 + 108e_3}; \quad p3B = \frac{108e_3}{24e_1 + 108e_3} \tag{30}$$

The next step leads to five different clusters: a chain, a star, a three-ring with an extra Si atom attached, a four-ring and a doublet of two three-rings (Fig. 12). The corresponding normalized probabilities are

$$p4A = \frac{24e_1}{Q_{3A}}p3A; \quad p4AA = \frac{8e_1}{Q_{3A}}p3A;$$

$$p4C = \frac{108e_4}{Q_{3A}}p3A, \tag{31}$$

$$p4AB = \frac{144e_{33}}{Q_{3A}}p3A + \frac{24e_1}{Q_{3B}}p3B;$$

$$p4BB = \frac{144e_{33}}{Q_{3B}}p3B, \tag{32}$$

where the normalizing factors Q_{3A} and Q_{3B} are

$$Q_{3A} = 32e_1 + 108e_4 + 144e_3,$$

$$Q_{3B} = 24e_1 + 144e_{33}.$$

The common denominator of all these fractions is interpreted as the nth approximation to the partition function.

Although we are still far from the adequate description of the situation, we can draw some useful information even at this stage. For example, assuming that the expressions e_1, e_3, etc., are just the Boltzmann factors related to the particular creations of bonds in a chain or in a three-ring, $e_1 = e^{-E_1/kT}$, $e_3 = e^{-E_1/kT}$, respectively, we can limit from above the difference $E_3 - E_1$ requiring that no more than
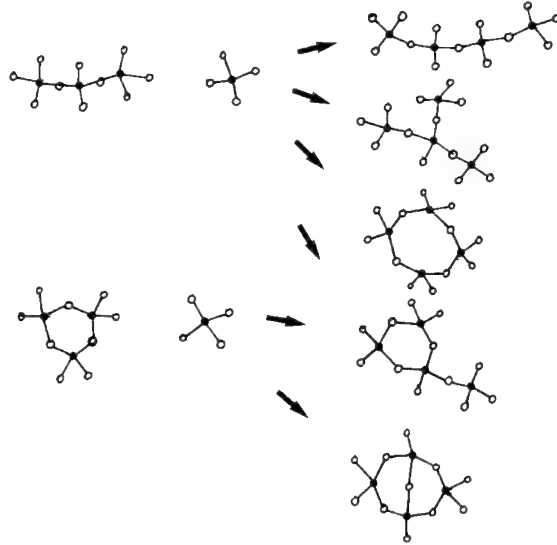
Fig. 12. The five configurations with five Si atoms and the pathways leading to their creation.

3% of Si atoms are found in the three-rings. To do so, it is enough to solve

$$p3B = 9e_3/(2e_1 + 9e_3) \le 0.03 \tag{33}$$

so that

$$e^{-(E_3 - E_1)/kT} \le 2/291, \tag{34}$$

which gives $(E_3 - E_1)/kT \ge -\ln(2/291) = 4.98$.

At $T = T_g \sim 1500$ K, this gives a reasonable estimate of the energy cost of formation of a three-ring: $E_3 - E_1 \ge 0.698$ eV.

We can also evaluate the approximate partition function:

$$Z_{(l)} \sim \left[2\pi M_{(l)}kT\right]^{3N_{(l)}/2} \prod_{\alpha=1}^{N_{(l-1)}} Q_\alpha^{(l)}, \tag{35}$$

where $N_{(l)}$ is the number of different clusters of the lth step, $M_{(l)}$ is their average mass and $Q_\alpha^{(l)}$ is the normalization factor of the pathway labeled α, $\alpha = 1, 2, \ldots, N_{(l-1)}$.

We have calculated the approximation to the specific internal energy, $u_{(l)}$, as usual:

$$u_{(l)} \sim \left(1/M_{(l)}\right)kT^2(\partial/\partial T) \ln Z_{(l)}. \tag{36}$$

Then we have found c_V by differentiating it with respect to T. The results (for B_2O_3 glass, Ref. [12]) are displayed in Fig. 13.
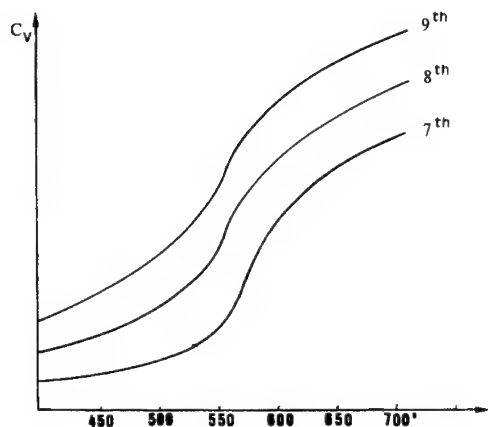
Fig. 13. The C_V curves for B_2O_3.

The work along the lines exposed above is still being pursued. We intend to perform the analysis of cluster formation up to the stage when the multiple coupled rings of the Si–O-bonds start to appear, i.e., up to the 13th or even 15th step of agglomeration, when we will be able to use the energies evaluated in Section 3 of this article.

References

[1] R. Kerner, J. Non-Cryst. Solids 135 (1991) 155.
[2] M. Micoulaut, C.R. Acad. Sci. Paris, Ser. II 316 (1993) 1679.
[3] R.A. Barrio and R. Kerner, in: Lectures on Thermodynamics and Statistical Mechanics, ed. M. Lopez de Haro and C. Varea (World Scientific, Singapore, 1993) p. 196.
[4] R.A. Barrio, J.P. Duruisseau and R. Kerner, submitted to Philos. Mag; R. Kerner and M. Micoulaut, J. Non-Cryst. Solids 176 (1994) 271.
[5] R. Kerner, K. Penson and K.H. Bennemann, Europhys. Lett. 19 (1992) 363.
[6] F.L. Galeener, R.A. Barrio, E. Martinez and R.G. Elliott, Phys. Rev. Lett. 53 (1984) 2429.
[7] F.L. Galeener, in: Physics and Technology of Amorphous SiO₂, ed. R. Devine (Academic Press, New York, 1988) p. 1.
[8] R. Kerner, C.R. Acad. Sci. Paris, Ser. II 304 (1987) 109.
[9] R. Kerner and D.M. dos Santos, Phys. Rev. B37 (1988) 3881.
[10] P.J. Bray, R.V. Muller and E.J. Holupka, J. Non-Cryst. Solids 75 (1985) 37.
[11] P.J. Bray, G.E. Geissberger, F. Bucholtz and I.A. Harris, J. Non-Cryst. Solids 52 (1982) 45.
[12] J.C. Phillips, J. Non-Cryst. Solids 34 (1979) 153; 43 (1981) 37.
[13] D.M. dos Santos-Loff, M. Micoulaut and R. Kerner, Europhys. Lett. (1994) in press.

Bethe lattice studies in glasses

Rafael A. Barrio [a,*], Gerardo G. Naumis [a], Chumin Wang [b]

[a] *Instituto de Física, Universidad Nacional Autónoma de México, Apartado Postal 20-364, 01000 México, Distrito Federal, Mexico*
[b] *Instituto de Investigaciones en Materiales, Universidad Nacional Autónoma de México, Apartado Postal 20-370, 01000 México,*
Distrito Federal, Mexico

Abstract

The Bethe lattice has been extensively used to study amorphous and glassy solids, due to the abundant and easily obtainable analytical results. However, not much attention has been paid to the unphysical and spurious features that make the calculations difficult to interpret. In this paper, some of the results extracted from Bethe lattice studies are critically reviewed and their most serious drawbacks are discussed, particularly the effects of an unphysical surface on local and long range correlations. A study of the localization of states in the Bethe lattice is also included.

1. Introduction

The most important difficulty when studying glasses, or amorphous solids in general, is the absence of long range translational symmetry. However, as discussed by Frank L. Galeener [1], one usually finds local chemical order and some type of intermediate range order in these, otherwise, disordered solids. Covalent amorphous semiconductors and AX_2 glasses, for instance, present nearest neighbour fixed geometry and regular coordination. This fact makes the Bethe lattice an appropriate network to simulate these glassy structures, since, as we shall see below, it is possible to define a local unit (or effective site) preserving the local short range order, and construct an infinite random network without long range order. This method is sometimes more convenient than building disordered clusters with free ends or periodic boundary conditions, since it is

free from unwanted finite size effects and artificial periodicities, although care must be taken when interpreting the results due to the unphysical properties of the Bethe lattice. The main advantage of Bethe lattice models is that most results are obtained analytically.

In this paper we present a new discussion of the properties of the Bethe lattice and revise a series of Bethe lattice models for glasses made in collaboration with Galeener in the past ten years, and referred to in the following text.

2. Properties of the Bethe lattice

Suppose one is interested in calculating the magnetic properties of a large system, and one approximates it by a small cluster. The difficulty in doing so is that the magnetization of the atoms in the surface of the cluster differs from those in the interior. One can impose periodic boundary conditions, but one is likely to obtain spurious results due to the artificial periodicity. The idea then is to attach to the surface

* Corresponding author. Tel: +52-5 622 5085. Telefax: +52-5 616 1535. E-mail: barrio@sysul2.ifisicacu.unam.mx.

atoms some effective medium imposing the condition that the magnetization of the surface should be equal to the atoms in the interior of the cluster. This is called the Bethe–Peierls approximation [2].

If one asks the question whether there is a network in which the Bethe–Peierls approximation is the exact result, the answer is the Bethe lattice [3]. If one studies the vibrations of a tetrahedron with five atoms and devises an imaginary impedance attached to the four surface atoms, imposing the condition that the amplitude of vibration for any atom in the cluster should be the same, one is talking about the 'structural potential approximation' [4] which, not surprisingly, turns out to be the Bethe lattice again.

Topologically, the Bethe lattice is the Cayley tree [3], which can be visualized as a simply connected network of identical units with constant coordination, Z, and without closed loops of paths. From this point of view, the Bethe lattice is a first approximation to any regular network, in which all connected diagrams without closed loops are summed exactly. There are two important observations: the first is that there is no long range order or periodicity in the Bethe lattice, and second is that there is only one path from one given site to another.

The first observation has been used as a justification to simulate amorphous infinite networks and calculate electronic [5], vibrational [6] and magnetic [7] properties. The second is responsible for the drawbacks and non-physical features of the results. If there is only one way to transit from one place to another, one should expect that the network is very similar to the linear chain; in fact, some of the properties of the Bethe lattice are as for a one-dimensional system, and a linear chain can be considered as a Bethe lattice of coordination $Z = 2$. However, as we see below, the linear chain is singular and different from the other Bethe lattices. If one chooses a given site in the Bethe lattice as being the center, the number of steps, n, to go to another site defines a shell shared by $Z(Z - 1)^{n-1}$ sites. Then, as the lattice grows, the number of sites in the surface, or the last shell, grows exponentially. The total number of sites in a Bethe lattice with n shells is $1 + Z\sum_{i=0}^{n-1}(Z - 1)^i = [Z(Z - 1)^n - 2]/(Z - 2)$. Therefore, as the number of shells tends to infinity, the proportion of surface sites tends to $(Z - 2)/(Z - 1)$.

Except for $Z = 2$, in the infinite Bethe lattice, the number of sites in the surface is not negligible, as it is in any other physical network. More than half of the sites belong to the surface and, as we see below, this unphysical fact is responsible for *all* the undesirable properties of the Bethe lattice.

In order to illustrate the procedure to solve analytically a problem in the Bethe lattice, let us take the simplest possible Hamiltonian

$$\mathscr{H} = V\sum_{i,j} |i\rangle\langle j|, \tag{1}$$

where sites i and j are nearest neighbours. The equations of motion for the Green's function $g = (E - H)^{-1}$ are explicitly

$$Eg_{00} = 1 + Vg_{01}, \tag{2}$$

$$Eg_{01} = Vg_{00} + (Z - 1)Vg_{02},$$

$$\vdots$$

$$Eg_{0n} = Vg_{0(n-1)} + (Z - 1)Vg_{0(n+1)},$$

$$\vdots$$

where g_{0n} is the correlation between the central atom and any of the atoms in shell n. The usual way of solving this set of equations is by defining a transfer function $g_{0n} = tg_{0(n-1)}$, which is obtained by substituting it in the equations of motion and solving for a quadratic equation to give

$$t = \frac{E \pm [E^2 - 4V^2(Z - 1)]^{1/2}}{2V(Z - 1)} \tag{3}$$

and

$$g_{00} = (E - ZVt)^{-1}. \tag{4}$$

The reason for assuming that t does not depend on n is that one has neglected the surface atoms at shell N, which obey a different equation:

$$Eg_{0N} = Vg_{0(N-1)}. \tag{5}$$

This neglect is wrong, because there are as many atoms in the surface as there are in the interior. There is an elegant and computationally efficient way of solving the system with a surface, which is considering the shell-dependent transfer functions $g_{0n} = T_n g_{0(n-1)}$ and using the Tschevicheff functions of the second kind $U(X/2)$, where $X =$

$E/(V\sqrt{Z-1})$ [8]. Eq. (5) shows that $T_N = 1/(X\sqrt{Z-1})$ and iterating one finds

$$T_1 = U_{N-1}(X/2)/\left(U_N(X/2)\sqrt{Z-1}\right).$$

In this case the self-correlation function is written as $g_{00} = [E - ZVT_1]^{-1}$. As the lattice tends to infinity,

$$\lim_{N \to \infty} T_1 = \frac{(Z-1)^{-1/2}}{X - [1/X - (1/X - \ldots)]}$$

$$= \frac{X \pm (X^2 - 4)^{1/2}}{2\sqrt{Z-1}} = t \qquad (6)$$

which means that for a large enough Bethe lattice the effect of the surface on the self-correlation is very small.

One could say that properties involving only the density of states, $\rho(E)$, are not strongly affected by the surface, since

$$\rho(E) = -(1/\pi)\,\mathrm{Im}[E - ZVt]^{-1} \qquad (7)$$

is the same for an infinite lattice with or without a surface, giving a band of width $W = 4V\sqrt{Z-1}$, according to Eq. (3). However, there is a subtle point: if one neglects the surface, one finds that perfectly coherent states (constant and equal amplitude in all sites) at $E = \pm ZV$ exist *out* of the band, since they are eigenstates of Eq. (2), their weight being inversely proportional to the total number of atoms. If one takes into account the surface, $\pm ZV$ is *not* an eigenstate; thus, the presence of an ever-growing surface prevents the existence of coherent states and the band shrinks. One may say that even the very local properties of the Bethe lattice are affected by the surface.

The case is even worse when one attempts to calculate properties that depend on long range correlations, for instance, the infrared, Raman and inelastic neutron cross-sections [9] are related to the imaginary part of quantities like

$$\sum_N = \sum_{j=1}^{N} g_{0j} \qquad (8)$$

which can be calculated in the Bethe lattice [10]

$$\sum_N = \left(1 - ZV(Z-1)^N g_{0N}\right)/(E - ZV). \qquad (9)$$

This equation shows that the result is entirely domi-nated by the surface for $Z > 2$ because of the very large factor $(Z-1)^N$. Again, if one incorrectly ne-glects the surface (i.e., $g_{0N} = 0$), there appears a δ-function response at $E = ZV$, but if the surface is taken into account the weight of the δ function is zero because $g_{0N}(E = ZV) = 1/[ZV(Z-1)^N]$.

As a final point, let us say some words about the effects of the surface in the localization of states of the Bethe lattice. Let the amplitude of the wave function of a site in shell n be ϕ_n, and define a transfer matrix

$$\mathbf{T} = \begin{pmatrix} \dfrac{E}{(Z-1)V} & \dfrac{1}{(Z-1)} \\ 1 & 0 \end{pmatrix}$$

such that $\mathbf{T}c_{n-1} = c_n$, where $c_n = (\phi_n, \phi_{n-1})$. The eigenvalues of $\mathbf{T}$ are

$$\lambda_\pm = |\lambda|\,e^{\pm i\beta},$$

where $|\lambda| = (Z-1)^{-1/2}$ and $\beta = \arctan\sqrt{4(Z-1) - E^2}/E$. From here one defines the lo-calization distance, ξ, through

$$|\phi_n| = |\lambda|^n = e^{-n/\xi}$$

or $\xi = 2/\ln(Z-1)$. In the linear chain the states are extended ($\xi = \infty$) but in any other Bethe lattice the states are localized, explaining the 'discreteness' of the continuum discussed elsewhere [11]. The same result is obtained defining the localization distance as the inverse of the Lyapunov exponent calculated with the norm of the transfer matrix. One could say that the shrinking of the band is due to this localiza-tion of states, that prevents the existence of coherent states in the Bethe lattice. The energies of the states in the band can be written as $E = 2V\,e^{-1/\xi}\cos\beta$ and the energy gap, Δ, between the edge of the band and ZV is

$$\Delta/V = \left(e^{1/\xi} - 1\right)^2 \geq 1/\xi^2, \qquad (10)$$

which can be understood in general if one considers that for long wavelengths $E \sim p^2$, and $\xi p \geq 1$, therefore $E \geq 1/\xi^2$.

3. Bethe lattice models for glasses

We first used the Bethe lattice to study electronic and vibrational excitations in amorphous silicon [12].

Then, when I met Frank we started trying to model a random network of AX_4 units to study glasses as SiO_2, GeO_2, GeS_2, BeF_2, etc. We obtained reasonable densities of vibrational states and, as Frank was an excellent experimenter, our aim was to compare the results of the theoretical model with Frank's infrared, Raman and neutron scattering experimental spectra. Consequently, we obtained analytical expressions with Bethe lattice models to simulate and compare the measurements. The results were in general quite satisfactory [13], except for one feature that became Galeener's obsession: there were sharp peaks in the Raman spectra of some glasses, like SiO_2, which were too narrow to be expected in a disordered structure [3]. Galeener postulated [14] that these features were the signature of regular intermediate range order structures or local defects. Thus, we started using the cluster Bethe lattice method [15] to study local defects in a cluster, as broken bonds, wrong bonds, double bonds, and square rings [16], with the surface atoms linked to appropriate Bethe lattices. The results showed that, although some of the defects could produce peaks at the right frequencies, none were as sharp as in the experiment because it was impossible to disconnect the defect from the rest of the lattice. This failure is important, because some people were assigning the sharp Raman peaks to local defects based on cluster calculations, without taking into account that they should be connected to a network.

The experimental evidence supported the idea that the sharp peaks were due to regular and almost planar threefold and fourfold rings of bonds [14]. We were able to show that threefold rings could be detached from the rest of the lattice at the Raman active mode if the ratio between central and angular forces was in a range of values, perfectly reasonable for the real materials. We reproduced the experimental peaks for threefold [17] and fourfold rings [18] with our models.

Galeener was also interested in vitreous boron oxide B_2O_3, which is supposed to contain large numbers of threefold planar rings [19]. Therefore, we built up a Bethe lattice of rings and obtained reasonable results for the density of vibrational states [20] and for the vibrational spectroscopies [21].

At this point it is worthwhile to mention that the expressions for the spectral responses have to be taken with care, as there are problems with δ-function unphysical responses in the Bethe lattice. For instance, if one calculates the infrared response from a simple effective point charge $e(n)$ model in amorphous silicon, one obtains

$$I = \sum_{n,m} e(n) e(m) g_{\alpha\alpha}(n, m; \omega)$$

$$= e^2 g \left[1 + \frac{4}{3} \left(\frac{t_\parallel}{1 - t_\parallel} + \frac{2 t_\perp}{1 - t_\perp} \right) \right]^{-1},$$

where g is the displacement–displacement autocorrelation and $t_\parallel$ and $t_\perp$ are the components of the transfer function parallel and perpendicular to the bond direction, respectively. It can be shown that this expression gives a δ function at the maximum frequency, ω_{max}, where there is no mode.

The Raman scattering response from a bond polarizability model can be obtained

$$R = g \frac{1}{1 + \frac{4}{3} \left[\frac{t_\parallel}{1 - t_\parallel} + \frac{2}{3} \left(\frac{t_\perp}{1 - t_\perp} + \frac{2 a t_\perp}{1 - a t_\perp} \right) \right]},$$

where $a = \cos 3\varphi$, and φ is the dihedral angle. For random angles ($a = 0$), this expression gives a broad response highly peaked towards the optic modes, which is qualitatively correct, but for the staggered case ($a = 1$) the response is again a δ function at ω_{max}. The neutron scattering response is more complicated to obtain [9], but the result also predicts a δ function response, which is unreasonable.

All these problems are due to the significance of the enormous surface in the Bethe lattice, but they can be corrected if instead of t one uses qt (with $q \sim e^{-1/\xi} \leq 1$) in all the above expressions. This means that the coherence of the response is destroyed within a distance of the order of ξ, due to the localization of the states.

In the models for the vibrational responses for SiO_2 we used a bond polarizability model only in a local environment around the defect, based on the fact that in a disordered solid the coherent responses fade out fairly quickly. The results for the Raman response for SiO_2, GeO_2 and B_2O_3 agree extremely well with the experimental results. Even a study of a disordered Bethe lattice with three-coordinated and

four-coordinated boron atoms in B_2O_3 to simulate Li-doped boron oxide gives satisfactory answers [22].

4. Conclusions

The Bethe lattice has been very helpful to study glasses and amorphous solids. The theoretical results agree extremely well with experimental probes and allow one to test hypotheses about some structural and physical properties of glasses. We have presented some examples of the use of these models, almost exclusively those made in collaboration with Frank, and we mentioned the main problem when interpreting the results. No attempt has been made to mention numerous works made by other people using the Bethe lattice.

We have discussed the unphysical features of the Bethe lattice from a new point of view that relates all these features to the existence of an enormous surface. In practice, when modeling disordered solids one can avoid the surface by arguing that there is a decay in the long range correlations due precisely to disorder; therefore, one can calculate responses locally and also deal with local defects with the Bethe lattice and be confident that the results are reasonable.

References

[1] F.L. Galeener, J. Non-Cryst. Solids 123 (1990) 182.
[2] H.A. Bethe, Proc. R. Soc. (London) A126 (1935) 45;
  R.E. Peierls, Proc. Camb. Philos. Soc. 32 (1936) 477.
[3] C. Domb, Adv. Phys. 9 (1960) 145;
  M.F. Thorpe, in: NATO ASI series, B78 (Plenum, New York, 1982) p. 85.
[4] M.F. Thorpe, D. Weaire and R. Alben, Phys. Rev. B7 (1973) 3777.
[5] D. Weaire and M.F. Thorpe, Phys. Rev. B4 (1972) 2508.
[6] R.A. Barrio and R.J. Elliott, J. Phys. C15 (1982) 4493.
[7] E. Müller-Hartmann and J. Zittartz, Phys. Rev. Lett. 33 (1974) 893.
[8] R.A. Barrio, Kinam 5 (1983) 337.
[9] R.J. Elliott, R.A. Barrio and M.F. Thorpe, Kinam 4C (1982) 55.
[10] Felix Yndurain, R.A. Barrio, R.J. Elliott and M.F. Thorpe, Phys. Rev. B28 (1983) 3576.
[11] J.F. Nagle, J.C. Bonner and M.F. Thorpe, Phys. Rev. B4 (1972) 2233.
[12] R.A. Barrio, R.J. Elliott and M.F. Thorpe, J. Phys. C16 (1983) 3425.
[13] R.A. Barrio, F.L. Galeener and E. Martínez, Phys. Rev. B31 (1985) 7779.
[14] F.L. Galeener, Solid State Commun. 44 (1982) 1037.
[15] J.D. Joannopoulos and F. Yndurain, Phys. Rev. B10 (1974) 5164.
[16] F.L. Galeener and R.A. Barrio, unpublished.
[17] F.L. Galeener, R.A. Barrio, E. Martínez and R.J. Elliott, Phys. Rev. Lett. 53 (1984) 2429.
[18] F.L. Galeener, R.A. Barrio, E. Martínez and R.J. Elliott, Phys Rev. B218 (1993) 15672.
[19] J. Krogh-Moe, J. Non-Cryst. Solids 1 (1969) 269.
[20] R.A. Barrio, and F.L. Galeener, in: Anais do Simposio Latino-Americano de Fisica dos Sistemas Amorfos, ed. E. Anda, Vol. 2 (Centro Latino-Americano de Física, Rio de Janeiro, 1985) p. 381.
[21] R.A. Barrio, F.L. Castillo-Alvarado and F.L. Galeener, Phys. Rev. B44 (1991) 7313.
[22] R.A. Barrio and F.L. Castillo-Alvarado, Phys. Rev. B46 (1992) 3779.

Section 2. Structure

The role of topology and geometry in the irradiation-induced amorphization of network structures

Linn W. Hobbs *

Department of Materials Science and Engineering, Massachusetts Institute of Technology, Room 13-4062, Cambridge, MA 02139, USA

Abstract

Network structures are characterized by some measure of directed bonding and more arbitrary connectivity. Crystalline networks additionally exhibit long-range translational periodicity and orientational order. The irradiation-induced loss of both latter features – commonly known as amorphization and geologically as metamictization – actually represents a loss of topological order and provides a measure of the structural redundancy in the network. Because of its similarity to glass formation, the metamict transition can provide potential insights into the structures of network glasses. High-resolution electron microscopy and energy-filtered electron diffraction provide important, though unfortunately limited, information about the process and the products of the topological disordering.

1. Introduction

The structure of aperiodic networks has exercised its fascination on three generations of structural chemists, solid-state physicists and ceramists, not least the late Frank Galeener who made the seminal contributions to our understanding of intermediate-range order and defect structures in network glasses that we here honor. *Network structures* are characterized by a well-defined measure of directed bonding and may be distinguished from *compact structures* by some arbitrariness in the remaining bonding. Compact structures are characterized by pronounced structural intimacy of polyhedral coordination units, which seriously constrains their ability to form glasses, whereas in network structures such units display more marginal connections to each

other and possess greater freedom to take on aperiodic arrangements. As a consequence, structural topology is more central to a description of network structures than the packing or space-filling considerations afforded compact solids [1].

It has been suspected since 1914 [2] and confirmed in 1939 [3] that certain initially crystalline structures – at first silicates, but now comprising a range of ceramic, metal and organic solids – can be induced to lose all vestiges of crystallinity under bombardment by energetic radiation. Geological minerals rendered aperiodic by (it is now known) alpha-decay of incorporated U or Th impurities were originally classified as *metamikt* [4], and use of the term *metamictization* has gained some currency [5] – in preference to the less accurate (but also less unwieldy) epithet *amorphization*, which has regrettably but ineradicably entered the radiation effects lexicon. It is the displacement of atoms which is responsible for the disordering transformation, usually in ballistic collision cascades engendered by the

* Corresponding author. Tel: +1-617 253 6835. Telefax: +1-617 252 1020. E-mail: hobbs@mit.edu.

displacive, rather than the ionizing, component of particle radiation; however, radiolytic mechanisms function in silica and silicates (Section 4) and organic crystals, and metamictization by *single* ballistic displacements occurs in quartz [6] and SiC [7]. The transformation is functionally complete at displacement densities approaching one displacement per atom (dpa), a radiation dose one to two orders of magnitude lower than encountered in other radiation-damage phenomena such as void swelling [8]. Nevertheless, amorphization may involve dimensional changes in excess of 15% in some systems.

Fig. 1 depicts the progress of a typical transformation in real and reciprocal spaces, in this case the radiolytic amorphization of quartz in a 200 keV electron beam [9]. It is clear from the electron diffraction patterns and the high-resolution transmis-

sion electron microscopy (TEM) images that long-range translational correlations are lost, but it is also evident from the diffraction haloes that *orientational* correlations are likewise lost. In solids which amorphize within collision cascades or by overlap of collision cascades, remanent crystalline islands actually appear slightly rotated with respect to each other [10], but for solids which amorphize by single displacements the origin of the loss of orientational order is more obscure (see Section 4). Loss of both translational and orientational correlations corresponds to *topological disordering* [11], and the metamict state is clearly a topologically disordered one. Glasses are topologically disordered too, although it is not apparent that metamict solids exhibit a glass transition and should be called glasses: metamict materials tend to recrystallize when heated,
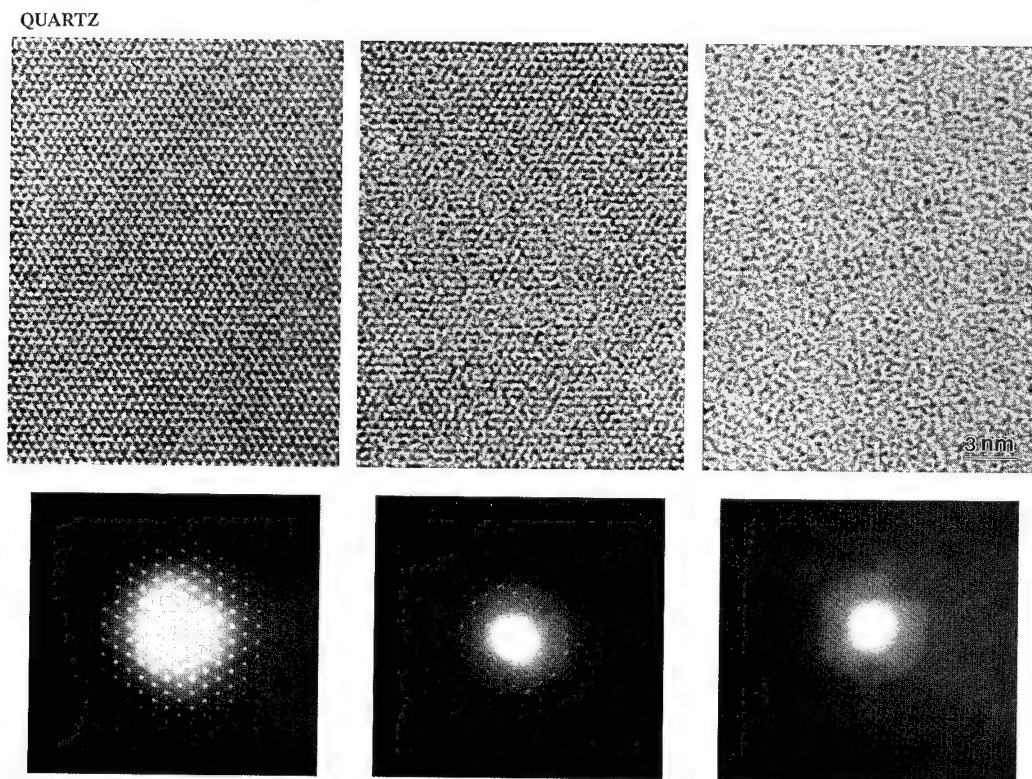
QUARTZ

Fig. 1. High-resolution axial TEM images along [0 0 1] for three different stages of the metamict transformation in α-quartz, with corresponding diffraction patterns [9].

epitaxially if a crystalline interface is available [12], and may recrystallize as fast as they disorder during irradiation above a critical temperature.

2. Experimental procedures

Irradiations reported in this study were performed with fast electrons, fission-reactor fast neutrons and energetic ions. Synthetic α-quartz crystals from the General Electric Company, UK, irradiated between 333 and 375 K in a low-intensity fission reactor at Oak Ridge National Laboratory with fission neutron fluences (> 0.1 MeV) from 10^{21} to 1.5×10^{24} n/m², were obtained from R.A. Weeks at Vanderbilt University. Hydrothermally grown α-quartz crystals for electron irradiation were obtained from Sawyer Research Company, Eastlake, OH, USA. Samples were thinned to electron transparency by a combination of mechanical polishing and 5 keV Ar-ion thinning. These were irradiated in situ by the scanned focussed electron probe of a 100 kV scanning transmission electron microscope (STEM) or in the highly focussed beam of a 200 kV high-resolution transmission electron microscope (HRTEM) to fluences between 10^{23} and 10^{27} e/m² at room temperature. High-resolution images were recorded in an Akashi-ISI 002B HRTEM with 200 kV electrons and conditions close to Scherzer focus without an objective aperture. Sawyer α-quartz crystals were also implanted along [0 0 1] with 150 keV Si$^+$ ions to a fluence of 2×10^{21} ions/m² at Naval Research Laboratories.

Natural cristobalite (collection catalogue number 128694) and tridymite (collection catalogue number 119881) crystals in the form of powders were obtained from the Harvard University Mineralogical Museum. Electron-transparent specimens of both materials were made by dispersing the powders in methyl alcohol and collecting the powders on holey carbon films supported on copper grids. These materials were electron-irradiated at room temperature similarly to α-quartz.

Lead pyrophosphate ($Pb_2P_2O_7$) single crystals were grown by slow cooling of a melt containing equimolar ratios of PbO and $(NH_4)_2H_2PO_4$, each starting compound with < 10 ppm nominal impurity, in a platinum crucible first heated to 775 K to decompose the ammonium dihydrogen phosphate and then cooled from 1150 K at a rate of 1 K/h. The resulting large ($40 \times 30 \times 0.3$ mm³) micaceous crystals grown were implanted at room temperature 7° off [0 0 1] with 100 keV P$^+$ ions to fluences between 10^{17} and 2×10^{20} ions/m².

The computer code TRIM-91 [13] was used to compute ion implantation depths, rate of displacement energy deposition as a function of depth, and the damage energy density required for amorphization from the critical amorphization fluence, for the ion implantations described above and for a number of ion irradiations carried out by other investigators reporting a critical ion fluence for amorphization in other materials. Displacement energies of between 15 and 60 eV were assumed for atoms in all solids considered [8], although choice of values made little difference to the critical damage energy densities calculated. The damage energy was taken to be the energy deposited by the primary ion into primary knock-on atoms less the losses to ionization and phonons in the subsequent collision cascades.

Energy-filtered electron diffraction (EFED) data were used to provide information about radial correlations in the metamict state and were acquired at room temperature in 100 keV (Vacuum Generators HB5) and 300 keV (Vacuum Generators HB603) field-emission STEM instruments operating in a selected-area diffraction mode with an approximately parallel incident scanned beam ~ 1 μm in diameter. Inelastically scattered electrons were removed by scanning the diffraction pattern across the entrance slit of a serial electron energy-loss spectrometer, operating with an energy window of about 2 eV centered on zero energy loss [14]. The angular range scanned corresponded to a scattering vector $q \equiv 2(\sin \Theta/2)/\lambda < q_{max} = 16$ nm^{-1} (Θ is the full scattering angle, $\lambda = 3.7$ pm for 100 keV electrons). A reduced radial density function

$$g(r) = 4\pi r^2 \left[\rho_e(r) - \bar{\rho}_e \right]$$

$$= 8\pi r \int_0^\infty q S(q) \sin(2\pi qr) M(q) \, \mathrm{d}q \qquad (1)$$

was derived by Fourier transformation of the Zernike–Prins [15] function

$$S(q) = \frac{I(q) - I(0)\delta_{q0}}{N_c \bar{f}^2} - \frac{1}{\bar{f}^2} \sum_{uc} f_j^2 \qquad (2)$$

as modified by the Lorch [16] function

$$M(q) = \frac{\sin(\pi q/q_{max})}{\pi q/q_{max}},\qquad(3)$$

where ρ_e is the scattering density for electrons, $I(q)$ is the measured scattered intensity, N_c is the number of units of composition (uc), and $\bar{f} = f_{Si} + 2f_O$ is a sharpening function derived from the atomic scattering amplitudes f_{Si} and f_O for electrons.

Simple modelling of initial stages of metamictization in α-quartz was carried out using the Nagoya University Molecular Structure Display Program [17] to draw perspective diagrams representing atoms and bonds, and a simple computer code [18] was used to minimize the sum of the weighted squares of deviations from equilibrium interatomic distances. The routines were carried out on a VAX Station II computer. Ring counts for crystalline silica polymorphs were carried out using connectivity tables derived from handbuilt models using a Symbolics computer programmed in Lisp.

3. Topology and amorphization

There are two fundamentally intriguing questions about the metamict transformation: how a (damaged) structure possesses the necessary freedom to form a topologically disordered arrangement, and why crystallization does not readily recur. Amorphization, like glass formation, represents fundamentally a failure to crystallize. Such questions are topological in nature [1].

The first question involves an assessment of what may be called 'structural freedom'. Many elemental solids and compounds exhibit multiple polymorphic crystalline forms, but the ability to adopt or retain more arbitrary atomic arrangements following a disordering event involves rather more. Structural freedom is governed by connectivity and is most easily demonstrated in two-dimensional analogues (Fig. 2). Structures can be thought of as comprising identical rigid structuring elements (generically 'polytopes') connected together by corner-, edge- or face-sharing. In compounds, these are most conveniently the cation coordination polyhedra; in elemental solids, like Si, they are more representational than physical, with
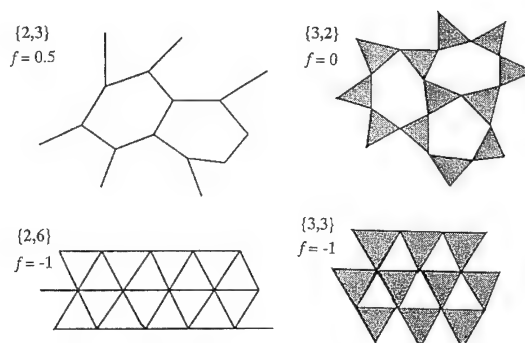
Fig. 2. Four two-dimensional networks constructed using one-dimensional rod and two-dimensional triangular polytopes, with the corresponding connectivities and structural freedoms indicated.

their vertices defined at the mid-points of inter-atomic bonds.

Fig. 2 illustrates one-dimensional rod polytopes and two-dimensional triangular polygons. Representing the connectivity by $\{V, C\}$, where V is the number of vertices per polytope and C is the number of polytopes sharing a vertex, the structures in Fig. 2 are, respectively, $\{2, 3\}$, $\{2, 6\}$, $\{3, 2\}$ and $\{3, 3\}$. The degree of structural freedom, f, is represented by the number of degrees of freedom for each vertex, equal to the dimensionality, d, of the structure, less the number of constraints, h, imposed by connections to neighboring elements. Gupta and Cooper [11,19] show that, for polytope dimension, δ,

$$f = d - C\{\delta - [\delta(\delta+1)/2V]\} - (d-1)(Y/2)$$
$$- [(p-1)d - (2p-3)](Z/p),\qquad(4)$$

where Y is the fraction of edge-sharing vertices and Z is the fraction of vertices sharing p-sided faces.

The $\{2, 3\}$ two-dimensional ($d = 2$) arrangement of rods ($\delta = 1$) in Fig. 2 highlights an important geometrical consideration: closure; such structures must close on themselves to form closed circuits or rings, if the density of self-similar elements is not to increase exponentially [1]. For the structure illustrated, one-third of the angles between adjacent rods are specified by the vertex condition and half by the average necessity for closure, leaving one-sixth of the network angles still to be chosen; the structure is therefore underconstrained and free to adopt an arbitrary configuration, as reflected by the value of $f = +0.5$ from Eq. (4). By contrast, the $\{2, 6\}$ ar-

rangement of rods, for which $f = -1$, is overconstrained and is required to be crystalline. Values of $f > 0$ therefore imply freedom to arbitrarily rearrange, while values of $f < 0$ imply rigid crystalline options. The $\{3, 2\}$ arrangement of triangles in Fig. 2, for which $f = 0$, is marginally constrained; there is no freedom once the boundary is set, but altering the boundary permits other possibilities. In three-dimensions (where $f = +1$), this is the structure of B_2O_3, a facile glass-former whose (underconstrained) structuring polytopes are corner-sharing $[BO_3]$ triangles. Finally, the two-dimensional $\{3, 3\}$ arrangement of triangles is again overconstrained and always crystalline, with $f = -1$.

If the two-dimensional $\{3, 2\}$ network of triangles is decorated with points and these points joined similarly, the result is a $\{2, 3\}$ network. The latter tiles (or tesselates) the two-dimensional space, with the useful property that each point has three rings passing through it; application of Euler's theorem shows that the average size of these rings is sixfold. There is, of course, an infinite number of larger rings also passing through a point in an infinite network, but attention is usefully restricted to those rings which are not the sum of two smaller rings; these will be called 'primitive' rings [20]. For a number of reasons, it is advisable for triangular and three-dimensional structuring polytopes to take the rings as

passing through the edges of the polytope; the two-dimensional $\{3, 2\}$ network in Fig. 2 thus has three primitive rings of average size 6 passing through each triangle, one through each edge. In three-dimensional networks, rings no longer tile the (three-dimensional) space, but it is nevertheless useful to retain primitive rings as a descriptor. The set of primitive rings passing through the edges of a given polytope defines a set of polytopes belonging to those rings which comprise the local cluster of that polytope. The five crystalline network polymorphs of silica can be uniquely described by their local clusters (see Section 4), without recourse to the crystallographic language of symmetry and periodicity [21], so this approach is equally applicable to describing non-crystalline glassy and metamict structures [22].

In three-dimensional networks (Fig. 3), the common structuring polytopes are triangles (as in B_2O_3), tetrahedra and octahedra. All silicas but stishovite and all framework silicates are based exclusively on full corner-sharing of $[SiO_4]$ tetrahedra (or substituted tetrahedra); such tetrahedral network arrangements are marginally constrained ($f = 0$). Analogous $[PO_4]$ tetrahedra in P_2O_5 and phosphates share only three of the four available vertices and are underconnected ($f \approx +0.4$). The corner-sharing octahedra in the ReO_3 structure, of which perovskites (e.g., $CaTiO_3$) are a stuffed derivative, are only somewhat

Table 1
Coordination, connectivity, structural freedom and amorphizability for some network structures

Structure	Polyhedra : sharing	$\{V, C\}$	f	Amorphization dose (eV/atom) [a]
SiC	Tetrahedra : corners	$\{4, 4\}$	-3	44 [26]
Si_3N_4	Tetrahedra : corners	$\{4, 3\}$	-1.5	> 700 [29]
$CaTiO_3$	$\sim$ Octahedra : corners	$\{6, 2\}$	< -1	66 [12] [b]
ReO_3	Octahedra : corners	$\{6, 2\}$	-1	
SiC [c]	Tetrahedra : corners	$\{4, 2\}$	< 0	44 [26]
$ZrSiO_4$	Dodecahedra : edges; tetrahedra : edges		$-3 \ll f < -1$	36 [31]
$CaSiO_3$	Octahedra : edges; tetrahedra : corners		$-1.33 < f < 0$	11 [31]
Si [c]	Tetrahedra : corners	$\{4, 2\}$	< 0	11 [32]
SiO_2	Tetrahedra : corners	$\{4, 2\}$	0	7 [31]
$Pb_2P_2O_7$	$\sim$ Tetrahedra : corners	$\{4, 1.75\}$	$< +0.4$	< 0.5 [42] [b]
P_2O_5	Tetrahedra : corners	$\{4, 1.75\}$	$+0.38$	
Si	Rods : ends	$\{2, 4\}$	$+1$	11 [32] [b]
B_2O_3	Triangles : corners	$\{3, 2\}$	$+1$	

[a] Low-temperature values for critical energy density required for amorphization.
[b] Not measured.
[c] Based on atom-centered polytopes which are not coordination polyhedra (see text).

B_2O_3
$\{3, 2\}$

P_2O_5
$\{4, 1.75\}$

SiO_2
$\{4, 2\}$

Si_3N_4
$\{4, 3\}$
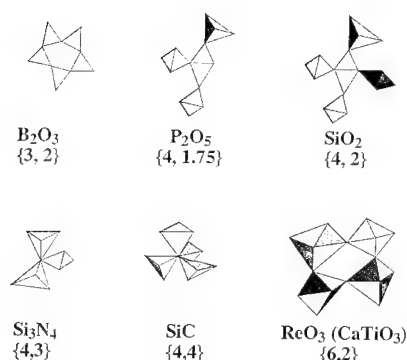
SiC
$\{4, 4\}$

$ReO_3 (CaTiO_3)$
$\{6, 2\}$

Fig. 3. Triangle, tetrahedron and octahedron polytope connectivity in some three-dimensional structures.

more constrained ($f = -1$), but addition of edge- (and face-) sharing introduces serious structural redundancies. Rutile (TiO_2; also the structure of the high-pressure silica polymorph stishovite and a polymorph of GeO_2), for example, features edge-sharing of only partly corner-shared octahedra, with a large ($f = -4$) reduction in structural freedom. Octahedra in the rocksalt structure are fully edge-shared ($f = -10$) and are so seriously overconstrained as to be unlikely ever to be found in more random aperiodic arrangements [23].

Table 1 indicates connectivities and structural freedom for the tetrahedral network structures Si, SiO_2, Si_3N_4 and SiC, as well as B_2O_3, P_2O_5, two silicates, a phosphate and the largely corner-shared octahedral structure of $CaTiO_3$. The connectivity of Si can be described as $\{2, 4\}$, but the rigid tetrahedral bonding makes it topologically more accurate to describe tetrahedra surrounding each Si atom (less space-filling than the Voronoi [24] polyhedra) with unoccupied vertices at the bond mid-points (cristobalite without the oxygen) with $\{4, 2\}$ connectivity and $f = 0$. The consequential requirement that the Si–vertex–Si angles *must* be 180° adds an additional constraint, so that f may be < 0.

Ease of metamictization must correlate in some way with structural freedom, because the fundamental question is how atoms rearrange themselves, perhaps within the confines of unaffected surrounding crystal, after a local disordering event. The criteria are not unlike those for identification of floppy (zero-frequency) mode thresholds [25] which also involves constraint counting (see also Section 4).

Given few enough constraints and sufficient structural options, the rearrangement can be arbitrary and stochastic, so that the transformation is essentially irreversible, and the crystal can be recovered only by full-scale recrystallization – for example epitaxially at the interface with unaffected crystal – given sufficient atomic mobility at high temperatures. There is therefore a strong temperature dependence for metamictization, so that some amorphizable solids will amorphize only at low or cryogenic temperatures. SiC, for example, amorphizes at room temperature at about 0.6 dpa [26], but not at 1000 K where it instead remains crystalline to displacement doses of 100 dpa and undergoes dislocation-climb-driven void swelling [27]. Silicas amorphize equally efficiently at 4 K [28] and well above room temperature.

Table 1 indicates also, where a critical radiation fluence was measured, the calculated critical energy deposited in atomic displacements to amorphize the network solids listed with energetic ions at room temperature or below. To a large extent, the order matches with broad category shifts defined by the type of connectivity. The underconnection of phosphate tetrahedra, for example, shows up very clearly in the extreme susceptibility of the pyrophosphate $Pb_2P_2O_7$ to amorphization; even though there is some edge sharing with larger Pb polyhedra, corner-sharing of three-connected $[PO_4]$ tetrahedra clearly dominates. The correlation works even for the smaller structural differences among silicates: the introduction of larger polyhedra and edge-sharing in wollastonite ($CaSiO_3$) and zircon ($ZrSiO_4$) clearly increases connectivity and decreases amorphizability. There are a few anomalies: $CaTiO_3$ and other perovskites exhibit a surprisingly low amorphization dose for strongly-ionic solids, which suggests that the large eight-coordinated alkali or alkaline-earth cation may be less important structurally than the corner-sharing octahedra. There is a precipitous increase in amorphization dose in going from silicas, in which $[SiO_4]$ tetrahedra are shared two to a vertex, to Si_3N_4, in which $[SiN_4]$ tetrahedra are shared three to a vertex; in fact, Si_3N_4 may not be amorphizable at all [29] at room temperature, some earlier reports to the contrary [30] being likely due to the influence of implanted ions at high concentration.

SiC, with four $[SiC_4]$ (or $[CSi_4]$) tetrahedra to a vertex, is only somewhat more difficult to amorphize

at room temperature than silicas or Si, and is clearly out of place with respect to its apparent redundant connectivities. SiC may be anomalous because of the arbitrariness of assigning the centers of tetrahedra to C or Si atoms (the choice of tetrahedra is not unique) and the possibility of antisite disorder; the atom sites (without regard to atom species) of β-SiC are in fact those of Si, so it may be more appropriate to consider SiC (like GaAs [30]) in the same structural category as Si. From a mechanistic point of view, the connectivity redundancy at a multiply-shared vertex represents a liability: displacement of a single vertex atom destroys four tetrahedra.

4. Structure of metamict silica

Silicas represent an informative case study for metamictization because the $[SiO_4]$ tetrahedron is evidently robust and there exist five precursor crystalline network polymorphs. Three of these (quartz, cristobalite and tridymite) with well-defined local clusters are listed in Table 2. Cristobalite and tridymite have *only* primitive six-rings, twelve in the local cluster, which encompasses respectively 29 and 27 tetrahedra. Quartz, with a much large local cluster comprising 63 tetrahedra, is dominated by primitive eight-rings; these are highly convoluted and double back on themselves, increasing the density by over 14%. Fig. 4 shows the density changes attendant upon neutron irradiation of quartz and vitreous silica; the largest rate of density change for quartz corresponds to the largest rate of loss of topological order as evidenced in diffraction observations. Fig. 5 indicates that progress to the metamict state is heteroge-
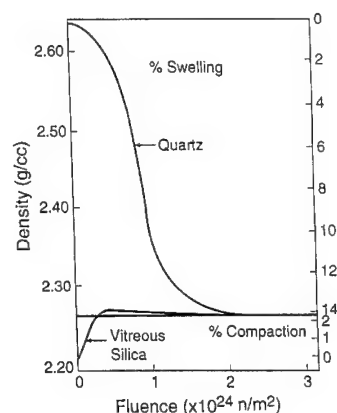

Fig. 4. Density changes in fission neutron-irradiated quartz and vitreous silica [8].

neous at this stage of neutron irradiation, with single or overlapping collision cascades providing the metamict nuclei observed to give rise to the strain-field and structure-factor contrast in the image. The highly geometric inelastic scattering in the accompanying diffraction pattern is notable in that it resembles similar distributions seen in soft phonon-mode transitions and could be associated with floppy modes involved in the restructuring. Both quartz and vitreous silica precursors approach a common terminal density during irradiation, quartz expanding by over 14%, vitreous silica compacting by almost 3%. The observed correlation of density and ring content in silicas [21] suggests that the structures of vitreous and metamict silica, with densities near that of tridymite, should be dominated by six-rings, as is found in iteratively-optimized models [33] and the best simulations currently available [34]. Similarly,

Table 2
Silica polymorph topology [21]

Polymorph	Stability regime	Density	Primitive ring content	Third neighbors	Local cluster size
Quartz	low temperature (810–1143 K)	2.65	6 6-rings 40 8-rings	30	63
Cristobalite	high temperature (1743–2001 K)	2.32	12 6-rings	24	29
Tridymite	high temperature (1143–1743 K)	2.26	12 6-rings	25	27
Metamict	low temperature	2.26	$\bar{n} \sim 6$?		
Vitreous	high temperature ($T_g \sim 1333$ K)	2.21	$\bar{n} < 6$		

assuming both metamict and vitreous silica remain fully-connected, with a small ($< 1\%$) concentration of point defects, the 3% density difference suggests that metamict silica may have on average some larger rings than vitreous silica. This may be expected also on the basis of polymorph formation temperatures, metamict silica being a low-temperature form. The lower-temperature forms of silica (quartz, keatite and, equivalently, high-pressure coesite) have larger ring sizes compared to those of the higher-temperature forms (cristobalite, tridymite, vitreous silica) [21].

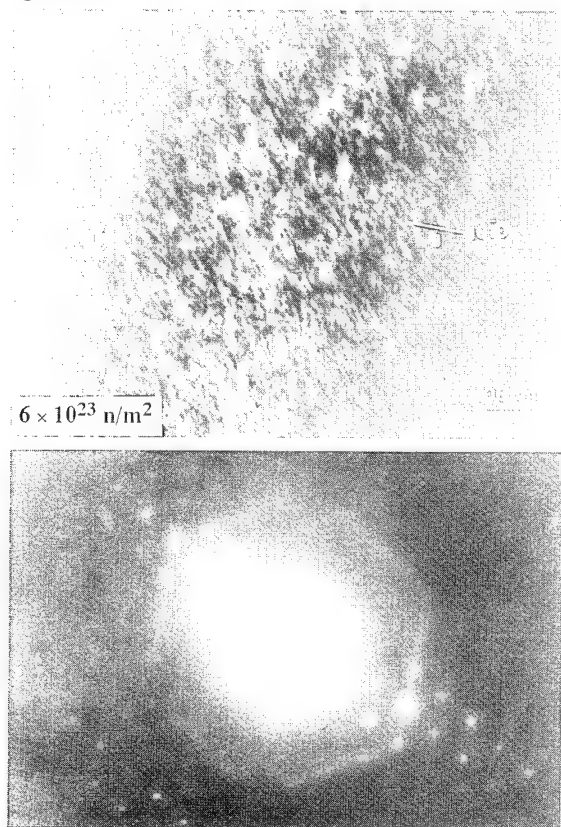Fig. 6. Proposed radiolytic displacement mechanism in tetrahedral silicas [35].

QUARTZ

Fig. 5. Weak-beam dark-field TEM image and corresponding diffraction pattern of α-quartz fission-neutron irradiated to a fluence of 6×10^{23} n/m², near the maximum rate of density change. Both structure differences and strain-field contribute to contrast in this imaging mode. The highly geometric inelastic scattering distribution in the diffraction pattern may be related to floppy modes involved in the restructuring.
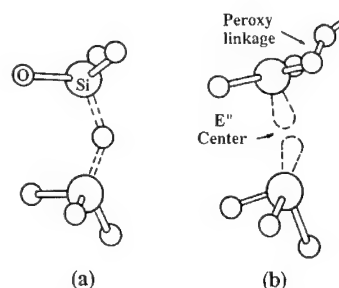
Crystalline tetrahedral silicas amorphize by electron irradiation, as shown in Fig. 1, by a more uniform radiolytic process, a proposed mechanism for which [35] is illustrated in Fig. 6. Excitonic excitation of the Si–O bond results in a configurational instability of the oxygen atom, which moves off-center and immediately (or eventually) joins a neighboring (or more distant) oxygen in an $[O_2]$ peroxy linkage. The result is an oxygen Frenkel pair: an oxygen vacancy (an E' center in some indeterminate charge state) and a molecular oxygen crowdion interstitial. Evidence for an analogous exciton-powered radiolytic displacement mechanism operating in vitreous silica has been found in paramagnetic resonance spectra after exposure to sub-gap excimer laser light [36].

In either vitreous or crystalline network silicas, generation of the Frenkel pair effectively breaks the connectivity of the silica network, and either or both adjacent $[SiO_4]$ units remaining may relax into a triangular, rather than tetrahedral, structuring polytope, with concomitant increase in structural freedom. Accumulation of a critical density of such broken linkages evidently results in local structural collapse and stochastic rebonding. The network thus restructures nearly bond-by-bond into a topologically-disordered arrangement.

Structural redundancy is particularly relevant in this case, and network silicas – having none – are locally free to restructure with even a single pair of proximate broken linkages (a bond switch), although steric considerations presumably require a rather higher critical density of breakages. Fig. 7 illustrates the orientational disorder attendant upon even one

such bond switch. The problem here is to determine how many Si–O–Si linkages need to be broken in some prescribed volume to impart local floppiness to the network sufficient to allow the rebonding; this problem is in part analogous to that addressed more globally by Thorpe [25] in tetrahedral glasses and by Dove et al. [38] in silica networks, both marginally constrained systems ($f = 0$).

The high-resolution transmission electron microscope provides a convenient source of radiolytic excitations, in the ionizing component of fast-electron energy loss, while imaging the progress of amorphization. Complete transformation takes place over a period of one to several minutes under high-resolution conditions after a total absorbed ionization dose of about 1 GGy. Of the three polmorphs described above, cristobalite transforms fastest, with tridymite not far behind; quartz is the slowest [39]. Cristobalite and tridymite progress seamlessly to the metamict state (Fig. 8(a)). The radiolytic transformation in quartz, however, must be nucleated heterogeneously – along extended defects (twin boundaries, dislocation cores), at point defect sites (e.g., hydrolyzed bonds), or at surfaces of thin-foil specimens [28]. Metamict inclusions, which begin as strained trigonal prisms [35] (Fig. 8(b)), grow until they

intersect or are engulfed by a transformation front nucleated at foil surfaces. The necessity for nucleation is apparent from Table 2. The metamict regions must expand by 14%, generating enormous accommodation strains, and – if the metamict structure is indeed dominated by six-rings as in cristobalite and tridymite – the transformation must involve a change from the 30 third-neighbor tetrahedra in quartz to 24 or 25 in the metamict region. The contrasting seamless transition from cristobalite or tridymite suggests that the structure, like the density, of the metamict state is similar to these crystalline precursors. The fact that the transformation nucleates at surfaces of quartz is also expected on the basis of there being fewer structural constraints at the surface.

The small volumes transformed under highly focussed electron beams preclude high-resolution neutron diffraction studies of the metamict state, but electron diffraction has proven convenient and surprisingly informative, despite a range of scattering vector only a quarter that accessible to neutron diffraction [40]. The result for metamict quartz (Fig. 9) shows that the radial density functions for electron-amorphized quartz and (only slightly electron-irradiated) vitreous silica are in very close agreement; the Si–O (0.16 nm) and O–O (0.26 nm) bond
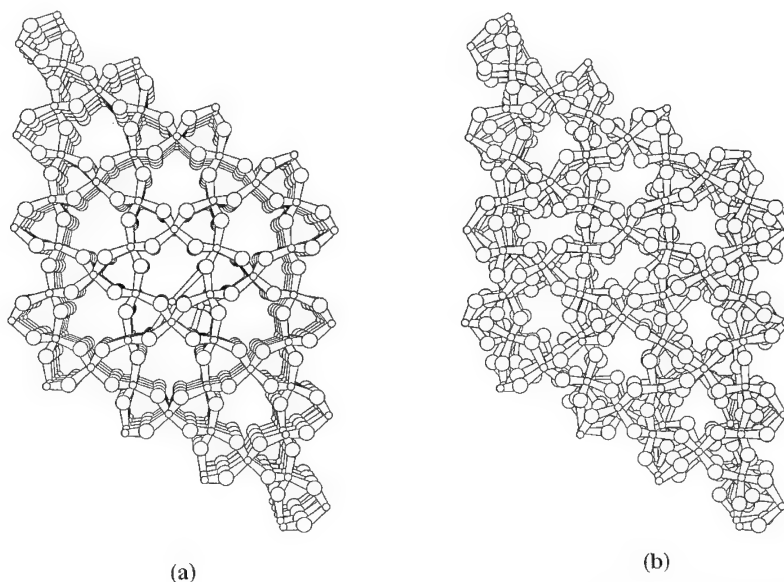

(a)   (b)

Fig. 7. Representation of 64 unit cells of α-quartz (a) with two central tetrahedra rebonded and (b) the resulting structure relaxed by minimum weighted square deviations from equilibrium interatomic distances [37].

lengths are the same as in unirradiated vitreous silica, which suggests the $[SiO_4]$ structuring tetrahedron is largely preserved intact. A small reduction in the Si–O peak area for electron-metamict quartz, corresponding to a small reduction in first-shell oxygen coordination about silicon, is in accord with the proposed radiolytic damage mechanism (Fig. 6). Neutron-metamict quartz shows significant differences – in particular, a much-reduced density of Si–O first-shell coordination, measurable change in the vicinity of the (unresolved) Si-Si correlations, and other differences at longer range. A similar comparison of polymorphic precursors (Fig. 10) reveals that, while radial density functions for

electron-metamict cristobalite and tridymite appear nearly identical, they both differ from the result for electron-metamict quartz – in particular, exhibiting a much-enhanced O–O correlation peak and a significant shift in the radial position of the intermediate-range peak at 0.4 nm. These differences were reproducible for two sets of samples, two different field-emission STEM instruments (Vacuum Generators 100 kV HB5 and 300 kV HB601) with different energy-loss spectrometers, and two different electron energies (100 and 300 keV). While a detailed interpretation of these results in terms of probable network topologies has still to be made, it is clear that both the crystalline precursor and the mechanism of
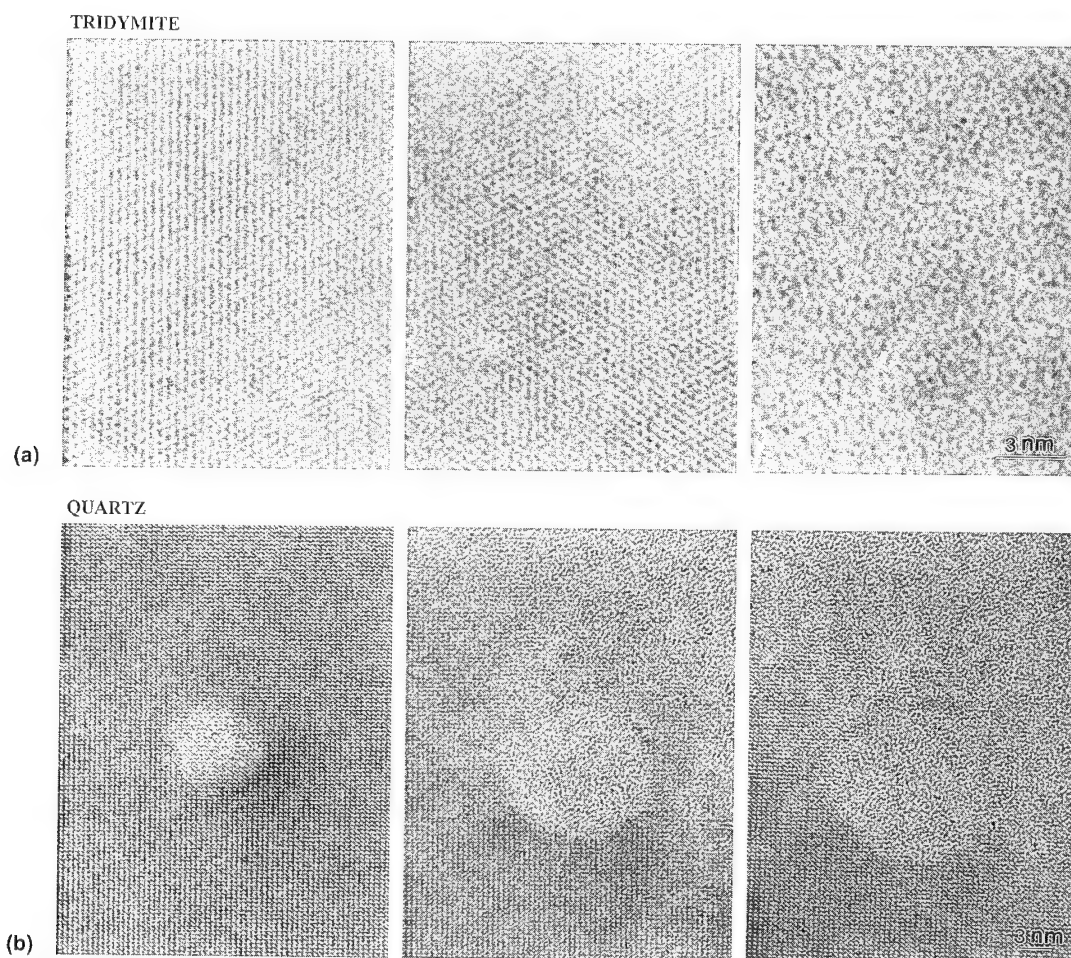

Fig. 8. Radiolytic metamictization at room temperature of 200 keV electron-irradiated silica polymorphs imaged in high-resolution TEM: (a) seamless progress to the metamict state in β-tridymite, imaged axially along [0 0 1]; (b) nucleation of strained metamict inclusions in α-quartz, imaged axially along [1 0 0].
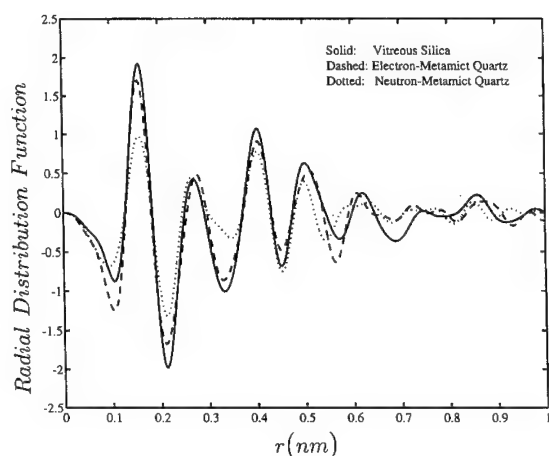
Fig. 9. Reduced radial distribution functions for vitreous silica, 100 keV electron-amorphized α-quartz and fission neutron-amorphized α-quartz, derived from energy-filtered electron diffraction [41].

formation influence the structure of the resulting metamict state.

The potenitally artefactual role of ions implanted to high concentrations in affecting amorphization – an ever-present concern in ion-induced amorphization [29] – is readily appreciated in observed changes in radial distribution functions as a function of ion fluence. Fig. 11 depicts the changes in single crystals of the pyrophosphate $Pb_2P_2O_7$ amorphized with three

Fig. 10. Reduced radial distribution functions for 100 keV electron-amorphized α-quartz, β-cristobalite and β-tridymite, derived from energy-filtered electron diffraction [41].
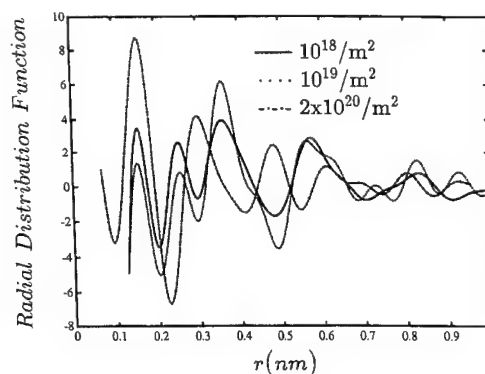

Fig. 11. Reduced radial distribution functions for single-crystal $Pb_2P_2O_7$, amorphized at room temperature by the indicated fluences of 100 keV P^+ ions, derived from energy-filtered electron diffraction [42].

different 100 keV P^+ ion fluences. While the two lower fluences yielded similar results, fluences $> 10^{20}$ ions/m² (corresponding to a peak implanted ion concentration $> 0.1\%$) yielded large shifts in the second and subsequent real-space correlation peaks. Substantial differences were similarly noted between neutron-amorphized quartz and quartz amorphized by 150 keV Si^+ ions to a fluence of 2×10^{21} ions/m². An analogous contribution from the implanted ion to the critical amorphization dose for $Pb_2P_2O_7$ or $CaTiO_3$ is unlikely in these materials, given the very low amorphization fluences ($< 5 \times 10^{16}$ 100 keV P^+ ions/m² [42] and 2×10^{18} 100 keV Pb^+ ions/m² [12], respectively) which correspond to implanted ion concentrations of $< 10^{-6}$ and 10^{-4}. An effect *has* been observed for Si_3N_4 [29] and is very likely for Al_2O_3 and MgO which amorphize only at ion fluences three to four orders of magnitude greater [23,30] and implanted ion concentrations of several percent.

In both phosphate and silica systems, ion implantation resulted in a large depression and displacement to higher q of the first sharp diffraction peak (FSDP). The evolution in the FSDP in topologically disordered silicas can clearly be seen in Fig. 12 in going from vitreous silica to electron-metamict quartz to neutron-metamict quartz to ion-implanted metamict quartz. The FSDP represents radial near-periodic propagation of characteristic intermediate-range structure over longer correlation lengths [43]; an appropriate sort of characteristically propagated in-
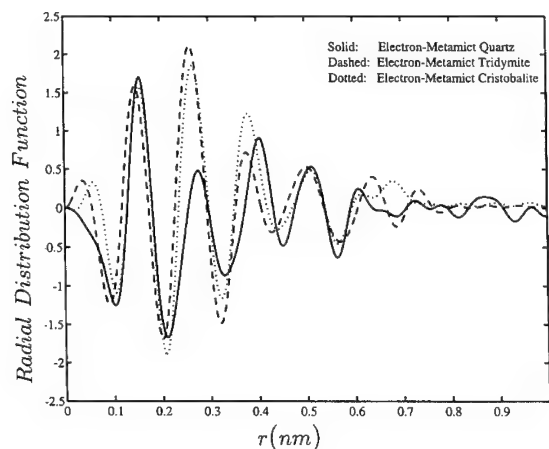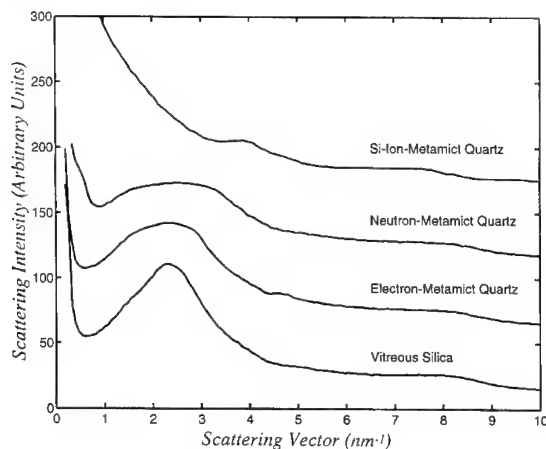
Fig. 12. The first sharp energy-filtered electron diffraction peak in vitreous silica, electron-metamict quartz, neutron-metamict quartz, and quartz rendered metamict by implantation with 2×10^{21} 150 keV Si^+ ions/m². Each pattern has been offset by 50 arbitrary intensity units from the next for clarity.

termediate-range feature could be structural voids – the void polytopes bounded by six-rings, for example – which could easily fill with implanted ions. Stuffing silica with Na^+ ions similarly quenches the FSDP [44], although without an observed shift in q.

5. Conclusions

Irradiation is an intriguing way to introduce topological disorder into network solids, and ease of amorphization provides a useful measure of the structural freedom inherent in a given structure. The topological basis for this freedom is evident from the combinatorial geometry underlying network connectivity and confirmed by the correlation of these connectivities with amorphizability. High-resolution electron microscopy provides limited information about the progress of amorphization, while electron diffraction measurements highlight the lack of uniqueness in the metamict state, whose structures depend on precursor states and irradiation modes.

References

[1] L.W. Hobbs, 'Network topology in aperiodic networks', in: Proc. 6th Int. Conf. on Non-Crystalline Materials, Prague, Aug.–Sept. 1994, J. Non-Cryst. Solids, in press.
[2] A. Hamberg, Geol. För. Förh. 36 (1914) 31.
[3] M.v. Stackelberg and E. Rottenbach, Z. Kristallogr. 102 (1939) 173, 207.
[4] W.C. Brøgger, 'Amorf', in: Salmonsens store illustrede Konversationslexikon 1 (1893) p. 742.
[5] R.C. Ewing, B.C. Chakoumakos, G.R. Lumpkin and T. Murakami, MRS Bull. XII (4) (1987) 58.
[6] H. Inui, H. Mori, T. Sakata and H. Fujita, J. Non-Cryst. Solids 116 (1990) 1.
[7] C.K. Kinoshita, Nihon Genshiryoku Gakkaishi 28 (1986) 1009.
[8] F.W. Clinard Jr. and L.W. Hobbs, in: Physics of Radiation Effects in Crystals, ed. R.A. Johnson and A.N. Orlov (Elsevier, Amsterdam, 1986) ch. 7, p. 387.
[9] L.C. Qin and L.W. Hobbs, Mater. Res. Soc. Symp. Proc. 279 (1993) 387.
[10] W.J. Weber, R.C. Ewing and L.-M. Wang, J. Mater. Res. 9 (1994) 688.
[11] P.K. Gupta, J. Am. Ceram. Soc. 76 (1993) 1088.
[12] J. Rankin, L.W. Hobbs, L.A. Boatner and C.W. White, Nucl. Instrum. Meth. B32 (1988) 28.

[13] J.F. Ziegler, J.P. Biersack and U. Littmark, The Stopping and Range of Ions in Solids (Pergamon, New York, 1985).

[14] L.C. Qin, A.J. Garratt-Reed and L.W. Hobbs, in: Proc. 50th Ann. Meeting Electron Micros. Soc. America, ed. G.W. Bailey, J. Bentley and J.A. Small (San Francisco Press, 1992) p. 350.

[15] F. Zernike and J.A. Prins, Z. Phys. 41 (1927) 184.

[16] E. Lorch, J. Phys. C2 (1969) 229.

[17] Y. Beppu, Computation News of Nagoya University 9 (1978) 123.

[18] W.L. Meier and H. Villiger, Z. Kristallogr. 129 (1969) 419.

[19] P.K. Gupta and A.R. Cooper, J. Non-Cryst. Solids 123 (1990) 14.

[20] C.S. Marians and L.W. Hobbs, Diff. Defect Data 52&53 (1987) 31.

[21] C.S. Marians and L.W. Hobbs, J. Non-Cryst. Solids 124 (1990) 242.

[22] C.S. Marians and J.K. Burdett, J. Non-Cryst. Solids 124 (1990) 1.

[23] L.W. Hobbs, Nucl. Instrum. Meth. B91 (1994) 30.

[24] G.F. Voronoi, J. Reine Angew. Math. 134 (1908) 198; J.L. Finney, Proc. R. Soc. (London) A319 (1970) 165.

[25] M.F. Thorpe, these Proceedings, p. 135; N. Mousseau and M.F. Thorpe, Phys. Rev. B48 (1993) 5172.

[26] W.J. Weber, private communication (1994).

[27] R.J. Price, J. Nucl. Mater. 48 (1973) 47.

[28] M.R. Pascucci, J.L. Hutchison and L.W. Hobbs, Radiat. Eff. 74 (1983) 219.

[29] S.J. Zinkle, Nucl. Instrum. Meth. B91 (1994) 234.

[30] P.J. Burnett and T.F. Page, Radiat. Eff. 97 (1986) 283.

[31] R. Eby, R.C. Ewing and R.C. Birtcher, J. Mater. Res. 7 (1992) 3080.

[32] J.K.N. Lindner, R. Domres and E.H. Te Kaat, Nucl. Instrum. Meth. B62 (1989) 306; J.K.N. Lindner, R. Zuschschlag and E.H. Te Kaat, Nucl. Instrum. Meth. B62 (1992) 314.

[33] L.F. Gladden, J. Non-Cryst. Solids 119 (1980) 318.

[34] P. Vashishta, A. Nakano, R.K. Kalia and I. Ebbsjö, these Proceedings, p. 59.

[35] L.W. Hobbs and M.R. Pascucci, J. Phys. (Paris) 41 (1980) C6-237.

[36] T.E. Tsai and D.L. Griscom, Phys. Rev. Lett. 67 (1991) 2517.

[37] U. Jain, A.C. Powell and L.W. Hobbs, Mater. Res. Soc. Symp. Proc. 209 (1991) 201.

[38] M.T. Dove, A.P. Giddy and V. Heine, J. Am. Cryst. Assoc. 27 (1993) 65.

[39] L.C. Qin, in: Proc. 51st Ann. Meeting Micros. Soc. America, ed. G.W. Bailey and C.L. Rieder (San Francisco Press, 1993) p. 1102.

[40] L.C. Qin and L.W. Hobbs, Mater. Res. Soc. Symp. Proc. 284 (1993) 331.

[41] L.C. Qin and L.W. Hobbs, 'Energy-filtered electron diffraction study of vitreous and amorphized silicas', in: Proc. Sixth Int. Conf. on Non-Crystalline Materials, Prague, Aug.–Sept. 1994, J. Non-Cryst. Solids, in press.

[42] A.N. Sreeram and L.W. Hobbs, Mater. Res. Soc. Symp. Proc. 321 (1994) 26.

[43] S.F. Elliott, these Proceedings, p. 40.

[44] M. Misawa, D.L. Price and K. Suzuki, J. Non-Cryst. Solids 37 (1980) 123.

Extended-range order, interstitial voids and the first sharp diffraction peak of network glasses

S.R. Elliott [*]

Department of Chemistry, University of Cambridge, Lensfield Road, Cambridge, CB2 1EW, UK

Abstract

The structural origin of the first sharp diffraction peak (FSDP), a prepeak in the structure factor of network-forming amorphous materials which exhibits anomalous behaviour with respect to temperature, pressure and composition, is ascribed to the structural ordering of interstitial voids. This void-based model gives a quantative description of the behaviour of the FSDP. The real-space quasi-periodicity in the structure of amorphous network materials necessary to produce an FSDP as a pseudo-Bragg peak has been identified in an ultra-large model of a-Si. This extended-range order is found to result from the propagation of short-range order (second-neighbour correlations) in the case of a-Si, or of medium-range order (fourth-neighbour correlations) in the case of AX_2-type materials.

1. Introduction

The nature and extent of medium-range order (MRO) in network-forming amorphous solids remains one of the most controversial issues in the field of non-crystalline materials [1,2]. One feature that has often been taken to be a signature of MRO is the so-called 'first sharp diffraction peak' (FSDP) in the structure factor of network-forming glasses and melts. However, the real-space structural origin of this peak continues to be the subject of much controversy [2–8].

It has not been clear in the past [5,7,8] precisely which peaks should be termed FSDPs since, of course, by definition, every diffraction pattern must have a first peak. In this paper, I reserve the term FSDP for those *prepeaks* to the main diffraction pattern that behave in an anomalous way compared with other diffraction peaks, as a function of temperature, pressure or composition; such FSDPs are characteristic of cross-linked network-forming amorphous solids [4,5]. A prepeak is a peak lying at a value of scattering vector, $Q_1 (= 4\pi \sin \theta / \lambda)$, smaller than Q_p, the position of the principal peak of the diffraction pattern, which is determined by the nearest-neighbour distance, r_1, in real space. For the case, for example, of a dense random packing (DRP) of hard spheres with diameter $\sigma (= r_1)$, the principal-peak position is given approximately by [8,9]

$$Q_p \simeq 7.7/r_1. \tag{1}$$

Since $Q_1 < Q_p$, this implies that a prepeak corresponds to real-space structural correlations on length scales appreciably larger than r_1 [8], i.e., in the MRO range.

Prepeaks can arise for a variety of structural reasons, and in amorphous materials with very different structures [10]. Thus, *molecular* systems, e.g.,

---

[*] Corresponding author. Tel: +44-223 336 525. Telefax: +44-223 336 362.

liquid CCl_4 [11,12] and as-evaporated films of As_4S_4 [13], exhibit intense, narrow prepeaks that result from molecular packing correlations. In such cases, the overall measured structure factor can be written as the sum of two terms:

$$S(Q) = f_m(Q) + D_m(Q), \qquad (2)$$

where $f_m(Q)$ is the molecular form factor associated with *intramolecular* scattering, and $D_m(Q)$ is the molecular-packing structure factor describing *intermolecular* interference. It is the interplay between these two terms that leads to the formation of a prepeak in this case.

Prepeaks can also occur in *ionic* amorphous systems, where a number of structural causes may be operative [10]. Perhaps the simplest mechanism is Coulombic ordering [14], wherein highly charged cations (e.g., Y^{3+} in YCl_3) are forced to be well separated due to their mutual Coulombic repulsion; this charge-induced structural ordering produces a prepeak in the cation–cation partial structure factor [14]. Similar Coulombic effects have been invoked [7,10] for $ZnCl_2$, an example of AX_2-type glass-forming materials. The charge imbalance between doubly-charged cation and singly-charged anion would be expected to lead to a depletion of cation density at the next-nearest-neighbour length scale, and beyond (i.e., in the MRO range), leading to the production of a prepeak [7,10]. Prepeaks can also arise in ionic systems as a result of a 'size-ratio effect' [10,15]; in simulations of the charged, hard-sphere AX_2 system, prepeaks appear only for values of the radius ratio, $R = \sigma_A / \sigma_X$, in the range $0.25 < R < 0.5$ [15].

From an experimental point of view, Coulombic effects do appear to be significant since prepeaks are observed for AX_2 melts [7] in the Bhatia–Thornton [16] concentration–concentration partial structure factor, $S_{CC}(Q)$, for the two-component (A, X) atom system which, in turn, is related to the charge–charge structure factor, $S_{ZZ}(Q)$, via [7]

$$S_{CC}(Q) = c_A c_X S_{ZZ}(Q). \qquad (3)$$

Such experimentally observed fluctuations in charge on MRO length scales are at variance, however, with the lack of such fluctuations found in hard-sphere simulations where, nevertheless, prepeaks are found for certain values of radius ratio, R [15]. This implies, in fact, that charge-related effects are *not*

essential to the production of prepeaks, but that network formation can play a dominant role in the formation of a prepeak or, in other words, an FSDP. This conclusion is borne out by the case of the monatomic tetravalent systems, a-Si and a-Ge, where prepeaks are also observed [6,17] and where, of course, charge interaction effects are completely absent. However, charge interactions may act to accentuate prepeak formation, when it is otherwise caused, through charge ordering effects.

2. The FSDP

Earlier in this paper, an FSDP has been defined as being a prepeak (for a network-forming amorphous material) that exhibits *anomalous* behaviour as a function of temperature, pressure or composition compared with the other peaks in $S(Q)$. In the case of the network-forming materials a-Si(Ge), AX_2-type glasses and melts (oxides and chalcogenides), etc., the FSDP lies at a value of scattering vector, Q_1, in the range $1-2$ $\mathring{A}^{-1}$.

The anomalous temperature dependence of the FSDP is that, in general, its intensity *increases* with increasing temperature (e.g., as exemplified by a-As_2S_3 [18]), unlike the other peaks in $S(Q)$ which decrease in intensity according to the normal Debye–Waller behaviour. The FSDP even persists, essentially unchanged in intensity, into the molten state of chalcogenides [7]. In this regard, v-SiO_2 seems to be somewhat anomalous since the FSDP intensity has been found to be temperature independent when measured by X-ray scattering [19], whereas it decreases with increasing temperature when measured by neutron diffraction [19]. This behaviour has been ascribed [4] to the very low thermal expansivity of v-SiO_2, together with the fact that X-ray and neutron scattering preferentially probe different types of atom pairs, themselves subject to varying degrees of dynamic disorder. By contrast, prepeaks resulting from intermolecular cluster correlations, e.g., as in CCl_4 [11], decrease in intensity with increasing temperature in the normal Debye–Waller fashion.

The anomalous pressure dependence of the FSDP is that the intensity *decreases* strongly (and shifts to larger Q) with increasing pressure, unlike the other peaks in $S(Q)$ which are relatively unaffected; this
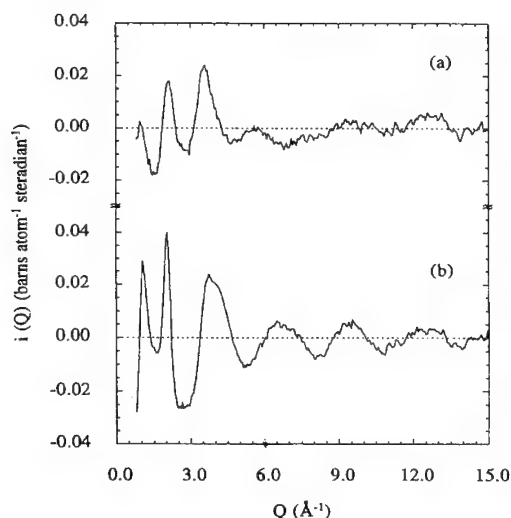
Fig. 1. Distinct neutron scattering function, $i(Q)$, for glassy $Li_2S–SiS_2$ with: (a) ^6Li enriched isotope $(b > 0)$; (b) ^{nat}Li $(b < 0)$ [25].

behaviour is observed for both glassy chalcogenides [20] and silica [21].

Finally, the FSDP is anomalous in its behaviour with composition, specifically modifier-ion content. In general, the FSDP intensity decreases strongly with increasing modifier-ion content, e.g., as in sodium silicate glasses [22] and Ag–Ge–Se glasses [23]; this behaviour is even observed for a-Ge alloyed with Mo [24]. By contrast, the behaviour of the neutron scattering FSDP intensity with incorporation of Li is anomalous; addition of Li leads to an *increase* in the peak height, as in lithium silicate glasses [22]. This behaviour has been ascribed [4] to the effect of the negative value of the neutron scattering length, b, for ^{nat}Li. This hypothesis has been verified by a neutron diffraction study of glassy $Li_2S–SiS_2$ [25], in which isotopic substitution of the Li was performed, using ^6Li $(b > 0)$ and ^{nat}Li $(b < 0)$. As can be seen from Fig. 1, of the isostructural samples, that containing the modifier having a negative b (^{nat}Li) gives the most intense FSDP.

It is clear from the above that the anomalous behaviour of the FSDP for network materials, compared with that of the other peaks in $S(Q)$, implies that it has essentially a completely different structural origin from the rest of the structure factor, by contrast, say, with the prepeaks originating from

intermolecular cluster correlations in molecular liquids and amorphous solids. This being the case, it would appear to be a valid procedure then to isolate the FSDP and to analyse its real-space structural origin, for example by means of Fourier transformation [8]. Regarding the FSDP as an isolated peak in reciprocal space, i.e., a pseudo-Bragg peak, implies that the real-space structural correlations responsible for the feature are *quasi-periodic* in nature, with an effective periodicity, R, given by

$$R \approx 2\pi/Q_1. \tag{4}$$

The correlation length, D, over which such quasi-periodic real-space density fluctuations are maintained can be obtained from the full width at half maximum (FWHM), ΔQ_1, of the FSDP using the expression [5,8]

$$D \simeq 2\pi/\Delta Q_1. \tag{5}$$

Correlation lengths in the range 15–30 Å are found in this way [6,26]. However, no attention has been paid previously to the nature and origin of such extended-range quasi-periodicity in real space necessary to generate the FSDP; this topic forms the subject of Section 4. Before that, I discuss a model for the FSDP which, uniquely at present, is capable of offering a quantitative explanation for various aspects of the FSDP.

3. Void-based model for the FSDP

It has been proposed [3,4] that the atomic-density fluctuations responsible for the FSDP can be represented by a structural model in which ordering of interstitial voids occurs in the structure: specifically, ordering of the voids is assumed to take place around cation-centred 'clusters' in the structure (e.g., $AX_{4/2}$ tetrahedra in AX_2-type glasses). That voids in an amorphous structure can lead to the production of prepeaks has also been demonstrated by Červinka et al. [27] in 2D simulations, and by Blétry [28] and Dixmier [6] in analyses of the transformation of DRP structures to low-coordination (e.g., tetravalent) structures by the incorporation of voids. The hole-inflation scheme [6] is shown schematically in the insets to Fig. 2. Starting with a DRP structure (assumed to be characterized by twelve-fold coordina-

tion in each of the two coordination shells around a central atom shown in Fig. 2(a)), holes can be introduced into the first shell such that the overall coordination becomes tetravalent and, as a result, a prepeak (FSDP) at Q_1 is produced below Q_p (Fig. 2(b)). Introduction of additional holes into the second coordination shell then converts the overall coordination from tetravalent to 4:2, characteristic of AX_2-type materials, and yet another prepeak (FSDP) is produced at Q_1' (Fig. 2(c)).

In this picture, the FSDP is simply the prepeak in the concentration–concentration structure factor, $S_{CC}(Q)$, (in the Bhatia–Thornton (BT) formalism [16]) reflecting the chemical ordering of voids in the structure represented as a packing of atoms [28], or cation-centred clusters [3,4], and voids. In this case,

Fig. 3. Partial {atom, void} structure factors in the Bhatia–Thornton formalism calculated [29] for a 13 824 atom model of a-Si [30].

Fig. 2. Structure factors for: (a) DRP-like structure (a-Ni-P); (b) a tetravalent structure (a-Si); and (c) a 4:2 structure (a-GeSe$_2$) [6]. The Q scales have been normalized to Q_p, the position of the principal peak determined by the nearest-neighbour distance. Peaks at values of Q smaller than Q_p are prepeaks, the lowest-lying being the FSDP. Shown inset are the hole-inflation rules to transform a DRP (12-coordinated) structure (a) into a four-coordinated structure (b) and a 4:2 coordinated structure (c). Filled circles in (b) and (c) are four-coordinated atoms, filled squares are two-coordinated atoms and open circles are voids.

the overall neutron scattering cross-section can be written as [16]

$$\frac{d\sigma}{d\Omega} = N\Big[\langle b\rangle^2 S_{NN}(Q) + 2\langle b\rangle(b_1 - b_2)S_{NC}(Q)$$
$$+ (b_1 - b_2)^2 S_{CC}(Q)\Big], \qquad (6)$$

where N is the number of atoms, b_i is the neutron scattering length of component i (atom/cluster or void), $\langle b\rangle = \Sigma c_i b_i$ is the compositionally-weighted average scattering length and the subscripts, N and C, refer to number and concentration, respectively.

Support for this identification of the FSDP with a chemical-order prepeak in $S_{CC}(Q)$ for an atom/cluster–void packing comes from a void analysis [29] of an ultralarge (13 824 atom) model of a-Si [30], where a strong peak in $S_{CC}(Q)$ accounts for almost all of the FSDP intensity (Fig. 3). It is significant that there is very little contribution to the FSDP from $S_{NN}(Q)$, while this function accounts for practically all the intensity of the second peak in $S(Q)$ at $Q_2 \simeq 3.5$ Å^{-1} as expected, since this is the principal peak determined by the nearest-neighbour separation.

Further support for the void-based interpretation comes from a similar analysis [4] made for a model of v-SiO$_2$, where again the FSDP is found to be due primarily to a prepeak in $S_{CC}(Q)$ for the {atom cluster, void} packing. (It should be emphasised that

the approach adopted here, and previously [3,4,17,29], is to apply the BT formalism to the structure regarded as a packing of atoms/clusters and voids; this should be distinguished from the analysis of Salmon [7], who uses the BT formalism applied to two different *atomic* species, A, X, in binary AX_2 systems.)

Blétry [28] has given a very simple formula for estimating the position of the prepeak in the atom/cluster–void $S_{CC}(Q)$, namely, the FSDP, in terms of d, the nearest-neighbour interatomic distance for monatomic, tetravalent systems, generalized to the intercluster separation (equal to the cation–cation nearest-neighbour distance) for AX_2-type materials [3,4], namely

$$Q_1 \simeq 3\pi/2d. \tag{7}$$

Use of Eq. (7), or modifications of it to take account of size differences between clusters and voids or atom–cluster overlap, give estimates for the FSDP positions in good agreement (to within 20%) with experimental values for a number of tetravalent and AX_2-type amorphous materials [3,4].

The anomalous temperature dependence of the FSDP intensity can be understood by writing the isobaric temperature dependence of the scattering intensity, I, for any peak in $S(Q)$ as [4]

$$(\partial I/\partial T)_p = (\partial I/\partial T)_\rho + (\partial I/\partial \rho)_T (\partial \rho/\partial T)_p. \tag{8}$$

For all peaks other than the FSDP, $(\partial I/\partial T)_p$ is a *negative* function since $(\partial I/\partial T)_\rho$ is negative due to the Debye–Waller effect and, although $(\partial I/\partial \rho)_T$ is found to be nearly zero or positive from simulations [31], the thermal expansivity $(\partial \rho/\partial T)_p$ is almost always negative (except, for example, v-SiO_2 at low temperatures). For the FSDP $(\partial I/\partial T)_\rho$ is still negative, but now $(\partial I/\partial \rho)_T$ is also *negative* [31], and hence the overall sign of $(\partial I/\partial T)_p$ depends on the balance between the two terms on the RHS of Eq. (8), but is generally positive. As the density of an amorphous material is increased, obviously the void volume is concomitantly reduced, and hence the prepeak intensity in $S_{CC}(Q)$ will also decrease, leading to a negative sign for the term $(\partial I/\partial \rho)_T$ [4].

For the pressure dependence of the peak intensity in $S(Q)$, the important factor is again the term

$(\partial I/\partial \rho)_T$, namely, [4]

$$\left(\partial I/\partial_p\right)_T = \left(\rho/B\right)(\partial I/\partial \rho)_T, \tag{9}$$

where B is the bulk modulus. As seen previously, for the FSDP, $(\partial I/\partial \rho)_T$ is negative and hence the pressure coefficient $(\partial I/\partial_p)_T$ should also be negative, as observed, and the estimated value [4] for the coefficient is in good agreement with experiment [20].

The void-based model also allows an understanding of the anomalous behaviour of the FSDP intensity with modifier-ion content, if it is assumed that the extrinsic atoms simply occupy some of the interstitial voids. For modifier ions with *positive* neutron scattering lengths, b, the contrast term $(b_1 - b_2)^2$ multiplying $S_{CC}(Q)$ in Eq. (6) will therefore be decreased compared with the unmodified case ($b_2 = 0$), leading to a diminution in the FSDP intensity, as observed [22–24]. On the other hand, for modifier ions having *negative* values of b, the FSDP intensity will be *increased* because of the contrast term, as found for Li-modified glasses [22] – see Fig. 1. Simulations [32] involving stuffing the interstices in a model of v-SiO_2 with Na or Li atoms show that, indeed, the incorporation of modifier ions having positive/negative neutron scattering lengths leads to a diminution/enchancement of the FSDP intensity (Fig. 4).
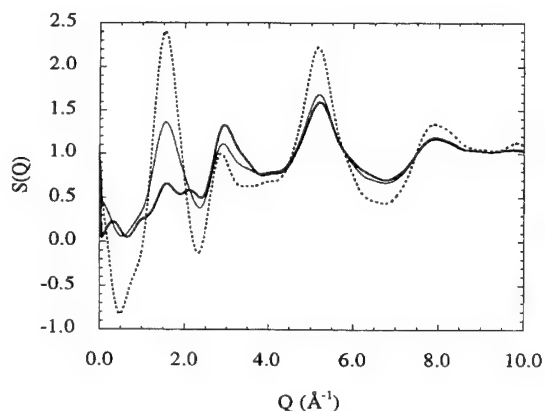

Fig. 4. Calculated total structure factors for a model of v-SiO_2 [32]: ———, unmodified; (- - - - - -) Li-stuffed; (▄▄▄▄▄) Na-stuffed. The compositions of the alkali-stuffed structures were $(M_2)(SiO_2)_2$ (M = Li, Na).

4. Origin of the extended-range real-space quasi-periodicity

Thus far, I have considered *how* FSDPs arise, but not *why* they appear. The atomic-density fluctuations in the structure of amorphous (network) materials responsible for the FSDP have been represented, equivalently, as corresponding to a packing of atoms / clusters and voids. However, the nature, and origin, of the quasi-periodicity of such atomic-density fluctuations necessary to produce the pseudo-Bragg-like FSDP has not been addressed previously. A theoretical study of oscillations in atomic density extending over correlation lengths, $D \simeq 20$–30 Å, as obtained from Eq. (5) [26], necessitates the analysis of ultralarge structural models. We have therefore analysed [17,29] the structural characteristics of ultralarge models of a-Si [30], that contain 13 824 and 110 592 atoms and have cubic box lengths of 66 and 132 Å, respectively. Even the smaller model, which has been most studied, satisfies the criterion [33] for the minimum size of model necessary to ensure that

the (discrete) calculated diffraction pattern be effectively continuous (with respect to the experimental resolution) in the region of the FSDP, namely

$$a_{min} \simeq 44.4/Q_1. \tag{10}$$

For the case of a-Si, for which $Q_1 \simeq 1.9$ Å^{-1} [34], Eq. (10) gives $a_{min} \simeq 23$ Å, considerably smaller than the actual cell dimension of $a_0 = 66$ Å.

The atom–atom RDF of the 13 824-atom model of a-Si appears effectively featureless beyond ~ 10 Å when plotted on a normal scale (Fig. 5). However, when magnified by a factor of 20, weak, but quasi-periodic, density fluctuations are evident [17], extending to the largest calculable distance of $a_0/2 (= 33$ Å). This extended-range order (ERO) is equally apparent in the atom–void and void–void partial RDFs (Fig. 6); it can be seen that ERO oscillations in the atom–atom and void–void partials are in phase with each other, and in antiphase with atom–void correlations, for $r \geq 10$ Å [29]. It should be noted in passing that the observation of such well-defined ERO in the atom–void partial RDF (Fig. 6)
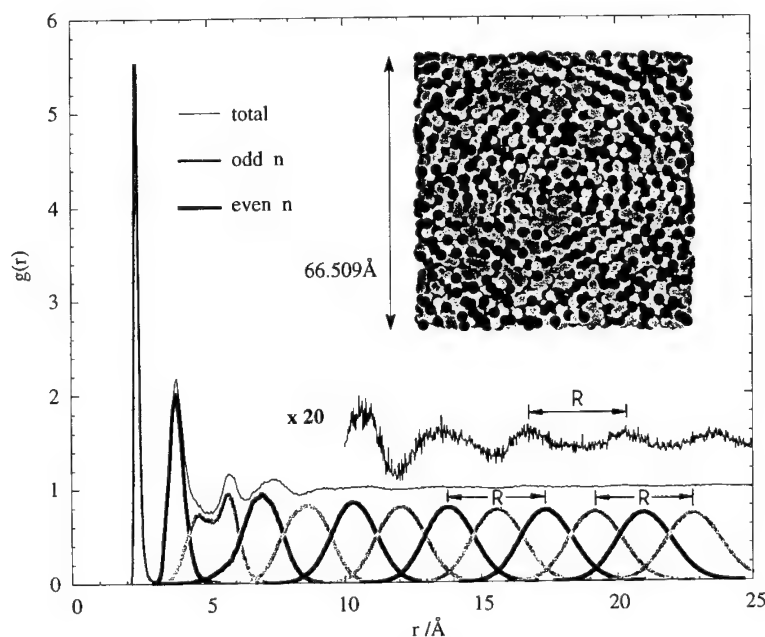
Fig. 5. RDF, $g(r)$, of a 13 824-atom model of a-Si [30] (solid line), resolved into neighbour-specific partial functions, $g_n(r)$, ($n = 1$–13), due to nth-neighbour atoms. A 20-fold magnification of the large-r portion reveals the ERO oscillations. The inset shows a projection of a 12 Å slice through the model, containing 2 476 atoms with an origin atom at the centre. Odd neighbours ($n = 1$–25) of the origin atom are drawn in grey, even neighbours ($n = 2$–26) are in black [17].

is direct evidence in support of the hypothesis for the chemical ordering of voids that forms the basis of the void model for the FSDP (Section 3).

The origin of this ERO can be begun to be understood with reference to the neighbour-specific partial pair distribution functions, $g_n(r)$, where n is the 'topological distance' between a given atom and an origin atom, which is simply the number of bonds in the shortest percolation path between the pair of atoms. It can be seen from Fig. 5 that the $g_n(r)$ distributions are remarkably well defined, and that the 'period' of the ERO oscillations, $R \simeq 3.4$ Å, averaged over the full spatial range of the oscillations, is the same as the separation between *alternate* (even–even, odd–odd) peaks in $g_n(r)$. (In fact, R is *not* strictly constant, but decreases slightly with increasing r.) This quasi-periodicity is also clearly apparent in a projection of the atomic positions in a slice of the model when the atoms are shaded according to their topological distance from a central origin atom (see inset to Fig. 5). It can be seen that the ERO quasi-periodicity exhibits *radial* symmetry about every atom, taken as origin; there is no evidence for the existence of microcrystalline domains with parallel planes of atoms. (Confusingly, the (111) interplanar spacing of the diamond–cubic crystal structure of c-Si is $d_{111} \simeq 3.2$ Å, very close to the ERO period, $R \simeq 3.4$ Å. One can speculate that

Fig. 7. Three-body conditional probability function, $\rho_{\Delta n}(\delta)$, for the probability that, given an atom 0 at the origin and another, i, at a distance r_i ($= 14 \pm 0.05$ Å) which is an nth neighbour of 0, there is a third atom, j, which is the Δnth neighbour of i, at a separation, δ, from i. The dominant distribution function is for $\Delta n = 2$, and its peak lies at $\delta \simeq 3.4$ Å. The schematic diagram shown in the inset illustrates how different conformations can lead to only a small dispersion in separations, δ, for second neighbours of i, and hence dominance of $\rho_2(\delta)$ [17].

Fig. 6. Partial RDFs for the {atom, void} system of the 13 824-atom model of a-Si [30] for the extended range of distances 10–33 Å [29].

the limiting value of the ERO period, in the limit of very large r, would, in fact, be d_{111}, since this would correspond to linear percolation paths for the topological distance between pairs of very distantly separated atoms.)

The true origin of the quasi-periodic ERO oscillations lies, we believe [17,29], in the *propagation* of structural order, but this can be understood only in terms of a three-body conditional probability distribution, rather than a conventional pair distribution function. The quantity of interest is the probability, $\rho_{\Delta n}(\delta)$, that, given an atom, 0, at the origin and another atom, i, at a distance, r_i, from the origin atom, 0, which is an nth neighbour of 0 (where n is variable), there is a third atom, j, at a distance, $\delta = r_j - r_i$, from i which is an $(n + \Delta n)$th neighbour of 0. Evaluation of $\rho_{\Delta_n}(\delta)$ for the 13 824-atom model of a-Si, with the arbitrary choice, $r_i = 14 \pm 0.05$ Å, shows [17] that the dominant $\rho_{\Delta n}(\delta)$ function is for $\Delta n = 2$ and this peaks at $\delta = 3.4$ Å (Fig. 7). A geometric explanation for this finding is shown in the inset to Fig. 7. Hence, any density fluctuation (positive or negative) at a distance, r_0, from an origin atom is preferentially propagated with a peri-

odicity of $R \simeq 3.4$ Å. Thus, it is *short-range order* (specifically next-nearest-neighbour, $\Delta n = 2$ correlations) that is propagated in the case of a-Si (or Ge). It should be noted, however, that the peak in $\rho_2(\delta)$ does not occur at the average second-neighbour separation characteristic of a-Si, namely 3.83 Å, but instead at a value appreciably smaller than this.

For the case of, say, AX_2-type materials, by analogy, it would be expected that ERO would be associated with $\Delta n = 4$ correlations (i.e., A–X–A–X–A, or even X–A–X–A–X), treating the AX_2-type structure as a decoration of a tetravalent framework of A atoms with divalent X atoms. A crude estimate of the ERO period, R, for v-SiO$_2$ can be obtained by scaling the result for a-Si to the Si–O–Si distance in v-SiO$_2$ (3.077 Å [35]) and normalizing by the nearest-neighbour Si–Si distance in a-Si (2.38 Å [30]), namely, $R(SiO_2) = 3.4 \times (3.077/2.38) = 4.4$ Å. (Such a calculation neglects the effects on $\rho_{\Delta n}(\delta)$ of fluctuations in both Si–O–Si bond angles and dihedral angles (Si–O–Si–O correlations), necessarily absent for a-Si.) In an experimental X-ray diffraction pattern [35] for v-SiO$_2$ (where Si–Si correlations are more heavily weighted), there is evidence (see Fig. 8) for a residual ERO periodicity of $R \simeq 4.1$ Å, close to the above estimate. A periodicity of $R \simeq 4.1$ Å is also necessary to give an FSDP at the observed value of $Q_1 \simeq 1.53$ Å^{-1} [33] using Eq. (4).

The quasi-periodic ERO atomic-density oscillations evident in the model of a-Si (Fig. 5), or in the experimental X-ray data for v-SiO$_2$ (Fig. 8), are what is required to produce an FSDP as a pseudo-Bragg peak, with the peak position related to the period by Eq. (4). (It should be mentioned in passing that the generally observed asymmetry in peak shape for the FSDP [33,34] can be associated with the decrease in period of the ERO oscillations with increasing r [29].) In fact, Fourier transformation of $g(r)$ for the model of a-Si for $r \geq 10$ Å shows that the weak ERO oscillations in this region contribute about half of the intensity of the FSDP [29], i.e., as much as the more intense, but much less periodic, density fluctuations in $g(r)$ for < 10 Å. However, examination of Fig. 5 shows that, although the peaks in $g(r)$ at low r may be aperiodic, the neighbour-specific partial functions, $g_n(r)$, for $n = 3$–6 approximately preserve the periodicity evident at larger r, and this periodicity in real-space atomic density contributes to the FSDP intensity.

5. Conclusions

This paper has sought to show that, by viewing the structure of network glasses as packings of atoms/clusters and voids, the FSDP is simply a chemical-order prepeak in the concentration–concentration structure factor for such a binary packing. This void-based model allows a quantitative interpretation of the position, and temperature, pressure and composition dependence of the intensity, of the FSDP. The quasi-periodic, real-space atomic-density fluctuations responsible for producing the FSDP as a pseudo-Bragg peak have been revealed in an ultra-large (13 824-atom) model of a-Si. Such extended-range order has been shown to arise from propagated short-range order in the case of a-Si (propagated medium-range order in the case of AX_2-type glasses).

Fig. 8. RDF, $r^3 D(r)$, for v-SiO$_2$ obtained from X-ray diffraction [35]. A residual periodicity with period $R \simeq 4.1$ Å is evident above the 1.65σ significance level at large r.

References

[1] S.R. Elliott, Physics of Amorphous Materials, 2nd Ed. (Longman, London, 1990).
[2] S.R. Elliott, Nature 354 (1991) 445.
[3] S.R. Elliott, Phys. Rev. Lett. 67 (1991) 711.

[4] S.R. Elliott, J. Phys.: Condens. Matter 4 (1992) 7661.

[5] S.C. Moss and D.L. Price, in: Physics of Disordered Materials, ed. D. Adler, H. Fritzsche and S.R. Ovshinsky (Plenum, New York, 1985) p. 77.

[6] J. Dixmier, J. Phys. I (Paris) 2 (1992) 1011.

[7] P.S. Salmon, Proc. R. Soc. (London) A437 (1992) 591.

[8] P.S. Salmon, Proc. R. Soc. (London) A445 (1994) 351.

[9] J. Blétry, Z. Naturforsch. 33a (1978) 327.

[10] M. Wilson and P.A. Madden, Phys. Rev. Lett. 72 (1994) 3033.

[11] M. Misawa, J. Chem. Phys. 91 (1989) 5648.

[12] M. Misawa, J. Chem. Phys. 93 (1990) 6774.

[13] M.F. Daniel, A.J. Leadbetter, A.C. Wright and R.N. Sinclair, J. Non-Cryst. Solids 32 (1979) 271.

[14] H. Tatlipinari, Z. Akdeniz, G. Pastore and M.P. Tosi, J. Phys.: Condens. Matter 4 (1992) 8933.

[15] H. Iyetomi and P. Vashishta, Phys. Rev. B47 (1993) 3063.

[16] A.B. Bhatia and D.E. Thornton, Phys. Rev. B2 (1970) 3004.

[17] A. Uhlherr and S.R. Elliott, J. Phys. Condens. Matter 6 (1994) L99.

[18] L.E. Busse, Phys. Rev. B29 (1984) 3639.

[19] S. Susman, K.J. Volin, D.G. Montague and D.L. Price, Phys. Rev. B43 (1991) 11076.

[20] Ke. Tanaka, Philos. Mag. Lett. 57 (1988) 183.

[21] S. Susman, K.J. Volin, D.L. Price, M. Grimsditch, J.P. Rino, R.K. Kalia, P. Vashishta, G. Gwanmesia, Y. Wong and R.C. Liebermann, Phys. Rev. B42 (1991) 1194.

[22] M. Misawa, D.L. Price and K. Suzuki, J. Non-Cryst. Solids 37 (1980) 85.

[23] R.J. Dejus, S. Susman, K.J. Volin and D.L. Price, J. Non-Cryst. Solids 106 (1988) 34.

[24] J.B. Kortright and A. Bienenstock, Phys. Rev. B37 (1988) 2979.

[25] J.H. Lee, A. Pradel, M. Ribes and S.R. Elliott, to be published.

[26] A.P. Sokolov, A. Kisliuk, M. Soltwisch and D. Quitmann, Phys. Rev. Lett. 69 (1992) 1540.

[27] L. Červinka, J. Komrska and J. Mikeš, J. Non-Cryst. Solids 75 (1985) 69.

[28] J Blétry, Philos. Mag. B62 (1990) 469.

[29] A. Uhlherr and S.R. Elliott, to be published in Philos. Mag.

[30] J.M. Holender and G.J. Morgan, J. Phys.: Condens. Matter 3 (1991) 7241.

[31] H. Iyetomi, P. Vashishta and R.K. Kalia, Phys. Rev. B43 (1991) 1726.

[32] J.H. Lee and S.R. Elliott, Phys. Rev. B50 (1994) 5981.

[33] A.C. Wright, R.A. Hulme, D.I. Grimley, R.N. Sinclair, S.W. Martin, D.L. Price and F.L. Galeener, J. Non-Cryst. Solids 129 (1991) 213.

[34] J. Fortner and J.S. Lannin, Phys. Rev. B39 (1989) 5527.

[35] J.H. Konnert and J. Karle, Acta Crystallogr. A29 (1973) 702.

Short and medium range order in ternary borate glasses

M. Massot, S. Souto, M. Balkanski *

Laboratoire de Physique des Solides de l'Université P. et M. Curie, associé au CNRS, 4 place Jussieu, F-75252 Paris cédex 05, France

Abstract

Low frequency Raman scattering experiments are described in ternary lithium borate glasses (B_2O_3–0.6 Li_2O–yLi_nX with $n = 1$, X = F, Cl, Br and I; or $n = 2$, X = SO_4). The 'boson peak' is analyzed in terms of a correlation length of phonon propagation and of a phonon–photon coupling. The concentration and the chemical composition dependance of the sound velocity, as well those of the structural correlation length deduced from the Raman spectra are discussed. Using a linear dependance for the coupling parameter, the experimental density of vibrational states is obtained and compared with those calculated in binary lithium borate glasses. Two different structural modifications depending on the nature of the anions of the 'doping salt' (halide or sulfate ions) are proposed to describe the glass network conformation.

1. Introduction

Raman scattering in glasses is commonly used as sensitive probe of local order, structure and coordination, by the way of examination of the frequencies, linewidths, relative intensities and degrees of polarization, of the spectral features contained in a typical spectrum. Structural glass forming units can be identified from the analysis of the high frequency part of the Raman spectra [1–4].

Although a great deal of information has been obtained from the vibrational spectra of glasses, very little is known about the nature of the 'boson peak' which is predominant in the low frequency part of the spectra. The 'boson peak' is commonly ascribed to disorder induced first order light scattering from acoustic modes. It was originally suggested that it reflects the crossover between long wavelength vibrations propagating into the continuous medium and highly localized acoustic vibrations in ordered domains [5]. For the Stokes Raman scattering, the intensity, $I(\omega)$, is proportional to the vibrational density of states, $g(\omega)$, through the expression

$$I(\omega) = C(\omega) g(\omega) [n(\omega) + 1] \omega^{-1},$$

where $C(\omega)$ is the light-vibration coupling coefficient and $n(\omega)$ is the Bose–Einstein population factor.

Recently, it has been argued that it is an excess in the density of vibrational states in the low energy range which is responsible for the 'boson peak' [6] rather than a maximum in $C(\omega)$ [7]. A characteristic

* Corresponding author. Tel: +33-1 44 27 58 94. Telefax: +33-1 44 27 58 96.

structural correlation length (SCL), $2R_c$, can be deduced using the 'boson peak' frequency, ω_{max}, and the sound velocity, V, according to $2R_c \approx V/\omega_{max}$. Different models have been proposed for the spectral dependance of the coupling coefficient, in which $C(\omega)$ is mainly proportional to ω^P [8].

Several attempts to correlate the 'boson peak' with the first sharp density peak of the static structure factor $S(q)$, have been made [9,10]. Recently, different results have been obtained and the previous 'universal' correlation between the positions of the FSDP and the 'boson peak' seems to fail [11,12].

Lorösch et al. [13] have observed, that in the binary borate glasses B_2O_3–M_2O (where M = Li, Na, K, Rb, Cs or Tl) the correlation range deduced from the Martin and Brenig model increases with the size of the modifier's cation. The structural correlation length does not exceed the dimension of two six-membered rings and the alkali oxide addition causes a decrease of the correlation range as the BO_3 triangles are transformed into BO_4^- tetraedra or as non-bridging oxygen atoms appears.

2. Short range or chemical order in borate glasses

When combined with oxygen, boron can assume either planar trigonal co-ordination or four-fold-co-ordination with sp^3 hybridization. Pure boron oxide B_2O_3 in the glassy state consists of boron atoms trigonally coordinated with oxygen, which can be associated to form six-membered boroxol rings (Fig. 1(a)) [14].

Neutron scattering investigations suggests that 60% of the boron atoms are included in boroxol rings [15]. In the boroxol rings, according to X-ray studies, the B–O–B angle is 120° and the angle of the connecting B–O–B units is about 130° [16]. Raman scattering was used by Galeener and Thorpe [17] to investigate the structure of v-B_2O_3 which presents a very sharp peak in the polarized spectra. This sharp peak in the Raman spectrum has been attributed to the symmetric vibration characteristic of the planar boroxol rings [18].

As alkali oxide modifiers are added to B_2O_3, trigonal boron atoms are transformed into fourfold or tetrahedral coordinated boron atoms. The four oxygens of each BO_4 are bridging oxygens and these units increase the coherence of the glass network. They are included initially in tetraborate units; then, with the increase of the lithium oxide content, they form diborate units with two BO_4 in next neighbouring position (Fig. 1(c)) [19]. Each tetrahedral BO_4 has a negative charge and the alkali cations are located in the vicinity of these negative sites. The ionic transport becomes possible and these glasses are ionic conductors. With the increase of the oxide content, the electrostatic interaction between negative BO_4 sites increases, the activation energy for the ionic motion decreases and the ionic conductivity increases [20].

With further addition of alkali oxide, the extra oxygens are accommodated as non-bridging oxygen atoms, one for each borate triangle [4,19]. The boron–oxygen network is depolymerized and its connectivity decreases (Fig. 1(d)). The transport properties result from the competition between two types of negative site with different binding energy for the alkali cations: the first are the BO_4^- units where the negative charge is distributed around the site and the second are the non-bridging oxygen atoms where the negative charge is localized on the B–O bond. These later sites have the deeper potential well and act as traps for the ionic transport [20]. The two mechanisms of the boron–oxygen network
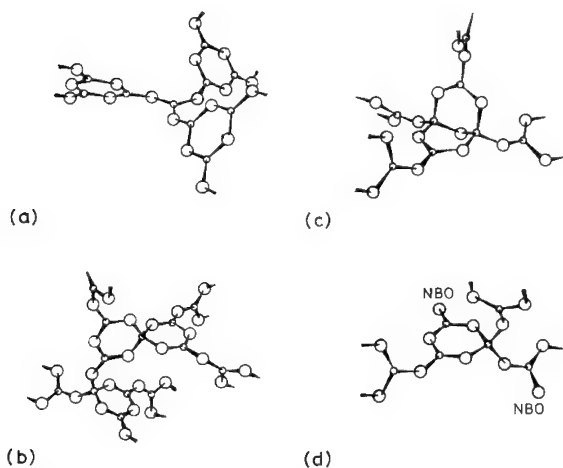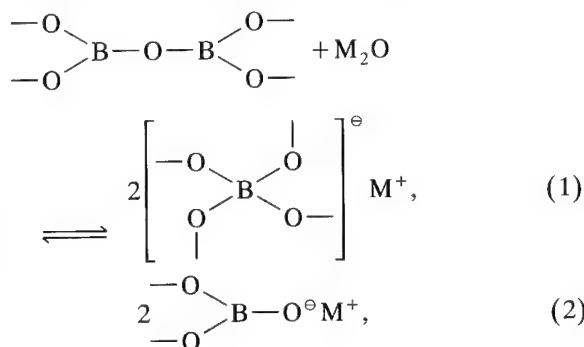

Fig. 1. Perspective of v-B_2O_3 and of some structural units in borate glasses: (a) B_2O_3 network, (b) tetraborate, (c) diborate, (d) borate network with non-bridging oxygen atoms (NBO).

modification under the addition of alkali oxides are described by the following equations:

$$2 \left[\begin{array}{c} \text{---O} \\ \text{---O} \end{array} \!\! \searrow \!\! B \!\! \diagdown \!\! \begin{array}{c} \text{O} \\ \text{O---} \end{array} \right]^{\ominus} M^+, \qquad (1)$$

$$\rightleftharpoons 2 \begin{array}{c} \text{---O} \\ \text{---O} \end{array} \!\! \searrow \!\! B \!\! - \!\! O^{\ominus} M^+, \qquad (2)$$

where the oxygen atoms labelled O^- are non-bridging atoms.

After the addition of a modifier alkali oxide, the glass former B_2O_3, becomes able to dissolve a third constituent: the 'doping salt'. The resulting ternary glass displays an enhanced cationic conductivity. If the network conformation is mainly governed by the O/B ratio, structural investigations [4] have nevertheless evidenced the role played by the anions of the 'doping salt': the four-coordinated boron atoms are redistributed inside of the matrix and the network is weakened to accommodate the halide anions interstitially. In this process, the BO_4^- ions have a tendency to form pairs included in diborate rings which contribute to the lowering of the activation energy and to the increase of the ionic conductivity.

Because of their negative charges, it is expected that the anions are located at a relatively large distance from the BO_4^- units and their repulsive interaction contributes to the weakening of the boron–oxygen matrix by the redistribution of the BO_4^- tetrahedra into the network. This is revealed also by changes in glass physical properties, such as density, molar volume or glass transition temperature, t_g [21].

Oxyanions such as SO_4^{-2} can also be used as 'doping salts' in alkali borate glasses. Spectroscopic investigations on lithium sulfo-borate have shown that lithium sulfate addition in glasses with low lithium oxide content produced the formation of four coordinated boron atoms [2]. In glasses with high modifier content near the diborate composition, lithium sulfate will induce a reconstruction of the network which affects the BO_3^- triangle (with non-

bridging oxygen atom) and the trigonal BO_3 units. In this mechanism, described by the Eq. (3), the two groups interact and will be transformed into BO_4^- tetrahedra [2,22]:
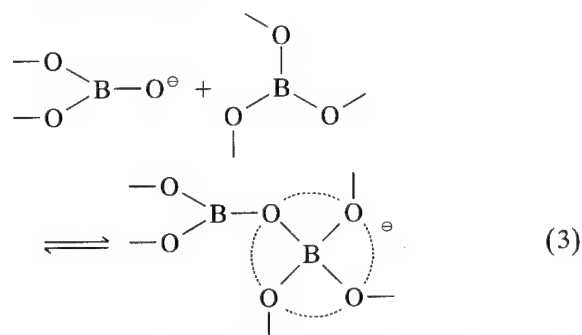
In this case diborate rings are also present in the glass and contribute by the same mechanism, as for the halogenoborates, which leads to the decrease the activation energy, and to the enhancement of the ionic conductivity.

3. Experimental techniques

Sample preparation and characterization have been described previously [4].

3.1. Measurements of the acoustic wave velocity

An acoustic pulse experimental setup, in double-transducers configuration has been used to measure the acoustic wave velocity [23] at room temperature. Samples, $4 \times 3 \times 3$ mm³, with polished faces were prepared. They were pressed between two glass buffers on which piezoelectric transducers are bonded. X-cut and Y-cut quartz transducers resonating at a fundamental frequency of 15 MHz were used for the generation and the detection of the longitudinal and transverse wave, respectively.

3.2. Measurements of the glass density

Glass density was measured by immersion in glycerine to avoid problems with glass hygroscopicity. Samples were chosen free from cracks or inclusions and were cleaned in methanol to remove surface contamination which could interfer with wetting by immersion fluid.

3.3. Light scattering spectroscopy

The Raman spectra have been recorded using the right angle scattering geometry in the spectral range 4–200 cm^{-1}. A double monochromator Jobin-Yvon U 1000 equipped with Jobin-Yvon 1800 g/mm, 500 nm 'blazed' holographic gratings was used to dispersed the scattered light. A cooled ITT FW130 photomultiplier tube (S20 cathode) and a computerized EG & G photo-counting system were used for the detection. For all the spectra reported here, the incident light was polarized in the direction perpendicular to the scattering plane while the scattered light was analyzed in a cross-polarization configuration. The low frequency spectra of all the glasses were excited with a power of about 100 mW from the 514.5 nm line of an ionized argon laser focussed on the sample. Each spectrum is the result of the averaging of 10 successive scans. A reasonable signal-noise ratio was obtained with a spectral resolution of 1 cm^{-1}.

4. Experimental results

4.1. Acoustical properties of the ternary borate glasses B_2O_3–0.6 Li_2O–yLi_nX

The elastic properties of some borate glasses have been studied by Brillouin scattering (binary glasses)
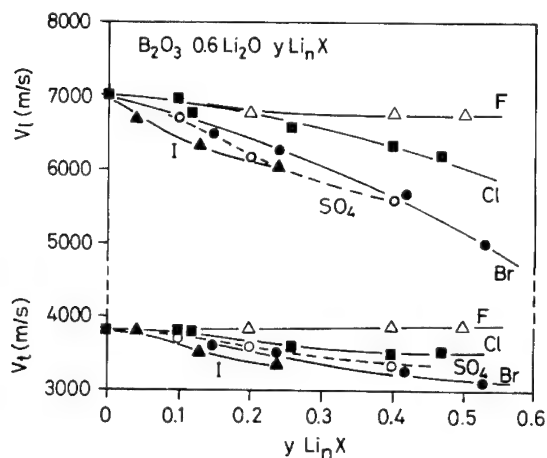
Fig. 2. Velocity of longitudinal and transverse acoustic waves, V_l and V_t, respectively, in the ternary system B_2O_3–$0.6Li_2O$–yLi_nX versus the 'doping salt' concentration.
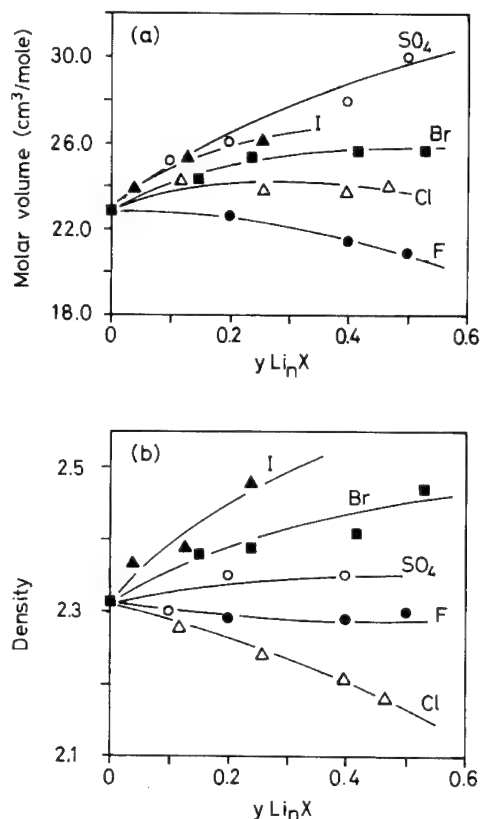
Fig. 3. Variations of the molar volume (a) and of the density (b) in the ternary system B_2O_3–$0.6Li_2O$–yLi_nX versus the 'doping salt' concentration.

[13] or by ultrasonic measurements (chloroborate glasses) [24]. The variations of the 15 MHz longitudinal and transverse acoustic wave velocities – V_l and V_t – are shown in Fig. 2 as a function of the 'doping salt' concentration, y, for different lithium salts. The measured values for the undoped glasses or for the lithium chloroborate glasses are comparable with those reported in Refs. [13,24]. A relative decrease, between 10 and 20%, of the two velocities is observed with the salt concentration and depends of the nature of the anion of the 'doping salt'.

According to the relations $V_l = (C_{11}/\rho)^{1/2}$ and $V_t = (C_{44}/\rho)^{1/2}$, where C_{11} and C_{44} are the elastic constants and ρ the density, it is clear that these variations are not due to an increase of the glass density.

In Fig. 3 are presented the variations of the molar volume and the density as a function of the dopant

concentration. The addition of lithium halide into the binary system B_2O_3–0.6 Li_2O produces an expansion of the molar volume with the increase of the anion size of the doping salt (Fig. 3(a)) except for lithium fluoride. The use of the molar volume in the discussion of the acoustical properties is preferable because the analysis in terms of density might be misleading. It is possible that dilatation of the glass network might be undetected if the mass of the ion responsible for the dilatation effect is considerably greater than that of the ion which it replaces. The density variations in such a case do not properly relate to the expansion of the network.

So, the variations of the two velocities are the result of the decrease of the elastic constants C_{11} and C_{44} produced by the weakening of the boron-oxygen network by breaking of the B–O–B bridges with the salt addition which have induced the redistribution of the BO_4^- tetrahedra that are grouped preferently by pairs to form diborate units. Spectroscopic investigations have revealed that the resulting diborates are connected between them by chains of trigonal BO_3 and BO_3^- triangles with non-bridging oxygen atoms to allow the accommodation of the lithium salt by the boron–oxygen network [25]. Fig. 4 shows that

Fig. 5. Raman spectra of B_2O_3–0.6Li_2O–yLiBr.

the network connectivity is also affected by the nature of the salt anions: heavy anions with large ionic radii produce a more important decrease of the elastic constants by distortion of the covalent network and reduction of the connectivity.

Fluoride glasses are a peculiar case because direct participation of the fluoride ions has been evidenced in nuclear magnetic resonance (NMR) experiments with the observation of BO_2F_2 and BO_3F tetrahedral units [26]. The system can be characterized as an interrupted network obtained by the cutting of the B–O–B bridges. No new diborate groups are formed [25] and the connectivity of the network is less affected by the fluoride addition. This agrees also with the behaviour of the sound velocities (Fig. 2) which present a small decrease or are practically constant with the lithium fluoride addition.

4.2. The low frequency Raman spectra in glasses

4.2.1. Medium range order in ternary borate glasses

Glasses and amorphous materials exhibit an anomalous low frequency vibrational behaviour not
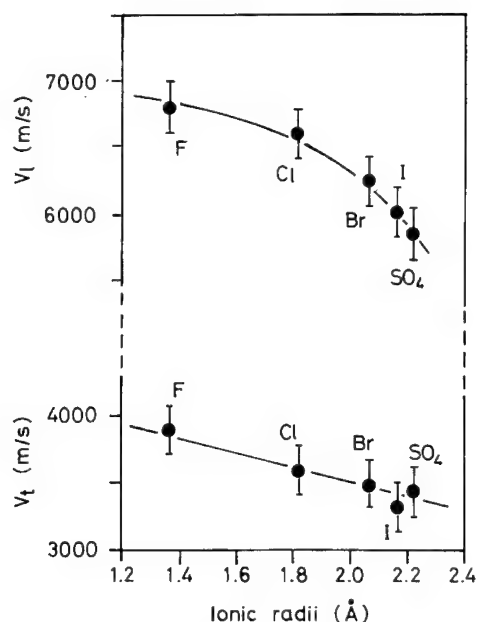

Fig. 4. Size effects on the velocity of longitudinal and transverse acoustic waves in B_2O_3–0.6Li_2O–0.26Li_nX for different anions.
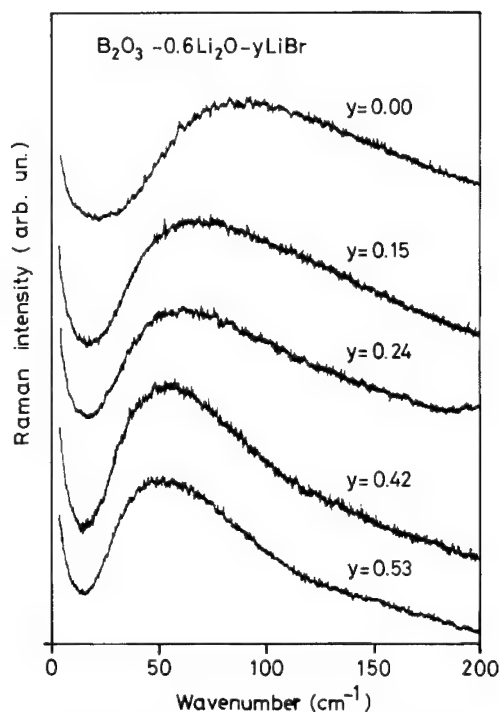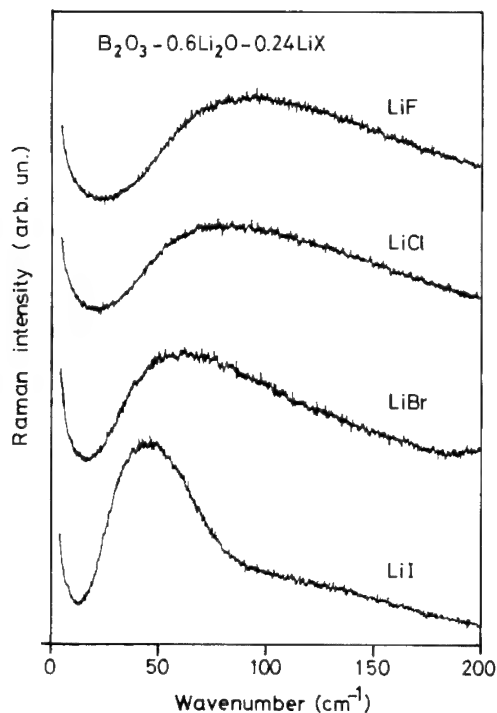
Fig. 6. Raman spectra of B_2O_3–$0.6Li_2O$–$0.24LiX$ for the four lithium halide salts.

Fig. 7. Variations of the structural correlation length, $2R_c$, as the function of the 'doping salt' concentrations in B_2O_3–$0.6Li_2O$–yLi_nX.

given glass matrix ($y = 0.24$), the frequency shift of ω_{max} to lower frequency increases with the size of the halide anions.

The frequency of the 'boson peak' has been determined by a mean-square fit of the Raman spectra around the position of the maximum with a polynomial function. Using Eq. (4) (below), the values of the structural correlation length, $2R_c$, determined by the fit of the I_{VH} intensity are plotted in

found in their crystalline forms and observed in low frequency Raman scattering [5,27], infrared absorption [28] and inelastic neutron scattering [6,29]. These anomalies are also revealed by an excess of specific heat in glasses as compared to the Debye prediction for crystals [30] and by a plateau in the thermal conductivity [31] in the temperature range 5–30 K. In the Raman spectra, the manifestation of the anomalous low frequency behaviour is exhibited by a broad peak, the 'boson peak', in the frequency range between 10 and 150 cm^{-1} [32].

The Raman spectra in the VH polarization are presented in Fig. 5 as a function of the lithium bromide concentration in the ternary system B_2O_3–$0.6 Li_2O$–$yLiBr$. The frequency of the maximum of the 'boson peak', ω_{max}, decreases as the lithium bromide content increases.

Addition of other lithium halides or lithium sulfate into the binary B_2O_3–$0.6Li_2O$ gives rise also to a systematic shift of the 'boson peak' toward the lower frequencies with the lithium salt content. Fig. 6 shows the effect of the anionic substitution, for a

Fig. 8. Size effects on the structural correlation length, $2R_c$, in the ternary glasses B_2O_3–$0.6Li_2O$–$0.24Li_nX$ for different halide anions.

Figs. 7 and 8 as a function of the 'doping salt' concentration for the different ternary systems and the ionic radii of the salt anions, respectively. The values of the structural correlation length (SCL) obtained in these ternary glasses agrees very well with those reported in binary alkali-borate glasses [13], or in lithium chloroborate glasses [37] and obtained by means of the Martin and Brenig model.

For all the salts, $2R_c$ increases with the salt content. If the variations of the SCL are small in fluoride, chloride and sulfate glasses, they are enhanced for bromide and iodide glasses. In particular, the effect of addition of lithium iodide to B_2O_3–$0.6Li_2O$ is a significant increase of the value of $2R_c$ from about 4.5 Å at $y = 0$ to 8.2 Å at $y = 0.24$. Fig. 7 shows that size effects contribute also to the variation of the SCL. For a given ne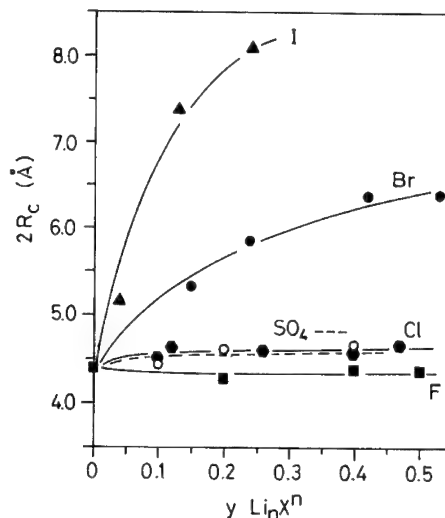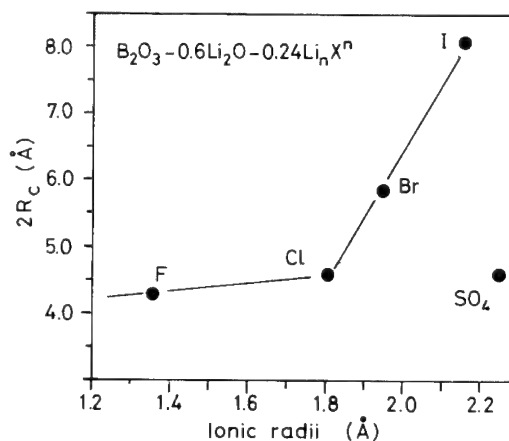twork, the SCL increases with the size of the salt anion excepted for lithium sulfate doped glasses where it seems that ion size effect can not be taken into account to explain the smallest variations of $2R_c$.

In fluoroborate or chloroborate glasses, the SCL is of about 4.5 Å, and agrees with the estimation of the average size of diborate units [38,39]. The addition of LiBr or of LiI gives rise to an enhancement of the SCL: $2R_c$ reaches 8.2 Å in iodoborate glasses. This indicates that in bromoborate and in iodoborate glasses, the medium-range order involves at least two diborate units and confirms that the BO_4^- tetrahedra have tendency to form diborate clusters to

Fig. 10. Correlation between the ionic conductivity and the structural correlation length, $2R_c$, in the ternary glasses B_2O_3–$0.6Li_2O$–$0.24LiX$ for different halide anions.

accommodate large size anions into the boron–oxygen network [25]. The comparison of the SCL values with characteristic lengths of the structure of crystalline diborate seems to indicate that the lithium halogenoborate glassy matrix consists of a random network of different ordered diborate-like configuration depending of the size of the halide anion [40].

Fig. 7 shows also that in sulfoborate glasses, the correlation length is practically unaffected by the lithium sulfate addition ($2R_c \approx 4.5$ Å). Recently, ^{11}B NMR-MAS (magic angle spinning) experiments have shown changes in the structural units by lithium sulfate addition and have pointed out the modifying action of the sulfate ions [41]. It has been found that, over a wide range of composition, addition of the lithium sulfate to a lithium borate glass promotes the conversion of the trigonal BO_3 units into BO_4^- tetraedra and that the sulfate anions are coordinated to BO_4 units and form new sulfoborate groups. Previous infrared reflectivity experiments have shown the first effect [42]. The sulfate ions induce the interaction of one trigonal BO_3 and one triangle BO_3^- with a non-bridging oxygen atom and BO_4^- tetrahedra probably grouped by pair into complexe sulfoborate units are formed. The direct participation of the sulfate ions to the glass matrix produces the reconstruction of the connectivity of the network and explains the small variations of the SCL observed in sulfoborate glasses. A possible model of reconstruc-
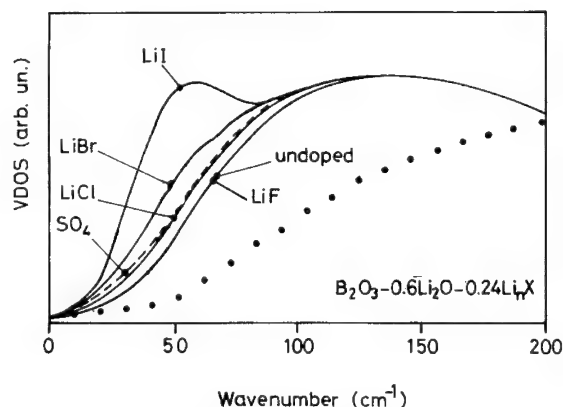

Fig. 9. Experimental vibrational density of states (VDOS) of B_2O_3–$0.6Li_2O$–yLi_nX glasses compared with the calculated VDOS of B_2O_3–$0.5Li_2O$ (●●●●) [43].
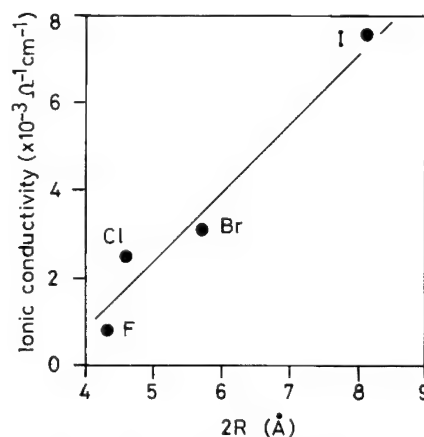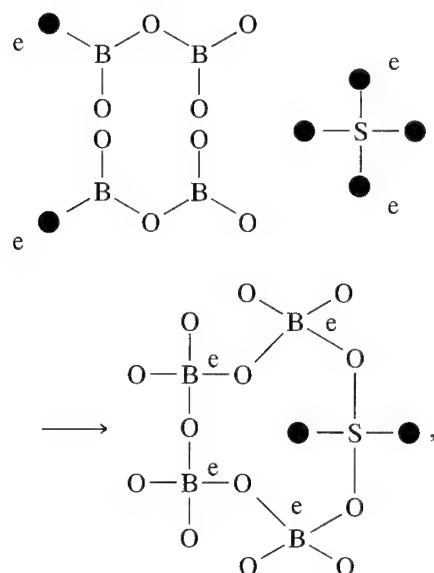
tion of the glassy network under the sulfate addition [41] is represented in the scheme

where ○ is a bridging oxygen and ● is a non-bridging oxygen.

With the assumption that the coupling coefficient, $C(\omega)$, has a linear frequency dependance in the range of the 'boson peak' [36], the vibrational density of states, $g(\omega)$, (VDOS) can be obtained and compared with those calculated by Barrio and Castillo-Alvarado [43] for binary borate glasses. The amorphous network was simulated by a Bethe lattice in which are incorporated only three structurals features: (1) the presence of tetraedral boron sites, (2) the disorder both topological and substitutional, (3) the activity of the different modes. Fig. 9 presents the comparison between the experimental curves of $g(\omega)$ for the ternary borate glasses B_2O_3–$0.6Li_2O$–$0.24Li_nX$ with those calculated for the binary system B_2O_3–$0.5Li_2O$. The calculated curves exhibit an increase of the VDOS in the low frequency range less important than that observed for the undoped glass B_2O_3–$0.6Li_2O$. This difference can be explained by the simple description used for the glass where the authors do not take account of more important structural features like tetraborate or diborate units. With the addition of lithium salts, the low frequency VDOS increases as the size of the halide anions increases. From Barrio, the main contribution to the low frequency VDOS comes from vibrations

of the bridging oxygen atoms between two three-co-ordinated boron atoms. The observed increase of the low frequency density of states with the salt addition is explained by the localization of vibrations in diborate clusters that are isolated by the weakening of the boron–oxygen network principally composed of B^{III}–O–B^{III} bridges. With the addition of a lithium salt, the covalent network is progressively weakened to accommodate anions of large size. By contrast, the small increase of the VDOS observed in the case of the sulfoborate confirms the participation of sulfate ions in the glass network conformation.

Fig. 10 shows the variation of the ionic conductivity [46] versus the correlation length in ternary halogenoborate glasses and shows that a direct correlation must exist between the ionic conductivity and the medium range order in these glasses.

5. Discussion

The anomalies in the low energy vibrational behaviour in glasses and amorphous materials are ascribed to the strong phonon scattering caused by density fluctuation domains in the amorphous network. Inside such domains, short-range and medium-range order is conserved and outside the material presents a homogeneous and isotropic structure. Phonon localization occurs when the phonon mean-free path, l, is comparable to the size of the domains $(l \approx 2R_c)$ and that is responsible for the excess of vibrational states observed in the low vibrational energy range [33].

From the Ioffe–Regel condition $(q \cdot l \approx 1)$, if q is the phonon wavevector and v is the sound velocity $(q = \omega/v)$, the structural correlation length $2R_c$, defined as the size of the domains, can be deduced from the frequency of the maximum of the 'boson peak', ω_{max}, and is given by [34]

$$2R_c \approx v/\omega_{max}. \tag{4}$$

Using the assumption that the correlation lengths of the vibrational modes are small compared to optical wavelengths, Shuker and Gammon [5] have shown that the intensity of the disorder induced one phonon contribution to the Stokes–Raman spectra can be represented by

$$I_{ij}(\omega, T) = C_{ij}(\omega) g(\omega)[1 + n(\omega, T)]/\omega, \tag{5}$$

where $n(\omega, T)$ denotes the Bose distribution at temperature T, C_{ij} is the Raman coupling coefficient, i and j are the polarization components of the incident and scattered light and $g(\omega)$ is the vibrational density of states. The anti-Stokes scattering intensity is simply obtained by replacing $1 + n(\omega, T)$ by $n(\omega, T)$ in Eq. (5). From this equation, it would be possible to determine the vibrational density of states from the Raman spectra if the frequency dependence of $C(\omega)$ is known.

Different analytical forms have been proposed to describe the spectral dependance of the coupling coefficient. Shucker and Gammon [5] have supposed that $C(\omega) = $ constant. Later, using a plane waves approximation for the acoustic vibrations, Martin and Brenig [7] have shown that $C(\omega)$ may have a more complicated frequency dependence which is

$$C(\omega) \propto \omega^2 \exp\left[-(2\omega R_c/v)^2\right], \qquad (6)$$

where v is the sound velocity. Then, $C(\omega)$ has a maximum at the frequency $\omega_{max} = v/2R_c$.

However, it was later shown, by comparison of the Raman spectra of amorphous materials with inelastic neutron scattering data which yield directly $g(\omega)$, that some of the predictions or assumptions about this model are wrong: the vibrational density of states has not Debye behaviour and the spectral dependance of the light-phonon coupling coefficient has no maximum in the frequency range of the 'boson peak' [6].

Comparison of low frequency Raman scattering spectra of various glasses with heat capacity data have shown that, in a broad frequency range, the Raman intensity is proportional to the number of vibrational excitations (vibrational density of states $g(\omega)$ multiplied by the Bose factor, $n(\omega)$) [35]. In a wide frequency range (from 5–8 cm^{-1} up to about 100 cm^{-1}) $C(\omega)$ is well approximated by a linear frequency dependance law. The linear dependance of $C(\omega)$ has been recently confirmed by comparison of low frequency Raman scattering results with vibrational density of states obtained from inelastic neutron scattering. In inorganic glasses such as SiO_2 or B_2O_3, it was found that $C(\omega) \propto \omega^2$ at very low frequency ($\omega \leq 20$ cm^{-1}) and that $C(\omega) \propto \omega$ at low frequency ($\omega \geq 20$ cm^{-1}) [36].

6. Conclusion

The description of the 'boson peak' on the basis of the phonon localization model is a useful tool to show the medium range order in glasses. In the ternary system studied here, the lithium salt addition in the binary matrix produces modifications of the medium-range ordering which depends on the concentration of lithium salt and on the size of the anion of the 'doping salt'.

In the lithium halide glasses, a redistribution of the BO_4^- units into diborate groups is observed. With large size anions such as bromide or iodide anions, the size of the BO_4^- tetrahedral cluster increases and structural correlation range, which involves at least two diborate groups, is shown. Simultaneously, the boron–oxygen network is weakened and there is localization of vibrations inside the clusters. These effects are observed in the experimental vibrational density of states which is enhanced in the low frequency range when large size halide anions are included in the glass.

The modifications of the conformation of the boron–oxygen network, observed with the lithium salts addition, are important for the ionic transport in these materials where the increase of the conductivity seems principally due to a decrease of the activation energy and not to an increase of the lithium ion concentration [44,45]. In the structural changes induced by the 'doping salt', the distance between BO_4^- groups is reduced and thus leads, by electrostatic interactions between negative sites, to a lowering of the energy barriers for the ionic motion.

References

[1] W.L. Konijnendijk, Phillips Res. Rep. suppl. 1 (1975).
[2] E.I. Katmitsos, M.A. Karakassides and G.D. Chryssikos, J. Phys. Chem. 90 (1986) 4528.

[3] M. Tatsumisago, M. Takahashi, T. Minami, N. Umesaki and N. Iwamoto, Yogyo Kyokai Shi 94 (1986) 464.

[4] M. Massot, E. Haro, M. Oueslati and M. Balkanski, in: Solid State Ionics, ed. G.A. Nazri, R.A. Huggins and D.F. Shriver, Materials Research Symposium Proceedings, Vol. 135 (Materials Research Society, Pittsburgh, PA, 1989) p. 207.

[5] R. Shuker and R.W. Gammon, Phys. Rev. Lett. 25 (1970) 222.

[6] V.K. Malinowski, V.N. Novikov, P.P. Parshin, A.P. Sokolov and M.G. Zemlyanov, Europhys. Lett. 11 (1990) 43.

[7] A.J. Martin and W. Brenig, Phys. Status Solidi b64 (1974) 163.

[8] E. Duval, N. Garcia, A. Boukenter and J. Serughetti, J. Chem. Phys. 99 (1993) 2040.

[9] A.P. Sokolov, A. Kisliuk, M. Soltwish and D. Quitmann, Phys. Rev. Lett. 69 (1992) 1540.

[10] S.R. Elliott, Phys. Rev. Lett. 67 (1991) 711.

[11] L. Börjesson, A.K. Hassan, J. Swensson and L.M. Torell, Phys. Rev. Lett. 70 (1993) 1275.

[12] L. Börjesson, A.K. Hassan, J. Swensson and L.M. Torell, Phys. Rev. Lett. 70 (1993) 4027.

[13] J. Lorösch, M. Couzi, J. Pelous, R. Vacher and A. Levasseur, J. Non-Cryst. Solids 69 (1984) 1.

[14] J. Krogh-Moe, Phys. Chem. Glasses 6 (1966) 46.

[15] P.A.V. Johnson, A.C. Wright and R.N. Sinclair, J. Non-Cryst. Solids 50 (1982) 281.

[16] R.L. Mozzi and B.E. Warren, J. Appl. Crystallogr. 3, (1970) 251.

[17] F.L. Galeener and M.F. Thorpe, Phys. Rev. B28 (1983) 5802.

[18] F.L. Galeener, R.A. Barrio, E. Martinez and R.J. Elliott, Phys. Rev. Lett. 53 (1984) 2429.

[19] P.J. Bray, J. Non-Cryst. Solids 95&96 (1987) 45.

[20] M. Massot, M. Balkanski and A. Levasseur, in: Microionics-Solid State Integrable Batteries, ed. M. Balkanski (Elsevier, Amsterdam, 1991) p. 139.

[21] D.P. Button, R. Tandon, M.H. Velez, H.L. Tuller and D.R. Uhlmann, J. Non-Cryst. Solids 49 (1982) 129.

[22] M. Massot, C. Julien and M. Balkanski, Infrared Phys. 29 (1989) 775.

[23] M. Balkanski, S. Souto, D. Ivanov and D. Royer, in: Solid State Ionics, ed. M. Balkanski, T. Takahashi and H.L. Tuller (Elsevier, Amsterdam, 1992) p. 381.

[24] M. Devaux, J.Y. Prieur and W. Wallace, Solid State Ionics 10 (1983) 593.

[25] M. Massot, C. Julien and M. Balkanski, Infrared Phys. 29 (1989) 775.

[26] D. Kline and P.J. Bray, Phys. Chem. Glasses 7 (1966) 41.

[27] R.J. Nemanich, Phys. Rev B16 (1977) 1665.

[28] U. Strom and P.C. Taylor, Phys. Rev B16 (1977) 5512.

[29] U. Buchenau, M. Prager, N. Nücker, A.J. Dianoux, N. Ahmad and W.A. Phillips, Phys. Rev. B34 (1986) 5565.

[30] N. Ahmad, K.W. Hutt and W.A. Phillips, J. Phys. C19 (1986) 3765.

[31] J.E. Graebner, B. Golding and L.C. Allen, Phys. Rev. B34 (1986) 5696.

[32] V.K. Malinowski and A.P. Sokolov, Solid State Commun. 57 (1986) 757.

[33] E. Akkermans and R. Maynard, Phys. Rev. B32 (1985) 7850.

[34] S.R. Elliott, Europhys. Lett. 19 (1992) 201.

[35] A.P. Sokolov, A. Kisliuk, D. Quitmann and E. Duval, Phys. Rev. B48 (1993) 7692.

[36] T. Achibat, A. Boukenter and E. Duval, J. Chem. Phys. 99 (1993) 2046.

[37] L. Borjesson, in: Dynamics of Disordered Materials, ed. D. Richter, A.J. Dianoux, W. Petry and J. Texeira (Springer, Berlin, 1989) p. 316.

[38] J. Chandrasekhar, J.G. Andrade and P.R. Schleyer, J. Am. Chem. Soc. 103 (1981) 5609.

[39] N. Uschida, T. Maekawa and T. Yokokawa, J. Non-Cryst. Solids 85 (1986) 290.

[40] J. Krogh-Moe, Acta Crystallogr. B24 (1968) 179.

[41] P. Mustarelli, S. Scotti, M. Villa and P.R. Gandhi, Solid State Ionics 39 (1990) 217.

[42] M. Massot, C. Julien, M. Balkanski, A. Krol and W. Nazarewicz, Mater. Sci. Eng. B3 (1989) 307.

[43] R.A. Barrio and F.L. Castillo-Alvarado, Phys. Rev. B46 (1992) 13779.

[44] D.P. Button, PhD thesis, Cornell University (1972).

[45] I. Darianian, thèse de l'Université P. et M. Curie (1988).

[46] A. Levasseur, J.C. Brethous, J.M. Reau, P. Hagenmullers and M. Couzi, Solid State Ionics 1 (1980) 177.

Molecular dynamics simulations of covalent amorphous insulators on parallel computers

Priya Vashishta [a,*], Aiichiro Nakano [a], Rajiv K. Kalia [a], Ingvar Ebbsjö [b]

[a] *Concurrent Computing Laboratory for Materials Simulations, Department of Physics and Astronomy and Department of Computer Science, Louisiana State University, Baton Rouge, LA 70803-4001, USA*
[b] *University of Uppsala, Studsvik Neutron Research Laboratory, S-61182 Nyköping, Sweden*

Abstract

Algorithms are designed to implement molecular dynamics (MD) simulations on emerging concurrent architectures. A highly efficient multiresolution algorithm is designed to carry out large-scale MD simulations for systems with long-range Coulomb and three-body covalent interactions. Large-scale MD simulations of amorphous silica are carried out on systems containing up to 41 472 particles. The intermediate-range order represented by the first sharp diffraction peak (FSDP) in the neutron static structure factor shows a significant dependence on the system size. Correlations in the range 4–11 Å are found to play a vital role in determining the shape of the FSDP correctly. The calculated structure factor for the largest system is in excellent agreement with neutron diffraction experiments, including the height of the FSDP. Molecular dynamics simulations of porous silica, in the density range 2.2–0.1 g/cm^3, are carried out on a system of 41 472 particles. The internal surface area, pore surface-to-volume ratio, pore-size distribution, and other structural correlations are determined as a function of the density. Various dissimilar porous structures with different fractal dimensions are obtained by controlling the preparation schedule and temperature. Pore interface growth and the roughness of internally fractured surfaces in silica glasses are investigated by MD simulations of 1.12 million particles. During uniform dilation, the pores coalesce and grow in size. When the mass density is reduced to 1.4 g/cm^3, the pores grow catastrophically to cause fracture. The roughness exponent for fracture surfaces, $\alpha = 0.87 \pm 0.02$, supports experimental claims about the universality of α. The nature of the phonon density-of-states due to low-energy floppy modes in crystalline and glassy states of the high-temperature ceramic Si_3N_4 is investigated. Floppy modes appear continuously in the glass as the connectivity of the system is reduced. In the crystal, they appear suddenly at 30% volume expansion. The density-of-states due to the floppy modes varies linearly with energy, and the specific heat is significantly enhanced by the floppy modes.

1. Introduction

Despite significant recent developments in materials simulation techniques [1–11], the goal of reliably predicting the properties of new materials in advance of fabrication and measurement has not yet been achieved. The primary reason for this lack of success is the inability of sequential machines to handle large-scale simulations. For example, molecular dynamics (MD) simulations for long-range interactions scale as N^2 where N is the number of particles in the system. In many physical systems, the desired system sizes are in the range of 10^6 particles. These are beyond the computing power of most sequential

* Corresponding author. Tel: +1-504 388 1157. Telefax: +1-504 388 5855. E-mail: priyav@bit.csc.lsu.edu.

machines. However, the MD technique has considerable inherent parallelism. By exploiting this parallelism on emerging parallel architectures, it is possible to perform large-scale simulations for complex materials [3–6].

Diffraction experiments provide useful information about structural correlations in glasses. The intermediate-range order (IRO) of covalently bonded oxide and chalcogenide glasses manifests itself as the first sharp diffraction peak (FSDP) in diffraction patterns [12–14]. Molecular dynamics simulations have been used successfully to investigate the microscopic origin of the FSDP [15]. The FSDP in $GeSe_2$ has been shown to arise mainly from Ge–Ge and Ge–Se correlations between 4 and 10 Å [15]. To investigate the IRO by MD simulations, special attention must be paid to finite-size effects in simulations. Typical MD simulations containing less than 1000 particles have linear dimensions of ~ 25 Å. In such small systems, the periodic boundary condition may impose additional implicit constraints on the IRO which supposedly extends up to 10–15 Å [14]. We have performed MD simulations on amorphous SiO_2 systems containing up to 41 472 particles to investigate the finite-size effect on the IRO [16].

There has been a growing interest in porous materials because of their many technologically important applications [17–23]. Much of the recent work has focused on aerogel silica, a form of porous SiO_2 which is prepared by hypercritical drying of an alcoholic silica gel. It is an environmentally safe material with a large thermal resistance which makes it a suitable alternative to chlorofluorocarbon (CFC) foamed plastic in thermal insulation of commercial and household refrigerators [17]. The application of porous glasses results from their unique selective separation capabilities, molecular transport, thermal resistance and mechanical properties. All of these characteristics depend crucially on structural correlations such as the pore size, internal surface area, surface-to-volume ratio, and interface texture.

In recent years, a great deal of progress has been made in understanding the morphology of surfaces and interfaces. Scale-invariant surface fluctuations related to different growth processes have been observed in a wide variety of systems [24,25]: vapor deposition; fluid flow in porous media; sedimentation of granular materials; and thin-film growth. The

root mean square surface fluctuations averaged over a distance, l, obey the scaling relation [24,25], $W \propto l^{\alpha}$. Recent experiments on a wide variety of materials reveal that fracture surfaces exhibit the scaling properties with the roughness exponent, $\alpha \approx 0.8$ [26,27]. This has led to the suggestion that the roughness exponent for fracture surfaces has a universal value. However the universality of the roughness exponent on the nanometer scale is still an unresolved issue [28].

We investigate the structural correlations [23] and the roughness of internally fractured surfaces in SiO_2 glasses [29] by MD simulations on systems of 1.12 million particles using parallel computer architectures. Interparticle potentials used in our simulations include two-body (V_2) and three-body (V_3) terms [30,31].

Silicon nitride is a very promising material for high-temperature applications [32,33]. It has a strong resistance against thermal shock, high strength at high temperatures, corrosion resistance against fused metals, chemical inertness and oxidation resistance at high temperatures. Because of these excellent characteristics, there are numerous applications of silicon nitride as engineering components. Amorphous silicon nitride, prepared by chemical vapor deposition (CVD), is used as a dielectric layer in microelectronics technology.

We have investigated the low-energy modes in silicon nitride with MD simulations. Low-energy modes play an important role in determining the properties of glasses. Phillips introduced the idea of *underconstrained* and *overconstrained* glasses in terms of the number of constraints, n_c, and the degrees of freedom, n_d [34]. Thorpe extended these ideas and introduced the notion of rigidity percolation, where a glass at lower coordinations may be viewed as consisting of rigid and floppy regions [35,36]. In an idealized random network model, the rigidity percolation transition is found when the average coordination, $\langle r \rangle$, reaches a critical value, $\langle r_c \rangle = 2.4$; for $\langle r \rangle < 2.4$, there is a finite fraction of zero-energy modes in the network. If additional stabilizing interactions are added to improve the mechanical stability of the network, the rigidity percolation transition is washed out [36]. However, even for $\langle r \rangle$ greater than $\langle r_c \rangle$ there are floppy regions in the glass which give rise to low-energy modes rather

than zero-energy modes, as envisioned in the original analysis [37–40].

In our MD simulations for the high-temperature ceramic silicon nitride, low-energy modes emerge in the amorphous and crystalline systems under uniform external negative pressures. In the glass, the number of low-energy floppy modes increases continuously with a decrease in the density and the average coordination of the system. The behavior of Si_3N_4 crystal is quite unusual: upon expansion from 3.2 to 2.8 g/cm^3, the crystal undergoes distortions due to stretched N–N bonds (the Si–N bond length remains unchanged) and the maximum energy, ω_{max}, in the density-of-states (DOS) shrinks by 30%. With further expansion to 2.4 g/cm^3, the crystal undergoes sudden decohesion which transforms it into an amorphous state. At the same time, the DOS at low energy exhibits a linear region due to floppy modes. In addition, ω_{max} increases by 30% and it continues to increase as the density of the system is further lowered. ω_{max} for the amorphous system at 2.0 g/cm^3 is 15% higher than ω_{max} for the crystal at the normal density (3.2 g/cm^3). Low-energy floppy modes cause a substantial enhancement in the specific heat over the temperature range of 50–400 K.

In this paper, we describe our recent work on parallel algorithms for the MD approach and simulation results for structural and dynamical properties of network glasses. The outline of this paper is as follows. Parallel MD algorithms are discussed in Section 2. Finite-size effects on the intermediate-range order in amorphous SiO_2 are analyzed in Section 3. Simulation results for structural properties of porous SiO_2 glasses and the roughness of fracture surfaces in SiO_2 glasses are discussed in Sections 4 and 5, respectively. Section 6 contains simulation results on low-energy floppy modes in Si_3N_4. Concluding remarks are given in Section 7.

2. Parallel molecular dynamics algorithms

The MD approach has played a key role in our understanding of physical systems [1]. In the MD approach, one obtains the phase-space trajectories of particles from the numerical solution of Newton's equations. Physical properties of a system are calculated from phase-space trajectories of the constituent particles.

For systems with a finite-range interparticle interaction, an efficient way to calculate interparticle interactions is to use the linked-list method [1]. A major advantage of the linked-cell list technique is that the computation time is proportional to the number of particles, N. Further, with the linked-list method the minimum-image convention can be implemented efficiently on distributed-memory multiple instruction multiple data (MIMD) machines [4–6].

The computation of forces can be further reduced with the multiple time-step (MTS) approach [2]. The MTS approach exploits the fact that the force experienced by a particle can be separated into a rapidly varying primary component and a slowly varying secondary component. The primary interaction arises from nearest neighbors of a particle (within a range of r_a), whereas the secondary forces are due to other particles within its range of interaction. The primary component is calculated at every MD step. On the other hand, the secondary component is calculated at intervals of five and 15 steps. In between, the secondary component is extrapolated according to the Taylor series.

We have used the divide-and-conquer strategy based on domain decomposition [3] to implement the parallel MTS–MD algorithm [4,5]. The total volume of the system is divided into p subsystems of equal volume, and each subsystem is assigned to a node. The data associated with particles of a subsystem are assigned to the corresponding node.

The three-body force calculation is a time-consuming part of the MTS–MD algorithm. Speed-up of the three-body force calculation is achieved by decomposing the three-body potential into a separable form [5,7].

The most prohibitive computational problem is associated with the Coulomb potential. Because of its long range, each atom interacts with all the other atoms in the system. Therefore the evaluation of the Coulomb potential for an N-particle system requires $O(N^2)$ operations, which makes large-scale MD simulations difficult. Recently, we have implemented MD simulations involving the Ewald summation [8] for Coulomb interaction on distributed-memory MIMD machines [4]. The parallel algorithm we have designed for the Ewald summation reduces the com-

putational complexity from $O(N^{3/2})$ to $O(N)$. This is achieved by ensuring that both the real-space and Fourier-space contributions scale linearly with the size of the system while maintaining the desired level of precision – 0.01% in the total potential energy.

Recent hierarchical algorithms [9,10] have revolutionized the computation of the Coulomb potential. The fast multipole method (FMM) uses the truncated multipole expansion and local Taylor expansion for the Coulomb potential field [10]. By computing both expansions recursively on a hierarchy of cells, the Coulomb potential is computed with $O(N)$ operations. In many materials simulations, periodic boundary conditions are used to minimize surface effects. The summation over infinitely repeated image charges must be carried out to compute the Coulomb potential. Ding et al. have developed the reduced cell multipole method (RCMM) which makes the computation of the Coulomb potential feasible for multimillion-particle systems with periodic boundary conditions [11]. In the RCMM, distant images of multimillion particles are replaced by a small number of fictitious particles with the same leading multipoles as the original system. With little computational effort, the Ewald summation is applied to these reduced images. We have developed a highly efficient MD algorithm based on multiresolutions in both space and time [6]. The long-range Coulomb potentials in periodic systems are calculated with the RCMM and FMM, while the intermediate-range,
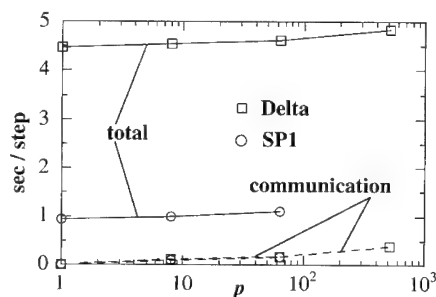
Fig. 2. Execution time (solid curves) and communication time (dotted) per MD time step for SiO_2. Circles and squares represent the results on the IBM SP-1 and Intel Touchstone Delta, respectively. Here p is the number of nodes. The size of the system, N, increases as $8232 p$.

non-Coulombic potentials are calculated by the MTS method (see Fig. 1).

Performance of the multiresolution algorithm is tested for SiO_2 systems on the 512-node Intel Touchstone Delta machine at Caltech and the 128-node IBM SP-1 system at Argonne National Laboratory [6]. Fig. 2 shows the execution time per MD step as a function of the number of processors, p. The number of particles is taken to be $8232 p$. For a 4.2 million particle system, the program requires only 4.84 s per MD step on the 512-node Delta. Communication accounts for only 8% of the total elapsed time. On the IBM SP-1, the computation part runs 4.8 times faster than on the Delta, while the communication performs at about the same speed.

(a) (b) (c)
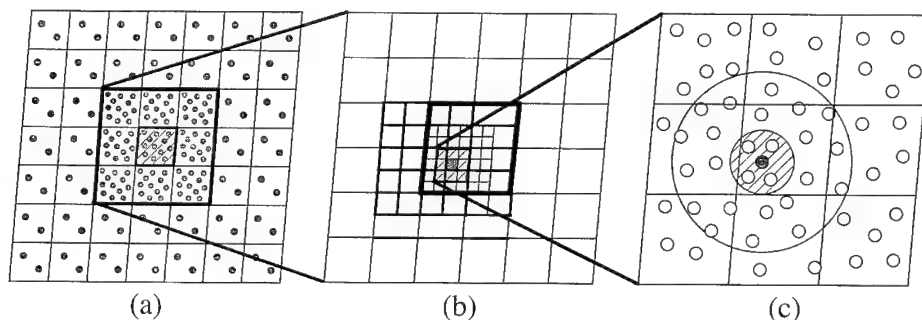
Fig. 1. Multiresolution in space. (a) Periodically repeated images of the original MD box. Replacing far images by a small number of particles with the same multipole expansion up to a certain order reduces the computation enormously while maintaining the necessary accuracy. (b) A hierarchy of cells used in the fast multipole method. (c) The near-field force on a particle is due to primary, secondary and tertiary neighbor particles.
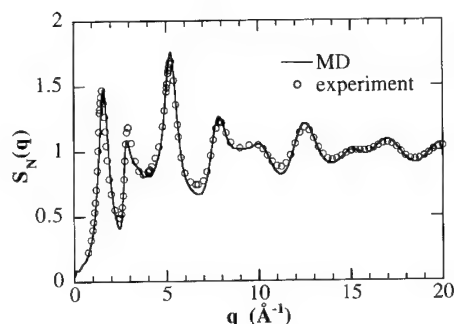
Fig. 3. Neutron-scattering static structure factor of amorphous SiO$_2$. ———, the MD result for a 41 472-particle system at 300 K; ○, neutron diffraction experiment [42] at 10 K.

3. First sharp diffraction peak and intermediate-range order in amorphous silica

Molecular dynamic simulations are performed for normal-density (2.2 g/cm^3) amorphous SiO$_2$ systems of three different sizes, i.e., the numbers of particles, $N = 648$, 5184, and 41 472. Periodic boundary conditions are imposed on the systems.

In Fig. 3, the solid curve represents the MD result for the neutron-scattering static structure factor calculated at 300 K for a 41 472-particle system. Results of neutron diffraction experiments are represented by open circles [42]. The MD result agrees well with the neutron diffraction experiment, including the height of the FSDP. Among the different system sizes, little difference in the pair distribution function is observed. The finite size, however, does affect the neutron-scattering static structure factor calculated from the Fourier transform of the pair distribution function. The height of the FSDP depends strongly on the system size. The height of the FSDP increases rapidly with increased system size, but then saturates. The asymptotic value ~ 1.5 agrees very well with neutron diffraction experiments [42]. The correlations in the range 4–11 Å has been shown to play a vital role in the shape of the FSDP [16].

4. MD simulations of porous silica

Structural correlations in porous silica span many hierarchical regimes. The short-range (< 4 Å) corre-

lations are known to arise from the structure of the SiO$_4$ tetrahedral unit [30]. The intermediate-range (4–11 Å) correlations, manifested as the first sharp diffraction peak (FSDP) in neutron- and X-ray diffraction experiments, arise from the connectivity of the tetrahedral units [30,16]. Both these correlations exist at normal density as well as in low-density amorphous silica. Beyond the intermediate range, small-angle neutron scattering (SANS) [18,19] and small-angle X-ray scattering (SAXS) [20,21] experiments on porous silica reveal a fractal structure.

The first MD simulation of 1500-particle porous SiO$_2$ was performed by Kieffer and Angell [22]. We present the results of our MD simulations of porous SiO$_2$ at densities in the range of 2.2–0.1 g/cm^3 [23]. The first system we simulated consisted of 41 472 Si and O atoms. Even at the lowest density, 0.1 g/cm^3, the length of the MD box (240 Å) covers all the hierarchical correlation regimes mentioned above. Simulations reported here took 1200 h on the eight-node iPSC/860 system at CCLMS.

The porous SiO$_2$ systems are prepared by successive uniform expansions of a well thermalized glass at the normal glass density 2.2 g/cm^3 and 300 K [22,23]. At the condensed amorphous phase above 1.6 g/cm^3, the amorphous system possesses only short- and intermediate-range correlations. However, as the density is lowered below 1.6 g/cm^3, density fluctuations that give rise to pores of various sizes set in. A close examination of these snapshots reveals self-similarity at length scales between 5 and 25 Å.
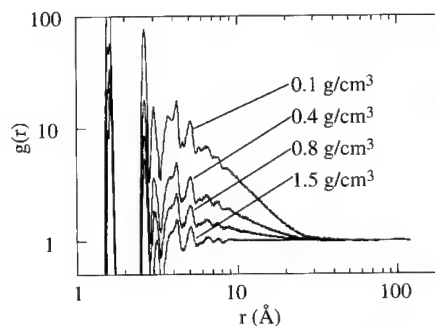

Fig. 4. Log–log plot of pair distribution functions, $g(r)$, of 41 472-particle silica glasses at densities at 0.1, 0.4, 0.8 and 1.5 g/cm^3 at 300 K.

In Fig. 4, we show a log–log plot of the pair distribution function, $g(r)$, at various densities. Short-range correlations manifest themselves as peaks at distances < 5 Å. Some of the peaks split at lower densities, but the peak positions change very little over the entire range of density. In the range 5–25 Å, a power-law decay is superimposed on the peak structures. From the power-law, the fractal dimension, d_f, is calculated as $d_f = 3 + d \log[g(r)]/d \log(r)$ [22,23].

In real materials, the value of d_f depends on the aggregation process and sample preparation conditions such as pH value [18–21]. To investigate the effect of kinetic processes, we performed another set of MD simulations where the temperature was kept at 1000 K instead of 300 K during the expansion process. At the high temperature, larger d_f is observed. Kinetic processes during the expansion determine the structure of the resulting glass. For higher temperatures, larger diffusion overcomes the correlation in immediate neighbors and more global configuration space is searched. As a result, energetically favored packed networks with larger d_f are formed. By controlling the balance between diffusion and correlation via temperature and expansion schedule, various dissimilar porous glasses with different d_f can be produced in MD simulations.

5. Roughness of fracture surface of amorphous silica

We have performed large-scale MD calculations on 1.12-million particle amorphous silica systems to investigate the growth of pores with a decrease in the density of the system [29]. The low-density MD glasses were obtained by uniformly expanding the normal-density glass. The pores begin to form when the density of the system is reduced to 1.8 g/cm³. Further decrease in the density of the system causes an increase in the number of pores and also the pores coalesce to form larger entities. There is a dramatic increase in the size of pores when the mass density is reduced to the critical value, $\rho_c = 1.4$ g/cm³. At that critical density, some pores percolate through the entire system by catastrophic growth. In Fig. 5(a) we show one of the surfaces of the percolating pore.

The roughness of this internally fractured surface
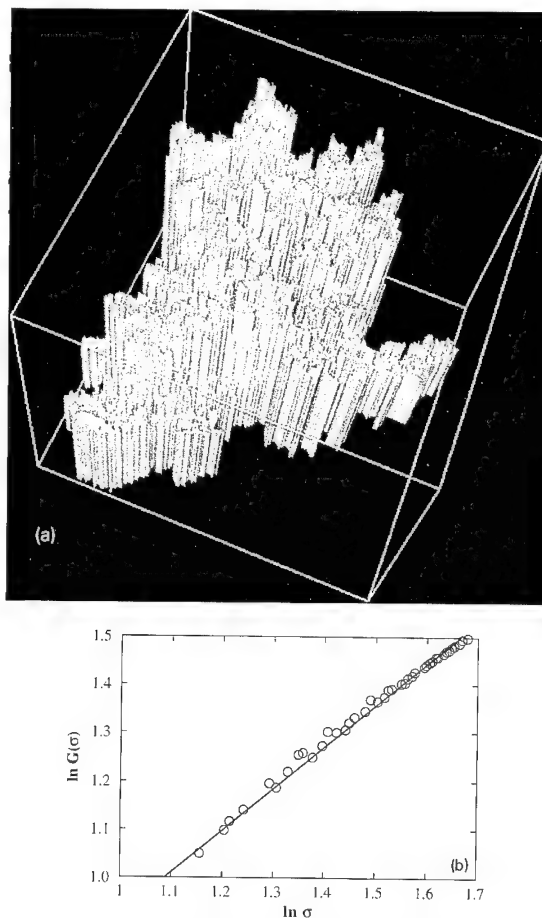
Fig. 5. (a) Snapshot of an internally fractured surface resulting from a percolating pore in silica glass at a mass density of 1.4 g/cm³. (b) Height–height correlation function (○) versus the in-plane distance, σ, for the fracture surface of a 1.12 million particle silica system computed on IBM SP-1. The solid curve is the best fit, $G(\sigma) \propto \sigma^\alpha$, with $\alpha = 0.87 \pm 0.02$ for $\sigma < 100$ Å.

is calculated from the height–height correlation function [29],

$$G(\sigma) = \langle [h(y + y_0, z + z_0) - h(y_0, z_0)]^2 \rangle^{1/2},$$

where $\sigma = (y^2 + z^2)^{1/2}$ and $h(y, z)$ is the highest vertical coordinate at the point (y, z). Fig. 5(b) shows that the MD results for $G(\sigma)$ are well described by the relation, $G(\sigma) \propto \sigma^\alpha$ with $\alpha = 0.87 \pm 0.02$ for $\sigma < 100$ Å. Experimental measurements on bakelite, concrete, steel and aluminum alloys indicate that the roughness exponent, α, has a universal value 0.8 [26,27]. The MD results for the
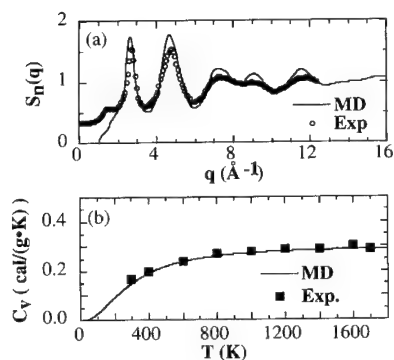
Fig. 6. (a) MD and experimental [48] results for the static structure factor of a-Si_3N_4 at a density of 2.8 g/cm^3. (b) Specific heat for Si_3N_4: MD and experiment at 3.2 g/cm^3 for α-crystal.

roughness exponent agree with experimental measurements, thus lending further support to claims that the roughness exponent of fracture surfaces is a material-independent quantity. Further, the MD results indicate that the universality of the roughness exponent may prevail even at length scales ≤ 10 nm.

6. Molecular dynamics simulations of silicon nitride

Recently we have also performed MD simulations for silicon nitride [41]. Fig. 6(a) shows the MD results for the static structure factor in amorphous Si_3N_4. The result is in satisfactory agreement with neutron structure factor measurements [43]. The specific heat of the α-crystal at normal density is calculated, and the results along with experimental data [32] are shown in Fig. 6(b). The MD results for the specific heat agree very well with the experimental results.

Low-energy phonon modes play an important role in determining the properties of glasses. In our MD simulations for the high-temperature ceramic silicon nitride, low-energy modes emerge in the amorphous and crystalline systems under uniform external negative pressures. In the glass the number of low-energy floppy modes increases continuously with a decrease in the density and the average coordination of the system. Fig. 7 shows the phonon density-of-states (DOS) in the frequency region below 15 meV: as the
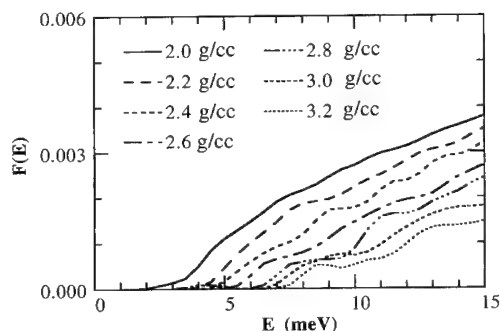
Fig. 7. Linear behavior of the low-energy part of the phonon DOS, $F(E)$, for Si_3N_4 glasses at densities between 3.2 and 2.0 g/cm^3.

connectivity is reduced, low-frequency floppy modes give rise to a linear energy dependence of the DOS.

Results for the low-energy floppy modes in the α-crystal are shown in Figs. 8(a)–(d). The DOS for
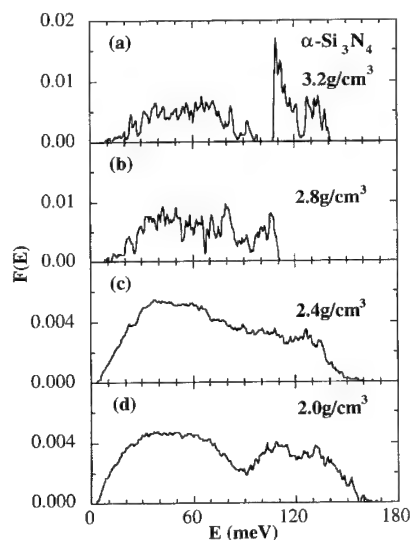
Fig. 8. Phonon DOS at different stages of decohesion of the α-crystal due to volume expansion at 300 K. (a) DOS for the crystal at normal density, 3.2 g/cm^3. (b) Expanded crystal at 2.8 g/cm^3. There is 30% contraction in the energy range of the DOS and a disappearance of the energy gap at 100 meV. (c) At 2.4 g/cm^3 there is an abrupt decohesion of the crystal and the emergence of a linear region in the DOS due to low-energy floppy modes. Further, the maximum energy in the DOS increases from 110 meV at 2.8 g/cm^3 to 150 meV at 2.4 g/cm^3, which is larger than the maximum energy of 140 meV in the α-crystal at 3.2 g/cm^3. (d) DOS for the system at 2.0 g/cm^3 from decohesion of the α-crystal is practically the same as for the glass at 2.0 g/cm^3 which was obtained from the melt. Also, the maximum energy in the DOS at 2.0 g/cm^3 is higher than that at 2.4 g/cm^3.

the normal crystal is in good agreement with Raman and IR experiments of Wada et al. [44]. Fig. 8(b) shows that, although the system at 2.8 g/cm³ is stretched, there are still sharp peaks in the DOS indicating the crystalline nature of the system. However, at 2.8 g/cm³ the 10 meV gap in the DOS of the normal crystal disappears, the point group symmetry of the original crystal is destroyed and the maximum frequency in the DOS is reduced from 140 to 110 meV. Note that the Si–N bond is robust and the nearest-neighbor N–N and Si–Si distances change to accommodate expansion, thereby distorting the tetrahedra. (This is different from the early stages of uniform expansion of a monatomic crystal where all bonds stretch uniformly and the point group symmetry of the crystal is maintained.) As the density is further reduced to 2.4 g/cm³, the system undergoes an abrupt decohesion. This represents the most profound rearrangement of the system – voids/pores grow and bonds are broken and reassembled within the clusters and in the intercluster regions. The crystalline symmetry is completely lost and a linear part in the DOS appears below 20 meV. At the same time the maximum frequency in the DOS increases from 110 to 150 meV. As the connectivity of the system is further reduced at 2.0 g/cm³ (Fig. 8(d)), the magnitude of the linear part of the DOS increases, the spectrum from 110 to 150 meV acquires more weight, and the maximum frequency increases to 165 meV.

Low-energy floppy modes have been found to cause a substantial enhancement in the specific heat over the temperature range of 50–400 K [41].

7. Conclusion

Algorithms have been designed to implement molecular dynamics simulations on emerging concurrent architectures. Million particle MD simulations for covalent amorphous insulators have been performed on parallel computers. We believe that for the next ten years, there is an enormous opportunity to develop new and efficient algorithms for parallel computers to solve grand challenge problems in materials science.

References

[1] M.P. Allen and D.J. Tildesley, Computer Simulation of Liquids (Oxford University, Oxford, 1990).

[2] W.B. Streett, D.J. Tildesley and G. Saville, Molec. Phys. 35 (1978) 639.

[3] D.C. Rapaport, Comput. Phys. Commun. 62 (1991) 217.

[4] R.K. Kalia, S.W. de Leeuw, A. Nakano and P. Vashishta, Comput. Phys. Commun. 74 (1993) 316.

[5] R.K. Kalia, S.W. de Leeuw, A. Nakano, D.L. Greenwell and P. Vashishta, Supercomputer 54(X-2) (1993) 11; A. Nakano, P. Vashishta and R.K. Kalia, Comput. Phys. Commun. 77 (1993) 303.

[6] A. Nakano, P. Vashishta and R.K. Kalia, Comput. Phys. Commun., in press; W. Li, R.K. Kalia, S.W. de Leeuw, A. Nakano, D.L. Greenwell and P. Vashishta, Mater. Res. Soc. Symp. Proc. 291 (1993) 267.

[7] D. Frenkel, in: Simple Molecular Systems at Very High Density, ed. A. Polian and P. Loubeyre (Plenum, New York, 1989).

[8] S.W. de Leeuw, J.W. Perram and E.R. Smith, Proc. R. Soc. (London) A 373 (1980) 27.

[9] J. Barnes and P. Hut, Nature 324 (1986) 446.

[10] L. Greengard and V. Rokhlin, J. Comput. Phys. 73 (1987) 325.

[11] H.-Q. Ding, N. Karasawa and W.A. Goddard, Chem. Phys. Lett. 196 (1992) 6; J. Chem. Phys. 97 (1992) 4309.

[12] S.C. Moss and D.L. Price, in: Physics of Disordered Materials, ed. D. Adler, H. Fritzsche and S.R. Ovshinsky (Plenum, New York, 1985) p. 77.

[13] S.R. Elliott, Phys. Rev. Lett. 67 (1991) 711.

[14] A.P. Sokolov, A. Kisliuk, M. Soltwisch and D. Quitmann, Phys. Rev. Lett. 69 (1992) 1540.

[15] P. Vashishta, R.K. Kalia and I. Ebbsjö, Phys. Rev. B39 (1989) 6034; P. Vashishta, R.K. Kalia, G.A. Antonio and I. Ebbsjö, Phys. Rev. Lett. 62 (1989) 1651.

[16] A. Nakano, R.K. Kalia and P. Vashishta, J. Non-Cryst. Solids 171 (1994) 157.

[17] J. Fricke, J. Non-Cryst. Solids 121 (1990) 188; 147&148 (1992) 356.

[18] T. Freltoft, J.K. Kjems and S.K. Sintra, Phys. Rev. B33 (1986) 269.

[19] R. Vacher, T. Woignier, J. Pelous and E. Courtens, Phys. Rev. B37 (1988) 6500; J. Non-Cryst. Solids 106 (1988) 161; J. Pelous, M. Foret and R. Vacher J. Non-Cryst. Solids 145 (1992) 63.

[20] D.W. Shaefer and K.D. Keefer, Phys. Rev. Lett. 56 (1986) 2199.

[21] T. Lours, J. Zarzycki, A.F. Craievich and M.A. Aegerter, J. Non-Cryst. Solids 121 (1990) 216.

[22] J. Kieffer and C.A. Angell, J. Non-Cryst. Solids 106 (1988) 336.

[23] A. Nakano, L. Bi, R.K. Kalia and P. Vashishta, Phys. Rev. Lett. 71 (1993) 85; Phys. Rev. B49 (1994) 9441.

[24] F. Family and T. Vicsek, J. Phys. A18 (1985) L75; M. Kardar, G. Parisi and Y.C. Zhang, Phys. Rev. Lett. 56 (1986) 889; J. Villain, J. Phys. I (Paris) 1 (1991) 19.

[25] F. Family and T. Vicsek, eds., Dynamics of Fractal Surfaces (World Scientific, Singapore, 1991).

[26] E. Bouchaud, G. Lapasset and J. Planès, Europhys. Lett. 13 (1990) 73.

[27] K.J. Måløy, A. Hansen, E.L. Hinrichsen and S. Roux, Phys. Rev. Lett. 68 (1992) 213.

[28] V.Y. Milman, R. Blumenfeld, N.A. Stelmashenko and R.C. Bull, Phys. Rev. Lett. 71 (1993) 204.

[29] A. Nakano, R.K. Kalia and P. Vashishta, Phys. Rev. Lett. 73 (1994) 2336.

[30] P. Vashishta, R.K. Kalia, J.P. Rino and I. Ebbsjö, Phys. Rev. B41 (1990) 12197.

[31] The same interparticle potential has been used sucessfully in MD simulations of densified silica glasses: W. Jin, R.K. Kalia, P. Vashishta and J.P. Rino, Phys. Rev. Lett. 71 (1993) 3146.

[32] S. Somiya, M. Mitomo and M. Yoshimura, eds., Silicon Nitride – 1 (Elsevier, New York, 1990); P.T.B. Shaffer and A. Goel, Silicon Nitride (ART, Buffalo, NY, 1993).

[33] X.S. Ning, T. Okamoto, Y. Miyamoto, A. Koreeda and K. Sugawara J. Mater. Sci. 24 (1989) 2865; L. Zambov, G. Peev, V. Shanov and S. Drumeva, Vacuum 43 (1992) 227; W. Braue, H.J. Dudek and G. Ziegler, J. Non-Cryst. Solids 56 (1983) 185.

[34] J.C. Phillips, J. Non-Cryst. Solids 34 (1979) 153; 43 (1981) 37.

[35] M.F. Thorpe, J. Non-Cryst. Solids 57 (1983) 355.

[36] H. He and M.F. Thorpe, Phys. Rev. Lett. 54 (1985) 2107; Y. Cai and M.F. Thorpe, Phys. Rev. B40 (1989) 10535.

[37] I.P. Swainson and M.T. Dove, Phys. Rev. Lett. 71 (1993) 193; N. Ahmad, T. Hussain and C.J. Adkins, J. Phys.: Condens. Matter 5 (1993) 147.

[38] U. Buchenau, M. Prager, N. Nucker, A.J. Dianoux, N. Ahmad and W.A. Phillips, Phys. Rev. B34 (1986) 5665.

[39] S.S. Yun, H. Li, R.L. Cappelletti, R.N. Enzweiler and P. Boolchand, Phys. Rev. B39 (1989) 8702.

[40] W.A. Kamitakahara, R.L. Cappelletti, P. Boolchand, B. Half-pap, F. Gompf, D.A. Neuman and H. Mutka, Phys. Rev. B44 (1991) 94; M. Garcia-Hernandez, F.J. Bernejo and B. Fak, Phys. Rev. B48 (1993) 149.

[41] P. Vashishta, R.K. Kalia and I. Ebbsjö, submitted to Phys. Rev. Lett.

[42] P.A.V. Johnson, A.C. Wright and R.N. Sinclair, J. Non-Cryst. Solids 58 (1983) 109.

[43] M. Misawa, T. Fukunaga, N. Niihara, T. Hirai and K. Suzuki, J. Non-Cryst. Solids 34 (1979) 313.

[44] N. Wada, S.A. Solin, J. Wong and S. Prochazka, J. Non-Cryst Solids 43 (1981) 7.

Molecular dynamics study of brittle fracture in silica glass and cristobalite

Thomas P. Swiler [a,1], Joseph H. Simmons [a,*], Adrian C. Wright [b]

[a] *Department of Materials Science and Engineering, University of Florida, Gainesville, FL 32611, USA*
[b] *Department of Physics, J.J. Thomson Laboratory, University of Reading, Whiteknights, Reading RG6 2AF, UK*

Abstract

A non-equilibrium molecular dynamics simulation approach is used to model the structure of silica glass and cristobalite using a two-body and a two-body/three-body potential. A comparison of the total correlation function is made between the two simulations and neutron scattering data. Differences in structure obtained by each simulation method show the influence of a lack of directional bond components in the two-body potential simulation and the result of strong directional components in the three-body potential simulation. The effect of an applied uniaxial strain on the structure of the simulated glass and crystalline phases is studied by following the resulting longitudinal stress. Data analysis shows that the glass exhibits a large strain-rate dependence in the maximum stress sustained, while the crystal does to a lesser extent or none at all depending on the potential function. The large strain rate dependence in the glass is interpreted as arising from a rearrangement of the free volume structure, whereby, at low strain rates, strain added uniformly to the structure is allowed to flow from higher density regions of the glass to lower density regions. This effect leads to coalescence of voids eventually causing fracture propagation through the simulated structure. The crystal, having no ability to assimilate the applied strain, can only stretch its bonds until fracture.

1. Introduction

Brittle fracture is a dynamic, non-linear process which involves a large ensemble of atoms acting cooperatively to relieve the build up of elastic potential energy through atomic motions and the formation of free surfaces. While the initiation of fracture can be predicted by the application of energy balance concepts first developed by Griffith [1], neither the

path of the crack, nor its propagation characteristics, nor the structure of the freshly formed surfaces are currently within range of either theory or experiment. The major reason for this lack of understanding results from the fact that crack formation and propagation in brittle media are dependent on the local atomic dynamics in the strained solid, and from the lack of any experimental method for examining these dynamics in detail. This type of problem, therefore, can only be investigated with simulation methods like molecular dynamics (MD). These methods can simulate the dynamic interatomic interactions and therefore can yield models of the manner in which an ensemble of particles bonded together to form a solid will react to an imposed stress or strain. By

---

* Corresponding author. Tel: +1-904 392 6679. Telefax: +1-904 392 6359. E-mail: simmons@silica.msc.ufl.edu.
[1] Present address: Sandia National Laboratories, Albuquerque, NM, USA.

examining the details of this response, it is possible to determine some of the processes which comprise the act of brittle fracture in the solid [2].

Experimental studies of brittle fracture in glass have exhibited a number of characteristic properties. These properties must be separated between sudden fracture and 'slow crack growth'. In the latter, the environment, especially water, is allowed to interact with strained bonds at the tip of existing cracks and can induce physi- and chemi-sorption processes which weaken the bond and allow the crack to advance slowly [3,4]. In the former, the crack is assumed to propagate without interaction with the environment. Because MD studies are based on classical interatomic potentials, they cannot provide a good basis for chemical reactions. Therefore, this paper only considers the case of sudden fracture in which the failure process is totally determined by mechanical considerations. Several ab initio [5] and semi-empirical molecular orbital [6] studies have addressed the other problem of strain induced chemisorption processes at the crack tip which control the 'slow crack growth' phenomenon.

Properties of the sudden brittle fracture phenomenon are obtained from fractography studies which yield structural descriptions of the fracture surface after the fact [7], and from fractoemission studies which give descriptions of particle, electron, acoustic and light emission during fracture [8]. Fractography shows regions of mirror, mist and hackle, corresponding to increasing degrees of roughness on the fracture surface, and a fractal surface structure in all three regions over a scale range from macroscopic to the submicrometer scale [9]. Fractoemission studies have shown the ejection of atomic and ionic particles from the fracture surface as well as acoustic and light emission during sudden brittle fracture [8].

The ultimate strength of a material without preexisting surface flaws that fails by brittle fracture can be calculated based on a knowledge of its structure and the properties of its interatomic bonds. This value is known as the cohesive strength of the material, and it can be calculated for a material given the Young's modulus, E, the surface energy, γ, the atomic structure and an assumption of the form of the interatomic potential [10].

A reasonable cohesive strength calculation has been achieved using the Morse interatomic potential function with the following result:

$$\sigma_{th} = \sqrt{E\gamma/4r_0} \, ,$$

where r_0 is the interatomic spacing. For vitreous silica, with $E = 7.3 \times 10^{10}$ Pa, $\gamma = 4.56$ J/m^2, and $r_0 = 1.62 \times 10^{-10}$ m, the theoretical strength given by the Morse potential is 23 GPa. This value compares favorably with the highest strength of 18 GPa measured for treated silica fibers in liquid nitrogen by Proctor [11], but is about two orders of magnitude greater than the measured strength for bulk silica or untreated silica fibers [12]. Maximum crack velocities during sudden brittle fracture have been calculated and measured to be between 40 and 60% the speed of sound [13].

Discrepancies between theoretical strengths and measured strengths are due to surface flaws and can be calculated using Griffith's equation [1], relating the maximum tensile stress, σ_c, which can be supported by a sample of material containing a crack of length, c, which, for a sheet with an edge crack is given by

$$\sigma_c = \sqrt{2E\gamma/\pi c} \, .$$

2. Molecular dynamics simulations

In this paper, the mechanisms of brittle fracture are investigated in a silica glass and in low cristobalite using the same MD algorithm and the same force function so that the only difference between the two materials is the contrast between order and disorder. Cristobalite is of interest because its low density structure (α- or low cristobalite) is the most comparable to the vitreous phase, of all the polymorphs of silica. Although quartz is the equilibrium phase, the cristobalite phase can be relatively stable when quenched to room temperature because the reconstructive transformations between the major phases are slow. Within the cristobalite polymorph, two sub-polymorphs are present, high, or β-, and low, or α-, cristobalite, which undergo a displacive transformation within the temperature range of 470–540 K. This displacive transformation results in a symmetry change from the high temperature cubic

symmetry to the lower temperature tetragonal symmetry upon cooling.

The structure of high cristobalite [14] is similar to the diamond structure. The silicon atoms are in the diamond positions and oxygen atoms are located between each pair of silicon nearest neighbors. The symmetry of high cristobalite is cubic, and the structure belongs to the $Fd3m(O_h^7)$ space group. The unit cell of high cristobalite has an edge length of 7.16 Å at 560 K and contains eight formula units.

The structure of low cristobalite has the same connectivity as the high cristobalite structure. Although this phase has tetragonal symmetry with prism dimensions $a_0 = 4.96$ Å and $c_0' = 6.92$ Å, the structure is pseudocubic when the cell is rotated by 45° about the c-axis and the sides a_0 are transformed into diagonals of the base of the prism, i.e., $a_0' = \sqrt{2} a_0 = 7.02$ Å and $c_0 = c_0' = 6.92$ Å. In this description, the structure is a relatively small distortion of the high cristobalite structure. The unit cell of low cristobalite contains four formula units and belongs to the space group $P4_12_1(D_4^4)$.

Initially, comparisons are conducted between two- and three-body force functions to select the most appropriate simulation method. In the case of silica, the potential functions that are commonly used either model silica as a purely ionic system [15], a pseudo-ionic system [16], an ionic system with a pseudo-covalent character [17], a modified ionic system with charge-polarization interactions with a pseudo-covalent system [18] or a pseudo ionic-covalent system [19]. All these potential functions have limitations. Comparisons of the fits of the total real space correlation function with neutron scattering data [20] can be analyzed using a reliability factor, R_χ, derived by Wright [21]. Using this approach, it is found that the Soules potential function yields $R_\chi = 10\%$, Feuston–Garofalini 15%, Vashishta 4% and Vessal 9%. A consideration of the fit quality, number of adjustable parameters and speed of calculation led us to use the Soules (six parameters) and Feuston-Garofalini (15 parameters) potentials to test the structural differences between two-body and three-body force functions. The Vessal function uses 40 adjustable parameters in a piecewise continuous Buckingham potential consisting of four segments; therefore, it was not tested here since the high number of adjustable parameters do not justify the

marginal fitting improvement. The Vashishta potential gives the best fit with 19 adjustable parameters, however it requires much longer computer times than the other two functions. Its application to simulations of glass structure is described in a paper by Vashishta in this volume [22].

Both the Soules (S) and Feuston–Garofalini (FG) potentials use a truncated Born–Mayer–Huggins function for the two-body component of the force. This potential function has the form

$$\phi_{2uv}(r) = \frac{q_u q_v}{r} + \beta_{uv} b \, \exp\left(\frac{(\sigma_u + \sigma_v) - r}{\rho} \right) + C_{uv} r^{-6} + D_{uv} r^{-8},$$

where: u, v signify atom types; ϕ_{uv} is the potential between atoms of type u and v as a function of r; r is the separation distance between atomic centers; q_u, q_v are charges on atoms of types u and v, respectively; σ_u, σ_v are radius repulsive parameters; b is a positive constant; ρ is a hardness parameter; C_{uv}, D_{uv} are the coefficients of dipole–induced dipole and dipole–induced quadrupole terms, respectively; β_{uv} is the Pauling coefficient, given by

$$\beta_{uv} = \left(1 + \frac{Z_u}{n_u} + \frac{Z_v}{n_v} \right);$$

Z_u, Z_v are the units of charge of type u and v, respectively; and n_u, n_v are the numbers of valence electrons of u and v, respectively. The multipole terms become important when the atoms are highly polarizable and are separated by small distances, but are generally neglected in the simulation of silica glass. Some have questioned the accuracy of this simplification since oxygen exhibits a high degree of polarization and the atoms are closely spaced in condensed phases. The justification for ignoring these terms is that atoms within a solid are generally constrained to the point that these terms would have minimal effect, and these terms involve many-body interactions that are computationally difficult.

In a simulation, it is desirable to have a potential of limited range in order to minimize the number of particle interactions. However, the Coulombic portion of the Born–Mayer–Huggins potential decays slowly and many neighbors would be required for calculations of all potentially significant interactions. To overcome this problem, a screening or truncation

function is used to limit these interactions. This truncation process simulates the result of a lattice of alternating charges as used in the calculation of a Madelung constant.

The FG potential uses an Ewald sum [23] approach to calculate the screening function, in which a different denominator is used with each interatomic interaction:

$$\text{Trunc}(r) = \text{erfc}(r/\epsilon L),$$

where: erfc ( ) is the complementary error function; ϵ is a constant, typically 0.175–0.35 [24]; and L is a linear dimension of the molecular dynamics cell or r_{max}. The Soules function uses a simple power law truncation term which reduces by one the number of adjustable parameters and yields a truncation process which is independent of cell size. The truncation term is applied to the force function instead of the potential function:

$$\text{Trunc}(r) = \left[1 - (r/r_{max})^{n}\right].$$

In silica, the truncation distance, r_{max}, is 5.5 Å and the exponent, n, is 3. Since the range of the FG Ewald sum truncation is about 5 Å, it is necessary to conduct simulations with boxes of at least 11 Å in order to avoid having particles bond twice to the same particle from the periodic images in neighboring cells.

The parameters of the Soules force function are given in Table 1.

The Feuston–Garofalini potential includes an ad-

Table 1
Parameters used in the Soules force and potential functions

Potential function parameters	
$\rho = 0.290023$ Å	
$A_{Si-Si} = 3300$ p erg	
$A_{Si-O} = 3000$ p erg	
$A_{O-O} = 2300$ p erg	
$q_{Si} = +4e$ [a]	
$q_O = -2e$ [a]	
Truncation function parameters	
$r_{max} = 5.5$ Å	
$n = 3$	

[a] e is the electron charge.

Table 2
Parameters used in the Feuston–Garofalini potential function

Two-body potential parameters	
$\rho = 0.290023$ Å	
$A_{Si-Si} = 1880$ p erg	
$A_{Si-O} = 2960$ p erg	
$A_{O-O} = 720$ p erg	
$q_{Si} = +4e$ [a]	
$q_O = -2e$ [a]	
$\beta_{Si-Si} = 2.29$	
$\beta_{Si-O} = 2.6$	
$\beta_{O-O} = 2.34$	
Non-zero three-body potential parameters	
$\lambda_{O-Si-O} = 180$ p erg	
$\lambda_{Si-O-Si} = 3$ p erg	
$\gamma_{O-Si-O} = 2.6$ Å	
$\gamma_{Si-O-Si} = 2.0$ Å	
$r^c_{O-Si-O} = 3.0$ Å	
$r^c_{Si-O-Si} = 2.6$ Å	
$\cos \theta^c_{O-Si-O} = -1/3$	
$\cos \theta^c_{Si-O-Si} = -1/3$	

[a] e is the electron charge.

ditional three-body function of the form developed by Stillinger and Weber [25] as follows:

$$\phi_{\theta uvw}(r_{ij}, r_{jk}, \theta_{ijk})$$
$$= \begin{cases} \lambda_{uvw} \exp\left[\dfrac{\gamma_{uvw}}{(r_{ij} - r^c_{uvw})} + \dfrac{\gamma_{uvw}}{(r_{jk} - r^c_{uvw})}\right] \\ \quad \times (\cos \theta_{ijk} - \cos \theta^c_{uvw})^2, \\ \quad r_{ij} < r^c_{uvw}, \; r_{jk} < r^c_{uvw}, \\ 0, \quad r_{ij} \geq r^c_{uvw}, \; r_{jk} \geq r^c_{uvw}. \end{cases}$$

The parameters used in this potential function are shown in Table 2.

Molecular dynamics simulations were conducted using the Verlet algorithm [26] principally. Tests using the fifth-order Gear predictor–corrector method [27] yielded the same results and were abandoned due to the greater computational time. Full periodic boundary conditions were used in all directions. The calculation time step used was 0.5 fs as determined by previously published tests [28]. The fundamental phonon vibration of the system was approximately 40 fs. Except when otherwise noted, all calculations were conducted under an isothermal constraint by

Fig. 1. Comparison of the total real space correlation function derived from neutron diffraction experiment (———) and the molecular dynamics simulation using the two-body Soules potential function (- - - - - -).

Fig. 2. Comparison of the total real space correlation function derived from neutron diffraction experiment (———) and the molecular dynamics simulation using the three-body Feuston–Garofalini potential function (- - - - - -).

which all particle velocities were scaled to maintain constant temperature.

The cristobalite phase was formed at low temperature, then heated to 300 K and annealed for 2 ps

before testing. The glass phase was formed by two methods. In the first, the glass was formed from a crystal structure heated to 12 000 K, then cooled to room temperature at 0.5 K/fs, then annealed at room
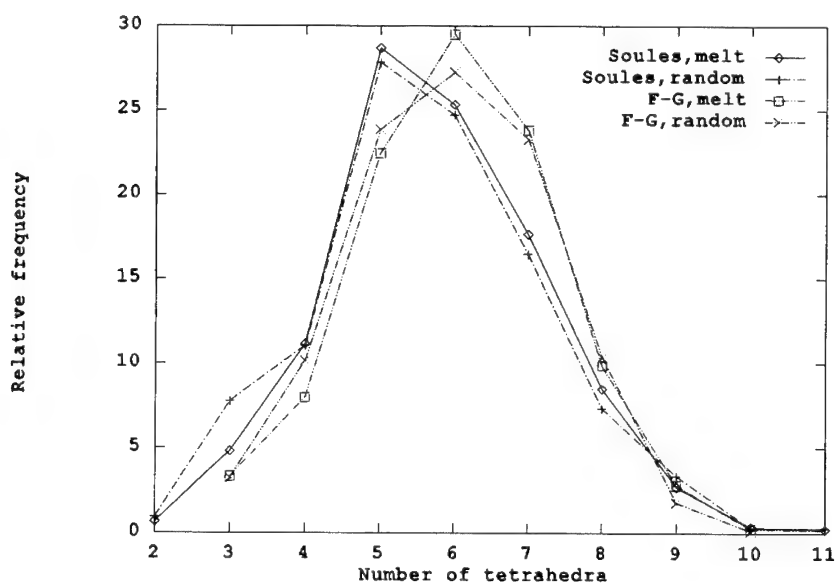
Fig. 3. Comparison of ring size distributions for vitreous silica derived from the two-body S-potential function and the FG-potential function for two different preparation conditions. 'Melt' signifies that the glass was formed from a crystal structure heated to 12 000 K, then cooled to room temperature at 0.5 K/fs, then annealed at room temperature for 2ps. 'Random' signifies that the glass was formed from a random lattice at 12 000 K, then cooled as for 'melt'.
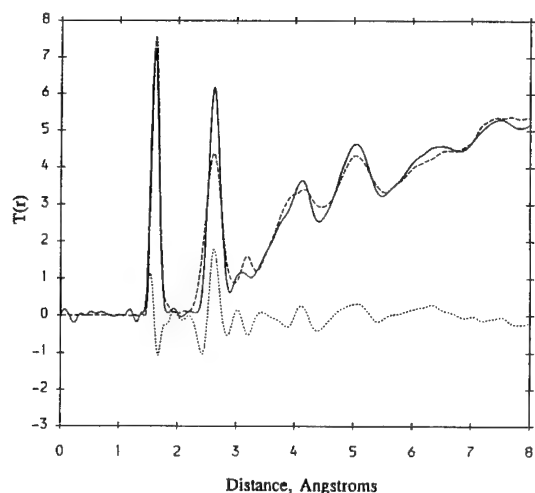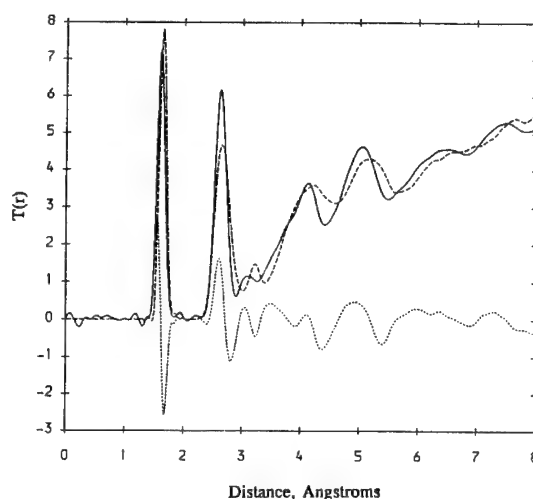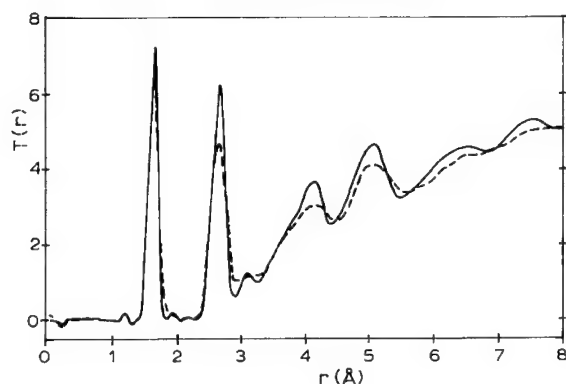
Fig. 4. Comparison of the total real space correlation function derived from neutron diffraction experiment (———) and the molecular dynamics simulation using the three-body Vessal potential function (- - - - - -) [20]

temperature for 2 ps. In the second, the glass was formed from a random lattice at 12 000 K, then cooled as in the first method.

An uniaxial strain was applied to a box ($40 \times 20 \times 20$ Å) along the long direction, by appropriately scaling the particle positions along that axis. There-

fore, the strain was applied uniformly to all particles. Strain rates were used which varied from the speed of sound to about 1/1000 the sound velocity.

3. Results

3.1. Structural studies

The structures of the silica glass and cristobalite samples were compared using the S and FG potentials. In general, the S potential gave a better fit of the glass total correlation function and a less stable crystal than did the FG potential. However, there were differences. For example, the FG potential gave a narrower fit of the O–O first correlation peak, in better agreement with data. The FG function exhibited a maximum in the ring size distribution at six, while the S function had a five-membered ring maximum. There were no other differences at other ring sizes. The S function had a greater concentration of over and under coordinated silica, and a slightly broader bond angle distribution. Both functions

Fig. 5. Stress–strain curves at various strain rates for low cristobalite formed using the two-body S-potential function.

showed a maximum at 110° for the O–Si–O angles and at 155° for the Si–O–Si angles. The S function exhibited the correct density at low pressures for both the glass and crystal, while the FG potential required a relatively higher pressure, 300 and 120 kbars for the crystal and glass, respectively. However, the two-body cristobalite melted at 10 000 K, while the three-body cristobalite melted at 8000 K. The fitted total correlation functions for both two- and three-body glasses are shown in Figs. 1 and 2. Ring statistics comparisons are shown in Fig. 3. The fit of the Vessal simulation is shown in Fig. 4 for comparison.

3.2. Fracture studies

3.2.1. Low cristobalite

Structures of low cristobalite were strained along the (100) axis at strain rates varying from 0.05 to 5.0 ps^{-1}. Both isothermal and adiabatic fracture experiments were performed in order to better understand the thermodynamics of fracture. Stress–strain curves

Fig. 7. Stress–strain curves at various strain rates for vitreous silica formed using the two-body S-potential function.

for cristobalite are shown in Fig. 5 for the S-potential simulation and in Fig. 6 for the FG-potential simulation. The curves show an elastic increase in stress up
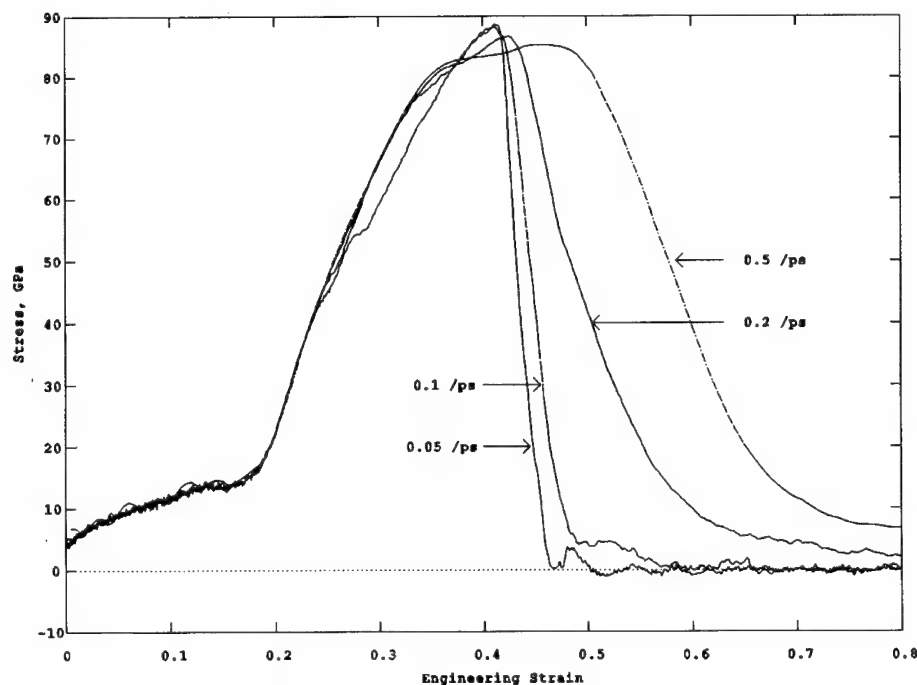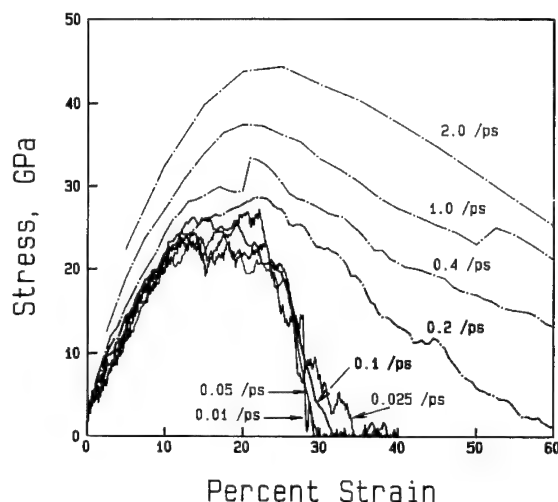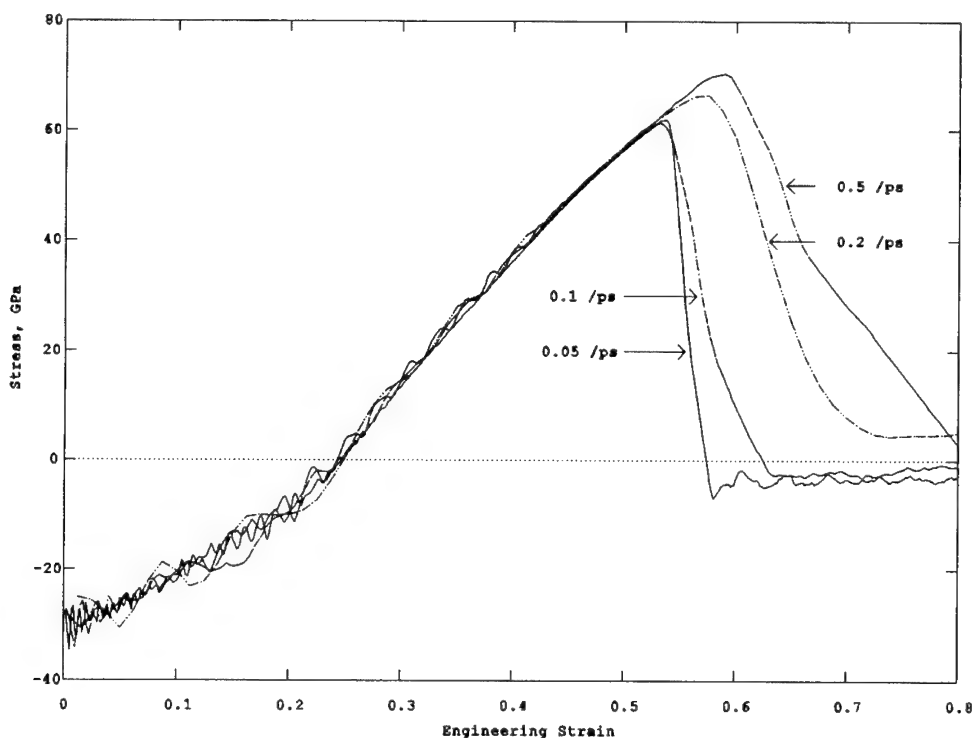

Fig. 6. Stress–strain curves at various strain rates for low cristobalite formed using the three-body FG-potential function.

to a maximum, followed by an abrupt drop to zero at low strain rates. At higher strain rates ($> 0.5/ps$), the curves do not drop to zero for strains of $\geqslant 100\%$, indicating that the sample has not broken into separate parts.

3.2.2. Vitreous silica

Stress–strain curves for the silica glass are shown in Fig. 7. Here, there were no differences between the two potentials used. The curves show a rapid drop to zero stress (complete fracture) at strain rates below 0.2/ps. The drop to zero stress also occurs at higher strain rates, but it takes place at very large strains ($> 100\%$).

4. Discussion

4.1. Structure studies

The Soules two-body potential yields an unexpectedly good fit of the real space correlation function of the glass phase (Fig. 1). The tetrahedral structure is obtained using large attractive Si–O and large repulsive O–O and Si–Si forces which drastically constrain any radial deviation in the symmetric tetrahedral structure. However, there is some flexibility in the relative positions of the oxygens at the corners of the tetrahedra. This is evident in the O–O correlation peak which appears broader than the experimental data. This problem is partially resolved by the FG potential which uses an angular-dependent restoration force on the oxygen ions to bring them back to tetrahedral symmetry. In both simulations, the Si–Si correlation peak occurs at too large a distance. This result is consistent with an Si–O–Si bond angle distribution maximum at 155°, instead of 140–145° as in Mozzi and Warren [29]. The higher order correlation peaks are reasonably well fitted by the two-body potential, probably indicating a better truncation scheme.

Improvements in the classical force functions are still useful for future studies in which engineering data are sought. The two simulations conducted here yield a Young's modulus about twice that measured experimentally so there is still room for improvements. However, one of the great utilities of molecular dynamics studies is the ability to examine particle dynamics in an ensemble, and, as shown below, the remaining differences from the ideal fit of the correlation function do not have a severe effect on the ability of the simulations to provide insight into the fracture process.

4.2. Fracture studies

In describing the stress–strain relationships, the point of *failure* will be defined as the point where stress reaches a maximum. The point of *fracture* will be the point where the stress drops to zero after reaching a maximum. Ordinarily, in brittle fracture experiments, these are close to each other, since once failure begins the material breaks catastrophically under constant applied stress as the strain diverges. However, since these experiments are conducted at constant strain rate, there is no catastrophic failure as the constant strain rate condition keeps the material together, and the stress decreases past failure. The time to fracture after failure can be used to calculate the fracture velocity.

4.2.1. Low cristobalite

The change in modulus observed in the S potential simulation (Fig. 5) at about 20% strain corresponds to an instability of the crystal structure. The FG potential exhibits a more regular behavior for the elastic modulus; however, the stress begins at a large negative value because of the large pressure needed to achieve the desired cristobalite density. The failure/fracture process appears similar for both simulations, although the FG sample shows a small increase in maximum strength. This appears to be a result of the symmetry of the crystal and the periodicity of the simulation, by which the material must have all its bonds broken before separation takes place. At the lower strain rates, thermal motions allow the alignment of the failure fronts so that they may reach across the box.

The S-potential simulation shows a strain-rate independent failure at 85 GPa. This greater value than the FG potential simulation is due to the combination of two factors: (1) the crystal fails by breaking Si–O bonds, and (2) the Si–O bond strength is greater in the S-potential simulation. The strain-rate

independence of the maximum stress in the S-potential simulation seems to be associated with the transformation occurring at 20% strain. Examination of the crystal structure reveals the formation of twinning defects. These defects provide the structural instability which leads to failure. By contrast, the FG system retains its symmetry and therefore has no weak link, thus exhibiting a maximum failure stress which increases with strain rate.

An analysis of the partition of energy between elastic and thermal components shows the elastic energy of the crystal increasing steadily until failure, while the thermal energy during the adiabatic runs remains low until failure where it climbs abruptly. Surface melting is observed in all crystals.

4.2.2. Vitreous silica

An examination of the behavior of the S-potential simulation reveals that the low strain rate samples exhibit a strain-rate independent maximum failure stress. At high strain rates, the failure stress increases drastically. In agreement with previous studies [30], the lower failure stress at low strain rates corresponds to a compliance of the system provided by the thermal vibrations, through which voids may coalesce to relieve the stress developed. In physical terms, one can imagine a process whereby, at low strain rates, the uniformly applied strain flows through regions of high density to regions of lower density through the thermal motions of the atoms. The details of these motions have been described previously [30]. At the higher strain rates, the increase in maximum stress corresponds to failure without any appreciable yield and should approach the theoretical strength of the material as discussed in the introduction. In fact, because of the higher modulus of the simulated glass, the fracture strengths are larger than those of silica glass by the same ratio.

Fracture velocities calculated by dividing the cross-sectional dimension of the cell by the time interval between onset of failure and fracture, are found to be about 40% of the phonon velocity.

Surface melting is also observed in these systems, and the thermal energy differs from the crystal by increasing gradually during the straining period. This indicates that bonds are being broken gradually in the yield region before failure occurs, and the fracture event is not as abrupt as in the crystal.

4.2.3. Surface behavior

Surface reconstruction has been discussed previously and an oxygen surface layer is observed in these studies for both the crystal and the glass, as predicted by our previous studies [31]. The surfaces are rough and exhibit a fractal character (to be described elsewhere). In the glass, the surface roughness appears to vary with strain rate. At higher strain rates, the surface appears much rougher than at low strain rates.

5. Conclusions

Simulations of the structure of silica glass and cristobalite were conducted using a two-body Coulomb potential and a two-body/three-body potential. Both demonstrated reasonably representative structures for silica glass. Fracture studies revealed major differences between glass and crystalline forms. The crystalline forms exhibited a larger maximum strength than the glass structure, by more than a factor of three. An analysis of void volumes in the crystal and glass phases showed that the glass has voids with radii as large as 4.5 Å while the largest crystalline void has a 2.5 Å diameter. If the initial diameter of the internal voids controlled the material's strength according to Griffith's equation, then the ratio of void radii necessary to produce a strength ratio of 3 would have to be 9. This ratio is not observed. The failure of the glass appears to come from a gradual growth and coalescence of large voids during the strain application due to the atomic motions of thermal vibrations. This rearrangement of void space during strain build-up seems to occur by the rejection of strain from the high density regions of the glass and passage to the low density regions. This void volume coalescence in the glass explains the lower than expected strength of the glass phase. Surface melting and reconstruction are observed in the crystalline and glass phases. The reconstructed surfaces are rough and have a fractal character.

Further studies include tests of better potential functions, and a fractal analysis of the reconstructed surfaces. Recently submitted results [32] indicate that the fracture process in the glass is fully chaotic, therefore a study of its implications to fracture deter-

minism and the statistical nature of brittle failure is in order.

References

[1] A.A. Griffith, Philos. Trans. R. Soc. A221 (1921) 163.

[2] J.H. Simmons, in: Experimental Techniques of Glass Science, ed. C.J. Simmons and O.H. El-Bayoumi (American Ceramic Society, Columbus, OH, 1993) p. 315.

[3] S.M. Wiederhorn, in: Mechanical and Thermal Properties of Ceramics, National Bureau of Standards Special Publication 303 (1969) p. 217; S.M. Wiederhorn, J. Am. Ceram. Soc. 50 (1967) 407.

[4] T.A. Michalske and S.W. Freiman, J. Am. Ceram. Soc. 66 (1983) 284; T.A. Michalske and B.C. Bunker, J. Appl. Phys. 56 (1984) 2686.

[5] Wong Ng, G.S. White and S.W. Freiman, J. Am. Ceram. Soc. 75 (1992) 3097.

[6] J.K. West and L.L. Hench, submitted to J. Mater. Sci. (1994); J.K. West and L.L. Hench, submitted to J. Mater. Sci. (1994).

[7] J.J. Mecholsky, S.W. Freiman and R.W. Rice, in: ASTM STP 645 (American Society for Testing and Materials, Philadelphia, PA, 1978) p. 363.

[8] S.C. Langford, Ma Zhenyi and J.T. Dickinson, J. Mater. Res. 4 (1989) 1272.

[9] J.J. Mecholsky, D.E. Passoja and K.S. Feinberg-Ringel, J. Am. Ceram. Soc. 72 (1989) 60; J.J. Mecholsky, T.J. Mackin and D.E. Passoja, in: Advances in Ceramics 22: Fractography of Glasses and Ceramics, (American Ceramic Society, Columbus, OH, 1988) p. 127.

[10] E. Orowan, Rep. Progr. Phys. 12 (1948) 185.

[11] B.A. Proctor, Phys. Chem. Glasses 31 (1990) 78.

[12] C.R. Kurkjian and U.C. Paek, Appl. Phys. Lett. 42 (1983) 251.

[13] J.E. Gordon, D.M. Marsh and M.E.M.L. Parratt, Proc. R. Soc. (London) Ser. A249 (1959) 59.

[14] R.W.G. Wyckoff, Crystal Structures, 2nd Ed., Vol. 1 (Wiley, New York, 1963) ch. 4, p. 27.

[15] L.V. Woodcock, C.A. Angell and P. Cheeseman, J. Chem. Phys. 65 (1976) 1565.

[16] T.F. Soules, J. Non-Cryst. Solids 123 (1990) 48.

[17] B.P. Feuston and S.H. Garofalini, J. Chem. Phys. 89 (1988) 5818; B.P. Feuston and S.H. Garofalini, J. Chem. Phys. 91 (1989) 564.

[18] P. Vashishta, Rajiv K. Kalia, José P. Rino and Ingvar Ebbsjö, Phys. Rev. B41 (1990) 12197; A. Nakano, K. Kalia and P. Vashishta, J. Non-Cryst. Solids 171 (1994) 157.

[19] B. Vessal, M. Amini, D. Fincham and C.R.A. Catlow, Philos. Mag. B60 (1989) 753; B. Vessal, M. Amini and C.R.A. Catlow, J. Non-Cryst. Solids 159 (1993) 184.

[20] D.I. Grimley, A.C. Wright and R.N. Sinclair, J. Non-Cryst. Solids 119 (1990) 49.

[21] A.C. Wright, J. Non-Cryst. Solids 159 (1993) 264.

[22] P. Vashita, A. Nakano, R.K. Kaka and I. Ebbsjö, these Proceedings, p. 59.

[23] P. Ewald, Ann. Phys. 64 (1921) 253.

[24] Thomas F. Soules and Robert F. Busbey, J. Chem. Phys. 75 (1981) 969.

[25] Frank H. Stillinger and Thomas A. Weber, Phys. Rev. B31 (1985) 5262.

[26] Loup Verlet, Phys. Rev. 159 (1967) 98.

[27] J.M. Haile, Molecular Dynamics Simulation: Elementary Methods (Wiley, New York, 1992).

[28] Romulo Ochoa and Joseph H. Simmons, J. Non-Cryst. Solids 75 (1985) 413; Romulo Ochoa, PhD dissertation, Catholic University of America, Washington, DC (1985).

[29] R.L. Mozzi and B.E. Warren, J. Appl. Crystallogr. 2 (1969) 164.

[30] Romulo Ochoa, Thomas P. Swiler and Joseph H. Simmons, J. Non-Cryst. Solids 128 (1991) 57.

[31] Joseph H. Simmons, Thomas P. Swiler and Romulo Ochoa, J. Non-Cryst. Solids 134 (1991) 179.

[32] T.P. Swiler, T. Vargese and J.H. Simmons, J. Non-Cryst. Solids 181 (1995) 238.

ELSEVIER

The vibrational modes of vitreous B_2O_3: inelastic neutron scattering and modelling studies

Alex C. Hannon [a,*], Adrian C. Wright [b], John A. Blackman [b], Roger N. Sinclair [c]

[a] *ISIS Facility, Rutherford Appleton Laboratory, Chilton, Didcot, Oxon OX11 0QX, UK*
[b] *J.J. Thomson Physical Laboratory, Whiteknights, Reading RG6 2AF, UK*
[c] *AEA Technology, Harwell Laboratory, Didcot, Oxon OX11 0RA, UK*

Abstract

Inelastic neutron scattering, Raman scattering and model calculations play complementary roles in the understanding of the vibrational modes of amorphous solids. These roles are illustrated by new and recent results for vitreous B_2O_3 from both inelastic neutron scattering and modelling. The well known boroxol ring breathing mode is clearly observed in the neutron data which show the mode to be enhanced in the Raman HV and HH spectra by factors estimated at 6.3 and 40, respectively. The observed width of the mode (FWHM 1.7 meV) is comparable with the resolution of the measurement (1.6 meV). This width could not be fully reconciled with Raman results. Full details are given of modelling studies of the vibrational density of states of ball-and-stick models which take into account non-central forces. In these studies, indirect methods have been developed for probing the nature of the calculated modes by considering the study of the effects of force constant variation and of isotopic substitution.

1. Introduction

Inelastic neutron scattering, Raman scattering and model calculations play complementary roles in the understanding of the vibrational modes of amorphous solids. The effective vibrational density of states (VDOS) measured by inelastic neutron scattering is more closely related to the true VDOS than that given by any other form of vibrational spectroscopy. Also inelastic neutron scattering provides reciprocal space (i.e., Q-dependent) information which relates to the atomic displacements for the vibrational modes. The spectra measured by Raman scattering suffer from matrix element enhancement of vibrational modes, making them less reliable as a means of measuring the relative importance of different features in the VDOS. However, this enhancement of modes makes Raman scattering a very sensitive probe for detecting regular structures such as planar rings in glasses. In addition, Raman scattering can provide a great deal of information on the nature of vibrational modes by means of either isotopic substitution studies or temperature-dependent studies. However, a full understanding of the experimental results from inelastic neutron scattering and Raman scattering can only be achieved in conjunction with model calculations. Recent and new work on the vibrations of vitreous B_2O_3 (v-B_2O_3) are presented here to illustrate the complementary roles played by inelastic neutron scattering, Raman scatter-

* Corresponding author. Tel: +44-235 445 358. Telefax: +44-235 445 720. E-mail: ach@isise.rl.ac.uk.

ing and model calculations in an understanding of the atomic vibrations of an amorphous material.

The vibrational modes of v-B_2O_3 have received a great deal of attention due to the numerous features in the Raman spectra of this material, the most prominent of which is an extremely intense, narrow and highly polarised peak at 808 cm^{-1} [1]. The structure of v-B_2O_3 is generally thought to involve a continuous random network (CRN) formed by comer-sharing between triangular BO_3 structural units [2,3], but in order to explain the Raman spectra it has been proposed that the structure involves a high concentration of a larger superstructural unit known as a boroxol group [4]. The B_3O_6 boroxol group is composed of three corner-sharing BO_3 tri-angles which form a very highly planar ring and the 808 cm^{-1} peak has been assigned to the breathing mode of the B_3O_3 boroxol ring, as shown in Fig. 1. This assignment has been confirmed by elegant Ra-man isotopic substitution experiments [5–7]. There is, however, still considerable controversy [8] sur-rounding the boroxol model due, first, to the failure of molecular dynamics calculations to predict the presence of boroxol groups. Second there have been suggestions that the boroxol group is actually a structural feature of insignificant occurrence, but that the boroxol ring breathing mode is grossly enhanced in the Raman spectra.

2. Experimental details and results

An inelastic neutron scattering experiment was performed on v-B_2O_3 using the direct geometry HET spectrometer at the ISIS pulsed neutron source at the Rutherford Appleton Laboratory. The boron in the sample was enriched to 99.57% ^{11}B in order to minimise the absorption of neutrons by ^{10}B. An incident neutron energy of $E_0 = 130$ meV was used so as to optimise the resolution at the energy of the boroxol ring breathing mode 100.2 meV (1 meV $\equiv$ 8.06614 cm^{-1}). Fig. 2 shows a calculation of the resolution for the measurement, full details of which are given in Ref. [8]. The sample temperature was maintained at 15 K in order to minimise multi-phonon scattering.

Fig. 3 shows the inelastic neutron scattering mea-surement of the VDOS of v-B_2O_3 in the region of

Fig. 1. The triangular BO_3 basic structural unit of the continuous random network used to describe the structure of v-B_2O_3, to-gether with the B_3O_6 boroxol group showing the motion (dashed arrows, SS) involved in the boroxol ring breathing mode.
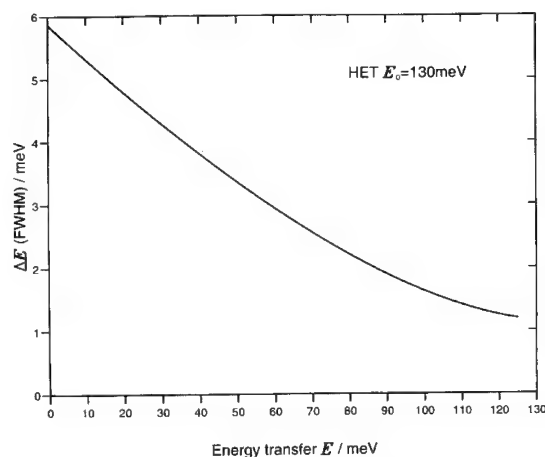
Fig. 2. The calculated resolution (FWHM) of the HET spectrome-ter for an incident energy, E_0, of 130 meV.
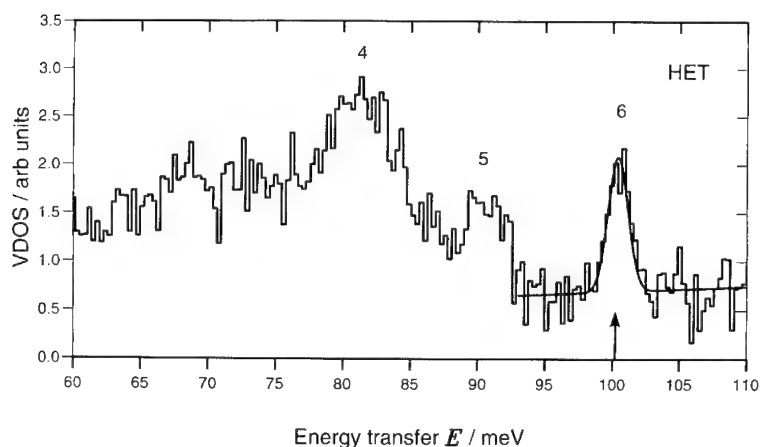
Fig. 3. The VDOS of vitreous v-B_2O_3 (after the multiple scattering correction) in the region of the boroxol ring breathing mode as measured by inelastic neutron scattering. The continuous line indicates the fit described in the text while the vertical arrow indicates the energy at which the boroxol ring breathing mode is observed in the Raman spectra. The peak numbering system corresponds to that used by Galeener and Thorpe [12].
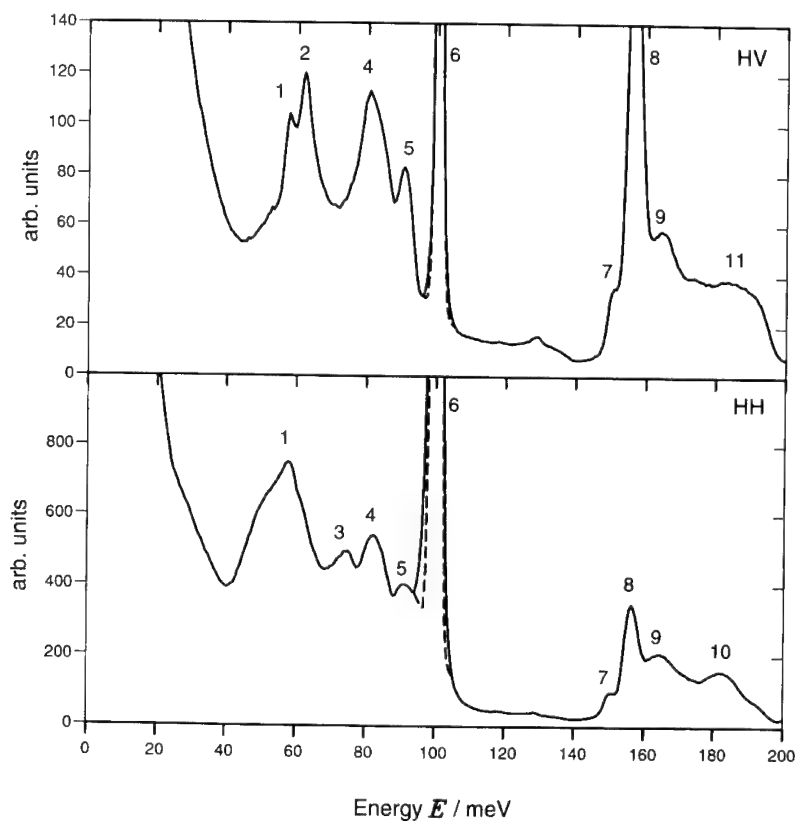
Fig. 4. The Raman spectra of v-B_2O_3 [1], without removal of the exciting line. The dashed lines show the fits described in the text, and the peak numbering system is that used by Galeener and Thorpe [12].

the boroxol ring breathing mode. The detectors on the HET spectrometer are all at relatively low scattering angle (10.4–29.6°) and hence there was a large proportion of multiple scattering. The data shown in Fig. 3 have been corrected for multiple scattering using a simple fitting approach, the details of which are given in Ref. [8].

3. Discussion

3.1. The width of the boroxol ring breathing mode peak

The measured VDOS of v-B_2O_3 has a relatively broad band of modes at approximately 82 meV and two narrower peaks at approximately 90 and 100 meV. Clearly the 100 meV peak can be identified with the 808 cm^{-1} Raman peak which is due to the breathing mode of the boroxol ring. The experimental results were fitted in the region of the boroxol ring breathing mode by a Gaussian plus linear background, giving the results shown in Table 1. The calculated experimental energy resolution at the energy of the boroxol ring breathing mode is 1.63 meV, and this is strikingly similar to the fitted width of the Gaussian, 1.74 ± 0.18 meV. Clearly the true width of the peak in the VDOS due to the boroxol ring breathing mode is small compared with the experimental resolution. The narrowness of this peak is evidence of the high degree of planarity of the boroxol groups in v-B_2O_3.

Fig. 4 shows the Raman HV and HH spectra for v-B_2O_3 at room temperature [1] together with fits to the boroxol ring breathing mode which were performed in the same way as for the neutron data. While the Gaussian does not fit the tails of the Raman peaks well, it is a satisfactory fit for the present purpose of providing widths, positions and areas which may be compared directly with those for the inelastic neutron scattering result. (In fact the original paper [1] describing these Raman data reports the width of the boroxol ring breathing mode to

[1] The data shown here are those of Galeener et al. [1] without removal of the exciting line since unfortunately this is the only form in which these data are now available.

Table 1
The results from fitting the boroxol ring breathing mode peak

	Gaussian position (meV)	Gaussian FWHM (meV)	Scaled Gaussian area
Neutron (HET)	100.38 ± 0.04	1.74 ± 0.18	0.971
Raman HV	100.22 ± 0.01	2.18 ± 0.04	6.1
Raman HH	100.06 ± 0.01	2.22 ± 0.04	38.7
Random model	100.37 ± 0.07	2.03 ± 0.15	1.03
Alternate model	100.59 ± 0.16	1.89 ± 0.33	1.17

be ~ 15 cm^{-1} (~ 1.9 meV) which is consistent with the widths in Table 1. In this particular case, the width of the peak observed by inelastic neutron scattering is actually narrower than the widths of the Raman peaks. The spectral slit width for the Raman data shown here was reported to be less than 5 cm^{-1}, and hence the Raman peak widths in Table 2 do not arise mainly from resolution. This is to be contrasted with the observation that the neutron peak width is due mostly to resolution. In part this difference in observed peak width may be explained by the effect of temperature. Ramos et al. [9] have found that the Raman FWHM changes approximately from 10 cm^{-1} at 4.2 K to 13 cm^{-1} at room temperature (the spectral slit width was less than 2 cm^{-1}), and a change in the distribution of dihedral angles with temperature was suggested on the basis of their results. Walrafen et al. [10] have also shown that the FWHM of the Raman peak at 808 cm^{-1} increases as the temperature is increased, with similar numerical values to Ramos et al. However, this temperature effect is not able to fully explain the discrepancy between the neutron and Raman peak widths; the Raman low temperature data indicate a natural width of approximately 1.2 meV, whereas the neutron result (which was measured with a sample temperature of 15 K) indicates a natural width which, on the assumption that widths add in quadrature, may be estimated to be in the region of 0.6 meV. It

Table 2
The ball-and-stick models used for the calculations

Model	Number of atoms	Relaxed	Ref.
No boroxol rings	1344	No	[20,21]
Random	1262	Yes	[22]
Alternate	1249	No	[22]

may be suggested [8] that this discrepancy arises from one of the differences between the nature of these two experimental techniques. First, inelastic neutron scattering involves finite values of momentum transfer, Q, whereas Raman scattering is a zone-centre technique ($Q = 0$). Second, Raman scattering involves a matrix element enhancement effect which does not occur for inelastic neutron scattering. Third inelastic neutron scattering experiments tend to take a much longer time than Raman experiments, leading to the possibility that the difference in peak widths could be due to a relaxation effect.

In the past, inelastic neutron scattering has suffered from having a poor energy resolution by comparison with that of Raman scattering. However, the present results show that, with the advent of modern pulsed neutron source spectrometers, this is no longer the case.

3.2. The area of the boroxol ring breathing mode peak

A comparison of the Raman spectra with the neutron VDOS shows that the boroxol ring breathing mode is greatly enhanced in both Raman spectra. However, the relative magnitudes of the 82 and 90 meV peaks seem to be similar for the Raman spectra and for the neutron VDOS. Hence the final column of Table 1 gives the area of the fitted Gaussian divided by the height of the 82 meV peak in order to give some measure of the boroxol ring breathing mode enhancement. (The 82 meV peak seems to be relatively broad in comparison with the experimental resolution so that its height should not be so sensitive to the effects of resolution.) The scaled Gaussian area indicates that the boroxol ring breathing mode is enhanced by factors of approximately 6.3 in the HV Raman spectrum and 40 in the HH Raman spectrum. A comparison of the neutron and Raman data indicates that the Raman peaks at 62.2 meV (502 cm^{-1}) and 74.6 meV (602 cm^{-1}) are also enhanced. Galeener et al. [11] have previously compared the neutron, Raman and infrared spectra for tetrahedral amorphous systems (SiO_2, GeO_2, BeF_2) and made the observation that the Raman HV spectrum mimics the VDOS while the HH spectrum is dominated by matrix element effects. In the case of v-B_2O_3, it appears that matrix element effects have an influence on both Raman spectra, but that the effect is smaller for the HV spectrum.

4. Model calculations of the vibrational density of states of v-B_2O_3

4.1. Introduction and theory

Galeener and Thorpe [12] have previously performed calculations of the VDOS of v-B_2O_3 by application of Sen and Thorpe's [13] central force analysis. This method involves a calculation of the band edges of the VDOS as a function of bridging oxygen bond angle. It was found that a network of triangles gave a general form to the VDOS which was much less structured than the Raman spectra and could not reasonably reproduce a symmetric mode at 808 cm^{-1}. A network of boroxol groups gave a VDOS which was much more structured and similar to the Raman spectra; in particular, it exhibited an energy gap similar to that observed in the experimental data with a delta-function at the low-energy edge of the gap similar to the 808 cm^{-1} Raman line. Thence it was concluded that the boroxol network showed better agreement with the experimental data than did the network of independent BO_3 triangles. The discrepancies which remained were ascribed to the need to include non-central forces in the calculation. The purpose of the study reported here was thus to perform calculations of the VDOS for v-B_2O_3 using a force model which includes non-central forces. However, the Sen and Thorpe analysis is applicable only when the force model contains only central forces, and for this reason the present calculations used the approach pioneered by Bell and Dean [14] whereby the VDOS is calculated numerically for a large ball-and-stick model of the structure. In fact such calculations were first called for by Galeener et al. [1] as a consequence of their original Raman study of v-B_2O_3.

The theory of network dynamics is presented here in a form involving 'sub-matrices' and 'dyads', which is particularly suited to the formulation of the calculations discussed below. To the authors' knowledge, this formulation of the theory of network dynamics has not been presented in the literature before. The aim of the calculations is to obtain the VDOS of an

assembly of atoms, assuming only harmonic forces between atoms. It can be shown that in the harmonic approximation it is possible to derive the eigenvalues of the system purely by considering the classical problem [15], in which case the VDOS is the normalised distribution of the frequencies ω_s, where ω_s^2 are the eigenvalues of the dynamical matrix, $\mathbf{W}$ ($\mathbf{W}\tilde{y} = \omega_s^2 \tilde{y}$).

Let the ith atom suffer a small displacement $\boldsymbol{u}_i$, from its equilibrium position. The contribution to the force on atom i due to the displacement of atom j may then be written in the form $-\sqrt{m_i m_j}\,\mathbf{W}_{ij}\boldsymbol{u}_i$ where the 3×3 sub-matrices, $\mathbf{W}_{ij}$, are the elements of the dynamical matrix. For the calculations discussed below, a Born force was assumed to act between atoms. This force has two components, one parallel to the bond (the central force) and one perpendicular to the bond (the non-central force). It was assumed that there is only one bond type (and hence only one set of force constants) and that only forces between bonded atoms are significant. In this case the elements of the dynamical matrix are

$$\mathbf{W}_{ii} = \frac{1}{m_i} \sum_{j,j \neq i} \left[\left(\lambda^c - \lambda^{nc} \right) \hat{d}_{ij}\hat{d}_{ij} + \lambda^{nc}\mathbf{I} \right] \qquad (1)$$

and

$$\mathbf{W}_{ij} = -\frac{1}{\sqrt{m_i m_j}} \left[\left(\lambda^c - \lambda^{nc} \right) \hat{d}_{ij}\hat{d}_{ij} + \lambda^{nc}\mathbf{I} \right], \qquad (2)$$

where $\mathbf{I}$ is a unit matrix, $\hat{d}_{ij}$ is the unit bond vector from atom i to atom j, and λ^c and λ^{nc} are central and non-central force constants respectively. The j-summation is over all atoms in the sample bonded to atom i, and the symbol $\boldsymbol{ab}$ is known as a dyad [16] and is used to represent the matrix which is the outer product of the two vectors $\boldsymbol{a}$ and $\boldsymbol{b}$.

The Born force represents a very simplistic force model because it does not contain a true bond-bending force, and it is not theoretically correct since it is not rotationally invariant. However, it has previously been found in calculations for amorphous Si and Ge [17] and for SiO_2 [18] that in most respects it is an excellent approximation to a more realistic force model [19], and thus the Born force was used in the work discussed here. It is of course possible that the rather unique structure of v-B_2O_3 requires a more sophisticated force model constructed to constrain

the bond and torsion angles in the boroxol group, but even if that should prove to be the case it is still worthwhile to present the approaches to the problem which have been developed for the case of the Born force.

4.2. Calculation method

Calculations of the VDOS were performed for three different ball-and-stick models of the structure of v-B_2O_3, as given in Table 2. Each of the three models is a CRN of BO_3 triangles, but the 'no boroxol rings' model contains no boroxol groups while the other two models have 75% of boron atoms in boroxol groups. In the 'random' model, the two types of structural unit (independent BO_3 triangles and boroxol groups) are arranged at random, whereas in the 'alternate' model there is an alternating arrangement of units. Modelling studies [20] favoured the structure of the random model. (For further discussion of the structures of these models, see Ref. [8] and references contained therein.) The number of surface atoms is very small for these models due to their large size and relatively low connectivity. For example the random model has 24 non-bridging oxygens which represents only 1.9% of the atoms in the model. This is to be contrasted with the case of the original Bell and Dean [14] model of SiO_2 for which 19% of the atoms were non-bridging oxygens. Thus the effect of the surface was not considered.

The VDOS of each model was calculated by use of the Sparspak package of Fortran subroutines [23], after adaptation to implement the negative eigenvalue theorem of Dean and Martin [24]. For these calculations it was found to be convenient to describe the force model in terms of a central force constant, λ^c, and a force constant ratio, $r = \lambda^{nc}/\lambda^c$. Since vibrational frequencies scale as $\sqrt{\lambda/m}$ for harmonic forces, the calculations were performed as a function of a dimensionless 'normal' frequency $\omega' = (\text{amu(kg)}/\lambda(\text{N/m}))^{1/2}\omega(\text{rad/s})$. This enables the calculations to be performed with atomic masses in atomic mass units (amu) and with the central force constant, λ^c, set to one. The calculated VDOS may subsequently be put on an energy axis according to $E(\text{meV}) = 16.1526\sqrt{\lambda^c(N/m)}\,\omega'$, where the value

of λ^c is chosen to give agreement with experimental data. This is similar to the situation for lattice dynamics where force constants are selected to give agreement with inelastic neutron scattering measurements of dispersion curves.

4.3. Optimisation of the calculated VDOS by comparison with the Raman spectra

In a calculation of the type reported here, a direct identification of the nature of the modes in a particu-
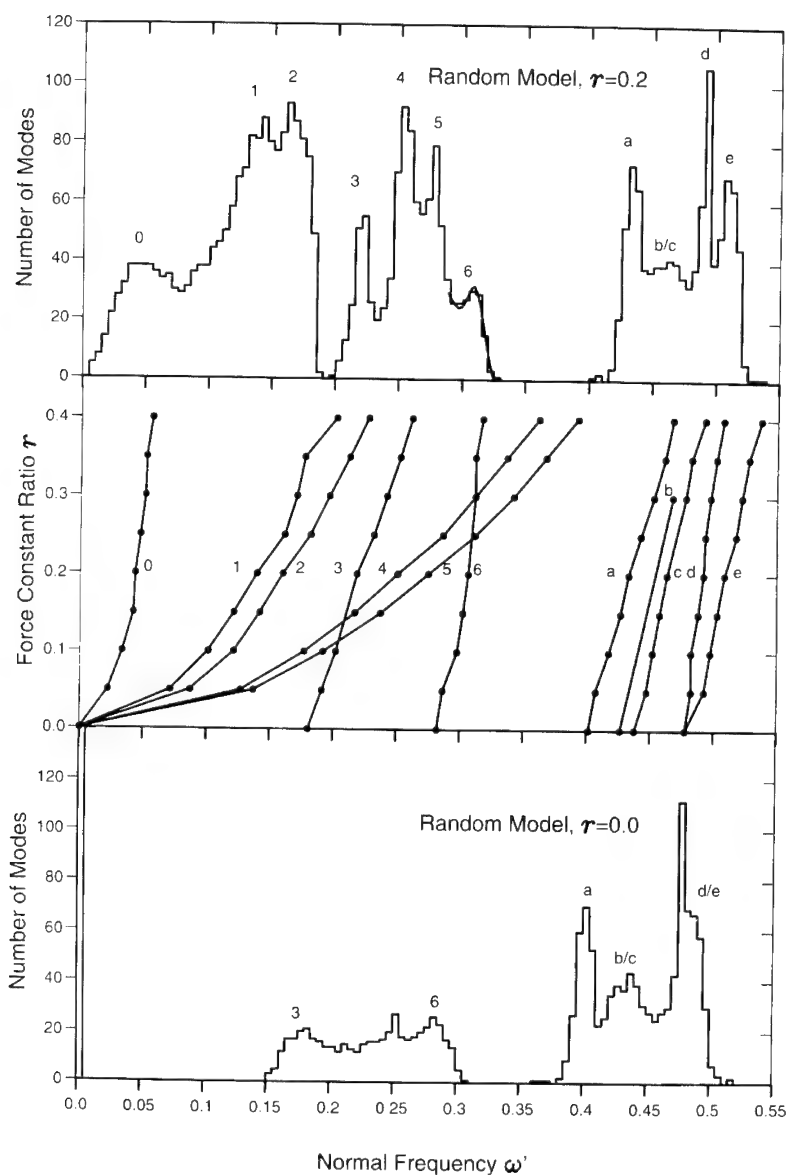

Fig. 5. The VDOS calculated for the random model for $r = 0.2$ (top; with the fit described in the text shown as a continuous line) and for $r = 0.0$ (bottom), together with the r-dependence of the features of the VDOS.

lar peak of the VDOS cannot be made since only eigenvalues have been calculated and not eigenvectors. Hence two new calculational techniques were developed to enable information about the atomic motions associated with the modes to be inferred. The first of these techniques involves a study of the effect of the force constant ratio, r, while the second technique involves a simulation of Raman isotopic substitution data.

Fig. 5 shows the VDOS of the random model calculated for force constant ratios $r = 0.0$ (i.e. a central forces only calculation) and $r = 0.2$, together with the r-dependence of the features of the VDOS. The $r = 0.0$ result shows great similarity to the central force result obtained by Galeener and Thorpe [12] for a CRN of boroxol groups. The correct value of r is not known, of course, but a value of order 0.2 is conventionally thought to be reasonable. For $r = 0.2$, the general form of the calculated VDOS may be described as two bands of modes followed by an energy gap and then a further band of modes, and this is the characteristic form for the VDOS of a CRN of BO_3 triangles [25–27].

For reasonable values of r (of order 0.2), the random model VDOS has a peak (6) at the lower edge of the energy gap. This is where the boroxol ring breathing mode is found experimentally, and hence the peak 6 is a likely candidate to be identified as the boroxol ring breathing mode. In fact the only other candidate below the energy gap is peak 3. The

reason for this is that for the boroxol ring breathing mode the oxygen displacements have a non-zero component along the B–O bonds and consequently this mode must occur at finite frequency for a ($r = 0.0$) central forces only calculation. However, peak 3 is a much less promising candidate since it is not possible to adjust r so that the VDOS has an energy gap with peak 3 at the lower edge of the gap.

Fig. 6 shows the effect of isotopic substitution (i.e., either the substitution of ^{10}B for ^{11}B or of ^{18}O for ^{16}O) on the VDOS calculated for the random model using a value $r = 0.2$. The shifts for the peaks of the VDOS are quantified in Table 3, where the following definitions have been used:

$$\Delta \omega'_B = \omega'(\text{natural}) - \omega'(^{10}\text{B}) \qquad (3)$$

and

$$\Delta \omega'_O = \omega'(^{18}\text{O}) - \omega'(\text{natural}), \qquad (4)$$

where $\omega(\text{natural})$, $\omega(^{10}\text{B})$ and $\omega(^{18}\text{O})$ are the frequencies at which the mode occurs for $^{11}B_2^{16}O_3$, $^{10}B_2^{16}O_3$ and $^{11}B_2^{18}O_3$ respectively. The experimental Raman isotopic substitution data have been very important in confirming the identification of the 808 cm^{-1} Raman peak with the breathing mode of the boroxol ring, and Table 4 contains the experimental Raman isotopic substitution peak shifts given by Galeener and Thorpe [12]. An important property of the boroxol ring breathing mode is that it involves only oxygen motion so that $\Delta \omega'_B = 0$ and Tables 3 and 4 show this to be the case for the calculated peak 6, as well as for the experimentally observed peak,

Table 3

The isotopic substitution peak shift data for the calculated VDOS of the random model

Fea-ture	ω' (natural)	^{10}B → ^{11}B substitution		^{18} → ^{16}O substitution	
		$\omega'(^{10}\text{B})$	$\Delta\omega'_B / \omega'(^{10}\text{B})$	$\omega'(^{18}\text{O})$	$\Delta\omega'_0 / \omega'$ (natural)
0	0.0458	0.0474	−0.033	0.0458	0
1	0.1420	0.1420	0	0.1373	−0.033
2	0.1623	0.1623	0	0.1521	−0.063
3	0.2217	0.2217	0	0.2069	−0.067
4	0.2522	0.2624	−0.039	0.2522	0
5	0.2773	0.2874	−0.035	0.2718	−0.020
6	0.3070	0.3070	0	−	−
a	0.4321	0.4524	−0.045	0.4321	0
b	0.4524	0.4673	−0.032	0.4470	−0.012
c	0.4618	0.4775	−0.033	0.4571	−0.010
d	0.4923	0.5072	−0.029	0.4822	−0.021
e	0.5072	0.5267	−0.037	0.4970	−0.020

Table 4

The fractional Raman isotopic substitution peak shifts given by Galeener and Thorpe [12]

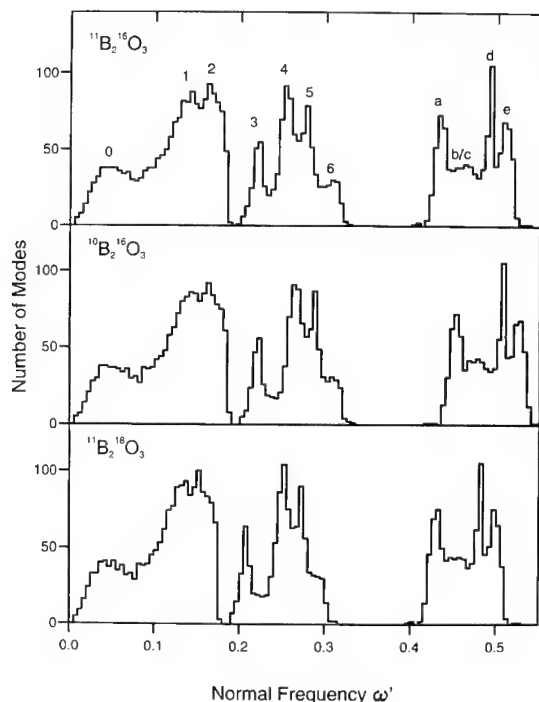| Feature	Energy (cm^{-1})	Energy (meV)	$\Delta\omega_B / \omega(^{10}\text{B})$	$\Delta\omega_0 / \omega'(\text{natural})$
1	470	58.3	−0.002	−0.053
2	502	62.2	−0.004	−0.056
3	602	74.6	−0.005	−0.058
4	660	81.8	−0.029	−0.006
5	732	90.7	−0.031	−
6	809	100.3	0	−0.059
7	1212	150.3	−0.022	−0.026
8	1261	156.3	−0.020	−0.020
9	1327	164.5	−0.032	−0.007
10	1467	181.9	−0.030	−0.010
11	1510	187.2	−0.029	−

Fig. 6. The effect of isotopic substitution on the VDOS calculated for the random model.

supporting the identification of peak 6 as the boroxol ring breathing mode.

A comparison of the fractional isotopic substitution peak shifts in Tables 3 and 4 supports an identification of the peaks 1–6 of the random model VDOS with the Raman peaks 1–6 (the peak numbering scheme used for the calculated VDOS was chosen to be consistent with the numbering scheme adopted for the Raman spectra by Galeener and Thorpe [12]). For all of these peaks, the motion involves predominantly only one of the two elements; peaks 1, 2, 3 and 6 involve mostly oxygen motion, while peaks 4 and 5 involve mostly boron motion. The behaviour with isotopic substitution of the Raman spectra for peaks below 1 has not been reported. However, peak 0 of the random model VDOS can probably be identified with the Raman peaks at 130 cm^{-1}($\equiv$ 16.1 meV) and 145 cm^{-1} ($\equiv$ 18.0 meV).

Clearly the calculated VDOS of the random model shows a high degree of correspondence with the experimental data below the energy gap. The r-de-

pendence data shown in Fig. 5 can thus be used to determine a reasonable value for r; when $r = 0.15$ peaks 3 and 4 are merged, while peaks 5 and 6 are merged when $r = 0.25$. Since peaks 3, 4, 5 and 6 are found experimentally to be clearly separated and to occur in the order in which they are numbered, the correct value of r must lie between these two values. Hence a value of 0.2 for r is seen to be ideal.

A comparison of the calculated normal frequency of mode 6 with its experimentally observed energy leads, by use of Eq. (12), to a value of 401.4 N m^{-1} for λ^c. However, if the same comparison is performed for modes 1–5 it is found that, while modes 3–6 require a value for λ^c of about 400 N m^{-1}, modes 1 and 2 require a value of about 600 N m^{-1}. Galeener and Thorpe [12] have previously suggested that a higher value should be used for λ^c for bonds outside boroxol rings than for bonds inside boroxol rings and, since mode 6 involves only bonds inside a boroxol ring, this suggests that the value $\lambda^c \sim 400$ N m^{-1} should be associated with bonds inside boroxol rings, while the value of $\lambda^c \sim 600$ N m^{-1} should be associated with bonds outside boroxol rings. Galeener et al. [1] obtained a value $\lambda^c = 612$ N m^{-1} for a CRN composed solely of independent BO$_3$ triangles which agrees well with the value deduced here to apply to bonds outside boroxol rings. Further, the work of Bril [28] on the Raman spectra of crystalline and vitreous borates indicates a value of λ^c for bonds inside boroxol rings which is about 30% smaller than the value for bonds outside boroxol rings, in good agreement with the current results.

An inadequacy of the results obtained by Galeener and Thorpe [12] is that the calculated modes above the energy gap occur at too low an energy, requiring an 'ad hoc gap expansion' to obtain satisfactory agreement with the experimental data. It was suggested that this is due first to the lack of non-central forces and second to the need for differing central force constants for bonds inside and outside boroxol rings. However, the calculated r-dependence plotted in Fig. 5 shows that the energy of the modes above the energy gap depends relatively little on the strength of the non-central force constant, λ^{nc}. Hence the first of the suggested mechanisms for a gap expansion is contradicted by the present results, and only the second suggestion of a variation in the central force constant remains as a viable possibility. (Since the

energy of the modes above the energy gap depends only weakly on the non-central force constant of the Born force, it is doubtful whether any other force with a non-central component, such as the Keating potential [29], would be successful at achieving the required gap expansion.)

Galeener and Thorpe [12] have identified five peaks, labelled 7–11, above the energy gap in the Raman spectra, although peak 11 appears to be very broad and ill-defined. The random model VDOS also has five peaks above the energy gap, labelled a–e, although it is perhaps questionable whether b and c really represent two separate peaks. The main evidence suggesting that b and c are separate peaks is the VDOS of the alternate model where they appear as two quite distinct features; it can then be argued that these peaks are almost merged in the random model VDOS as a result of the relaxation procedure. A comparison of the model and experimental oxygen isotopic substitution data suggests that the model peak a should be identified with the experimental peak 9 since both show very small shifts, and possibly that the calculated peak c can be identified with the observed peak 10. If these identifications are correct then they require a value of approximately 600 N m^{-1} for the central force constant, λ^c. The Raman spectra show that the band of modes above the energy gap extends from 145 to 197 meV, and if a single value is used for λ^c then the modes of the random model above the energy gap cover the range from 140 to 164 meV for $\lambda^c = 400$ N m^{-1}, or 171–201 meV for $\lambda^c = 600$ N m^{-1}. Hence the suggestion that the ad hoc gap expansion can be justified in terms of two central force constant values appears to be correct.

In their central force calculations, Galeener and Thorpe [12] chose to fit their model VDOS to features 1 and 6 in order to determine the two parameters of the calculation (central force constant λ^c and mean bridging oxygen bond angle, θ, outside boroxol rings). However, according to the present results, non-central forces are essential in describing the motion associated with the peak labelled 1, since it occurs at zero frequency for the central forces only calculation ($r = 0.0$, see Fig. 5). The band edge in Galeener and Thorpe's calculated VDOS which was fitted to peak 1 of the Raman spectra is found to become a significant peak on the addition of non-

central forces and should have been fitted to peak 3 of the Raman spectra. This discrepancy in identification of peaks is the reason why the central force constant, $\lambda^c = 470$ N m^{-1}, obtained by Galeener and Thorpe for a network of boroxol groups does not agree well with the present value of $\lambda^c \sim 400$ N m^{-1} for bonds inside boroxol rings. The present study indicates that non-central forces are essential to an understanding of peaks 0, 1, 2, 4 and 5, but suggests that a central-forces-only model with a variation in central force constant should be able to explain peaks 3, 6 and 7–11, contrary to Galeener and Thorpe's conclusion that a correct explanation of features 7 and 8 requires non-central forces.

Barrio et al. [30] have recently given a report of calculations for a Bethe lattice of boroxol groups subject to a generalised Born force. This report questions the identification of peak 6 as the boroxol ring breathing mode given previously in a brief preliminary report of the present calculations [31]. Instead it is concluded that peak 3 represents the boroxol ring breathing mode (as discussed above, this peak is the only likely candidate, other than peak 6). Since a calculation of the eigenvectors is not feasible for a large ball-and-stick model, it is not possible to determine directly the nature of the vibrations for a particular peak in the VDOS for a calculation of the type presented here. Instead indirect means must be used and in the present case an attempt has been made to identify the boroxol ring breathing mode by virtue first of its position at the lower edge of the energy gap and second of the successful reproduction of the Raman isotopic substitution data. Since these indirect methods must be used to infer the nature of a mode it is not possible to directly contradict the alternative mode identification of Barrio et al. However, a difficulty with this alternative is that the boroxol ring breathing mode should be at the lower edge of the energy gap, but the model presented here cannot give a result where peak 3 is in such a position since peaks 4 and 5 are always at a higher energy than peak 3. Also the present identification of peaks seems to reproduce the Raman isotopic substitution data well. Nevertheless it is not possible to rule out the possibility that a more sophisticated force model would be capable of giving a result with peak 3 at the lower edge of the energy gap without having caused other peaks to
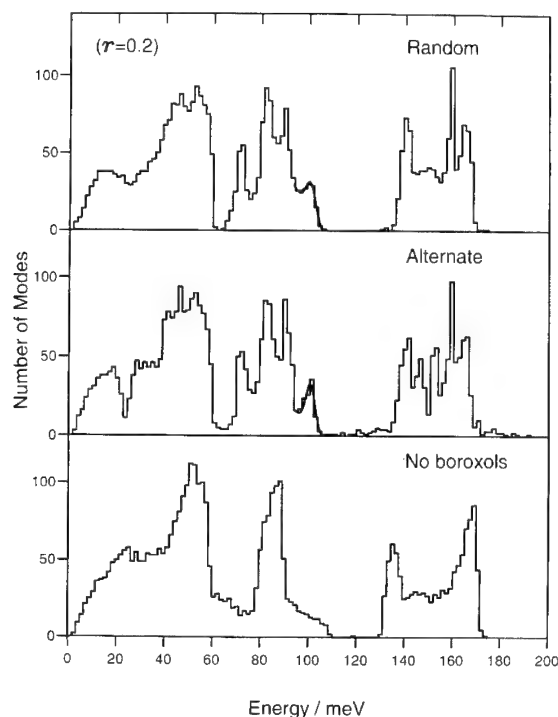
Fig. 7. The calculated VDOS for each model. The fits described in the text are shown by a continuous line.

move into the energy gap. However, the VDOS calculated by Barrio et al. exhibits a peak at about 108 meV and thus far there has been no experimental observation of such a peak by inelastic neutron scattering, or any other technique. (We note in passing, however, that both inelastic neutron scattering [27] and Raman scattering observe a mode at approximately 130 meV that has so far been neglected in all modelling studies.) Finally it may be noted that Barrio et al.'s VDOS shows little correspondence with lower energy inelastic neutron scattering results [25–27].

4.4. Comparison with the inelastic neutron scattering result

Fig. 7 shows the VDOS calculated for Wright et al.'s [22] random and alternate models and for Williams and Elliott's [20,21] model, in each case using $r = 0.2$ and a value of 401.4 N m^{-1} for λ^c (chosen so that the energy of the calculated peak 6 coincides with the energy of the boroxol ring breath-

ing mode). All three models have the energy gap typical of the triangular BO_3 CRN. However, only the models containing boroxol groups have a peak at the low-energy edge of the energy gap which may be identified as the boroxol ring breathing mode. This peak was fitted using the same procedure as had been used for the experimental data, yielding the results given in Table 1. The scaled Gaussian area for the models containing boroxol groups shows good agreement with the result from the neutron-weighted VDOS. For both of these models the fraction of boron atoms in boroxol groups is $f = 0.75$, and hence this agreement supports the results from neutron diffraction [8] and from nuclear magnetic resonance [32] that $f = 0.80 \pm 0.05$ and $f = 0.82 \pm 0.08$ respectively. The model peak widths given in Table 1 are relatively large in comparison with the peak width indicated by the experimental data, and this discrepancy may be ascribed to the effect of the relaxation procedure used for the models [8].

5. Conclusions

The boroxol ring breathing mode of vitreous B_2O_3 has been clearly observed by inelastic neutron scattering with an energy resolution comparable with that of Raman scattering. The results show that the mode is enhanced in the Raman HV and HH spectra by factors estimated at 6.3 and 40, respectively. The observed width of the mode is similar to that of the experimental resolution, indicating that the natural width is extremely small.

Calculations of the vibrational density of states for ball-and-stick models subject to a force including a non-central component show that only models containing boroxol groups give rise to a result of a complexity comparable with that observed previously by Raman scattering and now by inelastic neutron scattering. It has been shown that the nature of the atomic motions associated with features in the calculated vibrational density of states can be inferred by the use of indirect methods which involve the study of the effects of force constant variation and of isotopic substitution. The vibrational density of states for a model containing boroxol groups shows agreement with Raman isotopic substitution data below the energy gap. The calculated modes

above the energy gap occur at too low an energy, but there is evidence that this situation would be improved by having two central force constants, one of about 400 N m^{-1} for bonds inside boroxol rings, and one of about 600 N m^{-1} for bonds outside boroxol rings.

References

[1] F.L. Galeener, G. Lucovsky and J.C. Mikkelsen Jr., Phys. Rev. B22 (1980) 3983.

[2] W.H. Zachariasen, J. Am. Chem. Soc. 54 (1932) 3841.

[3] B.E. Warren, H. Krutter and O. Morningstar, J. Am. Ceram. Soc. 19 (1936) 202.

[4] J. Goubeau and H. Keller, Z. Anorg. Allg. Chem. 272 (1953) 303.

[5] F.L. Galeener and A.E. Geissberger, J. Phys. (Paris) Coll. C9 (1982) 343.

[6] C.F. Windisch Jr. and W.M. Risen Jr., J. Non-Cryst. Solids 48 (1982) 307.

[7] W.M. Risen Jr., J. Non-Cryst. Solids 76 (1985) 97.

[8] A.C. Hannon, D.I. Grimley, R.A. Hulme, A.C. Wright and R.N. Sinclair, in: Proc. 1st PAC RIM Meeting, Hawaii, Nov. 1993, J. Non-Cryst. Solids 177 (1994) 299.

[9] M.A. Ramos, S. Vieira and J.M. Calleja, Solid State Commun 62 (1987) 455.

[10] G.E. Walrafen, S.R. Samanta and P.N. Krishnan, J. Chem. Phys. 72 (1980) 113.

[11] F.L. Galeener, A.J. Leadbetter and M.W. Stringfellow, Phys. Rev. B27 (1983) 1052.

[12] F.L. Galeener and M.F. Thorpe, Phys. Rev. B28 (1983) 5802.

[13] P.N. Sen and M.F. Thorpe, Phys. Rev. B15 (1977) 4030.

[14] R.J. Bell and P. Dean, Discuss. Faraday Soc. 50 (1970) 55.

[15] P. Dean, Rev. Mod. Phys. 44 (1972) 127.

[16] J. Mathews and R.L. Walker, Mathematical Methods of Physics (Benjamin, New York, 1970).

[17] R. Alben, D. Weaire, J.E. Smith Jr. and M.H. Brodsky, Phys. Rev. B11 (1975) 2271.

[18] R.B. Laughlin and J.D. Joannopoulos, Phys. Rev. B17 (1978) 2790.

[19] F.L. Galeener, R.A. Barrio, E. Martinez and R.J. Elliott, Phys. Rev. Lett. 53 (1984) 2429.

[20] S.J. Williams and S.R. Elliott, in: The Structure of Non-Crystalline Materials, ed. P.H. Gaskell, J.M. Parker and E.A. Davis (Taylor and Francis, London, 1982) p. 407.

[21] S.J. Williams and S.R. Elliott, Proc. R. Soc. (London) A380 (1982) 427.

[22] A.C. Wright, D.J. Sumner and A.G. Clare, in: The Structure of Non-Crystalline Materials 1982, ed. P.H. Gaskell, J.M. Parker and E.A. Davis (Taylor and Francis, London, 1982) p. 395.

[23] A. George, J.W. Liu and E. Ng, University of Waterloo, Research Report CS-78-30, (1980).

[24] P. Dean and J.L. Martin, Proc. R. Soc. (London) A259 (1960) 409.

[25] A.C. Hannon, R.N. Sinclair and A.C. Wright, in: The Physics of Non-Crystalline Solids, ed. L.D. Pye, W.C. LaCourse and H.J. Stevens (Taylor and Francis, London, 1992) p. 67.

[26] A.C. Hannon, R.N. Sinclair and A.C. Wright, Physica A201 (1993) 375.

[27] A.C. Hannon, A.C. Wright and R.N. Sinclair, in: Fundamentals of Glass Science and Technology (Stazione Sperimentale del Vetro, Venice, 1993) p. 479 (supplement to Riv. Staz. Sper. Vetro XXIII (1993)).

[28] T.W. Bril, Philips Res. Rep. Suppl. 2 (1976).

[29] P.N. Keating, Phys. Rev. 145 (1966) 637.

[30] R.A. Barrio, F.L. Castillo-Alvarado and F.L Galeener, Phys. Rev. B44 (1991) 7313.

[31] A.C. Hannon, R.N. Sinclair, J.A. Blackman, A.C. Wright and F.L. Galeener, J. Non-Cryst. Solids 106 (1988) 116.

[32] G.E. Jellison Jr., L.W. Panek, P.J. Bray and G.B. Rouse Jr., J. Chem. Phys. 66 (1977) 802.

Section 3. Defects

Properties of bonded hydrogen in hydrogenated amorphous silicon and other hydrogenated amorphous silicon alloys

G. Lucovsky [a,c,d,*], Z. Jing [a], Z. Lu [a], D.R. Lee [d], J.L. Whitten [b]

[a] *Department of Physics, North Carolina State University, Raleigh, NC, 27695-8202, USA*
[b] *Department of Chemistry, North Carolina State University, Raleigh, NC, 27695-8202, USA*
[c] *Department of Materials Science and Engineering, North Carolina State University, Raleigh, NC, 27695-8202, USA*
[d] *Department of Electrical and Computer Engineering, North Carolina State University, Raleigh, NC, 27695-8202, USA*

Abstract

This paper discusses bonding configurations of hydrogen atoms (H) in amorphous silicon and amorphous-silicon-based alloys. Recent experiments combined with theoretical calculations have identified two new aspects of bonded H that have not previously been addressed: (i) the formation of H bonds between H atoms on Si–H groups and electronegative atoms or groups such as O atoms or NH groups; and (ii) an inherent metastability of H-bonded clusters as driven by the trapping of charged carriers. Both of these are shown to play important roles in (i) a photo-induced defect metastability such as the Staebler–Wronski effect, and (ii) hydrogen evolution from amorphous silicon nitrides. Finally, the concepts developed for a-Si:H alloys apply equally well to defect metastability at $Si–SiO_2$ interfaces as in metal–oxide–semiconductor devices including insulated-gate field-effect transistors.

1. Introduction

Infrared (IR) absorption spectroscopy has been shown to one of the most important techniques for establishing the local bonding arrangements of H atoms in hydrogenated amorphous silicon (a-Si:H) and silicon-based alloys (a-Si:X:H, where X is an alloy element such as O, N, C, etc.) [1,2]. Of particular importance have been comparisons of vibrational properties of films prepared using precursor molecules such as silane (SiH_4) and deuterated silane (SiD_4). The frequency changes brought about by substitution of D for H depend not only on the

nominal 1:2 mass ratio of H to D but also on the extent to which other near-neighbor atoms participate in the vibrational motion, i.e., through an effective mode mass [3]. Studies performed on a-Si:H and a-Si:D films, coupled with empirically-based calculations have identified the effects of mode-mass differences, thereby confirming assignments for the major features observed in the IR and Raman spectra (see Table 1) [4,5]. These assignments have generally relied on combinations of bond-stretching and bending features to distinguish between (i) monohydride (Si–H) and polyhydride (SiH_m, $m \geq 2$) arrangements; (ii) isolated and polymerized polyhydride groups such as SiH_2, and $(SiH_2)_n$, respectively; and (iii) bond-bending, rocking and wagging modes of polyhydride configurations.

A second aspect of bonded H in a-Si:H films that

---

* Corresponding author. Tel: +1-919 737 3301. Telefax: +1-919 515 7331.

contain other atomic species in addition to Si and H focuses on changes in Si–H bond-stretching frequencies that are induced by (i) near neighbors in the network, specifically atoms or groups that are more electronegative than Si and are back-bonded to the Si atoms of the Si–H groups [6,7], as well as (ii) changes in the average electronegativity of silicon alloy networks such as SiO_x, $0 < x \le 2$ and SiN_x, $0 < x < 1.33$ [8,9]. The frequencies of the Si–H stretching vibrations scale with the partial charges on the Si atom [7], and this is expressed as a function of the partial charge (e'_{Si}) by

$$\nu_{Si-H} = \nu_0 + \beta e'_{Si} = (1975 + 651 e'_{Si} \pm 13) cm^{-1}, \tag{1}$$

where e'_{Si} is calculated using the empirical procedures of Ref. [10]. The values of ν_0 and β were determined empirically. The frequency of the bond-stretching vibration for an Si–H group in a Si host approaches 1985 cm^{-1} in a-Si:H alloys with low hydrogen concentrations [H] [11]. This frequency is increased to (i) ~ 2000 cm^{-1} in a-Si:H with [H] ~ 10 at.%, (ii) ~ 2150 cm^{-1} in a-Si$_3$N$_4$ [9] and (iii) ~ 2250 cm^{-1} in a-SiO$_2$ [8].

Inductive effects have also been used to establish a non-statistical association of H and alloy atoms such as O and N atoms in a-Si:H networks with low concentrations of O or N atoms [8,9]. Near-neighbor
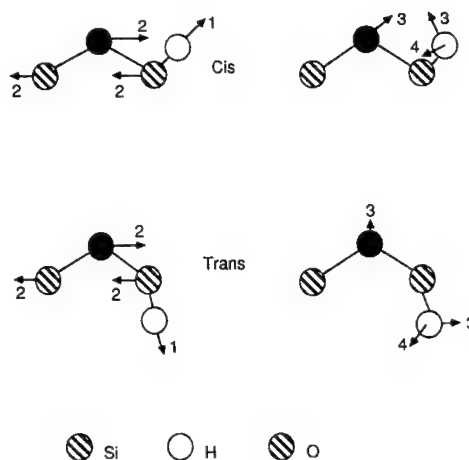

Fig. 1. Atomic motions for vibrational modes of O and H atoms bonded to a common Si atom. Mode 3 for the cis geometry is a coupled mode involving significant O and H atom motions. Mode 3 for the trans geometry and mode 4 for both geometries are localized Si–H bond-bending modes with no significant O atom motions.

bonding groups involving two different alloy atoms, e.g., H and O, can also lead to coupled modes with frequencies that are not found in the normal bonding arrangements of either alloy atom by itself. Fig. 1 shows an example of such a bonding geometry along with the eigenvectors of a coupled mode to be discussed below [12,13]. For a coupled mode to exist two conditions must be satisfied: (i) the atomic vibrations of the two atoms must be in the same frequency range, and (ii) each of the alloy atoms must vibrate in the same plane with their separate motions projecting on a common axis. As shown in Fig. 1, this occurs for Si–O–Si vibrations ($\sim 600–980$ cm^{-1}) and Si–H vibrations (630 to 2100 cm^{-1}) in a cis bonding geometry but not in trans geometry configuration.

Other experimental probes such as nuclear magnetic resonance (NMR) have also been used to study H atom incorporation in a-Si:H materials [14]. One example relates to NMR experiments that have established boron (B) and phosphorus (P) atoms in fourfold-coordinated doping configurations have near-neighbor H atoms occurring as second neighbors in H–Si–P$^+$–Si chains, and as first neighbors in H–B$^-$–Si chains [15]. These bonding geometries are

Table 1
Frequencies of IR-active vibrations

	Frequency (cm^{-1}) H	Frequency ratio D for H substitution
Monohydride SiH		
Bond-stretching	2000	1.37
Bond-bending	630	1.24
Isolated dihydride SiH$_2$		
Bond-stretching	2090	1.37
Scissors-bending	870	1.37
Rocking	630	1.26
Polymerized polyhydride (SiH$_2$)$_n$		
Bond-stretching	2100	1.38
Scissors-bending	890	1.37
Wagging-bending	845	1.33
Rocking	630	1.26

consistent with what is expected from the electronegativities of P^+ and B^- relative to Si and H [16,17].

Another aspect of H incorporation involves H bonding in which relatively weak electrostatic bonds are formed between H atoms with a positive partial charge and strongly electronegative atoms or groups. This has been studied for OH and NH groups in a-Si:O:H and a-Si:N:H, respectively [18,19]. Two different types of H bonding associated with the H atoms of OH groups have been reported in a-Si:O:H, and are distinguished by the spectral shape of the O–H stretching band between about 3200 and 3700 cm^{-1}. For isolated Si–OH groups in a-SiO$_2$, the H bond is between the H atom of the OH group and a bridging O atom of the network in an Si–O–Si geometry. This absorption band has an asymmetric shape indicative of a statistical distribution of H–O distances. It is also possible to have nearest-neighbor pairs OH groups, as in a-SiO$_2$:H films formed by low-temperature plasma deposition [19]. These groups can be cycled in and out of the films by sequential exposures to atmospheric moisture (or water) and low-temperature ($\sim 200°C$) annealing [19,20]. The bond-stretching spectral feature for nearest-neighbor Si–OH groups is a symmetric band centered at ~ 3300 cm^{-1}, and is easily differentiated from the asymmetric OH band in films prepared in different ways.

This paper focuses on new aspects of H bonding interactions involving H atoms of Si–H groups rather than H atoms of OH or NH groups. We review recent experimental results which suggest that chemically specific groups such as NH play a role in the light-induced metastability of defects in a-Si:H and a-Si:H-based alloys. We then indicate how these results, coupled with complementary experimental studies of H evolution and theoretical studies of bond energies and instabilities, have led to the development of a new model for defect metastability, e.g., as in the Staebler–Wronski effect (SWE) [21–23]. The model relies on trapping of charge carriers to promote metastable bond rearrangements [24]. Many of the traditional explanations for the SWE have invoked some type of diffusive H motion, whereas the new model is based on displacive H motion induced by charged carrier trapping, and thereby provides a mechanism by which the initial pre-light-soaked state can be restored exactly.

2. Summary of experimental results

2.1. Amorphous silicon alloys

Experimental evidence for chemically specific metastable defects in hydrogenated amorphous silicon alloys derives from a series of experiments recently reported for a-Si:N:H alloys [25]. Films were deposited by remote plasma enhanced carbon vapor deposition (PECVD) at a substrate temperature of 250°C using two different N atom source gases, N$_2$ or NH$_3$. Of importance to defect-related properties is an observation that films prepared from N$_2$ with [N] to at least up to 12 at.% do not display IR-detectable SiN–H absorptions, whereas films deposited from NH$_3$ display weak Si–NH absorptions for [N] $\approx$ 10–12 at.%.

Most of properties of these a-Si:N:H alloys as a function of [N] are independent of the N atom source gas including (i) the photon energy at which the absorption coefficient, $\alpha \approx 10^4$ cm^{-1} (the E_{04} optical gap), (ii) the dark conductivity activation energy, E_a, (iii) the photoconductivity, σ_{ph}, and (iv) the ambipolar diffusion length, L_{amb}, determined by the steady-state photo-grating (SSPG) method. The variations of E_a and L_{amb} with [N] are indicative of a transition from n-type doping for [N] $\lesssim$ 3 at.% to alloying for [N] $>$ 5 at.%.

The SWE has been studied in a-Si:N:H with [N] $\approx$ 10–12 at.% ($E_{04} \approx$ 2.1–2.2 eV), and in PV-grade a-Si:H ($E_{04} \approx$ 1.9 eV). a-Si:N:H alloys were prepared form two different N atom source gases, N$_2$ and NH$_3$. Metastable defects were induced by an extended exposure ($\sim$ 1000 min) to white light at a level of $\sim$ 200 mW/cm^2, and were monitored by the ratio of the initial photoconductivity to its value after 1000 min of light-soaking ($[\sigma_{ph}]0/[\sigma_{ph}]_{1000 \text{ min}}$) [24,25]. This ratio was $\sim$ 10 $\pm$ 3 for (i) a-Si:H and (ii) a-Si:N:H deposited from N$_2$, but was significantly increased, $\sim$ 50 $\pm$ 15 for (iii) a-Si:N:H deposited from NH$_3$; a value of $\sim$ 10 is typical of PV-grade a-Si:H for this light-soaking condition [21–23]. In spite of these differences in the SWE, annealing at $\sim$ 150–200°C for $\sim$ 2–3 h returned the photoconductivies to their initial values for all three types of film. The activation energy for annealing was $\sim$ 0.9 eV, independent of the incorporation of nitrogen, or the particular N atom source gas. These observations may be unique to films prepared by

remote PECVD, or other PECVD processes which also can provide sufficient control over reaction pathways to limit the multiplicity of different local bonding environments; in this case, these processing constraints inhibit the formation of SiN–H groups in films prepared from the N_2 source gas [26].

2.2. IR studies of annealed nitride films

These studies have shown that for a-Si:N:H films deposited at 300°C by remote PECVD with NH_3 as the N atom source gas, the absorption constants of the IR vibrations associated with Si–H and SiN–H groups decrease beginning at about 400°C indicating a release of bonded H similar to results reported elsewhere [27]. The release of H persists to temperatures up to 1000–1200°C at which the IR absorptions for the Si–H and N–H groups are below the level of detection; however, at temperatures above about 800–900°C, there is an increase in the IR absorption associated with Si–N bonds that is interpreted as a linking-up of Si and N atom dangling bonds formed by the removal of H from near-neighbor Si–H and SiN–H groups. Since the bond energies of Si–H and N–H in the Si–H and SiN–H groups are ∼ 3.5 and 5.0 eV, respectively, the release of H atoms at temperatures as low as 400–500°C must be a cooperative phenomenon involving the formation of molecular hydrogen, H_2. Estimates of the activation energies for this H atom removal, as determined from the IR data for a sample with approximately equal Si–H and Si–NH concentrations, are approximately 2–3 eV, and less than the 3.5–5.0 eV bond energy range.

3. Bond energies

Preliminary calculations were performed at the Hartree–Fock self-consistent field (SCF) level and were used in order to determine relative values of bond energies, and the extent to which a particular atomic arrangement was stable. In order to obtain more reliable values for the bond energies and bond lengths, correlation effects are incorporated into calculations which are performed using the MP2 perturbation scheme (see, for example, Ref. [28]). These calculations were performed on finite clusters in

Table 2
Si–H bond energies

Group	Si–H bond length (nm)	Si–H bond energy (eV)
Isolated Si–H	0.149	3.48
Positively charged ammonium $(Si_2-N-H_2)^+$	0.101	4.97
Neutral ammonium $(Si_2-N-H_2)^0$ (→ H)	unstable	− 1.51
Positively charged oxonium $(Si_2-O-H)^+$	0.96	5.65
Neutral oxonium $(Si_2-O-H)^0$ (→ H)	unstable	− 3.35

which atoms at the perimeter of the clusters were H-terminated. Table 2 includes results for four atomic arrangements that will be discussed below in the context of defect metastability. These are shown in Fig. 2 and are (i) a positively charged ammonium complex–H_2–N^+–Si_2, (ii) a neutral ammonium complex–H_2–N–Si_2, (iii) a positively charged oxonium complex–H–O^+–Si_2, and (iv) a neutral oxo-

Ammonium Complexes

Oxonium Complexes
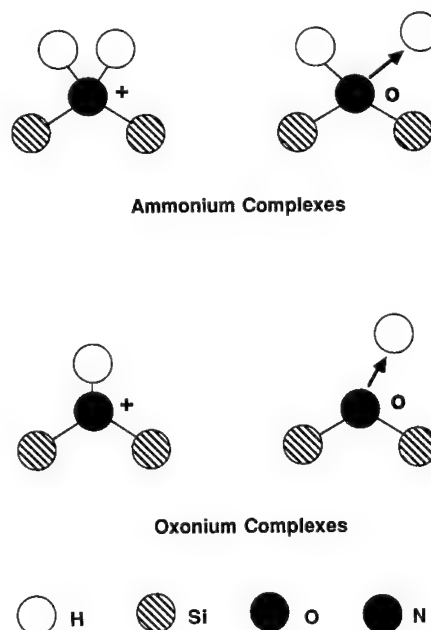
◯ H   ▨ Si   ⬤ O   ⬤ N

Fig. 2. Local atomic arrangements in positive in charged and neutral ammonium and oxonium clusters. The positively-charged clusters (a) and (c) are stable. The neutral clusters are unstable with respect to the loss of a single H atom (indicated by the arrow).

nium complex–H–O–Si$_2$. The results in Table 2 indicate that the charged ammonium and oxonium centers are stable, with N$^+$–H and O$^+$–H bond energies of ~5.0 eV and 5.6 eV, respectively, whereas the neutral centers are unstable against the release of a H atom by −1.5 and −3.3 eV, respectively.

We have also considered H atom removal from metastable ammonium centers that can be induced by either electron trapping at low temperatures (< 300°C) without H$_2$ formation or by electron trapping at high temperatures (> 400°C) which includes H$_2$ formation (see Section 4). The energy calculations needed to describe these effects must include any electrostatic interactions between the N atom and Si atom dangling bonds formed during the high-temperature H–release processes. These calculations demonstrate that, for Si–N distances of the order of 0.25–0.3 nm, there are relatively strong electrostatic interactions that result from the dangling bonds being charged rather than neutral; the N dangling bond is doubly occupied and negatively charged and the Si dangling bond is unoccupied and positively charged. These charge states are in accordance with the relative electronegativies of these N and Si atoms. For example, for a Si–N distance of 0.25 nm, the electrostatic bond energy is calculated to be ~2.3 eV.

4. Defect model

4.1. General aspects of defect metastability and hydrogen release

The proposed model for defect metastability is illustrated in Fig. 3, where a complete cycle of
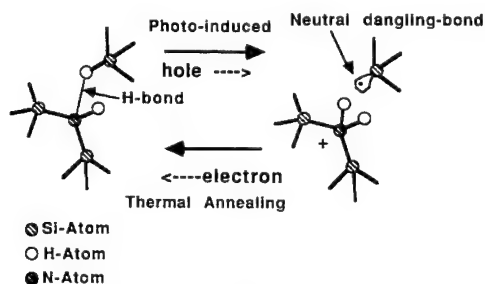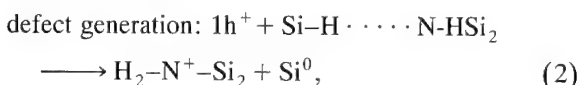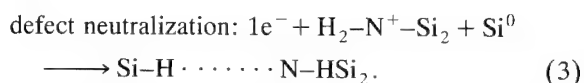

Fig. 3. Metastability cycle proposed for the Staeble–Wronski effect for clusters that couple Si–H and Si–NH groups by H bonds.

metastable bonding including defect creation and defect creation and defect neutralization is shown. The model is based on the ab initio calculations presented in Section 3, and includes a novel activation/neutralization mechanism in which trapping of charged carriers at local clusters with H bonding arrangements provides a mechanism that promotes low-temperature defect metastability without the loss or diffusion of H atoms. In this model, the equations governing (i) defect creation by trapping of a hole, and (ii) defect neutralization by trapping of an electron are given by

defect generation: $1h^+ + \text{Si–H} \cdots\cdots \text{N–HSi}_2$

$$\longrightarrow H_2\text{–}N^+\text{–Si}_2 + \text{Si}^0, \qquad (2)$$

and

defect neutralization: $1e^- + H_2\text{–}N^+\text{–Si}_2 + \text{Si}^0$

$$\longrightarrow \text{Si–H} \cdots\cdots\cdot \text{N–HSi}_2. \qquad (3)$$

The dotted lines in Eqs. (2) and (3) indicate a H bond between the H atom of the Si–H group and the N atom of the SiN–H group; the superscript (^{0}) indicates a neutral dangling bond. N–HSi$_2$ is a symbolic rather than a structural formula, e.g., the N atom is bonded to two Si atoms and one H atom. The trapping of a hole at an initially neutral site initiates the metastability cycle leading to the creation of charged ammonium center, $H_2\text{–}N^+\text{–Si}_2$, and a neutral Si atom dangling bond, Si^0. The ab initio results in Table 2 have established the stability of the positively charged ammonium center. The trapping of an electron at the positively charged ammonium center destabilizes that center, leading to the detachment of one of the H atoms, which in the low-temperature limit then becomes re-attached to the Si atom dangling bond. This results in the formation of Si–H and N–HSi$_2$ groups connected via the H bonding interaction and therefore in the initial bonding arrangement. The coinage in this defect metastability process is the displacive motion of the H atom which is driven by the sequential trapping of holes and electrons. The H atom is initially bonded to the Si atom, and weakly associated with the NH group by a H bond with Si–H and N $\cdots\cdots\cdot$ H distances of ~0.15 and 0.20 nm, respectively. After hole trapping, the Si–H distance is increased to > 0.2 nm, and the N–H bonding distance is decreased to ~0.10 nm.

The defect metastability cycle described by Eqs. (2) and (3) can occur at low temperatures, i.e., below about 300°C, where release of H atoms from the defect configuration is highly improbable. However, if electron hole and trapping occur at elevated temperatures, from about 400°C and up to 900–1000°C, then H_2 release from Si and N atoms and the linking up of the defect state Si and N atom dangling bonds are possible (see Fig. 4). This sequence of events is represented in Eqs. (4)–(6), which illustrate
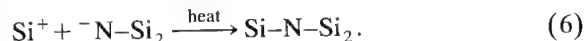(i) hole trapping

$$1h^+ + Si-H \cdots \cdots \cdots N-HSi_2$$
$$\xrightarrow{heat} H_2-N^+-Si_2 + Si^0, \tag{4}$$
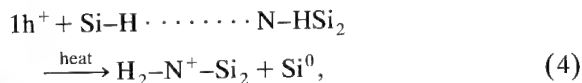
(i) electron trapping, followed by release of an H_2 molecule

$$1e^- + H_2-N^+-Si_2 + Si^0 \xrightarrow{heat} Si^+ + N-Si_2 + H_2, \tag{5}$$
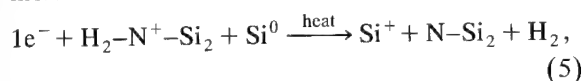
and (iii) bond healing

$$Si^+ + {}^-N-Si_2 \xrightarrow{heat} Si-N-Si_2. \tag{6}$$

The ab initio calculations of Section 3 indicate that both of the dangling bonds in Eq. (5) are charged and this is indicated by the superscripts ' − ' and ' + '. The N dangling bond is doubly occupied and negatively charged (' − '), and the Si dangling bond is unoccupied and positively charged (' + ').
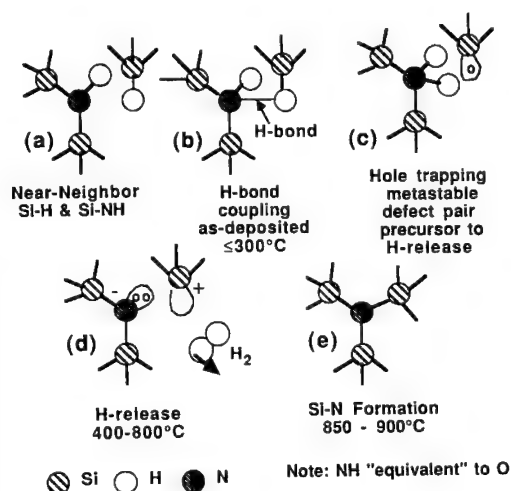

Fig. 4. Local bonding configurations for the release of H_2 molecules from clusters that couple Si–H and Si–NH groups by H bonds.
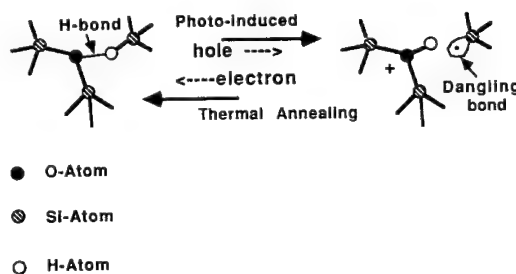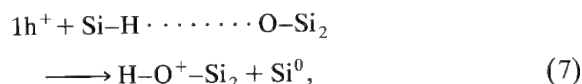

Fig. 5. Metastability cycle proposed for the Staebler–Wronski effect for clusters that couple Si–H and Si–O–Si groups by H bonds.

The experimental results presented in Section 2 have demonstrated that defect metastability (Eqs. (2) and (3)) is promoted by light-soaking and low-temperature annealing ($< 250°$C), whereas H_2 formation followed by defect healing is driven at higher temperatures: 400–800°C for H_2 formation, and $>$ 800°C for defect healing as indicated in Eqs. (4)–(6).
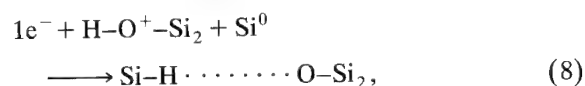
An analogous defect metastability mechanism applies to materials with bonded O, as in hydrogenated silicon oxides. The link between the NH and O bonding arrangements derives from the fact that NH groups and O atoms are chemically equivalent (i.e., isoelectronic), with each being capable of forming two partially covalent bonds in their normal neutral bonding states and three partially covalent bonds when positively charged as for example in the respective ammonium and oxonium configurations, NH_4^+ and OH_3^+.

The local bonding arrangements for these O atom groups in a defect metastability cycle are shown in Fig. 5, and the reaction equations for defect generation and neutralization are given below:
(i) defect generation

$$1h^+ + Si-H \cdots \cdots \cdots O-Si_2$$
$$\longrightarrow H-O^+-Si_2 + Si^0, \tag{7}$$

(ii) defect neutralization

$$1e^- + H-O^+-Si_2 + Si^0$$
$$\longrightarrow Si-H \cdots \cdots \cdots O-Si_2, \tag{8}$$

where the dotted line between the H of the Si–H group and the O of the Si–O–Si string indicates the H bond. Elimination of bonded H from Si–H and

Si–H groups, with the formation of H_2, can occur via a series of reactions that parallel Eqs. (4)–(6). A second type of process in which H_2O molecules can be eliminated is from near-neighbor Si–OH groups that are interconnected through H bonding interactions [19,20].

4.2. Defect metastability in a-Si:H and a-Si:N:H

Studies of photo-induced metastability in a-Si:H have shown that the SWE is accompanied by an increase in the electron spin resonance (ESR) signal, and that the level of light-induced defect generation saturates in the low to mid-10^{17} cm^{-3} range [21–23]. These studies also demonstrated that the Si dangling bonds responsible for the ESR signal are separated by more than ~ 1 nm from other Si dangling bonds, and in addition do not have a back-bonded H neighbor [29]. This infers that photo-induced defects contain only one Si atom dangling bond, and perhaps another defect associated bonding arrangement that does not include a second Si dangling bond. Many of the studies of the SWE indicate correlations between increases in the magnitude of the SWE and impurity atom concentrations of electronegative species such as oxygen and nitrogen [22,23]. The quantitative differences in the SWE in a-Si:N:H alloys in films prepared by remote PECVD from the different N atom source gases, N_2 and NH_3, and the differences in local bonding groups for H atoms has led us to propose the following model of the SWE.

The proposed model is based on an inherent charge-trapping-induced metastability of local bonding arrangements that include an Si–H group and a near-neighbor SiN–H group in which the H atom of the Si–H group makes a H bond with the N atom of the SiN–H group. The complete cycle of defect generation and defect neutralization are described by the following steps.

(i) Under solar illumination, electron–hole pairs are produced by absorption when the photon energy of the incident light exceeds the effective optical band gap of the a-Si material.

(ii) A relative small fraction of the holes are trapped at the Si–H$\cdots\cdots\cdots$N–HSi$_2$ sites, converting these into a Si dangling bond, and a positive ammonium center with two H atoms, $Si^0 + H_2-N^+-Si_2$ (see Eq. (2)).

(iii) During continued exposure to light, there are two possible processes that can take place:

(a) conversion of normal bonding arrangements into Si dangling bond and ammonium centers by hole trapping (Eq. (2)), or

(b) conversion of ammonium centers and Si dangling bonds back to their normal bonding arrangement by electron trapping (Eq. (3)).

(iv) After a period of time dictated by (a) the generation rate of electron–hole pair production by the incident light, (b) the trapping cross-sections of the normal (σ_0) and defect (σ_+) structures for holes and electrons respectively and (c) the concentration of normal centers (N_0) that serve as precursor sites for defect generation, a steady state is reached wherein the number of defect centers ($N_{d(+)}$) comprised of the Si atom dangling bond and the charged ammonium center approaches a constant value approximately equal to

$$N_{d(+)} \approx \{\sigma_0/\sigma_\perp\}N_0. \tag{9}$$

(v) If the light source is removed, then the material will remain in the defect state for a period of time dictated by the thermal generation rate of electrons.

(vi) If the sample is subjected to thermal annealing, then the kinetics of this process display an activation energy that is determined by the thermal rate of generation of electrons. The activation energy for annealing is determined by the position of the Fermi level relative to the conduction band, which in materials dominated by electron transport is the simply the dark conductivity activation energy in the light-soaked state.

A similar situation will prevail for other bonding arrangements in which Si–H bonds are in close proximity to strongly electronegative atoms (e.g., O) or groups (e.g., OH), that can also participate in H bonding interactions with the H atom of the Si–H group. The bonding configurations which are most susceptible to these H bonding reactions are those in which there is at least one strongly electronegative atom (O or N) or group (OH or NH) back-bonded to the Si atom of the Si–H group. This generates a positive partial charge on the H atom of the Si–H group promoting the H bonding interaction.

4.3. Application to a-Si:H

Consider a-Si:H alloys with no intentional additions of O, N or NH groups. From secondary ion mass spectrometry (SIMS) analyses performed on PECVD materials, the oxygen concentrations of these materials are typically the order of 3×10^{19} cm^{-3} [30]. We take this as the number of precursor sites by assuming that in the a-Si:H network a bridging O atom will be encapsulated by an internal a-Si surface which will include Si–H terminations. Since the precursor state is neutral, the capture cross-section will of the order of atomic dimensions squared, i.e., $\sim 5 \times 10^{-16}$ cm^2 [31]. The efficiency of defect generation is determined by the concentration of precursors, their capture cross-section, and the concentration and capture cross-section of the sites which characterize any competitive processes such as shallow trapping as in the hole transport process. A hole lifetime against shallow-trapping can be estimated from the drift mobility; alternatively, if the microscopic hole mobility is assumed to be of order 1 cm^2/V s, then the measured drift hole mobilities of $\sim 10^{-3}$ cm^2/V s mean that the hole is free for capture by other centers $\sim 0.1\%$ or 10^{-3} of the time. This is defined here as the fraction of time, t_{free}, that is free or available for other trapping and recombination processes such as in the defect formation process. If it is further assumed that every Si atom is a potentially shallow trapping site for transport limitations, then the quantum efficiency (QE_g) for defect generation is approximated by

$$QE_g \sim \left(N_0 / N_{d(a-Si)} \right) t_{\text{free}}, \tag{10}$$

where $N_{d(a-Si)}$ is the atomic density of a-Si:H, $\sim 4 \times 10^{23}$/cm^3. Taking $N_0 \approx 3 \times 10^{19}$ cm^{-3} gives $QE_g \approx 8 \times 10^{-8}$, in agreement with estimates derived from the light-intensity time products that are known to generate the approximately $\sim 10^{17}$ defect states/cm^3 associated with the light soaking/induced defect formation [21–23].

Consider next the typical number of defect states created by light soaking. The room-temperature trapping cross-sections for uncharged and Coulomb attractive centers are approximately 5×10^{-16} cm^2, and 10^{-13} cm^2, respectively [31]. Using Eq. (9), the

number of defect states expected under steady-state conditions is

$$N_{d(+)} \approx \left\{ \frac{\sigma_0}{\sigma_+} \right\} N_0 \sim \frac{5 \times 10^{-16} \text{ cm}^2}{10^{-13} \text{ cm}^2} 3 \times 10^{19} \text{ cm}^{-3}$$
$$\approx 1.5 \times 10^{17} \text{ cm}^{-3}, \tag{11}$$

and in quantitative agreement with experiment. In addition experiments performed by Crandall [22] have demonstrated that the Staebler–Wronski effect increases linearly with increasing O atom concentration, also in agreement with Eq. (9).

The characteristic activation energy for defect relaxation after removal of the light source and associated with low-temperature (150–250°C) thermal annealing in the dark has been found to be ~ 0.9 eV, which, as predicted by the model, is approximately equal to the dark conductivity activation energy after light soaking. Finally, in agreement with ESR data, this model predicts only one Si atom dangling bond per defect center, and the dangling bond site does not necessarily include a an additional H atom back-bonded to the Si of the Si–H group.

4.4. Application to a-Si:N:H alloys

In applying the model to a-Si:N:H alloys three assumptions are made: (i) the concentration of O precursor sites remains unchanged by adding either NH or N groups; (ii) the addition of N atoms into a-Si:N:H alloys by deposition from N$_2$ does generate new precursor states, since N atoms bonded only to Si atoms do not readily participate in H bonding interactions; whereas (iii) the addition of NH groups to a-Si:N:H alloys by deposition from NH$_3$ adds new precursor states in direct proportion to number of incorporated NH groups.

Using these assumptions, the experimental results support the model discussed above; e.g.,

(a) the Staebler–Wronski effect, as manifested in the ratio of the rested to the fatigued state photocurrent, is the same in a-Si:N:H alloys grown from N$_2$ as in a-Si:H alloys. In the context of this model the precursor cluster is the same as in a-Si:H, i.e., an Si–H and an Si–O–Si linkage coupled via a H bond;

(b) the Staebler–Wronski effect, as reflected by the ratio of the rested to the fatigued state photocurrent, is increased in a-Si:N:H alloys grown from

$\mathrm{NH_3}$ with respect to a-Si:H alloys. In the context of the model there are two precursor sites: (i) the H bond coupled Si–H to an Si–O–Si group; and (ii) the H bond coupled Si–H to Si–NH–Si group.

If one assumes the same cross-sections for hole capture at the two precursor sites in the a-Si:N:H alloys grown from $\mathrm{NH_3}$, then the steady-state number of defects is expected to be larger than for a-Si:H, and a-Si:N:H grown from $\mathrm{N_2}$. It must be emphasized again that this is anticipated for a-Si:N:H alloys grown by remote PECVD because of the control of local bonding inherent in the remote excitation process [26]. In a conventional PECVD or glow discharge (GD) process, similar considerations relative to N and NH populations will not generally apply, and the SWE is expected to increase with [N] in a-Si:N:H alloys independent of the N atom source gas. If we designate $N_{0(O)}$ and $N_{0(NH)}$ as the concentrations of the two precursors and assume that the neutral and charged state capture cross-sections are the same for the two defect configurations, then the maximum number of positively charged oxonium and ammonium sites will be given by

$$N_{d(+)} \approx \{ \sigma_0 / \sigma_+ \}(N_{0(O)} \text{ and } N_{0(NH)}). \qquad (12)$$

However, this expression will overestimate the number of sites because it does not take into account (i) near-neighbor Si–O–Si and Si–NH–Si environments, and (ii) changes in the capture kinetics when positively charged centers increase to the point where their respective spheres of influence overlap and their effective capture cross-section are reduced.

Using spectroscopic data to estimate the density of NH centers for the alloys studied in Ref. [25], $N_{0(NH)}$ is at most of the order of 10^{21} cm^{-3}, and according to Eq. (10) we would then expect a steady-state density of defects of $\sim 10^{19}$ cm^{-3}, about 20 times higher than is inferred from the fivefold increase in the degradation ratio of the photoconductivity. Alternatively, the Coulomb cross-section for capture by a charge center can be used to estimate a maximum density of charged defects. Assuming that charged defects can be no closer than about two times the radius associated with their capture cross-section, this estimate yields an upper density of charged traps to be of the order of 9×10^{17} cm^{-3}, in quantitative agreement with a defect density of (5–7

$\times 10^{17}$ cm^{-3} as determined from the increased degradation ratio for the photoconductivity.

### 4.5. Elimination of H from Si–H and Si–NH bonds in a-Si:N:H alloys

The IR results discussed above, coupled with aspects of network topology, have led to the proposal of the following model for the simultaneous release of H atoms for Si–H and SiN–H from a-Si:N:H alloys. Fig. 4(a) indicates an SiN–H group and Si–H group in close proximity. If the distance between the H atom of the Si–H group and the N atom of the SiN–H group is between about 0.25 and 0.3 nm (2.5–3.0 Å), there will be a sufficiently strong electrostatic interaction between the H atom to promote the formation of a H bond [32]. Typical energies of these H bonds range from about 0.2 to 0.8 eV. The H bond interaction is included (Fig. 4(b)) and it can promote metastability with respect to the trapping of charged carriers, thereby forming a structural basis for the SWE. Fig. 4(c) illustrates a possible intermediate step of the H release process in which hole trapping by the N atom results in both H atoms becoming bonded to a positively charged N atom of the SiN–H group (the ammonium center in Fig. 2(a)). The conjugate defect, a neutral Si atom dangling bond, is formed in the same process. The formation of this new configuration is due to displacive, rather than diffusive motion of the H atom which was originally closer to the Si atom than the N atom (~ 0.15 nm, as compared with ~ 0.2–0.3 nm); after hole trapping, the relative distances are reversed, ~ 0.1 nm from the N atom, and ~ 0.25 nm from the Si atom. Fig. 4(d) illustrates the release of a hydrogen molecule ($\mathrm{H_2}$), driven in part by electron trapping, and resulting in the formation of two dangling bond defects, one on the N atom and one on the Si atom. As noted in Section 3, ab initio calculations suggest that the N atom dangling bond is doubly occupied and negative, and the Si atom dangling bond is unoccupied and positive. Fig. 4(e) illustrates the temperature-driven recombination of these dangling bonds to form an Si–N bond, which then completes the network healing processes.

The reaction equations governing this H release process have been presented above (see Eqs. (4)–(6)). Two reaction equations along with the energy bal-

ance are given below. The first of these is for the high-temperature process that includes formation of an H_2 molecule where the dot–dash line ($\cdot-\cdot-\cdot-\cdot$) indicates an electrostatic attraction between the charged dangling bonds:

$$1e^- + H_2-N^+-Si_2 + Si^0$$
$$\longrightarrow Si^+ \cdot -\cdot-\cdot-\cdot \; {}^-N-Si_2 + H_2:$$
$$E = -3.9(\pm 0.5) \text{ eV}, \tag{13}$$
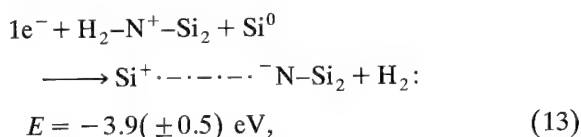
and the second is for the low-temperature defect metastability process in which trapping of electron restores the bonding arrangement to the precursor state:

$$1e^- + H_2-N^+-Si_2 + Si^0$$
$$\longrightarrow Si-H \cdot \cdots\cdots N-HSi_2:$$
$$E = -5.2(\pm 0.2) \text{ eV}. \tag{14}$$
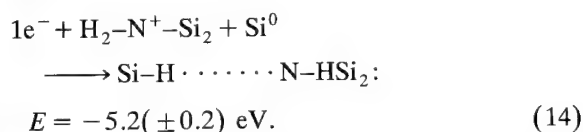
From the energies for the two processes in Eqs. (13) and (14), it can be concluded that defect metastability is favored at low temperature (Eq. (13)), while H_2 elimination and the creation of charged defect pair is more likely at higher temperatures (Eq. (14)). This is in agreement with the experimental results presented above. Above about 800°C, the IR data indicate the formation of Si–N bonds according to a reaction equation given by

$$Si^+ \cdot -\cdot-\cdot-\cdot \; {}^-N-Si_2 \longrightarrow Si-N-Si_2. \tag{15}$$
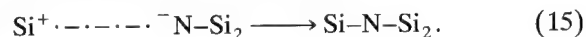
4.6. Defects in MOS and MIS devices

Metal–oxide–semiconductor (MOS) capacitors were formed by a 300°C two-step remote plasma-assisted process [33]. The in situ steps were (i) a remote plasma-assisted oxidation using either O_2 or N_2O; followed by (iii) a remote plasma-enhanced chemical vapor deposition (PECVD) of SiO_2 using downstream injected SiH_4 as the Si atom source gas, and N_2O, coexcited with He, as the O atom source gas. In addition, some of the MOS devices were also exposed to N species produced by the direct or remote plasma excitation of NH_3 [34,35]. MOS devices were prepared by conventional techniques including (i) the sputter deposition of A as a metal electrode, (ii) photolithographic patterning to define devices with areas of $\sim (1-4) \times 10^{-3}$ cm^2, and (iii)

Table 3
Electrical properties at Si–SiO$_2$ interfaces

	Mid-gap D_{it} (cm^{-2} eV^{-1})	Nitrogen at interface	
		species	cm^{-2} ($\times 10^{14}$)
Plasma oxidation (O$_2$)			
400°C processing	1.3×10^{10}	N	1.6
Plasma oxidation (N$_2$O)			
400°C processing	1.1×10^{10}	N	8.5
Exposure to NH$_3$ plasma			
400°C Processing	$2-5 \times 10^{11}$	NH	>5
900°C RTA	$\sim 1 \times 10^{10}$	N	>5

a 400°C post-metallization anneal (PMA) in an N_2 atmosphere. Table 3 includes mid-gap defect state densities, D_{it}, determined from capacitance–voltage ($C-V$) measurements using the conventional high–low-frequency method of data analysis performed on three types of MOS device prepared with pre-deposition oxidations using (i) either (a) O_2 or (b) N_2O [36], and with no post-deposition exposures to excited NH_3, and (ii) O_2, but with post-deposition exposures to excited species from an NH_3 plasma. Also included in the table are interfacial densities of N atoms as determined from an analysis of SIMS data. The results in Table 3 demonstrate (i) about the same D_{it} values for MOS devices which included pre-deposition oxidation steps using O_2 and N_2O, and with no exposures to plasma-excited NH_3, but (ii) significantly higher values of D_{it} for MOS devices which included pre-deposition oxidation using O_2 followed by an exposure to species from an NH_3 plasma after the oxide deposition and before the metallization. Based on SIMS data and $C-V$ studies, and under processing conditions including a 400°C PMA, it has been found that (i) the incorporation of N atoms (as contrasted with NH groups) in the immediate vicinity of the Si–SiO$_2$ interface does not lead to significant changes in D_{it} with respect to interfaces (they are not intentionally processed to increase N atom concentrations), whereas (ii) the incorporation of NH groups at the Si–SiO$_2$ interface can lead to significant increases in D_{it}. Three different experimental situations using plasma-excited NH_3 have given this same result with respect to increases in D_{it}: (i) the exposure of oxide dielectrics to species from an NH_3/He discharge with no film deposition during the exposure [34]; (ii) the deposition of nitride
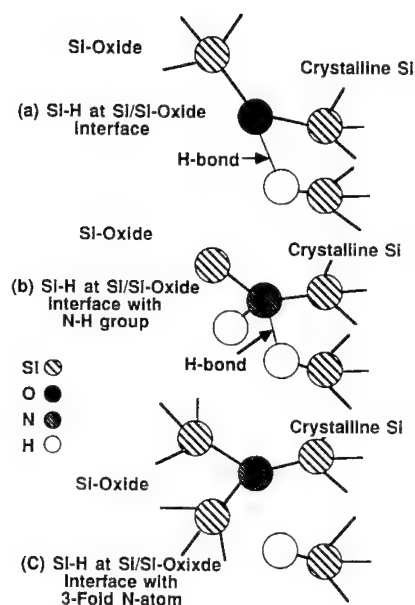
Fig. 6. Local bonding arrangements at Si–SiO$_2$ interfaces. (a) and (b) display H bonding interactions between H atoms of Si–H groups at the Si side of the interface with O atoms, and NH groups respectively. (c) indicates the absence of H bonding interactions when N atoms are threefold-coordinated to only Si atoms.

layers that are incorporated into oxide–nitride–oxide (ONO) dielectrics [34]; and (iii) the deposition of homogeneous oxynitride alloy dielectrics onto pre-plasma-oxidized Si surfaces [35]. When the devices with ONO or oxynitride dielectrics were subjected to a 30 s post-deposition rapid thermal anneal (RTA) at 900°C, D_{it} values were reduced to approximately the same levels as for devices processed without any NH$_3$ exposures [34,35]. We propose that these differences are due to aspects of the local bonding arrangements that involve H bond formation (see Fig. 6). This type of bonding is possible when Si–H groups are in close proximity to either Si–O–Si and Si–NH–Si groups as in Si–SiO$_2$ interfaces with NH groups, but not when N atoms bonded only to Si are in close proximity to Si–H bonds at Si–SiO$_2$ interfaces.

Since N atoms bonded only to Si atoms at Si–SiO$_2$ interfaces cannot produce additional H bonding configurations, but only reduce the number of such interactions involving near-neighbor Si–H groups and Si–O–Si linkages, we would expect no increases in D_{it} at Si–SiO$_2$ interfaces processed with the N$_2$O

pre-oxidation step, even though the number of N atoms in the immediate vicinity of the Si–SiO$_2$ interface is increased by a factor of about five when N$_2$O is substituted for O$_2$ (see Table 3). By contrast, the values of D_{it} are significantly higher if NH species are allowed to accumulate at the Si–O–Si interface during processing [34,35].

The increase in D_{it} derives from two effects: (i) the accumulation of Si–NH–Si linkages in close proximity to Si–H groups at the SiO$_2$ interface, and (ii) the temperature of 400°C for the post metallization anneal used with the Al gate electrodes. If these two groups are in close proximity and linked through a H bonding interaction then, as shown in Fig. 6, H atoms can be released from these environments following the mechanism given above (see Eqs. (4)–(6)). This will lead to simultaneous increases in both D_{it} and Q_f, since Si atoms dangling bonds are created which contribute to D_{it}, and positively charged centers are created which contribute to Q_f. The experiments to date have shown coupled effects for NH atom accumulation: (i) increases in D_{it}, and (ii) negative shifts in the flatband voltage due to positive fixed charge (increases in Q_f). Finally, the inclusion of a 30 s 900°C RTA prior to Al metallization results in capacitor structures with ONO and oxynitride dielctrics that have D_{it} and Q_f values essentially the same as devices processed without any NH exposures, and with oxide dielectrics. This is consistent with a 900°C defect healing process described by Eq. (15).

Interrupted charge to breakdown experiments indicate increases in D_{it} occur before breakdown [37]. An integrated charge of about 1 C/cm^2 typically increases D_{it} from the 10^{10} cm^{-2} range to the low to mid 10^{11} cm^{-2} range. Since one Coulomb of charge corresponds to ~ 6.3×10^{18} charged carriers, this means that the quantum efficiency for this process in which D_{it} is increased is ~ $10^{11}/(6.3 \times 10^{18})$ or approximately 1.6×10^{-8}, and is therefore comparable with the effective quantum efficiency (QE) for the defect generation step in the SWE. Interestingly enough, this type of defect generation is reversible before breakdown of the capacitor structure [38].

The similarities in the numerical values for the QEs for the D_{it} increase at Si–SiO$_2$ interfaces and for the SWE in a-Si materials are fortuitous. The

factors that contribute to the QE for the D_{it} increase are (i) the number and trapping cross-section of precursor sites at the Si–SiO$_2$ interface, and (ii) a kinetic factor given by the ratio of the transit time through the interface region to the lifetime against trapping at the precursor sites. Since the fractional coverage of precursor defect sites at the interface is the product of their area density, $\sim 10^{12}$ cm^{-2}, times their cross-section, $\sim 5 \times 10^{-16}$ cm^2, this gives a value of $\sim 5 \times 10^{-4}$. The kinetic factor is approximated by $t_{transit}/t_{lifetime}$, where $t_{transit}$ is the transit time through the interface region. Assume an effective interface thickness of 0.5 nm and a velocity, $v \simeq 5 \times 10^5$ cm/s, $t_{transit} = 5 \times 10^{-8}$ cm/5 $\times$ 10^5 cm/s = 10^{-13} s. The lifetime is given by the usual expression, $t_{lifetime} = (v N_t \sigma_t)$, where N_t is the trap density, and σ_t is the capture cross-section. Therefore $t_{lifetime} = 1/(5 \times 10^5$ cm/s $\times 10^{18}$ cm^{-3} $\times 5 \times 10^{-16}$ cm^2) $= 4 \times 10^{-9}$ s, so that the ratio, $t_{transit}/t_{lifetime}$, is given by 2.5×10^{-5}, thereby yielding a QE for defect generation at Si–SiO$_2$ interfaces of $\sim 1.2 \times 10^{-8}$, close to the approximate experimental value of $\sim 1.6 \times 10^{-8}$.

5. Discussion

The results presented in this paper have demonstrated a new mechanism for the formation of metastable defects that is triggered by charge trapping in atomic clusters that include H bonds. In the examples discussed, the important components of the precursor sites are (i) an Si–H bond with at least one of the back-bonds to the Si atom involving a strongly electronegative atom or groups such as O or N, or an NH or OH group, and (ii) an electronegative atom or group such as O, or an NH or OH group that participates in the H bonding interaction with the H atom of the Si–H group. Trapping of a hole at these environments generates a Si atom dangling bond, and an over-coordinated, positively charged O or N atom in an oxonium or ammonium bonding arrangement, respectively. If the material system with the over-coordinated groups is maintained at room temperature, or annealed at low temperatures, typically below about 300°C, then trapping of an electron will destabilize the defect center comprised of the Si atom dangling bond, and the positively charged oxo-

nium or ammonium center will return to its normal state via a displacive motion of the H atom. On the other hand, trapping of an electron at higher temperatures, or simply the application of temperatures in excess of about 400°C, will result in the elimination of H, and the formation of stabilized defect centers. These defect centers consist of charged dangling bonds on Si$^+$ and O$^-$, or Si$^+$ and N$^-$ atoms and can be neutralized by annealing at sufficiently high temperatures which allow structural relaxation. For example, temperatures of the order of 900°C for 30 s are required for healing defects in nitrides, oxynitrides and at oxide–nitride interfaces internal to ONO dielectrics.

References

[1] M.H. Brodsky, M. Cardona and J.J. Cuomo, Phys. Rev. B16 (1977) 3556.
[2] J.C. Knights, G. Lucovsky and R.J. Nemanich, Philos. Mag. B37 (1978) 467; G. Lucovsky, R.J. Nemanich and J.C. Knights, Phys. Rev. B19 (1979) 2064.
[3] G. Lucovsky, J. Yang, S.S. Chao, J.E. Tyler and W. Czubatyj, J. Non-Cryst. Solids 59&60 (1983) 609; G. Lucovsky, S.S. Chao, J. Yang, J.E. Tyler and W. Czubatyj, J. Vac. Sci. Technol. A2 (1984) 353.
[4] G. Lucovsky and W.B. Pollard, in: The Physics of Hydrogenated Amorphous Silicon II, ed. J.D. Joannopoulos and G. Lucovsky (Springer, Berlin, 1984) p. 301.
[5] W.B. Pollard and G. Lucovsky, Phys. Rev. B26 (1982) 3172.
[6] G. Lucovsky, Solid State Commun. 29 (1979) 571.
[7] G. Lucovsky, AIP Conf. Proc. 73 (1981) 100; G. Lucovsky, J. Phys. (Paris) C4, 42 (1981) 741.
[8] D.V. Tsu, G. Lucovsky and B.N. Davidson, Phys. Rev. B40 (1989) 1795.
[9] G.N. Parsons and G. Lucovsky, Phys. Rev. B41 (1990) 1664.
[10] R.T. Sanderson, Chemical Bonds and Bond Energy, 2nd Ed. (Acadmic Press, New York, 1976).
[11] D.V. Tsu and G. Lucovsky, J. Non-Cryst. Solids 97&98 (1987) 839.
[12] G. Lucovsky and W.B. Pollard, J. Vac. Sci. Technol. A1 (1983) 313.
[13] G. Lucovsky, Solar Energy Mater. 8 (1982) 165.

[14] J.C. Knights, in: The Physics of Hydrogenated Amorphous Silicon II, ed. J.D. Joannopoulos and G. Lucovsky (Springer, Berlin, 1984) p. 5.

[15] J.B. Boyce, S.E. Ready and C.C. Tsai, J. Non-Cryst. Solids 97&98 (1987) 345.

[16] G. Lucovsky, Z. Jing and J.L. Whitten, J. Non-Cryst. Solids 137&138 (1991) 119.

[17] J. Zing, J.L. Whitten and G. Lucovsky, Phys. Rev. B45 (1992) 13978.

[18] D.V. Tsu, S.S. Kim, J.A. Theil and G. Lucovsky, J. Vac. Sci. Technol. A8 (1990) 1430.

[19] J.A. Theil, D.V. Tsu, S.S. Kim and G. Lucovsky, J. Vac. Sci. Technol. A8 (1990) 1374.

[20] Z. Yin, D.V. Tsu, G. Lucovsky and F.W. Smith, J. Non-Cryst. Solids 114 (1989) 459.

[21] D.L. Staebler and C.R. Wronski, Appl. Phys. Lett. 38 (1980) 456.

[22] R.S. Crandall, in: Tetrahedrally-Bonded Amorphous Semiconductors, ed. D. Adler and H. Fritzsche (Plenum, New York, 1985) p. 315.

[23] D.E. Carlson, in: Tetrahedrally-Bonded Amorphous Semiconductors, ed. D. Adler and H. Fritzsche (Plenum, New York, 1985) p. 165.

[24] G. Lucovsky, M.J. Williams, S.M. Cho, Z. Jing and J.L. Whitten, Mater. Res. Soc. Symp. Proc. (1994) 275.

[25] M.J. Williams, S.S. He, S.M. Cho and G. Lucovsky, J. Vac. Sci. Technol. A12 (1994) 1072.

[26] G. Lucovsky, D.V. Tsu, R.A. Rudder and R.J. Markunas, in: Thin Film Processes II, ed. J.R. Vossen and W. Kern (Academic Press, New York, 1991) p. 565.

[27] W. Beyer and H. Mell, in: Disordered Semiconductors, ed. M.A. Kastner, G.A. Thomas and S.R. Ovshinsky (Plenum, New York, 1987) p. 641.

[28] Z. Jing, G. Lucovsky and J.L. Whitten, Surf. Sci. 296 (1993) L33.

[29] K. Tanaka, J. Non-Cryst. Solids 137&138 (1991) 1.

[30] K. Tanaka and A. Masuda, Mater. Sci. Rep. 2 (1987) 139.

[31] A. Rose, Concepts in Photoconductivity and Allied Problems (Interscience, New York, 1972), ch. 7.

[32] T.A. Cotton and G. Wilkinson, Advanced Inorganic Chemistry (Interscience, New York, 1963) ch. 3;
L. Pauling, The Nature of the Chemical Bond, 2nd Ed. (Cornell University, Ithaca, NY, 1939) ch. 7.

[33] T. Yasuda, Y. Ma, S. Habermehl and G. Lucovsky, Appl. Phys. Lett. 60 (1992) 434.

[34] Y. Ma, T. Yasuda, and G. Lucovsky, J. Vac. Sci. Technol. A11 (1993) 952; Y. Ma, T. Yasuda, S. Habermehl and G. Lucovsky, J. Vac. Sci. Technol. B11 (1993) 1533.

[35] Y. Ma and G. Lucovsky, J. Vac. Sci. Technol. B12 (1994) 2504.

[36] D.R. Lee and G. Lucovsky, J. Vac. Sci. Technol. A13 (1995) in press.

[37] G.G. Fountain and R.J. Markunas, unpublished data.

[38] J. Maserjian and N. Zamani, J. Appl. Phys. 53 (1982) 559.

Photoluminescence and electron spin resonance in nitrogen-rich amorphous silicon nitride

D. Chen [a], J.M. Viner [a], P.C. Taylor [a,*], J. Kanicki [b,1]

[a] *Department of Physics, University of Utah, Salt Lake City, UT 84112, USA*
[b] *IBM Thomas J. Watson Research Center, Yorktown Heights, NY, 10598, USA*

Abstract

Electron spin resonance (ESR) and photoluminescence (PL) measurements have been employed to investigate some electronically important defects in nitrogen-rich amorphous silicon nitride films (a-SiN$_x$:H where $x > 1.3$) prepared using plasma-enhanced chemical vapor deposition. The PL intensity decreases with time (fatigues) when excited with UV light. This fatigued PL can be restored (bleached) with the application of visible light. There exists an ESR signal in as-deposited films of a-SiN$_x$:H which is temperature dependent. This ESR signal can be increased by irradiation with UV light, and the increased ESR signal can be bleached by application of visible light. Microscopic models for the defects responsible for these effects are discussed.

1. Introduction

Amorphous films of silicon nitride are of interest for a variety of applications where insulating layers are required [1]. This material is normally grown using the plasma-enhanced chemical vapor deposition (PECVD) technique by decomposition of mixtures of ammonia (NH$_3$) and silane (SiH$_4$). The films are termed 'nitrogen-rich' when the nitrogen content exceeds that of the stoichiometric crystalline compound Si$_3$N$_4$ (i.e., a-SiN$_x$:H where $x > 4/3$). The optical band gap of these films for $x = 1.6$ is about 5 eV.

The most common neutral defect in nitrogen-rich a-SiN$_x$:H is the K center which has been identified as a paramagnetic dangling bond on a silicon atom that is back-bonded to three nitrogen atoms [2–4]. A second important neutral defect is the so-called N center which is a paramagnetic dangling bond on a nitrogen atom that is back-bonded to two silicon atoms [3–5]. Under certain conditions these defects exist in measurable densities in as-prepared films, but one can also enhance the densities of the neutral K centers by application of ultraviolet (UV) light ($E > 3.5$ eV) [6–8]. When the ESR spin density increases due to the application of UV light, then there is a concomitant increase in a subgap optical absorption [9] and decrease in (fatigue of) the photoluminescence (PL) signal [10].

It has been suggested [3] that the K centers exhibit a negative effective electron–electron correlation energy (negative U_{eff}) such as that proposed earlier for the dominant defects in the amorphous chalcogenides [11,12]. It has also been suggested that, because a-SiN$_x$:H is a wide-gap insulator, the defects exhibit positive U_{eff} but strong potential fluctu-

---
* Corresponding author. Tel: +1-801 581 3538. Telefax: +1-801 581 4801. E-mail: craig@mail.physics.utah.edu.
[1] Present address: Department of Electrical Engineering and Computer Science, University of Michigan, Ann Arbor, MI 48109, USA.

ations produce charged defect states [13]. In this paper we review the experimental evidence from photoluminescence (PL) and electron spin resonance (ESR) that relates to the K defects and discuss the implications for the two models that have been proposed. We also discuss optically induced absorption measurements that have an influence on the interpretation.

2. Experimental details

The thin films of nitrogen-rich a-SiN$_x$:H were prepared by PECVD using an ammonia-to-silane ratio of 12. Substrates were roughened to reduce the fringing effects on the PL lineshapes. Substrate temperatures were 400°C for all samples discussed in this paper. The value of x for these films was approximately 1.6, and the films had an index of refraction [14] of 1.77 in the energy range well below the optical gap. Sample thicknesses were approximately 1 μm. The PL spectra, PL excitation spectra, and fatiguing and bleaching of PL were measured at 300 K using a spectrofluorimeter (SPEX) with both visible and UV capabilities. Details of the PL measurements are available elsewhere [10,15].

The ESR measurements were made on a spectrometer (IBM ER200-SRC) operating at approximately 9 GHz. Variable temperatures were obtained using a gas flow system (Helitran) over the temperature range from 4 to 300 K. Signal averaging techniques were employed to increase the signal-to-noise ratios. At all but the lowest temperatures appropriate microwave powers could be chosen to avoid saturation effects. Details of the ESR measurements are also available elsewhere [16].

3. Photoluminescence measurements

The room-temperature PL spectra for a sample of a-SiN$_x$:H grown at a substrate temperature of 400°C are shown in Fig. 1. The PL lineshape peaks at about 3 eV with a full width at half maximum of about 1.4 eV. The PL peak position corresponds to an energy that is a little more than half of the optical gap energy. The curve labeled (a) is for the sample after annealing at 300°C for 30 min to eliminate any
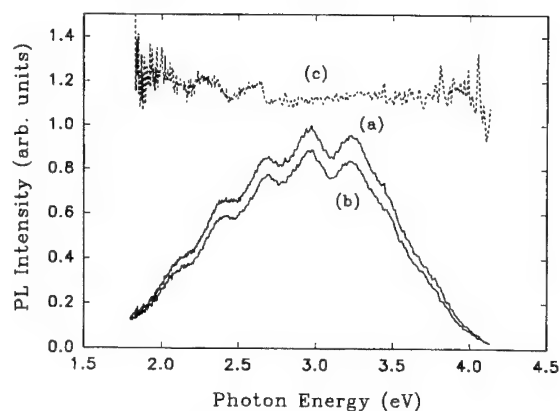

Fig. 1. Room-temperature photoluminescence spectra for an a-SiN$_{1.6}$:H film grown at a substrate temperature of 400°C (a) thermally annealed at 300°C for 30 min, (b) thermally annealed and then illuminated under 4.8 eV UV light for 120 min. The PL excitation light energy is 4.8 eV. Curve (c) is (a) divided by (b).

possible fatiguing effects. The spectrum labeled (b) is after illumination of the sample at 4.8 eV for 120 min. One can see from this figure that the fatiguing represents approximately a 10% effect for this particular sample. Fatiguing of up to about 30% has been observed in some samples under similar conditions. The fatiguing effect is uniform across the PL spectrum and therefore does not change the PL lineshape. This result can be seen in Fig. 1 by examining the ratio of curves (a) and (b) which is presented as curve (c). The fact that curve (c) is essentially flat shows explicitly that the PL lineshape is not altered by the fatiguing process. A Gaussian lineshape with a peak maximum at 2.9 eV and a full width at half maximum of 1.4 eV provides a good fit to the PL spectrum.

The PL fatigue does not follow a simple exponential relationship, but appears to involve a fairly broad distribution of time constants. At high photon energies ($E > 4.5$ eV), the efficiency of the PL fatiguing follows the optical absorption edge. This fact implies that at these energies the fatiguing is proportional to the number of absorbed photons and is independent of energy. At energies between 3.5 and 4.5 eV, there is an additional fatiguing 'band' where the fatiguing efficiency peaks near 4 eV. Below 3.5 eV there appears to be no measurable fatiguing effect. Annealing of the fatigued sample at 300°C for about 30 min restores the room temperature PL to its original
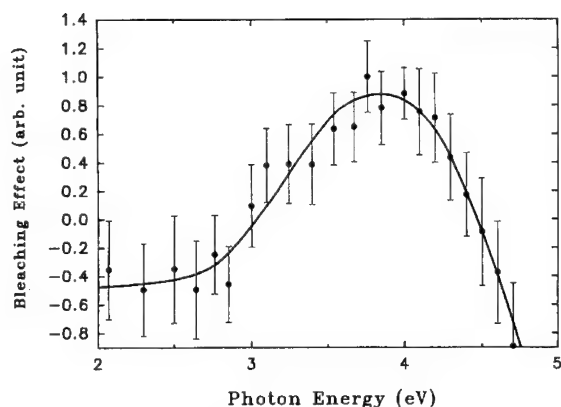
Fig. 2. Increase of room-temperature photoluminescence spectrum due to photobleaching for an a-SiN$_{1.6}$:H film grown at a substrate temperature of 400°C. The increase of PL is from a fatigued condition (film irradiation at 4.8 eV for 60 min) to a photobleached condition (film irradiation at a given bleaching energy for 30 min) relative to the fatigued condition. (See text for details.)

unfatigued state. The fatiguing process is therefore completely reversible upon annealing at temperatures below the temperature at which the sample was originally deposited.

After fatiguing, the PL can be restored (the fatiguing can be bleached) by irradiation with light whose energy is below the optical gap energy. Fig. 2 shows the bleaching spectrum for the same sample as that used in Fig. 1. Note that there is an onset to the bleaching process around the 3 eV, an energy which roughly corresponds to the peak of the PL spectrum as shown in Fig. 1. The error bars in Fig. 2 represent the estimated contribution from random errors, but there appears to be a systematic error in these data as well since the data below 3 eV are negative in Fig. 2. (At 300 K, the bleaching experiments are complicated by the fact that there is a thermal decay of the fatiguing effect at this temperature that partially restores the fatigued PL even in the absence of light [15]. The data of Fig. 2 have been corrected for this room-temperature annealing effect.) Regardless of this complication, the general features of the bleaching band are apparent from Fig. 2. In particular, the fall-off of the bleaching effect above about 4 eV is clear and is probably related to the competition between the fatiguing and bleaching effects in this spectral range.

The PL excitation (PLE) spectrum has also been measured for nitrogen-rich a-SiN$_x$:H films and shown to follow the absorption edge over the range from about 3 to 4.5 eV where the values of the absorption coefficient, α, vary from 1 to 300 cm^{-1}. Above 4.5 eV, the PLE spectrum bends over faster than the absorption [10].

4. Electron spin resonance measurements

The optically induced changes in the PL and ESR spectra are clearly related in nitrogen-rich a-SiN$_x$:H. While UV irradiation produces a fatiguing of the PL spectrum, this light also produces an increase in the ESR response attributed to the neutral K center [6,8]. There is also an increase in the sub-gap optical adsorption that looks very much like a shift of the very broad absorption edge to lower energies [9,16]. The excitation spectra for these three effects (PL fatigue, ESR increase, optical absorption increase) are similar in that they all appear to follow the absorption coefficient, α, above about 4.5 eV.

The optically induced ESR may also be photobleached in analogy with the bleaching of the fatigued PL described above [6]. Also for this effect there is a rough parallel between the excitation spectra for the PL bleaching and ESR bleaching effects; however, the bleaching of the ESR appears to extend to lower energies [6] than that for the PL.

The PL and ESR results presented thus far for nitrogen-rich a-SiN$_x$:H are very similar to those that have been observed in the amorphous chalcogenides [17]. There is an important difference in the optically induced absorption that is discussed below. There is also an additional ESR result that has no parallel with the chalcogenide glasses. This result is the fact that there is a dark ESR signal in most of the annealed films of nitrogen-rich a-SiN$_x$:H and this ESR signal is temperature-dependent [16] as shown in Fig. 3. The samples employed for the ESR measurements are made under the same conditions as those used for the PL and optical absorption measurements.

Because the dark ESR signal is small ($< 10^{16}$ spins/cm^3), there are technical difficulties, such as that due to microwave saturation of the signal, that hinder accurate measurements of the ESR intensities.
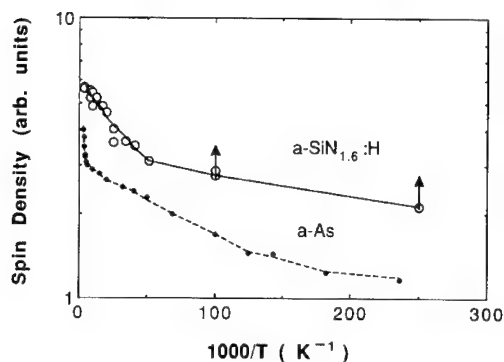
Fig. 3. Spin densities in a-SiN$_{1.6}$:H and a-As as functions of temperature over the range $4 \leq T \leq 300$ K. Solid and dashed lines are aids to the eye. See text for details.

For this reason the temperature dependence of the ESR signal in nitrogen-rich a-SiN$_x$:H is compared with that observed in a sample of a-Si:H that has a similar spin density at 300 K. In a-Si:H the spin density is well known to be temperature-independent.

The temperature-dependent ESR signal in nitrogen-rich a-SiN$_x$:H is also compared with that previously observed [18] in amorphous arsenic (a-As). The nitrogen-rich a-SiN$_x$:H and a-As samples appear to have qualitatively similar behaviors over the temperature range shown in Fig. 3. The arrows on the datapoints for the nitrogen-rich a-SiN$_x$:H sample at $1000/T$ equal to 100 and 250 represent lower bounds since the signals are saturated at these temperatures at the lowest microwave powers available. It is probable that the ESR intensities in the nitrogen-rich a-SiN$_x$:H become essentially temperature-independent at the lowest temperatures. This behavior is quantitatively different from that observed in a-As where the ESR signal continues to decrease at the lowest temperatures measured.

5. Discussion

As mentioned above, there are many parallels between the optically induced effects on the ESR, PL and optical absorption spectra in nitrogen-rich a-SiN$_x$:H and the semiconducting chalcogenide glasses. In addition, the average nearest-neighbor coordination number, n_{av}, for nitrogen-rich

a-SiN$_x$:H alloys can be significantly less than that of the stoichiometric composition. In the stoichiometric composition, where $x = 1.33$, $n_{av} < 3.43$ (if one ignores the hydrogen concentration) while in the nitrogen-rich alloys, where $x = 1.6$, $n_{av} < 3.38$. For these reasons, the first models to explain the K centers were based on the concept of a negative effective electron–electron correlation energy (negative U_{eff}) for these centers [2,19]. If the K centers constitute a negative U_{eff} system, then the reaction

$$2K^0 \rightarrow K^+ + K^- \tag{1}$$

is exothermic, where K^0 is the neutral, metastable paramagnetic center and K^+, K^- are, respectively, the positively and negatively charged diamagnetic ground states for the defect system. According to this model, by exposure to band-gap light the K^+ and K^- states can be photoexcited to the metastable K^0 state. In thermal annealing or bleaching with below-gap light, the metastable K^0 centers can be reconverted to K^+ and K^- centers as described in Eq. (1).

There are some difficulties with the application of the negative U_{eff} model to the defects in nitrogen-rich a-SiN$_x$:H films. First, there should be no dark ESR signal in any of these films if negative U_{eff} K centers are the only defects. This deficiency can be avoided if other defects, such as charged nitrogen dangling bonds (N centers), are also important [20].

A second problem with the negative U_{eff} model is the existence of a temperature dependence to the dark ESR signal as shown in Fig. 3. In principle, one can avoid this problem also by assuming that there exists a broad distribution of values for U_{eff} that includes both positive and negative values [10]. (There is nothing inherently special about $U_{eff} = 0$ since it represents an arbitrary cancellation of the effects due to Coulomb repulsion and lattice relaxation.) This situation describes the behavior in a-As very well [18].

A third problem with the negative U_{eff} interpretation, which is more difficult to overcome, is the fact that, although the ESR results in nitrogen-rich a-SiN$_x$:H and a-As are similar, the optically induced absorption is very different in these two materials [16]. As mentioned above, the optically induced absorption in nitrogen-rich a-SiN$_x$:H depends exponentially on energy and closely resembles a shift of the absorption edge to lower energies [9,13]. On the

other hand, the optically induced absorption in a-As exhibits a sharp rise at an energy equal to half the optical gap and is essentially constant above this onset energy [17,21]. This behavior is identical with that which occurs in the chalcogenide glasses. Because there is no well defined onset energy for the optically induced absorption in nitrogen-rich a-SiN$_x$:H, it is difficult to infer a well defined metastable defect level in the middle of the gap for the K^0. Therefore, in addition to the existence of a range of effective correlation energies that includes both positive and negative values such as occurs in a-As, one must also assume that the metastable defect energies themselves extend over a wide range within the energy gap. It has been difficult to construct a microscopic model that provides such distributions in a natural way.

On the other hand, nitrogen-rich a-SiN$_x$:H is an ionic material so it is natural to assume that the metastable changes in the ESR, PL and optical absorption are due to rearrangements of charges trapped at various valence states of defects due to the fact that the potential fluctuations are larger than the correlation energies [13,22,23] In these potential-fluctuation models, charged defects analogous to K$^+$ and K$^-$ will exist even for a positive value of U_{eff} provided that the potential fluctuations are larger than U_{eff}. The critical assumption in models that rely on potential fluctuations to produce charged states of defects is that local inhomogeneities, such as those due to bond angle or bond length distortions, are such that dipolar or higher-order potential fluctuations cannot be screened by the continuous density of states near the Fermi level [22]. The presence in nitrogen-rich a-SiN$_x$:H of Si–N and N–H bonds [24], which are highly ionic, at least allows the possibility of producing large potential fluctuations.

Although the optically induced absorption does not provide a well defined 'onset' energy, the bleaching of the fatigued PL as shown in Fig 2 does suggest an onset energy near 3 eV. A similar, although slightly higher, onset energy is indicated in the fatiguing measurements [15]. In addition, measurements of bleaching of the optically induced ESR suggest the possibility of an onset near 1.8 eV [6]. Clearly, any detailed microscopic model must be consistent with these specific results. The fact that nitrogen-rich a-SiN$_x$:H alloys have band gaps of 5 eV or greater suggests that the defects that contribute to the metastabilities in this system are characteristically different from those that are important in the much narrower-gap amorphous semiconductors. The possibility that large potential fluctuations play an important role in influencing the charge states of the defects in nitrogen-rich a-SiN$_x$:H may be an important ingredient for microscopic models of the predominant defects.

6. Summary

The metastable optical effects that occur in the PL, ESR and optical absorption measurements of nitrogen-rich a-SiN$_x$:H films are qualitatively similar to metastable effects that occur in some amorphous semiconducting systems.

References

[1] Various device applications are discussed in : Amorphous and Microcrystalline Semiconductor Devices, ed. J. Kanicki (Artech House, Boston, MA, 1991, 1992).

[2] P.M. Lenahan, D.T. Krick and J. Kanicki, Appl. Surf. Sci. 39 (1989) 392.

[3] W.L. Warren, J. Kanicki, F.C. Rong and E.H. Poindexter, J. Electrochem. Soc. 139 (1992) 880.

[4] W.L. Warren, F.C. Rong, E.H. Poindexter, G.J. Gerardi and J. Kanicki, J. Appl. Phys. 70 (1991) 346.

[5] W.L. Warren, P.M. Lenahan and J. Kanicki, J. Appl. Phys. 70 (1991) 2220.

[6] M.S. Crowder, E.D. Tober and J. Kanicki, Appl. Phys. Lett 57 (1990) 1995.

[7] D.T. Krick, P.M. Lenahan and J. Kanicki, J. Appl. Phys. 64 (1988) 3558.

[8] J. Kanicki, M. Sankaran, A. Gelatos, M.S. Crowder and E.D. Tober, Appl. Phys. Lett. 576 (1990) 598.

[9] C.H. Seager and J. Kanicki, Appl. Phys. Lett. 57 (1990) 1378.

[10] D. Chen, J.M. Viner, P.C. Taylor and J. Kanicki, in: Amorphous Silicon Technology – 1992, ed. Y. Hamakawa, P.G. LeComber, A. Madan and E.A. Schiff, Vol. 258 (Materials Research Society, Pittsburgh, PA, 1992) p. 661

[11] P.W. Anderson, Phys. Rev. Lett. 34 (1975) 953.

[12] R.A. Street and N.F. Mott, Phys. Rev. Lett. 35 (1975) 1293.

[13] H. Fritzsche and Y. Nakayama, Philos. Mag. B (1994) in press.

[14] N. Voke and J. Kanicki, Mater. Res. Symp. Proc. 68 (1986) 175.

[15] D. Chen, J.M. Viner, P.C. Taylor and J. Kanicki, in : Amorphous Silicon Technology – 1994, ed. E. Schiff, M. Hack, A. Madan, M. Powell and A. Matsuda (Materials Research Society, Pittsburgh, PA, 1994) p. 619.

[16] D. Chen, J.M. Viner, P.C. Taylor and J. Kanicki, Phys. Rev. B49 (1994) 13420.

[17] S.G. Bishop, U. Strom and P.C. Taylor, Phys. Rev. B15 (1977) 2278.

[18] P.C. Taylor, E.J. Friebele and S.G. Bishop, Solid State Commun. 28 (1978) 247.

[19] J. Kanicki, W.L. Warren, C.H. Seager, M.S. Crowder and P.M. Lenahan, J. Non-Cryst. Solids 137&138 (1991) 291.

[20] W.L. Warren, J. Robertson and J. Kanicki, Appl. Phys. Lett. 63 (1993) 2685.

[21] E. Mytilineou, P.C. Taylor and E.A. Davis, Solid State Commun. 35 (1980) 497.

[22] H.M. Branz and M. Silver, Phys. Rev. B42 (1990) 7420.

[23] Y. Bar-Yam, D. Adler and J.D. Joannopoulos, Phys. Rev. Lett. 57 (1986) 467.

[24] M.M. Guraya, H. Ascolani, G. Zampieri, J.I. Cisneros, J.H. Dias da Silva and M.P. Cantao, Phys. Rev. B42 (1990) 5677.

Optical and electrical properties of proton-implanted amorphous SiO_2, GeO_2–SiO_2, MgO–P_2O_5 and nanocrystalline $MgIn_2O_4$: novel materials by proton implantation

Hideo Hosono [a,*], Naoyuki Ueda [b], Hiroshi Kawazoe [a,b], Noriaki Matsunami [c]

[a] *Research Laboratory of Engineering Materials, Tokyo Institute of Technology, Nagatsuta, Midori-ku, Yokohama 227, Japan*
[b] *Institute for Molecular Science, Myodaiji, Okazaki 444, Japan*
[c] *School of Energy Science and Engineering, Nagoya University, Nagoya 464, Japan*

Abstract

The optical and electrical properties of proton-implanted SiO_2, GeO_2–SiO_2, MgO–P_2O_5 glasses and nanocrystalline $MgIn_2O_4$ (spinel-type structure) films were examined and several drastic changes in them were observed. The results obtained are summarized as follows. (1) Fast proton conduction (conductivity at 300 K = ~ 10^{-5} S cm^{-1}) was obtained in $Mg(PO_3)_2$ glasses implanted with H^+ ions to a fluence of 10^{18} cm^{-2}. (2) Nanocrystalline Ge colloid particles were created by implantation of H^+ ions into $1GeO_2$–$9SiO_2$ glasses without post heat treatment. (3) Electronic conductivities in $MgIn_2O_4$ sputter-deposited films at 300 K increased from 10^{-7} S cm^{-1} to 1.5×10^1 S cm^{-1} on implantation of H^+ to a fluence of 2×10^{16} cm^{-2}. (4) Peroxy radicals in SiO_2 glasses were created primarily by electronic excitation with 1.5 MeV H^+ ions.

1. Introduction

A proton has several properties very different from those of other monovalent cations (Ernsberger [1] called it a 'non-conformist ion'). It has the smallest mass, its mobility varies over ten orders of magnitude with chemical bonding state in the condensed phases and its chemical interaction with materials results in changes in chemical and physical properties. Modification of materials by chemical reactions with protons has been demonstrated in a

wide variety of fields. In most cases, however, chemical treatments of materials with hydrogen are performed at high temperatures to obtain significant reaction rates. Ion implantation is a low-temperature processing technique and a given ion can be introduced at a controlled depth to a desired concentration level [2–4]. Therefore we anticipate that implantation of protons offers novel possibilities for studying electronic excitation effects and for creation of new materials utilizing the unique properties of protons.

In this paper we report preliminary results on the following problems: (a) effects of electronic excitation on defect formation in ion-implanted amorphous SiO_2, (b) fabrication of fast proton conducting glasses by H^+ implantation, (c) formation of nanocrystalline

---

* Corresponding author. Tel: +81-45 922 1114 5359. Telefax: +81-45 922 5169. E-mail: hhosono@nc.titech.ac.jp.

Ge by H^+ implantation into GeO_2–SiO_2 glasses, and (d) generation of conduction carriers in nanocrystalline insulating $MgIn_2O_4$ (spinel-type structure) by H^+ implantation. Since the effects of implantation on modification of the properties of materials are in most cases governed by nuclear (elastic) collision processes [5], little concrete evidence [6] of electronic excitation effects has been reported so far to our knowledge. A concrete piece of evidence for electronic excitation effects on defect formation by ion beams is given by utilizing H^+ in (a).

Fast proton conducting materials are of importance in various applications such as solid electrodes for electrochromic displays and H_2–O_2 fuel cells. Although the fundamentals of protonic conduction in oxide glasses have been established by Abe and co-workers [7–9], no proton conducting glass showing high conductivity ($> 10^{-5}$ S cm^{-1}) has been obtained yet, to our knowledge. An approach for fabricating glasses with high proton conductivity is shown in (b).

Nanosized metal or semiconductor colloid particles embedded in glass are attracting considerable attention because of their novel optical properties such as a large third-order non-linear susceptibility originating from quantum confinement effects of electronic wave functions. Ion implantation is, undoubtedly, a favorable technique to fabricate these nanocomposite materials. All nanosized colloid particles in glass obtained by implantation have been synthesized by implantation of ions of a desired colloid [4,10,11]. Here, we show a novel approach utilizing the chemical reaction of implanted protons with the constituents in substrate glasses in (c).

Historically, a great success in the application of ion implantation is in carrier doping into semiconductors such as Si and GaAs [12]. However, no work showing efficient carrier generation in crystalline and amorphous oxides by implantation has been reported so far, to our knowledge. We show in (d) that the electronic conductivity in sputter-deposited films of $MgIn_2O_4$ (crystalline size 4–8 nm) with spinel type crystal structure at room temperature can be enhanced by over nine orders of magnitude by implantation of protons. The efficiency of carrier doping is ∼ 20% for nanocrystalline $MgIn_2O_4$ in the as-implanted state and increases to ∼ 40% on post annealing.

2. Experimental

Substrates used are plates of synthetic SiO_2 glasses (type III, OH content 200 wt ppm.), 10 GeO_2–90SiO_2 glasses (VAD method, OH content < 0.1 ppm), 50MgO–50P_2O_5 glasses and $MgIn_2O_4$ films (∼ 1 μm thick) deposited on SiO_2 glass substrates by the rf sputtering technique. Detailed preparation procedures of MgO–P_2O_5 glasses and $MgIn_2O_4$ thin films were described in Refs. [8] and [13], respectively.

The crystallite size of $MgIn_2O_4$ in these films, determined from the width of X-ray diffraction peaks using Scherrer's formula, was 4–8 nm [13].

Implantation of H^+ ions was performed at room temperature at an acceleration voltage of 50–150 kV or 1.5 MV. The total fluences and dose rate were 0.5×10^{16}–1×10^{18} cm^{-2} and ∼ 3 μA cm^{-2}, respectively. Substrates were wrapped with Al foil except for implanted parts during implantation to reduce charging effects [14].

Depth concentrations of peroxy radicals (POR) in 1.5 MeV H^+-implanted substrates were determined by a sectioning technique using mechanical grinding (accuracy ± 3 μm). For 160 keV Cr^+-implanted substrates, the POR depth profile was measured by an etch back technique using HF and the depth was determined (accuracy ± 30 nm) by comparing the Rutherford backscattering (RBS) spectra of implanted Cr^+ ions in substrates before etching with those after etching [15]. Concentrations of PORs were measured at 77 K by electron paramagnetic resonance (EPR) spectroscopy. Optical absorption spectra were measured by a conventional dual-beam spectrophotometer for 190–3000 nm or by a Fourier transform infrared spectrometer for 4000–2000 cm^{-1}. Measurements of Raman spectra were carried out with a triple-grating type spectrometer using an Ar^+ laser as excitation source.

Direct-current electrical conductivities were measured with an electrometer (detection limit 10^{-11} A). Platinum paste electrodes were used for H^+-implanted substrates in a two-probe configuration and sputtered Au electrodes were applied for $MgIn_2O_4$ films in a four-probe configuration. Conductivities in H^+-implanted substrates were measured in air and in an evacuated state (∼ 10^{-1} Pa). Hall effect measurements in $MgIn_2O_4$ films were carried out at room

temperature by the Van der Pauw method, applying a static magnetic field of 1 T. A Ga–In alloy was appropriate as an electrode to make a better Ohmic contact. Conductivity and Hall measurements were made by examining an Ohmic contact. The sign of the Seeback coefficient was measured at room temperature under a temperature gradient of $\sim 20°C$.

3. Results

3.1. Depth profile of implantation-induced PORs in SiO₂ glasses

Fig. 1 shows energy depositions and depth profiles of PORs in SiO_2 glasses implanted with 160 keV Cr$^+$ or 1.5 MeV H$^+$. Concentrations of PORs in

the Cr$^+$-implanted substrates have a maximum at ~ 100 nm from the surface and the profile is similar to that of nuclear energy loss. On the other hand, in the case of H$^+$ implantation, the depth concentrations of PORs gradually increase with depth, reach a maximum at ~ 20 μm, and decrease rapidly to below the detection limit. This profile is close to that of the electronic energy loss.

3.2. Effects of H$^+$ implantation on phosphate and silica glasses

Fig. 2 shows changes in UV–visible and infrared absorptions in magnesium phosphate glasses upon implantation of H$^+$ ions at 120 keV. It is evident that a broad absorption band peaking at ~ 3200 cm^{-1} is induced and its intensity increases with the
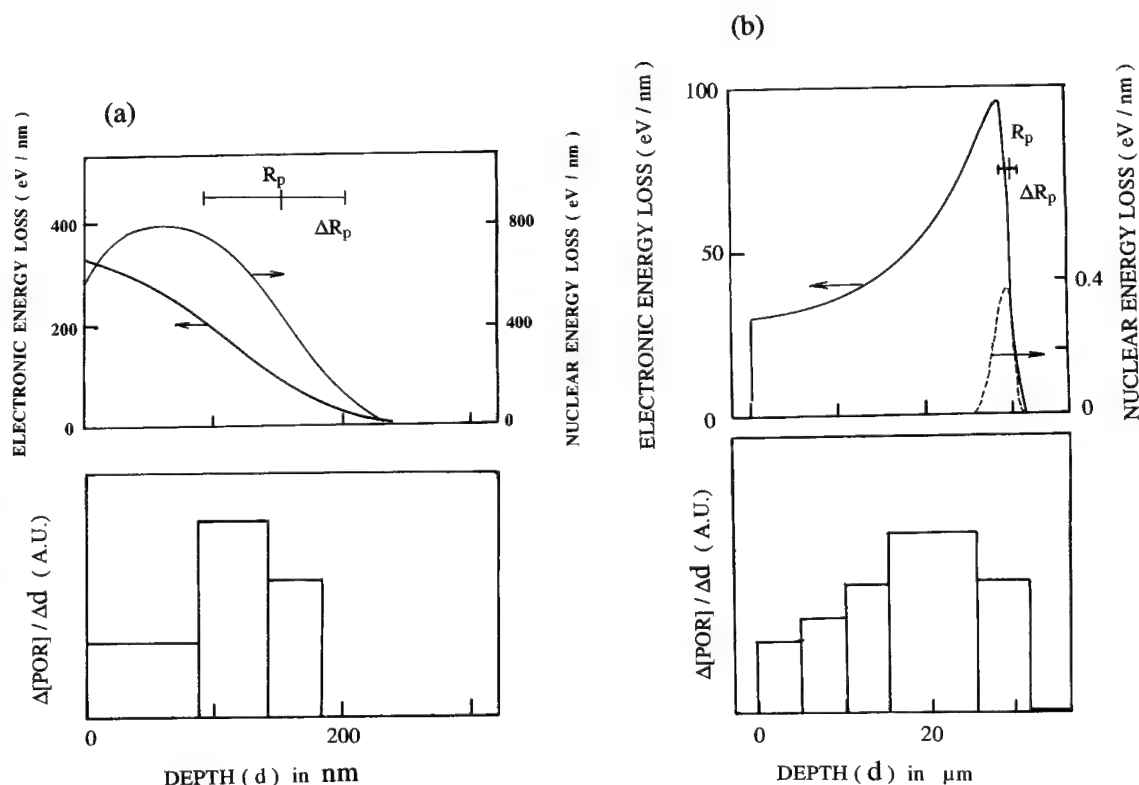
Fig. 1. Energy deposition and depth concentrations of peroxy radicals (POR). R_p and ΔR_p denote the projected range and range of straggling, respectively. Energy depositions, R_p, and ΔR_p were calculated with the TRIM code. (a) Implantation: Cr$^+ \rightarrow$ SiO$_2$ glass (type III, [OH] = 200 ppm), 160 keV. The depth POR concentrations was measured for substrates implanted to 0.5×10^{16} cm^{-2} by the chemical etch-back technique. (b) Implantation: H$^+ \rightarrow$ SiO$_2$ glass (VAD, [OH] < 0.1 ppm), 1.5 MeV. The depth POR concentrations were measured for substrates implanted to 1×10^{17} cm^{-2} by the mechanical sectioning technique.

fluence of protons. This band, which is close to that in substrates before implantation, is due to POH groups forming a strong hydrogen bonding with an oxygen attaching to the glass network [8]. However, a new band peaking at ~ 3400 cm^{-1}, marked by an arrow in the figure, becomes prominent in the substrate implanted to a fluence of 1×10^{18} cm^{-2}. This band is not seen for POH groups in the substrate before implantation and is tentatively attributed to molecular water H_2O [16] from its similarity to the peak position of H_2O in silicate glasses [17]. In UV–visible absorption spectra, absorptions extending from a deep UV region to ~ 2 eV are induced at fluences $\geq 1 \times 10^{17}$ cm^{-2} and their intensities increase rapidly at doses $> 3 \times 10^{17}$ cm^{-2}. Then the substrate changed from being colorless to reddish yellow. This absorption and coloring are close to that of amorphous red phosphorus colloids [18].

Fig. 3 shows the changes in infrared absorption spectra of SiO_2 glasses with implantation of 150 keV H$^+$. It is evident that two absorption bands centered at 3670 and 2230 cm^{-1}, which are due to Si–OH and Si–H groups [19], respectively, are induced by proton implantation. The presence of the latter band became clear by subtracting the spectrum

Fig. 3. Changes in infrared absorption spectra of SiO_2 glass (type IV) upon implantation of H$^+$ ions (150 keV, 1×10^{18} cm^{-2}). Two induced bands peaking at ~ 3670 and 2230 cm^{-1} are due to stretching vibrations of SiO–H and Si–H bonds.

Fig. 2. Visible–ultraviolet (left) and infrared (right) absorptions induced by implantation of protons. Each spectrum was obtained by subtracting the spectrum before implantation from that after implantation. The induced visible–UV absorptions appearing $\geq 3 \times 10^{17}$ cm^{-2} are ascribed to amorphous red phosphorus (a-P$_{red}$) colloids, referring to the spectra of a-P$_{red}$ colloids embedded in silica fabricated by P implantation. Absorptions appearing in the range 3800–2500 cm^{-1} are due to stretching vibrations of PO–H bonds. Note that a component (indicated by an arrow) which is seen only in the substrate implanted to a fluence of 1×10^{18} cm^{-2} is attributed to due to molecular water, H_2O.
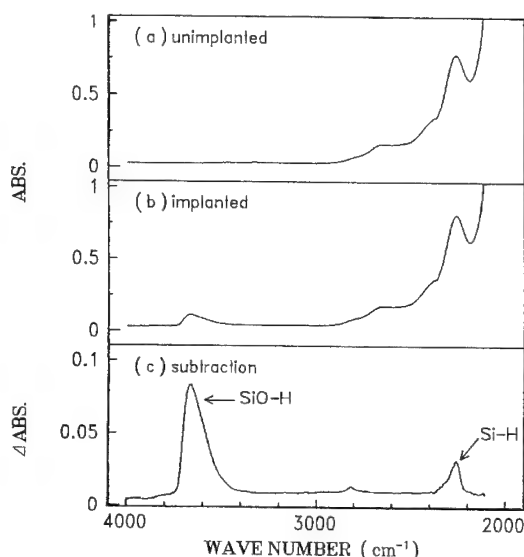
of the substrate before implantation from that after implantation. No formation of molecular water was seen. The concentrations of created SiOH and SiH, estimated from the infrared spectra, were 4.9×10^{17} and 3.7×10^{17} cm^{-2}, and the sum of these two concentrations is comparable with the concentration $(1 \times 10^{18}$ cm$^{-2})$ of implanted H$^+$ ions. In UV–visible absorption spectra (not shown), there is a band peaking at 5.8 eV and a shoulder at ~ 5 eV, both of which are ascribed to intrinsic point defects created by ion bombardment in silica.

Fig. 4 shows the electrical conductivities of 50MgO–50P$_2$O$_5$ glasses implanted with 120 keV H$^+$ to 1×10^{18} cm^{-2}. No difference in data was seen between samples measured in air and in an evacuated state within the experimental uncertainty ($\sim \pm 10\%$). Here, conductivities were calculated by postulating the thickness of conductive layers to be 1 μm, which corresponds to the calculated depth [20] of implanted protons. The conductivity at 300 K is $\sim 10^{-5}$ S cm^{-1} and the estimated activation energy was ~ 18 kJ mol^{-1} (0.19 eV). The conductivity at room temperature is larger by about ten orders of magnitude than that in the substrate (containing ~ 0.2 mol L^{-1} of residual OH) before implantation

(conductivities are controlled by protons [7, 21, 22]). Conductivities in SiO_2 glasses implanted with 150 keV H^+ to a fluence of 1×10^{18} cm^{-2} at ~ 300 K were $< 10^{-8}$ S cm^{-1}.

3.3. H^+-implanted GeO_2–SiO_2 glasses

Fig. 5 shows the changes in optical absorption spectra of $1GeO_2$–$9SiO_2$ glasses implanted with 1.5 MeV H^+ to a fluence of 1×10^{18} cm^{-2} with depth. No perceptible optical band except for a band peaking around 5 eV, which originates from Ge-related oxygen vacancies [23], was seen in the substrate before implantation. Absorptions extending from ~ 2 to > 7 eV are induced by implantation, and then the substrates appear to be yellowish brown. It is evident from the figure that induced absorptions are comprised of at least two components, the 5 eV band and absorption extending from a deep UV to visible range including a shoulder at ~ 3 eV. No such change was observed in the substrate implanted with 1.5 MeV He^+ to a fluence of 1×10^{18} cm^{-2} as shown in inset of the figure. Fig. 6 shows the Raman
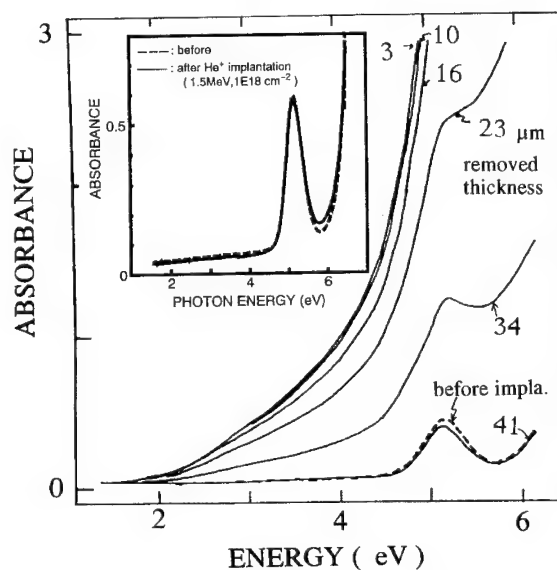
Fig. 5. Changes in optical absorption spectra of H^+-implanted (1.5 MeV, 1×10^{18} cm^{-2}) $10GeO_2$–$90SiO_2$ glass as a function of depth. Numbers in the figure denote the thickness removed by mechanical grinding. The trace of the spectrum of the substrate before implantation is drawn by the broken curve. The inset shows the optical absorption spectra of the substrate before and after He^+ (1.5 MeV, 1×10^{18} cm^{-2}) implantation.
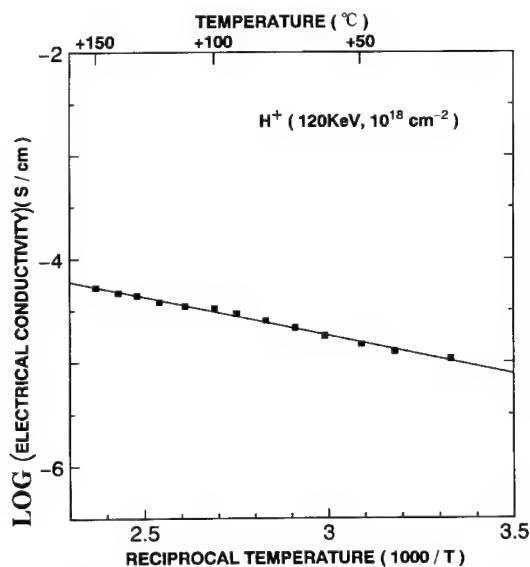

Fig. 4. Semi-logarithmic plot of the electrical conductivity of $50MgO \cdot 50P_2O_5$ glass implanted with 120 keV H^+ ions to a fluence of 1×10^{18} cm^{-2} as a function of the inverse absolute temperature. The curve is a least-squares fit (correlation factor 0.98) of the data of a linear function log (conductivity) = a $(1/T) + b$ (where a and b are constants to be determined).

spectra of substrates before and after implantation. A conspicuous spectral change upon implantation is noted, i.e., the emergence of a sharp band at ~ 300 cm^{-1} (shaded band). It is already known [24] that fine particles of Ge give an intense Raman scattering band (peaking at around 300 cm^{-1}) originating from resonance effects and the peak width provides information on the states and sizes of Ge particles. Therefore, the observed 300 cm^{-1} band is attributed to fine crystalline Ge colloid particles. The colloid size was estimated to be ~ 8 nm in diameter from a relation [24] between the linewidth of the band and the diameters of crystalline Ge particles embedded in amorphous SiO_2 matrix (the linewidth of amorphous Ge particles is much broader than that of crystalline particles [24]). The optical absorption [25] of Ge particles 7–10 nm in diameter is consistent with the observed absorption having a shoulder at ~ 3 eV. In infrared spectra, the formation of GeOH and SiOH groups was observed in the substrate after implantation as shown in inset to Fig. 6 (lower right). Fig. 7 shows the depth intensity of absorption at 3 eV, i.e.,
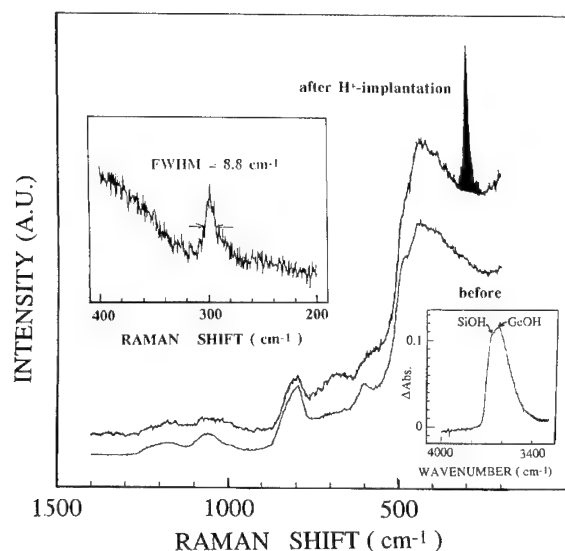
Fig. 6. Raman spectra of $10GeO_2-90SiO_2$ glass substrate before and after H^+ (1.5 MeV, 1×10^{18} cm^{-2}) implantation. The inset (upper left) shows a portion of the sharp band appearing at ~ 300 cm^{-1} measured at a resolution of 1 cm^{-1}. Excitation: Ar$^+$ laser (514.5 nm, 250 mW). Infrared absorption bands of SiOH and GeOH are observed in the substrate after implantation as shown in the inset (lower right).

the depth concentrations of Ge colloids and energy depositions. The profile of the electronic energy loss is similar to that of the absorption. No formation of Si particles was observed in $1GeO_2-9SiO_2$ or in
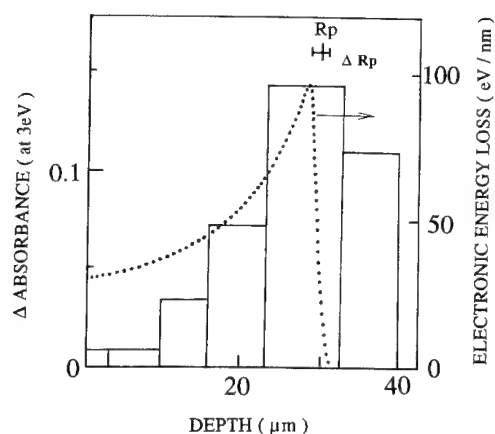
Fig. 7. Electronic energy loss and depth intensity of absorption at 3 eV. The electronic energy loss was calculated for $H^+ \rightarrow 1GeO_2-9SiO_2$ substrate with the TRIM code [20] and the depth intensity of the absorption at 3 eV was evaluated from Fig. 5. R_p and ΔR_p denote the calculated projected range and range of straggling, respectively.
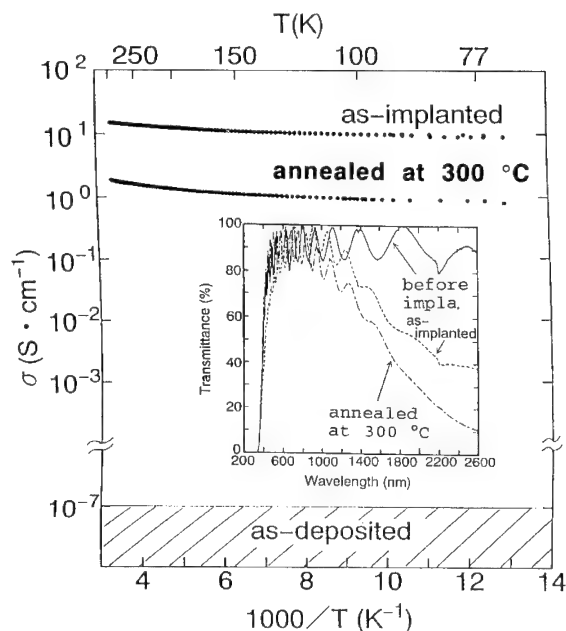

Fig. 8. Temperature dependence of the electrical conductivities of $MgIn_2O_4$ sputtered films. The conductivities in the substrate before implantation are $< 10^{-7}$ S/cm. As-implanted: H^+ ions were implanted at 50 keV to 1×10^{16} cm^{-2} and then at 80 keV to 1×10^{16} cm^{-2}. Annealed at 300°C: after annealing of as-implanted substrate at 300°C for 1 h in air. The inset shows the optical transmission spectra of substrates before and after implantation and the implanted substrate after post annealing at 300°C.

SiO_2 glasses (hydroxyl free type) implanted with protons under the same conditions.

3.4. Changes in optical and electrical properties of $MgIn_2O_4$ films

Fig. 8 shows the electrical conductivities of $MgIn_2O_4$ sputter-deposited films before and after H^+ implantation and after post thermal annealing. Conductivity at room temperature increased by more than eight orders of magnitude after implantation, i.e., from $< 10^{-7}$ to 1.5×10 S cm^{-1}. The mobility and carrier electron concentrations (the sign of Hall voltages showed that the electrons) evaluated by Hall effect measurements were 3 cm^2/V s and 3×10^{19} cm^{-3} at ~ 300 K in the as-implanted substrate. No such carrier generation was observed on implantation of He$^+$ ions. Two optical absorption bands were induced by proton implantation as shown in the inset to Fig. 8, a band centered at ~ 500 nm and a band extending from ~ 800 nm to > 2600 nm. When the

as-implanted substrate was annealed at 300°C for 1 h in air, the former band faded but the latter absorption developed. Then, conductivities were reduced over the entire temperature range by about an order of magnitude compared with those in the as-implanted substrate. The carrier concentration was enhanced from 3×10^{19} to 6×10^{19} cm^{-3}, whereas the mobility was reduced from 3 to 0.2 cm^2 V^{-1} s^{-1}. No change in X-ray diffraction pattern was perceived after implantation or post annealing of the as-implanted substrate.

4. Discussion

4.1. Two formation channels of PORs in implanted SiO₂ glass

Substrate silica glasses used for Cr$^+$ and H$^+$ implantation are type III (prepared by flame hydrolysis of SiCl$_4$) and contain ~ 200 ppm of residual SiOH groups. The predominant oxygen-associated paramagnetic defects in type III silica irradiated with ionizing radiation such as γ-rays is not a POR but a non-bridging oxygen hole center NBOHC, which is created via radiolysis of SiOH groups [26].

However, Tsai and Griscom [27] found in type III (wet) SiO$_2$ glasses irradiated with ArF excimer laser light (6.4 eV) that although the predominant oxygen hole center (OHC) is a NBOHC in the unfocused region as was already known, a POR becomes the major OHC in place of NBOHC in the focused region and the POR concentration is much higher than that of precursors even in the as-irradiated state (POR concentrations increase after annealing at 100–200°C through a reaction of E′ centers and molecular oxygens, which are created by dense electronic excitation). This finding indicates that dense electronic excitation of amorphous SiO$_2$ induces the formation of PORs from Si–O–Si bonds via an intrinsic mechanism. It is now established that self-trapped excitons (STE) are formed in crystalline and amorphous SiO$_2$ as in alkali halides by electronic excitation [28–30].

In 1979, Griscom [29] proposed a structural model of STE, which is composed of a peroxy radical and a E′ center. Recently Shluger and Stefanovich [30] proposed a structural model of STE in silica and a defect pair of an oxygen vacancy and an oxygen interstitial by self-consistent-field molecular-orbital calculations. The STE is composed of a hole localized on a singly bonded oxygen (Si–O–Si bonds are broken by energy localization) and an electron which is trapped in the Coulombic field of the localized hole. When the oxygen on which the hole is trapped moves to a neighboring oxygen, it results in a neutral oxygen vacancy and a peroxy bridge Si–O–O–Si. This structure is the proposed model of defect pairs created from decay of the STE. Both models may explain the formation of E′ centers and POR (in the latter model, the POR is created by trapping a hole on the peroxy bridge). Therefore, we consider that PORs in the H$^+$-implanted silica are created primarily by dense electronic excitation with energetic H$^+$ via an excitonic mechanism.

On the other hand, a similarity in depth profile between nuclear energy loss and PORs indicates that the PORs are created in the Cr$^+$-implanted substrates by knock-on events. As a consequence, it turns out that PORs are created in implanted amorphous silica either by electronic excitation or elastic collision. The present results strongly indicate that the primary factor, elastic or inelastic energy loss, controlling defect formation in amorphous SiO$_2$ is the mass of implanted ions (it was reported by Pfeffer [31] that ionization rather than atomic collision is the predominant defect formation mechanism in SiO$_2$ by fast electron irradiation). The major problem to be clarified first is to evaluate the efficiency of POR formation by these two mechanisms. The determination of a saturation fluence by examining the fluence dependence is indispensable for this evaluation.

4.2. Requirements for glasses with high proton conductivity

According to experimental works on protonic conduction in oxide glasses by Abe and co-workers [7,9,21,22], the conductivity, $\sigma_{417\,K}$ (S cm^{-1}), is related to the concentration of protons, [H$^+$] (mol l), and the peak wave number, ν_{OH} (cm^{-1}), of the infrared absorption band due to OH stretching vibration through

$$\sigma_{417\,K} = A_H[H^+]^2, \tag{1}$$

$$\log A_H = -0.0097\nu_{OH} + 17.1, \tag{2}$$

where $\sigma_{417\ K}$ is the conductivity at a reference temperature of 417 K and A_H is a constant depending on the glass composition, and is a measure of the protons mobility. These equations have been obtained from the experimental data for about 80 types of oxide glass containing only residual X–OH groups (X = Si, P and B) (*no molecular water is contained*). The activation energy, E (kJ mol^{-1}), in MgO–P$_2$O$_5$ glasses is also related to proton concentrations through

$$E = 110 - 12 \log[\text{H}^+]. \tag{3}$$

Let us calculate the conductivity and activation energy in H$^+$-implanted $(1 \times 10^{18}$ cm$^{-2})$ magnesium phosphate glasses. The produced POH concentration estimated from the peak height of POH band (at ~ 3200 cm^{-1}) using a molar absorption coefficient of 150 l cm mol^{-1} is 2.7 mol l^{-1}. Putting these values into Eqs. (1)–(3), we obtain $\sigma_{417\ K} = 10^{-12}$ S cm^{-1} and $E = 105$ kJ mol^{-1}. The observed conductivity $\sigma_{417\ K}$ is $\sim 10^{-4}$, which is larger by about eight orders of magnitude than the calculated one, and the observed activation energy is about one-sixth of the calculated one. These conspicuous discrepancies suggest that fast protonic conduction in H$^+$-implanted MgO–P$_2$O$_5$ glasses is not related to OH groups. We propose that the present results are related to the formation of molecular water. Since protons are transferred as H$_3$O$^+$ in acid solutions, we consider that the coexistence of acidic POH groups and H$_2$O results in easy formation of H$_3$O$^+$ and hence the mobility is greatly enhanced compared with the system involving no molecular water. In fact, H$_3$Mo$_{12}$PO$_4 \cdot 29$H$_2$O [32], H$_3$W$_{12}$PO$_4 \cdot 29$H$_2$O [32] and HUO$_2$PO$_4 \cdot 4$H$_2$O [33], all of which are known as fast protonic at room temperature, commonly contain both POH and H$_2$O.

In the case of H-implanted SiO$_2$ glasses, SiOH and SiH groups are created at comparable concentrations and the sum of these two groups is close to the concentration of implanted protons. These results indicate that most of the implanted H$^+$ ions react with Si–O–Si bonds to form Si–OH and Si–H, but the reaction does not proceed to reduction of Si^{4+} ions into the neutral state such as in the case of H$^+$-implanted MgO $\cdot$ P$_2$O$_5$ glasses. This difference may be attributed to that in thermodynamic stability of SiO$_2$ and P$_2$O$_5$, i.e., standard Gibbs' free energy

formation $\Delta G^f_{300\ K}(1/5\text{P}_2\text{O}_5) = -580$ kJ/mol $> \Delta G^f_{300\ K}(\text{SiO}_2) = -850$ kJ/mol.

4.3. Formation of nanosized Ge colloids by implantation of protons

It is worth noting that crystalline Ge particles are obtained in the as-implanted state without post thermal annealing. There are several works reporting that nanosized Ge particles embedded in amorphous silica and related materials can be synthesized by co-sputtering of Ge and silica or plasma-enhanced chemical vapor deposition using relevant gases. However, post thermal annealing at > 600–800°C of as-deposited films is necessary to obtain crystalline Ge particles [24,25]. It is interesting to note that when Ge ions are implanted into SiO$_2$ glasses, nanocrystalline Ge cannot be obtained in the as-implanted state and post annealing at temperatures > 600°C is needed [34].

The profile of the electronic energy deposition is similar to that of the absorption, suggesting that electronic excitation plays an important role in the formation of Ge colloids. It is, however, assumed from the result on the He$^+$ implantation that electronic excitation with a rare gas ion is much less efficient than that with H$^+$, i.e., chemical interactions of implanted protons with ions in the substrates play a key role in the formation of Ge colloids. Since SiOH and GeOH groups are produced with H$^+$-implantation, we consider that GeO$_2$ components in the substrate glasses are reduced to Ge particles (GeO$_2$ + 4 H $\rightarrow$ Ge + 4H$_2$O). In thermodynamic argument, whether the elementary state is formed or not is determined by the magnitude of free-energy changes, ΔG_f, in the formation of oxide of an ion. ΔG_f (~ -500 kJ mol^{-1} at 300 K) of GeO$_2$ is much larger than that (~ -850 kJ mol^{-1}) of SiO$_2$; hence, it is assumed that GeO$_2$ is much more easily reduced to elementary colloids compared with SiO$_2$. This is consistent with the experimental result. So far, colloid particles have been produced by implanting ions of a desired colloid into substrates, to our knowledge. The present method can be applicable to various colloids. An advantage of this method is that it is capable of creating colloids at much deeper regions from the surface.

4.4. Carrier generation in implanted $MgIn_2O_4$

Since no significant conductivity increase was observed in He-implanted substrates, we conclude that chemical interactions of implanted H^+ ions with ions in the substrate control key events. According to tight-binding calculations, the bottom of the conduction band of $MgIn_2O_4$ crystal is mainly constituted of the In 5s orbital and the dispersion near the Γ point is considerably large. The effective mass of the electron, m^*, which is inversely proportional to the carrier mobility, μ, can be related to the curvature of ϵ versus k (at the bottom of the band) through

$$1/m^* = (1/\hbar^2)(d^2\epsilon/dK^2). \tag{4}$$

Here ϵ and k denote the electronic energy and wave vector, respectively. It is therefore obvious that high mobility should be obtained in $MgIn_2O_4$ if carrier electrons can be injected into the conduction band. On the assumption that each implanted H^+ generates a conduction electron, the carrier generation efficiencies in the as-implanted substrate and in the post annealed substrate were ~ 20 and $\sim 40\%$, respectively.

An optical band at ~ 500 nm was induced in both the He- and H-implanted substrates. On the other hand, another induced band extending to the infrared region was not seen in the He^+-implanted substrate and its intensity increases on annealing of the as-(H^+)-implanted substrate. This intensity increase is parallel to an increase in concentration of carrier electrons. Thus, we attribute the former band and the latter absorption to be due to a color center produced by ion bombardment and to a plasma oscillation arising from generated carrier electrons, respectively. Since the optical band gap of $MgIn_2O_4$ is ~ 3.5 eV and the tail of the plasmon band almost ends at ~ 800 nm, H^+-implanted $MgIn_2O_4$ is almost colorless after annealing at 300°C but has high electrical conductivity, i.e., a novel transparent conducting oxide material has been created by carrier injection using proton implantation.

5. Summary

(1) Fast proton conducting glasses were obtained by implantation of protons (120 keV, 1×10^{18} cm^{-2}) into magnesium phosphate glasses. The conductivity at room temperature was $\sim 10^{-5}$ S cm^{-1} and the activation energy was ~ 18 kJ mol^{-1} (0.19 eV). We suggested that the coexistence of molecular water and OH groups is requisite to obtain fast H^+ conduction in glass.

(2) Nanocrystalline Ge colloids embedded in glass were fabricated only by implanting protons into germanosilica glass substrates. No post annealing was needed to crystallize Ge.

(3) Conduction carriers were generated efficiently in nanosized $MgIn_2O_4$ crystallites with spinel-type structure by proton implantation without post annealing. Electric conductivities at room temperature increased from $< 10^{-7}$ to 1.5×10 S cm^{-1}. We postulated that an implanted H^+ generates a carrier electron, the efficiency of carrier generation was $\sim 20\%$ for the substrate implanted with 50 keV 1×10^{16} cm^{-2} + 80 keV 1×10^{16} cm^{-2}.

(4) Peroxy radicals in amorphous SiO_2 implanted with 1.5 MeV H^+ were created primarily by electronic excitation.

References

[1] F.M. Ernsberger, J. Am. Ceram. Soc. 66 (1983) 747.
[2] P.D. Townsend, Rep. Prog. Phys. 50 (1987) 501.
[3] R.A. Weeks, in: Glasses and Amorphous Materials, ed. J. Zarzycki (VCH, Weinheim, 1991) p. 331.
[4] P. Mazzoldi, G.W. Arnold, G. Battaglin, R. Bertoncello and F. Gonella, Nucl. Instr. and Meth. B91 (1994) 478.
[5] See, for example, D.A. Thompson, Radiat. Eff. 56 (1981) 105;
A. Hiraiwa, H. Usui and K. Yagi, Appl. Phys. Lett. 54 (1989) 1106.
[6] B.C. Sales, R.A. Zuhr, J.C. McCallum and L.A. Boatner, Phys. Rev. B46 (1992) 3215.
[7] Y. Abe, H. Hosono, Y. Ohta and L.L. Hench, Phys. Rev. B38 (1988) 10166.
[8] H. Hosono, T. Kamae and Y. Abe, J. Am. Ceram. Soc. 72 (1989) 294.
[9] M. Kotama, K. Nakanishi, H. Hosono, Y. Abe and L.L. Hench, J. Electrochem. Soc. 138 (1991) 2928.
[10] H. Hosono, Jpn. J. Appl. Phys. 32 (1993) 3892.

[11] H. Hosono, in: Proc. E-MRS Symp., Strasbourg, May 1994, J. Non-Cryst. Solids, to be published.

[12] J.W. Mayer, L. Eriksson and J.A. Davis, Ion Implantation in Semiconductors (Academic Press, New York, 1970).

[13] H. Un'no, N. Hikuma, T. Omata, N. Ueda, T. Hashimoto and H. Kawazoe, Jpn. J. Appl. Phys. 32 (1993) L1260.

[14] N. Matsunami and H. Hosono, Nucl. Instr. and Meth. B80&81 (1993) 1233.

[15] H. Hosono and R.A. Weeks, Phys. Rev. B40 (1990) 10543.

[16] F.M. Ernsberger, J. Am. Ceram. Soc. 60 (1977) 91.

[17] E. Stolper, Contrib. Mineral. Petrol. 81 (1982) 1.

[18] H. Hosono, Y. Suzuki, Y. Abe, K. Oyoshi and S. Tanaka, J. Non-Cryst. Solids 142 (1992) 287.

[19] J.E. Shelby, J. Appl. Phys. 50 (1979) 3702.

[20] J.F. Ziegler, J.P. Biersack and U. Littmark, in: The Stopping and Range of Ions in Solids, ed. J.F. Ziegler (Pergamon, New York, 1985) ch. 8.

[21] Y. Abe, H. Shimakawa and L.L. Hench, J. Non-Cryst. Solids 51 (1982) 357.

[22] Y. Abe, H. Hosono, O. Akita and L.L. Hench, J. Electrochem. Soc. 141 (1994) L64.

[23] H. Hosono, Y. Abe, D.L. Kinser, R.A. Weeks and H. Kawazoe, Phys. Rev. B46 (1992) 11445.

[24] M. Fujii, S. Hayashi and K. Yamamoto, Jpn. J. Appl. Phys. 30 (1991) 687.

[25] R. Hayashi, M. Yamamoto, T. Tsunemoto, K. Kohno, Y. Osaka and H. Nasu, Jpn. J. Appl. Phys. 29 (1990) 756.

[26] M. Stapelbroek, D.L. Griscom, E.J. Friebele and G.H. Sigel, J. Non-Cryst. Solids 32 (1979) 313;
H. Imai, K. Arai, J. Isoya, H. Hosono, Y. Abe and H. Imagawa, Phys. Rev. B48 (1993) 3116.

[27] T.E. Tsai and D.L. Griscom, Phys. Rev. Lett. 67 (1991) 2517.

[28] N. Itoh, Adv. Phys. 31 (1982) 491.

[29] D.L. Griscom, in: Proc. 3rd Frequency Control Symp. (Electronic Industries Association, 1979) p. 98.

[30] A. Shluger and E. Stefanovich, Phys. Rev. B42 (1990) 9664.

[31] R.L. Pfeffer, J. Appl. Phys. 57 (1985) 5176.

[32] O. Nakamura, T. Kodama, I. Ogino and Y. Miyake, Chem. Lett. (1979) 17.

[33] M.G. Shilton and A.T. Howe, Mater. Res. Bull. 12 (1977) 701.

[34] J.R. Phillips, O.C. Hellman, N. Kobayashi, Y. Makita, H. Shibata, A. Yamada, P. Fons, Y. Tsai, S. Niki, M. Hasegawa and T. Iida, Mater. Res. Soc. Proc. 136 (1994) 475.

^{29}Si superhyperfine interactions of the E' center: a potential probe of range-II order in silica glass

D.L. Griscom [a,*], M. Cook [b]

[a] *Optical Sciences Division, Code 5612, Naval Research Laboratory, 4555 Overlook Ave, S.W., Washington, DC 20375-5000, USA*
[b] *Department of Chemical Engineering, University of Massachusetts, Amherst, MA 01003, USA*

Abstract

An electron spin resonance study has been carried out on E'_γ centers in γ-irradiated silica glasses of various ^{29}Si enrichments, with the object of measuring superhyperfine splittings due to ^{29}Si nuclei at the three closest silicon neighbors to the silicon of the unpaired spin. Experimental spectra obtained at X band (9.1 GHz) in the absorption mode and at Ka band (35.0 GHz) in the rapid-passage dispersion mode are compared with computer lineshape simulations based on a simple tight-binding model anchored to literature values of the so-called 'weak' ^{29}Si hyperfine splittings of the E'_1 center in α-quartz. Surprisingly few E'_γ sites are found in the glasses to exhibit such 'weak' splittings. To reconcile this result with the model assumption made by Mozzi and Warren and the supporting analyses of Galeener, it is suppose that dihedral angles in glassy silica might be relatively uniformly distributed and uncorrelated with the Si–O–Si angle distribution in the undamaged glass but that backward puckering relaxations (similar to that calculated by Rudra et al. for the E'_2 center in quartz) may be pervasive at E'_γ (oxygen vacancy) sites in glassy silica, causing dihedral angles in the range $100 \lesssim \alpha_1 \lesssim 140°$ to be 'read out' in the present experiment as falling in the range $80 \geq \alpha_1 \geq 40°$.

1. Introduction

Both amorphous and crystalline forms of silicon dioxide are materials of high technological importance, with the former playing critical roles in both fiber-optic and metal–oxide–semiconductor (MOS) applications, while α-quartz is widely used for crystal oscillators. Thus, for practical reasons, there is strong interest in knowledge of the structures of these materials. In addition, the structure of silica glass has been the object of intensive studies because it is a 'simple' single-component prototype for a host of practical network glasses. The structures of α-quartz and other crystalline polymorphs of SiO_2 are well known from diffraction studies [1]. The structures of various amorphous forms of silicon dioxide (which may depend strongly on preparation history) are knowable to a degree by the practice of 'amorphography', which, as defined by Wright [2–4], consists of the careful comparison of the predictions of various structural models against the results of high-precision diffraction experiments. It is critical to recognize the role of models in amorphography. For example, the well known distribution of Si–O–Si bond angles in silica glass derived by Mozzi and Warren [5] was based on the model assumption of a completely random distribution in dihedral angles (designated α_1 in Fig. 1). If a different distribution

---

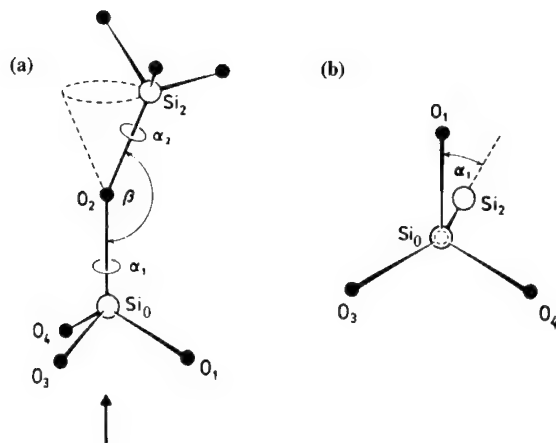* Corresponding author. Tel: +1-202 404 7087. Telefax: +1-202 404 8114.

Fig. 1. Definitions of Si–O–Si bond angle, β, and dihedral angles, α_1 and α_2. Dashed cone in (a) represents the locus of possible positions of Si_2 obtainable by varying α_1 for fixed β. Panel (b) is a view along direction of arrow in (a). (Adapted from Ref. [2].)

in α_1 had been assumed, a different distribution in Si–O–Si angle (denoted β in fig. 1) would have resulted from the analysis. Similar Si–O–Si bond angle distributions in silica glass have also been obtained from magic-angle spinning-sample NMR [6–8], although again not without model assumptions (e.g., linear proportionality between β and the chem-

ical shift, irrespective of α_1). Thus, while further refinements in these types of data may yet begin to constrain the distributions in both types of bond angle, it remains desirable to identify additional experimental techniques capable of providing independent information on the interconnection of adjacent structural units in amorphous SiO_2, i.e., the intermediate-range order defined by Galeener [9] or the similarly defined range-II order of Wright [4].

Radiation-induced defect centers in silica glasses have been extensively studied by various spectroscopic methods for about forty years [10–15]. Again, technology was a prime driving force for this work (although investigator curiosity was still an accepted motivation in the 1950s and 1960s). Windows and fiber optics must not black out under irradiation, nor must electrical charge be allowed to build up in the gate oxide of MOS transistors. Similarly, there is a concern that quartz crystal frequency standards be insensitive to nuclear or ionizing radiations. One of the early tasks of researchers in this field was to distinguish intrinsic color centers from defects associated with impurities, and one of the earliest successes was the identification of a family of intrinsic color centers associated with oxygen vacancies (the E' centers of Weeks [10,11]).
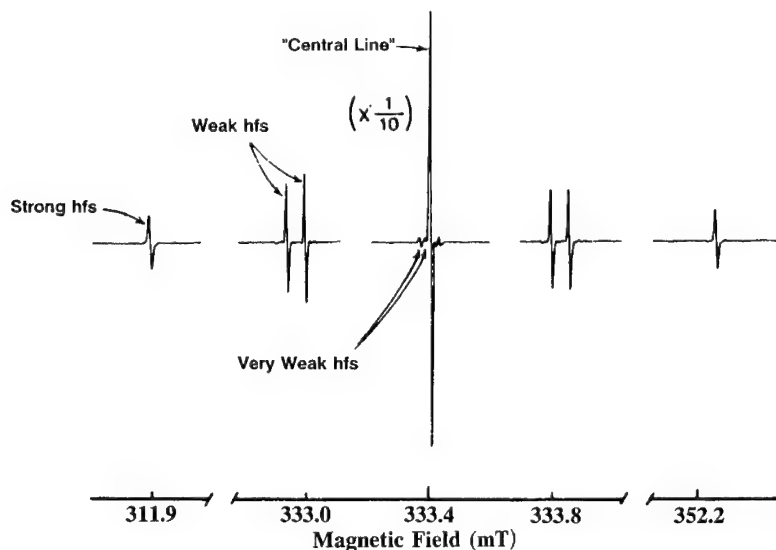

Fig. 2. ESR spectrum of E'_1 centers in irradiated α-quartz recorded with the direction of the applied magnetic field accurately parallel to the c-axis. Satellite lines are the so-called 'strong,' 'weak,' and 'very weak' hyperfine splittings of the 4.7% abundant ^{29}Si isotope. (Adapted from Ref. [21].) (The corresponding lines recorded for silica glasses are much broader and in some cases overlapping.)

Electron spin resonance (ESR) was, and remains, the experimental technique of choice to elucidate the atomic-scale structures of defects which are paramagnetic, i.e., those which contain an unpaired electron 'spin' in the highest occupied orbital. Weil has published two comprehensive reviews [16,17] on what has been learned from ESR studies of both intrinsic and impurity-related point defects in α-quartz. The ESR spectra of point defects in pure and doped oxide glasses have been reviewed by Griscom [18]. Families of E′ centers are known in both crystalline and glassy SiO_2.

1.1. E′ centers in crystalline quartz

The best information on the E′ centers comes from irradiated single crystals of α-quartz, since the angular-dependent line positions can be related to the crystal structure known from diffraction methods. For a general orientation of the direction of the applied magnetic field with respect to the crystal axes, the ESR spectrum of the E'_1 center in α-quartz comprises six equally intense symmetry-related lines; these coalesce into a single line when the field direction is made parallel to the c-axis [11,19–21]. Each of these six principal lines is flanked by several pairs of additional lines with relative intensities ∼ 2.5% [11,19–21]. These satellite pairs are recognized as hyperfine structure due to spin-$\frac{1}{2}$ nuclear species at or near the defect sites. As illustrated in Fig. 2, so-called 'strong', 'weak' and 'very weak' hyperfine pairs have been recorded, characterized by magnetic field splittings of about 41, 0.8 and 0.05 mT, respectively [21] (the descriptive nomenclature refers to the magnitudes of the splittings and not their intensities). For the E'_1 center, there is one 'strong' doublet and two each of the 'weak' and 'very weak' splittings [11,19–21]. Each of these pairs is believed to be due a hyperfine interaction with the ^{29}Si isotope, which is 4.7% abundant in nature and is possessed of a nuclear spin, $I = \frac{1}{2}$. The notion that the 'weak' pairs in quartz might be due to impurity protons (also $I = \frac{1}{2}$) was unambiguously dispelled by the careful electron–nuclear double resonance (ENDOR) measurements of Jani et al. [21]. The ^{29}Si origin of the 'strong' doublet is so universally accepted that no ENDOR experiment has been thought necessary. Nevertheless, in the case of silica

glass, a suggestion [22] that the 'strong' 42 mT splitting is due to an interaction with an impurity proton was definitively disproved by systematic ^{29}Si isotopic substitution experiments [23].

Angular dependence data recorded by Silsbee [20] for the 'strong' hyperfine splitting of the E'_1 center in α-quartz demonstrated the unpaired spin to be confined to an sp-type orbital of a single silicon atom, this orbital being oriented parallel to a 'short' Si–O bond direction in the quartz structure. (For each silicon, there are two 'long' and two 'short' Si–O bonds of lengths 1.611 and 1.604 Å, respectively.) This fundamental result was reconfirmed in meticulous studies by Feigl and Anderson [19] and Jani et al. [21]. Silsbee's analysis of the 'strong' hyperfine data, based on the local-hybrid model (for a review, see Cook and White [24]), indicated more specifically that the unpaired spin occupies an sp^3 (tetrahedral) orbital. Recently, weaknesses in the traditional application of this model have been pointed out by Edwards and Fowler [25], who argued that it may be impossible to extract the exact sp ratio from presently available theory. Nevertheless, the essential 'sp-type dangling orbital' picture of the defect evoked by Silsbee remains beyond challenge. However, for a period of a dozen years or so following Silsbee's work, there existed considerable puzzlement over the experimental evidence of the unpaired spin being confined to a single silicon dangling orbital, since two dangling orbitals point into each simple oxygen vacancy (Fig. 3(b)). (This led, for example, to the postulation of a silicon–oxygen divacancy model [11].) The asymmetric-relaxation model proposed in 1974 by Feigl et al. [26] and subsequently supported by the quantum-chemical calculations of a number of authors [27–31] has now explained this paradox (see Fig. 3(c)).

With the 'strong' splitting now understood as the ^{29}Si hyperfine interaction of the unpaired spin with the atom on which it is primarily localized, i.e., Si(0) in Fig. 3(c), the 'weak' and 'very weak' splittings may be supposed to be due to ^{29}Si nuclei in neighboring sites. Such near-neighbor hyperfine interactions are commonly referred to as superhyperfine structure (SHFS). Feigl et al. [26] assumed that one of the two 'weak' splittings could be due to a superhyperfine interaction with Si(1) in Fig. 3, and the calculations of Yip and Fowler [27] verified that

this model was a possibility by finding order-of-magnitude agreement between Silsbee's data [20] and their calculations on the model. However, Jani et al. [21], sensing a high degree of uncertainty in both the data and the model, obtained higher-precision angular dependence data for the two 'weak' hyperfine interactions of the E'_1 center in α-quartz. On the basis of their findings, it became apparent that the 'weak' interactions are almost certain to be with the silicons bonded to oxygens O(2) and O(3) in Fig. 3. For convenience we denote the nearest-neighbor silicons not shown at the bottom of Fig. 3 as Si(2), Si(3) and Si(4), according to the oxygens to which they are respectively bonded. Fig. 4(a) shows the positions of Si(2) and Si(3) with respect to the orientation of the sp orbital on Si(0) which comprises the E'_1 center in α-quartz. Not being able to explain the absence of a similar 'weak' interaction with Si(4), Jani et al. [21] tentatively proposed an oxygen vacancy at the O(4) position – in addition to the accepted one at the O(1) position. The increased precision of Jani et al.'s measurements, together with the controversial new divacancy model it spawned,

Fig. 4. (a) E'_1-center model from Fig. 3(c) expanded to show positions of near-neighbor silicon atoms (Si(2) and Si(3)) responsible for the 'weak' ^{29}Si hyperfine structure. The terminologies 'back bond' and 'equatorial bond' are explained in the text. (b) Definition of angles θ and η used in our tight-binding calculation. The z-axis in (b) is taken to be parallel to the dangling orbital represented by the 'balloon' in (a) and the y-axis lies in the plane z–Si(0)–O(2).

Fig. 3.(a) A fragment of the structure of α-quartz projected into the plane of Si(0), O(1), and Si(1). 'L' and 'S' designate the so-called 'long' and 'short' bonds. (b) An unrelaxed oxygen vacancy created by removal of O(1). If the vacancy is electrostatically neutral, the dangling sp orbitals on Si(0) and Si(1) (dashed 'balloons') contain a total of two electrons. (c) Feigl–Fowler–Yip asymmetric-relaxation model for the (positively charged) E'_1 center in irradiated α-quartz. Note that Si(0) puckers forward toward the vacancy, while Si(1) relaxes into the plane of its three coordinating oxygens. This model accounts for the available ESR and ENDOR data and is supported by numerous semiempirical and ab initio calculations. (Adapted from Ref. [26].)
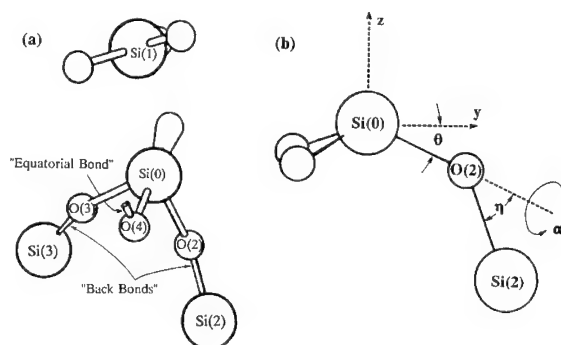
proved to be the catalyst for the next major step forward in theory of the E'_1 center.

Rudra and Fowler [28], taking into consideration the complexity of the quartz structure and the many possible structural relaxations, employed semiempirical molecular orbital methods – modified intermediate neglect of differential overlap (MINDO/3) and its open shell version MOPN – to perform calculations involving clusters of atoms (30–40) much larger than had previously been possible. In this way, they were able to examine the predicted ^{29}Si superhyperfine interactions of the E'_1 center at all of the nearest-neighbor silicon sites. From the standpoint of the present paper, the most interesting findings of Rudra and Fowler [28] were (i) calculations of the hyperfine interactions with Si(2) and Si(3) which were within 10–30% of the experimental 'weak' splittings and (ii) a calculated interaction with Si(4) which came out comparable in magnitude with the 'very weak' splittings without resort to positing a vacancy at the O(4) site. Rudra and Fowler [28] remarked that "the positions of only Si(2) and Si(3) are mutually equivalent with respect to the unpaired electron on Si(0), and the position of Si(4) is completely different in this regard". The meaning of this remark becomes transparent by reference to Fig. 4(a). We refer to bonds of the type Si(0)–O(2)–Si(2) and Si(0)–O(3)–Si(3) as 'back bonds' because they

point backwards from the direction of the dangling sp orbital on Si(0). As distinguished from this, we refer to bonds of the type Si(0)–O(4)–Si(4) as equatorial bonds since Si(4) (not shown in the figure) falls near the equator of a sphere centered on Si(0) with its polar axis pointing along the direction of the dangling orbital.

1.2. Rationale for the present work

We have become convinced that Rudra and Fowler [28] have hit upon something fundamental, although they had not fully spelled it out. In the present paper we attempt to generalize the model implications of the Rudra–Fowler 'weak' hyperfine structure (HFS) calculations by using a simple tight-binding model [32] to investigate theoretically the superhyperfine interactions of the E' center with ^{29}Si nuclei at nearest-neighbor silicon sites as a function of the dihedral angle, α_1, as defined in Fig. 1. We then employ computer lineshape simulation methods to extract the experimental 'weak' ^{29}Si hyperfine interactions of the E'$_\gamma$ center in silica glass (thought to be the nearest equivalent of the E'$_1$ center in quartz) and we use our theory to make inferences concerning the local bonding at these defect sites.

To set our experimental data in perspective, it should be kept in mind that the sharp spectral lines of Fig. 2 which characterize the E'$_1$ center in quartz become greatly broadened in the case of the E'$_\gamma$ center in silica glass, due to a combination of powder-pattern effects and the statistical influences of vitreous disorder (see, for example, Ref. [18]). For example, the 'strong' HFS of the E'$_\gamma$ center has been clearly observed [23,33] but was found to be two orders of magnitude broader than the 'strong' HFS lines of Fig. 2. By contrast, it was earlier concluded by one of us [34] that the E'$_\gamma$ center in silica glass does not exhibit any 'weak' ^{29}Si HFS at all. In Ref. [34], all spectral manifestations which could have qualified as 'weak' HFS were either demonstrated to arise from a proton-associated defect [35] or argued to result from quasiforbidden simultaneous electron–nuclear spin flips [36]. In the present paper, the data of Ref. [34] are re-analyzed under the (unproved) assumption that the spectral manifestations of E' centers in ^{29}Si-enriched glasses previously ascribed to quasi-forbidden transitions are indeed 'weak' ^{29}Si

superhyperfine structure interpretable by our theory. Even under this assumption, the implied differences between the dihedral angles in α-quartz and those in silica glass turn out to be profound. We discuss possible reasons for this outcome and offer our assessment of the prospects for using ^{29}Si SHFS of the E'$_\gamma$ center as a probe of range-II order in silica glass.

2. Theory

Fig. 4(b) is a schematic illustration of a molecular fragment representing the paramagnetic part of an E' center including the three nearest-neighbor oxygens and of one of its nearest-neighbor silicon atoms, Si(2). The unpaired spin is localized in an sp-type orbital on Si(0) projecting along the $+Z$ axis. Definitions of the angles, θ and η, to be used in our calculation are indicated in Fig. 4(b); the dihedral angle, α_1, is defined in Fig. 1. Specifically, α_1 is the angle between the Z–Si(0)–O(2) plane and the Si(0)–O(2)–Si(2) plane. In our definition, when the projection of the vector $r(\text{O}(2) \rightarrow \text{Si}(2))$ on the Z-axis reaches its most negative value, $\alpha_1 = 180°$.

We wish to investigate the dependence of the magnitude of the isotropic part of the superhyperfine interaction with Si(2), $a^{\text{Si}(2)}$. To do this, we construct a simple tight-binding model [32] for the interaction. The simplest form of this model gives the $a^{\text{Si}(2)}$ in the form

$$a^{\text{Si}(2)} \propto \left(c_{\text{d}}^{\text{Si}(2)\text{s}} \right)^2 | \psi_{\text{Si}}(0) |^2. \tag{1}$$

That is, the isotropic superhyperfine interaction with Si(2) is proportional to $(c_{\text{d}}^{\text{Si}(2)\text{s}})^2$, the square of the s-orbital coefficient on Si(2) in the defect level, and is also proportional to $| \psi_{\text{Si}}(0) |^2$, the valence s-orbital wavefunction density at the Si nucleus in the isolated atom. This form assumes that the primary mechanism for generating a superhyperfine interaction on Si(2) is the mixing of an Si(2) s-orbital into the defect level. In general, spin polarization effects should also contribute to the superhyperfine interactions. However, interatomic polarization is typically a rapidly decreasing function of distance, so at the Si(2) position the effect should not be large.

The Si(2) orbital is mixed into the defect level through the presence of off-diagonal elements of the secular matrix, which are often taken to be proportional to the overlap of the atomic orbitals. At the lowest reasonable level of approximation, this mixing would be modeled by a 2×2 secular matrix between the defect hybrid on Si(0) and an s-orbital on Si(2). If the Si(0) hybrid is primarily p-like, the overlap – and the interaction matrix element, V – becomes proportional to the cosine of the angle $Z-r(\text{Si}(0) \rightarrow \text{Si}(2))$. For fixed values of the angles, θ and η, the distance $|r(\text{Si}(0) \rightarrow \text{Si}(2))|$ is independent of the dihedral angle, α_1, and, hence, V has no explicit dependence on this distance in this case. For simplicity, we here take the distances $R(\text{Si}(0) \rightarrow O(2))$ and $R(O(2) \rightarrow \text{Si}(2))$ to be equal to an average Si–O bond length, R. It then becomes straightforward to show that the vector $r(\text{Si}(0) \rightarrow \text{Si}(2))$ has the form

$$r = \left(R \sin \alpha_1 \sin \eta, \ R\left[\cos \theta(1 + \cos \eta) \right.\right.$$
$$\left. + \sin \theta(\cos \alpha_1 \sin \eta)\right],$$
$$R\left[-\sin \theta(1 + \cos \eta) \right.$$
$$\left.\left. + \cos \theta(\cos \alpha_1 \sin \eta)\right]\right). \quad (2)$$

If the Si(0) hybrid is modeled by a p-orbital along the Z direction, then V is proportional to the cosine of the angle between Z and r,

$$V \propto \cos \theta_{Zr}. \quad (3)$$

From Eq. (2) we find the dependence of $\cos \theta_{Zr}$ on dihedral angle, α_1:

$$\cos \theta_{Zr}$$
$$= -\left[\sin \theta(1 + \cos \eta) - \cos \theta(\cos \alpha_1 \sin \eta)\right]$$
$$\times \left[2(1 + \cos \eta)\right]^{-1/2}. \quad (4)$$

In the approximation of a 2×2 interaction, the mixing coefficient of the Si(2) s-orbital into the defect level is proportional to V, and hence Eq. (1) implies

$$a^{\text{Si}(2)} = \text{constant} \times \cos^2 \theta_{Zr}. \quad (5)$$

In Fig. 5, expressions proportional to $\cos^2 \theta_{Zr}$ are plotted versus dihedral angle, α_1, for several values of the angle Si–O–Si ($\beta \equiv 180° - \eta$), assuming the tetrahedral value for θ ($\equiv 19.47°$). Here, we make no attempt to incorporate the results of orbital theory
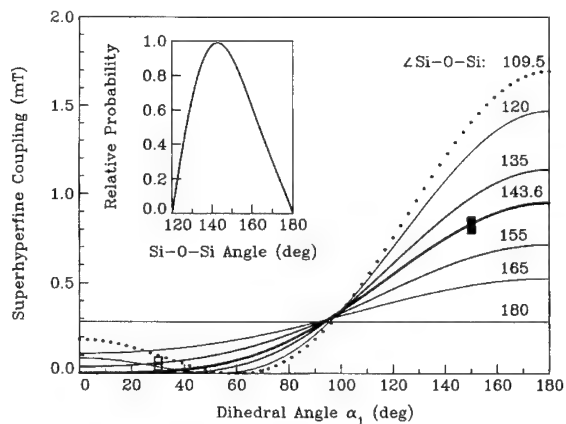

Fig. 5. Tight-binding calculation of superhyperfine coupling of an E'-type defect with a ^{29}Si nucleus at position Si(2) in Fig. 4(b). The curves are obtained by evaluating Eq. (5) as a function of dihedral angle, α_1, and Si–O–Si angle, $\beta \equiv 180 - \eta°$. Datapoints represent the isotropic 'weak' (■) and 'very weak' (□) ^{29}Si hyperfine coupling constants of the E'$_1$ center in α-quartz plotted at dihedral angles corresponding approximately to silicons Si(2) and Si(3) in Fig. 4(a) for the 'weak' splittings and to Si(4) for the 'very weak' splittings. Inset shows distribution of the angle, β, in silica glass taken from Ref. [5].

calculations [27] which suggest that the pucker angle, θ, should increase somewhat at E'$_1$ sites (see Fig. 3(c)). Nor do we include estimates of the (relatively small) $|r|$ dependence of the 'constant' in Eq. (5) which enters when β is allowed to take on different values.

For the (hypothetical) case of a tetrahedral $\angle$Si–O–Si, we see that $a^{\text{Si}(2)}$ goes to zero for $\alpha_1 = 60°$ (dotted curve in Fig. 5). This zero results from the fact that, at this combination of angles, Si(2) would be found in the nodal plane of the defect p-orbital on Si(0). Of course, this situation is unlikely in SiO$_2$, but it does accurately model the structure of crystalline silicon, which can be represented by replacing the basal oxygens in Fig. 4(b) with silicons and completing the other two tetrahedral bonds. In fact, important support for the present tight-binding model comes from self-consistent calculations [37] of dangling-bond defects on (111) silicon surfaces (P$_b$ centers) where, in good qualitative agreement with experiment, sizable superhyperfine interactions were found with second-neighbor silicons Si(2) at $\alpha_1 = 180°$ and nearly-zero interactions were calculated for second-neighbor silicons at $\alpha_1 = \pm 60°$.

3. Experimental details

Samples for this experiment consisted of small beads of silica glass fused from isotopically enriched powders containing 99.8% ^{28}Si or 95.3% ^{29}Si obtained from Oak Ridge National Laboratory (ORNL). In addition to glasses prepared directly from these as-supplied materials, a third sample was prepared by blending the two in 50:50 proportions. The masses of the 0% ^{29}Si and 50% ^{29}Si samples were 49 and 55 mg, respectively. Two separately fabricated 95% ^{29}Si samples were employed: (No. 1) 39 mg and (No. 2) 20 mg. All of these samples were annealed in air at 1000°C for 93 h before being irradiated by ^{60}Co γ-rays to a cumulative dose of 8.3×10^6 Gy (Si). Additional details concerning the physical and chemical natures of these materials and their histories have been given elsewhere [23]. For reference, an identically treated sample of a common high-purity synthetic silica (Suprasil 1) was also examined.

All samples were first investigated at room temperature by X-band (~ 9.1 GHz) ESR in the absorption mode, using 100 kHz field modulation resulting in the normal first-derivative display. As described elsewhere [23], both the E′-center 'central line' and the 42 mT 'strong' HFS were recorded and their microwave-power-corrected intensities quantified by numerical integration (Fig. 6). Most of the X-band spectra to be reported below were obtained at a microwave power level of 0.05 mW and a modula-

tion amplitude of 0.04 mT. A computer-averaged X-band spectrum of 95% ^{29}Si sample No. 2 was acquired as the sum of 46 sweeps under conditions of elevated power and modulation (0.5 mW and 0.16 mT, respectively).

To maximize the cavity filling factor with these small samples, ESR spectra were also recorded at Ka-band frequencies (~ 35 GHz), also at room temperature. Operation of the Ka-band bridge of the Varian E-9 spectrometer in the traditional absorption mode proved impossible due to inadvertent crosstalk with the dispersion signal. Therefore, all Ka-band measurements were made in the dispersion mode. The magnetic field was modulated at frequency $\omega_m / 2\pi = 100$ kHz with amplitude $H_m = 0.032$ mT, and the lock-in amplifier was set 90° out of phase (see Section 5.1 for explanation). The microwave power level was $P \approx 0.1$ mW for all of the Ka-band measurements to be described.

4. Experimental results

X-band ESR spectra of the four isotopically enriched samples are illustrated in Fig. 7 for identical conditions of microwave power, modulation amplitude and spectrometer gain. (The two 95% ^{29}Si samples were run only at $10 \times$ gain.) The central-line spectrum of Suprasil proved to be effectively identical in both shape (not shown) and mass-normalized intensity (Fig. 6, ◇) to that of the sample containing 99.8% ^{28}Si (Fig. 6, ▽). Note that 95% ^{29}Si sample No. 1 displays a strong impurity signal to the high-field side of the central line, while the central line in 95% ^{29}Si sample No. 2 appears anomalously weak. Spectra recorded as a function of increasing microwave power (not shown) revealed the weak feature near the position of the arrow in Fig. 7(a) to be less saturable than the central line.

Dispersion-mode Ka-band spectra of the 0 and 50% ^{29}Si samples and of 95% ^{29}Si sample No. 2 are reproduced in Fig. 8(a) from Ref. [34] (smooth unbroken curve, dashed curve, and noisy trace, respectively). The conditions of microwave power and modulation were identical for each of these spectra, while the ratios of (spectrometer gain) × (sample mass) were respectively 1:1.8:6.4, vis à vis expectation of 1:2:20. Here, the stronger-than-expected
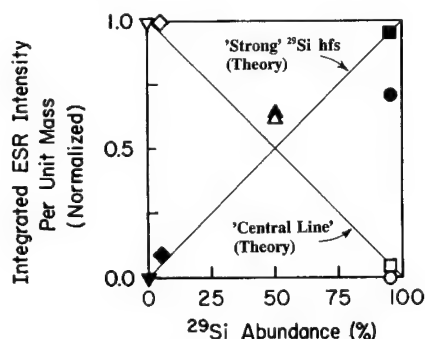

Fig. 6. ESR intensity per unit sample mass versus isotopic abundance for the E′$_\gamma$-center 'central line' (open symbols) and 'strong' ^{29}Si hyperfine structure (filled symbols) in the silica glasses of the present study. Deviations from the predicted behavior (diagonal straight lines) are tentatively ascribed to experimental error and/or slight differences in glass structure. (After Ref. [23].)

signal of 95% ^{29}Si sample No. 2 is tentatively ascribed to the higher cavity Q presumably attaching to the less massive sample. (By contrast, the Q of the much larger X-band cavity is expected to be insensitive to such small sample-mass variations, thus permitting reliable intensity measurements such as are portrayed in Fig. 6.)

5. Discussion

5.1. Interpretation of dispersion-mode lineshapes

It was previously shown [34] that the dispersion-mode spectra of Fig. 8(a) are in fact indistinguish-

able from the undifferentiated absorption curves .of the E' centers. (These shapes differ noticeably from those expected for the first derivative of the dispersion.) The same type of dispersion-mode lineshape effect has been previously observed by Portis [38] in the case of F centers in alkali halides. Portis explained this phenomenon as a rapid-passage effect associated with paramagnetic centers having long spin–lattice relaxation times and inhomogeneously broadened lineshapes. Portis' analysis was later extended and amplified by Hyde [39].

In general, the ESR spectra of E' centers in silica glasses are inhomogeneously broadened in consequence of the existence of site-to-site statistical distributions in spin-Hamiltonian parameters, as well as
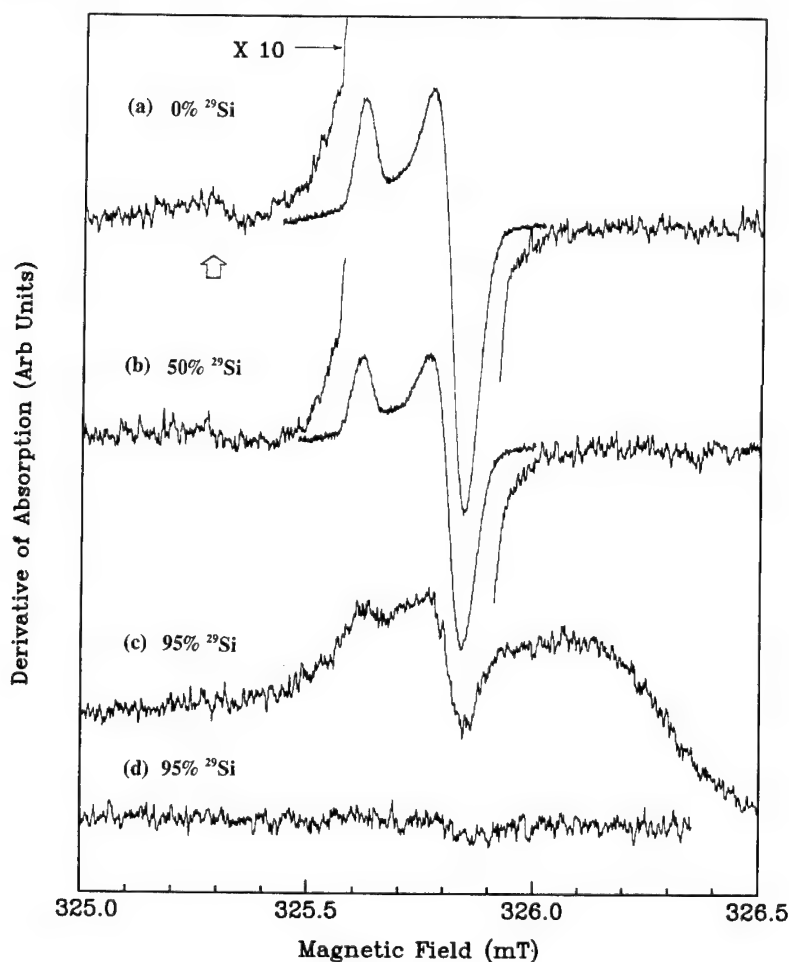
Fig. 7. X-band ESR spectra recorded at room temperature for γ-irradiated silica glasses of various isotopic enrichments: (a) 0% ^{29}Si; (b) 50% ^{29}Si; (c) 95% ^{29}Si No. 1; (d) 95% ^{29}Si No. 2. The central lines arise from E'$_\gamma$ centers. The feature indicated by the arrow in (a) is inferred to be an impurity effect (see text). The major baseline fluctuation in (c) is ascribed to a different impurity.

powder pattern effects [23]. The spin–lattice relaxation time at 300 K of these defects has been measured to be $T_1 \sim 2 \times 10^{-4}$ s [23]. For an inhomogeneously broadened line under saturation conditions, Portis [38] estimates the time of passage to be $t_{\text{passage}} \sim H_1 / \omega_m H_m$, where $2H_1$ is the peak transverse microwave field. Assuming the loaded Q of the cylindrical Varian Ka-band cavity to be ~ 5000, the value of H_1 in the present experiment was calculated from the relation [40]

$$H_1^2 \approx 10^{-3} PQ(V_w/V_c), \tag{6}$$

where V_w and V_c are the volumes of a section of the waveguide one guide wavelength long and the volume of the cavity, respectively. The resulting estimate of t_{passage} was $\sim 8 \times 10^{-8}$ s. Clearly, the condition for rapid passage, $t_{\text{passage}} \ll T_1$, is fulfilled

in the present case. According to the Portis theory [38], under such conditions a signal having the shape of the undifferentiated distribution in local resonance fields (i.e., the lineshape due to inhomogeneous broadening) will be detected in the dispersion mode at a phase angle $\phi = \tan^{-1}(\omega_m T_1)$. For the parameters of the present experiment, we calculate $\phi \approx 89.5°$. Thus, in the following section, the lineshapes of Fig. 8(a) (which were recorded at a setting of $\phi = 90°$) will be regarded as undifferentiated absorption curves.

5.2. Search for 'weak' HFS of the E' center in silica glass

Even without performing any analysis, one is surprised when inspecting Figs. 7 and 8(a) by the
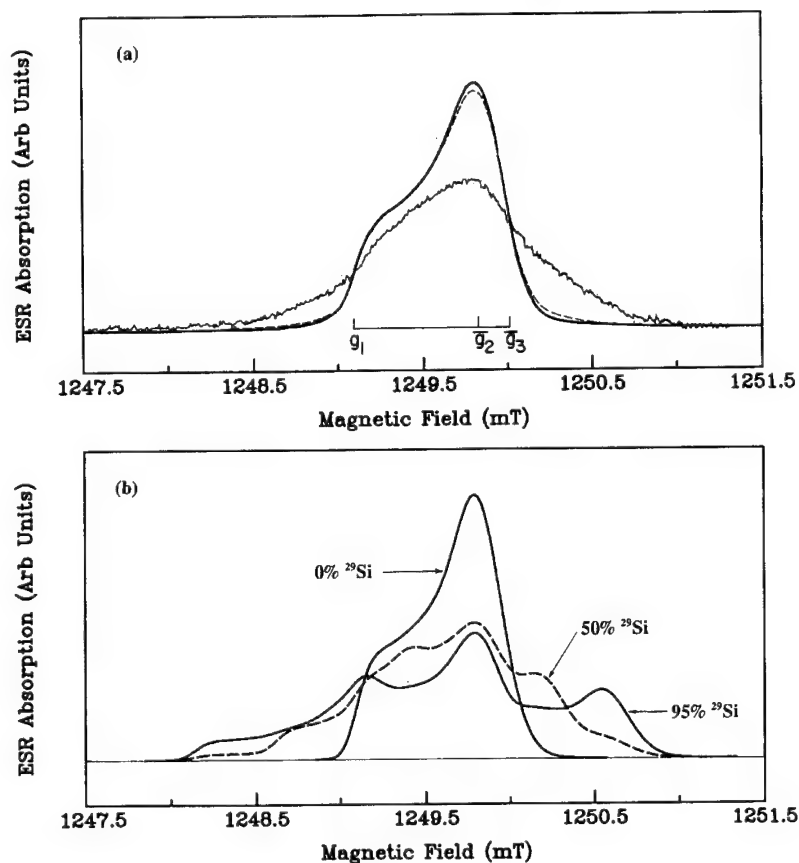
Fig. 8. (a) Rapid-passage dispersion-mode Ka-band ESR spectra recorded at room temperature for γ-irradiated silica glasses of various isotopic enrichments (smooth unbroken curve: 0% ^{29}Si; dashed curve: 50% ^{29}Si; noisy trace: 95% ^{29}Si). These spectra arise from E'$_\gamma$ centers. (After Ref. [34].) (b) Computer simulations of the corresponding spectra of E'$_1$ centers in a fictitious 'idealized amorphous quartz' (see text).

close similarity in shapes between the spectra for the samples containing 0 and 50% ^{29}Si. Indeed, one might be inclined to assess them as being identical in shape within experimental uncertainties. Based on this observation, it might be tempting to speculate that the actual isotopic enrichments of the samples are imprecisely known. However, the isotope effects clearly evident in the 'strong' and central-line intensities plotted in Fig. 6 reassure us that the isotopic enrichments given by the supplier were correct.

We have searched all of the spectra of Fig. 7 for possible evidence of 'weak' ^{29}Si splittings ($\sim$ 1.0 mT). The feature indicated by the arrow in Fig. 7(a) occurs in the proper position to be the low-field member such a 'weak' HFS doublet. Essentially the same feature also appears in the spectrum of Fig. 7(b) with comparable intensity relative to the central line. Since, on going from the sample of Fig. 7(a) (0.2% ^{29}Si) to that of Fig. 7(b) (50% ^{29}Si), the fraction of the silicon sites occupied by a ^{29}Si increases by a factor of $\sim$ 250, the designated feature clearly cannot be ascribed to ^{29}Si HFS associated with the E'_γ-center central line. Indeed, our microwave saturation studies indicate the presence of a less saturable impurity-related line of unknown origin at this position. Evidence has been given [34] that a 1.04 mT doublet, previously shown to arise from a (numerically minor) proton-associated E'-type defect [35], can also give rise to a feature at the same position. However, the 'strong' HFS due to the apex silicon should weaken the intensity of this 1.04 mT proton doublet in the ^{29}Si enriched samples in the same proportion that the E'_γ center is weakened, so that the former should be unmeasurably weak in the 95% ^{29}Si samples. We believe the most likely origin of the feature marked by the arrow in Fig. 7 to be the central member of an ^{14}N hyperfine triplet arising from a nitrogen-impurity defect [41]. In any event, evidence for ^{29}Si 'weak' HFS of the E'_γ center in the X-band spectra is inconclusive. It remains possible, however, that the 'weak' HFS of the E' centers in silica glass exists, but is overlapped by the impurity signal which we tentatively ascribe to the nitrogen center. If we have any chance to isolate this 'weak' HFS, it must be found in the Ka-band rapid-passage dispersion-mode spectra, where any lines due to less saturable impurity centers should be significantly suppressed.

To obtain a sense of the types of lineshape we might expect when 'weak' ^{29}Si HFS becomes important, we have performed computer lineshape simulations for a hypothetical material which we term 'idealized amorphous quartz'. Of course, it is well known from diffraction data and model building that silica glass cannot be constructed of units even vaguely resembling α-quartz [4], so the simulations illustrated in Fig. 8(b) are only to establish a point of reference. In these simulations we have used the average 'weak' ^{29}Si hyperfine coupling constants of the E'_1 center in α-quartz given by Silsbee [20] ($A_\parallel = 0.95$ mT and $A_\perp = 0.76$ mT) to compute the Ka-band absorption spectra for defects in samples of isotopic composition 0, 50 and 95% ^{29}Si. We did not assume statistical distributions in the values of A (the 'idealized' aspect) but we did incorporate the g-value distributions determined [23] for E' centers in silica glass. From the standpoint of isotope statistics, the fact that there are two 'weak' hyperfine interactions per E'_1 defect in α-quartz dictates that, in the 95% ^{29}Si samples, the fraction of the centers which interact with two ^{29}Si nuclei is $0.95 \times 0.95 = 0.9025$, while $0.95 \times 0.05 \times 2 = 0.095$ of the centers would interact with one ^{29}Si and only $0.05 \times 0.05 = 0.0025$ of the centers would experience no 'weak' hyperfine interactions. In the 50% ^{29}Si samples, the fraction interacting with two ^{29}Si falls to $0.5 \times 0.5 = 0.25$, while the fraction of the centers interacting with just one ^{29}Si rises to $0.5 \times 0.5 \times 2 = 0.5$. These effects show up rather dramatically in Fig. 8(b).

5.3. Model lineshape simulations

Fig. 8(b) models the expected ESR lineshapes of E'_1 centers in a hypothetical 'idealized amorphous quartz'. Clearly this is an unsuccessful model for the E' centers in silica glasses, since the simulations look nothing like the actual spectra given in Fig. 8(a). The model used here was admittedly quite crude. In the present section we invoke some more realistic models, taking advantage of the tight-binding theory developed in Section 2 to translate hypothetical distributions of bond angles into distributions in near-neighbor ^{29}Si coupling constants.

Our tight-binding theory is too crude to estimate the absolute magnitude of the superhyperfine coupling constants, but in plotting the curves of Fig. 5

we have chosen the constant factor in Eq. (5) so that the curve corresponding to the Si–O–Si bond angle in quartz (143.6°) passes through the published isotropic coupling constants (expressed in mT) of the E'_1-center 'weak' ^{29}Si HFS when these data are plotted ($\blacksquare$) at a dihedral angle of (150°) roughly appropriate for both Si(2) and Si(3). The E'_1 'very weak' HFS data are also shown in Fig. 5 plotted ($\square$) at a dihedral angle (30°) appropriate to Si(4) – although only one, and perhaps neither, of the two 'very weak' splittings may arise from Si(4). The largest of the two 'very weak' splittings lies ~ 0.07 mT above the Si(4) prediction of Fig. 5 (~ 0 mT) for the most probable case, $\angle Si–O–Si = 143.6°$. If indeed this 'very weak' splitting in α-quartz arises from Si(4), the small discrepancy in Fig. 5 may be due to neglect of the s-orbital component of the defect orbital in our tight-binding treatment. Since any such s-orbital contribution would be independent of α_1, we propose that the curves of Fig. 5 can be used to generate model predictions of the ^{29}Si SHFS of E'_γ centers in glassy silica accurate to within an additive constant ~ 0.07 mT.

To proceed with our analysis, we first consider what is known about bond-angle statistics in glassy silica. The inset to Fig. 5 shows the distribution in

Fig. 9. Histogram (bar graph) of E′-center ^{29}Si superhyperfine coupling constants developed from Fig. 5 by assuming a totally random (flat) distribution in dihedral angle, α_1, and the MW distribution in Si–O–Si angles. In principle, this distribution would independently apply to ^{29}Si s occupying each of the three near-neighbor silicon positions, Si(2), Si(3), and Si(4) in Fig. 4(a). The circles represent a Gaussian SHFS distribution discussed in the text.

Si–O–Si bond angles in silica glass experimentally derived by Mozzi and Warren (MW) [5] under the model assumption that all dihedral angles occur with equal statistical probability and are uncorrelated with $\angle Si–O–Si$. Galeener [42] has shown that a simple hard-sphere steric hindrance model incorporating the MW assumption in fact leads an Si–O–Si angle distribution similar to that extracted by Mozzi and Warren [5] from their diffraction data.

Acting then on the MW assumption that the Si–O–Si angle distribution is uncorrelated with dihedral angle, we divided the dihedral-angle axis of Fig. 5 into nine 'bins' of 20° width and used the MW $\angle Si–O–Si$ bond angle probabilities (inset) to determine the probabilities of recording ^{29}Si 'weak' interaction coupling constants falling in particular intervals on the y-axis of the figure. Following MW, we have assumed a uniform distribution in dihedral angle and have therefore histogrammed these probabilities versus the value of the ^{29}Si superhyperfine coupling constants by summing the equally weighted histograms of all nine dihedral-angle bins. The result is presented as the bar graph of Fig. 9.

When comparing our model predictions with experiment, we place the greatest weight on the Ka-band spectrum of 95% ^{29}Si sample No. 2, for reasons mentioned above. However, to ensure that we are not deceived in any way by the undifferentiated line-shapes and magnified g anisotropies which distinguish these rapid-passage dispersion-mode Ka-band spectra from those obtained at X band, we also test each model simulation against a signal-averaged X-band spectrum of the very same sample.

For our 'model-1' simulations, we assume a uniform distribution in just one of the three dihedral angles at the E′-center site, constraining the other two to be essentially equatorial ($\leq 60°$) and thus not contributing to the 'weak' ^{29}Si HFS. Although a radical departure from the MW model (which would predict a uniform distribution in all three of these angles), it is the easiest case to evaluate since the histogram of Fig. 9 can be used directly. The spectra simulated on this model are compared in Fig. 10 with the experimental spectra of E′ centers in 95% ^{29}Si sample No. 2. The Ka-band simulation (Fig. 10(a)) is fair in the central region but clearly under-represents the intensities in the wings. The X-band simulation (Fig. 10(b)) is credible, although we again
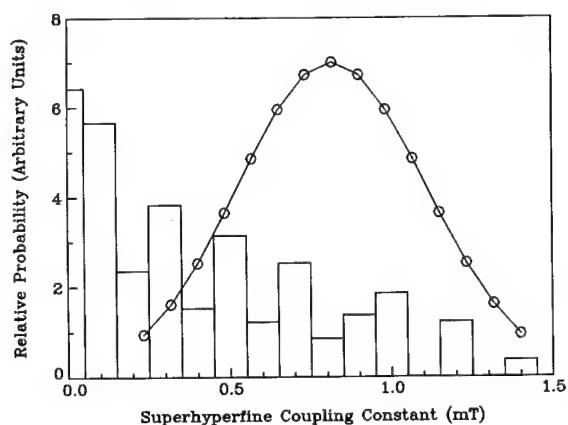
emphasize the poor quality of the X-band experimental spectrum. In particular, the spectrum of Fig. 10(b) was recorded at a microwave power level of 0.5 mW, resulting in a relative enhancement of the intensity of the low-field satellite line which we infer therefore to arise largely from an unrelated (nitrogen-impurity?) center.

For the 'model-2' simulations, we assign uncorrelated uniform distributions to two of the dihedral angles at the E'-center site, holding the third angle in the equatorial regime. Computer codes written by Friebele [43] were employed which generate powder patterns, accurate to second order in perturbation theory, of paramagnetic centers undergoing hyperfine interactions with two inequivalent nuclei. Again using the histogram of Fig. 9, we obtained the results shown in Fig. 11. Here, the Ka-band simulation is noticeably improved, but the X-band simulation is a palpable failure. Although we lack the codes to accurately calculate cases of uncorrelated distribu-
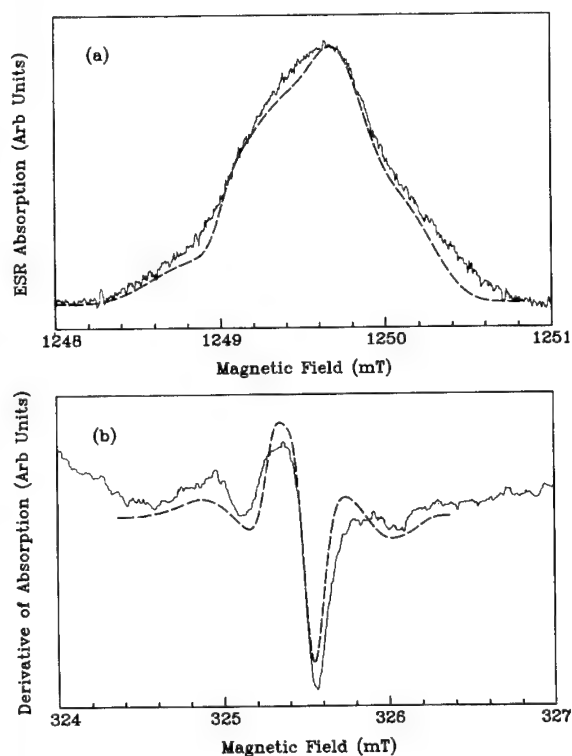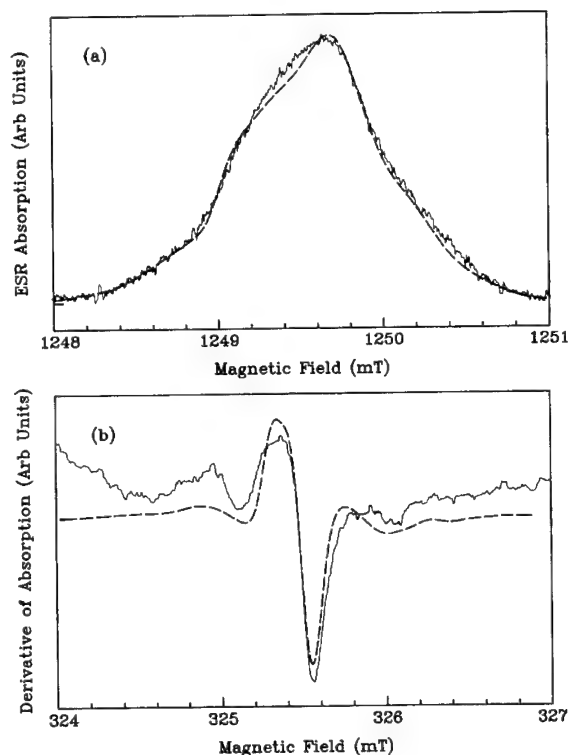

Fig. 11. 'Model-2' simulations (dashed curves) of (a) Ka-band and (b) X-band ESR spectra of E' centers in a γ-irradiated silica glass 95% enriched in ^{29}Si.

Fig. 10. 'Model-1' simulations (dashed curves) of (a) Ka-band and (b) X-band ESR spectra of E' centers in a γ-irradiated silica glass 95% enriched in ^{29}Si.

tions in all three dihedral angles, from inspection of Fig. 11(b) we advance the theorem that the X-band simulation would become significantly worse under the assumption of full randomness in dihedral angles implicit in the MW model, since the experimentally prominent central line would be totally obliterated in a simulation achieved by folding in the broad bargraph coupling-constant distribution of Fig. 9 a third time.

In Fig. 12, we have momentarily abandoned the MW model and arbitrarily assume one back bond ($\alpha_1 > 120°$) and two equatorial bonds ($\alpha_1 < 60°$) at each E' site in 50% of the cases. (The other 50% of the cases are assumed to have all equatorial bonds.) We have adopted Gaussian distributions in ^{29}Si coupling constants centered on the experimental values of $A_\parallel$ and $A_\perp$ for the 'weak' splittings in α-quartz and have optimized the fit by adjusting the full widths at half maximum of these distributions. For the 'model-3' simulations of Fig. 12, the distribution

in the isotropic part of the coupling constant is given by $\bar{A}_{iso} = 0.82$ mT and $\Delta A_{iso} = 0.67$ mT (circles in Fig. 9). This very simple ad hoc model does not fit the Ka-band spectrum well in the wings (Fig. 12(a)) and it also overaccentuates the satellite structure in the X-band simulation (Fig. 12(b)), given that much of the low-field satellite seems to be an impurity effect.

Guided by both the weaknesses and the strengths of the 'model-3' simulations of Fig. 12, we have considered one further model wherein some sites have no back bonds, some have one back bond and some have two back bonds. In this 'model 4', we have retained the same Gaussian coupling-constant distributions as used in the simulations of Fig. 12 and have carried out the simulations under the assumption that the coupling constants of the two-back-bond sites are completely uncorrelated. These simulations were optimized by varying only the fractional numbers of the three types of sites. For the

Fig. 12. 'Model-3' simulations (dashed curves) of (a) Ka-band and (b) X-band ESR spectra of E' centers in a γ-irradiated silica glass 95% enriched in ^{29}Si.

Fig. 13. 'Model-4' simulations (dashed curves) of (a) Ka-band and (b) X-band ESR spectra of E' centers in a γ-irradiated silica glass 95% enriched in ^{29}Si.

'model-4' simulations of Fig. 13, the ratios [0 back bonds] : [1 back bond] : [2 back bonds] were [35] : [40] : [25]. To our eyes, the fits of Fig. 13 are excellent. (Yet we may contemplate improving them further in the central region by plausible introduction of 'very weak' ^{29}Si HFS.) We believe it significant that these high-fidelity simulations were achieved under the effective constraint that the mean values of $A_{\parallel}$ and $A_{\perp}$ assigned to the back-bond sites remain identical to the corresponding values of the 'weak' ^{29}Si HFS of the E'_1 center in α-quartz.

In Fig. 14, we have applied the 'model-4' approach to the Ka-band spectrum of the 50% ^{29}Si–50% ^{28}Si glass. In this case, use of the identical [35] : [40] : [25] bond-type ratios (long dashed curve) results in very bad agreement with the experimental spectrum. A reasonably good fit (short dashed curve) was accomplished by greatly reducing the fractions of centers with back bonds, i.e., by using the ratios [80] : [13] : [7].
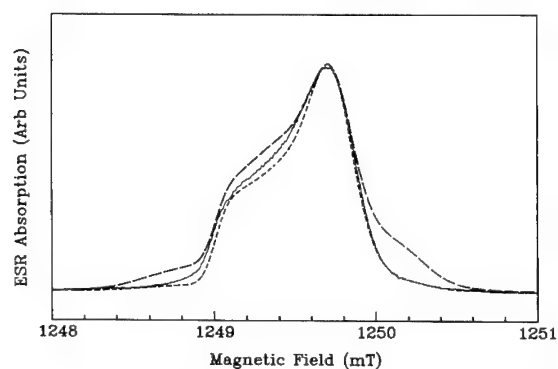
Fig. 14. 'Model-4' simulation (long dashed curve) of Ka-band ESR spectrum of E' centers in a γ-irradiated silica glass 50% enriched in ^{29}Si. Short-dashed simulation was accomplished by reducing the assumed fractions of sites with 'back bonds' (see text).

It is important in the context of the simulations of Figs. 13 and 14 to point out the fact that the possibility of sites involving three back bonds cannot be ruled out. Indeed, it is doubtful that we could distinguish the three-back-bond case from the one-back-bond case (in the present spectra), since their simulations would be effectively identical other than the fact that a small fraction $(1/4)$ of the intensity in the three-back-bond case would be split into a doublet separated by three times the single-back-bond coupling constant and would thus appear in the far 'wings,' where our spectra recede into the noise. Thus, a simulation [0 back bonds]:[1 back bond]:[2 back bonds] $= [x]:[y]:[z]$ is presently indistinguishable from the case [0 back bonds]:[3 back bonds]:[2 back bonds] $= [x]:[1.33y]:[z]$.

5.4. What does it all mean?

The spectral simulations of Figs. 10–14 are intriguing but they present some apparent internal contradictions (e.g., the dramatically different parameterizations of the successful simulations of Figs. 13 and 14) and a surprising disagreement with the reigning model assumption for the structure of silica glass (i.e., the presently favored distributions of dihedral angles differ greatly from the uniform distribution posited in Refs. [5,42].) What does it all mean?

We believe (but cannot presently prove) that the internal contradictions arise from actual differences

in glass structure, existing because each of the small samples underwent melting for a poorly controlled short period of time (∼ minutes). We suggest that 95% ^{29}Si sample No. 2 is a worse glass (i.e., it retains more crystallinity) than both 95% ^{29}Si sample No. 1 and the 50% ^{29}Si glass. Indeed, 95% ^{29}Si sample No. 2 had the appearance of being incompletely vitrified, by contrast with the 50% ^{29}Si sample which appeared as a clear glass. Second, the low X-band ESR intensity recorded for sample No. 2 is consistent with this sample being partially crystalline, since dose-for-dose defect yields in α-quartz are typically two orders of magnitude lower than in glassy silica. If we are correct in this assessment, then the short-dashed simulation of Fig. 14 gives the best information on the dihedral angles at E'-center sites in a silica glass derived from the melt. However, at face value, this information appears seriously at odds with the MW model assumption. We believe that this second dilemma may be resolved by recognizing that the E' centers which we are using as probes of glass structure are not probing typical sites in the glass network, but are sites where there is an oxygen vacancy. One possibility is that oxygen vacancies are selectively formed at sites with atypical bonding statistics. However, our feeling is that the very high 1.5 MeV γ-ray doses employed here should have created vacancies randomly across the full spectrum of site configurations present in the glass. Rather, we suppose that relaxations take place at the E' sites after vacancy creation which affect both the dihedral and Si–O–Si angles which existed before the vacancy was created. Nevertheless, it seems to us that steric constraints would prohibit relaxations which completely erase all record of the pre-existing order. Rather, we suppose that the only possible gross relaxation at the defect site would be a puckering of the defect silicon backward through the plane of three oxygens to which it remains bonded. We illustrate such a situation in Fig. 15.

The prevailing theory of the E'$_2$ center in quartz involves just such a puckering relaxation [44], and this particular E' species is characterized by the absence of any 'weak' ^{29}Si hyperfine interactions [11,19]. The single-crystal data unambiguously demonstrate that dangling Si sp orbitals of the E'$_1$ and E'$_2$ centers in α-quartz are located on the so-called 'short-bond' and 'long-bond' sides, respec-
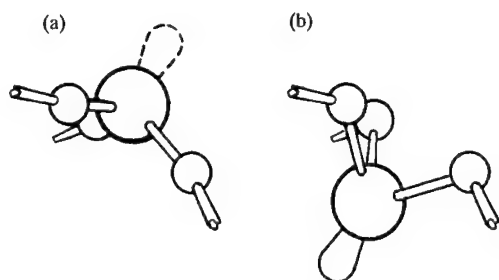
Fig. 15. Representation of a backward puckering E'-type defect. (a) Before relaxation, the dangling orbital (dashed 'balloon') projects into the oxygen vacancy. (b) After relaxation, the apex silicon has puckered backwards through the triangle of oxygens so that the dangling orbital points away from the vacancy and toward an interstice. In this particular example, all Si–O–Si angles are drawn close to 180° in the unrelaxed state.

tively, of the generic oxygen vacancy in the α-quartz lattice [11,19–21] (denoted 'S' and 'L' in Fig. 3(a)). As underscored in Fig. 4(a), the apex silicon at the E'_1 site has two back bonds with dihedral angles $\alpha_1 \sim 150°$ relative to the direction of the dangling bond. The near-neighbor silicons bridged by these back bonds give the 'weak' [29]Si HFS [21]. By contrast, before puckering, the apex silicon at the E'_2 site has two back bonds with dihedral angles of just $\sim 120°$. Quite possibly the relaxation energetics in both α-quartz and glassy silica are keyed to these back-bond dihedral angles. If so, guided by the apparent structure of the E'_2 center, we hypothesize that all E' sites in the glasses having two back bonds with dihedral angles $\leq 120°$ will pucker backwards – converting these back bonds into equatorial ones and thereby eliminating their 'weak' [29]Si hyperfine interactions altogether. Given that the Si–O–Si bond energy has a shallow minimum at $\angle$ Si–O–Si $\approx 144°$ [45], we envision further that a site with three Si–O–Si angles close to 180° (irrespective of dihedral angle) would similarly lower its energy by puckering backward (this case is illustrated in Fig. 15). If either or both of these effects should be general to all forms of SiO_2, then the global distribution in dihedral angles in the glasses (be it the MW uniform distribution or other) would not be accurately represented at the E' center sites. Rather, at the defect sites, a uniform global dihedral angle distribution would bifurcate into a predominance of sites with no back bonds (due to backward puckering) and a mi-

nority of sites with one or two back bonds with dihedral angles of perhaps $\geq 140°$ (which can only pucker forward into the vacancy). The successful ESR lineshape simulations of Figs. 13 and 14 are fully consistent with this view.

5.5. Recommendations for future work

Future work should begin with [29]Si-enriched silica samples of greater mass, higher purity and homogeneity, and better defined thermal histories. These might well be prepared by sol–gel chemistry. They could first be studied as low-fictive-temperature glasses and subsequently revisited as high-melting-temperature glasses. Thorough melting of these small but costly samples might be accomplished, e.g., by ultrasonic sample levitation and using a CO_2 laser as a power source. The radiation-induced central-line ESR spectra of the high-[29]Si samples should be examined at high gain in the far 'wings' in order to discriminate the one-back-bond 'weak' splittings from those arising from three back bonds. Besides recording the straight ESR spectra, ENDOR studies might also be carried out to obtain a more definitive measure of the 'weak' and 'very weak' HFS. A preliminary ENDOR study [46] performed on our samples gave tantalizing support for the present interpretations but as of this writing these results remain inconclusive.

Finally, reliable assessment of the hypotheses of Section 5.4. are likely to require improved ab initio calculations of structural relaxations at the E' sites as functions of the Si–O–Si and dihedral angles defining the vectors (Eq. (2)) joining the silicon of the dangling Si sp orbital with its three bonded silicon neighbors. Based on such calculations, more highly constrained models of the 'weak' HFS of E'_γ centers in silica glass could be developed and tested against experiment by ESR lineshape simulation methods.

6. Conclusions

The [29]Si superhyperfine structure of radiation-induced E'_γ centers in isotopically enriched silica glasses can be determined by model computer simulations of their ESR spectra and, potentially, from ENDOR measurements. These data provide a new

window on intermediate-range order in these glasses and potentially may be used as a supplement to diffraction methods for testing models of glass structure. However, for interpreting these data, new theoretical studies may be needed to account for local relaxations likely to occur at the defect sites; these relaxations may systematically transform the bond-angle distributions characteristic of the defect-free glasses.

References

[1] V.K. Leko, Glass Phys. Chem. 19 (1993) 351.
[2] A.C. Wright, G.A.N. Connel and J.W. Allen, J. Non-Cryst. Solids 42 (1980) 69.
[3] A.C. Wright, in: Experimental Techniques of Glass Science, ed. C.J. Simmons and O.H. El-Bayoumi (American Ceramic Society, Westerville, OH, 1993) p. 205.
[4] A.C. Wright, J. Non-Cryst. Solids 179 (1994) 84.
[5] R.L. Mozzi and B.E. Warren, J. Appl. Crystallogr. 2 (1969) 164.
[6] R. Dupree and R.F. Pettifer, Nature 308 (1984) 523.
[7] L.F. Gladden, T.A. Carpenter and S.R. Elliott, Philos. Mag. B53 (1986) L81.
[8] R.A.B. Devine, R. Dupree, I. Farnan and J.J. Capponi, Phys. Rev. B35 (1987) 2305.
[9] F.L. Galeener, J. Non-Cryst. Solids 123 (1990) 182.
[10] R.A. Weeks, J. Appl. Phys. 27 (1956) 1376.
[11] R.A. Weeks, Phys. Rev. 130 (1963) 570.
[12] G.W. Arnold and W.D. Compton, Phys. Rev. 116 (1959) 802.
[13] P.W. Levy, J. Phys. Chem. Solids 13 (1960) 287.
[14] E. Lell, N.J. Kreidl and J.R. Hensler, in: Progress in Ceramic Science, Vol. 4, ed. J. Burke (Pergamon, Oxford, New York, 1966) p. 1.
[15] D.L. Griscom, J. Ceram. Soc. Jpn. 99 (1991) 923.
[16] J.A. Weil, Phys. Chem. Miner. 10 (1984) 149.

[17] J.A. Weil, in: The Physics and Chemistry of SiO₂ and the Si–SiO₂ Interface 2, ed. C.R. Helms and B.E. Deal (Plenum, New York, 1993) p. 131.
[18] D.L. Griscom, in: Glass: Science and Technology, Vol. 4B, Advances in Structural Analysis, ed. D.R. Uhlmann and N.J. Kreidl (Academic Press, Boston, 1990) p. 151.
[19] F.J. Feigl and J.H. Anderson, J. Phys. Chem. Solids 31 (1970) 575.
[20] R.H. Silsbee, J. Appl. Phys. 32 (1961) 1459.
[21] M.G. Jani, R.B. Bossoli and L.E. Halliburton, Phys. Rev. B27 (1983) 2285.
[22] A.V. Shendrik and D.M. Yudin, Phys. Status Solidi B85 (1978) 343.
[23] D.L. Griscom, Phys. Rev. B20 (1979) 1823.
[24] M. Cook and C.T. White, Surf. Sci. Technol. 4 (1989) 1012.
[25] A.H. Edwards and W.B. Fowler, Phys. Rev. B41 (1990) 10816.
[26] F.J. Feigl, W.B. Fowler and K.L. Yip, Solid State Commun. 14 (1974) 225.
[27] K.L. Yip and W.B. Fowler, Phys. Rev. B11 (1975) 2327.
[28] J.K. Rudra and W.B. Fowler, Phys. Rev. B35 (1987) 8223.
[29] A.H. Edwards, W.B. Fowler and F.J. Feigl, Phys. Rev. B37 (1988) 9000.
[30] D.C. Alan and M.P. Teter, J. Am. Ceram. Soc. 73 (1990) 3247.
[31] K.C. Snyder and W.B. Fowler, Phys. Rev. B48 (1993) 13238.
[32] M. Cook and C.T. White, Mater. Res. Soc. Symp. Proc. 209 (1991) 561.
[33] D.L. Griscom, E.J. Friebele and G.H. Sigel Jr., Solid State Commun. 15 (1974) 479.
[34] D.L. Griscom, Phys. Rev. B22 (1980) 4192.
[35] T.-E. Tsai and D.L. Griscom, J. Non-Cryst. Solids 91 (1987) 170.
[36] J.A. Weil and J.H. Anderson, J. Chem. Phys. 35 (1961) 1410.
[37] M. Cook, and C.T. White, Phys. Rev. B38 (1988) 9674.
[38] A.M. Portis, Phys. Rev. 100 (1955) 1219.
[39] J.S. Hyde, Phys. Rev. 119 (1960) 1483.
[40] C.P. Poole Jr., Electron Spin Resonance: A Comprehensive Treatise on Experimental Technique (Wiley, New York, 1983) p. 166.
[41] T.-E. Tsai, D.L. Griscom and E.J. Friebele, Phys. Rev. B38 (1988) 2140.
[42] F.L. Galeener, Philos. Mag. B51 (1985) L1.
[43] D.L. Griscom and E.J. Friebele, Phys. Rev. B43 (1991) 7427.
[44] J.K. Rudra, W.B. Fowler and F.J. Feigl, Phys. Rev. Lett. 55 (1985) 2614.
[45] G.V. Gibbs, Am. Miner. 67 (1982) 421.
[46] M.D. Pace, private communication.

Section 4. Dynamics of glassy systems

Bulk and surface floppy modes

M.F. Thorpe [*]

Center for Fundamental Materials Research and Department of Physics and Astronomy, Michigan State University,
East Lansing, MI 48824, USA

Abstract

In this paper most of the ideas that have been put forward over the past ten years on constraint counting and the resultant floppy modes in random networks are collected together. It is shown how model systems can help us understand the phenomena via rigidity percolation. These ideas have been tested experimentally in bulk glasses where the most illuminating experiments involve low frequency phonons as seen by inelastic neutron scattering in chalcogenide glasses. Other experiments, such as measurements of the elastic moduli, have been disappointing in that the effects are not resolved. Marginal cases where the instability is caused by the surface, leading to the number of floppy modes scaling with the surface area, are also examined. These effects may be important in porous silica, zeolites and possibly biological systems.

1. Introduction

The study of network structures has fascinated scientists in many areas – engineering, mechanics and biology going back more than a century [1]. Maxwell was intrigued with the conditions under which mechanical structures made out of struts, joined together at their ends, would be stable (or unstable). To determine the stability, without doing any detailed calculations (that would have been impossible then except for the simplest structures), Maxwell devised the method of constraint counting. This counting is an approximate method that proves to be accurate for structures where the density (of struts or joints) is approximately uniform. Maxwell's constraint counting method is exact for some geometries that I will discuss in this paper. The idea of a constraint in a mechanical system goes back to La-

grange [2] who used the concept of holonomic constraints to reduce the effective dimensionality of the space. The difficult part is to determine which constraints are linearly independent. If the linearly independent constraints can be identified, then the problem is solved – however, in most large systems, this identification is not possible except using some numerical procedure on an actual realization.

The problem under consideration is a static one – given a mechanical system, how many independent deformations are possible without any cost in energy? These are the zero frequency modes, which I prefer to refer to as floppy modes because in any real system there will usually be some weak restoring force associated with the motion. Often it is more convenient to look at the system as a dynamical one, and assign potentials or spring constants to deformations of the various struts (bonds) and angles. It does not matter whether these potentials are harmonic or not, as the displacements are virtual. However it is convenient to use harmonic potentials so that the system is linear. It is then possible to set up a

Lagrangian for the system and hence define a dynamical matrix which is a real symmetric and as a consequence has real eigenvalues. These eigenvalues are either positive or zero. The number of finite (non-zero) eigenvalues defines the rank of the matrix. Thus our counting problem is rigorously reduced to finding the rank of the dynamical matrix. The rank of the matrix is also the number of linearly independent rows or columns in the matrix. Neither of these definitions is of much formal help, and a numerical determination of the rank of a large matrix is difficult and of course requires a particular realization of the network to be constructed in the computer. Nevertheless the rank is a useful notion as it represents the proper mathematics for this problem, which now becomes well posed.

The genius of Maxwell was to devise the simple constraint counting method that allows us to estimate the rank of the dynamical matrix and hence the number of floppy modes. In the next section, I discuss the application of these ideas to bulk covalent network glasses. In Section 3, I expand this work to look at the marginal case when surface floppy modes become important.

2. Large ($N \to \infty$) networks

2.1. Theory

We start by examining a large covalent network that contains no dangling bonds. I can describe such a network by the chemical formula $Ge_x As_y Se_{1-x-y}$ where the chemical element Ge stands for *any* fourfold-bonded atom, As for *any* threefold-bonded atom and Se for *any* twofold-bonded atom. Every atom has its full complement of nearest neighbors and I consider the system in the thermodynamic limit where the number of atoms $N \to \infty$. There are no surfaces or voids and the chemical distribution of the elements is not relevant, except that I assume there are no isolated pieces, like a ring of Se atoms. The total number of atoms is N and there are n_r atoms with coordination r ($r = 2$, 3 or 4); then

$$N = \sum_{r=2}^{4} n_r, \tag{1}$$

and I can define the mean coordination

$$\langle r \rangle = \left(\sum_{r=2}^{4} r n_r \Big/ \sum_{r=2}^{4} n_r \right) = 2 + 2x + y. \tag{2}$$

We note that $\langle r \rangle$ (where $2 < \langle r \rangle < 4$) gives a partial but very important description of the network. Indeed when questions of connectivity are involved, it is the key quantity as we shall see.

In covalent networks like $Ge_x As_y Se_{1-x-y}$, the bond lengths and angles are well defined and small displacements from the equilibrium structure can be described by the potential [3–5]

$$V = \frac{\alpha}{2} \sum_{\langle i,j \rangle} \left[(u_i - u_j) \cdot \hat{r}_{ij} \right]^2 + \frac{\beta}{2} \sum_{\langle ijk \rangle} l_{ij} l_{jk} (\Delta \theta_{ijk})^2. \tag{3}$$

I refer to this as the covalent potential [6]. Here u_i is the displacement of the atom i, and $\hat{r}_{ij}$ is a unit vector connecting nearest neighbor sites i, j; l_{ij} is the length of the bond ij and θ_{ijk} is the angle between the bonds ij and jk. The bond stretching force constant, α, and the bond bending force constant, β, are the largest forces in covalent glasses. The bond bending force is essential to the constraint counting approach. The other terms in the potential are assumed to be much smaller and can be neglected at this stage. If floppy modes are present in the system, then these smaller terms in the potential will give the floppy modes a small finite frequency. For more details, see Ref. [6]. If the modes already have a finite frequency, these extra small terms will produce a small uninteresting shift in the frequency. This division into large and small forces is absolutely essential if the constraint counting approach is to be of any use. It is for this reason that it is of little, if any, use in metals and ionic solids. It is fortunate that this approach provides a very reasonable starting point in many covalent glasses.

We regard the solution of the eigenmodes of the potential (3) as a problem in classical mechanics [7]. The dynamical matrix has a dimensionality $3N$ which corresponds to the $3N$ degrees of freedom. In a stable rigid network, we would expect all the squared eigenfrequencies $\omega^2 > 0$ with six modes to be at zero frequency. These six modes are just the three rigid translations and the three rigid rotations. I am assuming that our (large) network has free boundary

conditions. There are some more comments on this in Section 3. Of course these six modes have no weight in the thermodynamic limit. The total number of zero frequency modes can be estimated by the Maxwell counting algorithm. This approach was first done for glasses by Phillips [8].

The constraint counting proceeds as follows. There is a single constraint associated with each bond and we can assign as $r/2$ constraints associated with each r-coordinated atom. In addition there are constraints associated with the angular forces in Eq. (3). For a twofold-coordinated atom, there is a single angular constraint; for an r-fold coordinated atom, there are a total of $2r - 3$ angular constraints. The total number of constraints is

$$\sum_{r=2}^{4} n_r [r/2 + (2r - 3)]. \quad (4)$$

The fraction, f, of zero-frequency modes is given by

$$f = \left[3N - \sum_{r=2}^{4} n_r [r/2 + (2r - 3)] \right] / 3N, \quad (5)$$

which can be conveniently rewritten in the compact form

$$f = 2 - \tfrac{5}{6} \langle r \rangle, \quad (6)$$

where $\langle r \rangle$ is defined in Eq. (2). Note that this result only depends upon the combination $2x + y$ which is the relevant variable. When $\langle r \rangle = 2$ (e.g., Se chains), then $f = 1/3$; i.e., one third of all the modes are floppy. As atoms with coordination higher than two are added to the network as crosslinks, f drops and goes to zero at $\langle r \rangle = 2.4$ and the network becomes rigid, as it goes through the phase transition.

2.2. Experiments

The above findings have been confirmed using computations on model networks. Some of these results are shown in Fig. 1. The computed number of floppy modes (shown in the inset) closely follows Eq. (6) and the elastic constants approach zero from the high coordination side, also at $\langle r \rangle = 2.4$, which is referred to as the point at which rigidity percolation occurs. This is a phase transition from rigid to floppy, driven not by temperature, but rather by the mean coordination. Measurements of the elastic con-
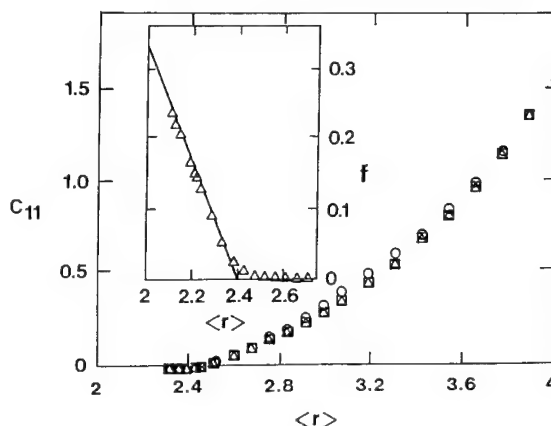
Fig. 1. The elastic constant, c_{11}, for a model network as a function of the mean coordination, $\langle r \rangle$, for three different series of random networks. In the inset, the fraction of floppy modes, f, is shown. The points are from computer simulation [3], and the solid line in the inset is the straight line given by Eq. (6).

stants [9] appear to be influenced considerably by the weak forces, and the phase transition is washed out as shown in Fig. 2. The best experimental confirmation of these ideas to date comes from inelastic neutron scattering measurements of the density of states [10], shown in Fig. 3. The agreement between theory and experiment is excellent, even when the weak forces are included in a very simple way and adjusted to bring the zero-frequency modes to the correct (low) frequency. Note that the weight in the floppy modes, given by constraint counting, is unaffected by the weak forces, even though there is some background response with which to contend.
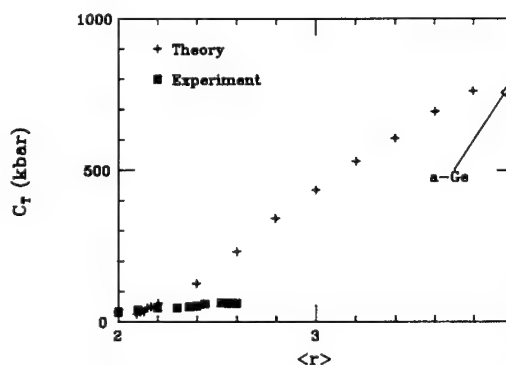

Fig. 2. The transverse elastic modulus, c_T, obtained with the weak forces included, is compared with experiment [3,6,9].
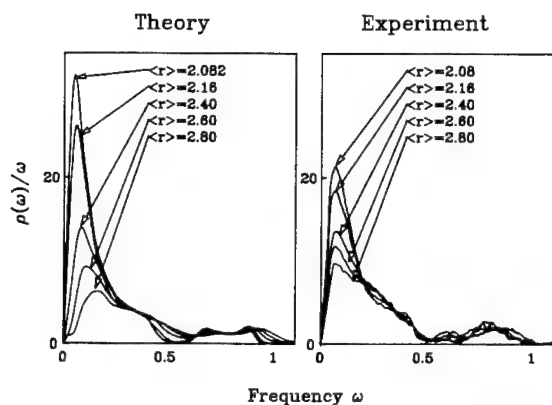
Theory   **Experiment**

Fig. 3. The density of states divided by the frequency, $\rho(\omega)/\omega$, for various values of the mean coordination, $\langle r \rangle$. The left hand set of graphs are theoretical [6] and the right set of graphs are from inelastic neutron scattering experiments [10] on $Ge_x Se_{1-x}$. The frequency is in units where the maximum frequency is unity.

2.3. Correction for dangling bonds

The previous section describes the situation when there are *no* dangling bonds present. The analysis fails when dangling bonds are present because the expression for the number of angular forces, $2r - 3$, gives -1 when $r = 1$, instead of the correct answer of zero. Thus formula (6) needs correction. This correction has recently been done in a compact way by a number of authors [11,12] following earlier efforts [13,14].

It is rather straightforward to extend formula (5) to include the summation over the dangling bonds ($r = 1$) and correct for miscounting the angular constraints to give

$$f = \left[3N - \sum_{r=1}^{4} n_r [r/2 + (2r - 3)] - n_1 \right] / 3N,$$

(7)

which now leads to the form

$$f = 2 - \tfrac{5}{6}\langle r \rangle - (n_1/3N),$$

(8)

where the definition of $\langle r \rangle$ is extended from Eq. (2) to *include* the dangling bonds. The transition now takes place at a lower mean coordination, $\langle r \rangle$, which is given by

$$\langle r \rangle = 2.4 - 0.4(n_1/N).$$

(9)

It is not surprising that the transition takes place at a lower $\langle r \rangle$ because the dangling ends play no role in the network connectivity. Indeed another conceptual approach is to strip the dangling ends away and define a skeleton network that has only two-, three- and four-coordinated atoms. The theory described in this section can then be applied to the skeleton network [15]. Eq. (9) has recently been applied to networks containing iodine, which forms a dangling end [12].

These ideas have also been applied to amorphous carbon networks by Tamor [16]. Amorphous carbon networks can be thought of as consisting of three type, of atom: fourfold (diamond-like) carbon, threefold (graphitic) carbon, and often considerable amounts of atomic hydrogen that ties off dangling ends and so is singly coordinated. Suppose that there are N atoms in the network, with a fraction x_4 of fourfold-coordinated carbon, a fraction x_3 of threefold-coordinated carbon and x_1 of singly boned atomic hydrogen. Then, by definition, we have

$$x_4 + x_3 + x_1 = 1.$$

(10)

To illustrate the use of the skeleton network, I apply it to this case. The mean coordination of the skeleton network, with the hydrogen removed is

$$\langle r \rangle = \frac{2(\text{number of bonds})}{\text{number of sites}}$$
$$= \frac{(4Nx_4 + 3Nx_3 + Nx_1) - 2Nx_1}{Nx_4 + Nx_3}$$

(11)

which gives

$$\langle r \rangle = \frac{4x_4 + 3x_3}{1 - x_1} - \frac{x_1}{1 - x_1}.$$

(12)

The important new term is the $2Nx_1$ in the numerator of Eq. (11), which removes the bonds between hydrogen and the rest of the network that are not present in the skeleton network. In deriving Eq. (12), it has been assumed [16] that there are no molecular fragments, like for example methane CH_4, that get detached from the network. If this were the case, then these fragments should also be eliminated for purposes of counting. It appears that the elastic moduli and especially the hardness properties of carbon networks [11] follow Eq. (12) closely. The hardness is measured, in a nano-indentation test, as
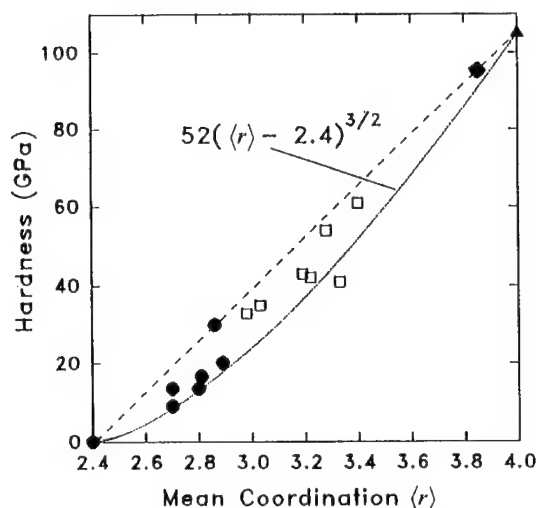
Fig. 4. The hardness (measured by nano-indentation) of various diamond films, some containing hydrogen, as a function of the mean coordination as defined by Eq. (12). The data were compiled and presented in this form by Tamor [16] based on work by Tamor [18] (●), Lossy et al. [19] (○) and Weiler et al. [20] (□) using various preparation techniques. The solid triangle is the result for diamond.

the depth a standard probe penetrates, when subject to the same external force. This is shown in Fig. 4, where the hardness is shown as a function of the mean co-ordination, $\langle r \rangle$. The hardness goes all the way from that of crystalline diamond at the one extreme, to mush when too much hydrogen is present. Also shown on the graph are a straight line and the form suggested by He and Thorpe [3] for the elastic constants and obtained via numerical computations. This form has also been confirmed recently by Franzblau and Tersoff [17], over the entire range of values of $\langle r \rangle$ from 2.4 to 4. The results seem to lie somewhere in between these two lines. It is always difficult to know precisely what is being measured by hardness and so this agreement with the elastic constants is interesting.

For the skeleton network, the number of floppy modes is still given by Eq. (6) as before. The total number of sites in the skeleton lattice is reduced to $N(1 - x_1)$, so that the total number of floppy modes, F, is given by

$$F = 3N(1 - x_1)\left(2 - \tfrac{5}{6}\langle r \rangle\right). \tag{13}$$

We now insert $\langle r \rangle$ from Eq. (12) into Eq. (13) and find that

$$F/3N = 2 - \tfrac{10}{3}x_4 - \tfrac{5}{2}x_3 - \tfrac{7}{6}x_1, \tag{14}$$

which of course reduces to the old result Eq. (6) if there is no hydrogen present so that $x_1 = 0$. The total number of floppy modes is not changed when the hydrogen is recombined with the skeleton network to reconstruct the original network that existed before the hydrogen was stripped off. This absence of change occurs because adding back a single hydrogen atom adds three extra degrees of freedom, but also adds three constraints (one for the central force associated with the bond, and two for the angular forces associated with attaching this bond to an atom in the network). Thus there is no change and all the floppy modes are associated with the skeleton network and *not* specifically with the hydrogen. No direct measurements of these modes have yet been carried out in carbon networks. Inelastic neutron scattering experiments in the low frequency region, similar to those carried out for chalcogenide glasses and shown in Fig. 3, would be very interesting.

The transition from rigid to floppy occurs when the number of floppy modes, F, goes to zero. By using Eq. (10), Eq. (14) can be written as $5x_1 = 8x_4 + 3x_3$ which, going back to the previous notation and using total numbers of atoms, can be written as

$$5n_1 = 8n_4 + 3n_3. \tag{15}$$

Of course this same result can be obtained directly from Eq. (8), without use of the skeleton network concept. From Eq. (15) we see that the amount of hydrogen is balanced against the amount of carbon to produce the transition. Without hydrogen there can be no transition, as the mean coordination lies between 3 and 4, which is well above the transition point of $\langle r \rangle = 2.4$.

3. Surface floppy modes

The analysis in the previous section has all been in the thermodynamic limit ($N \to \infty$), and the number of floppy modes, F, was a thermodynamic quantity proportional to the number of atoms, N. Thus the floppy modes can be thought of as extended bulk modes. Because there are N such modes, surface
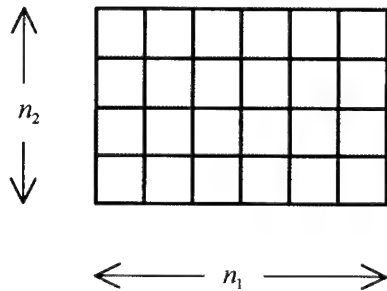
Fig. 5. A square net with free boundary conditions containing $n_1 n_2$ atoms.

effects are normally irrelevant and just small, negligible corrections. However, when the term proportional to N is zero, surface effects can become important and dominant. I will discuss this situation here.

3.1. Basic counting techniques

We use as an illustration the square net with $n_1 n_2$ sites shown in Fig. 5. I can apply the Maxwell constraint counting method here also, taking careful account of the sides and corners. The basic algorithm is unchanged; F, equals the number of degrees of freedom (twice the number of sites) minus the constraints (the number of bonds):

$$F_2 = 2n_1 n_2 - \left[\tfrac{4}{2}(n_1 - 2)(n_2 - 2) + \tfrac{3}{2}2(n_1 - 2) \right.$$
$$\left. + \tfrac{3}{2}2(n_2 - 2) + \tfrac{2}{2}4 \right],$$
$$= n_1 + n_2, \tag{16}$$

where the subscript 2 on F denotes two-dimensions. I have checked this computationally for a range of values of n_1 and n_2 and find that the formula (16) works exactly. Indeed it is likely that the constraint counting can be shown to be exact for any structure with free boundary conditions, containing no triangles of bonds [21]. The formula (16) is based on topological considerations and so it does not matter whether the network is distorted or not. I have also checked this computationally.

These planes can now be stacked up to form a simple cubic array and the result for F becomes

$$F_3 = n_3 F_2 + n_3(n_1 n_2) - (n_1 n_2)(n_3 - 1), \tag{17}$$

where the second term comes from the extra degrees of freedom and the last term is the additional constraints. Simplifying, I find that

$$F_3 = n_1 n_2 + n_2 n_3 + n_3 n_1. \tag{18}$$

This equation is clearly a surface term, as it is proportional to the number of surface atoms in a large sample.

We can now generalize to d dimensions:

$$F_d = n_d F_{d-1} + (n_d) \prod_{i=1}^{d} n_i - (n_d - 1) \prod_{i=1}^{d-1} n_i, \tag{19}$$

which gives

$$F_d = n_d F_{d-1} + \prod_{i=1}^{d-1} n_i. \tag{20}$$

We can solve this equation, using induction and the known answers for $d = 2$ and $d = 3$ to give

$$F_d = \left(\prod_{i=1}^{d} n_i \right) \left(\sum_{i=1}^{d} \frac{1}{n_i} \right). \tag{21}$$

This equation has been checked for various values of n_i for $d = 2$ and $d = 3$ and always works exactly for *both* distorted and undistorted networks.

A nice way of obtaining the equation for F_2 is to count the number of missing bonds at the surface and divide by 2. An example is shown in Fig. 6. Here there are 29 sites and 24 surface bonds shown by dashed lines. A little thought will convince the reader that the number of floppy modes is $24/2 = 12$. This number clearly reduces to the previous answer $n_1 + n_2$ for a rectangular shape, but generalizes the answer to other less regular shapes. Note that the site
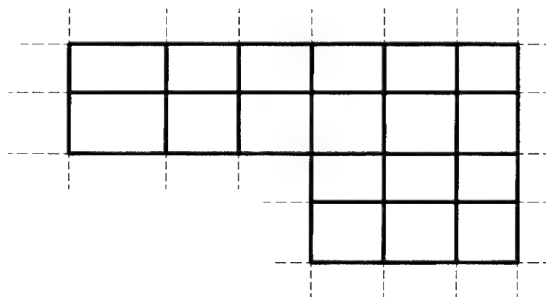

Fig. 6. A piece of a square net with 29 sites and 24 surface bonds shown by dashed lines. It is explained in the text that there are $24/2 = 12$ floppy modes of which two are the macroscopic rigid translations and one is the macroscopic rigid rotation.
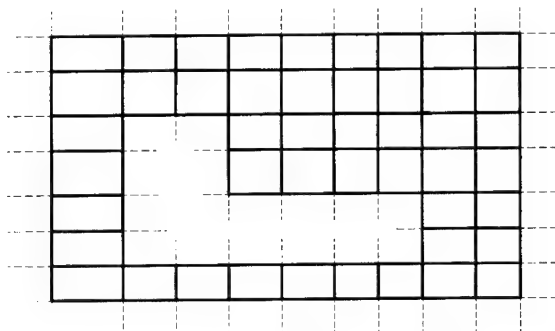
Fig. 7. A piece of a square net containing a void. Before the void was introduced there were $36/2 = 18$ floppy modes of which two are the macroscopic rigid translations and one is the macroscopic rigid rotation. The void introduces an additional $16/2 = 8$ floppy modes which can be seen by counting the dashed bonds.

in the indentation has all four bonds present, and so does not contribute, despite being a surface atom in some sense. This type of construction also works if there are internal voids, and hence surface bonds as in Fig. 7. Another way to look at this construction, is to dissect the network into distinct linear chains which decouple. Each linear chain has two (dashed) ends and a single zero frequency mode, leading immediately to the result above. This construction can be shown to be rigorously true if the network is made up of undistorted square plaquettes [21]. However the result is certainly much more general, but awaits a more general proof.

In Fig. 6, I show an example of an internal void, where there are an additional eight floppy modes introduced when the void is created. This type of counting obviously is easily extended to more complex internal void geometries, as long as the lattice is made up of square (or rectangular) plaquettes.

3.2. Problems with periodic boundary conditions

The periodic case is more difficult to understand, as symmetry now seems to play a more important role, with clear differences appearing between distorted and undistorted networks [22]. The reader may complain that the periodic case is of no more than academic interest. This complaint may be justified, but we cannot claim to understand this entire area until we do understand the periodic case also. Constraint counting always gives exactly 0 for any d

dimensional hypercubic lattice. This result is not exactly correct as there are always the d Goldstone modes, corresponding to the acoustic phonons in the long wavelength limit. For the *distorted* periodic case, I find numerically that this is the total − there are indeed always exactly d modes. The *undistorted* periodic case can be solved using Bloch's theorem. For a periodic hypercubic lattice, the eigenfrequencies are given by

$$\omega_r^i = \sqrt{k/M} \; | \sin(\pi r_i/n_r) |, \qquad (22)$$

where $r_i = 0, 1, 2 \ldots n_r - 1$. Because of the decoupling, there are

$$\frac{1}{n_r} \left(\prod_{i=1}^{d} n_i \right)$$

floppy modes associated with the direction r, so that the total number of floppy modes is again given by

$$F_d = \left(\prod_{i=1}^{d} n_i \right) \left(\sum_{i=1}^{d} \frac{1}{n_i} \right), \qquad (23)$$

which is the same answer I obtained for the square with free boundary conditions (Eq. (21)). This is because the cube can be dissected into F_d periodic linear chains, each with a single floppy mode, as in the case with free boundary conditions.

The difference is that the distortions reduce the number of floppy modes from F_d (given in Eq. (23)) to d in the periodic case, but the number of floppy modes is unchanged at F_d for free boundary conditions.

3.3. Silicate networks

Although the floppy modes that I have been discussing emanate from the surface, they are in no sense surface modes. The amplitude is not damped away from the surface. They are bulk in extent and involve the entire solid. It is only the total number that scales like the surface area. This concept is important in other marginal structures. Another two-dimensional example is the kagome lattice which consists of triangles joined at the corners. The most important three-dimensional example is provided by silicates $[SiO_2]$ where the SiO_4 tetrahedra are corner-sharing. This case has been examined extensively, both theoretically and experimentally recently [23]. These authors refer to these modes as rigid unit

modes (RUMs) in which the SiO_4 tetrahedra are not distorted. These modes can be seen using inelastic neutron scattering. This experiment is not so straightforward as in the chalcogenide glasses, because the number of RUMs is proportional to the surface area, $N^{2/3}$, rather than the bulk, N, where N is the number of atoms.

It is not yet clear if the exact results given for the number of surface floppy modes in this section, are exact or only approximately generalisable to the Kagome and silicate structures.

4. Summary

In this paper, I have tried to collect together some of the more important results regarding floppy modes and constraint counting in glasses that have emerged in the past decade. This work has provided a useful conceptual framework within which to discuss some of the physical properties of glasses. Some of the arguments in this area are subtle and still controversial. For example using a reduced dimensionality of two rather than three for layered materials like As_xSe_{1-x} does not seem to be correct to me, as these atoms are still embedded in a three-dimensional space [24]. It is true that using this reduced dimensionality does seem to improve agreement with experiment where the discontinuity seems to be at $\langle r \rangle = 2.67$ rather than $\langle r \rangle = 2.4$, but perhaps there are other explanations for this value.

Recent work on surface floppy modes is beginning to look interesting as a way of understanding open structures. So far the only serious application has been to bulk silicate networks [23], but this approach looks promising for other more complex structures such as porous silica, clays and zeolites, that contain internal surfaces or voids. Internal floppy modes may permit voids to alter their shape so as to facilitate chemical reactions and catalysis. This possibility remains to be seen. An even more distant hope is that this work may find applications in biological systems, where the ability of molecules to move at little cost in energy probably has important implications for enzyme activity and other biologically important interactions.

References

[1] J.C. Maxwell, Philos. Mag. 27 (1864) 294.
[2] J.L. Lagrange, Mécanique Analytique (Paris, 1788).
[3] H. He and M.F. Thorpe, Phys. Rev. Lett. 54 (1983) 2107.
[4] P.N. Keating, Phys. Rev. 145 (1966) 637.
[5] J.G. Kirkwood, J. Chem. Phys. 7 (1939) 506.
[6] Y. Cai and M.F. Thorpe, Phys. Rev. B40 (1989) 10535.
[7] See, for example, H. Goldstein, Classical Mechanics (Addison–Wesley, London, 1950).
[8] J.C. Phillips, Phys. Status Solidi B101 (1980) 473; J.C. Phillips, J. Non-Cryst. Solids 34 (1979) 153; 43 (1981) 37.
[9] S.S. Yun, H. Li, R.L. Cappelletti, P. Boolchand and R.N. Enzweiler, Phys. Rev. B39 (1989) 8702.
[10] P. Boolchand, R.N. Enzeiler, R.L. Capelletti, W.A. Kamitakahara, Y. Cai and M. F. Thorpe, Solid State Ionics 39 (1990) 81.
[11] J.C. Angus and F. Jansen, J. Vac. Soc. Am. A6 (1988) 1778.
[12] P. Boolchand and M.F. Thorpe, Phys. Rev. B50 (1994) 10366.
[13] G.H. Döhler, R. Dandaloff and H. Bilz, J. Non-Cryst. Solids. 42 (1980) 87.
[14] M.F. Thorpe, J. Non-Cryst. Solids 57 (1985) 355.
[15] N. Mousseau and M.F. Thorpe, Phys. Rev. B48 (1993) 5172.
[16] M. Tamor, private communication.
[17] D. Franzblau and J. Tersoff, Phys. Rev. Lett 68 (1992) 2172.
[18] M.A. Tamor, W.C. Vassell and K.P. Karduner, Appl. Phys. Lett. 58 (1991) 592.
[19] R. Lossy, D.L. Pappas, R.A. Roy, J.J. Cuomo and V.M. Sura, Appl. Phys. Lett. 61 (1992) 171.
[20] M. Weiler, R. Kleber, S. Sattel, K. Jung, H. Ehrhardt, G. Jungnickel, S. Deutschman, U. Stephan, P. Blaudeck and Th. Frauenheim, Diam. Relat. Mater. 3 (1994) 245.
[21] A. Bhattacharya, A.R. Day and M.F. Thorpe, unpublished.
[22] V. Heine, private communication.
[23] M.T. Dove, A.P. Giddy and V. Heine, Am. Crystal. Assoc., 27, (1993) 65.
[24] K. Tanaka, Phys. Rev. B39 (1988) 1270.

Lamb–Mössbauer factors as a local probe of floppy modes in network glasses

P. Boolchand [*], W. Bresser, M. Zhang, Y. Wu, J. Wells [1], R.N. Enzweiler [2]

Department of Electrical and Computer Engineering, Mail Location 30, University of Cincinnati, Cincinnati, OH 45221-0030, USA

Abstract

The temperature dependence of the Lamb–Mössbauer factor, $f(T)$, in a solid provides the first inverse, $\langle 1/\omega \rangle$, and second inverse, $\langle 1/\omega^2 \rangle$, moments of the vibrational density of states. In network glasses, these moments serve as local probes of low-frequency vibrational excitations, such as floppy modes, and provide a means to establish the rigidity percolation threshold. Lamb–Mössbauer results on prototypical chalcogenide glasses (Ge_xSe_{1-x}) correlate well with those of Raman scattering, inelastic neutron scattering and Mössbauer hyperfine structure experiments in indicating that the rigidity percolation threshold occurs near $\langle r \rangle_c = 2.46(4)$. These observations provide experimental support for predictions of the Phillips–Thorpe constraint theory, when provision is made for a small but finite concentration of broken bond-bending constraints around chalcogen sites.

1. Introduction

Vibrational excitations in glasses and corresponding crystals display similarities as well as differences. The similarities, in general, can be traced to elements of short-range order (SRO), i.e., to the nature of the building blocks of the network. Elastic scattering experiments [1] using a beam of X-rays or neutrons have shown over the years that elements of SRO between glasses and crystals are similar although not without exceptions [2]. On the other hand, differences in vibrational excitations between glasses and crystals possessing the same SRO arise in general from atomic correlations extending to larger distances. Glasses differ from crystals in that their networks do not possess long-range order. The vibrational features intrinsic to glasses, particularly in the low-frequency regime, continue to attract interest [3] because these are tied to elements of medium-range order (MRO), i.e., to the way and extent building blocks are correlated both spatially and vibrationally in a glass network.

Traditionally, the experimental methods used to establish the vibrational density of states (VDOS) in a glass have included inelastic neutron scattering [4], Raman scattering [5] and IR reflectance [6]. In this paper we introduce a new method – vibrational spectroscopy based on measurements of the Lamb–Mössbauer factors [7]. The Lamb–Mössbauer factor, also known as the f-factor, physically measures the probability for recoilless (zero phonon) emission or absorption of a γ-ray by a resonant atomic nucleus

---

[*] Corresponding author. Tel: +1-513 556 4758. Telefax: +1-513 556 7326. E-mail: pboolcha@ece.uc.edu.

[1] Present address: Thomas More College, Crestview Hills, KY 41017, USA.

[2] Present address: Northern Kentucky University, Highland Heights, KY 41099-1900, USA.

in a solid. It is akin to Debye–Waller factors for X-ray scattering. Broadly speaking, f-factors in a nuclear resonance experiment are determined by the integrated area under the observed lineshape. Physically, their magnitude at a given temperature is determined by two parameters, the energy of the γ-ray being resonantly absorbed or emitted or scattered as the case may be and, second, the hardness of the solid host material often described in terms of the Debye temperature, θ_D.

In this paper, we review results of specific Lamb–Mössbauer factor experiments on Sn-doped Ge_x-Se_{1-x} glasses that bear on the idea of rigidity percolation threshold predicted [8–10] by the Phillips–Thorpe constraint theory of glasses. The underlying low-frequency vibrational excitations in an undercoordinated network glass, also called floppy-modes, have been observed [11] directly in inelastic neutron scattering experiments. The presence of these floppy modes leads to a softening [12] of f-factors in undercoordinated glasses. Results of these neutron scattering and f-factor experiments correlate with the Raman A_1 breathing mode [13], the frequency shifts of $Ge(Se_{1/2})_4$ units and the Te Mössbauer site-intensity ratios [14], all studied systematically as a function of the glass composition. These results taken together provide persuasive experimental evidence for the existence of the stiffness threshold predicted by the constraint theory of glasses.

2. Lamb–Mössbauer factors as probe of low-frequency vibrational excitations

The probability of nuclear resonant absorption in a solid, f, is described [7] by the Lamb–Mössbauer factor

$$f = \exp\left(-\langle (\mathbf{k} \cdot \mathbf{u})^2 \rangle\right), \tag{1}$$

where $\mathbf{k}$ is the γ-ray wave vector and $\mathbf{u}$ is the displacement vector of the resonant nucleus; the angular brackets imply a thermal average. For a harmonic oscillator at low temperature, T ($T \to 0$), the mean-square displacement as $T \to 0$, is given by

$$\langle u^2 \rangle_{T \to 0} = \langle u^2 \rangle_0 = 3\hbar / 2M\omega, \tag{2}$$

while at high T ($T > \theta_D$)

$$\langle u^2 \rangle_T = 3k_B T / M\omega^2. \tag{3}$$

By combining Eq. (2) and (3) with Eq. (1), one obtains the first and second inverse moments of the vibrational density of states in a Debye solid

$$\langle 1/\omega \rangle = \left(2\hbar Mc^2 / E_\gamma^2\right)(-\ln f_0) \tag{4}$$

and

$$\langle 1/\omega^2 \rangle = \frac{\hbar^2 Mc^2}{E_\gamma^2} \frac{1}{k_B} \frac{d}{dT}(-\ln f). \tag{5}$$

In the harmonic approximation, Eq. (4) suggests that one can obtain the first inverse moment of the VDOS in a network glass by measuring f_0, the $T \to 0$ limit of the Lamb–Mössbauer factor. Eq. (5) shows that the second-inverse moment of the VDOS can be established by measuring the slope, $d(-\ln f)/dT$ at $T > \theta_D$. In general, the T-dependence of $f(T)$ in a harmonic solid possessing a Debye-like VDOS can be written [7] as

$$f = \exp - \left\{ \frac{6R}{k_B \theta_D} \left[\frac{1}{4} + \left(\frac{T}{\theta_D} \right)^2 \int_0^{\theta_D/T} \frac{x \, dx}{e^x - 1} \right] \right\}. \tag{6}$$

The first term on the right, which is T-independent, describes the zero-point motion contribution to the f-factor. The second-term is T-dependent and, for $T > \theta_D$, $\ln f(T)$ decreases linearly with T, with the slope being inversely proportional to θ_D^2, as illustrated in Fig. 1.

The second moment of the VDOS $\langle \omega^2 \rangle$ in a solid is also accessible from Mössbauer spectroscopy. It is obtained by measuring the T-dependence of the nuclear resonance lineshape centroid. This was first recognized by Pound and Rebka [15], and independently by Josephson [16], and is familiarly known as the thermal shift or second-order Doppler shift. This shift is given by

$$\frac{\delta \nu}{\nu} = -\frac{1}{2c^2} \left[\frac{9k_B \theta_D}{M} \left(\frac{1}{8} + \left(\frac{T}{\theta_D} \right)^4 \right) \right.$$
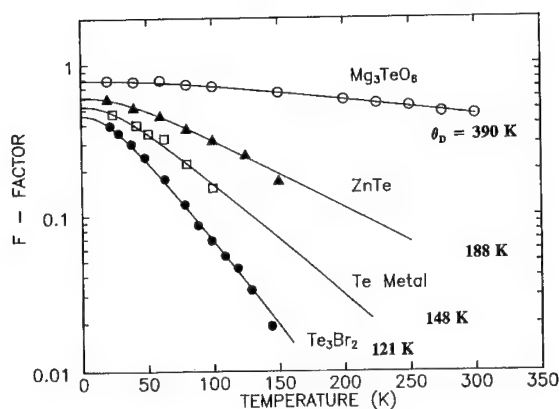$$\left. \times \int_0^{\theta_D/T} \frac{x^3 \, dx}{e^x - 1} \right]. \tag{7}$$

Fig. 1. Temperature dependence of Lamb–Mössbauer factors in indicated compounds using the 35.5 keV γ-ray in ^{125}Te. Note that f-factors saturate at $T = 0$. At high temperatures the f-factors decrease with T, with the slope $d(\ln f)/dT$ inversely proportional to θ_D^2. Further note that the f-factors decrease with average coordination of the compounds. Some parts of this figure are taken from the work of Bresser et al. [7].

In summary, the Mössbauer effect through the thermal shift becomes a sensitive probe of high-frequency vibrational excitations, through the $T \rightarrow 0$ limit of the f-factor, f_0, to intermediate-frequency vibrational excitations, and through the slope $d(-\ln f)/dT$, to low-frequency vibrational excitations in a solid. The latter two physical observables will be of special interest in context to floppy modes in a network glass, as we illustrate in the next section.

In a Mössbauer effect experiment, when the physical size of the absorbing grain becomes less than about 20 nm, such as in nanocrystalline materials or a molecular cluster in a network glass, then an unusual circumstance can prevail. The recoil energy, E_R, imparted to the mesoscopic grain during resonant absorption can become comparable with the natural linewidth, Γ_n, of the resonance (for ^{119}Sn, $\Gamma_n = 5.9 \times 10^{-8}$ eV), i.e.,

$$E_R = \Gamma_n. \tag{8}$$

Eq. (8) defines a critical grain size, d_c, which for the case of Sn absorption in GeSe$_2$ equals a value of about 20 nm. In samples with a grain size $d < d_c$, one can expect a decrease [17] in the f-factor in proportion to $(d_c - d)$ due to displacement of the grain upon nuclear absorption or emission. Thus f-factors in such solids have two broad contributions, one due to displacement of the absorbing atom within

a grain (or molecular cluster) known as the intragrain f-factor, f_{intra}, and the second from a motion of the grains in relation to each other known as the intergrain f-factor, f_{inter}. Thus the observed f-factor is the product of

$$f = f_{intra} f_{inter}, \tag{9}$$

These ideas will help us to understand differences in f-factors of glasses and crystals as we see below in Section 4.

3. Phillips–Thorpe constraint theory of glasses

For a covalent network constrained by bond-stretching, α, and bond-bending, β, forces, a mechanical critical point exists when the number of constraints per atom, n_c, equals the dimensionality or number of degrees of freedom, n_d, of the space in which is it embedded,

$$n_c = n_d. \tag{10}$$

This general condition, enunciated by Phillips [8] in 1981, has stimulated considerable interest in glass science. This condition is satisfied exactly in some of the best glass formers in nature such as As$_2$Se$_3$ and SiO$_2$. In SiO$_2$, the β constraint associated with O atoms is apparently broken as revealed by experiments and this ensures $n_c = n_d$. Eq. (10) is thought to describe the formation of optimally polymerized networks [8]. Thorpe [9,10] recognized that the glass condition (10) can be cast in the language of percolation theory. Specifically, he showed that for covalent networks in which the N atoms bond chemically with coordination numbers greater than or equal to two, the number of zero-frequency modes, $F = N$ $(n_d - n_c)$, vanishes when the average coordination number, $\langle r \rangle$, increases to 2.40,

$$\langle r \rangle = 2.40. \tag{11}$$

The character of a covalent network undergoes a qualitative change [9] from being easily deformable $\langle r \rangle < 2.40$ to being rigid at $\langle r \rangle > 2.40$.

Recently, Boolchand and Thorpe [18] have extended constraint theory to include networks containing singly coordinated atoms. Specifically, they have shown that rigidity will percolate in such networks at

$$\langle r \rangle = 2.4 - 0.4(n_1/N), \tag{12}$$

where (n_1/N) represents the concentration of singly coordinated atoms in the polymeric (backbone) network structure terminated by singly coordinated atoms.

These ideas based on the enumeration of α and β constraints lead to results that are mathematically well defined. The floppy modes represent zero-frequency modes or cyclical modes in the dynamical matrix. In practice these modes do not possess zero frequency, but are blue-shifted due to the presence of residual interactions such as van der Waals forces.

4. Rigidity percolation threshold in chalcogenide glasses

The prediction of a stiffness threshold or a rigidity percolation threshold in a glassy network at $\langle r \rangle = 2.40$ (based on Eq. (11)) has stimulated much experimental activity over the years. The binary glass systems Ge_xSe_{1-x} and Ge_xS_{1-x} in which cations and anions are known to be four- and two-fold-coordinated provide convenient test systems for these ideas. In these binaries, one can prepare homogeneous bulk glasses over a wide composition range $0 < x < 0.40$, in which the average coordination number of the network can be tuned to include $\langle r \rangle = 2.40$. According to constraint theory, one must exclude monomeric species such as S_8 or Se_8 units, which apparently phase-separate at low x ($x \leq 0.20$) in the respective networks, since these molecular clusters do not form part of the backbone structure to which the constraint arguments apply. Further, since the stoichiometric chemical compounds occur at $x = 0$ (Se or S), $x = 1/3$ ($GeSe_2$ or GeS_2) and $x = 1/2$ (GeSe and GeS), sufficiently far removed from the projected stiffness threshold composition at $x_c = 0.20$ (corresponding to $\langle r \rangle = 4x_c + 2(1 - x_c) = 2.4$), one is in a position to separate the more delicate mechanical effects from the overwhelming chemical ones associated with stoichiometric crystalline compound formation.

4.1. Inelastic neutron scattering

Direct evidence for the existence of floppy modes in binary Ge_xSe_{1-x} glasses has emerged from the inelastic neutron scattering measurements of Kami-
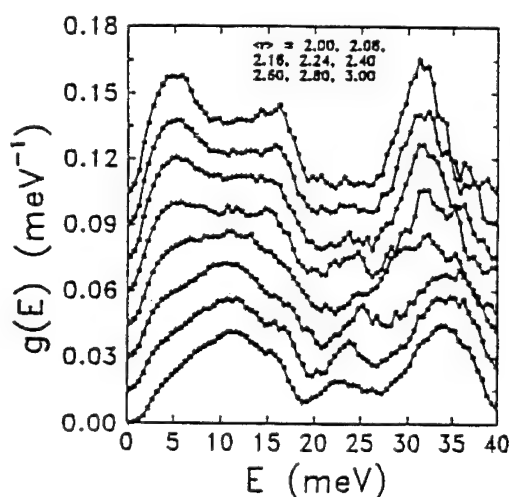
Fig. 2. VDOS for Se–As–Ge alloy glasses. Starting from the bottom ($\langle r \rangle = 3.00$), successive curves have been shifted up to 0.015 units on the vertical scale. The top curve ($\langle r \rangle = 2.00$) is for pure Se glass. The other alloy glasses in order are $\langle r \rangle = 2.08$, $Se_{96}Ge_4$; $\langle r \rangle = 2.16$, $Se_{89}As_{06}Ge_{05}$; $\langle r \rangle = 2.24$, $Se_{88}Ge_{12}$; $\langle r \rangle = 2.40$, $Se_{675}As_{250}Ge_{075}$; $\langle r \rangle = 2.60$, $Se_{63}As_{14}Ge_{23}$; $\langle r \rangle = 2.80$, $Se_{51}As_{18}Ge_{31}$; and $\langle r \rangle = 3.00$, $Se_{395}As_{210}Ge_{395}$. The peak at ~ 5 meV is identified as the floppy mode peak. This figure is taken from Ref. [11].

takahara et al. [11]. Fig. 2, taken from their work, shows a plot of the observed density of vibrational states, $g(E)$, as a function of average coordination number, $\langle r \rangle$. The prominent peak at about 5 meV in g-Se ($x = 0$) has an integrated intensity (over the energy range 0–8 meV), which is approximately one-third of the total spectral weight. This constitutes good evidence that the modes in question are floppy modes. For a Se chain, in which each atom is twofold-coordinated, there is one α and one β constraint yielding two constraints per atom, or one floppy mode per atom, or one-third of the modes are floppy as observed.

The first and second inverse moments of the VDOS deduced from these neutron scattering measurements [12] are displayed in Fig. 3 as a function of Ge concentration. There is some evidence of a change in slope in the first-inverse moment near the composition $x \simeq 0.20$, corresponding to the stiffness threshold. The scantiness of the data does not permit us to localize the threshold composition with any degree of accuracy, however. The second-inverse
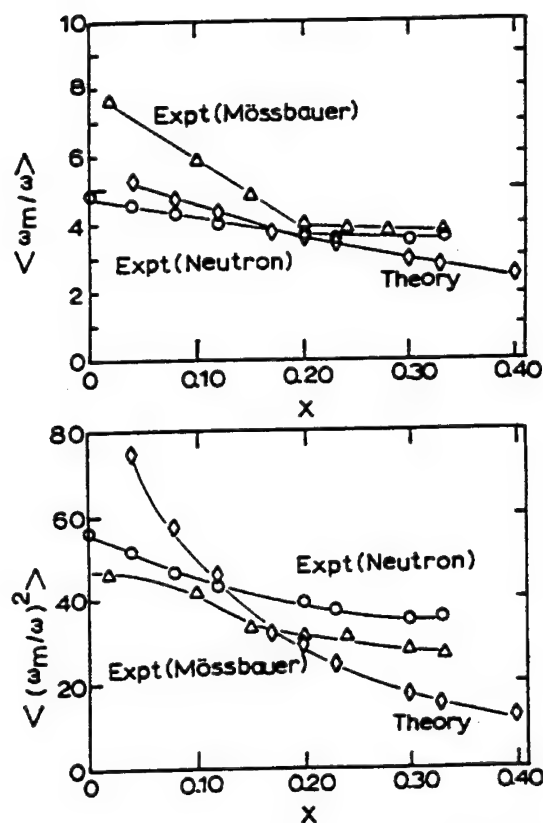
Fig. 3. First inverse $\langle \omega_m / \omega \rangle$ (top panel) and second inverse $\langle \omega_m^2 / \omega^2 \rangle$ (bottom panel) moments of the density of vibrational states deduced from inelastic neutron scattering (O), Lamb–Mössbauer factors ($\triangle$) and bond-depleted diamond lattice calculations ($\diamond$) as a function of Ge concentration, x. Note that $\langle \omega_m / \omega \rangle$ displays clear evidence of a break in slope near $x = 0.20$ corresponding to the rigidity threshold. This figure is taken from Ref. [12].

moment deduced from these neutron scattering measurements provides no evidence of any anomaly whatsoever near the composition $x = 0.20$, a point we shall return to later.

It is also clear from these neutron scattering results [11] that the floppy mode strength does not extrapolate to zero when x increases to 0.20 (corresponding to $\langle r \rangle = 2.4$) as predicted by the calculations of He and Thorpe [10]. There are clearly other modes in the low-frequency regime (< 10 meV) that apparently contribute to the VDOS when $x > 0.20$ which are most likely due to aspects of MRO emerging in these networks.

4.2. Raman scattering

An advantage in working with the $Ge_x Se_{1-x}$ binary system over the $Ge_x As_y Se_z$ ternary system is that in the bond-stretching regime one can closely monitor growth of Raman scattering from the A_1 symmetric stretch of $Ge(Se_{1/2})_4$ tetrahedral units at the expense of the A_1 stretch of Se_n chain units, as the Ge content, x, of the glasses is monotonically increased. Murase et al. [13] noticed that the A_1 mode frequency of $Ge(Se_{1/2})_4$ units blue-shifts systematically with x, at first linearly in the range $0.05 < x < 0.20$, and then superlinearly once $x > 0.25$ (see Fig. 4).

This blue-shift of A_1 modes is the natural consequence of network stiffening. In the absence of data in the critical range $0.20 < x < 0.25$, one choice is to draw a smooth curve (broken line) through the data as reported by Murase et al. [13]. It now appears that the datapoint at $x = 0.25$ is not only correct (i.e., not spurious), but it actually forms part of a smooth trend shown by the continuous line drawn in Fig. 4. It is clear from the trend of these Raman results at compositions $x > 0.25$, and those at $x < 0.20$, that there apparently exists some type of a discontinuity in the critical range $0.20 < x < 0.25$. The location and nature of this discontinuity remains to be established, however.

Raman scattering on the parallel $Ge_x S_{1-x}$ binary glass system was recently studied by us [19]. These measurements reveal the A_1 mode frequency of $Ge(S_{1/2})_4$ units to blue-shift in a fashion remarkably similar to those reported by Murase et al. [13] on the $Ge_x Se_{1-x}$ binary. In particular, we confirm the superlinearity of the A_1 mode frequency shift in the composition range $0.23 < x < 0.33$, and its linearity at lower Ge concentration $0.10 < x < 0.20$, with an apparent discontinuity existing in the range $0.20 < x < 0.23$. In retrospect, it is clear that Raman scattering data at compositions, x, in this range, in both the Ge–Se and Ge–S binaries, is crucially needed to better localize the stiffness threshold. Before this is achieved, however, the effective Ge concentration of the backbone structure responsible for percolation of rigidity in these glasses will also need to be established. Corrections to the actual glass compositions for the presence of S_8 rings and, to a lesser degree, Se_8 rings, molecular species that are known to

phase-separate in the respective binary glasses, particularly at low Ge concentrations ($x \lesssim 0.20$), will have to be made. Fortunately, A_1 modes of S_8 rings are partially resolved from those of S_n chains. A careful lineshape analysis of the observed vibrational bands (see Fig. 5) will establish the requisite chalcogen concentration present in the backbone network.
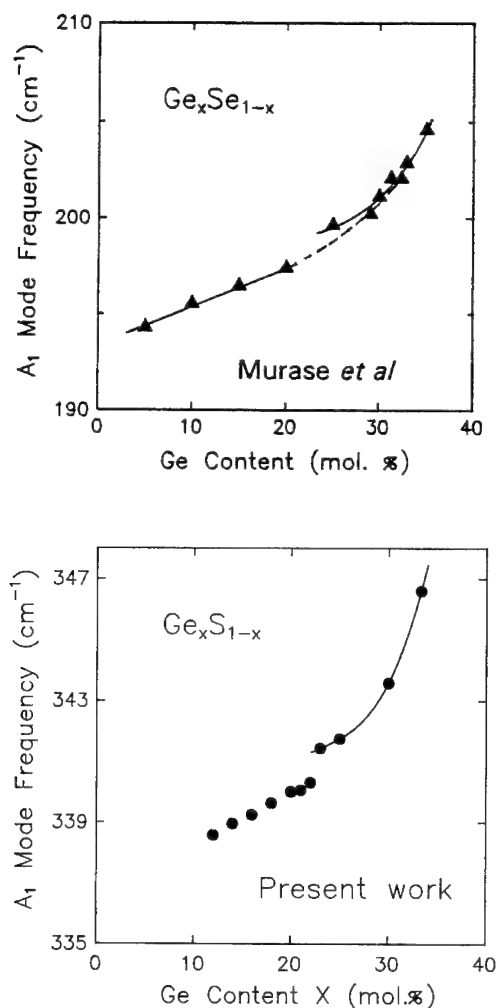

Fig. 4. Top panel shows the results on the Raman stokes shift of the A_1 mode of $Ge(Se_{1/2})_4$ units in Ge_xSe_{1-x} glasses as a function of x taken from the work of Murase and co-workers [13,22]. The broken line through the datapoints is the original trend drawn by the authors. The continuous lines are drawn by the present authors to highlight a likely discontinuity in the range $0.20 < x < 0.25$. Bottom panel shows similar results obtained on the Ge_xS_{1-x} system in the present work.
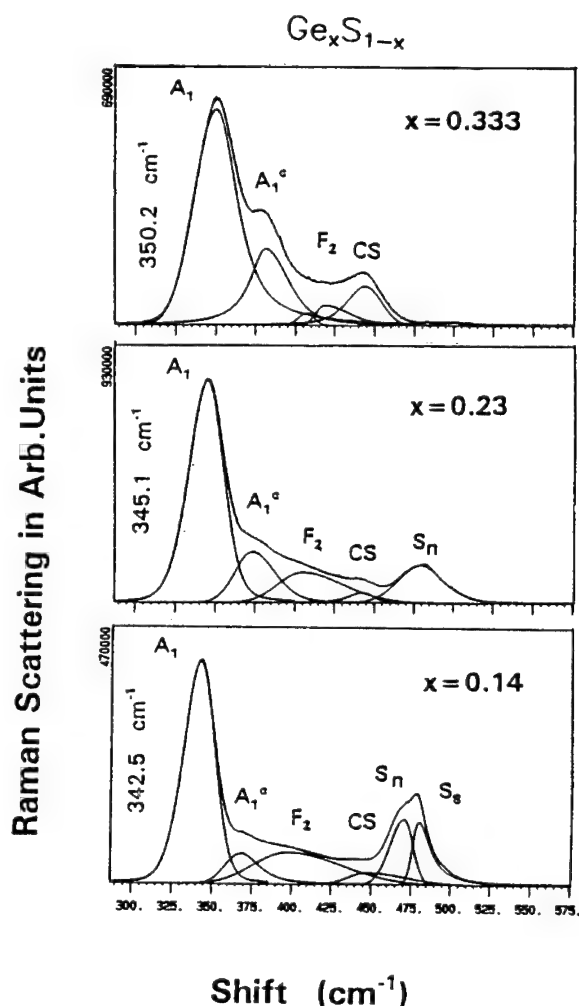
Fig. 5. Room-temperature Raman scattering results on indicated glasses obtained using the 514 nm exciting radiation from an Ar-ion laser. The A_1 mode frequency, obtained by least-squares fitting the lineshape, shows a clear blue-shift with Ge content.

4.3 Lamb–Mössbauer factors

Since neither Ge nor S or Se provide viable Mössbauer effect probes in these glasses, we have chosen to add traces of elemental Sn (enriched in ^{119}Sn, the resonant isotope) to prepare alloy glasses of the composition $(Ge_{0.995}Sn_{0.005})_x(S$ or $Se)_{1-x}$. The presence of traces of Sn in these glasses affects neither the glass transition temperatures, T_g, nor the Raman vibrational modes, but this amount of Sn is sufficient to observe the Mössbauer effect of 23.8

keV γ-rays in [119]Sn in these glasses using standard transmission geometry. There is overwhelming evidence [19,20] that in trace amount the isovalent Sn additive mimics the local bonding configurations of Ge sites in these binary glasses. In the composition range $0 < x < 0.32$, for example, one observes in Mössbauer spectroscopy a narrow resonance characteristic of tetrahedrally coordinated $Sn(X_{1/2})_4$ sites, where X = S or Se. These sites are chemically equivalent but their vibrational behavior, as studied by Lamb–Mössbauer f-factors, is found to depend on the glass composition in a fashion that closely parallels the vibrational behavior of $Ge(X_{1/2})_4$ units as studied by Raman scattering.

Unlike inelastic neutron scattering measurements, which require typically 10 g or more of a glass sample, Raman and Mössbauer spectroscopy require a miniscule amount ($< 1/10$ g) of sample. This amount can be an important consideration in glass investigations since it is not always usual that large-sized glass samples of uniform composition can be prepared. Further, the latter methods also lend themselves elegantly to examine thin films and to check sample inhomogeneities. Micro-Raman as a method is particularly diagnostic as a check of sample homogeneity. Such information can often be used to optimize processing conditions to achieve homogeneous glass samples.

Fig. 6 illustrates [20] the spectra of $(Ge_{0.99}Sn_{0.01})x(Se)_{1-x}$ glasses near the stoichiometric composition $x = 1/3$. Two types of Sn site are observed, a tetrahedral $Sn(Se_{1/2})_4$ site, labeled A, and a non-tetrahedral Sn-site, labeled B. Temperature dependences of the Lamb–Mössbauer factors for these sites of the stoichiometric ($GeSe_2$) glass composition were obtained by cooling the glass sample in a vibration-free He closed-cycle cryostat and exciting the nuclear resonance with an emitter of [119]Sn^m in a $CaSnO_3$ matrix kept at a fixed temperature (300 K) outside the cryostat. The integrated areas under the site A (single line) and site B (doublet) resonances were obtained by least-squares fitting the observed lineshape using standard procedures and plotted systematically as a function of temperature.

Fig. 7 and 8 provide an overview [12] of the results. The effective vibrational (Debye) temperature of site A of $\theta_D^A = 130(5)$ K is found to be significantly higher than that of site B of $\theta_D^B = 100(5)$
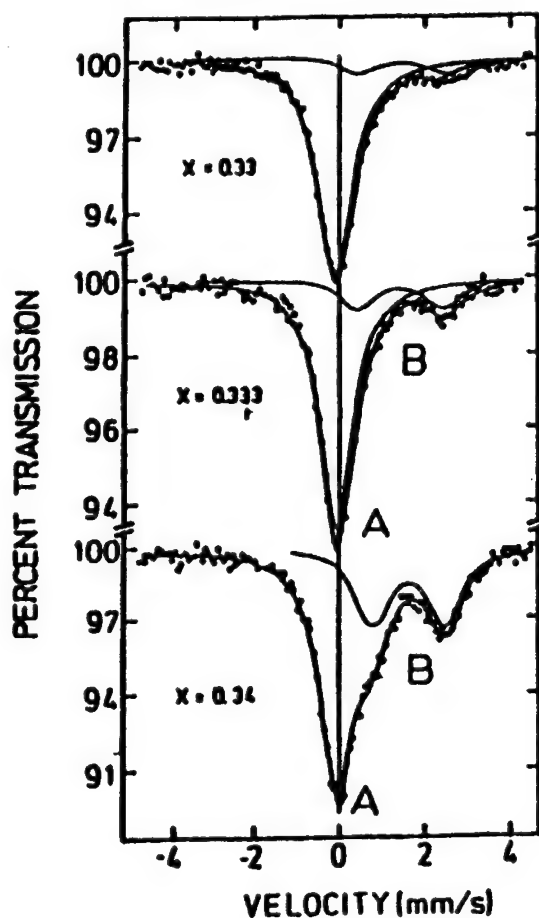
Fig. 6. [119]Sn Mössbauer spectra of $(Ge_{0.99}Sn_{0.01})_xSe_{1-x}$ glasses showing two sites (A,B) near the stoichiometric composition $x = 0.333$. This figure is taken from Ref. [12].

K. These sites represent the dopant (Sn) replacing available Ge sites in two distinct local environments: a tetrahedral one ($Ge(Se_{1/2})_4$) and a non-tetrahedral one ($Ge(Se_{1/2})_3Ge_{1/4}$). Raman scattering provides unambiguous evidence [21] for these building blocks (modes at 203 and 180 cm^{-1}, respectively). Since the masses of Ge and Se are nearly the same, it is difficult to understand their formation in the same polymeric network since the f-factors of the two sites are measurably different. On the other hand, if site A is formed in a large Se-rich cluster in which all cations are tetrahedral, and site B is formed in a much smaller Ge-rich cluster consisting of ethane-like units, then one can reconcile their different f-factors. The reduced f-factor of site B in relation to that of
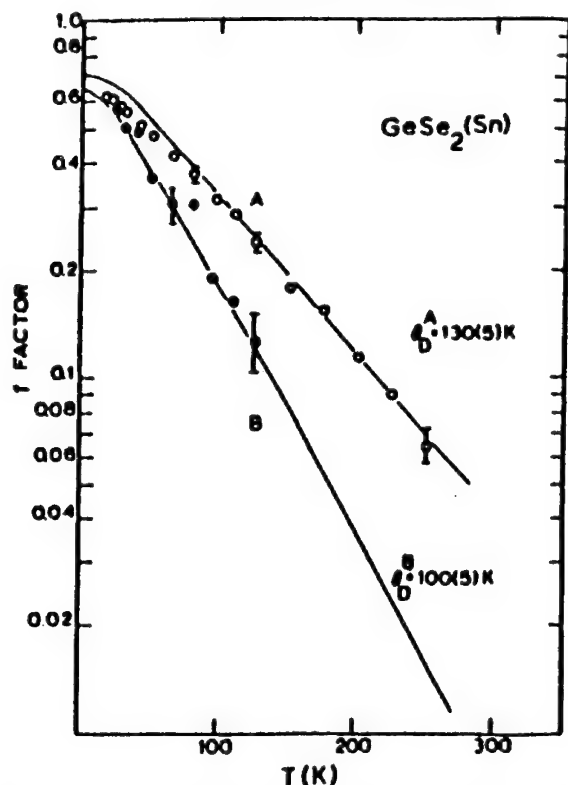
Fig. 7. Temperature dependence of the integrated intensity of site A (singlet) and site B (doublet) revealing the widely different vibrational (Debye) temperatures, θ_D. This figure is taken from Ref. [12].
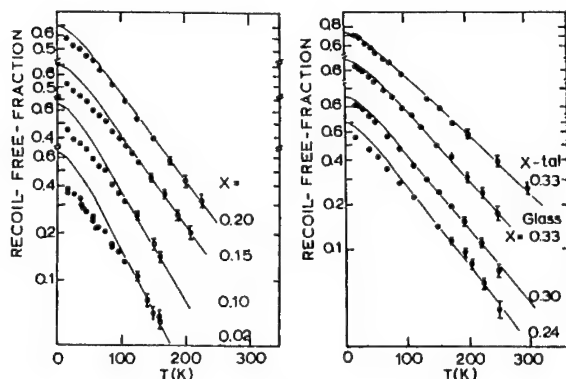

Fig. 8. Site A temperature dependence of the Mössbauer–Debye–Waller factor, $f(T)$, in $(Ge_{0.99}Sn_{0.01})_x Se_{1-x}$ glasses at indicated cation concentration, x. In c-$GeSe_2$, note that $f(T)$ is well fitted by one Debye temperature, while in glasses a softening of $f(T)$ is observed at low T on account of the floppy modes. This figure is taken from Ref. [12].

site A in such a model of the stoichiometric glass derives from intergrain effects and not intragrain ones, as alluded to in Section 2. A more subtle observation is the systematic misfit of the f-factor at $T < 100$ K to a unique Debye temperature. At these lower temperatures, the presence of some floppy modes in the VDOS (see Section 4.1.) at 5 meV leads to an enhanced mean square displacement that results in a softening of the f-factors.

These softening effects are understandably far more dramatic [12] as the Ge concentration in the glasses is systematically reduced. At a lower average coordination number, inelastic neutron scattering results reveal the floppy mode strength to increase progressively. A perusal of the f-factor results in Fig. 8 clearly demonstrates that the f-factor softening is rather dramatic in a Se-rich glass ($x = 0.02$) corresponding to an average coordination number of two.

To quantitatively compare these Lamb–Mössbauer f-factors to the neutron scattering results, we have obtained the normalized first and second inverse moments of the VDOS and these results appear in Fig. 3. These experimental results are compared with DOVS calculations based on a simple bond-depleted diamond lattice using a method developed by He and Thorpe [10]. These calculations utilize a Keating potential with α and β forces. In essence, the calculations contain the single most important parameter of the network, the SRO, or the average coordination number which apparently controls many of the physical effects observed [12].

The most striking experimental result to emerge from the f-factor measurements is the break in slope near $x = 0.20$ in the first inverse moment. This composition corresponds to an average coordination number, $\langle r \rangle = 2.4$, and thus serves to provide support for the prediction (Eq. (11)) of constraint theory. It is also clear that, based on these f-factor results alone, given the large compositional steps studied around $x = 0.20$ and given the accuracy to which values of f_0 have been extracted (data handling), one can do better and localize the stiffness threshold more accurately. There is an interest in refining these measurements further, because Raman scattering and independent Te Mössbauer site intensity ratio measurements on the same Ge_xSe_{1-x} binary provide evidence that the stiffness threshold in these glasses may be closer to $x = 0.23$ than to $x = 0.20$. This has
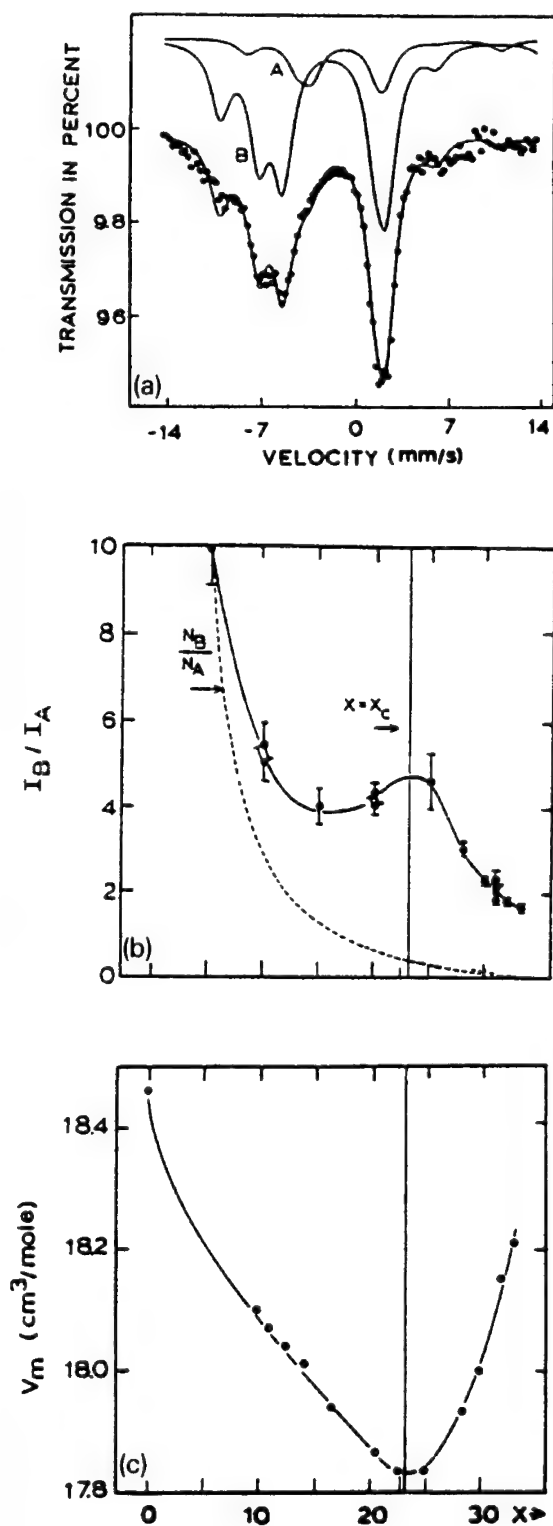
some important consequences which we discuss Section 5.

The second-inverse moment of the VDOS in Ge_xSe_{1-x} glasses reveals no apparent discontinuity near $x = 0.20$ in both the f-factor and the inelastic neutron scattering results. There may be an important message behind this result. It suggests that the second-inverse moment, which weighs lower-frequency vibrational excitations more than the first-inverse moment can, becomes less sensitive to the presence of these floppy modes because these modes are blue-shifted due to residual interactions. One can then expect bulk elastic constants which probe the low-frequency slope of $\omega(q)$ for acoustic phonons in these glasses to become even less sensitive to the stiffness threshold, a point that has generally not been recognized.

4.4. ^{129}I Mössbauer hyperfine structure in chalcogenide glasses

The use of ^{129}I Mössbauer emission spectroscopy as a probe of both SRO and the MRO in chalcogenide glasses was developed [23] several years ago. We also discussed these results in relation to the structural manifestations of the onset of rigidity in the Ge_xSe_{1-x} binary [24]. In the ^{129}I experiments, broadly speaking, we used traces of $^{129}Te^m$ dopant to probe the chalcogen chemical order. We inferred the SRO by decoding the multimodal distribution of sites through the nuclear hyperfine structure. In the Ge_xSe_{1-x} binary at $x \leq 1/3$, we expected, in general, three types of Te site to be populated: site A; twofold-coordinated to Ge nearest neighbors (nn)

Fig. 9. (a) ^{129}I Mössbauer emission spectrum of g-$Ge_x(Se_{0.99}Te_{0.01})_{1-x}$ alloy at $x = 0.20$ showing the presence of the two chemically inequivalent ^{129}I sites, A and B, with the ratio $I_B/I_A = 4.0 \pm 0.3$. A random cross-linked network model would require the ratio I_B/I_A to be an order of magnitude smaller. This figure is taken from Ref. [14]. (b) Mössbauer site intensity ratio, $I_B/I_A(x)$ studied as a function of x in g-$Ge_x(Se_{0.99}Te_{0.01})_{1-x}$ alloys. The I_B/I_A systematics reveal a peak centered at the critical composition, $x = x_c = 0.23(2)$. At $x = 0$ (i.e., g-Se) only B sites are observed corresponding to $I_B/I_A \to \infty$. The dashed curve represents a theoretical plot of the site population ratio $N_B/N_A(x)$ based on a random cross-linked chain model. This figure is taken from Ref. [14]. (c) Molar volumes of g-Ge_xSe_{1-x} alloys as a function of x, taken from Ref. [25].

resulting from a chalcogen site acting as a bridge between a pair of $Ge(Se_{1/2})_4$ tetrahedra; site B; twofold-coordinated to Se nns as in a Se chain or ring; and finally; site B′; twofold-coordinated to a Se and a Ge nn as would be formed at the Ge cross-links of Se_n chains or edges of $GeSe_2$-like planar fragments. The daughter ^{129}I sites resulting from this trimodal distribution of parent ^{129}Te^m sites, display a *bimodal* distribution of sites because of an increase in valence from Te to I. The daughter I resulting from site A is always found to be singly coordinated, forming an I–Ge σ-bond. The daughter I resulting from both site B and site B′ is also singly coordinated and forms an I–Se σ-bond for reasons discussed elsewhere. Since the ^{129}I nuclear quadrupole couplings of an I–Ge σ-bond (−890 Mhz) differ qualitatively from the coupling of an I–Se σ-bond (−1385 MHz), one can clearly resolve the concentration of these two ^{129}I sites from standard lineshape analysis of the Mössbauer lineshape (Fig. 9(a)). The ^{129}I site intensity ratios, I_B/I_A, have proved to be particularly insightful in decoding the elements of MRO in these glasses as discussed elsewhere.

Fig. 9(b) provides a summary of the results. If binary Ge_xSe_{1-x} glasses could be broadly described as a random network of Ge cross-linked chains of Se, one would expect the I_B/I_A ratio to decrease monotonically (dashed curve in Fig. 9(b)) with x and to extrapolate to zero at $x = 1/3$ when a chemically ordered network of corner- or edge-sharing $Ge(Se_{1/2})_4$ tetrahedra emerges at the stoichiometric $GeSe_2$ glass. The observed I_B/I_A ratio (continuous line) certainly does display some of this broad trend, but it also reveals a striking departure from this trend. One observes a local maximum in the site-intensity ratio centered around $x = 0.23$, with the ratio extrapolating to a finite value of 1.8 instead of zero at $x = 1/3$.

We have ascribed [14] the presence of this local maximum to a pair of competing processes. The increase in $I_B/I_A(x)$ in the range $0.10 < x < 0.23$ represents nucleation of edge-sharing (ES) Ge-$(Se_{1/2})_4$ tetrahedra in the network, while the reduction in the I_B/I_A ratio at higher x ($0.23 < x < 0.33$), represents lateral growth of these ES tetrahedra to form fragments of the two-dimensional ($2d$) form of $GeSe_2$. The finite concentration of site B at $x = 1/3$, is due to an intrinsic phase separation of the network

into Ge-rich and Se-rich clusters, with the site B signal representing Te dopant segragating to the edges of the Se-rich cluster.

The morphological structure of Ge_xSe_{1-x} glasses advanced above finds support in molar volumes [25] (Fig. 9(c)) and Raman scattering results. The latter reveal growth of the A_1 companion mode (A_1^c at 220 cm^{-1}) strength at $x \gtrsim 0.10$ which has now been positively identified as a mode of edge-sharing $Ge(Se_{1/2})_4$ units by Murase et al. [26]. The growth of such clusters eventually leads to phase separation into Ge-rich and Se-rich clusters. The Raman signature of the former is the mode at 180 cm^{-1} (Ge–Ge) and of the latter is the mode at 247 cm^{-1} (Se–Se), with the scattering strength of both modes nearly comparable in the stoichiometric glass.

In summary, the local maximum in I_B/I_A at $x = 0.23$ correlates with molar volumes and Raman A_1 mode frequency shifts of $Ge(Se_{1/2})_4$ units, ^{119}Sn Lamb–Mössbauer f-factors and suggests that the stiffness threshold in this binary occurs close to $x = 0.23$.

5. Discussion

Historically, once the foundations of constraint theory of glasses were laid, it appeared logical to measure bulk elastic constants in the chalcogenides. Since elastic constants provide a measure of network rigidity, one expected these constants to increase with $\langle r \rangle$ and to display a threshold behavior close to $\langle r \rangle = 2.4$. Careful experiments by Yun et al. [27] on Ge_xSe_{1-x} glasses have shown otherwise. One can begin to understand the reasons for this negative result. Residual van der Waals interaction between Se-chains blue shift floppy mode frequencies from zero to about 5 meV, as revealed by the inelastic neutron scattering measurements [11]. For this reason, the low frequency slope of $\omega(q)$ for acoustic phonons becomes only weakly sensitive [27,28] to changes in floppy mode strength as glass composition is altered. This suggestion is quite consistent with Lamb–Mössbauer factor results on these glasses which show that although the first-inverse moment $\langle 1/\omega \rangle$ can track the stiffness threshold at $\langle r \rangle \simeq 2.4$, the second-inverse moment $\langle 1/\omega^2 \rangle$ merely shows a

rounding of the transition. The $\langle 1/\omega \rangle$-moment weights more heavily the higher frequency vibrational excitations than is the $\langle 1/\omega^2 \rangle$ moment capable. Clearly the $\langle 1/\omega^2 \rangle$ moment provides a less sensitive probe of floppy modes than the $\langle 1/\omega \rangle$ moment. Bulk elastic constants track stiffness of a network using long wavelength acoustic modes. These can be expected to be even less sensitive than the $\langle 1/\omega^2 \rangle$ moment. For these reasons, the absence of a threshold in the longitudinal and the shear elastic constants, at $\langle r \rangle = 2.4$ in these glasses is not due to the absence of a rigidity percolation threshold but merely due to lack of sensitivity of this experimental method to probe vibrational excitations at such high energies (5 meV).

Bulk elastic constants in $Ge_x Se_{1-x}$ glasses display a threshold behavior close to $\langle r \rangle = 2.67$ corresponding to the chemical composition $GeSe_2$. Tanaka [29] in an extensive review has suggested that this result may represent a mechanical threshold of a covalent network composed of globaly 3D but locally planar (2D) fragments. This assumption would require tetrahedral building blocks of such layered fragments to be locally planar instead of 3D and to thus have three β constraints instead of five, a premise that is difficult to rationalize for such a building block. Finally, one would also have to justify calculating the left-hand side of Eq. (2) in 2D and equating it to the right hand-side of the equation calculated in 3D to obtain the result $\langle r \rangle = 2.67$. It appears to us that the most likely interpretation of the threshold at 2.67 is that it represents a chemical effect.

There is a basic interest to establish if the stiffness threshold in these 4–2-coordinated glassy networks occurs exactly at $\langle r \rangle = 2.4$ or at an $\langle r \rangle$ somewhat greater than 2.40. Theoretically, an increased $\langle r \rangle$ could arise if the β constraint around some of the twofold-coordinated anions is broken. Zhang and Boolchand have recently shown [30] that the stiffness threshold in a general covalent network containing a fraction m_2/N of twofold-coordinated sites around which the β constraint is broken is given by

$$\langle r \rangle = 2.4 - 0.4(n_1 - m_2)/N. \tag{13}$$

In a 4–2-coordinated glassy network, since there are no singly coordinated atoms, we have $n_1/N = 0$. If 15% of the anion sites in the network have their

angular constraint broken then, according to Eq. (13) the stiffness threshold is predicted to occur at

$$\langle r \rangle = 2.46, \tag{14}$$

a circumstance that could conceivably occur in the Ge–Se and Ge–S binaries. Of course, the celebrated example of a 4–2 glassy network for which all anion sites have their β constraints broken is the Zachariasen glass, SiO_2. We note in passing that, for this case, $n_1/N = 0$ and $m_2/N = 2/3$, and Eq. (14) predicts rigidity to percolate at $\langle r \rangle = 2.67$. This $\langle r \rangle$ corresponds exactly to the chemical composition SiO_2 and thus serves to demonstrate the propensity of this material to form a glass since the Phillips glass condition (Eq. (10)) is exactly satisfied in this case only when broken β constraints are taken into account.

We would be amiss not to mention the work of Tatsumisago et al. [31], which bears on thermal measurements of chalcogenide glassy liquids. Activation energies for enthalpy relaxation close to T_g, activation energies for viscosity, and the specific heat jumps, ΔC_p, at T_g examined in ternary Ge–As–Se glassy liquids, all reveal evidence of a threshold behavior close to $\langle r \rangle = 2.40$. Clearly these ideas on rigidity percolation in covalent networks apply not only to glassy solids but also extend to glassy liquids. This is expected given that the glassy solid evolves upon supercooling the liquid.

6. Conclusions

Raman A_1 mode frequencies of $Ge(Se_{1/2})_4$ units, ^{119}Sn Lamb–Mössbauer f-factors of $Sn(Se_{1/2})_4$ sites, ^{129}I Mössbauer site intensity ratios $I_B/I_A(x)$ and molar volumes, all studied as a function of x in the binary $Ge_x Se_{1-x}$ glass system provide persuasive evidence for the stiffness threshold to occur near the Ge concentration $x = 0.23$. This threshold can be understood in terms of Phillips–Thorpe constraint theory of glasses if 15% of the anion sites have their angular constraint broken.

References

[1] E.A. Porai Koshits, in: Glass Science and Technology, Vol. 4A, ed. D.R. Ulhmann and N.J. Kreidl, p. 1. Also see G.N. Greaves, in: Glass Science and Technology, Vol. 4B, ed. D.R. Uhlmann and N.J. Kreidl, Vol. 4B (Academic Press, Boston, MA, 1990) p. 1.

[2] A. Bienenstock, J. Non-Cryst. Solids 11 (1974) 447; R.N. Enzweiler and P. Boolchand, Solid State Commun. 62 (1987) 197.

[3] A.P. Sokolov, A. Kisliuk, M. Soltwisch and D. Quitmann, Phys. Rev. Lett. 69 (1992), 1540; S.R. Elliott, Phys. Rev. Lett. 67 (1991) 711.

[4] For a review see R. Zallen, The Physics of Amorphous Solids (Wiley, Chichester, 1983); F.L. Galeener and G. Lucovsky, Phys. Rev. Lett. 37 (1976) 1471; F.L. Galeener, Phys. Rev. B19 (1979) 4292; I.T. Penfold and P.S. Salmon, Phys. Rev. Lett. 67 (1991) 97.

[5] G. Lucovsky, F.L. Galeener, R.C. Keezer, R.H. Geils and H.A. Six, Phys. Rev. B10 (1974) 5134; J.E. Griffiths, G.P. Espinosa, J.P. Remeika and J.C. Phillips, Phys. Rev. B25 (1982) 1272; M. Tenhover, M.A. Hazzle and R.K. Grasseli, Phys. Rev. Lett. 51 (1983) 404.

[6] K. Murase, T. Fukunaga, Y. Tanaka, K. Yakushiji and I. Yunoki, Physica 117B&118B (1983) 962.

[7] W.E. Lamb Jr., Phys. Rev. 55 (1939) 190; R.L. Mössbauer. Z. Phys. 151 (1958) 124. For a more current description of the f-factor see: N.N. Greenwood and T.C. Gibb, Mössbauer Spectroscopy (Chapman and Hall. London, 1971) p. 9. For a recent example of such measurements using ^{125}Te Mössbauer spectroscopy, see W. Bresser, M. Zhang, L. Koudelka, J. Wells, P. Boolchand, G.J. Ehrhart and P. Miller, Phys. Rev. B47 (1993) 11663.

[8] J.C. Phillips, J. Non-Cryst. Solids 43 (1981) 37.

[9] M.F. Thorpe, J. Non-Cryst. Solids 57 (1983) 355.

[10] H. He and M.F. Thorpe, Phys. Rev. Lett. 54 (1985) 2107.

[11] W.A. Kamitakahara, R.L. Cappelletti, P. Boolchand, B. Half-pap, F. Gompf, D.A. Neumann and H. Mutka, Phys. Rev. B44 (1991) 94.

[12] P. Boolchand, R.N. Enzweiler, R.L. Cappelletti, W.A. Kamitakahara, Y. Cai and M.F. Thorpe, Solid State Ionics 39 (1990) 81.

[13] K. Murase, T. Fukunaga, K. Yakushiji, T. Yoshimi and I. Yunoki, J. Non-Cryst. Solids 5960, (1983) 883; also see J.C. Phillips, Phys. Rev. B31 (1985) 8157.

[14] W. Bresser, P. Boolchand and P. Suranyi, Phys. Rev. Lett. 56 (1986) 2493.

[15] R.V. Pound and G.A. Rebka Jr., Phys. Rev. Lett. 4 (1960) 274.

[16] B.D. Josephson, Phys. Rev. Lett. 4 (1960) 341.

[17] B. Kolk, in: Dynamical Properties of Solids, Vol. 5, ed. G.R. Horton and A.A. Maradudin (North-Holland, Amsterdam 1984) p. 109.

[18] P. Boolchand and M.F. Thorpe, Phys. Rev. B50 (1994) 10366.

[19] P. Boolchand, W. Bresser, M. Zhang, Y. Wu and H. Schaffer, unpublished.

[20] P. Boolchand in: Physical Properties of Amorphous Materials, ed. D. Adler, B.B. Schwartz and M.C. Steel (Plenum, New York, 1985) p. 221; M. Stevens, P. Boolchand and J.H. Hernandez, Phys. Rev. B31 (1985) 981.

[21] P. Boolchand, J. Grothaus, W.J. Bresser and P. Suranyi, Phys. Rev. B25 (1982) 2975.

[22] K. Murase and T. Fukunaga, in: Defects in Glasses, Mater. Res. Soc. Symp. 61 (1986) 101.

[23] W.J. Bresser, P. Boolchand, P. Suranyi and J.P. deNeufville, Phys. Rev. Lett. 46 (1981) 1689.

[24] P. Boolchand, Key Eng. Mater. 13–15 (1987) 131.

[25] A. Feltz, H. Aust and A. Bleyer, J. Non-Cryst. Solids 55 (1983) 179.

[26] K. Murase, K. Inoye and O. Matsuda in: Current Topics in Amorphous Materials: Physics and Technology, ed. Y. Sakurai, Y. Hamakawa, T. Masumoto, K. Shirae and K. Suzuki (Elsevier, Amsterdam, 1993) p. 47.

[27] S.S. Yun, Hui Li, R.L. Cappelletti, R.N. Enzweiler and P. Boolchand, Phys. Rev. B39 (1989) 8702.

[28] Y. Cai and M.F. Thorpe, Phys. Rev. B40 (1989) 10535.

[29] K. Tanaka, Phys. Rev. B39 (1989) 1270.

[30] M. Zhang and P. Boolchand, Science (25 Nov. 1994).

[31] M. Tatsumisago, B.L. Halfpap, J.L. Green, S.M. Lindsay and C.A. Angell, Phys. Rev. Lett. 64 (1990) 1549; C.A. Angell, J. Non-Cryst. Solids 73 (1985) 1.

ELSEVIER

Kohlrausch relaxation and glass transitions in experiment and in molecular dynamics simulations

J.C. Phillips *

AT&T Bell Laboratories, 600 Mountain Ave., Murray Hill, NJ 07971-0636, USA

Abstract

The field of residual Kohlrausch relaxation, either electronic or structural, is widely regarded as mysterious because there is no generally accepted theoretical model which predicts the way in which the details of such relaxation vary from one system to the next. It is shown that an electronic trap model, now about 20 years old, gives an accurate description of relaxation kinetics in systems which are homogeneously disordered. The electronic materials discussed include a-Si:H, a-C_{60}, TaS_3, spin glasses and vortex glasses in high-temperature superconductors. The molecular materials discussed include polymers, network glasses, alcohols, Van der Waals supercooled liquids and glasses and fused salts. In the intrinsic cases, the theory of $\beta(T_g)$ is often accurate to 2%, which is often better than the quoted experimental accuracies $\sim 5\%$. The extrinsic cases can be identified by explicit structural signatures. The discussion also includes recent molecular dynamical simulations which have achieved the intermediate relaxed Kohlrausch state and which have obtained values of the Kohlrausch stretching parameter, β, in excellent agreement with the prediction of the microscopic theory.

1. Introduction

As recently as ten years ago almost all of our knowledge of the glass transition came from a wealth of experiments [1]. Molecular dynamics simulations (MDS) suffered from serious limits on computational timeframe and sample size, and it was far from clear which of these was more serious. The available timeframe is seldom longer than 10^{-10} or 10^{-9} s, and sample sizes were smaller than $\sim 10^2$ atoms. Today the situation has changed radically. It has turned out that many of the older simulations, on hard- or soft-sphere, or excessively ionic models, failed because these 'materials' are simply not good glass-formers. As interatomic force fields have become more realistic, dramatic improvements have occurred in the simulated glass-forming tendency. Today the available timeframe has not expanded greatly, but sample size has expanded enormously, from ~ 200 atoms (1982) to ~ 5000 atoms (1990) to $\sim 40\,000$ atoms (1994). It has turned out that finite-size effects, and not the limited timeframe, were the second most serious problem, after that of poorly chosen force fields.

The agreement between simulated and experimentally measured structure factors is now very good, as described, for instance, for g-SiO_2 at this conference by Vashishta [2]. This means that the relaxation of such structure-factor peaks can be examined in detail, at least above the kinetic structural arrest transition temperature, T_t^*, of the MDS. Of course, because of MDS timeframe limitations, T_t^* is higher than the experimental T_g, but not much higher, and such differences themselves are instructive.

* Corresponding author. Tel: +1-908 582 2528. Telefax: +1-908 582 4702.

A remarkable aspect of structural relaxation in amorphous and glassy systems, both electronic and atomic, is that the more homogeneous the system (i.e., the lesser the extent of the onset of spinodal phase separation or microcrystallization), the more accurately its relaxation can be described by the stretched exponential function

$$K(t) = K_0 \exp\left[(-t/\tau)^\beta \right], \qquad (1)$$

which was observed and identified first by Kohlrausch in 1847, in the context of residual discharge of a Leyden jar. We have recently examined [3] the very large database of Kohlrausch exponents $\beta_\alpha(T)$ in disordered systems, α. As described in Section 2, our analysis concluded, contrary to the general opinion, that β has a well defined microscopic significance. Broadly speaking, $\beta_\alpha(T)$ is constant below an arrest temperature, T_α^*, that is related to the kinetic arrest temperature, T_t^*, in the sense that both describe a type of glass transition within the temporal frame used in the MDS. The constant value, $\beta(T_t^*)$, agrees with theoretical predictions in the cases of several recent MDS for metallic glasses and polymers, as discussed in Section 4.

One of the features which characterizes the microstructures of network glasses is medium-range order (MRO) [1]. The structural signature of MRO is the first sharp diffraction peak (FSDP). This peak has no analogue in crystalline powder patterns for glasses such as SiO_2, although it corresponds to the c-axis interlayer spacing in chalcogenide alloy glasses like As_2Se_3 and $GeSe_2$. Will the Kohlrausch constant, $\beta(T_t^*, Q_F)$, be the same as that for normal diffraction peaks, $\beta(T_t^*, Q_N)$? Will the structural arrest temperature for Kohlrausch relaxation, $T_t^*(Q_F)$, be the same as that for $T_t^*(Q_N)$? We discuss these questions and their microscopic implications in Section 3, where we also provide some much-needed interpretation of the MRO physical mechanisms which give rise to the FSDP.

2. Kohlrausch relaxation

Relaxation in homogeneous disordered atomic, molecular or electronic systems takes place in general in three stages: an initial transient stage, often

describable by a power-law or simple exponential time dependence; an intermediate or residual stage, which is the subject of this section; and a very long time coarsening or domain-formation stage where inhomogeneities (associated, for example, with phase separation or crystallization) form and grow in size. Relaxation in the intermediate time range, after dissipation of transients and before the onset of nucleation, is generally best described by the stretched exponential time dependence, $K(t)$, in Eq. (1). Hundreds of values for β are known, but it is generally believed [4,5] that no microscopic model exists which can explain those values of β which are intrinsic and which can be used to separate intrinsic from extrinsic effects. In practice often the Kohlrausch fit is not unique and in general one cannot be confident that the materials studied are sufficiently homogeneous to justify such fitting.

I have recently analyzed [3] a large body of data which span about 10^3 papers on both electronic materials, such as a-Si:H, a-C_{60}, TaS_3, spin glasses and vortex glasses in high-temperature superconductors, as well as molecular materials which include polymers, network glasses, alcohols, Van der Waals supercooled liquids and glasses, and fused salts. In the intrinsic cases, the theory of $\beta(T_g)$ is often accurate to 2%, which is often better than the quoted experimental accuracies $\sim 5\%$. The extrinsic cases are identified by explicit structural signatures which are discussed at length. A full discussion of the non-local diffusion-to-traps model [6], which gives

$$\beta = d/(d+2), \qquad (2)$$

where d is the effective dimensionality of the configuration space in which the particles relax, lies outside the scope of the present paper. However, we can easily see why this model leads to modifications of conventional Debye ($\beta = 1$) simple exponential local relaxation. Near $t = 0$, particles close to the traps diffuse to and are captured by the traps. At later times, the density of particles near the traps is depleted by previous captures. This depletion is itself a smooth, self-similar process, dependent on $(t/\tau)^\beta$, where the exponent, β, can be calculated in several ways. The function, $K(t)$, has no expansion in powers of t unless β is integral, and the slowing-down depletion process leads to $0 < \beta < 1$, corresponding to $0 < d < \infty$. The stretched exponential reverts, of

course, to simple exponential relaxation when $\beta = 1$, and this is the result within an effective-medium approximation. The problem also cannot be solved by perturbation theory based on powers, n, of the trap density, which corresponds to an expansion in terms of n-trap clusters, as this predicts power-law decay [3]. In other words, stretched exponential decay is inherently non-local, and it involves relaxation of the system as a whole. Of course, the solution depends essentially on a fully random trap distribution. If the randomness condition is violated, then the relaxation may appear to be describable by $K(t)$ over a short timeframe, but at longer times the fit will deteriorate.

In the absence of a microscopic theory of β_α, and an understanding of the α-dependent chemical trends, the overwhelmingly accepted view has been that β is only a fitting parameter [4,5]. Our analysis [3] showed that the physical meaning of d is the obvious one in simple cases where internal fields do not constrain particle motion, but it is modified in a subtle and profound way when those fields are present. The constraining effect of such fields can be calculated by axiomatic set-theoretic methods similar to those used to define the composition dependence of the glass-forming tendency in network glasses [1]. These methods are not yet part of most physicists' knowledge and this, together with many experimental ambiguities, may explain why this problem has remained unsolved for so long.

A full exposition of these mathematical techniques, together with a careful analysis of the experimental data, has been given in a paper [3] that is about five times longer than the present one. Here we mention a small number of the results. For an electronic excitation, the traps can represent centers where charges recombine. For molecular relaxation, the traps represent regions where the local free energy has secondary minima whose number, size and position have been established during transient relaxation and do not change appreciably during the residual relaxation period. These conditions are easily met in molecular dynamics simulations with current supercomputers, but they are generally not satisfied in many so-called random glasses or polymers. Many polymers, such as polyvinyl chloride or vinyl polybutadiene, are probably partially crystallized. An ideal non-crystallizing organic liquid is propylene

glycol, which is a mixture of two isomers, cannot crystallize, and is familiar to all as the essential component of antifreeze. Moreover, propylene glycol is available in both monomer and polymer forms ($M = 4000$), with respective values $\beta = 0.61(4)$ and $\beta = 0.42(4)$, both values being in accord with theory, as are values obtained for many other Van der Waals liquids and polymers which do not crystallize. With inorganic glasses, some crystallization or phase separation occurs in many nominally ideal glasses, such as SiO_2, GeO_2 and As_2S_3, as shown directly by β values and also by correlations between these values and the pressure dependence of certain narrow Raman bands. However, $Na_2O \cdot 2SiO_2$ and Ge–As–Se glass at the ideal glass-forming compositions behave nearly ideally so far as theory is concerned, because their ternary compositions are effective in suppressing crystallization and phase separation.

In physical systems without internal fields, d is simply the spatial dimensionality; usually $d = 3$ and $\beta = \beta_{SR} = 3/5$, for short-range forces. For Coulomb forces the situation is different. Then charge fluctuations (standing waves) do not contribute to relaxation, only diffusive current flow. The energy of such charge fluctuations is given by $\hbar\omega_p$, the plasmon energy, with $\omega_p^2 = 4\pi Ne^2/m$, where N is the density of a free charge confined to a glassy grain of volume $\Omega_0 = L^{\{d\}} = L^3$. The density of grains free of plasmon excitations is proportional to $f = (1 - \exp(-\hbar\omega_p/kT))$, and in the long-time limit $\hbar\omega_p \ll kT$ this scales like $L^{\bar{d}}$ with $\bar{d} = -3/2$. As L varies the effective volume available for diffusive flow, Ω_e, is related to Ω_0 by $\Omega_e = f\Omega_0 \propto L^d$, where $d = \{d\} - \bar{d} = 3 - 3/2 = 3/2$. Thus Kohlrausch charge relaxation is determined by $\beta = \beta_K = 3/7$. This value is observed in electronic relaxation at low temperatures in stable materials such as fullerene.

A surprising and very satisfying bonus of the theory is that it enables us to identify Coulomb relaxation as the dominant relaxation mode of long-chain polymers, in the absence of appreciable cross-linking. In a-Se this mode becomes dominant even in the supercooled liquid, i.e., below T_m and well above T_g, and it is also dominant in cis–trans polybutadiene, where Kohlrausch relaxation has been established over six decades in reduced time, as shown in Fig. 1 [7]. The reason Coulomb relaxation dominates is that the relaxation of such long chains is con-
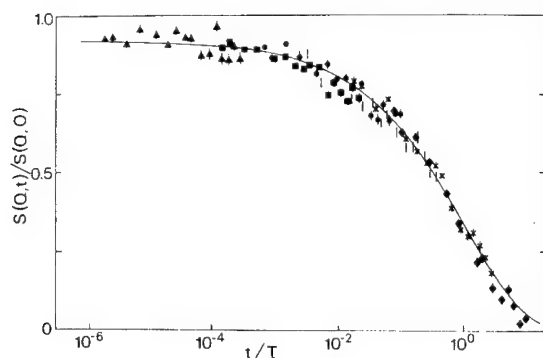
Fig. 1. Scaling representation of the neutron spin-echo data for relaxation of cis–trans polybutadiene at the maximum $Q = Q_1$ of the structure factor, $S(Q)$, where t is rescaled by τ so that the filled triangle data for $T = 200$ K lie to the left, while the diamond data for 280 K lie to the right. The smooth line is the Kohlrausch fit with $\beta = 0.45(2)$, all reproduced from Ref. [7] for the reader's convenience. Note that the fit spans more than six decades in the abcissa.

trolled by long-range interactions provided by infrared-active longitudinal optic phonons. Many other examples of this effect are analyzed elsewhere [3]. In particular, in a-Ge–As–Se alloys β crosses over from β_K to β_{SR} as the average coordination number, $\langle m \rangle$, varies from $\langle m \rangle = 2$ (a-Se) to $\langle m \rangle = 2.4$ (ideal glass formers) [8]. The values of β in mono- and poly-propylene glycol, quoted above, similarly match β_{SR} and β_K, respectively.

There are many different experimental methods for measuring β, and many different materials have been studied. The greatest complications have arisen in the measurements on fused salts (liquid electrolytes). These have all been resolved by the present theory. The prototypical material is the molten salt mixture $x \mathrm{Ca(NO_3)_2} (1 - x) \mathrm{KNO_3}$ (CKN), where β has been measured in neutron spin echo ($\beta_1 = 0.58(2)$) and ultrasonic ($\beta_2 = 0.44$) studies. The neutron measurements probe density fluctuations, which are dominated by short-range forces, so that $\beta_1 \approx \beta_{SR}$. Ultrasonic waves couple to internal electric fields and hence are controlled by long-range forces, so that $\beta_2 \approx \beta_K$. Finally, the puzzle of the fact that β increases significantly at low probe frequencies in dielectric relaxation experiments, up to $\beta \sim 0.75$ at

low frequencies, can be understood as the result of the crossover from microscopic to macroscopic relaxation. When the relaxation wavelength, as inferred from the velocity of sound, is larger than the sample dimensions, dominant relaxation occurs in the Gouy double layers at the electrode–electrolyte interfaces. It is possible that the combined relaxation in such double layers effectively has dimensionality $\{d\} = 6$, giving $\beta \sim 3/4$, as is observed to be the low-frequency limit for dielectric relaxation in CKN.

3. Clusters, morphology and the FSDP in network glasses

As mentioned in the Introduction, the FSDP (first sharp diffraction peak in $S(Q)$ at $Q = Q_F$) is a characteristic feature of the diffraction spectra of most network glasses [1,9]. One can search for explanations for the occurrence of this feature in two ways. First, the minimalist way: one postulates that the structure is a Zachariasen continuous random network, with alternating cations and anions, nearly fixed bond lengths, and as many nearly fixed bond angles as allowed by constraint theory. The average bond lengths and bond angles are adjusted to fit experiment, and MDS then produces an $S(Q)$ which may fit experiment very well if the interatomic force field is chosen judiciously and the sample size is large enough to minimize finite size effects. From the simulation one can calculate partial structure factors, $S_{\alpha\beta}(Q)$, and partial radial distribution functions, $P_{\alpha\beta}(r)$.

When this procedure is carried through, it is found that deletion of the peaks of $S_{\alpha\beta}(Q_F)$ has very small effects on $P_{\alpha\beta}(r)$, and that these small effects occur mainly at medium range distances $r \approx R_{mr} = 6 \pm 2$ Å, where the direct interatomic forces are quite weak. This means that most of the interaction energies which created MRO and the FSDP are large ring energies which involve correlation functions of $m \gg 2$ particles. The MDS n-ring populations, p_n, can be calculated, of course, but it is not easy to analyze them. In GeSe$_2$ they could be compared with the ring statistics of the high-temperature and low-temperature crystalline phases, and possibly their moments $(p_n - p_n)^{2m}$. In this way similarities of the glass structure to that of the high-temperature crys-

talline phase might be apparent, but this has not been done so far.

The second approach is based on the assumption that some physical mechanism must be responsible for the presence of the FSDP, and that this mechanism can only be the formation of clusters of a definite size, R_C, such that $Q_F R_C \gtrsim 1$. (This approach has been the one that has been used for modelling quasicrystals recently in terms of the crystal structure of crystalline approximants [10]; it was adopted after it was found that random tiling models, the Penrose analogue of Zachariasen's continuous random networks, gave physically unacceptable results (some very short bond lengths).) The internal topology of the cluster must be that of the high-temperature crystalline phase, and the surface of the cluster should be partially reconstructed, with some back or surface bonds replacing the outer intercluster bonds which exist in the crystal. A few examples of such clusters have been proposed, especially the outrigger raft model for $GeSe_2$ [1]. However, these methods, although highly informative in favorable cases, are not easily generalized to other glasses, such as SiO_2, and are not easily compared with MDS.

Another special feature of the chalcogenide glasses which makes them a happy testing ground for sophisticated theories is that the average coordination number, $\langle m \rangle$, can be varied smoothly by network substitution in both binary and ternary systems. Although the average trends depend almost entirely on $\langle m \rangle$, the extent of cluster formation and microcrystallization is expected to be much greater in binary than in ternary alloys, as there are several types of incompatible building unit in the latter. It seems likely that quantities like the FSDP will be very similar, for the same $\langle m \rangle$, in binary and ternary chalcogenide alloys, but it would be very interesting to test this conjecture by MDS.

A number of experiments on binary and ternary chalcogenide alloys have confirmed the presence of kinks in physical properties as functions of $\langle m \rangle$ near the critical coordination number $\langle m \rangle = m_c = 2.40$ predicted by constraint theory, but other experiments, similar in nature, have not found such kinks. This discrepancy can probably be traced to differences in quenching kinetics for small samples compared with large samples. The difference between

binaries and ternaries is small for $\langle m \rangle \leq m_c = 2.40$ (underconstrained glasses, where entropy is large), but it grows rapidly for $\langle m \rangle > m_c$ (overconstrained glasses, where clusters are enthalpically stabilized) [11]. One measure of the density of some trap states is the strength of the term in the specific heat which is linear in T, which shows a minimum at $\langle m \rangle = m_c = 2.40$, and a maximum at $\langle m \rangle = m' = 2.70$ [12]. The minimum is what one would expect from constraint theory, whereas the maximum occurs at the value identified by Tanaka and explained by him as associated with the structural transition from layered to three-dimensional structures [13]. Evidence for anomalous behavior associated with this transition has also been obtained in measurements of solubility and photostructural changes in ternary Ge–As–S alloys [3]. The change in slope of the softening of the elastic constants as m decreases through m_c expected by constraint theory is not observed in large samples, probably because of microcrystallization, but in much smaller samples probed by Mössbauer spectroscopy the predicted effect has been observed [10]. The microcrystallites have their largest effect at long wavelengths. At intermediate wavelengths ~ 30 Å, a 'floppy mode' peak in the density of vibrational states is observed whose strength decreases rapidly with $\langle m \rangle$ and which is quite small for $\langle m \rangle > 2.40$ [14].

When we review the many subtle aspects of clusters and their morphology as evidenced in chemical trends in chalcogenide alloys, we are led to the conclusion that in glassy $GeSe_2$ the presence of the FSDP is probably little affected by morphological subtleties. One reason for this is that the sizes of the unit cells of the two phases of $GeSe_2$ are very large (24 formula units in the low-T, three-dimensional phase, and 16 formula units in the high-T layered phase, compared with only eight formula units for the high-T (β-cristobalite) phase of SiO_2). Another reason is that MRO can develop at $R_c \sim 6$ Å at short times, whereas crystalline order may well develop only at longer distances ~ 30 Å and hence at much longer times. (This is consistent with the observed differences between small and large samples [13].) Thus the clusters that are responsible for the FSDP are merely incipient microcrystallites, precursors to Gibbs' critical nuclei that grow rapidly in non-glass-forming supercooled liquids with T just below T_m.

4. Kohlrausch relaxation in metallic and oxide glasses: simulations and experiments

Chalcogenide glasses are not the only glasses where Kohlrausch relaxation has been studied. MDS have examined [15] Kohlrausch relaxation in a proto-typical metallic glass Ni_xZr_{1-x} with $x = 0.5$. The central factor which leads to glass formation in this system is the elemental size differences, which produce a complex binary phase diagram with deep eutectics. Crystalline NiZr has the quasi-hexagonal CrB structure in which the smaller atoms form helical chains. No mention is made of whether such chain fragments are present in the description [15] of the MDS, but $\beta(T)$ has been calculated and it behaves as expected: $\beta(T) \rightarrow 1$ at high T, and near the structural arrest transition, $T_t^* \sim 1500$ K, $\beta(T^*) = 0.59(2)$, in excellent agreement with $\beta(d = 3) = \beta_{SR} = 0.60$. It is difficult to obtain experimental values for β, because metallic glasses crystallize very rapidly.

Oxide glasses are suitable for relaxation studies at low frequencies (stress relaxation), but most of the data collected in phenomenological studies [4] are quite old and these materials probably should be re-measured using modern instrumentation. In spite of these caveats, the data are in surprisingly good agreement with theory; for instance, $\beta(Na_2O \cdot SiO_2) = \beta(B_2O_3) = 0.6$, while $\beta(SiO_2) = 0.7$ and $\beta(GeO_2) = 1.0$. The latter two deviations are actually to be expected, especially for g-GeO_2, which has been shown by high-pressure Raman studies to contain microcrystallites of rutile c-GeO_2, which has sixfold-coordinated Ge, whereas in the glassy network Ge should be fourfold-coordinated [2]. One

Table 1
Systems for which $\beta \approx \beta_{SR} = 3/5$

Material	Method	β
Soft spheres	MDS	0.62 (3)
Metallic glass	MDS	0.59 (2)
Polymer	MDS	0.59 (4)
g-Ge–As–Se	stress	0.63 (3)
OTP [a]	neutron	0.62 (2)
CKN [a]	neutron	0.58 (2)
Salol	photon	0.60 (5)
Propylene glycol	specific heat	0.61 (4)

[a] Here OTP = orthoterphenyl, a three-ring planar molecule, while CKN = $(Ca, K_2)(NO_3)_2$.

Table 2
Systems for which $\beta \approx \beta_K = 3/7$

Material	Method	β
Glass	charge	0.43 (1)
a-Si:H	charge	0.45 (5)
a-C_{60}	charge	0.40 (5)
a-Se	stress	0.43 (3)
a-Se	neutron	0.42 (2)
PB ($f_v \sim 0$)	neutron	0.45 (1)
PVME	NMR	0.44 (2)
PVME	neutron	0.44 (2)
CKN	ultrasonic	0.44
Poly propylene glycol	stress	0.42
PPMS	stress	0.44
PVA	stress	0.43
PMA	stress	0.41

An interesting comparison can be made between propylene glycol ($\beta = 0.61 \approx \beta_{SR}$, Table 1) and polypropylene glycol ($M = 4000$, $\beta = 0.42 \approx \beta_K$). This illustrates the way that floppy, infrared-active polymerized chain modes shift β from β_{SR} to β_K. Compare also the value for CKN obtained with an electric-field probe with that in Table 1 for a neutral probe. The acronyms PXX... refer to various polymers (see Ref. [5]).

could wonder whether there is any correlation between $| \beta(T_g) - \beta_{SR} |$ and the strength of the FSDP, but the database at present is too sparse to permit conclusions to be drawn. From the remarks made above, it would seem that the formation of FSDP clusters is part of the exponential relaxation which precedes Kohlrausch relaxation, which in turns precedes spinodal coarsening and eventually microcrystalline nucleation and growth.

5. Conclusions

For the reader's convenience, we show in Tables 1 and 2 some examples of intrinsic relaxation in various materials where $\beta \approx \beta_{SR} = 0.60$ or $\beta \approx \beta_K = 0.43$ as measured by a variety of techniques. To appreciate fully the significance of these data, one must understand not only the mathematical background of the theory but also the chemical trends in β as they correlate with the degrees of homogeneous random disorder in different families of materials. These issues are discussed at considerable length elsewhere [3]. The tables are presented here merely to give the reader a taste for this subject, which has developed to a far greater extent than is generally

realized outside the community of chemists and physicists devoted to relaxation studies.

There are several open relaxation questions which can be examined by MDS. We expect that if the current timeframe ($\leq 10^{-9}$ s) is adequate, $\beta(T_t^*, Q_F)$ will be approximately equal to β_{SR}, but if it is not, $\beta(T_t^*, Q_F) > \beta(T_t^*, Q_N) \sim \beta_{SR}$. This would indicate that structural arrest is complete on the 3 Å scale, but not on the 6 Å scale. Thus, relaxation studies can be used to test how well annealed the sample is on different time and length scales. Another question of interest would be the demonstration for a suitable three-dimensional chain model of the way that Coulomb forces shift β from β_{SR} to β_K. The chains could consist of Se (where the charges are dynamical and depend on intrachain bond angles) or $-CH_2-$ (where the charges are static). Here again the timescale could be important, as one could find an apparent $\beta \sim \beta_{SR}$ at shorter times $\leq 10^{-9}$ s, where transverse relaxation is dominant, and a different $\beta \sim \beta_K$ at times $\geq 10^{-9}$ s, when transverse relaxation is nearly complete and the longitudinal relaxation involving the length scale of the chain fragments dominates. It is quite convenient that MDS at present cover times $\leq 10^{-9}$ s, while neutron spin echoes work best for times $\geq 10^{-9}$ s.

References

[1] J.C. Phillips, J. Non-Cryst. Solids 34 (1979) 153; 43 (1981) 37.

[2] P. Vashisha, R.K. Kalia, and J.P. Rino, Phys. Rev. B41 (1990) 12197; P. Vashishta, A. Nakano, R.K. Kalia and I. Ebbsjö, these Proceedings, p. 59.

[3] J.C. Phillips, J. Non-Cryst. Solids 172–174 (1994) 98. unpublished.

[4] W. Götze and L. Sjögren, Rep. Prog. Phys. 55 (1992) 241.

[5] R. Böhmer, K.L. Ngai, C.A. Angell and D.J. Plazek, J. Chem. Phys. 99 (1993) 4201.

[6] I.M. Lifshitz, Usp. Fiz. Nauk 83 (1964) 617 [Sov. Phys. — Usp. 7 (1965) 549;
R. Friedberg and J.M. Luttinger, Phys. Rev. B12 (1975) 4460;
P. Grassberger and I. Procaccia, J. Chem. Phys. 77 (1982) 6281.

[7] B. Frick, B. Farago and D. Richter, Phys. Rev. Lett. 64 (1990) 2921.

[8] R. Böhmer and C.A. Angell, Phys. Rev. B45 (1992) 10091;
Ch. Simon, G. Faivre, R. Zorn, F. Batallan and J.F. Legrand, J. Phys. I (Paris) 2 (1992) 2307.

[9] S.R. Elliott, Phys. Rev. Lett. 67 (1991) 711; these Proceedings, p. 40.

[10] M.V. Jarić and S.-Y. Qiu, Phys. Rev. B49 (1994) 6614;
K.M. Rabe, J.C. Phillips and P. Villars J. Non-Cryst. Solids 153–154 (1993) 530.

[11] M. Tatsumisago, B.L. Halfpap, J.L. Green, S.M. Lindsay and C.A. Angell, Phys. Rev. Lett. 64 (1990) 1549;
M. Zhang, S. Mancini, W. Bresser and P. Boolchand, J. Non-Cryst. Solids 151 (1992) 149.

[12] X. Liu and H. Vonlohneysen, Phys. Rev. B48 (1993) 13486.

[13] K. Tanaka, Phys. Rev. B39 (1989) 1270.

[14] W.A. Kamitakahara, R.L. Cappelleti, P. Boolchand, B. Halfpap, F. Gompf, D.A. Neumann and H. Mutka, Phys. Rev. B44 (1991) 94;
A.N. Sreeram, A.K. Varshneya and D.R. Swiler, J. Non-Cryst. Solids 128 (1991) 294.

[15] H. Teichler, Phys. Status Solidi (b)172 (1992) 325.

Odd rings and tunneling modes in glasses

Nicolas Rivier *

Laboratoire de Physique Théorique, Université Louis Pasteur, 3 rue de l'Université, F 67084 Strasbourg cédex, France

Abstract

Tunneling modes, elementary excitations of a large class of glasses, are local dynamical signatures of disorder. There is one tunneling mode per odd loop (a necklace through odd rings in the network), decoupled from other loops, and tunneling is forced by gauge invariance of the structure, the symmetry of disorder. Absence of tunneling modes in trivalent glasses (a-As or B_2O_3) is a notable consequence of this model. It is possible to decompose topologically a tetravalent network into a trivalent network, and to add a large proportion of boroxol rings with their characteristic but different dynamical signature.

1. Introduction

Tunneling modes constitute, together with long-wavelength phonons, the low-energy excitations in glass. Their tunneling nature has been established experimentally after 1973, confirming in qualitative details a model proposed independently by Anderson, Halperin and Varma, and by W.A. Phillips [1]. The experimental demonstration of tunneling modes has a long history, beginning in 1959 [2]. The four crucial sets of experiments ((i) specific heat, (ii) thermal conductivity, (iii) saturation or (non-linear) ultrasonic attenuation and (iv) echoes) were first performed by (i) Hornung et al. [3], and Zeller and Pohl, (ii) Anderson, Reese and Wheatley, (iii) Hunklinger, Arnold, Stein, Nava and Dransfeld, and Golding, Graebner, Halperin and Schutz, and (iv) Golding and Graebner, and Arnold and Hunklinger. The tunneling model was introduced after experiments (i) and (ii), but before (iii) and (iv) which

confirmed it as the only model explaining all four experiments. All this is well documented in Ref. [1] (except for the two precursors for which a specific reference [2,3] is given).

After a brief review of the four experimental signatures of tunneling modes, emphasizing the challenges which they present to any theory, an explanation for their origin and their nature is offered [4]: tunneling modes are associated with odd rings of bonds. Specifically, there is one tunneling mode per odd line, a necklace threading through odd rings and avoiding even rings [5]. Tunneling is imposed by the symmetry of disorder, a gauge invariance responsible for the long-range homogeneity of glasses and amorphous materials. Each tunneling mode, and thus each odd loop, is independent from the other. Tunneling modes are therefore local dynamical signatures of disorder. The explanation meets all the challenges and is predictive: no tunneling modes should occur in trivalent covalent glasses or amorphous materials such as borate, arsenate glasses or a-As. Any tunneling mode in amorphous III–V or II–VI semiconductors such as a-GaAs will correspond to a 'wrong' (As–As or Ga–Ga) bond. Quantitative predictions

---
* Corresponding author. Tel: +33 88 35 81 41. Telefax: +33 88 35 81 82. E-mail: nick@fresnel.u-strasbg.fr.

should soon be available, as the structure of tunneling configurations can now be described explicitly [4]. Mathematical details and explanations are omitted; they can be found in the published literature [4–6].

In the rest of the paper, we discuss the celebrated boroxol ring mode [7], which, although a local, dynamical signature of disorder, is not a tunneling mode. It is possible to transform topologically a tetravalent network (supporting tunneling modes) into a trivalent network with boroxol rings, which does not have tunneling modes.

2. Tunneling modes: experimental evidence

Glass has extraordinary physical properties at low temperatures [1], described as tunneling modes. Phonons of sufficiently long wavelength to ride over any inhomogeneity in the structure (i.e., > 4 nm) are elementary excitations of a solid piece of glass. We hear them as the glass rings. However, its specific heat is approximatively linear in temperature below 1 K. This linear specific heat cannot be due to metallic electrons, in a transparent glass or in a metallic glass made superconducting. Surely, one does not have a one-dimensional fractal material? Scaling of weight with the cube of the linear dimension shows that this is indeed a bulk three-dimensional solid, and the expected T^3 specific heat is swamped at low temperatures by additional excitations, specific to glass.

Heat conductivity, or ultrasonic attenuation, shows that phonons are absorbed or scattered by these additional excitations, which form a distribution of two-level systems. They are tunneling modes, as shown by the fact that they can be saturated (other, classical excitations are much higher in energy and not accessible at low temperatures) and can be made to produce an echo by returning in phase at the same time, as in spin-echo but without any electromagnetic contribution. This is a real 'acoustic' echo. The echo experiment also shows that tunneling modes are independent (their dephasing time, T_2, is longer than the long echo time).

These low-temperature properties are common to all glasses, covalent oxides, amorphous elemental semiconductors and metallic glasses. Only their in-

tensity and characteristic energy and temperature scales differ. For example, in amorphous silicon or germanium, the chemical bond is stiffer than in vitreous silica (where it is longer, and decorated by an oxygen atom). Consequently, the distribution of tunneling modes spans a broader range of energies, and the density of low-energy tunneling modes is, accordingly, one or two order of magnitude smaller. Nevertheless, tunneling modes have been observed in amorphous germanium [8]. Their echo has been heard in metallic glasses [9]. The similarity between low-energy atomic excitations in oxide and metallic glasses has been emphasized and reviewed by Black [10]. Tunneling modes are a general feature of disordered condensed matter. (Exceptions, like amorphous arsenic, or III–V compounds which have no odd rings, or hardly any (they imply the presence of wrong (Ga–Ga or As–As) bonds, which are energetically costly), are interesting and confirm the model. They are discussed below.)

Theoretically, one faces a dilemma. Either one presents an explanation so general as to be untestable, or one looks for a simple model, applicable to one type of glass only, which explains clearly the nature of tunneling modes, is predictive and falsifiable, but non-universal. The second approach is discussed in this paper: we will consider covalent glasses. Tunneling modes are located on odd rings of the networks. These odd rings form closed loops in the glass. There is one tunneling mode per odd loop. The density of odd loops, thus of tunneling modes, is determined by maximum entropy. The maximum entropy configuration of the loops is semi-dilute, with only one single length scale, thereby taking maximal advantage of mixing (small loops) and configuration (longest loops) degrees of freedom. A tetravalent network is also the generic scaffolding spanning the disordered elastic continuum representing polymeric glasses.

Another striking property of glass is its finite entropy (as measured through the specific heat, integrating C_p/T) at $T = 0$. Physically, this has no practical consequences since $C_p(T = 0) = 0$. The entropy of glass has two contributions. The first is physical, associated with heat transfer. It vanishes at $T = 0$. The second, which is finite at $T = 0$, is the structural information, the measure of the frozen-in disorder, or the algorithmic complexity of glass. We

will see that this structural entropy is concentrated on odd loops. The zero-point entropy, particularly as a function of the rate of cooling, is a measure of the density of tunneling modes. Analysis of the lowest energy states of glass, and of its elementary excitations, should explain its extraordinary properties.

The anomalous physical properties of glass (i)–(iv) below 1 K [1] are modelled by tunneling between independent pairs of potential valleys in configuration space. Thus, phase space is represented as a direct product of a pair of classical configurations (potential energy minima) which are nearly degenerate in energy. The ground state and first excited state of each pair are tunneling modes, superpositions of the classical configurations. Classical excitations in each potential well are at much higher energy, and are not excitable at low temperatures below 10 K, as would be classical transitions over a saddle point between potential wells if they were to exist. The local, tunneling modes and the long wavelength phonons therefore constitute the elementary excitations in glass.

(i) The specific heat is approximatively linear in temperature below 1 K, where a linear function exceeds the T^3 contribution of phonons in a three-dimensional system. There are therefore additional elementary excitations in glass besides phonons. A distribution of two-level systems yields a linear specific heat (as for electrons in metals: Boltzmann's distribution on a two-level system looks like Fermi–Dirac's, and the distribution, $P(\Delta_0)$, of energy spacing plays the part of the density of electronic states).

(ii) Heat is carried by phonons. Glass has a thermal conductivity lower than its corresponding crystalline material (quartz), so the phonons are absorbed by the additional two-level excitations.

(iii) If the power of the transducer is turned up, most two-level systems will have absorbed a phonon and be in their excited state. They can no longer absorb phonons, and the thermal conductivity of the crystal is recovered.

(iv) An echo can be set up on these excitations, as in any quantum two-level systems (spin 1/2). The echo delay time is approximatively 10 μs at 20 mK, which shows that the two-level systems are effectively decoupled (the dephasing time, T_2, is greater than this very long delay time).

Saturation and echo show that the two-level excitations are due to quantum tunneling (classical, thermal excitations are at much higher energy, out of reach at these low temperatures). The first two experiments could also be explained by classical excitations between potential wells, but not the last two. Further, the energy splitting between the two levels is very small (linear specific heat is observed between $< 10^{-2}$ K and 1 K in silica, which implies a continuous range of splittings between $< 10^{-6}$ and 10^{-4} eV). This splitting is therefore entirely the contribution of tunneling, Δ_0, between degenerate potential wells. Any departure from degeneracy, Δ, yields an additional energy difference ($> \Delta$ and Δ_0). It also implies that there are many atoms involved in the tunneling moving very little. (Inversion tunneling of one atom in a tetrahedron (a symmetrical ammonia molecule) would occur at a frequency higher by orders of magnitude.)

Tunneling modes (in all their four manifestations) have been seen in all glasses and amorphous materials, with a few notable exceptions which confirm the rule (the model which we now discuss).

Apart from the fact that one does not know precisely what tunnels, the presence of nearly *degenerate* (to within less than 10^{-4} eV) classical ground states (potential minima) in a system with no obvious symmetry to impose the degeneracy is astonishing: indeed, bulk condensed matter usually has one single ground state, and its potential energy has one single minimum in a many-dimensional configuration space. (Excitations about this minimum are phonons, which are also heard in glass.) Further, observation of echo (analogous to spin echo, but generated by sound pulses) suggests that different tunneling modes – different pairs of potential valleys – are *uncoupled* enough to preserve phase coherence between excitation and echo (∼ 10 μs at 20 mK).

3. Tunneling modes in covalent glasses

What then are these tunneling modes, why are they decoupled, and why are they degenerate, in a strongly correlated system of many atoms with the trivial space group?

The answers are provided by an analysis of the structure and elasticity of covalent glasses. Neither

are simple, and the argument is in several steps listed below which are stated without proof. Details have been published elsewhere [4].

3.1. Structure of network glasses

(1) The long-range homogeneity of glass is a gauge invariance. Glasses have perfect short-range order, imposed by chemistry: silicon atoms are tetravalent, boron or arsenic (in a-As) atoms trivalent. Each silicon atom can therefore be represented as a perfect tetrapod, each boron or arsenic by a perfect tripod. Beyond 4 nm, i.e., beyond a few rings, glasses are completely homogeneous, but this homogeneity is not the generative symmetry of crystals whereby the translated crystal is exactly superposable on the original. The translated glass is locally different, for example in the orientation of the nearby Si tetrapods, but this difference is physically irrelevant. The distinction is the same as between a forest in which one is lost, and a regular plantation: one tree in the forest is slightly different from another, but this difference is physically, globally or objectively irrelevant. It does not help us to find a way out. Thus, each Si atom in the network has, besides its position, a gauge parameter which connects it to its immediate environment (at this stage, it is easiest to think of the orientation of the tetrapod, but this will be refined as the group of permutations of its bonds). The gauge parameter changes slightly from atom to atom but the overall structure and physical properties of the glass are independent of these changes. Note that these local variations are altogether obligatory and macroscopically irrelevant in a disordered material. Note also that the variations, albeit local, are transmitted from atom to atom by the elasticity of the covalent bond linking them. These two remarks are generic properties of gauge symmetry, of which glass is the most concrete if not the simplest example.

(2) Glass structure is modelled by a continuous random network, i.e., as a regular graph. Each vertex of the network is a Si or B atom. It has $z = 4$ incident edges ($z = 3$ in the case of arsenic or boron), and each edge of the network represents one (in elemental glasses like a-As or a-Si) or two covalent bonds separated by an oxygen atom (in silicate, borate or arsenate glasses). The oxygen or selenium

atom only decorates the edge and plays no topological part. We will count the edges and call odd ring a ring made of an odd number of edges, of Si or B atoms. Thus, a boroxol ring, with three B–O–B edges, is odd. The vertices and edges of the network are physical objects. The constant vertex coordination, z, is imposed by chemistry, and the only connection between two vertices, an edge of the network, is a covalent bond (whether decorated by oxygen or not) which has some rigidity: it costs some energy to stretch, bend ot twist it, in decreasing order.

The continuous random network is a discrete, random scaffolding. This has two consequences. The first, already alluded to in (1), is that its physical properties will be gauge invariant, by symmetry. This means that, in addition to the topological position of each Si atom in the network, there is a local parameter, the 'gauge', which indicates how the atom is connected to its neighbours. In more familiar physical contexts, the gauge parameter is the phase of the wave function in quantum electrodynamics, or the local vertical in gravitation. Usually, the gauge parameter returns to its original value when one returns to the original atom after some closed path in the network. Not so if the closed contour is odd, in which case the gauge parameter must be changed: it will be entangled about odd rings, in one of two equivalent fashions. Since this entanglement is not physically relevant, tunneling must occur between the two equivalent fashions, giving rise to tunneling modes. Once again, we see the double role – obligatory and physically irrelevant – of gauge symmetry, the 'double agent' of disorder. The network itself, as a bare structural scaffolding, is topologically as trivial as can be. It is not entangled.

(3) The second consequence of randomness is that it has 'defects' as its structural signature. These defects are odd lines, necklaces threading through the odd rings of the network, while avoiding even rings [5]. Odd lines either close in as loops, or exit at the boundary of the material. The proof of this theorem is elementary: on any closed surface in the network (intersecting it at vertices, as for example a cell or a group of cells of the network), there is an even number of odd rings, thereby providing an exit for any odd line entering the surface. Thus, odd rings do not occur in isolation, but in loops. The theorem

is also valid for crystalline structures, but there, odd rings are rare or absent (only threefold rings are crystallographic), odd loops are very few and very small, and there is no gauge invariance to mould their dynamics. What are the physical effects of these odd lines? They are the seat of tunneling modes, and their density is measured by the zero-point entropy.

Gauge invariance and odd loops are the only essential ingredients of the structure of network glasses. I stress that they are natural ingredients, both in the physical (physical atoms and bonds in a continuous random network) and in the mathematical (simplest and generic) senses of the word.

3.2. Elasticity of z = 4 random networks

We now describe the classical elasticity of continuous random networks. The elastic energy is carried by the edges of the network, i.e., by the chemical bonds connecting two tetrapods. This potential energy consists of two terms [11–14]: a strong, bond-stretching, V_1, and a weaker, bond-bending contribution, V_2. V_1 can be written in terms of the relative displacement of two neighbouring atoms only. V_2 requires at least the direction towards a third atom as well. Its precise nature is not important for tunneling modes. From now on, we discuss the case of tetravalent networks ($z = 4$) only. We will return to the trivalent case later.

(4) Neglect V_2 in a first stage. The normal modes are a band of N phonons flanked by two sets of N degenerate modes [12,13]. One set has zero frequency and energy. The network is underconstrained (wobbly) in the absence of bond-bending forces. The ground state configuration(s) and the lowest energy excitations of the material are concentrated on the N floppy modes at $\omega = 0$.

The motion of an unstretched edge is given by one single number, the projection on the edge of the displacement of the two vertices bounding it. This number is like a current in an electrical network. The N floppy modes are independent currents [15]: they lie on bonds (edges) not on a spanning tree of the network, and each independent edge closes an independent circuit or ring. Any tree reaching all vertices of the network is called spanning. It is, of course, not uniquely defined, and selecting one spanning tree

partly fixes the gauge. The independent floppy modes form a basis for displacements leaving all bonds unstretched. They are the N $\omega = 0$ normal modes.

(5) Let us now stiffen the network by bond-bending forces, $V_2 \neq 0$. The floppy modes are reorganized, separated into ground states with elementary excitations, and modes of higher energy. Even rings are trivial (they have a single ground state). Odd rings have two stable configurations.

Let us measure the energy of a ring configuration. By definition, floppy modes have only bond-bending energy. For a given bond, α, this energy is measured by comparing the orientations of the two tetrapods (at i and $i\alpha$) which it links, or, equivalently, through a congruent transformation of the tetrapod, from its orientation at i to that at $i\alpha$. This energy is analogous to the bond energy, $S_i J_{ij} S_j$, in Ising magnetism, but it is seen not as some interaction between two identical objects (S_i and S_j), but as a *connection* (or synapse in neural networks) *from S_i to S_j*. The first point of view regards J as the standard for comparing directions of S_i and S_j; the second, adopted here, through the congruent transformation (flip or identity) J imposes on the spin.

Accordingly, the shared chemical bond (of label or colour, α) imposes a mirror reflection by connecting the two neighbouring tetrapods (the other three non-shared bonds may rotate). So, the congruent transformation is a rotatory reflection.

In a given configuration, the tetrapod must be returned to its original orientation (or an equivalent one) after being carried around the ring. Configuration of a n-sided ring is the product of n rotatory reflections. The product of rotatory reflections is therefore a covering transformation of the tetrapod, namely a permutation of the labels (colours) of its legs. If the ring is even, the permutation, a product of n reflections, is even. If the ring is odd, the permutation is odd. (This is because the number of legs, $z = 4$, is even. Elementary rotation about the shared bond, a cyclic permutation of the ($z - 1$) others, has parity $(-1)^z$.) Permutation is the gauge parameter indicating how the Si atom is connected to its neighbours through rings of covalent bonds. To this permutation can be associated a small quantitative energy, involving V_2 only, since bonds are unstretched.

(6) In fact, it is not the permutation which labels

the configuration, but only its class: let us go around two different rings in succession, starting from a common vertex, recording permutation **R** through one ring, permutation **Q** through the other. The total permutation is **P** = **Q** · **R**, or **P′** = **R** · **Q**, depending on the order of the circumnavigations, and, in general, **P** and **P′** are different. They are related by

$$\mathbf{P'} = \mathbf{R} \cdot \mathbf{P} \cdot \mathbf{R}^{-1} \qquad (1)$$

and belong to the same class of the permutation group. The physical configuration, which must be independent of the order of circumnavigations made to measure it, is labelled by the set which includes **P**, **P′**, etc., namely by the *class* of the permutation group to which they belong. Permutations belonging to the same class are identified physically.

The ground state of even rings clearly belongs to the identity class of the permutation group of degree $z = 4$, S_4. It is non-degenerate, and even rings are dynamically trivial. Only then can they be coloured consistently.

The configurations of odd rings are labelled by the two classes of odd permutations of S_4 (each containing six elements, $\{(\alpha\beta)\}$ and $\{(\alpha\beta\gamma\delta)\}$, so that odd rings have two distinct lowest-energy configurations (characterized by one permutation in each class, selected by choosing and colouring a spanning tree), separated by a large gauge transformation. It is easy to label consistently (colour, identity permutation) all even rings, and impossible to do so for odd rings. Change of labelling of the latter does not destroy consistency in the former (the physical meaning of Eq. (1)). Moreover, one odd ring is the sole, independent representative of an entire odd line, because all the other odd rings are linked to the first one by even rings and their bonds are permuted accordingly.

This shows that the odd line has two distinct classical ground states, separated by a large gauge transformation. The two classical ground states are represented in Fig. 1. Permutation class $\{(\alpha\beta)\}$ on the left has been realized by a connection algorithm labelling eclipsed bonds by the same colour. This gives the sequence of transformations $\alpha\beta \to \beta\alpha \to \alpha\beta \to \beta\alpha \to \alpha\beta \to \beta\alpha$, hence permutation $(\alpha\beta)$ for the ring. On the right, bonds of the same colour are rotated by by $2\pi/3$ about the shared bond, yielding the sequence $\alpha\beta\gamma\delta \to \beta\gamma\delta\alpha \to \gamma\delta\alpha\beta \to \delta\alpha\beta\gamma \to$
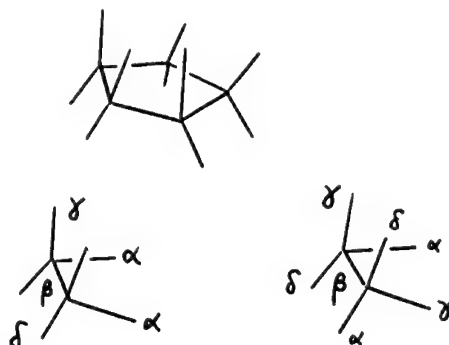
Fig. 1. The two classical configurations (bond labellings) about an odd ring. The label of indistinguishable bonds is not an observable quantity. Change of labelling algorithm is a gauge transformation. Frustration is inevitable and is seen as one of the two classes of permutations $(\alpha\beta)$ and $(\alpha\beta\gamma\delta)$.

$\alpha\beta\gamma\delta \to \beta\gamma\delta\alpha$, i.e., permutation $(\alpha\beta\gamma\delta)$ for the ring. Any colouring algorithm must lead to one or the other permutation class, but it is not a physical attribute since bonds are identical and odd rings cannot be coloured consistently (like the impossible triangles of the Swedish artist Reuterswärd). The physical attributes of the random network architecture are edges shared between two neighbouring atoms, and the fact that an odd cycle of shared edges imposes inevitable frustration for $z = 4$. Change of algorithm, and of class, is therefore a gauge transformation, leaving invariant the physical properties of the system, its energy, defects (odd loops, in base space) and physical properties (frustration on odd rings of shared bonds). Colouring is just a metaphor for bonds shared between two tetrapods. It is not the actual colouring which matters physically (bonds are identical), but whether consistent colouring is possible, and, when not, in how many essentially distinct ways.

Two different odd loops are independent since the bonds closing their representative odd rings are independent. All remaining rings are even, can be coloured consistently, and are in their ground state. Gauge transformation (a permutation) on one loop does not affect the class of permutation representing the structure of another (see Eq. (1)). Of course, higher excitations (non-trivial permutations on even rings) would couple two different odd loops. However, these excitations are at higher energies. Unlike the ground states discussed here, they also involve

the real energy cost of bond-bending, the rotation part of the rotatory-reflection connection.

3.3. Large gauge transformations and tunneling

(7) However, neither classical ground state configuration $\{(\alpha\beta)\}$ or $\{(\alpha\beta\gamma\delta)\}$ are gauge-invariant. Each is transformed into the other by a large gauge transformation **G**, **G**$|\{(\alpha\beta)\}\rangle = |\{(\alpha\beta\gamma\delta)\}\rangle$, **G**$|\{(\alpha\beta\gamma\delta)\}\rangle = |\{(\alpha\beta)\}\rangle$. They are therefore degenerate in energy. However, the physical configurations are given by the gauge-invariant linear combinations

$$|\pm\rangle = (1/\sqrt{2})[|\{(\alpha\beta)\}\rangle \pm |\{(\alpha\beta\gamma\delta)\}\rangle], \tag{2}$$

with one sign for the ground state and the other for the excited state. Tunneling, however slow, must take place to restore gauge invariance. Tunneling modes must exist in $z = 4$ glasses, and also in disordered elastic continua or in polymeric or mesoscopic glasses for which the tetrapod is the generic local frame of reference spanning the three spatial dimensions.

3.4. What is it that tunnels?

While saturation and echo experiments demonstrate the existence of tunneling modes, they do not show what it is that tunnels. It may be possible to observe tunneling modes directly on a glass undergoing the echo experiment, by using single-molecule spectroscopy (which yields fluorescence intensity autocorrelation at two different times) [16], or, less simply but in a direct structural measurement, by two, split and delayed and ultimately interfering structural probes (neutron or X-ray beam) on a glass undergoing the echo experiment. The echo effectively strobes the structure, since all odd loops are together in one of two classical configurations at the beginning and at the end of the experiment [14].

It is, of course, not possible to observe a system within the potential barrier through which it tunnels (illustrations in G. Gamov's Mr Tomkins notwithstanding). What can be done is to use the fact that, at two instants in an echo experiment, all tunneling modes are together in a classical configuration $((\alpha\beta)$ or $(\alpha\beta\gamma\delta))$ which is observable. Take a glass, prepared at $t = 0$ for an echo experiment. Use also neutron or X-ray diffraction as a structural probe. The beam is split and delayed: the first beam is diffracted by the glass at time t, then delayed by τ; the second beam is first delayed by τ and diffracted by the glass at $t + \tau$. The two beams are recombined and their interference is detected. The echo strobes the glass, so that, if the beams are in phase with the echo experiment *and* delayed by exactly the echo time, the interference produced by the tunneling atoms is constructive. It will be destructive otherwise. While this experiment was beyond the technical ability of detectors and beam intensity in 1984 when it was first proposed [14], it may now be suitable for consideration.

4. Topological entropy of glass and density of tunneling modes

The topological entropy is the entropy carried by odd loops. It is the entropy remaining in the glass at $T = 0$. We make the maximum entropy assumption that every face (smallest ring) of the continuous random network can be odd or even, independently of the others, without restriction apart from the very continuity of the odd lines, and that this part of phase space has been fully explored. Odd loops can move and be generated freely in the glass-forming liquid. The number of equivalent configurations of an arbitrary number of odd loops in any position, shape or length is simply two configurations per face of the network, with continuity guaranteed by keeping one face per cell as parity control, providing when necessary an exit for an odd line entering that cell, thus $\Omega = 2^{F-C}$ configurations in the network. The topological entropy is therefore

$$S = k_B \ln \Omega = k_B C(\langle f\rangle/2 - 1) \ln 2, \tag{3}$$

since a facet always separates two cells, and $\langle f\rangle$ is the average number of facets per cell, $2F = \langle f\rangle C$. For a froth ($z = 4$, all eclipsed edges), $\langle f\rangle = 13.4$. At the other extreme (random diamond, $z = 4$, all staggered edges), $f = 4$. There are on average $\langle f\rangle/2$ odd faces per cell, thus $\langle f\rangle/4$ odd lines per cell, which varies between 3.35 for all eclipsed edges and 1 for all staggered edges. The entropy is maximal,

and the configuration of odd loops is semi-dilute, the best compromise between mixing entropy (which favours many small loops) and configurational entropy (which favours a few very large loops). A loop is certain to traverse the neighbouring cell, but it may be part of the same loop or another.

The topological entropy (3) can be given per Si or B atom (N), using Euler's formula for a three-dimensional network and the valence relationship $zN = 2E$, valid for all regular networks (an edge is always bounded by two vertices, and z is fixed by chemistry), as [17]

$$S = k_B \ln \Omega = k_B N(z/2 - 1) \ln 2. \tag{4}$$

If the cooling rate has been too rapid for full exploration of phase space, the zero point is greater than (3), and the odd loops are no longer in a semi-dilute configuration.

5. No tunneling modes in $z = 3$ networks

There can be no tunneling modes in a random network with $z = 3$, which serves as a microscopic scaffolding for a-As or borate glass, for two reasons:

(i) for $z = 3$, an elementary rotation about the shared bond is an odd permutation, so that odd rings may here accommodate the identity permutation. Odd rings in $z = 3$ networks are not frustrated;

(ii) odd permutations of S_3 belong to one class only.

Tunneling modes are associated with odd rings, but do not occur in trivalent network glasses. Thus, the celebrated boroxol ring in B_2O_3 glasses is not a tunneling mode, even though the ring is odd (three boron–boron edges), the mode which it supports is local (classical, symmetrical breathing of the three oxygen atoms in the ring leaving boron atoms motionless) and decoupled from the other modes of the network. It shows up as a sharp Raman absorption peak at 100.2 meV, a high energy compared with the splitting of tunneling energy levels ($\leq 10^{-4}$ eV in silica), because it stretches bonds. This mode, discovered in 1953 by Goubeau and Keller [18], has been identified and explained by Frank Galeener [7]. It is not a tunneling mode, but, like tunneling modes, it is a dynamical signature of disorder.

6. Topological transformations between $z = 3$ and $z = 4$ networks

Several glasses (B_2O_3, As_2O_3, and the chalcogenides As_2S_3 and As_2Se_3, a-As) constitute trivalent networks (the oxygen, or chalcogen atoms only decorating the network). They do not have tunneling modes. However, the first two show sharp features in their Raman spectrum, which are absent in elemental network glasses like a-As. These localized excitations, decoupled from the rest of the network, have been shown [7] to be symmetrical breathing modes of the three oxygen atoms in boroxol rings. Decoupling from the network is due to the symmetry of the motion of the oxygen atoms, and to boron atoms remaining motionless in these normal modes (as shown by isotopic substitution [7]).

Although the network of B_2O_3 is trivalent, it is not a simple continuous random network as that of a-As. The structure contains a large number of boroxol rings, which are (planar) three-rings of $z = 3$ boron atoms (with edges decorated by oxygen, as usual, i.e., $(BO)_3$ rings), connected to the rest of the network by three edges.

As established by isotropic substitution [7], the symmetrical breathing mode of the three oxygen atoms in the boroxol ring is decoupled from the rest of the network, and shows up as a sharp Raman peak. Even though most recent experimental and theoretical evidence supports the result that 80% of the boron atoms in glassy B_2O_3 are in boroxol rings [19], their existence is still somewhat controversial (see the review of Hannon et al. in this volume [24]).

A boroxol ring can be regarded as the decoration of a $z = 3$ vertex by a triangle of eclipsed edges, called inverse T2 topological transformation in foams [20]. Decoupling to the rest of the network is best achieved if the bonds incident to the original vertex are staggered (Fig. 2). So, structurally, a boroxol ring is simply a decorated vertex in a trivalent continuous random network without three-rings, but, because it is constituted of six atoms (three moving oxygen), it has sufficient oscillator strength to show up dynamically as a sharp Raman absorbtion peak.

It is easy to construct a $z = 3$ network from a $z = 4$ continuous random network, simply by noticing that a $z = 4$ vertex can be split into two $z = 3$ vertices (separated by a staggered edge) by an ele-
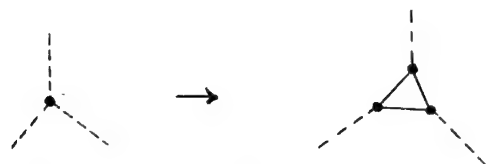
Fig. 2. Boroxol ring as a decoration of a $z = 3$ vertex (inverse T2 transformation). Dashed lines indicate staggered edges; plain lines indicate eclipsed edges.

mentary topological transformation, and relaxed. Because the new edge is staggered, it cannot support a flat interface and this transformation does not occur in foams where it is not topologically stable. It occurs in natural membranes, where it is a realization of the celebrated Bonnet transformation between T and G periodic minimal surfaces [21].

Consider three $z = 4$ vertices, linked by two bonds (Fig. 3). Split the middle vertex as above. The new $z = 3$ vertex gathers the new bond and the two linking bonds. Further splitting of the two side vertices completes the decomposition of the three $z = 4$ vertices into four $z = 3$ vertices. Inverse $T2$ decora-

tion of the central vertex creates the boroxol ring. If the two bonds of the original $z = 4$ network are staggered, the linking bonds, like the new bond, are also staggered, and the boroxol ring is best decoupled from the rest of the lattice. If one original bond is eclipsed, the linking bond is also eclipsed, and the decoupling, although possible, is less clear. Normal modes of a larger, planar structure of two or more boroxol rings separated from the network by staggered bonds will show up in the Raman spectrum.
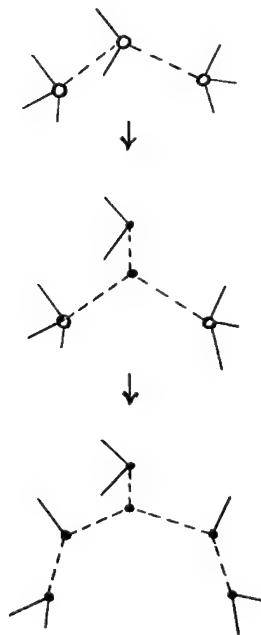
Recall that a $z = 4$ network is the natural scaffolding for a three-dimensional structure. The ease with which it can be split and decorated into boroxol rings make it understandable why so many boron atoms are on boroxol rings [19]. This construction can be applied to binary borate glasses, which are mixed $z = 3$ and $z = 4$ networks.

7. Conclusions

Tunneling modes are located on odd loops in $z = 4$ network glasses. They can be summarized in three statements. (1) Fig. 1 (two equivalent classical configurations about an odd ring, representative of a closed loop). (2) Gauge invariance implies that tunneling must occur (Eq. (2)). (3) This leads to a ground state landscape and excitation spectrum which is a direct product of independent tunneling modes between degenerate classical sectors. The experimental evidence that many tens of atoms are involved in the tunneling process is indeed consistent with the present model. Each classical configuration involves, at least, all the Si atoms on the rings constituting one odd loop. The average size of a loop can be inferred to be about 10 edge lengths, by maximum entropy consideration (see Section 4) or through the near-perfect homogeneity of glass beyond one unique length scale (≈ 4 nm in window glass), which is also the screening distance for stresses. This involves a considerable number of atoms, but moving very little.

Topological disorder shows up in the random network at two levels: the distribution of odd lines is random, and there is no generative symmetry. The space group is trivial, but even the involution associated with the bonds (reflection) never adds up to a consistent action on odd rings. It is indeed the action

Fig. 3. Construction of a trivalent network from a tetravalent continuous random network. Staggered edges are dashed. Full vertices have $z = 3$, open vertices $z = 4$.

of this involution which differentiates odd and even rings.

It is in the gauge parameter that the physical characteristics of the material are to be found, and one would have expected solid state physics to collect various gauges like stamps. Not at all. Gauge transformations, the permutations between bonds, are universal, like their sources, the odd loops in the network. They have spectacular and direct physical consequences in the low-temperature behaviour of glass. Odd loops have been observed indirectly by etch pits [22] and, probably, directly in electron microscopy by Liu et al. [23].

The chemical bond is the main actor in a gauge-invariant, disordered solid: as the energy-carrying connection, and as the geometrical constituent of the odd rings and loops responsible for frustration and tunneling modes. There is one pair of tunneling modes per odd loop. It is also the agent of the transformation from tetravalent to trivalent random networks, and decorates the vertices of the latter in boroxol rings.

Thus glasses, with their somewhat complicated ground state and very simple elementary excitations (direct product of tunneling modes or ring modes), are exact opposites from crystalline solids.

References

[1] S. Hunklinger and A.K. Raychaudhari, in: Progress in Low Temperature Physics Vol. 9, ed. D.F. Brewer (North-Holland, Amsterdam, 1986) p. 265;
W.A. Phillips, Amorphous Solids. Low-Temperature Properties (Springer, Berlin, 1981).

[2] P. Flubacher, A.J. Leadbetter, J.A. Morrison and B. Stoicheff, J. Phys. Chem. Solids 12 (1959) 53.

[3] E.W. Hornung, R.A. Fisher, G.E. Brodale and W.F. Giauque, J. Chem. Phys. 50 (1969) 4878.

[4] N. Rivier, J. Math. Chem. 13 (1993) 1; Philos. Mag. B69 (1994) 911.

[5] N. Rivier, Philos. Mag. A40 (1979) 859.

[6] N. Rivier, in: Geometry in Condensed Matter Physics, ed. J.F. Sadoc (World Scientific, Singapore 1987) p. 1.

[7] F.L. Galeener, in: The Structure of Non-crystalline Materials 1982, ed. P.H. Gaskell, J.M. Parker and E.A. Davis (Taylor and Francis, London, 1983) p. 337; F.L. Galeener and M.F. Thorpe, Phys. Rev. B28 (1983) 5802; F.L. Galeener and A.E. Geissberger, J. Phys. (Paris) Coll. C9 (1982) 343;
C.F. Windisch Jr. and W.M. Risen Jr., J. Non-Cryst. Solids 48 (1982) 307.

[8] J.Y. Duquesne and G. Belessa, J. Phys. C16 (1983) L65.

[9] G. Weiss and B. Golding, Phys. Rev. Lett. 60 (1988) 2547.

[10] J.L. Black, in: Glassy Metals I, ed. H.-J. Güntherodt and H. Beck (Springer, Berlin, 1981) p. 167.

[11] P.N. Keating, Phys. Rev. 145 (1966) 637.

[12] R. Alben, D. Weaire, J.E. Smith Jr. and M.H. Brodsky, Phys. Rev. B11 (1975) 2271.

[13] P.N. Sen and M.F. Thorpe, Phys. Rev. B15 (1977) 4030.

[14] N. Rivier, Adv. Phys. 36 (1987) 95.

[15] G. Kirchhoff, Pogg. Ann. Phys. 72 (1847) 32;
N. Biggs, Algebraic Graph Theory (Cambridge University, Cambridge, 1974).

[16] M. Orrit and J.L. Bernard, Phys. Rev. Lett. 65 (1990) 2716;
A. Zumbusch, L. Fleury, R. Brown, J. Bernard and M. Orrit, Phys. Rev. Lett. 70 (1993) 3584.

[17] N. Rivier and D.M. Duffy, J. Phys. C15 (1982) 2867.

[18] J. Goubeau and H. Keller, Z. Anorg. Allg. Chem. 272 (1953) 303.

[19] G.E. Jellison Jr., L.W. Panek, P.J. Bray and G.B. Rouse Jr., J. Chem. Phys. 66 (1977) 802;
A.C. Hannon, R.N. Sinclair and A.C. Wright, Physica A201 (1993) 375.
D.M. dos Santos-Loff, M. Micoulant and R. Kerner, Europhys. Lett. 28 (1994).

[20] D. Weaire and N. Rivier, Contemp. Phys. 25 (1984) 59.

[21] Y. Bouligand, in: Geometry in Condensed Matter Physics, ed. J.F. Sadoc (World Scientific, Singapore, 1987) p. 156.

[22] A. Chenevas-Paule, in: Semiconductors and Semimetals, ed. J. Pankowe (Academic Press, New York, 1984) ch. 12.

[23] B.X. Liu, C.H. Shang and H.D. Li, J. Phys.: Condens. Matter 3 (1991) 5769.

[24] A.C. Hannon, A.C. Wright, J.A. Blackman and R.N. Sinclair, these Proceedings, p. 78.

An interpretation of quasielastic neutron scattering and molecular dynamics simulation results on the glass transition

K.L. Ngai [a,*], C.M. Roland [a], G.N. Greaves [b]

[a] *Naval Research Laboratory, Code 6800, 4555 Overlook Ave., Washington, DC 20375-5320, USA*
[b] *EPSRC Daresbury Laboratory, Warrington, WA4 4AD, UK*

Abstract

Results of recent molecular dynamics simulations and quasielastic neutron scattering experiments performed on several glass-forming materials are discussed and analyzed to show that they are in agreement with the fundamental laws of relaxation proposed by the coupling model. Specifically, these results exhibit the existence of a temperature independent time, at which the correlation function crosses over from an exponential form, $\exp-(t/\tau_0)$, which holds for $t < t_c$ to a stretched exponential correlation function, $\exp-(t/\tau^*)^{1-n}$, which holds for $t > t_c$. Continuity of the correlation function at $t = t_c$ leads to the important relation: $\tau^* = [t_c^{-n}\tau_0]^{1/(1-n)}$ which has been formerly applied to explain many aspects of the dynamics of glass-forming materials. The characteristics of τ_0 indicate that it is the relaxation time of an independently relaxing species in accordance with the model.

1. Introduction

The glass transition is one of the oldest problems in physical science that has still not been resolved. One can date the first study of the glass transition to prehistoric times, when Babylonians and Egyptians made glass from desert sand. Over the course of time many different kinds of glass-forming materials have been found. Today we have glasses formed from inorganic, organic, metallic and polymeric materials. The study of the dynamics of glass-forming liquids and the search for a basic understanding of the glass transition phenomenon have not abated. In fact recently there is renewed interest from the physics community in this problem, as evidenced by the applications of microscopic probe experiments in-

cluding quasielastic neutron scattering [1–6] and molecular dynamics simulations [7–9]. We have also witnessed a surge in theoretical efforts to interpret these experiments [10–12]. Quasielastic neutron scattering (QENS) experiments and molecular dynamics simulations (MDS) can both monitor the dynamics of glass-forming liquids in the short time regime defined (approximately $10^{-14} < t < 10^{-9}$ s). This ability is to be contrasted with the much longer timescale (typically 10^2 s) associated with the conventional glass transition temperature, T_g. In spite of this disparity in timescales, QENS and MDS are crucial as microscopic probes that can critically test any microscopic theory or model of the glass transition.

QENS and MDS data have been published in the literature. The principal experimental results for diffusive motion of the atoms are contained in (i) the van Hove self-correlation function defined by $G_s(r, t) = \langle \delta[\{r_i(t) - r_i(0)\} - r]\rangle$, or (ii) equiva-

---
* Corresponding author. Tel: +1-202 767 6150. Telefax: +1-202 767 0546. E-mail: ngai@estd.nrl.navy.mil.

lently the intermediate scattering function defined by $F_s(Q, t) = \langle \exp\{-iQ[r_i(t) - r_i(0)]\}\rangle$, which is the spatial Fourier transform of $G_s(r, t)$, or (iii) the dynamic structure factor, $S_s(Q, \omega)$, given by the temporal Fourier transform of $F_s(Q, t)$ or (iv) the susceptibility, $\chi''(Q, \omega)$, which is the product $\omega S_s(Q, \omega)$. Experimental data represented by any of these functions contain contributions not only from the diffusive motion of the atoms but also from their vibrations (i.e., phonons). Thus, in comparing experiment with theory, it is of paramount importance to take into account the contribution of phonons to the relaxation data. There is evidence that relaxational and vibrational scattering are statistically independent processes, which justifies writing the intermediate scattering function as a product $F_s(Q, t) = F_{relax}(Q, t)F_{phonon}(Q, t)$ and the dynamic structure factor as a convolution $S_s(Q, \omega) = S_{relax}(Q, \omega) \otimes S_{phonon}(Q, \omega)$. This paper describes comparisons of experimental data with a theory of relaxation in complex correlated systems now generally referred to as the coupling model [13,14]. These comparisons show the Q and t dependences of $F_{relax}(Q, t)$ are in accord with the predictions of the coupling model. Parameters characterizing the relaxation process extracted from $F_s(Q, t)$ are found to have the physical meaning required by the coupling model.

2. The coupling model

The coupling model since its introduction in 1979 has repeatedly offered an accurate description of cooperative relaxation processes in dense packed correlated systems such as glass forming liquids [14]. It proposes the existence of a temperature insensitive crossover time, t_c, separating two time regimes in which the dynamics of relaxation differ. While the existence of t_c is suggested by theoretical considerations [13], its exact magnitude is not known a priori. Order of magnitude estimates of t_c obtained from comparing experimental data with the predictions of the coupling model locate it within the range $10^{-12} < t_c < 10^{-11}$ s for local segmental relaxation in polymers and translational and rotational motions in small molecular van der Waal liquids. An estimate roughly of 10^{-12} s has been suggested for ion motion in alkali borate glasses [15].

At short times, for $t < t_c$, the units relax independently, as if the intermolecular interaction had no effect, with a rate $W_0 \equiv 1/\tau_0$. However, for $t > t_c$, intermolecular interaction or constraints take hold, and on the average slow the independent relaxation rate. The result is that the effective relaxation rate obtained by averaging over all units has the time-dependent form $W(t) \propto W_0(t/t_c)^{-n}$, where n ($0 < n < 1$) is the coupling parameter indicating the degree of intermolecular cooperativity. As far as the normalized correlation function, $C(t)$, for translational or rotational motion is concerned, the immediate consequence are

$$C(t) = \exp(-t/\tau_0) \quad \text{for } t < t_c; \tag{1}$$

$$C(t) = \exp-(t/\tau^*)^{1-n} \quad \text{for } t > t_c. \tag{2}$$

The important relation between τ^* and τ_0 given by

$$\tau^* = [t_c^{-n} \tau_0]^{1/(1-n)}. \tag{3}$$

is a consequence of the requirement that the two forms (1) and (2) of the correlation function should be continuous at the crossover time, t_c. In many occasions in the past we have written a similar relation $\tau^* = [(1-n)\omega_c^n \tau_0]^{1/(1-n)}$ where the reciprocal of ω_c is the time at which the relaxation rate defined by $-(1/C(t)) \, \mathrm{d}C(t)/\mathrm{d}t$ are equal for the two correlation functions (Eqs. (1) and (2)). It can be easily shown that $t_c = (1-n)^{-1/n}\omega_c^{-1}$. Hence this relation and Eq. (3) are identical. The coupling parameter, n, through Eqs. (2) and (3) describes the effect that intermolecular interactions (or constraint dynamics) have in slowing the relaxation process.

The fractional exponential function given by Eq. (2) is identical to the relaxation function, $\exp[-(t/\tau)^\beta]$, first proposed by Kohlrausch [16] in 1847 to describe his electrical and mechanical relaxation data. Compilation of data taken over the past hundred and fifty years indicates that the Kohlrausch functions describe many relaxation processes in various families of materials rather well. Currently in the research community there are many efforts to explain the origin of the Kohlrausch function and meaning of the fractional exponent β. These efforts other than the coupling model include the mode–mode coupling theory of Götze and Sjögren [10,17], and the constraint theory of Phillips [18].

The three coupled relations given by Eqs. (1)–(3), were first proposed more than fourteen years ago and have remained unmodified [13,14]. They look deceptively simple but, in reality, when used together explain a host of important and often critical experimental fact concerning the viscoelastic response of amorphous polymers and small molecule glasses, and the diffusion of ions in glassy ionic conductors [14]. Most effective is the relation (3) between τ^* and τ_0, through which many previously puzzling properties have been explained (for a very recent review, see Ref. [14]). In these applications the experimental data had been obtained in the long time regime ($t \gg t_c$), which precludes direct observation of the crossover at t_c from exponential relaxation (1) to stretched exponential relaxation (2). Nevertheless, with the assumption of a temperature-insensitive t_c, the two coupled predictions (2) and (3) have been successful in explaining experimental data. Naturally, in view of this good agreement, it is desirable to directly verify the coupling model in its entirety (i.e., the existence of a temperature-independent t_c and the result in Eqs. (1)–(3)) either by rigorous theoretical proof or by performing experiments in time windows that span t_c. Recent attempts on the theoretical front based on the dynamics of chaotic Hamiltonians have produced encouraging results [13], although there is still a long way to go before the problem can be considered solved. On the other hand direct, experimental tests of the coupling model can be performed using QENS and MDS, which monitor

the dynamics in the time window of $10^{-14} < t < 10^{-9}$ s, where the expected crossover of relaxation dynamics at t_c can be observed directly.

3. Quasielastic neutron scattering

The quasielastic neutron scattering measurements were made by Colmenero and co-workers [5,6] using the TOF spectrometer IN6 at the Institut Laue–Langevin, Grenoble, France. The incoherent scattering function, $S(Q, \omega)$, was obtained for various scattering wavevectors, Q, in the range $0.2 < Q < 2$ Å^{-1} and energy transfer, $\hbar\omega$, up to 5 meV at constant temperatures in the range $T_g{-}8 < T < T_g + 100$ K. The poly(vinylchloride) (PVC) sample studied has a glass temperature $T_g = 358$ K and a number-averaged molecular weight $M_n = 4.55 \times 10^4$. The relaxation contribution, $S^{relax}(Q, \omega)$, to the scattering was isolated after removal of the harmonic vibrational contribution from the measured $S(Q, \omega)$, taking into account the instrument resolution. Fourier transform of $S^{relax}(Q, \omega)$ gives the normalized intermediate scattering function $I_0(Q, t) \equiv F_{relax}(Q, t)$. The results are reproduced in Fig. 1(a) for different temperatures at a constant Q value of 1.5 Å^{-1}. It can be seen that, independent of T and Q, all the intermediate scattering functions exhibit a break in curvature at a time of about 1.7 ps, signifying a crossover of $I_0(Q, t)$ from one regime at short times ($t < 1.7$ ps) to another at long times ($t > 1.7$ ps). This crossover
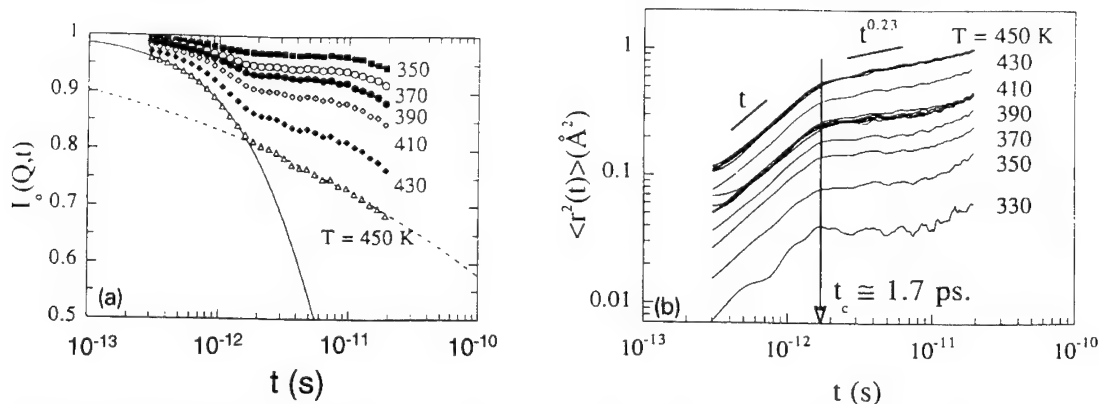
Fig. 1. (a) Normalized intermediate scattering function for PVC at $Q = 1.5$ Å^{-1} at different temperatures [5]. (b) Mean square displacement obtained from data in (a). For 450 K, data from different values of Q are plotted together [5].

between two different dynamic regimes is more clearly seen in the mean squared displacement of the scattering centers, $\langle r^2(t)\rangle$, which can be obtained from the $I_0(Q, t)$ data by solving the equation $I_0(Q, t) = \exp[-Q^2\langle r^2(t)\rangle/6]$. The values of $\langle r^2(t)\rangle$ so obtained [5,6] at different temperatures are plotted against time in Fig. 1(b), and the existence over a considerably large temperature range of a T-independent crossover time (approximately equal to 1.7 ps) is clear. In the short time regime of $t < 1.7$ ps, $\langle r^2(t)\rangle$ is proportional to t, while for $t > 1.7$ ps, $\langle r^2(t)\rangle \propto t^{1-n}$ with $n = 0.77$. This sublinear time dependence of $\langle r^2(t)\rangle$ was found previously using a longer time window of $10^{-11} < t < 10^{-8}$ s [19,20]. It has been shown to originate from the local segmental (alpha) relaxation of PVC, with a stretched exponential form, $\exp[-(t/\tau^*(Q, T))^{1-n}]$, for the intermediate scattering function.

To see if this crossover corresponds to the one proposed by the coupling model, the intermediate scattering function data in the short time regime was fitted by [5,6]

$$I_0(Q, t) = \exp - (t/\tau_0(Q, T)) \quad \text{for } t < 1.7 \text{ ps} \tag{4}$$

and the data in the long time regime by the stretched exponential (see Fig. 1(a))

$$I_0(Q, t) = \exp - [t/\tau^*(Q, T)]^{1-n}$$
for $t > 1.7$ ps $\tag{5}$

with the exponent $1 - n$ taken to be that obtained from $\langle r^2(t)\rangle \propto t^{1-n}$ (i.e., $1 - n = 0.23$ for $T = 430$

and 450 K (see Fig. 1(b))). While fits to Eq. (4) (solid curve in Fig. 1(a)) in the short time regime have been carried out successfully in the entire temperature range, fits to Eq. (5) in the long time regime can be carried out with confidence at only the two highest temperatures, 430 and 450 K, where the $I_0(Q, T)$ data decrease significantly with time, before being cut off by the long time edge of the time window. These fits, shown as dashed curves in Fig. 1(a), describe well the experimental $I_0(Q, T)$ at $T = 430$ and 450 K.

From these fits of the experimental data in the two separate time regimes using Eqs. (4) and (5), τ_0 and τ^* were obtained as a function of Q and T. For τ_0 it was found that

$$\tau_0(Q, T) \propto Q^{-2} \exp[(5.8 \text{ kcal/mol})/RT]. \tag{6}$$

The Q^{-2} dependence indicates simple diffusion of the scattering centers, consistent with independent relaxation of local segments without the intermolecular interaction expected for $t < t_c$. The Arrhenius temperature dependence is valid over a temperature range and has an activation enthalpy of about 6 kcal/mol. This enthalpy is comparable to the conformational energy barrier of a PVC chain deduced before from different measurements [21]. Such a temperature dependence provides additional support for the coupling model interpretation of the short time ($t < t_c$) dynamics. On the other hand, for τ^*, combining the current TOF neutron scattering data with the previously published neutron backscattering data, we find $\tau^* \propto Q^{-9}$, similar to earlier results
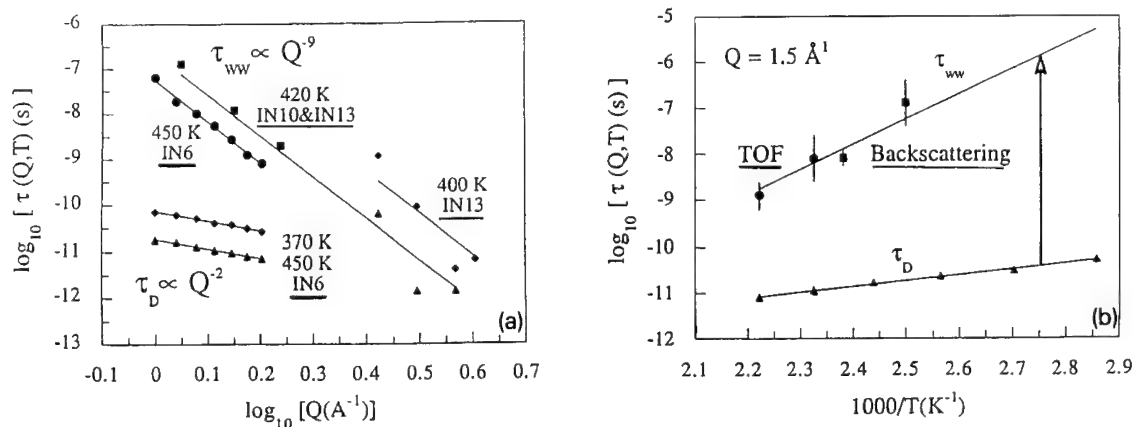
Fig. 2. (a) Q-dependences of τ_0 and τ^* [5]. (b) T-dependences of τ_0 and τ^* [5].

[19,20] based on backscattering data alone. Substituting $\tau_0(Q, T)$ given by Eq. (6) into Eq. (3), recalling the fact that t_c is independent of Q and T and $n = 0.77$, the coupling model predicts

$$\tau^*(Q, T) \propto Q^{-2/(1-0.77)}$$

$$\times \exp\{25 \ (\text{kcal/mol})/RT\}. \quad (7)$$

These predicted temperature and Q dependencies of τ_0 and τ^* are summarized and illustrated respectively in Figs. 2(a) and (b). The predictions are in good agreement with the experimental data. Similar results have been obtained for other polymers including poly(vinylmethylether), polybutadiene and polyisoprene [22]. Thus, we conclude that neutron scattering data directly corroborate the coupling model.

Questions can be raised on the plausibility of the observation of diffusive motion (consistent with the Q^{-2} dependence of τ_0 in Eq. (6)) in the short time regime of $3 \times 10^{-13} < t < t_c$. In fact, the existence of a multitude of high frequency vibrational (bond bending and stretching) modes provides the fast variables (i.e., heat bath) that enable 'diffusion' of the hydrogen as seen by the neutrons. In the next section we discuss molecular dynamics simulation of small molecule liquids and polymers. In these simulations [7–9], the same crossover phenomenon seen by incoherent neutron scattering are obtained, with similar t_c for both $F_s(q, t)$ and the reorientational time correlation function, $M_k(t) = \langle P_k[\cos\theta(t)]\rangle$, where $P_k(x)$ is the Legendre polynomial of order k, and $\theta(t)$ is the reorientation angle of a vector at time, t. For reorientational motion, the rotational diffusion relaxation time does not have any Q-dependence, and it is obvious that rotational diffusion can occur on timescales of the order of a picosecond.

4. Molecular dynamics simulations

In recent years improvement in the technique has made molecular dynamics simulation (MDS) a powerful tool to investigate the dynamics of molten salts [7], glass-forming small molecule liquids [8] and polymers [9]. Realistic potentials have been used to represent the interactions between the molecular units, making the results of computer experiments as quantitatively accurate as actual experiments. In ad-

dition, information extracted from MDS are often richer than that from real experiments. Thus, these MDS data provide additional tests of the theoretical basis of the coupling model. In this section we analyze one set of MDS data [9] and show that the results confirm the coupling model's description of the dynamics.

Roe [9] has performed MDS of polyethylene (PE). The intermolecular interactions are of the short range van der Waals kind, represented by Lennard–Jones potentials. $F_s(Q, T) = \langle \exp\{-iq \cdot [r_i(t) - r_i(0)]\}\rangle$, where $r_i(t)$ is the position of the ith segment at time, t, has been evaluated for different temperatures and several values of the wavevector, Q. Results for $Q = 1.38 \ \text{Å}^{-1}$ are shown in Ref. [9]. At temperatures < 108 K there is an initial decay of $F_s(Q, T)$ which can be ascribed to harmonic phonons, with no additional relaxation process observed in the time window. The assignment of the initial decay to harmonic phonons is consistent with the plateau value, $F_s(Q, T \rightarrow \text{large})$, being well described by the Debye–Waller factor, $\exp(-WQ^2 T)$, where W is a constant independent of Q and T [23]. A semilog plot of the Debye–Waller factor obtained from the low temperature $F_s(Q, T)$ data yields a straight line which can be used to extrapolate the phonon contribution to higher temperatures. This extrapolation clearly indicates that the contribution of phonons to $F_s(Q, T)$ has to be taken into consideration at all temperatures. At temperatures $\geqslant 132$ K, additional relaxation processes appear in the time window of Fig. 3, making it difficult to isolate the individual components. We can account for the harmonic phonon contribution to $F_s(Q, T)$ at higher temperatures by Fourier transformation of the $F_s(Q, T)$ data at low temperatures (say $T < 108$ K), where only the harmonic phonons contribute, followed by scaling of the resultant dynamic structure factor, $S(Q, \omega)$, by the Bose factor and the Debye–Waller factors [23]. The inverse Fourier transform of the scaled $S(Q, \omega)$ yields $F_s^{\text{ph}}(Q, t)$, the density–density correlation function from phonons at higher temperatures. Assuming that scattering by harmonic phonons and relaxation are statistically independent processes, we write the intermediate scattering function as a product $F_s(Q, t) = F^{\text{phonon}}(Q, t)F^{\text{relax}}(Q, t)$. Eq. (3) can be solved for $F^{\text{relax}}(Q, t)$ at any T. The results can be compared with the predictions of the coupling model in a
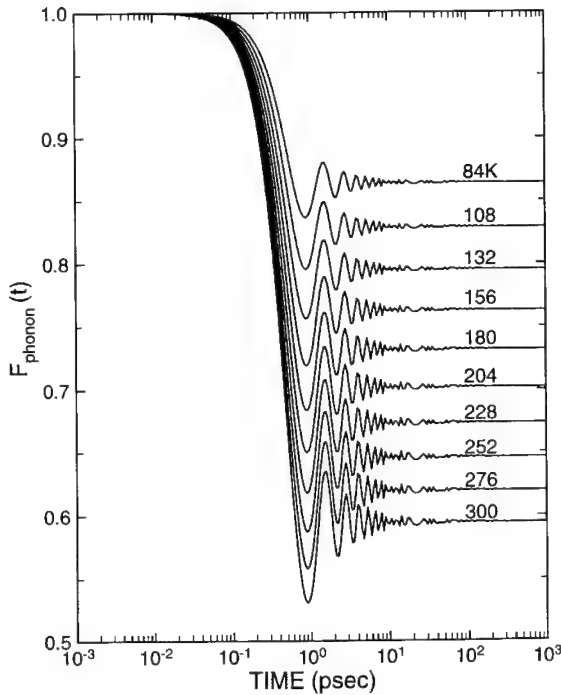
Fig. 3. $F_{phonon}(Q, t; T)$ plotted against t for $q = 1.38$ Å^{-1} at different temperatures.

similar manner as done previously by Colmenero and co-workers [5,6] using their QENS data.

In this paper we model the phonons contributing to $F_{phonon}(Q, t; T)$ at temperature, T, by a Debye spectrum with density of normal modes, $g_D(\omega)$, represented in the form of $g_D(\omega) = (3/2\pi^2)(\omega^2/c^2) \equiv K\omega^2$ for $\omega < \omega_D$ and $g_D(\omega) = 0$ for $\omega > \omega_D$. Although the Debye spectrum is only a gross approximation, we use it because of simplicity and to avoid the possibility of biasing the final results. Using a well known expression [24], $F_{phonon}(Q, t; T)$ is calculated for a Debye spectrum of phonons $g_D(\omega)$ according to the formula $F_{phonon}(Q, t; T) = \exp(-Q^2 W(t, T))$ at T, where

$$W(t, T) = KT^2 \int_0^{\omega_D} g_D(\omega)[1 - \cos(\omega t)]\,\omega^{-1}$$
$$\times [2/(\exp(\hbar\omega/kT) - 1) + 1]\,d\omega. \tag{8}$$

The parameters K and ω_D are adjusted to fit the experimental $F_s(Q, t; T)$ obtained at the lowest temperatures, where $F_{relax}(Q, t; T) = 1$ throughout the

experimental range of time. For the data of Roe [9] at $Q = 1.38$ Å^{-1}, we find $\omega_D = 5 \times 10^{12}$ rad/s and $K = 6.83 \times 10^{-30}$. The $F_{phonon}(Q, t; T)$ at all temperatures for which Roe has made his simulations are displayed in Fig. 3. We can now assess the coupling model by examining whether the experimental $F_s(Q, t; T)$ can be represented at each temperature by

$$F_s(Q, t; T) = F_{phonon}(Q, t; T)$$
$$\times \begin{cases} \exp - (t/\tau_0(T)) & \text{for } t < t_c \\ \exp - (t/\tau^*(T))^{1-n} & \text{for } t > t_c \end{cases}, \tag{9}$$

for a temperature-independent t_c such that the continuity condition, $\exp - (t/\tau_0(T)) = \exp - (t/\tau^*(T))^{1-n}$, is satisfied always at $t = t_c$. We start by first choosing a t_c and then for each temperature find two independent parameters, τ_0 and n (the third parameter τ^* is automatically fixed by Eq. (3)), such that the products on the right hand side of Eq. (9) give a good fit to the experimental $F_s(Q, t; T)$. In carrying out this, we find that for good fits at all temperatures can only be obtained for values of t_c limited to a narrow range around 2 ps.

The results of the best fits for $t_c = 2$ ps are shown in Fig. 4. The $F_{relax}(Q, t; T)$ used to obtain these fits are displayed in Fig. 5. At each temperature, $F_{relax}(Q, t; T)$ is comprised of two pieces: $\exp - (t/\tau_0(T))$ for $t < t_c$ and $\exp - (t/\tau^*(T))^{1-n(T)}$ for $t > t_c$. The relaxation times, τ_0 and τ^*, and the
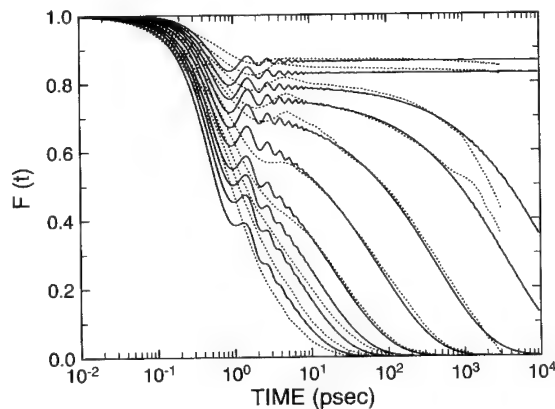
Fig. 4. Theoretical fits (solid curves) to experimental data (dotted curves) $F_s(Q, t;T)$ of polyethylene.
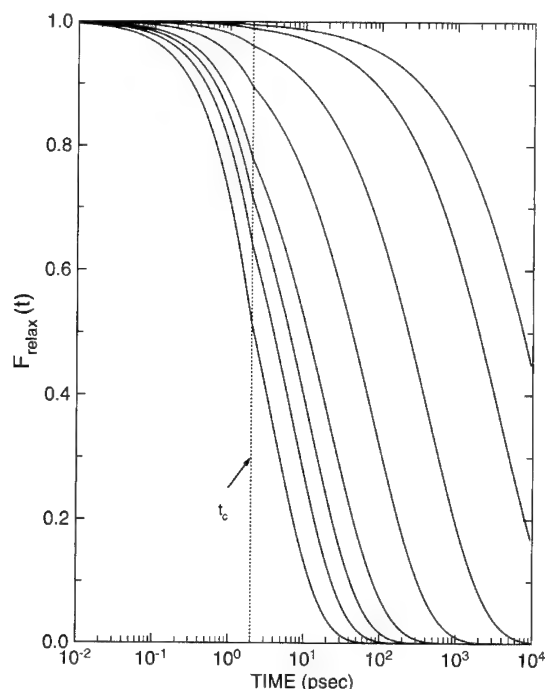
Fig. 5. $F_{relax}(Q, t;T)$ at different temperatures.

Fig. 7. The coupling parameter, n, as a function of temperature.

Fig 6. Arrhenius plot of τ_0 and τ^* of polyethylene.

coupling parameter, n, are plotted as a function of temperature in Fig. 6 and Fig. 7, respectively. The temperature dependence of τ_0 is approximately Arrhenius with an activation enthalpy of about $E_a = 2.4$ kcal/mol. It is apparent that the temperature dependence of τ_0 becomes milder at high temperatures ≥ 252 K, which makes the overall activation energy to appear smaller. Excluding the three highest tem-

peratures, the activation enthalpy is close to 3 kcal/mol.

The coupling parameter has the value of 0.40 and exhibits a decrease at high temperatures. This decrease of n at high temperatures may be correlated with the corresponding milder temperature dependence of τ_0 seen there. The value for E_a is roughly what is expected for the activation energy of the conformational energy barrier for a single polyethylene chain. As modelled by Roe, this is about 3 kcal/mol [9]. This is a striking agreement for the microscopic activation energy which governs local segmental motion of a single chain. The stretch exponent, $\beta \equiv 1 - n$, determined for polyethylene is close to that expected from the empirical correlation between β and the steepness of the polymer's cooperative plot [25]. The coupling parameter $n = 0.40$ for polyethylene is smaller than that of all other polymers with bulkier monomer structure. The much larger coupling parameter ($n = 0.77$) found for polyvinylchloride (PVC) from QENS as well as dielectric and mechanical measurements, arises from its larger intermolecular interaction due to the polar nature of the PVC backbone. The disparity of the values of n in PVC and PE is directly responsible for the different appearance of the $F_{relax}(Q, t; T)$s obtained for these two polymers (see Fig. 1(a) and Fig. 5). In PVC we see clearly a break in the $F_{relax}(Q, t; T)$ at the crossover time, t_c. For PE, the break at the crossover is less obvious (Fig. 5) due to the smaller n. Nevertheless, in PE the initial exp $-(t/\tau_0(T))$ decay for $t < t_c$ is necessary to explain the
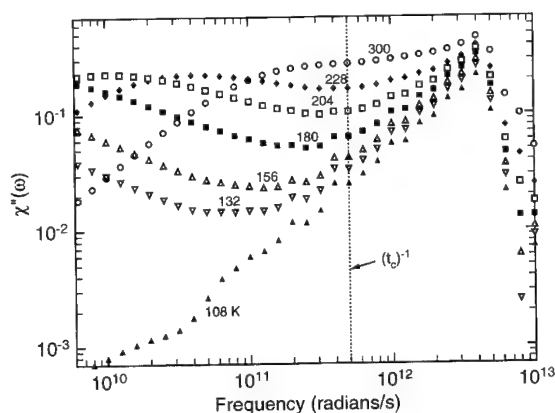
Fig. 8. Calculated $\chi''(\omega)$ at different temperatures.

departure of $F_s(Q, t; T)$ from the phonon contribution $F_{phonon}(Q, t; T)$ at short times.

Finally we calculate from $F_s(Q, t; T)$ by temporal Fourier transform the functions $S(Q, \omega; T)$ and $\chi''(Q, \omega; T)$. The results for $\chi''(\omega)$ are shown in Fig. 8. The resemblance of these results to those obtained by depolarized light scattering on $[Ca(NO_3)_2]_{0.4}[KNO_3]_{0.6}$ and salol [26] merits futher discussion, but is beyond the scope of the present paper.

5. Conclusion

Quasielastic neutron scattering and molecular dynamics simulation data provide critical tests of the basic premise of the coupling model. From the analyses of the data given above for two polymers and other glass-forming materials (including the molten salt $[Ca(NO_3)_2]_{0.4}[K(NO)_3]_{0.6}$ [7] and ortho-terphenyl [8]) not discussed here, we conclude that these experimental data are in agreement with the fundamental laws of relaxation (specifically, Eqs. (1)–(3) with a temperature-independent t_c) for interacting systems as postulated by the model. In addition to this simplicity, the model has the virtue of being applicable to different materials and phenomena. By means of Eq. (3), many observed anomalies can be explained. Some examples that support these claims can be found in a recent review [14].

References

[1] W. Knaak, F. Mezei and B. Farago, Europhys. Lett. 7 (1988) 529.
[2] B. Frick, B. Farago and D. Richter, Phys. Rev. Lett. 64 (1990) 2921.
[3] W. Petry, E. Bartsch, F. Fujara, M. Kiebel, H. Sillescu and B. Farago, Z. Phys. B83 (1991) 175.
[4] M. Kiebel, E. Bartsch, O. Debus, F. Fujara, W. Petry and H. Sillescu, Phys. Rev. B45 (1992) 10301.
[5] J. Colmenero, A. Arbe and A. Alegría, Phys. Rev. Lett. 71 (1993) 2603.
[6] J. Colmenero, Physica A201 (1993) 38.
[7] G.F. Signorini, J.L. Barrat and M.L. Klein, J. Chem. Phys. 92 (1990) 1294.
[8] L.J. Lewis and G. Wahnström, J. Non-Cryst. Solids 172–174 (1994) 69.
[9] R.J. Roe, J. Chem. Phys. 100 (1994), 1610; J. Non-Cryst. Solids 172–174 (1994) 77.
[10] W. Götze and L. Sjögren, Rep. Progr. Phys. 55 (1992) 241.
[11] X.C. Zeng, D. Kivelson and G. Tajus, J. Non-Cryst. Solids 172–174 (1994) 61.
[12] P.K. Dixon, N. Menon and S.R. Nagel, Phys. Rev. E50 (1994) 1717;
    H.Z. Cummins and G. Li, Phys. Rev. E50 (1994) 1720.
[13] K.L. Ngai, Comment Solid State Phys. 9 (1979) 127; K.L. Ngai and R.W. Rendell, J. Non-Cryst. Solids 131–133 (1991) 233; K.L. Ngai, S.L. Peng and K.Y. Tsang, Physica, A191 (1992) 523; K.Y. Tsang and K.L. Ngai, to be published.
[14] K.L. Ngai, in: Disorder Effects in Relaxation Processes, ed. A. Blumen and R. Richert (Springer, Heidelberg, 1994) p. 89.
[15] K.L. Ngai and H. Jain, Solid State Ionics 18&19 (1986) 362.
[16] R. Kohlrausch, Ann. Phys. (Leipzig) 12 (1847);
    G. Williams and D.C. Watts, Trans. Faraday Soc.66 (1970) 80.
[17] W. Götze and L. Sjögren, J. Non-Cryst. Solids 172–174 (1994) 16.
[18] J.C. Phillips, J. Non-Cryst. Solids 172–174 (1994) 98.
[19] J. Colmenero, A. Arbe, A. Alegría and B. Frick, Phys. Rev. Lett. 69 (1992), 478.
[20] K.L. Ngai, J. Colmenero, A. Arbe and Alegría, Macromolecules 25 (1992), 6727.
[21] K.L. Ngai and A.F. Yee, J. Polymer Sci. B: 29 (1991) 1493.
[22] J. Colmenero, private communication (1994).
[23] N.W. Ashcroft and N.D. Mermin, Solid State Physics (Holt, Rinehart and Winston, New York, 1976) appendix N.
[24] We thank Prof. Wolfgang Dieterich for an illuminating discussion.
[25] K.L. Ngai and C.M. Roland, Macromolecules 26 (1993) 6824.
[26] H.Z. Cummins, W.M. Du, M. Fuchs, W. Götze, A. Latz, G. Li and N.J. Tao, Physica A201 (1993) 23.

Dielectric relaxation in supercooled 1-propanol

B. Schiener, R. Böhmer *

Institut für Festkörperphysik, Technische Hochschule, D-64289 Darmstadt, Germany

Abstract

By combining time- and frequency-domain techniques, the dielectric response of 1-propanol has been measured in a spectral range covering eleven decades. In particular it has been demonstrated that the dielectric loss due to the main relaxation in 1-propanol exhibits the Debye width up to timescales of 1000 s. In order to extend the range in which the dynamics of propanol can be exploited to high temperatures, conductivity relaxation due to ionic impurities has been used. The occurrence of high-frequency relaxation processes has been studied in both isomers of propanol. It is shown that the 1-propanol data yield a master curve in a previously suggested scaling representation. However, owing to the presence of the high-frequency excitations, no agreement with the universal scaling form is obtained.

1. Introduction

Amorphous materials as diverse as supercooled liquids, metallic glasses and proteins exhibit a wealth of universal properties [1]. Well known are the low-energy excitations responsible for the anomalous thermal properties at temperatures, $T < 10$ K [2], and for the enhanced vibrational density of states as seen by neutron and light scattering techniques [3]. Also the vitrification process and the supercooled liquid state are typically described by such salient and universal features as non-exponential relaxation, departures from simple thermally activated response [4], physical aging [5] and cooling-rate-dependent thermodynamic signatures [6]. A correlation among several of these features has long been anticipated

[7,8]. By quantifying the behavior of amorphous matter using the fragility index, m [9], it has recently been documented that the deviations from the Arrhenius dependence of the relaxation times are connected with the degree of non-exponential relaxations as well as with many other properties for a large number of glass-forming materials [1,6,10,11]

It is well recognized, however, that monohydric aliphatic alcohols exhibit exceptions from some of these correlations in several respects. Although the hydrogen-network-forming alcohols are intermediately fragile, dielectric experiments revealed a monodispersive primary relaxation in the audiofrequency range [12,13]. Also the step $\Delta C_p(T_g)$ in the specific heat at the glass transition temperature, T_g, is much more pronounced than in non-hydrogen-bonded liquids of comparable fragility [14].

Some of these startling observations have been rationalized by pointing out that a self-micellization phenomenon may occur in these materials [14]. Hence the notion has developed that monohydric alcohols are heterogeneous liquids in the sense that a large portion of the molecules are involved in the self-as-

---

* Corresponding author. Present address: Institut für Physikalische Chemie, Johannes Gutenberg-Universität, Jakob Welder Weg 15, D-55099 Mainz, Germany. Tel: +49-6131 392 536. Telefax: +49-6131 394 196. E-mail: bohmer@pc-aak.chemie.uni-mainz.de.

sembling process, while a minor fraction (percent range) of molecules are not part of the network [12–14]. It is also pointed out that in nuclear magnetic resonance and low frequency viscoelastic experiments indications for strong deviations from monodispersive primary relaxation processes have been obtained [15].

In order to address the question concerning the nature of the primary relaxation in supercooled monohydric alcohols we have studied the dielectric relaxation primarily of supercooled 1-propanol (or n-propanol, $CH_2OH–CH_2–CH_3$) but also of 2-propanol (or iso-propanol, $CH_3–CHOH–CH_3$) covering a broad dynamic range. Moreover, conductivity relaxation has been investigated to determine the diffusion of mobile ions in propanol.

This paper is organized as follows. In the following section we give some experimental details. Then, in Section 3 the experimental results obtained in the frequency and time domains are presented. Finally in Section 4 master plots for the dielectric behavior of propanol are compared and the temperature dependence of the relaxation timescales are discussed.

2. Experimental procedures

The complex dielectric constant, $\epsilon = \epsilon' - i\epsilon''$, was measured using two experimental set-ups. In the frequency domain (40 Hz $< \nu <$ 4 MHz), measurements were carried out using an impedance analyzer (4192A from Hewlett-Packard) while ramping the temperature at rates of -0.5–2 K/min in order to avoid crystallization. For the time range 10^{-5}–10^4 s, a dielectric spectrometer was used [16] which is based on a design described by Mopsik [17]. Most time-domain experiments were carried out at relatively low temperatures at which the tendency to crystallize is less pronounced. Therefore the temperature could be stabilized, typically to within ± 0.1 K, during the entire data acquisition. The sample capacitors were of parallel plate design and exhibited empty cell capacitances of 10–20 pF. They were immersed into the liquids which had stated purities larger than 99% (1-propanol) and 99.7% (2-propanol).

3. Results

Some dielectric results of propanol as taken in the frequency domain are shown in Fig. 1. In the upper panel of this figure, the real part of the dielectric constant, $\epsilon'(T)$, of 1-propanol is seen to exhibit a Curie type of behavior at high temperatures, which for low frequencies is superimposed by conductivity contributions originating from the motion of mobile (impurity) ions.

The large steps in $\epsilon'(T)$ are associated with the primary or α-relaxation. At somewhat lower temperatures indications for another (α'-) relaxation process
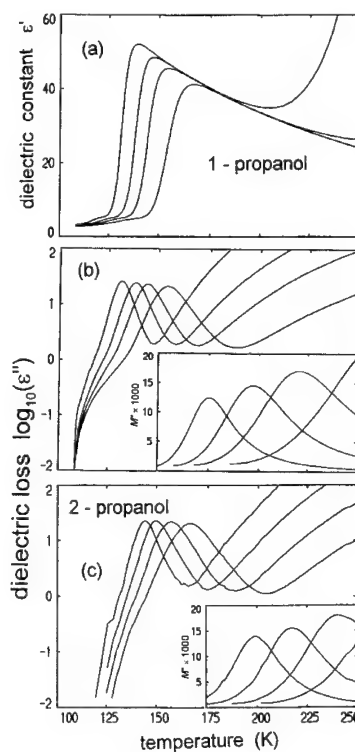
Fig. 1. Temperature dependence of the dielectric constant (a) and loss (b) of 1-propanol. For comparison, the dielectric loss of 2-propanol is also shown (c). Measurement frequencies were 0.35, 2.1, 7.9 and 47 kHz for 1-propanol and 0.4, 1.9, 8.6 and 40 kHz for 2-propanol. Note that the high-frequency permittivities of 1-propanol are $\epsilon_\infty = 5.2$ and $\epsilon'_\infty = 2.7$. The dielectric losses are plotted on a logarithmic scale. The insets show the temperature-dependent electrical modulus as calculated from the complex permittivity using Eq. (1). Frequencies are the same as given above. The data have been taken in steps of 1 K; for the purpose of clarity they are represented as lines.

can be obtained from the slightly frequency-dependent dielectric constant. Correspondingly, the dielectric loss, ϵ'', of 1-propanol, shown in Fig. 1(b) on a logarithmic scale, in addition to the main peak, exhibits a weak shoulder at low temperatures. This shoulder appears even weaker in 2-propanol (see Fig. 1(c)). At high temperatures, the ionic conductivities in both samples lead to an increase in ϵ'' with temperature.

The conductivity relaxation is most clearly seen from a modulus representation of the data. The insets of Fig. 1 show the imaginary parts of the electrical modulus

$$M'' \equiv \epsilon'' \left[(\epsilon')^2 + (\epsilon'')^2 \right], \tag{1}$$

for 1- and 2-propanol. It is clearly seen that $M''(T)$ peaks at temperatures much higher than the dielectric losses at the same frequencies. This observation is consistent with what has been reported previously for other supercooled liquids [18,19].

In order to measure the relaxation behavior of 1-propanol over a broad dynamical range we have used time-domain spectroscopy. The experiments were performed by applying an electric field to the sample and monitoring the time-dependent sample capacitance, $C(t)$, at constant field. The raw data from this study, i.e., the voltages across the feedback capacitor which are proportional to the variations in $C(t)$, are shown in Fig. 2 for a number of temperatures. The shape of the relaxation function, $C(t)$, appears to be invariant. However it is clearly seen that the position as well as the magnitude of the step in $C(t)$ depend strongly on temperature, consistent

Fig. 3. Real part (a) and imaginary part (b) of the dielectric constant of 1-propanol. The solid lines are calculated using the Debye expression, Eq. (3). This equation yields good fits except for frequencies that are much larger than the peak frequencies, ν_α.

with the observations apparent from Fig. 1. In order to allow for a direct comparison of both sets of data, we have transformed the $C(t)$ data into the frequency domain using [17]

$$\epsilon(\omega) = \epsilon_\infty + \frac{1}{C_0} \int_0^\infty C(t) \, e^{i\omega t} \, dt. \tag{2}$$

Together with the data measured directly in the frequency domain the complex dielectric constant, $\epsilon(\omega)$, of 1-propanol is thus obtained in a frequency range covering 11 decades (see Fig. 3). The solid lines in this figure have been calculated using the Debye form

$$\epsilon(\omega) = \epsilon_\infty + (\epsilon_s - \epsilon_\infty)(1 + i2\pi\nu\tau_\alpha)^{-1}. \tag{3}$$

This equation describes the dielectric response in systems in which the dynamics are governed by a single relaxation time τ_α. In Eq. (3) the high-frequency permittivity is denoted by ϵ_∞, and $(\epsilon_s - \epsilon_\infty)$

Fig. 2. Voltage, U, across the feedback capacitor versus the logarithm of time. The variation in U is proportional to the polarization of 1-propanol. Temperatures from left to right are 130.0–102.0 K in steps of 2.0 K.

is the dispersion strength. Eq. (3) provides a good fit to the experimental results except for frequencies about 1.5 orders of magnitude larger than the peak frequencies as can be seen in Fig. 3(b).

4. Discussion

The deviations from the Debye relaxation process are most clearly revealed by double-logarithmic plots of the dielectric loss, normalized to peak frequency, ν_α, and peak amplitude ϵ''_{max}. Master plots for both propanol isomers are shown in Fig. 4. It is clearly seen that the deviations showing up at high frequencies are more pronounced in 1-propanol. This observation is consistent with the fact that the low-temperature shoulders visible in the dielectric loss, $\epsilon''(T)$, presented in Fig. 1(c) are only relatively weakly developed. Therefore it can be ruled out that the high-frequency contributions to $\epsilon''(T)$ of 1-propanol are entirely due to those excitations which are universally observed in other amorphous materials [4,20]. This is most convincingly demonstrated by scaling the dielectric loss into the form $(1/W) \times \log_{10}[(\epsilon''/\epsilon''_{max})/(\nu/\nu_\alpha)]$ versus $(1/W) \times (1 + 1/W) \times \log_{10}(\nu/\nu_\alpha)$ shown in Fig. 5. This type of representation has been shown by Dixon et al. [4] to lead to the collapse of data from many different glass
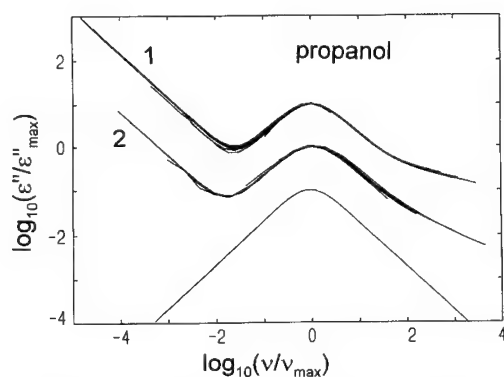
Fig. 4. Master plot of the dielectric losses (represented as solid lines) measured for 1-propanol (1) and 2-propanol (2). The data have been normalized with respect to the peak frequency, ν_α, and to the local maximum in the dielectric loss, ϵ''_{max}. The solid line shows the shape of the loss according to the Debye equation. The ordinate axis applies to 2-propanol. The data for 1-propanol have been shifted upwards by one order of magnitude.
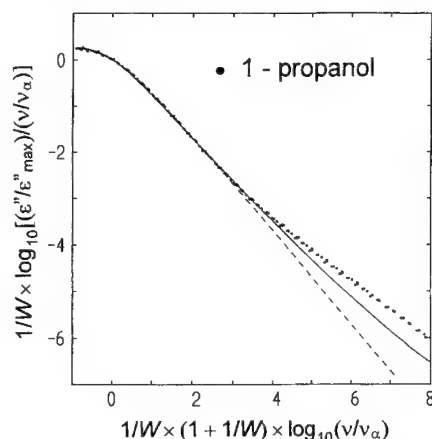
Fig. 5. Dielectric loss of 1-propanol, scaled according to the procedure suggested by Dixon et al. [4]. The results are compared with the scaled data of propylene glycol [16] (represented as solid line) which follow the master curve obtained by these authors. For comparison the stretched exponential (or Kohlrausch–Williams–Watts or KWW) form is represented as dashed line. Note that in this representation the KWW form is identical to the Debye form if W is properly adjusted. W is the normalized width of the dielectric loss (in decades). Note that propanol exhibits the Debye width, $W = 1$, for which this plot reduces to $\log_{10}[(\epsilon''/\epsilon''_{max})/(\nu/\nu_\alpha)]$ versus $2\log_{10}(\nu/\nu_\alpha)$.

formers onto a single curve if the width, W, is suitably chosen [21].

Fig. 5 shows that the results for 1-propanol which contain contributions from two different processes expectedly do not follow the scaling curve (shown as solid line). However 2-propanol shows only slight deviations from the universal curve at the highest frequencies (not shown). Nonetheless a master curve is obtained for 1-propanol, indicating that the two relaxation processes are closely related. In this context it is interesting to mention that it has been shown previously that the scaling does not work at high frequencies if contributions from β-relaxations are included [19]. However if only the α-relaxation is considered then the scaling works not only for supercooled liquids but also applies to the cases of amorphous polymers [22] and orientationally disordered crystals [23].

It is thus suggestive that the primary relaxation of propanol also obeys this scaling form. Then, by subtracting the low-frequency contribution, it is clear that the high-frequency process is to be characterized by a timescale and a spectral shape which are differ-

B. Schiener, R. Böhmer / Journal of Non-Crystalline Solids 182 (1995) 180–185
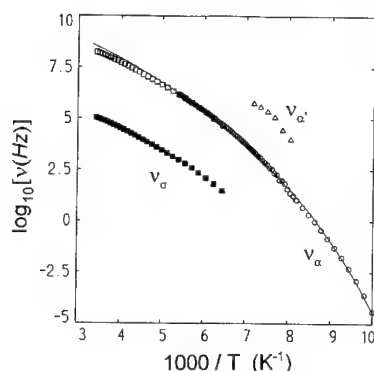
Fig. 6. Arrhenius plot of characteristic peak frequencies of 1-propanol. The open circles represent the primary (α-) relaxation rates. They have been fitted by the Vogel–Fulcher law, Eq. (4), represented as solid line. The α'-peaks appear at frequencies indicated by the triangles. The open squares were obtained from the peaks of the electrical modulus due to ionic conduction. They were shifted upwards by 2.4 orders of magnitude (■) in order to match the primary relaxation times in the overlapping temperature range.

ent than those obtained previously. Earlier workers [12,13] assumed that the dominant relaxation exhibits the Debye shape described by Eq. (3).

Finally we discuss the temperature dependences of the various relaxation processes observed for 1-propanol. The main relaxation represented by the open circles in Fig. 6 was followed over the most extensive frequency range. The peak frequencies, ν_α, were fitted to the Vogel–Fulcher law

$$\nu_\alpha = \nu_0 \, \exp\left[-B/(T-T_0)\right]. \tag{4}$$

The apparent activation energy normalized by the glass transition temperature, $T_g = T(\tau = \tau_g)$, with $\tau_g = (2\pi\nu_\alpha)^{-1} = 100$ s or the fragility index $m = (\partial \log_{10}\tau)/[\partial(T_g/T)]$ at $T_g = 105$ K is $m = 33$.

Conductivity relaxation times, $\tau_\sigma = (2\pi\nu_\sigma)^{-1}$, were obtained from the peak frequencies, ν_σ, of the modulus, $M''(\nu)$. The modulus peaks, within experimental uncertainty, exhibited the Debye shape. This indicates the predominance of dc conduction processes. In the temperature range where both conductivity and primary relaxation times can be determined, they can be made to overlap by shifting ν_σ by a factor of 1.6×10^3 to larger values. A close relationship between both quantities is in fact suggested by a combination of the Stokes–Einstein and the Nernst equations which gives

$$\nu_\sigma/\nu_\alpha = ne^2/(6\pi r\epsilon_0 \epsilon_\infty G_\infty). \tag{5}$$

The high-frequency shear modulus, G_∞, of propanol is known [24]. If one assumes that the mobile ions carry one unit charge and that their radius, r, is of the order of 0.1 nm, then their number density in our particular specimens is estimated to be $n \approx 2 \times 10^{18}$ cm^{-3}. The main relaxation rates are smaller by about a factor of 250 as compared with the high-frequency relaxation rates in accordance with previous studies [12,14].

Fig. 6 shows that at the highest temperatures the shifted conductivity relaxation rates do not fall exactly on top of the extrapolated Vogel–Fulcher fit to the main relaxation rates [25]. Similar deviations in other supercooled liquids have previously been taken to signal the return to Arrhenius behavior in the highly fluid state [26]. Another possibility is that the translational diffusion as seen by conductivity relaxation and the rotational diffusion monitored by the dielectric relaxation follow different temperature dependences in different temperature ranges. Of course both diffusion processes are expected to be intimately coupled at high temperatures [27].

5. Conclusions

Our broad-band dielectric investigations of 1-propanol have considerably extended the spectral range as compared with what has been available in previous studies. In particular we have shown that

(a) the main relaxation remains monodispersive at least down to the mHz frequency range;

(b) in addition to the main (primary) relaxation, low-temperature or high-frequency dielectric losses show up which are more pronounced in 1-propanol than in 2-propanol;

(c) the mean rates characterizing the two processes are separated by 2.4 decades for 1-propanol if the main relaxation is assumed to obey the Debye equation, Eq. (3);

(d) a collapse of the data can be achieved by using a scaling procedure which has previously been applied to supercooled liquids, amorphous polymers

and orientationally disordered crystals. While the data for 2-propanol almost obey the previously universally found master curve, clear deviations from the universal behavior were detected for 1-propanol.

We have analyzed the conductivity relaxation in propanol using the electrical modulus formalism and found that the conductivity relaxation time is consistent with a charge carrier concentration of 2×10^{-4} in our 1-propanol samples provided Eq. (5) is applicable.

Our investigations of supercooled propanol confirm the usefulness of the scaling procedure suggested by Dixon et al. However, no agreement with the universal scaling form is obtained. Although for most liquids it is not clear why the scaling procedure works, for propanol it does so because time–temperature-superposition is valid (cf. Fig. 4). Nonetheless, it would be most useful to obtain microscopic informations, e.g. from computer simulations, about the clustering phenomena in propanol in order to explain the similarities and differences in the dynamic behavior of both isomers.

References

[1] R. Richert and A. Blumen ed., Disorder effects on relaxational processes (Springer, Berlin, 1994).

[2] A.P. Sokolov, E. Rössler, A. Kisliuk and D. Quitmann, Phys. Rev. Lett. 71 (1993) 2062.

[3] J. Wuttke, J. Hernandez, G. Li, G. Coddens, H.Z. Cummins, F. Fujara, W. Petry and H. Sillescu, Phys. Rev. Lett. 72 (1994) 3052.

[4] P.K. Dixon, L. Wu, S.R. Nagel, B.D. Williams and J.P. Carini, Phys. Rev. Lett. 65 (1990) 1108.

[5] L.C.E. Struik, Physical Ageing in Amorphous Polymers and Other Materials (Elsevier, Amsterdam, 1976).

[6] I.M. Hodge, J. Non-Cryst. Solids 169 (1994) 211.

[7] C.A. Angell, in: Relaxation in Complex Systems, ed. K.L. Ngai and G.B. Wright (Naval Research Laboratory, Washington DC, 1984), p. 3; K.L. Ngai, J. Non-Cryst. Solids 95&96 (1987) 969.

[8] C.T. Moynihan and S. Cantor, J. Chem. Phys. 48 (1968) 115.

[9] R. Böhmer and C.A. Angell, Phys. Rev. B43 (1992) 10091.

[10] D.J. Plazek and K.L. Ngai, Macromolecules 24 (1991) 1222.

[11] R. Böhmer, K.L. Ngai, C.A. Angell and D.J. Plazek, J. Chem. Phys. 99 (1993) 4201; R. Böhmer, J. Non-Cryst. Solids 172–174 (1994) 628.

[12] R.H. Cole and D.W. Davidson, J. Chem. Phys. 19 (1951) 1484; F.X. Hassion and R.H. Cole, J. Chem. Phys. 23 (1955) 1756; W. Dannhauser and R.H. Cole, J. Chem. Phys. 23 (1955) 1762.

[13] S.S.N. Murthy and S.K. Nayak, J. Chem. Phys. 99 (1993) 5362.

[14] C.A. Angell, in: Hydrogen-Bonded Liquids, ed. J.C. Dore and J. Teixeira (Kluwer, Dordrecht, 1991) p. 59; M.A. Floriano and C.A. Angell, J. Chem. Phys. 91 (1989) 2537.

[15] M. Pöschl, G. Althoff, S. Killie, E. Wenning and H.G. Hertz, Ber. Bunsenges. Phys. Chem. 95 (1991) 1084; M. Butsch and H. Sillescu, to be published; T. Christensen and N.B. Olsen, unpublished.

[16] R. Böhmer, B. Schiener, J. Hemberger and R.V. Chamberlin, submitted to Z. Phys. B.

[17] F.I. Mopsik, Rev. Sci. Instrum. 55 (1984) 79.

[18] K. Pathmanathan and G.P. Johari, J. Chem. Phys. 95 (1991) 5990.

[19] L. Wu, Phys. Rev. B43 (1991) 9906.

[20] R.V. Chamberlin, Phys. Rev. B48 (1993) 15638.

[21] The width, W, is defined by the full width (in decades) at half maximum of the frequency-dependent dielectric loss divided by the width of 1.14 decades obtained from the imaginary part of Eq. (3).

[22] N. Menon and S.R. Nagel, Phys. Rev. Lett. 71 (1993) 4095; however, see also A. Schönhals, F. Kremer and F. Stickel, Phys. Rev. Lett. 71 (1993) 4096.

[23] D. Leslie-Pelecky and N.O. Birge, Phys. Rev. Lett. 72 (1994) 1232.

[24] R. Kono, T.A. Litovitz and G.E. McDuffie, J. Chem. Phys. 45 (1966) 1790.

[25] The possibility exists that the temperature dependence of the conductivity relaxation rates is to be connected with that of the α' relaxation which, however, mimics that of the α process in the range studied. Note that in our discussion we do not take into account a possible temperature dependence of G_∞.

[26] A. Schönhals, F. Kremer, A. Hofmann, E.W. Fischer and E. Schlosser, Phys. Rev. Lett. 70 (1993) 3459.

[27] F. Fujara, B. Geil, H. Sillescu and G. Fleischer, Z. Phys. B88 (1992) 195.

Section 5. Novel disordered materials

Structure and electronic properties of amorphous carbon: from semimetallic to insulating behaviour

Th. Frauenheim *, G. Jungnickel, Th. Köhler, U. Stephan

Fakultät für Naturwissenschaften, Institut für Physik, Technische Universität Chemnitz–Zwickau, PSF D-09107 Chemnitz, Germany

Abstract

Correlations between the atomic-scale structure and electronic properties in amorphous carbon and its hydrogenated analogues are analyzed. The metastable amorphous modifications with varying density 2.0–3.5 g/cm^3 and different amount of hydrogen have been generated by density-functional-based molecular dynamics applying different annealing regimes. The atomic-scale structure is characterized with special emphasis on comparing neutron scattering with simulated diffraction data. The global electronic band gap properties are related to the chemical bonding and π-cluster formation. While at low density the π–π* gap closes owing to the large size of π-clusters and the residual strain on the π-system from the rigid bonding environment, the internal strain at high density of 3.0 g/cm^3 is maximally reduced by the separation of smaller π-clusters. In the latter case, the π-bonds optimally relax consistent with the opening of large π–π* gaps up to 3 eV. While the internal strain again increases with further increase in the density, incorporation of hydrogen at 3.0 g/cm^3 additionally supports the removal of internal strain by enforcing two-phase separation tendencies between chemically differently bonded carbon atoms.

1. Introduction

Carbon in combination with hydrogen is one of the most promising chemical elements for molecular structure design in nature. An infinite richness of different structures with an incredibly wide variety of physical properties can be produced. Even the two crystalline inorganic modifications, graphite and diamond, show diametrically opposite physical properties. Whereas graphite with its typical layered sp^2 bonding planes is black, soft, lubricating, electrically conducting and absorbing, the fully three-dimensionally interconnected sp^3 hybridized brightly sparkling diamond is light, hard, brittle, electrically insulating and transparent. Graphite, in the planes, behaves as a semimetal due to a non-vanishing density of states (DOS) near the Fermi energy produced by delocalized π-states. By contrast, diamond behaves as an insulator due to its large σ-band gap.

By the successful handling of different deposition techniques, many metastable amorphous carbon modifications have been prepared during the past two decades [1]. These span the entire spectra of physical properties between graphite and diamond. When hydrogen is added during deposition, the structural spectrum is further enlarged by the polymeric and hydrogenated amorphous carbon modifications which also have interesting potential for technical applications.

---

* Corresponding author. Tel: +49-371 531 3146. Telefax: +49-371 531 3143. E-mail: frauenheim@physik.tu-chemnitz.de.

A fundamental investigation of structure–property correlations in carbon-based amorphous materials and obtaining insight into the structure formation under varying deposition conditions are central and rapidly developing topics in covalent amorphous semiconductor research. Whereas experimental thin-film analysis only provides a limited structurally averaged insight into these problems, molecular dynamics (MD) modeling of atomic-scale structures and related theoretical (structural, diffraction, vibrational, electronical, spectroscopical) data on the basis of a coupling between atomic and electronic degrees of freedom has become a powerful tool in elucidating structure–property relations and mechanisms for structure formation [2–5].

In the following we describe the current state of the art of atomic-scale and chemical-bonding-related characterization of amorphous carbon materials and their hydrogenated analogues by applying a density-functional-based molecular dynamics (DF-MD). The method and the simulation regime is briefly outlined in Section 2. The main part, in Section 3, reviews amorphous model structures that have been generated at different mass density and composition by applying different simulation regimes of various time extension. Amorphous structures of low density, 2.0 g/cm^3, high density, 3.0 g/cm^3, and diamond density, 3.52 g/cm^3, are characterized in their energetics, statistical structure and bonding properties including a detailed comparison with available neutron scattering data for thin-film materials having similar densities [6,7] and a fully four-fold-coordinated continuous distorted network (CDN) model generated according to the bond switch (WWW) method [8]. As one main goal, correlations between the global band gap properties and the detailed clustering of chemically differently bonded carbon atoms are derived by applying a local orbital analysis. The changes obtained in the band gap value and defect state distribution with a variation of density, hydrogen content and simulation regime are discussed. We examine the size distribution of π-clusters and check the ability of π-bonds in these clusters to relax under the constraint of a strained rigid bonding environment. Concluding in Section 4, the removal of internal strain from the amorphous network by the separation of small π-clusters between undercoordinated sites is discussed as the main source for developing

large defect-free band gaps with steep band edges. A further reduction of strain is enforced by the incorporation of hydrogen. This opens the possibility of controling the cluster effects in high-density amorphous carbon with special emphasis on band gap engineering in these materials.

2. Density-functional molecular dynamics

To model the structure formation in amorphous carbon modifications, we have carried out MD simulations for 128 carbon plus hydrogen atoms using fixed-volume cubic supercell arrangements of varying size in relation to the microscopic mass densities and compositions to be studied. The relaxation of the structures has been realized by applying a rapid cooling of a partly equilibrated liquid at a cooling rate 10^{15} K/s over 2 ps and an extended stochastic cooling regime over 8 ps [9].

The method which may be outlined as a hybrid density-functional (DF) non-orthogonal tight-binding molecular dynamics (MD) [4] includes first-principles concepts in relating the Kohn–Sham orbitals of the atomic configuration to a minimal basis of the localized atomic-like valence orbitals of all atoms. These valence electron orbitals represented by a set of twelve Slater-type functions along with the potentials of single atoms in free space are determined self-consistently within the local-density approximation (LDA). Making use of a simplified non-self-consistent DF scheme for the many-atom configuration, the effective one-electron potential in the Kohn–Sham Hamiltonian is approximated as a sum of contracted pseudoatom potentials. These pseudoatom potentials are introduced in consistency with limiting the range of the valence electron orbital extension by an additional potential of the type const.$(r/r_0)^2$, strongly increasing for $r \geq r_0$ ($r_0 \approx 2 \times$ the covalent atom radius). As a result, the charge densities are contracted similarly to self-consistently obtained charge densities in molecular and crystalline modifications. Consistent with this approximation, we take into account only two-center Hamiltonian matrix elements in the secular equation leaving a simplified general eigenvalue problem for determining the cluster electron eigenvalues and wave

functions [10]: $\sum_\mu c_\mu^i (h_{\mu\nu} - \epsilon_i S_{\mu\nu}) = 0$. The total energy of the system as a function of the atomic coordinates can now be decomposed into two parts, $E_{tot}(\{R_l\}) = E_{bind}(\{R_l\}) + E_{rep}(\{R_l - R_k\})$. The first term appearing as the sum over all occupied cluster electron energies represents the so-called band-structure energy, obtained at $k = 0$ to achieve a BZ sampling at the Γ-point for our relatively large supercells. The second term, as a repulsive energy, comprises the core–core repulsion between the atoms and corrections due to the Hartree double-counting terms and the non-linearity in the superposition of exchange–correlation contributions. The repulsive energy in a further approximation is described by short-range repulsive two-particle potentials which are fitted to the self-consistent (SCF) LDA cohesive energy curves of corresponding diatomic molecules and crystalline modifications over a wide range of the interatomic separations. Examining carbon microclusters [11], fullerenes [12], bulk-crystalline and amorphous modifications as well as diamond surfaces [13], experimentally found structures are reproduced. Moreover, the cohesive energy versus interatomic separation curves per carbon atom, as a function of structure and coordination, closely approximate results obtained by more sophisticated methods [14]. A more complete discussion of the transferability of the used DF-based non-orthogonal TB scheme to phases of varying coordination, finite systems and different atom-type combinations will be given elsewhere [15].

3. Examination of structure property correlation

As the result of the simulation we have obtained final metastable amorphous carbon modifications at different mass density, a selection of which is shown in Fig. 1 as side views. Different carbon hybrids and, in one single case, the incorporated hydrogen atoms are designated by different colours. From the structural images there is a clear tendency for the different hybrids to separate from each other, and to form small interconnected subclusters. Owing to the fixed composition and constant atom number in the hydrogen-free supercells, the cohesive energies at different densities have been compared to determine the high-density modifications of 3.0 g/cm^3 as the minimal energy metastable configurations under a given set of simulation conditions supporting previous results [4].

In this paper we focus on only three densities – 2.0, 3.0 and 3.52 g/cm^3 – that are most interesting from the point of deposition and application. As one main goal, we show how the structures and the chemical bonding change with the simulation regime, which has a significant influence on the energetic stability and the chemical-bonding-related global electronic properties of the amorphous modifications.

The increase in energy per carbon atom in the amorphous systems relative to the diamond cohesive energy, ΔE^{at}, together with the structural and electronic characteristics of the models are listed in Tables 1–3. In the upper part, we outline data from a pure statistical analysis of the structures [18], including the fraction of two-, three- and four-fold-coordinated atoms, C_2, C_3, C_4, the mean bond length, R_1, bond angle, θ, and their standard deviations, Δ, the CC coordination number, k_{CC}, and the number of rings according to a shortest path analysis, $N_{rings}^{(4\cdots8)}$.

To prove the validity of our model structures, we provide the calculated neutron scattering data for comparison with experiments. From the histograms of pair distances in the models, we compute an unbroadened reduced radial distribution function, $G'(R)$, the Fourier transform of which yields the total interference function of the models, $F(Q)$, where Q is the momentum transfer related to a scattering event. $F(Q)$ is directly proportional to the well-known structure factor $S(Q)$, which may be determined in neutron scattering experiments, $F(Q) = Q \times [S(Q) - 1]$. Since it is instructive to investigate the structure in real space, too, the experimental procedure in turn computes a radial distribution function (RDF) from the measured $F(Q)$. However, the RDF is usually broadened by means of a window

Fig. 1. (001) view of several models generated. (a) a-C, $\rho = 2.0$ g/cm^3, DF-MD rapid cooling; (b) a-C, $\rho = 2.0$ g/cm^3, DF-MD extended stochastic cooling; (c) ta-C, $\rho = 3.0$ g/cm^3, DF-MD rapid cooling; (d) ta-C, $\rho = 3.0$ g/cm^3, DF-MD extended stochastic cooling; (e) ta-C:H, $\rho = 3.0$ g/cm^3, DF-MD rapid cooling, $x_H = 30$ at.%; (f) a-dia, $\rho = 3.5$ g/cm^3, 512 atoms CDN model.
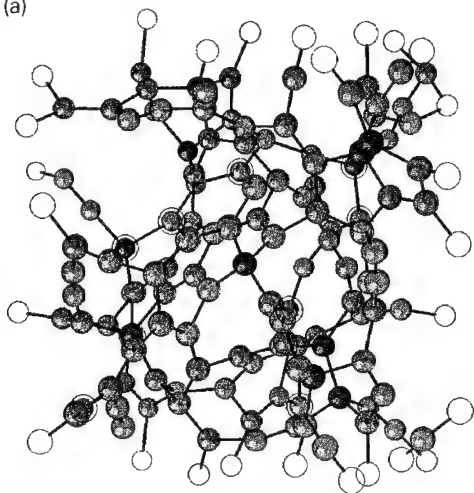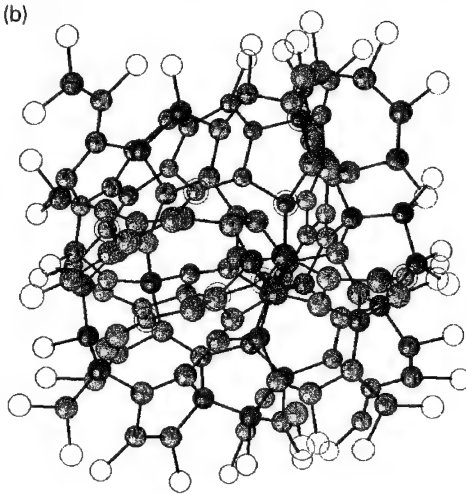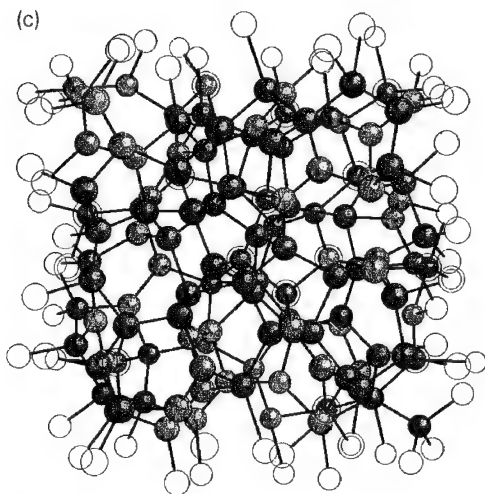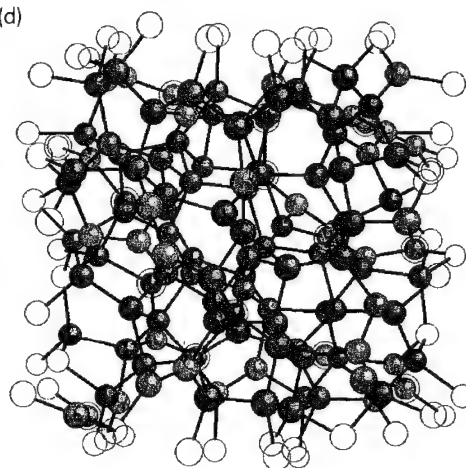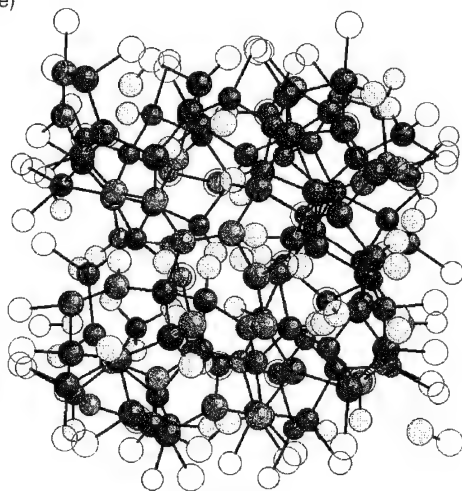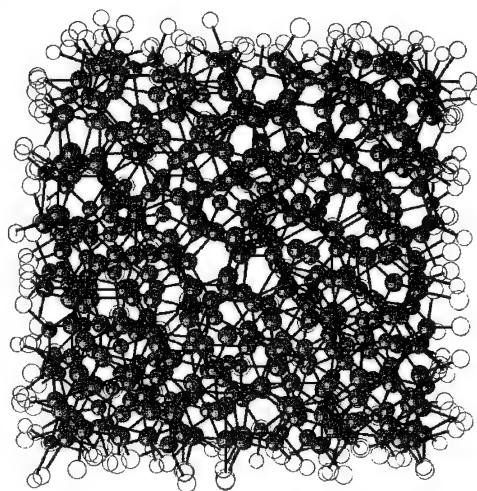
Table 1

Structure, chemical bonding and global band gap properties of low-density a-C models generated by rapid cooling and extended stochastic cooling; ΔE^{at} is the calculated cohesive energy decrease per carbon atom relative to the diamond energy

Data	a-C$_{2.0}^{rapid}$	a-C$_{2.0}^{extended}$
ΔE^{at} (eV):	0.95	0.76
C_2 (%):	27	8
C_3 (%):	64	73
C_4 (%):	9	19
$R_1 \pm \Delta R_1$ (Å):	1.43 ± 0.08	1.47 ± 0.08
$\theta \pm \Delta\theta$ (deg):	120.6 ± 16.9	116.2 ± 13.3
k_{CC}:	2.80	3.11
$N_{rings}^{(4\ldots8)}$:	1, 9, 5, 8, 9	2, 17, 28, 11, 7
$E_{\pi-\pi^*}$ (eV):	1.93	1.38
$N_{defects}$:	11	4
n_p/n_π:	0.077	0.036
$n_{p+\pi}/n\sigma$:	0.430	0.286
$\bar{I}_{pp}/I_{pp}^{max}$:	0.68	0.63
$N_{(size)}^{\pi-cl}$:	$14_2, 1_5, 2_6, 1_{15}, 1_{82}$	$12_2, 1_8, 1_{80}$

Table 3

Structure, chemical bonding and global band gap properties of amorphous diamond a-dia models generated by DF-MD and Monte Carlo simulated annealing using the WWW algorithm

Data	a-dia$_{3.52}^{rapid}$	a-dia$_{3.52}^{extended}$	a-dia$_{3.52}^{CDN}$
ΔE^{at} (eV):	0.81	0.70	0.99
C_3 (%):	12	8	0
C_4 (%):	88	92	100
$R_1 \pm \Delta R$ (Å):	1.53 ± 0.06	1.54 ± 0.06	1.54 ± 0.09
$\theta \pm \Delta\theta$ (deg):	109.6 ± 11.1	109.4 ± 10.4	109.0 ± 11.3
k_{CC}:	3.88	3.92	4.00
$N_{rings}^{(4\ldots8)}$:	5, 41, 79, 67, 33	1, 46, 98, 67, 18	0, 70, 86, 47, 15
$E_{\pi-\pi^*}$ (eV):	5.59	3.22	–
$N_{defects}$:	8	2	0
n_p/n_π:	1.0	0.2	–
$n_{p+\pi}/n\sigma$:	0.032	0.024	–
$\bar{I}_{pp}/I_{pp}^{max}$:	0.59	0.88	–
$N_{(size)}^{\pi-cl}$:	$1_2, 3_3$	5_2	–

function, $D(Q)$, that is multiplied by the pure $F(Q)$ before the Fourier transformation in order to avoid unphysical truncation ripples due to the experimental limits in momentum space [19]. As the window function we use a Gaussian, $\exp(-\beta \times Q \times Q)$, with a damping constant, $\beta = 0.003$, to obtain the experimental total reduced radial distribution functions,

Table 2

Structure, chemical bonding and global band gap properties of high-density highly tetrahedral ta-C(:H) models generated by rapid cooling and extended stochastic cooling

Data	ta-C$_{3.0}^{rapid}$	ta-C$_{3.0}^{extended}$	ta-C:H$_{3.0}^{rapid}$
ΔE^{at} (eV):	0.72	0.69	–
C_3 (%):	36	31	32
C_4 (%):	64	69	68
$R_1 \pm \Delta R$ (Å):	1.54 ± 0.08	1.54 ± 0.07	1.49 ± 0.06
$\theta \pm \Delta\theta$ (deg):	111.0 ± 11.7	110.9 ± 11.2	111.2 ± 12.3
k_{CC}:	3.64	3.69	3.25
$N_{rings}^{(4\ldots8)}$:	6, 36, 54, 32, 20	3, 43, 58, 39, 12	4, 17, 29, 25, 7
$E_{\pi-\pi^*}$ (eV):	2.88	2.07	3.30
$N_{defects}$:	4	4	3
n_p/n_π:	0.087	0.111	0.077
$n_{p+\pi}/n\sigma$:	0.108	0.085	0.079
$\bar{I}_{pp}/I_{pp}^{max}$:	0.60	0.67	0.73
$N_{(size)}^{\pi-cl}$:	$16_2, 4_3, 1_6$	$9_2, 1_4, 1_6, 1_8$	$11_2, 1_4, 1_{11}$

$G(R)$. The model RDFs to be compared are obtained by a convolution of $G'(R)$ with $D(R)$.

In the lower part of the tables, the global electronic parameters of the amorphous models are summarized. From the calculation of total and partial electronic densities of states (TDOS, s and p DOS) we have estimated the HOMO–LUMO $\pi-\pi^*$ band gap splitting, $E_{\pi-\pi^*}$, by eliminating the non-bonding p-states around the Fermi energy. All other data, the total number of electronic defects, $N_{defects}$, the ratios of non-bonded p- to bonding and antibonding π-states, n_p/n_π, as well as all p + π- to bonding and antibonding σ-states, $n_{p+\pi}/n_\sigma$, the mean p-orbital overlap between undercoordinated sites relative to that of a C_2H_4 double bond, $\bar{I}_{pp}/I_{pp}^{max}$, and the numbers of π-clusters having different size, $N_{(size)}^{\pi-cl}$, have been determined by a local orbital analysis according to Stephan et al. [24].

For further detailed discussion of amorphous carbon structures and hydrogenated analogues for a broad range of mass densities between 1.8 and 3.5 g/cm^3, we refer the reader to Refs. [4,16–18,20–24].

3.1. Low-density amorphous carbon, a-C, 2.0 g/cm³

The models presented in Figs. 1(a) and (b) were generated by running two different annealing regimes, rapid and extended, within the DF-MD

calculations. The characteristic structure, chemical bonding and electronic data are summarized in Table 1. It is found that the cohesive energy take-off per carbon atom relative to the diamond phase, ΔE^{at}, decreases when the relaxation time is extended and using optimized stochastic cooling regimes. In the rapidly cooled structure, formation of a homogeneous dense structure has not been achieved. The network has low connectivity incorporating a large fraction of two-fold-coordinated atoms, C_2, as also found by Wang et al. [3] at 2.2 g/cm^3 and, therefore, yielding a coordination number $k_{CC} < 3$. The corresponding tendency is to build up chain-like segments in this model in conjunction with the generation of double- and triple-like bonds, which, due to enhanced binding forces, drives the mean bond length, R_1, to be smaller and the mean bond angle, Θ, to increase in the rapidly cooled modification. These effects are additionally manifested by the relatively weak ring formation tendencies characterized by the total number of rings in this structure. The sp^3 fraction with 9% is low and the sp^2 clustering is additionally stabilized by the formation of π-bonding clusters which at the considered low densities percolate through the system.

By applying the extended stochastic cooling, the chemical bonding in the corresponding lower-energy a-C modification changes considerably compared with the rapid cooling. The fraction of twofold-coordinated atoms has dropped to 8%, simultaneously increasing the sp^3 fraction to 19%, which comes close to values obtained for smaller supercell configurations by Galli et al. [2] using SCF plane wave calculations within the Car–Parinello framework. The connectivity is strongly enhanced which is confirmed by the higher value of k_{CC} and the enhanced ring formation favouring six-fold relative to odd-membered rings.

Fig. 2(a) shows the reduced RDF for the low-density models. Both of the models are capable of reproducing the experimentally observed peaks regarding the position as well as the global form of each maximum. There is a misfit in the peak heights for the extended stochastically cooled model and some better agreement with the experimental curve for the rapidly cooled model. However, for the latter model the first correlation sphere is clearly shifted to smaller atomic distances, consistent with the shorter
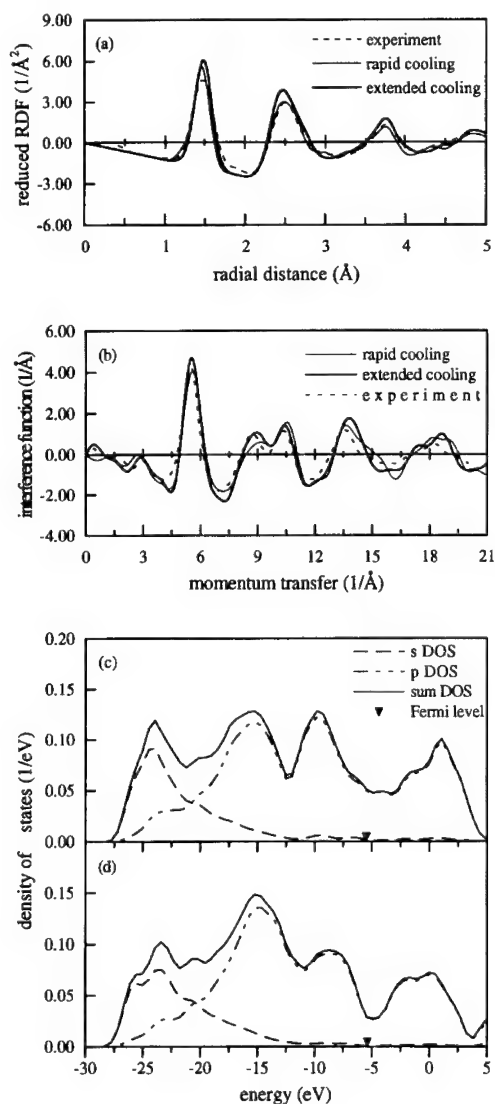
Fig. 2. Diffraction and electronic data for the low-density a-C models. (a) reduced radial distribution function in comparison with neutron scattering data. [6]; (b) interference function in comparison with neutron scattering data. [6]; (c) density of states for the rapidly cooled DF-MD model; (d) density of states for the extended stochastically cooled DF-MD model.

mean bond length in the presence of a relatively high sp fraction of this model. For further detail, Figs. 2(b)–(d) show the corresponding total interference functions $F(Q)$, of the two models in comparison with neutron scattering results [6] and the electronic

density of states for the rapid (c) and extended stochastic cooling (d). It should be pointed out that the behaviour of the central double peak in $F(Q)$ is different for the two low-density models. As a result of the different bond length statistics, there is a change in the form of the peak at $Q \approx 13.5 \ \text{Å}^{-1}$, too. The differences in the ring or medium-range structure discussed so far give rise to some peak shift and change in the curve form for low Q-values. Comparing with the neutron experiment, the better overall agreement of both curves in coordinate and momentum space is achieved for the extended stochastically cooled modification. However, this good coincidence of the scattering and radial distribution function for a given model is only one necessary condition for a realistic model structure.

Another typical feature of low-density amorphous carbon is the existence of a relatively small electronic gap. Therefore, let us now discuss the calculated DOS curves, shown in Figs. 2(c) and (d), and the global electronic parameters. As seen from the data listed in the lower part of Table 1, the number of non-σ-bonded orbitals equals the number of all p + π-states that dominate the TDOS behaviour near the Fermi energy. The structure of the π bands approximately follows from the ratio of the non-bonding to the bonding and antibonding states $n_p/n\pi$. For the two models, this ratio is very small, which describes the appearance of distinct bonding and antibonding π bands enclosing a strong pseudo-gap. In changing again the relaxation from rapid to extended cooling, the π–π* splitting decreases. This is mainly due to the formation of an energetically more favourable π-cluster distribution reducing the total number of defects considerably. Simultaneously the connectivity of the network is enhanced by forming a larger fraction of σ-bonds (lower ratio $n_{p+\pi}/n\sigma$) enforcing the strain on the π-bonds from the rigid bonding environment and consequently decreasing the mean p-orbital overlap compared with the rapidly cooled structure. The electronic DOS shows a clear σ valence band from 20 to 7 eV below the Fermi energy which is characterized by one mostly s-state dominated and one p-dominated peak. The additional two maxima on both sides of the Fermi energy correspond to the π and π* bands, the shape and separation of which are controlled by the particular π-cluster distribution in the two mod-

els. For a more detailed discussion, we refer to Ref. [21].

3.2. High-density, highly tetrahedral amorphous carbon, ta-C(:H), 3.0 g / cm³

The low-density structures discussed so far actually are electronically less interesting due to their strong π bands determining the gap behaviour and the minor fraction of fourfold coordinated sp³-like hybridized atoms. Therefore, many efforts were made to increase the fraction of these chemical species in hydrogen-free materials using ion beam techniques [25] and vacuum arc deposition [18,26]. Weiler et al. recently even reported on a new type of high-density a-C:H films prepared by a monoenergetic rf plasma beam source using C_2H_2 as working gas [22]. The characteristic properties of all of these films in relation to the density strongly depend on the energy of deposited carbon atoms. The sp³ content, compressive stress, hardness and optical gap are all found to pass through a maximum at highest density values. In the optimum energy range of about 90–100 eV per C atom, densities of 2.9–3.3 g/cm³ corresponding to sp³ fractions of 60–90% were reported. Independently, analogous structures have been found to represent metastable minimal energy configurations [4,5,18,24], which is confirmed by the cohesive energy increase per atom relative to diamond in Table 2 by comparison with less-dense and more-dense structures generated by identical MD simulation regimes in both rapid and extended versions (cf. Tables 1 and 3). Simultaneously the internal strain is maximally removed from the network by the separation of small, favourably even membered, π-clusters between undercoordinated sites. The separation of π-bonded pairs at 3.0 g/cm³ has also been reported by Drabold et al. [5] using smaller supercell configurations within ab initio local orbital MD. Table 2 and Fig. 3 show the results for the two ta-C models (cf. Figs. 1(c) and (d)) generated by the two cooling regimes. The fraction of fourfold-coordinated atoms at 3.0 g/cm³ density reaches about two thirds, which is slightly lower than usually reported experimentally and remarkably smaller than found by Drabold et al. within their calculation [5]. The sp³ fraction is almost unaffected by changing the simulation regime and the additional incorporation of hydrogen, yield-
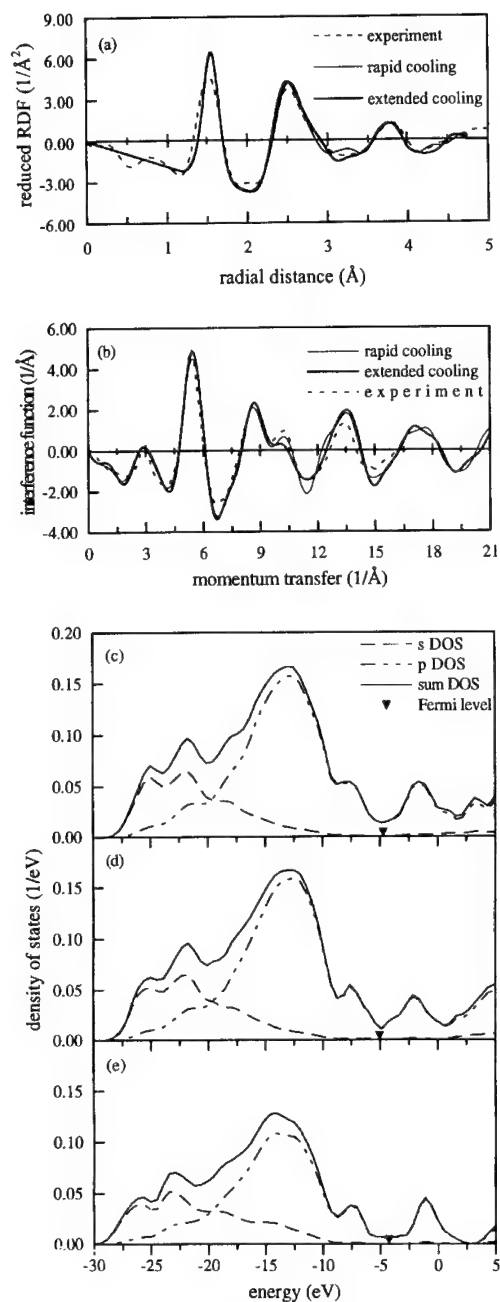
Fig. 3. Diffraction and electronic data for the high-density ta-C(:H) models. (a) reduced radial distribution function of the hydrogen-free models in comparison with neutron scattering data [7]; (b) interference function of the hydrogen-free models in comparison with neutron scattering data [7]; (c) density of states for the rapidly cooled DF-MD model; (d) density of states for the extended stochastically cooled DF-MD model; (e) density of states for the rapidly cooled hydrogenated DF-MD model.

ing the conclusion that the density constraints at 3.0 g/cm^3 are most important for determining the final chemical composition of the ta-C(:H) material. Whereas extended stochastic rather than rapid cooling does not significantly change the connectivity of the network, given by the ring statistics, the dilution by hydrogen favours the termination of a lot of bonds and reduces the number of rings drastically.

We have found 3.0 g/cm^3 as an optimal density at which a minimal defect concentration is established. At lower and higher mass densities, the total number of defects, N_{defect}, and the fraction of non-bonded p-electrons relative to the bonding and anti-bonding π-states increases as can be seen in the tables. The increase in the $\pi-\pi^*$ splitting up to 3 eV compared with low-density materials is mainly determined by the changing size distribution of π-clusters with respect to smaller ones (cf. values for $N_{size}^{\pi-cl}$ in the tables) and by the ability of the π-bonds to relax to a mean value of 0.6 of a C_2H_2 double bond under the constraint of a rigid sp^3 bonding environment. If we extend the annealing time using optimized stochastic cooling techniques at almost equal defect distribution, the $\pi-\pi^*$ splitting drops to 2.07 eV. The evolution of the $\pi-\pi$ gap in this structure is strongly influenced by shifting the size distribution of π-clusters to larger non-aromatic even-membered clusters of up to eight sp^2 sites, reducing the gap at an even slightly larger mean p-orbital overlap. Both hydrogen-free ta-C models have the highest cohesive energy and consequently the lowest internal stress of all DF-MD models obtained so far. The energetic stability considered at equal density, given by ΔE^{at} in Table 2, is even further enhanced with extended stochastic cooling. In consistency the bond length and bond angle deviations are lowest in the corresponding model, whereas the ring structure does not change significantly.

For completeness, we have included in Table 2 and Fig. 3 data for an equally dense hydrogenated model, ta-C:H, showing the hydrogen-induced structural consequences in the case of a rapid cooling run. The stability of such a high-density hydrogenated modification has recently been successfully demonstrated [22].

The addition of a relatively large amount of hydrogen (30 at.% in our studies) strongly favours a

further decrease of internal stress due to the reduction of the network connectivity, as can be seen by comparing the coordination numbers and numbers of rings in Table 2. In particular, the minimal defect densities given by the small n_p/n_π ratio and the very large $\pi-\pi^*$ splitting of 3.3 eV correspond with experimentally obtained thin-film structures [22,27]. Similar to the hydrogen-free counterparts of the same density, this verifies the high stability and high sp^3 fraction of these novel ta-C:H modifications. Although the size distribution of small π clusters and defects in both rapidly cooled ta-C and ta-C:H models are very similar, the mean p-orbital overlap in the hydrogenated structure reaches a maximum of 0.73 of a C_2H_4 double bond. This remarkably exceeds the corresponding values for both ta-C models and confirms the further removal of internal strain by the incorporation of hydrogen. As a result the π-bonds are strengthened in consistency with the widening of the $\pi-\pi^*$ splitting to 3.3 eV.

Fig. 3(b) shows excellent agreement of the rapidly cooled MD model interference function with available neutron diffraction data [7], which, in particular, compared with the neutron data at low densities, is characterized by a changing height ratio of the central double peak at 9 Å^{-1} and a shift of the peak near 13 Å^{-1} to the left. Owing to the strong similarity of the local order of the models in both relaxation regimes, the radial distribution functions given in Fig. 3(a) do not differ much. The peak positions and the peak slopes are described well for both models. The only remarkable difference in the height and width of the first coordination sphere when comparing it with the experimental scattering data indicates a slightly larger bond length deviation in the investigated thin-film structure.

The electronic DOS in Figs. 3(c)–(e) show a clear partition into a low-energy σ-like band and relatively weak but well resolved π and π^* shoulders below and above E_F, which still control the energy pap in the high-density ta-C:H modification, developing now steeper band edges as shown in Fig. 3(e). This is promising for doping which will be studied in future investigations. Further, it is apparent that all three valence band DOS are characterized by a third strong feature due to a split of the underlying partial s DOS. The reason for the low occupation of the s-states around 20 eV below Fermi level is under
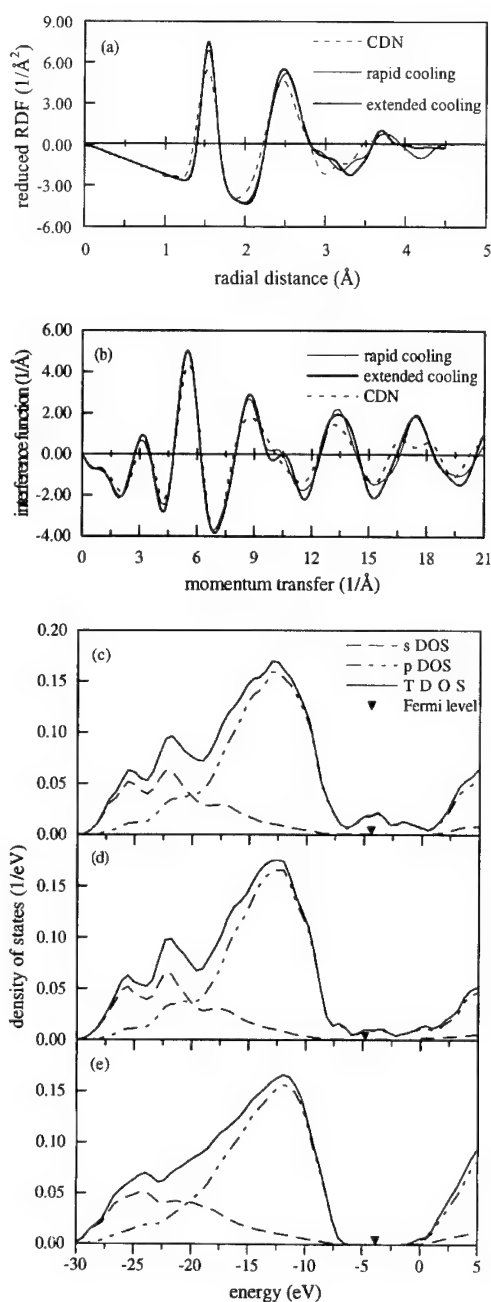
Fig. 4. Diffraction and electronic data for the diamond density a-dia models. (a) reduced radial distribution function in comparison with that of a four-fold-coordinated CDN; (b) interference function in comparison with that of a four-fold-coordinated CDN; (c) density of states for the rapidly cooled DF-MD model; (d) density of states for the extended stochastically cooled DF-MD model; (e) density of states for the 512 atoms WWW-CDN model.

present investigation and the discussion should be postponed to another paper [28].

3.3. Amorphous carbon with diamond density, a-dia, 3.52 g / cm³

Finally, let us consider the structure and physical properties of a series of models made at diamond density. We have generated two models by applying the two MD relaxation regimes and a Monte Carlo (MC) method, which is based on the WWW-bond switch procedure [8] originally successfully introduced to describe amorphous silicon properties. The model has been generated starting from a crystalline diamond cell inducing a sequence of locally relaxed bond transpositions preventing the formation of four-membered rings. After reaching a bond switch density of one transposition per atom, the model has been finally relaxed by extended Monte Carlo annealing techniques allowing both bond transpositions and atomic vibrations. The interatomic forces are described by using the Keating potential [29]. Details of the particular annealing procedure will be given elsewhere [28]. After an equilibration at 300 K, we obtained a completely fourfold-coordinated defect-free continuous distorted network (CDN) [30]. Fig. 1(f) shows the largest CDN generated in this way containing 512 carbon atoms.

Table 3 lists the properties of the two MD models by comparison with that of a CDN with 128 atoms. As one main outcome, we notice that the decrease in cohesive energy of the CDN relative to diamond is highest. Considering the rapidly cooled MD model, the cohesive energy decrease exceeds that of the corresponding ta-C model at 3.0 g/cm³ by 0.09 eV/atom. This again confirms the high stability of highly tetrahedrally bonded amorphous carbon modifications at mass densities around 3.0 g/cm³. Regarding the extended stochastically cooled MD model, however, the cohesive energy per atom is only slightly lower than in the ta-C case and represents the most stable configuration of a series of a-dia models. The three models differ significantly in their sp^3 fraction. We find that extended optimized MD cooling decreases the number of undercoordinated sites compared with the rapid cooling regime. The lowering of stress and further gain in cohesive energy mostly results from the changing size distri-

bution of π-clusters in consistency with a remarkable increase of the mean p-orbital overlap between undercoordinated sites. The connectivity of the network determined by the number of rings is enhanced during extended cooling. By comparing the DOS behaviour of both DF-MD models, shown in Figs. 4(c) and (d), it is obvious that in the rapidly cooled structure the large defect concentration dominates the Fermi energy region while the $\pi-\pi^*$ splitting is enhanced due to the topology of three-atom π-clusters even at lower mean p-orbital overlap indicating high strain on the π-system. Removing most of the defects and shifting the π-cluster distribution to only sp^2 pairs in the energetically more stable extended cooled DF-MD model (cf. values in Table 3) decreases the $\pi-\pi^*$ splitting. Nevertheless, it is still as high as 3.22 eV. This relatively high value results from optimal mean p-orbital overlap in the π-bonded sp^2 pairs.

Finally, for comparison let us characterize the properties of the CDN model. Despite the simple modeling procedure and the classical description of interatomic forces, the statistical properties of the CDN are in excellent agreement with the density-functional-based models. Moreover, the complete absence of p-defects is proven by the same π-bond analysis as applied for all the other models. The electronic density of states (see Fig. 4(e)) supports this impressively. There is a pure $\sigma-\sigma^*$ gap whereas both the MD models exhibit a non-vanishing DOS nearby the Fermi level (Figs. 4(c) and (d)). Further, it should be mentioned that the interference functions of the three models give very similar results except for some slight deviations in the width of the peak at $Q \approx 18 \text{ Å}^{-1}$ and in the weight of the right-hand peak in the central double peak feature, which becomes only a shallow flank in the absence of sp^2-like atoms. Regarding the reduced RDFs (see Fig. 4(a)), the broadening of the first peak for the CDN model is largest in agreement with the larger bond length deviation. Differences in the position of the second correlation spheres in comparing all three models reflect the effect of slightly different mean bond angles obtained (see Table 3). However, one should keep in mind that even this shell is strongly affected by correlations between atoms that are third neighbours counting the number of σ-bonds between them [18]. These correlations are strongly coupled to the

ring structure. The appropriate differences observed have a special influence on the shape of the second correlation sphere at large distances and change the behaviour between the second and third maxima in $G(R)$ remarkably. Considering the ring structure in the CDN, it is evident that the number of six-membered rings is lower than for the extended MD cooling and that the number of five-membered rings exceeds the number of seven-membered rings, by contrast with the MD models. This, in conjunction with the broadening due to the increased bond length deviation, could be one reason for the fact that the already mentioned third central peak in the valence band found in the DOS of the MD models vanishes for the CDN. Moreover, the presence of a lot of five-membered rings in the latter yields the lowest mean bond angle of the three models investigated.

4. Conclusion

Using DF-based MD modeling of amorphous carbon modifications depending on the density and the simulation regime, we confirm the stability of the high-density highly-tetrahedral modifications at 3.0 g/cm^3. The atomic-scale models represent metastable minimal energy configurations obtained under the constraint of constant volume conditions. We applied both rapid and extended stochastic cooling regimes. At this high mass density, the internal strain from the network is maximally removed due to the separation of small, favourably even-membered π-clusters between undercoordinated atoms. The size distribution and the degree of relaxation of these π-clusters dominantly determine the $\pi-\pi^*$ splitting and the corresponding electronic gap behaviour in these materials. While the distribution of mainly π-bonded pairs in the rapidly cooled model extends the $\pi-\pi^*$ splitting to 2.88 eV, the formation of larger π-clusters in the more stable, less strained extended cooled model gives rise to a narrowing of the $\pi-\pi^*$ splitting to about 2 eV even though the mean p-orbital overlap is higher. By the incorporation of hydrogen at the same density under rapid cooling, the strain on the π-system in ta-C:H is further reduced, forcing chemically differently bonded C-atoms to separate on a molecular level. So, in Fig. 1(e) we find one relatively large compact sp^3

microcluster (consisting of about 30 blue atoms) in the bottom left of the ta-C:H model which is embedded in the amorphous sp^2/sp^3 matrix in which smaller π-clusters between undercoordinated sites are separated in a rigid sp^3 bonding environment. The size distribution of π-clusters and the number of defects are very similar to that of the corresponding rapidly cooled hydrogen-free structure. The hydrogen is preferably bonded to sp^3 carbon partly saturating the sp^3 microcluster surface and filling reduced density regions in the sp^2/sp^3 matrix. As a result, the strain in the amorphous network and consequently on the π-clusters is reduced to the maximum degree observed so far. This gives rise to optimal p-orbital overlap between undercoordinated sites in consistency with the largest theoretically obtained $\pi-\pi^*$ band gaps. As the most advantageous configuration for maximum reduction of internal stress and thus developing large defect-free band gaps with steep band edges suitable for doping, an optimal distribution of π-bonded sp^2 pairs within a minimal strained sp^3 matrix should be established at certain low hydrogen concentration at high density. In this context, the comparable high stability of a corresponding CDN model of diamond density opening a well-defined large $\sigma-\sigma^*$ band gap should further stimulate experimental efforts to control the clustering of chemically differently bonded carbon atoms in order to achieve a band gap engineering in carbon-based amorphous materials.

Coordinates of the models discussed throughout this paper are available upon request from the corresponding author.

References

[1] Robertson, Diamond Related Mater. 2 (1993) 984.
[2] G. Galli, R.M. Martin, R. Car and M. Parrinello, Phys. Rev B42 (1990) 7470.
[3] C.Z. Wang, K.M. Ho and C.T. Chan, Phys. Rev. Lett. 70 (1993) 611.

[4] Th. Frauenheim, P. Blaudeck, U. Stephan and G. Jungnickel, Phys. Rev. B48 (1993) 4823.

[5] D.A. Drabold, P.A. Fedders and P. Stumm, Phys. Rev. B49 (1994) 16415.

[6] F. Li and J.S. Lannin, Phys. Rev. Lett. 65 (1990) 1905.

[7] P.H. Gaskell, A. Saeed, P. Chieux and D.R. McKenzie, Phys. Rev. Lett. 67 (1991) 1286.

[8] F. Wooten, K. Winer and D. Weaire, Phys. Rev. Lett. 54 (1985) 1392.

[9] Th. Köhler, Th. Frauenheim, G. Jungnickel and D.A. Drabold, submitted to Phys. Rev. B.

[10] G. Seifert, H. Eschrig and W. Bieger, Z. Phys. Chem. (Leipzig) 267 (1986) 529.

[11] P. Blaudeck, Th. Frauenheim, D. Porezag, G. Seifert and E. Fromm, J. Phys.: Condens. Matter 4 (1992) 6389.

[12] P. Blaudeck, Th. Frauenheim, H.-G. Busmann and Th. Lill, Phys. Rev. B49 (1994) 11409.

[13] Th. Frauenheim, U. Stephan, P. Blaudeck, D. Porezag, H.-G. Busmann, W. Zimmermann-Ebling and S. Lauer, Phys. Rev. B48 (1993) 18189.

[14] M.T. Yin and M.L. Cohen, Phys. Rev. Lett. 50 (1983) 2006.

[15] D. Porezag, Th. Frauenheim, G. Seifert and R. Kaschner, Phys. Rev. B, in press.

[16] P. Blaudeck, Th. Frauenheim, G. Jungnickel and U. Stephan, Solid State Commun. 85 (1993) 997.

[17] Th. Frauenheim, U. Stephan, P. Blaudeck and G. Jungnickel, Diamond Related Mater. 3 (1994) 462.

[18] G. Jungnickel, M. Kühn, S. Deutschmann, F. Richter, U. Stephan, P. Blaudeck and Th. Frauenheim, Diamond Related Mater. 3 (1994) 1056.

[19] C.N.J. Wagner, J. Non-Cryst. Solids 31 (1978) 1.

[20] G. Jungnickel, Th. Frauenheim, D. Porezag, P. Blaudeck, U. Stephan and R.J. Newport, Phys. Rev. B50 (1994) 6709.

[21] G. Jungnickel, M. Haase, Th. Köhler, S. Deutschmann, P. Blaudeck and Th. Frauenheim, J. Non-Cryst. Solids, in press.

[22] M. Weiler, S. Sattel, K. Jung, H. Ehrhardt and V.S. Veerasamy, Diamond Related Mater. 3 (1994) 608; M. Weiler, S. Sattel, K. Jung, H. Ehrhardt and J. Robertson, Appl. Phys. Lett. 64 (1994) 2797.

[23] M. Weiler, R. Kleber, S. Sattel, K. Jung, H. Ehrhardt, G. Jungnickel, S. Deutschmann, U. Stephan, P. Blaudeck and Th. Frauenheim, Diamond Related Mater. 3 (1994) 245.

[24] U. Stephan, Th. Frauenheim, P. Blaudeck and G. Jungnickel, Phys. Rev. B49 (1994) 1489.

[25] D.R. McKenzie, D. Muller and P.A. Pailthorpe, Phys. Rev. Lett. 67 (1991) 773.

[26] V.S. Veerasamy, G.A.J. Amaratunga, W.I. Milne, P. Hewitt, P.J. Fallon, D.R. McKenzie and C.A. Davis, Diamond Related Mater. 2 (1993) 782.

[27] Th. Frauenheim, G. Jungnickel, U. Stephan, P. Blaudeck, M. Weiler, S. Sattel, K. Jung and H. Ehrhardt, Phys. Rev. B50 (1994) 7940.

[28] G. Jungnickel, Th. Köhler, M. Haase, P. Blaudeck, U. Stephan and Th. Frauenheim, to be published in J. Non-Cryst. Solids.

[29] P.N. Keating, Phys. Rev. 145 (1966) 637.

[30] K. Winer, Phys. Rev. B35 (1987) 2366.

Comparison of diffraction and diffusion measurements in porous media

Martin D. Hürlimann [a], Thomas M. de Swiet [a,b], Pabitra N. Sen [a,*]

[a] *Schlumberger-Doll Research, Old Quarry Rd, Ridgefield, CT 06877-4108, USA*
[b] *Department of Physics, Harvard University, Cambridge, MA 02138, USA*

Abstract

Two manifestations of diffractive behavior in diffusion in a porous medium are reviewed. The measured amplitude, $M(q, t)$, in a pulsed field gradient spin echo (PGSE) experiment probes the pore structure using two length scales, the gradient length q^{-1} and the diffusion length $[D(t)t]^{1/2}$. For a suspension of monosized beads, $M(q, t)$ shows a diffraction bump at a wave vector $q = 2\pi/2R$, R being the radius of the beads. For large q, $M(q, t)$ is shown to be proportional to $\Gamma(t)(S/V_p)q^{-4}$, in analogy with the Debye–Porod law. Here $\Gamma(t)$ is a time-dependent function that depends on details of the geometry, and S/V_p is the surface to volume ratio. Experiments on two different suspensions of beads of known sizes in the 500 and 50 μm range, respectively, are used as illustrations. In PGSE, the measured signal amplitude is amplified over that in phase-suppressed magnetic resonance imaging and X-ray diffraction because the sample volume is replaced by the volume enclosed by a diffusion length.

1. Introduction

Classical diffraction phenomena using the scattering of waves such as X-rays, neutrons and electrons are commonly employed in the structure determination of condensed matter. In a periodic structure, sharp peaks are seen in the scattered intensity when k, the difference between the wave vectors of the incident and the scattered waves, equals a reciprocal lattice vector. In liquids and amorphous media, no such sharp peaks are seen, but the scattered intensity might show oscillations and bumps as a function of k. In porous media, no bumps are generally seen, but the intensity for large values of k falls off as $(S/V_p)k^{-4}$, where S/V_p is the surface to volume

ratio of the pore space, which is known as the Debye–Porod law [1]. Debye et al. studied porous catalyst support materials by X-ray scattering and used this large-k behavior successfully to extract S/V_p.

More recently, diffraction effects have been seen in the NMR pulsed gradient spin echo (PGSE) experiment in which the measured amplitude, $M(q, t)$, is given by the Fourier transform of the diffusion propagator. Callaghan et al. [2] observed that $M(q, t)$ of water confined in a pack of mono-sized beads has a diffraction bump at a wave vector $q = 2\pi/2R$, R being the radius of the beads. This has stimulated much interest [3,4] in obtaining structural information from PGSE. Similarly, we have recently observed the analog of the Debye–Porod behavior in the context of diffusion [5]. We found that $M(q, t)$, is proportional to $(S/V_p)q^{-4}$ for large q, in analogy with the Debye–Porod law. In this paper we review

---
* Corresponding author. Tel: +1-203 431 5225. Telefax: +1-203 438 3819. E-mail: Sen@ridgefieldsdr.slb.com.

these two results both theoretically and experimentally.

In standard diffraction, or elastic scattering, the intensity pattern comes from the interference of wavelets coming instantaneously from different parts of the system. Thus the scattered intensity is related to the Fourier transform of the density–density correlation function. By contrast, in PGSE experiments the interference is between signals from a diffusion walker at two different space–time locations. The signal, $M(q, t)$, is given by the Fourier transform of the diffusion propagator and is thus a function of time, t, as well as the wave vector, q, both of which can be controlled in an experiment. A feature of the diffusive case is that interference can only occur between two points that are visited by the same Brownian particle and thus, for example, interference cannot occur between disconnected pores.

In any experimental PGSE system, one can also perform standard magnetic resonance imaging (MRI). This can be used to obtain precisely the same information as a classical diffraction experiment [6]. However, as we see below, for analysis of structure on short length scales, there is a great enhancement of signal to noise in PGSE experiments as compared with MRI. Structure on long length scales, however, is not accessible to PGSE which is limited by how far a particle can diffuse during the lifetime of the experiment (this is determined by the NMR relaxation time). Thus each technique has its natural domain.

2. Diffraction and MRI

In this section we review the theory of diffraction in a porous medium. For simplicity, and ease of comparison with PGSE, we define a porous medium by two random interconnected spaces, one labeled pore and one grain. The pore space is taken to be filled with a uniform density of isotropic, elastic scattering particles and the grain space is taken to be transparent, i.e. neither absorbing nor scattering.

It is convenient to define the two point correlation function, $S_2(r)$, as

$$S_2(r) \equiv (1/V) \int dr' \, \chi(r') \chi(r' + r), \qquad (1)$$

where $\chi(r)$ is unity in the pore space and zero otherwise. The diffraction signal is then given by

$$I(k) = (1/V_p \phi) \int dr \, \exp(ik \cdot r) S_2(r). \qquad (2)$$

Note that the integration above is over the entire sample volume, V, and the normalization is chosen such that $I(k = 0) = 1$. Here V_p is the pore volume, $V_p = \phi V$; ϕ is the porosity. In periodic structures, $S_2(r)$ has delta function peaks when r equals a lattice vector, R_1, so $I(k)$ has peaks when k equals a reciprocal lattice vector. Eq. (2) may be simplified in an isotropic, homogeneous medium where $S_2(r) = S_2(|r|) = S_2(r)$. We then obtain

$$I(k) = \frac{4\pi}{\phi V_p} \int dr \, r^2 \frac{\sin(kr)}{kr} S_2(r). \qquad (3)$$

It is clearly important to understand what information about the pore space is contained in $S_2(r)$. In fact $S_2(r)$ has several interesting features which are discussed in Ref. [7]. For example, the slope at the origin is proportional to the surface-to-volume ratio of the pore space:

$$\partial S_2(r)/\partial r \,|_{r=0} = -S/(4V). \qquad (4)$$

In Fig. 1, we show a schematic representation of $S_2(r)$ for a pack of spheres and the geometrical information contained in it. Since $S_2(r)$ is constrained at $r = 0$ and ∞, one can factor out the limiting behavior and define a new function, $f(r)$,
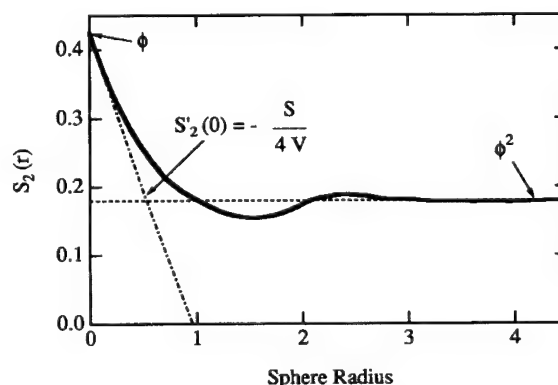
Fig. 1. Structure factors, $S_2(r)$, for model materials composed of impenetrable spheres.

containing the dynamic range of $S_2(r)$:

$$S_2(r) = \phi^2 + \phi(1 - \phi)f(r),$$

$$f(0) = 1, \quad f(\infty) = 0. \tag{5}$$

Clearly $f(r)$ is zero beyond a distance which is much larger than the largest relevant length scale, λ_{max}, of the porous medium.

We can easily see that, if $S_2(r)$ has oscillations, $I(k)$ will have bumps. To give a concrete example, consider a random pack of impenetrable spheres, a system with a structure factor similar to Fig. 1. It has been found that the numerically generated $S_2(r)$ for impenetrable spheres [4] can be fitted well [8], for r up to the sphere radius, R, by

$$f(r) = e^{-r/a} \sin(q_1 r)/(q_1 r). \tag{6}$$

Here $1/a = -f'(0) = [S/(4V_p)]/(1 - \phi) = 3/(4R\phi)$, and $q_1 \approx \pi/R$. It follows that

$$I(k) = \frac{8\pi}{\phi V_p} \frac{a^3(1 - \phi)}{\left[1 + (k - q_1)^2 a^2\right]\left[1 + (k + q_1)^2 a^2\right]}$$

$$\times (1 - \delta_{k,0}) + \delta_{k,0}. \tag{7}$$

This shows a bump when $k \approx q_1$. Note that, in a more complicated porous medium, $S_2(r)$ will not have oscillations and hence $I(k)$ will not show any bumps. For example, Debye found that typically catalyst support materials produce a diffraction signal corresponding to $f(r) = e^{-r/a}$, i.e., $q_1 = 0$, and the 'bump' in diffraction has disappeared. In these types of porous media where the diffraction signal does not have an obvious signature of the porous medium, Debye [1] used the large-k behavior to probe the system.

The large-k behavior is brought out by simple integrations by parts:

$$I(k) \rightarrow -\frac{8\pi}{\phi V_p k^4} \frac{\partial S_2(r)}{\partial r}\bigg|_{r=0} + O\left(\frac{1}{k^6}\right). \tag{8}$$

Now, using the identity [1] $\partial S_2(r)/\partial r|_{r=0} = -S/(4V)$, where S is the total surface area, we find that the coefficient multiplying k^{-4} on the right-hand side of Eq. (8) gives the surface-to-volume ratio, S/V_p:

$$I(k) \rightarrow \frac{2\pi}{V_p} \frac{1}{k^4} \frac{S}{V_p}. \tag{9}$$

Eq. (9) is known as the Debye–Porod law [1].

3. Diffraction in diffusion

The PGSE experiment was originally proposed in some pioneering papers [9], by Stejskal and Tanner, who clearly showed the relationship between the measured signal, $M(q, t)$, and the diffusion propagator:

$$M(q, t) = \int d\mathbf{r} \, d\mathbf{r}_1 \, \exp(i\mathbf{q} \cdot \mathbf{r}) G(\mathbf{r}_1, \mathbf{r}_1 + \mathbf{r}, t)$$

$$\times m(\mathbf{r}_1, t=0). \tag{10}$$

Here the diffusion propagator, $G(\mathbf{r}_1, \mathbf{r}_2, t)$, is the conditional probability density of finding a Brownian walker (in fact a nuclear spin in the pore space) at $\mathbf{r}_2$ at a time, t, given that it was initially at $\mathbf{r}_1$, and $m(\mathbf{r}_1, t=0)$ is the initial density of magnetization. In many experiments in porous media, the pore space is initially uniformly magnetized, so from now on we assume that $m(\mathbf{r}_1, t=0) = 1/V_p$, where V_p is the total pore volume. We shall assume that there are no spins contributing to the signal which are in the grain. The experimentally tunable parameters are wave vector, q, and diffusion length, $\sqrt{6Dt}$, where D is the diffusion coefficient. For water filling the pore space in rocks, the diffusion length can be as large as 100 μm.

Given the bulk molecular diffusion constant, D_0, the conditional probability density function, G, satisfies the equation

$$\frac{\partial G(\mathbf{r}_1, \mathbf{r}_2, t)}{\partial t} = D_0 \nabla^2 G(\mathbf{r}_1, \mathbf{r}_2, t), t > 0;$$

$$G(\mathbf{r}_1, \mathbf{r}_2, t=0^+) = \delta(\mathbf{r}_1 - \mathbf{r}_2), \tag{11}$$

with the boundary condition

$$\hat{n} \cdot \nabla G(\mathbf{r}_1, \mathbf{r}_2, t) + \rho G(\mathbf{r}_1, \mathbf{r}_2, t)|_{r \in \Sigma} = 0,$$

at the pore–grain interface, Σ, with an outward (from pore to grain) normal $\hat{n}$. For homogeneous isotropic systems, Eq. (10) reduces to

$$M(q, t) = 4\pi \int d\mathbf{r} \, r^2 \frac{\sin(qr)}{qr} \mathscr{G}(r, t);$$

$$\mathscr{G}(r, t) \equiv \frac{1}{V_p} \int d\mathbf{r}_1 \, G(\mathbf{r}_1, \mathbf{r}_1 + \mathbf{r}, t). \tag{12}$$

Note that isotropy means $\mathscr{G}(\mathbf{r}, t) = \mathscr{G}(r, t)$, i.e., the probability density of having traversed a distance, $\mathbf{r}$,

after a time, t, averaged over all initial positions is independent of direction.

Stejskal [9] pointed out that it was useful to study this Fourier transform of the data. In the case of a medium of isolated pores, such as the yeast cells studied by Cory and Garroway [10], the diffusion propagator becomes flat within a pore, at long times. Each spin has equal probability of diffusing anywhere in the pore, independent of starting position. $\mathscr{G}(r, t)$ becomes the density autocorrelation function of a pore, averaged over the distribution of pore shapes in the sample. For well connected pores, the diffusion propagator does not reveal information of interest so easily. The initial papers by Callaghan et al. [2] and the book by Callaghan [3] provide many key ideas for general understanding of the diffraction-like feature, i.e., the 'bump' in the context of diffusion. They also contain substantial theoretical discussions about obtaining pore-structure factors in

a scattering analysis of PGSE. To simplify the link between PGSE measurements and the pore geometry we proposed a simple ansatz [4]. This ansatz links the measured amplitude directly to the two-point pore space correlation function, $S_2(r)$, and leads to a 'diffraction bump' in the PGSE experiment, as we show in Section 3.1. In Section 3.2., we present rigorous results for the large q asymptotics of $M(q, t)$.

3.1. Diffraction bump in diffusion

Previously, numerical calculations in Ref. [4] showed that both the ansatz as well as the random walk simulations with a numerically generated structure factor for a pack of hard spheres exhibit a 'diffraction' bump. To show analytically the origin of this bump, we use an ansatz for $\mathscr{G}(r, t)$, which was proposed for the regime where the diffusion
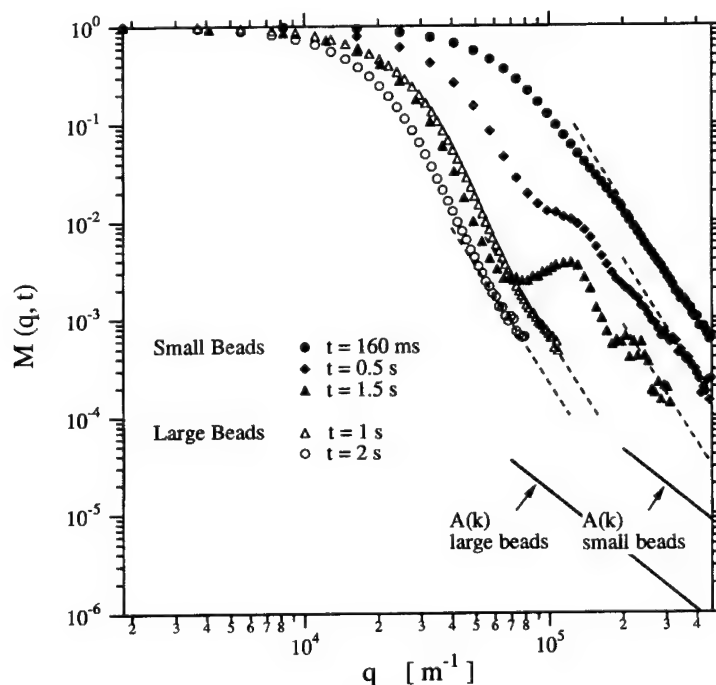
Fig. 2. PGSE signal, $M(q, t)$, as a function of q for two different bead packs, one with diameter in the range 380–515 μm for diffusion times $t = 1$ s and 2 s, and another with diameter of 52 μm for diffusion times $t = 160$ ms, 500 ms and 1.5 s. The dashed line marks the large-q asymptote. A clear diffraction peak develops at a wave vector $q_d = \pi/R = 1.21 \times 10^5 \text{m}^{-1}$ for the small beads. The calculated signal, $A(k)$, for a phase-suppressed imaging experiment is also shown.

length is much larger than the structure of interest. It is the product of an effective Gaussian

$$C(t)\left[\exp\{-r^2/4D_1(t)t\}\right]/\left[4\pi D_1(t)t\right]^{3/2}$$

and $S_2(r)$, the structure factor, where $C(t)$ is a normalization coefficient and $D_1(t)$, the width of the Gaussian, is chosen by fitting the mean square displacement of Brownian particles in the pore space as predicted by the ansatz to the observed value. The mean square displacement as a function of time is simple to obtain from experimental data or a numerical simulation. $D_1(t)$ equals the free diffusion coefficient for the geometries considered here to within a factor of two at all times. Physically the ansatz expresses the fact that the conditional probability density is some smooth Gaussian-like distribution in the pore space and precisely zero in the grain space.

Using this ansatz [4], we find that with the structure function of Eq. (6), $M_A(q, t)$ is given in terms of error functions. In the limit $ql_{D_1} \gg 1$, where $6l_{D_1}^2 \equiv 6D_1(t)t$ corresponds to the mean square displacement, we find in this case

$$M_A(q, t)$$

$$= C(t)\left\{\phi^2 \exp\left[-D_1(t)q^2t\right] + \frac{\phi(1-\phi)}{\sqrt{\pi}}\right.$$

$$\left. \times \frac{a^3}{l_{D_1}^3\left[1 + (q-q_1)^2 a^2\right]\left[1 + (q+q_1)^2 a^2\right]}\right\}.$$

$$(13)$$

This equation shows the 'bump' at $q \approx q_1$ and that $M_A(q, t)$ has a q-independent plateau if $qa \ll 1$. The height of this plateau decreases as $(a/l_{D_1})^3$. This dependence eventually rolls over to q^{-4} behavior as $qa \gg 1$. The height of the 'bump' decays at long times as $a/(l_{D_1}^3 q_1^2)$. In Fig. 2 we show examples of both 'bump' and q^{-4} behavior for data on a pack of beads. We discuss the data in more detail below.

3.2. Large-q asymptotics

One of the clearest connections of the diffusion problem to diffraction theory is afforded by the large-q behavior of $M(q, t)$ [5]. Following Debye et al. [1], a straightforward integration by parts of Eq.

(12) gives for values of q much greater than $(D_0 t)^{-1/2}$ and the inverse of all geometrical lengths such as S/V_p,

$$M(q, t) \to -\frac{8\pi}{q^4} \frac{\partial \mathcal{G}(r, t)}{\partial r}\bigg|_{r=0} + O\left(\frac{1}{q^6}\right). \quad (14)$$

We have used the fact that $\mathcal{G}(r, t)$ goes to zero at large r, since $\mathcal{G}(r, t)$ falls off at least as fast as a Gaussian of width $\sim \sqrt{D_0 t}$. The exponent of q changes to 2 and 3 in 1D and 2D systems, and to non-integers for fractal systems. The generalization to fractals is straightforward, but will not be considered here. Some rocks are believed to be fractal, but only at the 10–100 Å level. In the PGSE experiments, the ruler size is set by the largest value of q or the smallest values of pulse times. For currently available experimental conditions, these lengths are typically larger than 1 μm if water is the fluid filling the pore space.

We demonstrated in Ref. [5] that the derivative of $\mathcal{G}(r, t)$ is proportional to the total probability of return to the origin at the surface:

$$\frac{\partial \mathcal{G}(r, t)}{\partial r}\bigg|_{r=0} = -\frac{1}{4V_p} \int d^2r_s\, G(\mathbf{r}_s, \mathbf{r}_s, t), \quad (15)$$

where the integration is over all the surface area and $\mathbf{r}_s$ denotes surface points. Although the surface average of the return to the origin probability is not an experimentally known quantity, the bulk average is simply $\mathcal{G}(r = 0, t) = [4\pi/(2\pi)^3] \int dq\, q^2 M(q, t)$ [11]. We define the ratio of these two quantities to be the dimensionless function

$$\Gamma(t) \equiv \Gamma(l_D/\{\lambda\}) = \frac{V_p}{S} \frac{\int d^2r_s\, G(\mathbf{r}_s, \mathbf{r}_s, t)}{\int d^3r\, G(\mathbf{r}, \mathbf{r}, t)}.$$

$$(16)$$

This depends on the diffusion length, l_D, and the full set of relevant length scales, $\{\lambda\}$, which characterizes the porous medium. Combining Eqs. (14)–(16), we find that for $ql_D \gg 1$, $q\lambda_{min} \gg 1$,

$$M(q, t) \to \frac{2\pi}{q^4} \Gamma(t) \mathcal{G}(r = 0, t) \frac{S}{V_p}. \quad (17)$$

This equation is the diffusive analogue of the Debye–Porod law, Eq. (9).

It is obvious now that one could estimate S/V_p using Eq. (17), if $\Gamma(t)$ were known. However, if S/V_p is measured by another method, it is also interesting to study $\Gamma(t)$ instead, to probe the full set of relevant length scales $\{\lambda\}$. We have shown rigorously that $\Gamma(t)$ starts out with a value of 2 for $l_D \ll \lambda_{min}$, the smallest relevant length scale, and reaches unity for $l_D \gg \lambda_{max}$, the largest relevant length scale, in a porous medium where all the pores are connected. We point out that the ansatz discussed above satisfies Eq. (17) with $\Gamma(t) = 1$.

4. Comparison of MRI and PGSE

Systems which may be studied by PGSE may also be examined with MRI. In fact, since the only difference between the two measurements is the NMR pulse sequence, the same apparatus can usually perform both of them. It is therefore worthwhile to compare the two experiments. In the imaging experiment the spatial information is encoded by applying a single magnetic field gradient pulse, ∇B_z of duration, δ, so that a spin at a given location, r, is given a phase, $\phi(r) = k \cdot r$, where $k = \gamma \nabla B_z \delta$. The measured signal, $A(k)$, is the total magnetization, or $\Sigma \exp(i\phi(r))$, and is thus the Fourier transform of the density of nuclei, $\rho(r)$. As emphasized by Barrall et al. [6], the phase-suppressed imaging data, $|A(k)|^2$, are identical to what is measured in a classical diffraction experiment and its Fourier transform is related to the two-point density–density correlation function, i.e., the Patterson function. The loss of the phase information makes image reconstruction impossible, but they have emphasized that these NMR Patterson functions can be acquired at a rate which is orders of magnitude faster than comparably resolved MRI, because k-space does not have to be sampled as densely. More precisely, to take an image one requires the spacing of sample points in k-space to be $\Delta k \approx \pi/L$, where L is the sample size, but to measure the two-point correlation function one only needs $\Delta k \approx \pi/\lambda_{max}$, where λ_{max} is the largest correlation length. Because the structure function can decay over a length scale much smaller than the system size, $\lambda_{max} \ll L$. In addition the

structure function is often isotropic, which greatly reduces the size of the region of k-space that must be sampled. Thus, this type of phase suppression makes it possible to acquire statistical information about small structural features that could not be imaged economically.

The unrefined PGSE experiment consists of two gradient pulses instead of the one pulse of the imaging sequence. As with imaging, one neglects diffusion during the pulse itself so that after the first pulse a spin at position, r_1, picks up phase, $q \cdot r_1$, where the wave vector, $q \equiv \gamma \delta \nabla B_z$. Now we wait a time, t, and let the spin diffuse to position, $r_1 + r$, with a probability given by the diffusion propagator, and apply another gradient pulse with a field gradient of the opposite sign and the same duration. The resulting signal is what we have used above. The main idealizations in this derivation are that we can make the pulse short enough to neglect movement during the pulse, and that gradients due to the inhomogeneous Larmor frequency are negligible compared with the applied gradients.

Let us now compare the signal strengths of the two measurements. The Debye–Porod regime is best understood and thus most amenable to comparison. For PGSE, the signal at large q per unit volume of sample is given by Eq. (17). Neglecting factors of order unity we obtain

$$M(q, t) \sim \langle G(r_s, r_s, t) \rangle q^{-4} S/V_p,$$

where $\langle G(r_s, r_s, t) \rangle$ is the surface average of the return to the origin probability. The probability of return to the origin is a measure of the height of the peak of the diffusion packet emitted from a given point. A good estimate for this is given by an inverse diffusion volume, $\langle r^2(t) \rangle^{-3/2}$, where $\langle r^2(t) \rangle$ is the mean square displacement. At short times this is approximately $(6D_0 t)^{-3/2}$, at longer times it will be determined by the length scale of geometrical restrictions. Thus we obtain

$$M(q, t) \sim \langle r^2(t) \rangle^{-3/2} q^{-4} S/V_p.$$

Now consider the case of imaging. From Eq. (9) above we have the form for the square of the measured signal, $|A(k)|^2 \sim k^{-4} S/V_p^2$. For comparison with PGSE we must use the signal itself,

$$|A(k)| \sim k^{-2} \sqrt{S}/V_p.$$

Comparing this with $M(q, t)$ we see that

$$M(q, t)/|A(k)| \sim (q^2\langle r^2\rangle)^{-1}\sqrt{S/\langle r^2\rangle},$$

where we have of course set $k = q$. Thus at large enough q the imaging experiment actually has better signal-to-noise. However this is not the experimentally observed regime. Consider the case for 500 μm diameter beads in water. To observe the large-q behavior one requires $q\langle r^2\rangle^{1/2} \gg 1$; in practice a value of 5 has proved ample in experiments. Diffusion lengths longer than 100 μm are uncommon and sample sizes are usually not much less than 1 cm. We can estimate the surface area as the ratio of sample volume to bead radius. Using these numbers we expect PGSE to have better signal-to-noise by a factor of 25. This number will be even larger if either the bead size or the diffusion length is reduced compared with the linear dimension of the sample.

On the other hand, diffusion lengths do not exceed hundreds of μm, since the spin relaxation time limits the interval between the PGSE pulses. Thus structure functions with longer length scales are inaccessible. If one is interested in seeing coherence peaks at distances much more than 100 μm phase-suppressed imaging must be done. For the case of large-k asymptotics, the situation is less clear-cut and, although the PGSE technique is clearly the better of the two below 100 μm, both techniques can be used to study bead packs in water on the millimeter scale. However as a general rule the imaging signal-to-noise becomes relatively stronger for coarser systems where the specific surface area is reduced.

5. Experimental results

To illustrate the Debye–Porod behavior and diffraction bump in diffusion experiments, we have performed PGSE measurements on two different unconsolidated sphere packs, saturated with distilled water. In both samples, we measured $M(q, t)$ as a function of q for several diffusion times, t. All measurements were performed at a Larmor frequency of 85 MHz and at a temperature of 25.0°C. The NMR pulse sequence is based on the stimulated spin echo, so that the diffusion time is limited by T_1, rather than by the shorter T_2 relaxation time. Effects

due to background gradients are attenuated by using the sequence of Cotts et al. [12].

The diameter of the beads, $2R$, was 52 μm in the first sample and in the range of 380–515 μm in the second sample. The values of S/V_p were determined by an analysis of the short-time behavior of the diffusion coefficient [4,13] on the same samples, and found to be $S/V_p = (5.3\ \mu\text{m})^{-1}$ and $S/V_p = (48.4\ \mu\text{m})^{-1}$, respectively. These values are in agreement with the expected values for mono-sized sphere packs, assuming random packing and a porosity of $\phi = 0.38$.

In Fig. 2, the measured amplitudes, $M(q, t)$, are plotted as a function of ln q for the different diffusion times indicated. The echo amplitudes are normalized with respect to the extrapolated amplitude, $\lim_{q \to 0} M(q, t)$, obtained from data with $l_S^{-1} \ll q \ll l_D^{-1}$, where l_S is the length of the sample. At small q, our data follow a Gaussian function, $M(q, t) \simeq \exp\{-q^2 l_D^2\}$ with a diffusion length, l_D, of 43.9 and 59.6 μm for the large beads, and 15.8, 28.7 and 46.3 μm for the small beads, respectively. At larger q, the magnetization eventually decreases as q^{-4}, shown by the dotted lines in Fig. 2.

In the measurements on the small beads, the diffusion length becomes comparable with the bead diameter for the longer diffusion times, t. In this case, a clear diffraction peak develops at a wave vector $q_d = \pi/R = 1.21 \times 10^5\ \text{m}^{-1}$, as was first observed by Callaghan et al. [2]. For the large beads, the diffusion length is always significantly smaller than the bead diameter. In this case, the Gaussian behavior goes smoothly over into the q^{-4} behavior.

The signal of a phase-suppressed MRI experiment as calculated from the square root of Eq. (9) is also plotted in Fig. 2. The signal from such an experiment is below the noise level for the beads sizes and NMR apparatus used here.

Additional analysis of the data shows that the dynamic range of Γ is small, as one might expect for a simple bead pack. All values of Γ, determined experimentally, fall between the theoretical values of $\Gamma(0) = 2$ and $\Gamma(\infty) = 1$.

6. Conclusion

We have shown that the diffusive PGSE measurement bears a strong resemblance to classical diffrac-

tion. In porous media both the coherence peak and the large wave vector asyptotics can be reproduced. However a major qualitative difference between the two experiments is that the diffractive behavior in PGSE is cut off at length scales larger than the diffusion length. This is both a drawback and an advantage. Large structural features cannot be studied by PGSE. However, in the regime where PGSE does exhibit diffractive behavior, there is a major enhancement of signal-to-noise. For the case of proton NMR in water, PGSE provides a non-invasive probe in the 10–1000 μm range – a range of length scales which is not readily accessible to MRI or other standard techniques such as X-ray and small-angle neutron scattering.

References

[1] P. Debye, H.R. Anderson Jr. and H. Brumberger, J. Appl. Phys. 28 (1957) 679;
G. Porod, in: Small Angle X-ray Scattering, ed. O. Glatter and O. Kratky (Academic Press, New York, 1982) p. 17.

[2] P.T. Callaghan, A. Coy, D. MacGowan, K.J. Packer and F.O. Zelaya, Nature 351, (1991) 467; P.T. Callaghan, D. MacGowan, K.J. Packer and F.O. Zelaya, J. Magn. Reson. 90 (1990) 177.

[3] P.T. Callaghan, Principles of Nuclear Magnetic Resonance Microscopy (Clarendon, Oxford, 1991); P.T. Callaghan, A. Coy, T.P.J. Halpin, D. MacGowan, K.J. Packer and F.O. Zelaya, J. Chem. Phys. 97 (1992) 651.

[4] P.P. Mitra, P.N. Sen, L.M. Schwartz and P. Le Doussal, Phys. Rev. Lett. 68 (1992) 3555; P.P. Mitra, P.N. Sen and L.M. Schwartz, Phys. Rev. B47 (1993) 8565; P.P. Mitra, and P.N. Sen, Phys, Rev. B45 (1992) 143; P.N. Sen, L.M. Schwartz and P.P. Mitra, Magn. Res. Imaging 12 (1994) 227; L.L. Latour, P.P. Mitra, R.L. Kleinberg and C.H. Sotak, J. Magn. Reson. A101 (1993) 342.

[5] P.N. Sen, M.D. Hürlimann and T.M. de Swiet, preprint (1993); P.P. Mitra, PhD, thesis, Harvard University (1993).

[6] G.A. Barrall, L. Frydman and G.C. Chingas, Science 255 (1992) 714;
P. Mansfield and P.K. Grannell, J. Phys. C6 (1973) L422; P. Mansfield and P.K. Grannell, Phys. Rev. B12 (1975) 3618.

[7] J.G. Berryman and S.C. Blair, J. Appl. Phys. 60 (1986) 1930.

[8] P.N. Sen and M.D. Hürlimann, J. Chem Phys. 101 (1994) 5423.

[9] E.O. Stejskal and J.E. Tanner, J. Chem. Phys. 42 (1965) 288; E.O. Stejskal, J. Chem. Phys. 43 (1965) 3597; J.E. Tanner and E.O. Stejskal, J. Chem. Phys. 49 (1968) 1768; J.E. Tanner, J. Chem. Phys. 52 (1970) 2523.

[10] D.G. Cory and A.N. Garroway, Magn. Res. Medicine 14 (1990) 435.

[11] P.P. Mitra, presented at 2nd Int. Meeting on Recent Advances in Magnetic Resonance Applications to Porous Media, Kent, UK (1993) (unpublished).

[12] R.M. Cotts, M.J.R. Hoch, T. Sun and J.T. Markert J. Magn. Reson. 83 (1989) 252.

[13] M.D. Hürlimann, L.L. Latour and C.H. Sotak, Magn. Reson. Imaging 12 (1994) 325.

Dynamic effective conductivity of porous silicon

J. Tagüeña-Martínez [*], J.A. del Río, J.E. Lugo

Laboratorio de Energía Solar, Instituto de Investigaciones en Materiales, UNAM, Ap. Postal 34, Temixco 62580, Morelos, Mexico

Abstract

The dynamical effective conductivity for a model of periodic columns simulating porous silicon is analyzed using the volume averaging method. The results are compared with experimental data for crystalline and porous silicon and with a theoretical model for quantum silicon wires.

1. Introduction

Porous silicon (PS) can be produced from its crystalline counterpart by electrochemical dissolution in hydrofluoric acid and when it is highly porous it presents efficient photoluminescence of visible light at room temperature [1]. This feature, which can have important applications [2], has generated a lot of interest in the subject. Many experimental efforts have been made to characterize the structure and properties of PS using a wide variety of techniques [3]. From transmission electron microscopy (0 0 1) oriented silicon columns as narrow as 2 nm [4] have been found. The surfaces of the silicon columns are hydrogenated as a consequence of the production process; it could be said that PS is formed by three components – crystalline silicon in the bulk, hydrogenated silicon with a certain degree of amorphicity on the surface and air.

An interesting debate regarding the origin of the luminescence is taking place. On one hand the luminescence could be due to quantum confinement [5],

but on the other hand it could be due to new compounds formed on the surface (in particular siloxenes) [6]. First principles electronic structure calculations of silicon quantum wires indeed confirm that the gap widens and shifts to become direct. However, surface effects cannot be ignored, as the efficiency in luminescence in PS is closely related to the H passivation of the surface and aging (oxidation) of the samples degrades the luminescence [7]. Another important aspect to consider is the possibility of phonon-assisted transitions to produce luminescence [8].

Most of the work has been directed to optical properties. Particularly, from the above-mentioned first-principles calculations in a silicon quantum wire, the imaginary part of the dielectric function, $\epsilon_2(\omega)$, shows the expected peak in the visible region [9]. The conductivity properties are experimentally hard to study because PS is a very fragile material, but there are a few results that indicate that the PS has high resistivity [10]. Theoretically, we have calculated the static effective electrical conductivity for a periodic array of crystalline silicon columns, with a classical approach called the volume averaging method [11]. From our results, we concluded that at low porosities (much lower than the luminescence

---
[*] Corresponding author. Tel: +52-73 250 046. Telefax: +52-73 250 044. E-mail: jtp@coatl.iimtenix.unam.mx.

range) the surface contribution could increase the bulk value for the effective conductivity. Nevertheless, on passing the percolation threshold, the conductivity decreases with the porosity to reach zero at 100%.

Although quantum effects are undoubtedly important in nanostructures, transport in heterogeneous materials can be studied, in our scale, in an analogous description to that of a homogeneous material. With this idea in mind, we chose the volume averaging method, which has been successful in treating mass and energy transport in porous media [12]. It averages point transport equations over a volume whose radius is much bigger than the characteristic length of the microstructure, but much smaller than the macroscopic scale. In the case of PS, this situation is clear, since it presents a microstructure at nanometer level while the macroscopic scale is of the order of millimeters. The average transport equations are written in terms of effective parameters which include physical properties of the components and the specific geometry of the microstructure.

In this work we complete our study of the effective conductivity, Σ, of porous silicon, addressing this time the problem of the dynamic conductivity. In order to do so, we use the linear response result which connects $\epsilon_2(\omega)$ with $\Sigma(\omega)$. Our goal is to analyze the dynamic behavior, which can be very useful for certain applications as frequency filters, and to compare it with the crystalline silicon case. Finally, we compare our results with a silicon wire quantum calculation and PS experimental results.

2. Model and method

The simplest possible geometry is to consider porous silicon as a periodic network of parallel cylinders (see Fig. 1). These cylinders are characterized in their bulk by crystalline silicon measurements while for their surface properties, hydrogenated amorphous thin-film results are the appropriate ones. As we mentioned in the Introduction, PS has three components, crystalline silicon in the bulk, a-Si:H on the surface, and air. Instead of having a fluid transported through the voids, as we normally have in porous media, here the transport is through the solid and the air is an insulator.
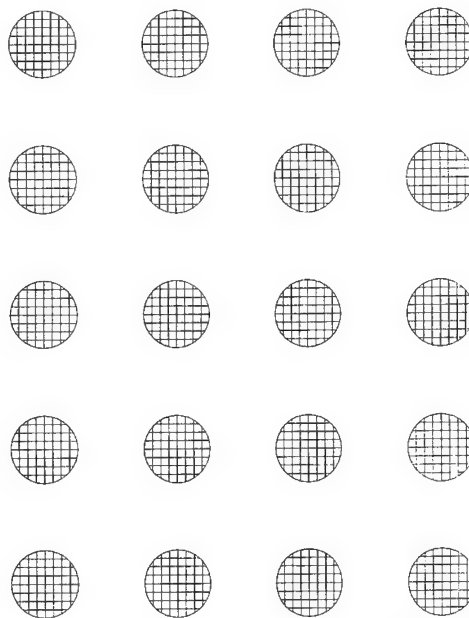
Fig. 1. Geometrical model for porous silicon: parallel cylinders in a periodic network.

The description of transport in heterogeneous materials is quite complex, since it varies from point to point. However, under certain circumstances, on the macroscopic scale, it is justified to develop an analogous description to that of a homogeneous material. This approach enormously simplifies the mathematical complexity of the problem together with its physical interpretation. The volume averaging method takes this approach. Fig. 2 shows the relevant scales involved in a two-component system. The average is performed in a volume characterized by r_0, where $L \gg r_0 \gg l$; this means that the averages are space-dependent.

For the purpose of clarity, let us repeat part of the procedure of our previous calculations [11]. The local problem is given by the equations

$$(\partial \rho_c / \partial t) + \boldsymbol{\nabla} \cdot \boldsymbol{J} = 0 \tag{1}$$

and

$$(\partial \rho_a / \partial t) + \boldsymbol{\nabla} \cdot \boldsymbol{J}_a = \boldsymbol{J} \cdot \boldsymbol{n}^{cv} \text{ on } A^{cv} \tag{2}$$

where ρ_c is the carrier density concentration in crystalline silicon, ρ_a is the surface carrier density concentration in a-Si:H, $\boldsymbol{J}$ is the current density, $\boldsymbol{J}_a$ is the surface current density and $\boldsymbol{n}^{cv}$ is the normal vector to the cylindrical Si–air interface, A^{cv}. For
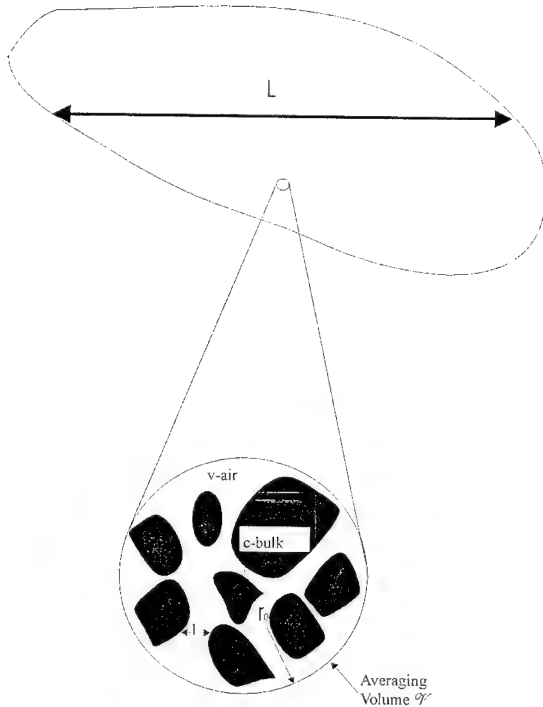
Fig. 2. Relevant scales in a two-component system. v refers to the vacuum and c to the medium: air and silicon in our case.

Ohm's law we should use the external electric field contribution, given by

$$J = -\sigma_c \nabla \phi_c, \tag{3}$$

where ϕ_c is the electric potential and σ_c is the electrical conductivity for the crystalline silicon. A similar equation must consider the surface region. The effective transport equation to be solved can be written as

$$(1-P)\left(1 + \frac{a_v K}{1-P}\right)\frac{\partial}{\partial t}\langle \rho_c \rangle = \nabla \cdot (\Sigma \cdot \nabla \langle \phi_c \rangle), \tag{4}$$

where the angular brackets $\langle\ \rangle$ indicate the spatial average, P is the porosity (void/averaging volume), a_v is the superficial area of the interface per unit of total volume, $K = \rho_a/\rho_c$, and Σ is the effective conductivity tensor given by

$$\Sigma = (1-P)\sigma_c\left(I + V^{-1}\int_{A^{cv}} n^{cv}\Omega f \, dA\right) + a_v K\sigma_a I. \tag{5}$$

Here $\Omega = 1 + (2HK\ (\sigma_a/\sigma_c))$, with H being the curvature of the cylinders, σ_a is the conductivity in a-Si:H, I is the unit tensor and f is a vector which depends on the parameters σ_c, σ_a, K and the microstructure of the PS (for details see Ref. [13]). Although there are many other averaging methods to study transport in heterogeneous media [14], none of them can deal with the surface contribution in a way simple as the volume averaging method. Further, since there is no explicit time dependence, this relation is valid in ω space.

It is obvious that the value of f in Eq. (5) is not needed in the axial component, because the product $n^{cv} \cdot k$ is zero for any microstructure of constant cross-section in the k direction. However, in the transverse direction this term must be calculated by solving the closure problem. This solution may be analytical if the representative cell is taken as a cylinder inside another cylinder, the so-called Chang approximation [13]. However, in the Chang model, the percolation limit cannot be attained. Thus, for our case, that is a cylinder in a square, the closure equation for f has to be solved numerically for low porosities.

In our geometrical model, a change of porosity means a change in the cylinder radius. We are considering a fixed volume and, therefore, to increase the porosity implies a reduction in the cylinder radius. Within our model, a cylinder within a cube, the percolation limit will be given when the circles touch the square, at a $P = 1 - \pi/4$. Luminescent samples of PS are well above this concentration, so we calculates only the simpler and analytical axial component, in porosities over 70%.

In order to calculate the dynamical conductivity for different porosities, we need to introduce experimental information. There are results available for the frequency-dependent dielectric function of c-Si [15], a-Si:H [16], PS [17] and silicon wires [9]; the first three are experimental and the fourth one is a first-principles calculation of silicon quantum wires up to about 1.5 nm using density-functional theory within the local-density approximation for the exchange–correlation energy, where the silicon dangling bonds at the surface are saturated with hydrogen atoms.

From the dielectric function, $\epsilon = \epsilon_1 + i\epsilon_2$, as a function of the frequency, ω, using a well known

result from linear response, the real part of the conductivity, σ, can be calculated as

$$\mathrm{Re}(\sigma) = \epsilon_2 \omega \epsilon_0, \tag{6}$$

where ϵ_0 is the permittivity in vacuum. One has to be careful in interpreting the conductivity calculated like this because it does not correspond to the experimental dc conductivity, since this relation includes the polarization contribution.

Once all the ingredients are given, we proceed to show the results.

3. Results

As we have already explained, the advantage of using the volume averaging method is that the surface contribution can be treated explicitly. However, we will start by only considering the bulk contribution. In Fig. 3 we show the effective conductivity for crystalline silicon (0% porosity) and porous c-Si obtained from Eq. (5) without the surface contribution; we are comparing this result with that of a silicon quantum wire using Eq. (6). As can be seen, the plots are very different, not only in shape but in the range of frequencies where the response takes place. In Fig. 4 we have the normalized results of introducing the surface effect as the frequency-dependent conductivity of a thin a-Si:H film, for a

Fig. 4. Normalized dynamic conductivity of PS at $K = 10^{-8}$ compared with c-Si and silicon quantum wire results [7] and experimental PS data [15].

certain value of K which characterizes the quality of the surface (for instance, $K = 10^{-7}$ is a well saturated surface) and we also compare with PS experimental data. Clearly, to consider the surface gives a behavior closer to the silicon quantum wire and the experimental PS.

In Fig. 5 we plot the experimental and theoretical normalized dynamic effective conductivity of PS with different surfaces varying the K values.

Fig. 3. Dynamic effective conductivity of c-Si, porous c-Si and silicon quantum wire [7].
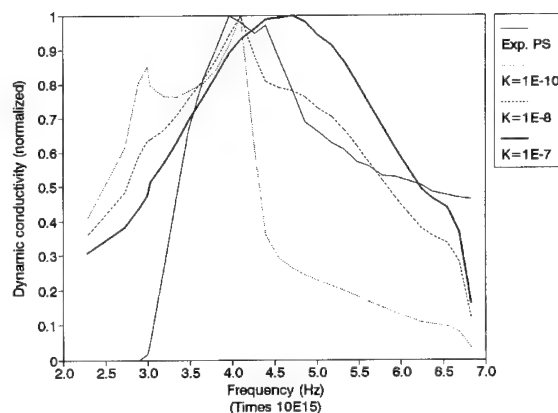
Fig. 5. Theoretical and experimental normalized effective dynamic conductivity of PS at (a) $K = 10^{-10}$, (b) $K = 10^{-8}$ and (c) $K = 10^{-7}$.

4. Discussion

It is important to establish the limits of our approach. As in any spatial integration method, our results are in the framework of mean-field approximation, i.e., we describe global behavior. Moreover, our results use the linear response approximation for the relation between the dielectric function and the electrical conductivity. However, because our analytical results allow us to study the volumetric and the superficial contributions independently, we can explore the role of the surface on the effective response.

When the quantum Si wire result for the dielectric function [8] is compared with the PS experimental data [17], it is clear that quantum confinement could be behind the peak in the visible range which explains the luminescence of Si wires. If quantum confinement can change the relevant range of energies of crystalline Si for a certain response, the question is then whether the surface contribution can have the same tuning effect. To answer this question, we start comparing porous crystalline Si (without surface) with the quantum Si wire effective conductivity calculation (Fig. 3) and we conclude that merely introducing holes in a crystalline bulk decreases the height, but does not shift the response. Afterwards, we consider the surface effect (see Fig. 4) and observe that now the relevant energies can be shifted in the right direction for a certain surface.

To compare our model theoretical results with the PS experimental plot, we try different K values (Fig. 5) and we again observe that the surface plays the role of tuning, shifting both the frequency range of the response and the peak position. It must be pointed out that real PS samples, particularly the passivation of their surfaces, depend heavily on the process of fabrication.

5. Conclusions.

Quantum confinement calculations in silicon wires are consistent with many observations in PS. Even the fact that the highly PS has a very high electrical resistivity can be explained in terms of very localized carriers, separated from the delocalized states by a large activation energy [5]. However, our results

seem to indicate that the surface effects might have similar consequences, at least regarding the range of relevant frequencies for the effective dynamic conductivity. Also, within our model, at high porosities, PS has to be more insulating than c-Si. The tuning role of the surface as a result of our theoretical calculation supports the possibility that the surface effects may be responsible for a change in the energy range of a response. This goes further than merely comparative arguments with experimental data [6], which have been used suggesting the relevance of the surface for the luminescent PS.

There are few experimental results reported at the moment for the effective electrical conductivity of PS. It is promising that PS has already been used for a solar cell although with a very high series resistance [10]. It would be interesting to explore further the effective dynamic conductivity.

References

[1] L.T. Canham, Appl. Phys. Lett. 57 (1990) 1046.

[2] M.A. Tischler, R.T. Collins, M.L.W. Thewalt and G. Abstreiter, eds., Silicon-Based Optoelectronic Materials, Mater. Res. Soc. Symp. Proc. 298, (Materials Research Society, Pittsburgh, PA, 1993).

[3] S.S. Iyer, R.T. Collins and L.T. Canham, eds., Light Emission from Silicon, Materials Research Soc. Symp. Proc. 256, (Materials Research Society, Pittsburgh, PA 1992).

[4] A.G. Cullis and L.T. Canham, Nature 353 (1991) 335.

[5] A.J. Read, R.J. Needs, K.J. Nash, L.T. Canham, P.D.J. Calcott and A. Qteish, Phys. Rev. Lett 69 (1992) 1232.

[6] P. Deák, M. Rosenbauer, M. Stutzmann, J. Weber and M.S. Brandt, Phys. Rev. Lett. 69 (1992) 253.

[7] M.A. Tischler, R.T. Collins, J.H. Stathis and J.C. Tsang, Appl. Phys. Lett. 60 (1992) 639.

[8] P.D.J. Calcott, K.J. Nash, L.T. Canham, M.J. Kane and D. Brumhead, J. Phys.: Condens Matter 5 (1993) L91.

[9] F. Buda, J. Kohnoff and M. Parrinello, Phys. Rev. Lett. 69 (1992) 1272.

[10] G. Smestad, M. Kunst and C. Vial, Solar Energy Mater. Solar Cells 26 (1992) 277.

[11] J.A. del Río, J. Tagüeña-Martínez and J.A. Ochoa-Tapia,

Solid State Commun. 87 (1993) 541; J. Tagüeña-Martínez, J.A. del Río and J.A. Ochoa-Tapia, Solid State Commun. 90 (1994) 411.

[12] S. Whitaker, Transport Porous Media 1 (1986) 3.

[13] J.A. Ochoa-Tapia, J.A. del Río and S. Whitaker, Chem. Engg. Sci. 48 (1993) 2061.

[14] D.J. Bergman, Phys. Rep. C43 (1978) 377; W.L. Mochán and R.G. Barrera, Phys. Rev. B32 (1985) 4984.

[15] G.E. Jellison Jr., Opt. Mater. 1 (1992) 41.

[16] M. Fried and T. Lohner, J. Appl. Phys. 71 (1992) 5260.

[17] N. Koshida, Appl. Phys. Lett. 63 (1993) 2774.

Layer rigidity in 2D disordered Ni–Al layer double hydroxides

S.A. Solin [a,*], D. Hines [a], S.K. Yun [b], T.J. Pinnavaia [b], M.F. Thorpe [c]

[a] *NEC Research Institute, Inc., 4 Independence Way, Princeton, NJ 08540, USA*
[b] *Department of Chemistry and Center for Fundamental Materials Research, Michigan State University, East Lansing, MI 48864, USA*
[c] *Department of Physics and Astronomy and Center for Fundamental Materials Research, Michigan State University, East Lansing, MI 48864, USA*

Abstract

A series of layer double hydroxide carbonates with the chemical composition $[(CO_3)_{x/2} \cdot y(H_2O)]-[Ni_{1-x}Al_x(OH)_2]$, $0 < x < 0.4$, $0 < y < 1.2$ has been prepared. The composition dependence of the basal spacing of these compounds has been determined from X-ray diffraction measurements and has been computed using an extended version of the discrete finite-layer rigidity model which includes both intra- and inter-layer rigidity effects. The inter- and intra-layer rigidity parameters of $Ni(OH)_2$ were found to be ~ 5 and 2.44, respectively, from which we conclude that the host $Ni(OH)_2$ spans class II and class III layered solids. On the basis of our X-ray measurements and steric considerations, it is determined that the carbonate ion is oriented in the host gallery with its threefold axis essentially parallel to the host c-axis.

1. Introduction

1.1. Rigidity and classification

Layered solids have been qualitatively classified into three distinct subgroups based on their degree of transverse layer rigidity vis-à-vis out-of-plane distortions [1,2]. According to this classification scheme, class I layered solids comprise only graphite and boron nitride, the layers of which are of monatomic thickness and are thus 'floppy' with respect to transverse distortions. Class II materials include the layered dichalcogenides, iron oxychloride and several other materials, the layers of which are typically composed of three interconnected planes of atoms. This interconnectivity enhances the layer rigidity of

Class II materials relative to that of Class I. The most rigid layered materials known are those falling into Class III which includes, for example, layered silicate clays and layered perovskites. They typically consist of five or more interconnected planes of atoms.

The weak (van der Waals) interlayer interaction in layered solids engenders the process of intercalation in which a variety of guest species can be ingested into the galleries between host layers. In Class I and II solids, intercalation necessitates charge exchange between the guest and host layer. Thus graphite, which is amphoteric, can accommodate either donor or acceptor guest species into its galleries [3]. By contrast, layered silicate clays possess a fixed (negative) layer charge and intercalation into these materials typically constitutes ion exchange of one guest cation for another [4].

To establish a quantitative measure of layer rigidity and thus justify the qualitative classification

* Corresponding author. Tel: +1-609 951 2610. Telefax: +1-609 951 2615. E-mail: solin@research.nj.nec.com.

scheme described above, Solin and co-workers developed experimental methods and supporting theoretical models which are based on the variation of the c-axis repeat distance or basal spacing with the composition of a 2D disordered solid solution intercalated into the galleries of the host solid [5,6]. The generic formula for such a system is $A_{1-x}B_xL$ where $0 < x < 1$, A is the smaller guest ion or a vacancy, B is the larger guest ion and L represents the host layer. In layer rigidity studies carried out to date [5,6], the composition of the host layer was independent of the composition of the intercalated 2D solid solution. In this paper we report the first systematic study of the layer rigidity in a layered solid for which the host layer composition depends on that of the guest layer. We show that the solid of interest here $[(CO_3)_{x/2} \cdot y(H_2O)]–[Ni_{1-x}Al_x(OH)_2]$, a layer double hydroxide (LDH) clay (where the entities in square brackets represent the [guest]–[clay] layers), exhibits several novel features in its layer rigidity (including dual classification) and we account quantitatively for those features with an augmentation of previously developed layer rigidity models [5,6]. Although several authors [7–9] have previously studied the structural properties of the Ni–Al LDHs, a quantitative explanation of their composition-dependent properties has not been given.

1.2. Structural properties of Ni–Al LDHs

Pure $Ni(OH)_2$ crystallizes in the cadmium iodide (or, equivalently, the brucite) structure and belongs to the hexagonal space group $P3m1$ (No. 164) with cell parameters $a = 3.126$ Å and $c = 4.065$ Å. [10,11] The structure is composed of close-packed planes of hydroxyl ions which themselves lie on a triangular lattice. The Ni ions occupy the octahedral holes between alternate pairs of OH planes and thus occupy a triangular lattice identical to that adopted by the OH ions. The unit cell of this structure contains one formula unit of $Ni(OH)_2$ and thus one layer of the host structure. We consider $Ni(OH)_2$ to be a brucite-like clay host.

Using the sample synthesis techniques described below, Ni^{2+} ions in nickel hydroxide can be substitutionally replaced by Al^{3+} ions with the concomitant insertion of carbonate ions and water into the gallery to provide overall charge neutrality in the
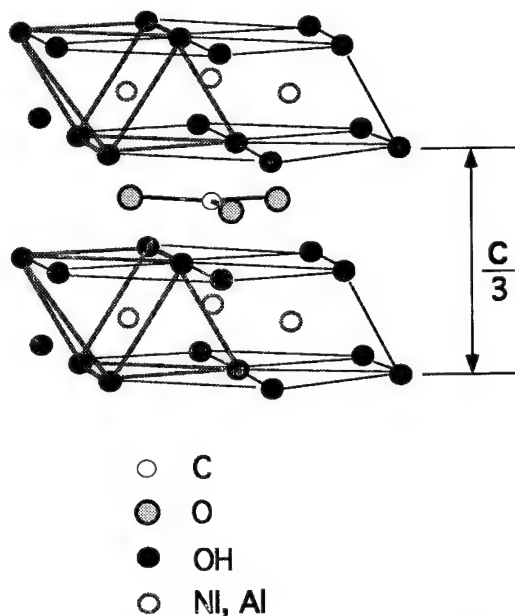
Fig. 1. Schematic illustration of the structure of $[(CO_3)_{x/2} \cdot y(H_2O)]–[Ni_{1-x}Al_x(OH)_2]$. The orientation of the carbonate ion about its C_3-axis is not fixed but its planar arrangement is correctly depicted. Residual water in the gallery is not shown. The circles depicting the ionic constituents are not drawn to scale.

presence of the positively charged host layer. The resultant compound, $[(CO_3)_{x/2} \cdot y(H_2O)]–[Ni_{1-x}Al_x(OH)_2]$, a cationic clay, is a member of the pyroaurite–sjögrenite group of hydroxy carbonates [7–9] which possess the characteristic structure shown schematically in Fig. 1 (gallery water is not shown). The aluminum distribution on the triangular metal ion lattice depends on composition and may or may not be random [7–9]. The carbonate and water are presumed to randomly occupy the octahedral sites between the clay layers and the rotational orientation of the carbonate about its c-axis is undetermined. The planar orientation of the carbonate ion shown in Fig. 1. is justified below.

2. Experimental procedure

2.1. Sample synthesis

Reagent-grade chemicals $Ni(NO_3)_2 \cdot 6H_2O$, $Al(NO_3)_3 \cdot 9H_2O$ and NaOH from Aldrich, and

Na_2CO_3 from Fisher together with deionized water were used for the preparation of all aqueous solutions used in sample synthesis. The reaction pH was controlled by a Fisher selective ion analyzer Model 750.

2.1.1. $Ni(OH)_2$

Into 100 ml H_2O pre-adjusted at pH 8.5 at 40°C was slowly added 1M Ni^{2+} nitrate solution (100 ml) with vigorous stirring. The reaction pH was kept at 8.5 (± 0.1) by a 2M NaOH solution through the delivery of Ni^{2+} nitrate solution. After complete delivery, the resultant suspension was further stirred for 1 h under the same conditions. Following 40 h digestion of the suspension with vigorous stirring at 70°C, the suspension was cooled to room temperature. The green $Ni(OH)_2$ product was then filtered, washed repeatedly with water and dried in air at room temperature.

2.1.2. $[(CO_3)_{x/2} \cdot y(H_2O)]–[Ni_{1-x}Al_x(OH)_2]$

A series of Ni–Al LDH carbonates, $[(CO_3)_{x/2} \cdot y(H_2O)]–[Ni_{1-x}Al_x(OH)_2]$, $((1-x)/x = 1.10, 1.50,$ 2.00, 2.33, 3.00, 4.00, 5.00), were prepared by a modification of the coprecipitation method [12]. A 150 ml portion of 1M mixed metal nitrate solution of Ni^{2+} and Al^{3+} ($Ni^{2+}/Al^{3+} = 1.10, 1.50, 2.00, 2.33,$ 3.00, 4.00, 5.00) was slowly added into 150 ml water, pre-adjusted with NaOH to pH 8.5, with vigorous stirring at 40°C. The reaction pH was kept at 8.5 (± 0.1) by the addition of a mixed base solution of 2M Na_2CO_3 ($CO_3^{2-}/Al^{3+} = 1.5$) and 2M NaOH. After complete delivery of the mixed nitrate solution, the suspension was further stirred for 1 h. Following 40 h digestion at 70°C with vigorous stirring, the suspension was cooled to room temperature. The greenish precipitate was then filtered, washed repeatedly with water free of the sodium ion and dried in air at room temperature. For the preparation of $[(CO_3)_{x/2} \cdot y(H_2O)]–[Ni_{1-x}Al_x(OH)_2]$, $((1-x)/x = 9.00)$, the same experimental procedure was adopted except that 0.5M solutions of mixed nitrate and base were used instead of 2M solutions.

2.1.3. Chemical properties

Elemental analyses of all samples were performed by inductively coupled plasma (ICP) emission spectroscopy [13] at the Toxicology Lab at Michigan

Table 1

Composition parameters for the Ni/Al LDH carbonates $[(CO_3)_{x/2} \cdot y(H_2O)]–[Ni_{1-x}Al_x(OH)_2]$

Ni/Al	x ($\pm 1\%$)	y ($\pm 5\%$)	y_{max}	L_a (Å) ($\pm 5\%$)	L_c (Å) ($\pm 5\%$)
1.5	0.400	1.03	1.7148	80	43
2.0	0.333	0.86	1.7770	121	79
2.33	0.303	0.84	1.8053	109	53
3.0	0.250	0.72	1.8547	109	89
4.0	0.200	0.69	1.9013	97	58
5.0	0.167	0.65	1.9324	– [a]	37
9.0	0.100	0.55	1.9945	– [a]	15
∞	0.000	0.06	2.0878	267	118

[a] Not determined because the (110) reflection is not resolved.

State University (MSU). About 30 mg of the samples were dissolved in 100 ml HNO_3 solution (20 vol.%) for each analysis. Energy-dispersive X-ray analysis in a scanning electron microscope (Hitachi Model S-2700) equipped with a detector system (PGT Model 1M1X) was used to test for microscopic phase separation. All particles of all solid solution samples in the range $1.1 < (1-x)/x$ were found to exhibit the same morphology and to contain both nickel and aluminum and showed no evidence of phase separation. We found it impossible to prepare homogeneous solid solutions of Ni–Al LDH carbonates with lower concentrations of nickel as such samples would always contain phase-separated aluminum hydroxide. We also found that water cointercalated with the carbonate ion in all the samples but the pure $Ni(OH)_2$. The water content (y value) was determined from thermogravimetric analysis (TGA) measurements which are described in detail elsewhere [14]. The results of these determinations for each of the samples studied are shown in Table 1.

2.2. X-ray diffraction

X-ray powder patterns were acquired using an Enraf Nonius rotating-anode X-ray generator with a vertical tube tower. A bent crystal graphite monochromator selected a horizontal line source of Cu Kα radiation. This radiation was incident on a sample mounted on a four-circle diffractometer (Huber). The diffractometer was in a horizontal configuration and was controlled by a motor controller (Klinger Motion Master). A NaI scintillation detector was

mounted on the 2θ arm of the diffractometer and was connected to electronics (Ortec). The motor controller and electronics were computer-controlled using Spec X-ray diffraction software which ran under UNIX on a 386/20 MHz PC. The maximum resolution of this instrument is 0.0024 $\mathring{A}^{-1}$ as determined from the width of the [111] reflection of single-crystal silicon. The basal spacing of each solid solution ($x > 0$) sample was obtained from a q-plot [15] containing at least three (00l) reflections.

3. Results

The powder X-ray diffraction patterns of each of the samples studied are shown in Fig. 2. As can be seen from that figure, the (00l) reflections dominate the diffraction patterns of the solid solution samples. Those powder patterns are consistent with the pyroaurite 3R polytype structure of the pyroaurite–sjögrenite group [7–9] and have been indexed accordingly. The pattern for pure Ni(OH)$_2$ is indexed to the brucite structure, the unit cell of which contains only one nickel hydroxide layer [16]. Although several of the reflections from the solid solutions are broad they are still sufficiently well developed to preclude microscopic phase separation. There is also no evidence of interstratification [18] which would be indicated by multiple sets of basal reflections. Thus, the X-ray results support the SEM analysis. The X-ray data of Fig. 2 have been used in conjunc-

Fig. 3. The composition, x, dependence of the measured room-temperature basal spacing of $[(CO_3)_{x/2} \cdot y(H_2O)]$–$[Ni_{1-x}Al_x$-$(OH)_2]$ obtained from a q-plot of the (00l) reflections of the powder patterns shown in Fig. 2. (See text.)

tion with the Scherrer formula [17] to determine the in-plane and c-axis correlation lengths, L_a and L_c, respectively. These correlation lengths are listed in Table 1. Note that the in-plane correlation lengths are consistently larger than those of the c-axis.

The composition dependence of the basal spacing, d, of the Ni–Al LDHs is shown in Fig. 3 together with the inset. (For the pyroaurite 3R polytype, $d = c/3$, where c is the c-axis lattice constant.) This basal spacing response is, to our knowledge, unique since it exhibits a distinct maximum in contrast to other 2D solid solutions which exhibit a monatonic increase in the range $0 \leq x \leq 1$ [5,6]. The expanded scale of the inset of Fig. 3 shows that the actual maximum in the basal spacing occurs at about $x = 0.2$. Also noteworthy in Fig. 3 is the unusually large jump in basal spacing at x between 0 and 0.1.

In order to relate the composition-driven c-axis expansion of all layered solids including the Ni–Al LDHs to one another we defined [5] the normalized basal spacing, $d_n(x)$, as

$$d_n(x) = \frac{d(x) - d(0)}{d(1) - d(0)}. \tag{1}$$

Thus $d_n(0) = 0$ and $d_n(1) = 1$ by the definition of Eq. (1). For the Ni–Al LDHs, $d(0)$ is the basal spacing of pure Ni(OH)$_2$ while $d(1)$ is the basal spacing of $(CO_3)_{1/2}Al(OH)_2$, a compound which, to our knowledge, does not exist in nature but whose basal spacing if it did exist can be determined from

Fig. 2. The composition, x, dependence of the room-temperature, Cu Kα powder X-ray diffraction patterns of $[(CO_3)_{x/2} \cdot y(H_2O)]$–$[Ni_{1-x}Al_x(OH)_2]$. These patterns were acquired with an instrument resolution of 0.006 $\mathring{A}^{-1}$.
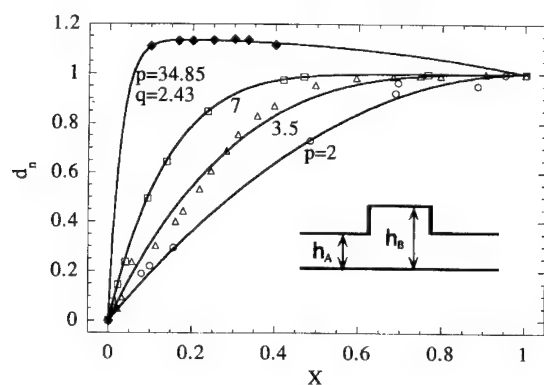
Fig. 4. The composition, x, dependence of the normalized basal spacing of the Ni–Al LDH carbonates ($\blacklozenge$) (see Fig. 3 for error bars) compared with that of other characteristic layered solids [19] ($\bigcirc$, Li_xC_6; $\triangle$, Li_xTiS_2; $\square$, Cs_xRb_{1-x} – vermiculite (error bars are smaller than the size of the datapoints)). The solid lines are non-linear least-squares fits to the data using Eq. (8) for the LDH and Eq. (4) for the others. The parameters p and q yielding these solid lines are also shown in the figure. Inset – schematic illustration of layer puckering in the discrete finite layer rigidity model (see text).

the data of Fig. 3, as we show below. The composition dependence of the normalized basal spacing of $[(CO_3)_{x/2} \cdot y(H_2O)]–[Ni_{1-x}Al_x(OH)_2]$ is shown in Fig. 4 together with the normalized basal spacings of other layered solids [19] which have been previously studied.

4. Discussion

4.1. The finite layer rigidity model

4.1.1. Composition-independent host layer thickness

In previous studies of the layer rigidity of intercalated layered solids, Solin and co-workers [5,6] have developed the finite layer rigidity (FLR) model in both a discrete and a continuum version to account for the observed composition dependence of the basal spacing. Because the physical parameters of the continuum FLR model such as the elastic stiffness constants are not known for the Ni–Al LDHs we focus here on the discrete FLR. We briefly review this model and show how it can be extended to encompass the unique behavior of the Ni–Al LDHs. Before proceeding, however, it is important to note that the discrete FLR model incorporated two

key assumptions. First, the host layer composition was independent of the composition of the solid solution in the gallery. Thus, when x is changed in $A_{1-x}B_xL$, L is unaffected. Second, the host layer may pucker in the region around a large (B) ion but its thickness remains constant.

The discrete FLR model as originally formulated [20] is based on the two-layer construction shown in the inset of Fig. 4. If h_B is the height of the B ion ($=$ twice the radius if the ion is spherical) and h_A is the height of the A ion, then a pillbox-like distortion will occur in the upper layer in the region around the B ion. The puckered area around the B ion, called the catchment area, will contain an average of, say, p lattice sites and is dependent on the layer rigidity. Thus p is defined to be the rigidity parameter. Then the effective height of the gallery between layers, [20] $h(x)$ is

$$h(x) = h_A(1-x)^p + h_B\left[1 - (1-x)^p\right] \qquad (2)$$

and the basal spacing is

$$d(x) = t + h_A(1-x)^p + h_B\left[1 - (1-x)^p\right], \qquad (3)$$

where t is the composition-independent host layer thickness. Upon substituting Eq. (3) into Eq. (1) to obtain the normalized basal spacing in the discrete FLR model, we find that

$$d_n(x) = 1 - (1-x)^p. \qquad (4)$$

Note from Eq. (4) that, within the formulation of the FLR model, the rigidity parameter can be obtained directly from the slope of $d_n(x)$ as $x \to 0$. Also note that for $p = 1$, which corresponds to zero rigidity since the large ion puckers only its own site, $d_n(x) = x$. This is Vegard's law [21] which is the expected result for perfectly floppy layers. (In the discrete FLR model, the A and B ions are assumed to have zero width and thus cause point-like vertical distortions of the host layers.)

4.1.2. Composition-dependent host layer thickness

For the Ni–Al LDH carbonates, both the gallery height and the host layer thickness are composition-dependent. Let the latter be designated $t(x)$. In the spirit of the discrete FLR model, we write the thickness of the hydroxide layer as

$$t(x) = t_{Ni(OH)_2} - 2(r_{Ni} - r_{Al})x^q, \qquad (5)$$

where $t_{Ni(OH)_2}$ is the thickness of the pure $Ni(OH)_2$ which for the structure of that compound discussed above is equal to its basal spacing of 4.75 Å, $r_{Ni} = 0.69$ Å [22] is the ionic radius of Ni^{2+}, and $r_{Al} = 0.51$ Å [22] is the ionic radius of Al^{3+}. The parameter, q, can be thought of as an intralayer rigidity parameter which measures the rigidity against puckering due to substitutions within the layer itself. In Eq. (5) it is explicitly assumed that the basal spacing of the fictitious compound $(CO_3)_{1/2}Al(OH)_2$ can be computed by subtracting the differential height of Ni and Al from the basal spacing of $Ni(OH)_2$.

The composition dependence of the gallery height, $h(x)$, can be obtained directly from the discrete FLR model if we view the guest pair as the CO_3 ion plus a vacancy. If we let s be the fraction of *available* carbonate ion sites that are filled, then

$$h(s) = h_{CO_3}\left[1 - (1-s)^p\right] + h_{Ni(OH)_2} \qquad (6)$$

where h_{CO_3} is the effective height of the carbonate ion in the LDH gallery and $h_{Ni(OH)_2}$ is the gallery height in $Ni(OH)_2$. There are two possible choices for the relation of s to x. The chemically defined relation is $s = x/2$ since only one carbonate is required for every pair of nickel ions replaced by aluminum ions. However, from the point of view of the FLR, the maximal occupancy of the gallery by carbonate is achieved when the nickel in the host layer is completely replaced by aluminum. Moreover, the water that necessarily cointercalates with carbonate ions into the gallery may contribute to the propping apart of the host layers. Unfortunately, the amount of water present is not a known analytic function of x (see discussion below). We therefore make the approximation that the gallery is fully occupied when nickel replacement is complete in which case $s = x$. With this definition we find

$$d(x) = d_{Ni(OH)_2} + h_{CO_3}[1 - x^p]$$
$$- 2(r_{Ni} - r_{Al})(1-x)^q, \qquad (7)$$

where $d_{Ni(OH)_2} = t_{Ni(OH)_2} + h_{Ni(OH)_2}$ is the basal spacing of pure nickel hydroxide. From the substitution of Eq. (7) into Eq. (1) we find

$$d_n(x) = \frac{h_{CO_3}[(1-x^p)-1] - 2(r_{Ni}-r_{Al})[(1-x)^q - 1]}{2(r_{Ni}-r_{Al}) - h_{CO_3}}. \qquad (8)$$

4.1.3. Applying the model and interpreting the results

We have used Eq. (8) with the above specified values of r_{Ni} and r_{Al} and with h_{CO_3}, p and q as adjustable parameters to obtain a non-linear least-squares fit to the data of Fig. 4 for the Ni–Al LDHs. The model yields an excellent fit to the data as can be seen from the solid lines in Fig. 4 and the corresponding adjusted parameters are: $h_{CO_3} = 3.09 \pm 0.02$ Å, $p = 35.31 \pm 2.80$ and $q = 2.44 \pm 0.73$. The corresponding fit to $d(x)$ obtained by inserting these parameters into Eq. (7) is shown as a solid line in Fig. 3. We now interpret these results.

The carbonate ion must be oriented in the gallery with its threefold symmetry axis essentially parallel to the c-axis of the host structure. Such an arrangement leads to a value of h_{CO_3} close to the van der Waals diameter of oxygen, 2.80 Å [22], in agreement with observation. The analogous height if the threefold axis was perpendicular to the c-axis would be twice the effective radius of the CO_3 ion or 5.35 Å (see discussion following Eq. (9) below). Such a height is clearly incompatible with the measured value of h_{CO_3}.

We believe that the interlayer rigidity parameter, p, has been fictitiously enhanced for the following reason: the water which is present will tend to solvate (bind to) the charged carbonate ions and thus, given its similar height, contributes to the propping apart of the host layers. However, account for this effect is not explicitly expressed in Eq. (8) because the observed functional dependence of y on x which is shown in Fig. 5 is not known analytically. We have used a steric model to calculate the maximum value of y as a function of x assuming the gallery area per Ni ion is fully occupied by a monolayer containing water molecules and carbonate ions. Then

$$A_{Ni} = y_{Max} A_{H_2O} + (x/2) A_{CO_3}, \qquad (9)$$

where $A_{Ni} = 25.45$ Å, $A_{H_2O} = 12.19$ Å and $A_{CO_3} = 22.73$ Å are the areas per Ni site, per water molecules and per carbonate, respectively, in $Ni(OH)_2$. The latter two values were determined from the radius of the smallest circle that could inscribe the molecule whose dimensions were obtained from the known bond lengths [11], bond angles [11] and the Van der Waals radii [22] of the constituents.
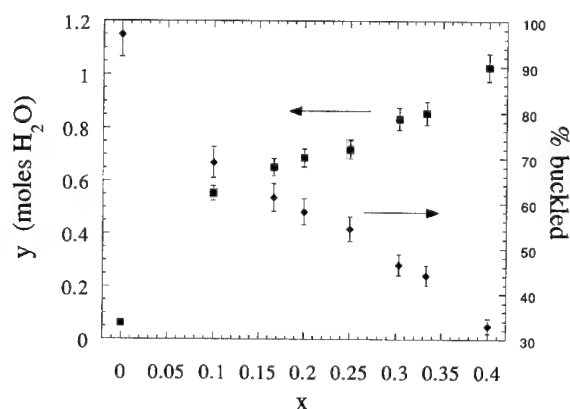
Fig. 5. The composition, x, dependence of the water content in the Ni–Al LDH carbonates (diamonds) and the percentage of host layer area that is buckled between solvated carbonate pillars (squares).

The values of y_{Max} deduced from Eq. (9) are listed in Table 1 for all of the samples studied. In every case they significantly exceed the actual water content which is thus apparently not controlled by planar steric hindrance. In further support of the lack of planar steric hindrance, we note from Fig. 5. and Table 1 that y increases with x over the range studied. However, if planar steric hindrance controls the water content, as more CO_3 is added to the gallery, the area available for water and thus y is reduced. To understand the contrasting observed behavior, recall that in the FLR model the host layer can collapse/buckle somewhat to yield a reduced gallery height in the lateral space between solvated

carbonate pillars. The amplitude of this buckling necessary to vertically exclude additional water can be quite small (< 0.1 Å). We estimate the percentage of host layer area that is buckled to be

$$\%\text{Buckled} = \left(1 - \frac{yA_{H_2O} + (x/2)A_{CO_3}}{A_{Ni}} \right) \times 100. \tag{10}$$

This function is plotted in Fig. 5. using the data from Table 1. As can be seen from that figure, the buckled area decreases with increasing x, thus resulting in increased water incorporation in qualitative agreement with observation. In this analysis, $Ni(OH)_2$ is fully (100%) collapsed and contains no gallery water.

The effect of the ficticious enhancement of the interlayer rigidity parameter can be roughly approximated by a re-scaling of the composition axis for the interlayer rigidity parameter as shown previously by Lee et al. [6] for the case of H_2 and D_2 physisorbed into KC_{24}. In effect, the gallery expansion reaches and retains its maximum value when very few carbonate ions are present, i.e., at x lower than that deduced from the chemical formula. As can be seen from Figs. 3 and 4, this value of x is approximately 0.15 where the rapid increase in d_n terminates. Thus the actual interplanar rigidity parameter is approximated as $p \sim 0.15 \times 34.85 = 5.22$. This is the (rounded) value we have entered into Table 2 where

Table 2
Classification and relevant parameters for layered solids

Host	Class	Intersite distance a (Å)	Site ratio α	Inter-layer		Intra-layer	
				rigidity parameter, p $\pm 5\%$	healing length, λ_d^{inter} $\pm 3\%$	rigidity parameter, q $\pm 5\%$	healing length, λ_d^{intra} $\pm 3\%$
Graphite	I	2.4704 ± 0.0001	3	2	3.16	–	–
Titanium disulfide	II	3.410 ± 0.005	1	3.5	3.35	–	–
Nickel hydroxide	II–III	3.126 ± 0.005	1	~ 5 [a]	~ 3.7	2.44	2.56
Vermiculite	III	5.344 ± 0.003	1	7	5.34	–	–

[a] This is the corrected value; the measured value is 35.31; see text.

we compare our results for nickel hydroxide with previous measurements on other layered solids.

The discrete version of the FLR model relates the interlayer rigidity parameter to the interlayer discrete healing length, λ_d^{inter}, through the relation

$$p = \pi \left(\lambda_d^{inter} \right)^2 / \alpha A_0. \tag{11}$$

The analogous expression for the intralayer rigidity parameter is

$$q = \pi \left(\lambda_d^{intra} \right)^2 / \alpha A_0, \tag{12}$$

where α is the ratio of the area per site of the saturated ($x = 1$) guest layer to the area per host site and A_0 is the area per lattice point of the host. The numerator in Eq. (11) is just the area of the puckered region around the large guest ion. For $Ni(OH)_2$, the Ni and Al ions occupy a triangular lattice so $\alpha = 1$ and $A_0 = 2(\sqrt{3}/4)a^2$ where $a = 3.13$ Å is the in-plane lattice constant. The inter- and intra-planar healing lengths of $Ni(OH)_2$ deduced from Eqs. (11) and (12) are compared with the inter-planar lengths of other layered solids in Table 2.

On the basis of inter-layer rigidity, graphite is much more floppy than nickel hydroxide while vermiculite is more rigid as expected from their class designations. The comparison with TiS_2 is more interesting because it, like $Ni(OH)_2$, crystallizes in the cadmium iodide (or brucite) structure. The metal chalcogen bond distances in the two compounds are 3.692 and 3.331 Å, respectively. Therefore, one would expect the Ti–S bonding in TiS_2 to be weaker than the Ni–OH bonding in $Ni(OH)_2$, which would yield a larger rigidity parameter for the latter, in agreement with observation.

Nickel hydroxide is the only layered solid for which the intra-layer rigidity parameter has been determined. Like the parameter, p, the parameter, q, will depend in a complex way on the elastic stiffness constants but, unlike the case for p, the explicit dependence of q on these constants has not yet been deduced. Moreover, the stiffness constants of $Ni(OH)_2$ have not been measured. Nevertheless, it is apparent from Table 2 that the rigidity of the $Ni(OH)_2$ layer with respect to transverse contraction caused by replacement of Ni ions by smaller Al ions is considerably less than the rigidity of the layer to externally induced puckering.

5. Conclusions

The Ni–Al layer double hydroxide carbonates constitute a novel system with which to study the transverse layer rigidity of intercalated layered solids. They offer the versatility of changing both the composition of the host layer itself as well as that of the intercalated layer which allows for the first determination of the intra-layer rigidity parameter, $q = 2.44$. While that parameter has been determined with reasonable accuracy, the inter-layer rigidity parameter, $p \sim 5$, can only be roughly estimated due to the necessity of rescaling the measured value to approximate the pillaring effect of water in the gallery. Within the limits of this rescaling approximation, the Ni–Al layer double hydroxides exhibit an interlayer rigidity which spans that associated with class II and class III layered solids. They therefore appear to represent one of the least rigid clay systems and at the same time one of the most rigid chalcogenide-like layered solids. We plan to develop a quantitative model of the composition dependence of the water/carbonate ratio in order to more accurately establish the value of p.

The layer rigidity model which we have employed here assumes a random distribution of both the intra-layer metal ions and the gallery cations. The Ni and Al adopt a lattice-gas-like arrangement on the triangular metal ion net but there is new preliminary magnetic evidence [14] and older structural evidence [7] for (subtle) non-random correlations in the Ni sites. Such correlations are clearly sufficiently short-range and mild so as to not perturb the validity of the FLR model as employed here. The random arrangement of the carbonate ions and water molecules in the gallery is best characterized as a 2D solvated liquid with a large excluded volume associated with the lateral regions where the host layers are buckled.

References

[1] S.A. Solin, J. Molec. Catal. 27 (1984) 293.

[2] S.A. Solin, in: Intercalation in Layered Materials, ed. M.S. Dresselhaus (Plenum, New York, 1986) p. 291.

[3] S.A. Solin and H. Zabel, Adv. Phys. 37 (1988) 87.

[4] R.E. Grim, Clay Mineralogy, 2nd Ed. (McGraw-Hill, New York, 1968).

[5] H. Kim, W. Jin, S. Lee, P. Zhou, T.J. Pinnavaia, S.D. Mahanti and S.A. Solin, Phys. Rev. Lett. 60 (198) 2168.

[6] S. Lee, H. Miyazaki, S.D. Mahanti and S.A. Solin, Phys. Rev. Lett. 62 (1989) 3066.

[7] H.F.W. Taylor, Mineral. Mag. 39 (1973) 377.

[8] D.L. Bish and G.W. Brindly, Am. Miner. 62 (1977) 458.

[9] G.W. Brindley and S. Kikkawa, Am. Miner. 64 (1979) 836.

[10] U.S. National Bureau of Standards Circ. 539, 6 (1956) 30.

[11] A.F. Wells, Structural Inorganic Chemistry, 5th Ed. (Clarendon, Oxford, 1993).

[12] S. Miyata, Clays Clay Miner. 28 (1980) 50.

[13] V.A. Fassel and R.N. Kniseley, Anal. Chem. 48 (1976) 611A.

[14] S.A. Solin, D. Hines, G. Seidler, S.K. Yun, T.J. Pinnavaia and M.F. Thorpe, unpublished.

[15] B.R. York, S.A. Solin, N. Wada, R.H. Raythatha, I.D. Johnson, and T.J. Pinnavaia, Solid State Commun. 54 (1985) 475.

[16] Mineral Powder Diffraction File Search Manual (International Center for Diffraction Data, Swarthmore, 1993) PDF No. 14-117, p. 674.

[17] A. Guinier, X-Ray Diffraction (Freeman, San Francisco, 1963) p. 124.

[19] See Ref. [6] and references therein.

[20] M.F. Thorpe, Phys. Rev. B39 (1989) 10370.

[21] L. Vegard, Z. Phys. 5 (1921) 17.

[22] C.D. Hodgman, ed., Handbook of Chemistry and Physics, 44th Ed. (CRC, Cleveland, OH, 1962).

JOURNAL OF
NON-CRYSTALLINE SOLIDS

Author index

Subject index